



BIROn - Birkbeck Institutional Research Online

Enabling Open Access to Birkbeck's Research Degree output

Investigating seismic activity and channel formation in Grojta Valles, Elysium Planitia, Mars

<https://eprints.bbk.ac.uk/id/eprint/54621/>

Version: Full Version

Citation: Brown, Jason Robert (2024) Investigating seismic activity and channel formation in Grojta Valles, Elysium Planitia, Mars. [Thesis] (Unpublished)

© 2020 The Author(s)

All material available through BIROn is protected by intellectual property law, including copyright law.

Any use made of the contents should comply with the relevant law.

[Deposit Guide](#)
Contact: [email](#)

**INVESTIGATING SEISMIC ACTIVITY AND CHANNEL
FORMATION IN GRJÓTÁ VALLES, ELYSIUM PLANITIA, MARS**

Jason Robert Brown

A thesis submitted for
the Degree of Doctor of Philosophy

School of Natural Sciences
Birkbeck, University of London

April 2024

(Revised — October 2024)

AUTHOR'S DECLARATION

I, Jason Robert Brown, confirm that the work presented in this thesis is my own. Where information has been derived from other sources, I confirm that this has been indicated in the thesis.

Signed:

Date: 30/04/2024

ABSTRACT

This thesis aims to provide comprehensive insights into the geological processes within Mars's northernmost Cerberus Fossae region, focusing on channel formation, boulder mobilisation, and seismic activity. By amalgamating observations from various sources, including satellite imagery and geological analyses, this study seeks to elucidate the area's structural and geomorphic evolution.

Beginning with a review of the geological background of the Cerberus Fossae and the methodology employed in this thesis, the research is divided into two main segments. The first segment investigates evidence of palaeoseismicity, seeking to determine the occurrence and timing of seismic events in the region. Utilising high-resolution imagery from NASA's Mars Reconnaissance Orbiter (MRO), boulder populations and their trails are analysed to discern patterns indicative of past seismic activity. The findings suggest the occurrence of large-magnitude paleo-marsquakes, shedding light on the area's seismic history.

The second segment focuses on the formation of channel systems within the study area. By constructing a detailed regional map and analysing satellite imagery, the study identifies and analyses channel-to-source relationships, determining the mechanisms and timing of channel formation. The results indicate episodic channel formation, with channels propagating further eastward over time, and provide insights into the potential sources of the flood events.

The discussion chapter synthesises the observations and discusses their implications in the broader context of Martian geological history. Based on the evidence gathered, the thesis concludes by formulating hypotheses regarding the Cerberus Fossae region's structural, geomorphic, and geological evolution.

Drawing upon previous publications by the first author, the thesis builds upon and extends the research presented in peer-reviewed journal articles. By delving deeper into nuanced aspects not extensively covered in the original publications, this study contributes to our understanding of Martian geology and the potential for past tectonic and hydrological activity on the planet.

TABLE OF CONTENTS

AUTHOR'S DECLARATION	2
ABSTRACT.....	3
CHAPTER 1. INTRODUCTION	15
1.1. Introduction	15
1.2. Channels and their Formation	22
1.3. Recent seismicity and palaeoseismicity of Cerberus Fossae.....	34
1.4. Aims	40
1.5. Objectives and Methodologies.....	40
1.6. Thesis Structure	42
1.7. Portions Included from or Based on First Author Publications	43
CHAPTER 2. LITERATURE REVIEW.....	44
2.1. Introduction	44
2.2. Geological History of Mars	44
2.2.1. Introduction	44
2.2.2. Pre-Noachian Epoch (4.6–4.1 Ga).....	45
2.2.3. Noachian Epoch (4.1–3.7 Ga).....	46
2.2.4. Hesperian Epoch (3.7–3.0 Ga).....	47
2.3. Water on Mars—Evolution and Evidence	49
2.3.1. Early Martian Water Discoveries	49
2.3.2. Martian Channels and Water Flow—Key Early Findings	49
2.3.3. Water Evolution on Mars: Three Mineralogical Eras.....	50
2.3.4. Modern Discoveries and Current Martian Water	50
2.3.5. Geological Features Shaped by Water and Ice	51
2.3.6. Implications for Habitability and Future Exploration.....	51
2.3.7. Conclusion.....	52
2.4. Vulcanicity	52
2.4.1. Introduction	52
2.4.2. Key Findings	52
2.4.3. Aqueous or Lava?.....	54
2.4.4. Concluding Remarks.....	55
2.5. Seismicity	56
2.5.1. Introduction	56
2.5.2. Key Findings	56
2.5.3. Concluding Remarks.....	57
2.6. Surface and Subsurface Geological Processes on Mars	57
2.6.1. Introduction	57

2.6.2. Evidence from Geological and Seismic Activity	58
2.6.3. Geological Significance of Cerberus Fossae	59
2.6.4. Concluding Remarks	59
2.7. Recent and Ongoing Activity on Mars	59
2.7.1. Introduction	59
2.7.2. Volcanism and Tectonic Activity in Elysium Planitia	59
2.7.3. Seismic Activity Detected by InSight	60
2.7.4. Impact Cratering and Martian Subsurface Probing	60
2.7.5. Evidence of Water Activity	60
2.7.6. Cerberus Fossae: A Key Region for Understanding Recent Geological Activity	61
2.7.7. Mars' Geological History and Its Broader Implications	61
2.7.8. Conclusion	61
CHAPTER 3. METHODS	63
3.1. Introduction	63
3.2. Identifying Boulder Trails and Fallen Boulders—High-Resolution Imaging Science Experiment (HiRISE) Images	64
3.2.1. Measuring Features Identified in HiRISE Images Using Google Earth	70
3.2.2. Potential Problems and Alternative Software Options	71
3.2.3. Measurements, Data Collection, and Analysis	72
3.2.3.1. Boulder Trails Measurement	72
3.2.3.2. Boulder Trail Width Measurement	74
3.2.3.3. Measuring Throw Across the Graben	76
3.2.3.4. Methods Used to Substantiate the Hypothesis	77
3.2.4. Identifying Outflow Channels in Grjótá Valles—Context Camera (CTX) and High-Resolution Imaging Science Experiment (HiRISE) with Mars Orbiter Laser Altimetre (MOLA) Point Data	77
3.2.5. Construction of a Regional Map and Location Maps and Cross- Sectional Profiles using CTX, HiRISE, and MOLA PEDR Data	81
3.3. FiSH Code	85
3.3.1. Introduction	85
3.3.2. What Is FiSH Code?	86
3.3.3. FiSH Code Relevancy and Usage in the Chapter 4 Research— Seismicity	86
3.3.4. FiSH Code Relevancy and Usage in the Chapter 5 Research— Dike Propagation	91
3.4. Concluding Remarks	92
CHAPTER 4. POSSIBLE EVIDENCE FOR VARIATION IN MAGNITUDE FOR MARSQUAKES FROM FALLEN BOULDER POPULATIONS, GRJÓTÁ VALLES, MARS	93

4.1. Introduction	93
4.2. Background	97
4.2.1. Cerberus Fossae	97
4.2.2. Cerberus Fossae—Recent seismic activity and natural seismometers	103
4.3. Method	112
4.3.1. Identifying, counting, and measuring boulder trails.....	114
4.3.1.1. Results	119
4.3.1.2. Discussion.....	124
4.3.2. Release of boulders by melting ice	125
4.3.3. Effect of local differences in lithology and weathering/erosion.....	125
4.3.4. Higher cliffs supply more boulders	129
4.3.5. Boulder mobilisation caused by nearby impacts.....	132
4.3.6. The relevance of boulder track density.....	134
4.3.7. Variation in the incidence angle of the images	135
4.3.8. Multiple single rockfalls	135
4.3.9. Inaccurate statistical treatment of boulder trail anomalies	138
4.3.10. Mobilisation of boulders due to seismic shaking.....	139
4.3.11. Comparison of mobilised boulder populations from different graben within the Cerberus Fossae	141
4.4. Conclusions.....	148
CHAPTER 5. OUTFLOW CHANNELS IN GRJÓTÁ VALLES. EVIDENCE FOR REPEATED, CROSS-CUTTING AND SPATIALLY MIGRATING OUTFLOW CHANNEL FORMATION.....	150
5.1. Introduction	150
5.2. Background.....	151
5.2.1. Grjótá Valles outflow channel system.....	151
5.2.2. Outflow channels in Cerberus—what formed them?	154
5.2.3. Aqueous origin.....	155
5.2.4. Lava origin	157
5.3. Methods	158
5.4. Results	163
5.4.1. Location 1 (Fig. 5.4)	163
5.4.1.1. Descriptions of landforms at Location 1	165
5.4.1.2. Interpretation of five geomorphic landforms at Location 1.....	167
5.4.1.3. Summary.....	169
5.4.1.4. Observations of the relative chronology of geomorphic features.....	169
5.4.1.5. Interpretation of the relative chronology of geomorphic features.....	170

5.4.1.6. Channel sources	170
5.4.1.7. Summary	172
5.4.2. Location 2 (Fig. 5.6)	173
5.4.3. Location 3 (Fig. 5.7)	175
5.4.4. Location 4 (Fig. 5.8)	176
5.4.5. Location 5 (Fig. 5.9)	178
5.4.6. Location 6 (Fig. 5.10)	180
5.4.7. Location 7 (Fig. 5.11)	183
5.4.8. Outlying Supplementary Locations A through D (Fig 5. SL A through Fig 5. SL D)	186
5.4.8.1. Supplementary Location A (Fig 5.12 SLA)	186
5.4.8.2. Supplementary Location B (Fig. 5.13 SL B)	187
5.4.8.3. Supplementary Location C (Fig 5.14 SL C)	189
5.4.8.4. Supplementary Location D (Fig 5.15 SL D)	190
5.4.9. Construction of the regional map and channel profiles	192
5.5. Discussion	194
5.6. Conclusion	198
CHAPTER 6. DISCUSSION	200
6.1. Introduction	200
6.2. Key findings	202
6.2.1. Using fallen boulder trail populations in the fault system of the northernmost Cerberus Fossae as a proxy seismograph	202
6.2.2. Geomorphology of Outflow Channels in the Area of the Northernmost Cerberus Fossae, Grjótá Valles Suggests Multiple Flow Episodes	205
6.3. Approach and methodology	206
6.3.1. FiSH Code—frequency–magnitude curve and seismicity estimates	206
6.3.2. Parameter Selection and Justification for FiSH Code Modelling of Cerberus Fossae	207
6.3.2.1. Introduction	207
6.3.2.2. Shear Modulus of the Martian Crust	207
6.3.2.3. Slip Rate and Seismic Moment	208
6.3.2.4. Recurrence Time (Tmean)	208
6.3.2.5. Conclusion	209
6.4. Results	209
6.4.1. Magnitude of completeness	209
6.4.2. FiSH Code Results: Frequency–magnitude curve and seismicity estimates	211
6.4.3. FiSH Code: Slip rates and dike propagation	214
6.5. Conclusion	218

6.6. Future work	219
6.6.1. Extended seismicity record and improved seismograph sensitivity	219
6.6.2. Enhanced crater counting for accurate age determination	219
6.6.3. Importance of future work	220
6.6.4. Summary	220
LIST OF REFERENCES.....	221
APPENDICES	247
Appendix A. The Mars Global Surveyor’s Mars Orbiter Laser Altimeter (MOLA) Precision Experiment.....	247
Appendix B. Boulder trail length and width data.....	248
Appendix C. Brown, J. R., and Roberts, G. P. (2019). Possible evidence for variation in magnitude for marsquakes from fallen boulder populations, Grjota Valles, Mars. Journal of Geophysical Research: Planets.....	250
Appendix D. Brown, J. R., and Roberts, G. P. (2023). Repeated, cross- cutting and spatially migrating outflow channel formation, Grjótá Valles, Mars.....	272

LIST OF FIGURES

Figure 1.1. Cerberus location map (NASA/JPL-Caltech/ASU).....	19
Figure 1.2. (a) Location map of the Northernmost Cerberus Fossae.....	20
Figure 1.3. (a) Location map of the northernmost Cerberus Fossae.	21
Figure 1.4. a. Location map THEMIS Day IR with colourised MOLA elevation 100 metre/pixel Global Mosaic version 13.4.....	23
Figure 1.5. a. Location map. THEMIS Day IR 100 metre/pixel Global Mosaic version 13.4. of the Southern Cerberus Fossae, and the lateral extent of the Athabasca Valles flow channel	24
Figure 1.6. a. Location map. THEMIS Day IR 100 metre/pixel Global Mosaic version 13.4. of the Southern Cerberus Fossae and a section of the Athabasca Valles	25
Figure 1.7. a. Location map THEMIS Day IR with colourised MOLA elevation 100 metre/pixel Global Mosaic version 13.4 of the Cerberus plains	27
Figure 1.8. Figures a and b. Seam-corrected and seam-mapped mosaic of Mars rendered at 5.0 m/px using Context Camera (CTX) data from the Mars Reconnaissance Orbiter	29
Figure 1.9. Figures a, b and c. Seam-corrected and seam-mapped mosaic of Mars rendered at 5.0 m/px using Context Camera (CTX) data from the Mars Reconnaissance Orbiter	38
Figure 3.1. a. and b. Location map for the northernmost Cerberus Fossae c. The exact position of the HiRISE footprints (orange rectangles) along the northernmost Cerberus Fossae (red).	65
Figure 3.2. a. Seam-corrected and seam-mapped mosaic of Mars rendered at 5.0 m/px using Context Camera (CTX) data from the Mars Reconnaissance Orbiter	67
Figure 3.3. Three images of full-resolution HiRISE stamp.....	69
Figure 3.4. An example of a boulder trail density measurement.....	73
Figure 3.5. Boulder trail lengths and widths were counted and re-counted by the authors Brown, J. R., and Roberts, G. P. (2019).	75
Figure 3.6. a–b Regional Map (centred at 15.25° N, 162.85° E) of the study area	78
Figure 3.7. a–b. CTX image mosaic detail of a section from Location 1 from the study of flow channels in Grjótá Valles.....	80
Figure 3.8. Regional Map (centred at 15.25° N, 162.85° E) of the study area marking the source areas of the five flows and the extent of each flow.	82
Figure 3.9. Maps and topographic profiles of Location 1 centred at 15.70° N, 161.61°E showing details of channels and cross-cutting relationships.....	84
Figure 3.10. Idealised frequency–magnitude graph showing the earthquake/marsquake magnitude bin sizes on the x-axis, with magnitude increasing to the right. The y-axis measures log frequency.....	87
Figure 3.11. A logarithmic plot illustrating seismic event data, specifically Marsquakes, based on findings from Ceylan et al. (2002).....	87

Figure 3.12. Truncated Gutenberg–Richter (GR) frequency–magnitude graph produced using FiSH code in MATLAB (v.R2011B) to create a frequency–magnitude curve of seismic events annually against moment magnitude.	88
Figure 3.13. a–f: Truncated Gutenberg–Richter (GR) frequency–magnitude graphs produced using FiSH code in MATLAB (v.R2011B) to create frequency–magnitude curves of seismic events annually against moment magnitude.....	90
Figure 3.14. Illustration to show how crater counting provides an age control to allow for estimates of surface processes such as dike/graben propagation and channel source migration.....	92
Figure 4.1. Hypotheses to explain the characteristics of the widest examples of boulder trails formed by the mobilised boulder populations due to seismic shaking and boulders' release from cliffs by ice melting.....	95
Figure 4.2. Location maps.	96
Figure 4.3. (a to d): Geological and geomorphological interpretations of Images 1, 3, 9 and 12, taken from HiRISE images.....	99
Figure 4.4. The relationship between the map trace of the graben and vertical offsets constrained by Mars Orbiter Laser Altimeter (MOLA) data.	101
Figure 4.5a. (a): (i) Location map of the area - Seam-corrected and seam-mapped mosaic of Mars rendered at 5.0 m/px using Context Camera (CTX) data from the Mars Reconnaissance Orbiter.....	108
Figure 4.6. Example of a boulder trail density measurement for two images: (a) Image 4 (HiRISE Image ESP_025011_1965) and (b) Image 8 (HiRISE Image ESP_026712_1960).	115
Figure 4.7. (a) Plot showing absolute elevation values for the plain to the south of the graben, the plain north of the graben, and the floor of the graben versus longitude. (b) Graph of longitude versus boulder trails per kilometre. (c) Graph of longitude versus boulder trail widths. (d) The location of the graben is associated with the two sets of boulder populations.....	117
Figure 4.8. Boulder trail lengths and widths were counted and re-counted along Boulder Trail Anomaly 1 and Boulder Trail Anomaly 2.	118
Figure 4.9. b. Location map of the northernmost Cerberus Fossae with Boulder Trail Anomalies 1 and 2 marked.	120
Figure 4.10. (a) Seam-corrected and seam-mapped mosaic of Mars rendered at 5.0 m/px using Context Camera (CTX) data from the Mars Reconnaissance Orbiter (MRO) showing the location of the northernmost Cerberus Fossae.	122
Figure 4.11. CRISM data, although having limited lateral extent and hence availability, showed no noticeable change in lithology of the rocks forming the walls to graben concerning oxidised iron minerals, mafic mineralogy, hydroxylated silicates, bound water or water ice, <i>and CO₂ ice</i>	127
Figure 4.12. NASA Mars Odyssey spacecraft imagery of the northernmost Cerberus Fossae in (a) daytime infrared and (b) night-time infrared (NASA/JPL/Arizona State University).....	128
Figure 4.13. Seam-corrected and seam-mapped mosaic of Mars rendered at 5.0 m/px using Context Camera (CTX) data from the Mars Reconnaissance Orbiter (MRO) showing a section of the northernmost Cerberus Fossae.	130
Figure 4.14. The geological setting and modes of ground acceleration for mobilised boulders.....	131

Figure 4.15. a) Detail from HiRISE image (ESP_055845_1955_RED) of part of the northernmost Cerberus Fossae and an area to the south of the northernmost Cerberus Fossae that contains three dark-coloured impact craters (b). (c) A close-up of one of the three craters.	133
Figure 4.16. Solar incidence data show little variation along the strike of the graben.	135
Figure 4.17. Mars Orbiter Camera (MOC) image MOC2-1222b of boulder trails within a south mid-latitude crater	136
Figure 4.18. An example of a mobilised boulder from Iceland with coarse-grained talus and no raised levees, in contrast to the examples in Figure 4.5 (d).	137
Figure 4.19. (a) and (b) are InSAR data showing the 24th August Mw 6.2 earthquake in central Italy jumping across an area where no surface faulting was reported in the earthquake or on geological maps recording longer-term deformation.	140
Figure 4.20. Compares the data from the northernmost Cerberus Fossae with similar data from work on the Southern Cerberus Fossae.	142
Figure 4.21. Two graphs that compare: (a) the ten widest boulder trails (m) against boulder trails per km of the Southern Cerberus Fossae (purple) with the two sections of the northernmost Cerberus Fossae, Boulder Trail Anomaly 1 (red) and Boulder Trail Anomaly 2 (green), and; (b) maximum boulder trails per km against the length of boulder trail anomaly (km) of the Southern Cerberus Fossae (purple) with the two sections of the northernmost Cerberus Fossae, Boulder Trail Anomaly 1 (red) and Boulder Trail Anomaly 2 (green).	146
Figure 4.22. Position of the three most prominent signals detected by the InSIGHT seismometer (S0183a, S0235b, and S0173A—marked as orange ellipses) in relation to the northernmost Cerberus Fossae, which is equidistant between S0183a and S0235b, and the larger Northern and Southern Cerberus Fossae, to the south of the northernmost Cerberus Fossae.	147
Figure 5.1. a. Regional location map of the study area	152
Figure 5.2. Regional Map (centred at 15.25° N, 162.85° E) of the study area marking the source areas of the five flows and the extent of each flow.	159
Figure 5.3. Schematic summary of cross-cutting relationships between channels.	160
Figure 5.4. Maps and topographic profiles of Location 1 centred at 15.70° N, 161.61°E showing details of channels and cross-cutting relationships	164
Figure 5.5. Panels a. through j. show the approximate location of the source area for each flow	171
Figure 5.6. Maps and topographic profiles of Location 2 centred at 15.60° N, 162.07° E showing details of channels and cross-cutting relationships	173
Figure 5.7. Maps and topographic profiles of Location 3 centred at 15.58° N, 162.37° E showing details of channels and cross-cutting relationships	175
Figure 5.8. Maps and topographic profiles of Location 4 centred at 15.60° N, 162.75° E showing details of channels and cross-cutting relationships	177
Figure 5.9. Maps and topographic profiles of Location 5 centred at 15.13° N, 163.21° E showing details of channels and cross-cutting relationships	179
Figure 5.10. Maps and topographic profiles of Location 6 centred at 15.60° N, 163.30° E showing details of channels and cross-cutting relationships	181

Figure 5.11. Maps and topographic profiles of Location 7 centred at 15.46° N, 163.28° E showing details of channels and cross-cutting relationships.....	184
Figure 5.12. <i>SL A</i> :Supplementary Location A (centred at 16.15° N, 162.90° E) and topographic profiles.....	187
Figure 5.13. Supplementary Location A (centred at 16.15° N, 162.90° E) and topographic profiles.	188
Figure 5.14. <i>SL C</i> : Supplementary Location A (centred at 16.15° N, 162.90° E) and topographic profiles.....	190
Figure 5.15. <i>SL D</i> : Supplementary Location A (centred at 16.15° N, 162.90° E) and topographic profiles.....	192
Figure 5.16. Shows the base elevations of identified flow channels in Locations 1 through 7	193
Figure 6.1. a, b, c, and d: Comparison of data from the Northernmost Cerberus Fossae.....	204
Figure 6.2. The graph displays a logarithmic plot with the cumulative count of events on the y-axis and decreasing magnitude on the x-axis after data from Ceylan et al. (2002).	210
Figure 6.3. Truncated Gutenberg–Richter (GR) frequency–magnitude graph produced using FiSH code in MATLAB (v.R2011B) to create a frequency–magnitude curve of seismic events annually against moment magnitude.	211
Figure 6.4. a–f: Truncated Gutenberg–Richter (GR) frequency–magnitude graphs produced using FiSH code in MATLAB (v.R2011B) to create frequency–magnitude curves of seismic events annually against moment magnitude.....	213
Figure 6.5. The extent of the Grjótá Valles flow tract.....	216

LIST OF TABLES

Table 3.1. Shows the HiRISE images used in the research, the number assigned to each number by the author, and the latitude and longitude together with the map projected scale.....	66
Table 4.1. HiRISE images used in the study of the northernmost Cerberus Fossae.....	113
Table 6.1. A summary of the parameters used in the FiSH code for this analysis.	209
Table 6.2. A summary of dike propagation and fault opening rates for Flows 1, 3, 4, and 5.....	217

ACKNOWLEDGEMENTS

I would like to express my sincere gratitude to several individuals who have played a pivotal role in the completion of this thesis. Firstly, I extend my heartfelt thanks to Gerald Roberts, whose guidance, expertise, and unwavering support have been invaluable throughout this journey. His mentorship has profoundly shaped my academic and research endeavours. I am deeply grateful to Gerald for his continuous support and encouragement, which served as a source of inspiration and motivation during challenging times. Gerald's belief in my abilities has driven me towards excellence.

Special appreciation goes to Keith Aleandri for his unwavering support and moral assistance throughout this endeavour. His encouragement and guidance have been immensely valuable in helping me navigate through the complexities of research and academia.

Finally, I would like to extend my heartfelt gratitude to my wife, Elena, and daughter, Milla, for their unwavering encouragement and emotional support. Their patience and understanding have been the cornerstone of my success, and I am profoundly grateful to them both for their support.

To all those mentioned above and to countless others who have contributed in various ways, I extend my heartfelt thanks. Your support has been indispensable, and I am deeply appreciative of your role in shaping this academic achievement. Thank you all.

CHAPTER 1.

INTRODUCTION

1.1. Introduction

The Cerberus Fossae are a set of linear graben that trend northwest to southeast on the Cerberus plains and vary in length, depth and width. The Cerberus Fossae are of great interest because recent research has shown that seismicity is ongoing within this region (Horvath et al., 2021). Studies of the areas surrounding the fossae reveal channels shaped by lava and aqueous flow and possibly a mix of both (Plescia, 2003). Research on the northernmost Cerberus Fossae, the least studied of the fossae, and the channels that have formed in the vicinity of the northernmost Cerberus Fossae sets out to establish whether the northernmost Cerberus Fossae is still seismically active, what are the possible causes of this seismicity, what formed the channels around the northernmost Cerberus Fossae, and to discern whether these channels were formed in one-off events or where there series of events over time (Kedar et al., 2022). Should the region remain seismically active, potentially owing to subsurface igneous activity, and ongoing flow events—whether lava or aqueous—persist, and if liquid water exists on Mars, such findings would hold immense significance. The presence of liquid water on Mars offers hope for finding extra-terrestrial life (Carr & Head, 2009).

The Cerberus Fossae, southeast of Elysium Mons, lie on the Cerberus plains, the youngest large-scale region on the Martian surface, dated to Late Amazonian (1 Gyr to present) (Tanaka, 1986, Tanaka et al., 1992; Greeley et al., 1987; Plescia, 1990, 2003) (Figure 1.1 a and b). The Cerberus plains contain various geological features, including lava formations, outflow channels, and fractures known as the Cerberus Fossae. These depressions are long, linear, narrow, highly segmented, and run in echelon formation. The trend of all the fossae is in a northwest-to-southeast direction. The Northern and Southern Cerberus Fossae (Fig 1 b) have been extensively studied (Burr et al., 2002; Plescia, 2003); the northernmost Cerberus Fossae (Fig 1 c) is much less so. Hall et al. (1986) demonstrated that the stress field induced by the Tharsis rise, an enormous volcanic plateau in the western hemisphere of Mars, could contribute to the formation of the fossae through a flexural loading model. It is believed that the fossae were formed in a regional extensional stress setting due to either pure graben faulting (Vetterlein and Roberts, 2010) or fracturing processes above growing dike(s) at depth (e.g., Berman and Hartmann, 2002; Burr et al., 2002; Head et al., 2003; Nahm et al., 2015, 2016; Plescia, 1990) as observed on Earth (e.g., Gudmundsson, 1984;

Hjartardóttir et al., 2016; Magee and Jackson, 2021; Mouginis-Mark et al., 2007; Rubin, 1992; Rubin and Pollard, 1988; Tentler, 2005). Numerous studies have also noted the local influence of the combined effect of dike intrusion and subsurface cryospheric melting, which may have led to large lava flows and catastrophic flows of meltwater at the surface of Mars that subsequently shaped the surrounding plains of the near-fossae regions (e.g., Burr et al., 2002; Cassanelli and Head, 2018; Nahm et al., 2015, 2016; Pendleton, 2015; Plescia, 2003;).

Work by Perrin et al. (2022) on parts of the Cerberus Fossae, namely the Northern and Southern Cerberus Fossae (Fig 1 b), revealed a range of morphological features associated with dike activity at depth. The team observed that the widths and throws of the fossae decrease towards the east, indicating the long-term direction of propagation of the dike-induced graben system. The connection between the width of the fossa and the distance of the throw indicates that the formation of fossae is primarily due to volcanic–tectonic processes. The fossae would most likely have been formed by the propagation of dikes at depth, a possible consequence of the rise of Elysium Mons, located northwest of the fossae.

Dike intrusions, a plausible cause of the surface fractures/graben, and a possible heat source that melted frozen water to release flows within this region emanated from a sub-surface volcanic source that underlay the region (Genova et al., 2016; Golder et al., 2020). Other authors have suggested the remnants of a sea or lake of ice (Balme et al., 2008; Murray et al., 2005; Sakimoto, 2006; Xiong et al., 2021). Dundas et al. (2018, 2021) and Harish et al. (2020) confirmed exposed shallow subsurface water ice on Mars, although these observations are limited to mid- and high-latitudes of Mars. Work by Alberti et al. (2012) considered the subsurface material of the Cerberus plains, with results suggesting high porosity underlying material in this region. Work by Morgan et al. (2015) revealed an extensive layer of sediments, possibly mixed with lava, to the south of Cerberus Fossae. Meng et al. (2020) reported an approximately 40 m thick lava layer over possible water–ice deposits in the area west of Elysium Mons. Xiong et al. (2021) studied the shallow subsurface of the central Cerberus plains and estimated a permittivity value of 3.12, suggesting that the region holds shallow subsurface water ice. However, dry, low-density materials could also be present (Watters et al., 2007).

Taylor et al. (2013) have inferred that Cerberus Fossae might be an active tectonic structure capable of releasing a seismic moment ranging from 10^{15} to 10^{17} Nm yr⁻¹. These studies associated this relatively recent tectonic activity (i.e., less than 10 million

years old) with evidence of volcanic activity, specifically young lava flows, as indicated by Vaucher et al. (2009). Furthermore, Horvath et al. (2021) identified a pyroclastic volcanic deposit in the central region of the fossae, which is estimated to be less than 250,000 years old, thereby supporting the notion that geological activity persists in the present time. Since 2019, the InSight mission has confirmed multiple seismic events, referred to as marsquakes, with magnitudes around $M_w \sim 2-3$ originating in the vicinity of Cerberus Fossae (Giardini et al., 2020). These findings align with pre-mission estimations by Böse et al. (2017), Panning et al. (2017), and Brown and Roberts (2019). However, it is believed that these marsquakes, despite their moderate magnitudes, are unlikely to trigger surface ruptures. Roberts et al. (2012) and Brown and Roberts (2019) conducted studies on paleo-marsquakes that occurred along the Southern Cerberus Fossae and northernmost Cerberus Fossae, respectively, by analysing along-strike distributions of boulders triggered by ground shaking. Brown and Roberts (2019) studied paleo-marsquakes along the northernmost Cerberus Fossae. Both research papers concluded that each area was seismically active in the very recent past. Through observations of the positions of mobilised boulders within the fossae, both teams noted a signature or pattern unique to boulders mobilised by seismicity (Keefer, 1984; Roberts et al., 2011; Brown and Roberts, 2019).

Insights into the processes that have shaped this enigmatic region of Mars and what lies beneath the Cerberus Fossae will help us to expand our understanding of subsurface and surface processes that have shaped this region of Mars and potentially other rocky planets and moons in our Solar System. One approach to gaining new knowledge is to study locations in this region that appear to have had recent activity.

The work in this thesis looks at the evidence for two disparate yet potentially connected topics: recent seismicity along the northernmost Cerberus Fossae and channel-forming flow episodes in the Amazonian (Middle Amazonian epoch) emanating from the northernmost Cerberus Fossae and flowing northeast, east and southeast. The connection between the topics lies with the region's proximity to Elysium Mons and the smaller Albor Tholus volcanoes, and the possible ongoing subsurface volcanic activity of these volcanic regions. As Berman and Hartmann (2002) point out, "... an intimate sequential intermixing of fluvial, volcanic, and tectonic activity" exists within the Cerberus plains. Perrin et al. (2022) studied the northernmost Cerberus Fossae and noted that the fissures become smaller in size further east. In their examination of both the Northern and Southern Cerberus Fossae, the team noted that the widths and vertical throws diminish from west to east change. They proposed that igneous activity below Elysium Mons is responsible for generating the melts and

driving the regional tectonics that resulted in dike development and stress propagation extending southeastward. Perrin et al. suggest that sub-surface dikes may be active and move radially from the volcanic region to the southeast, as evidenced by the radial fractures that run northwest to southeast. These dikes may have formed the surface faults, fissures, and graben, and observed seismicity in this area could be due to dike movements. Furthermore, the team linked flow episodes to dike movement, with dikes melting ice that precipitates the flow episodes. The fact that the younger flow episodes are found further southeast suggests that the dikes continually move in this direction.

In this thesis, results are reported that the area of the northernmost Cerberus Fossae and part of the Grjótá Valles channel system were areas where paleoseismic events and several channel flow episodes occurred prior to the formation of the surface manifestations of the faults responsible for the palaeoseismicity. The hypotheses formed in this thesis are that the seismicity now proven by others since the initiation of this PhD work may be linked to both the palaeoseismicity and channel-forming episodes. The thesis develops a model of how these processes are linked and interact, giving new insights into processes on rocky planets that complement what we know from studies of terrestrial geology.

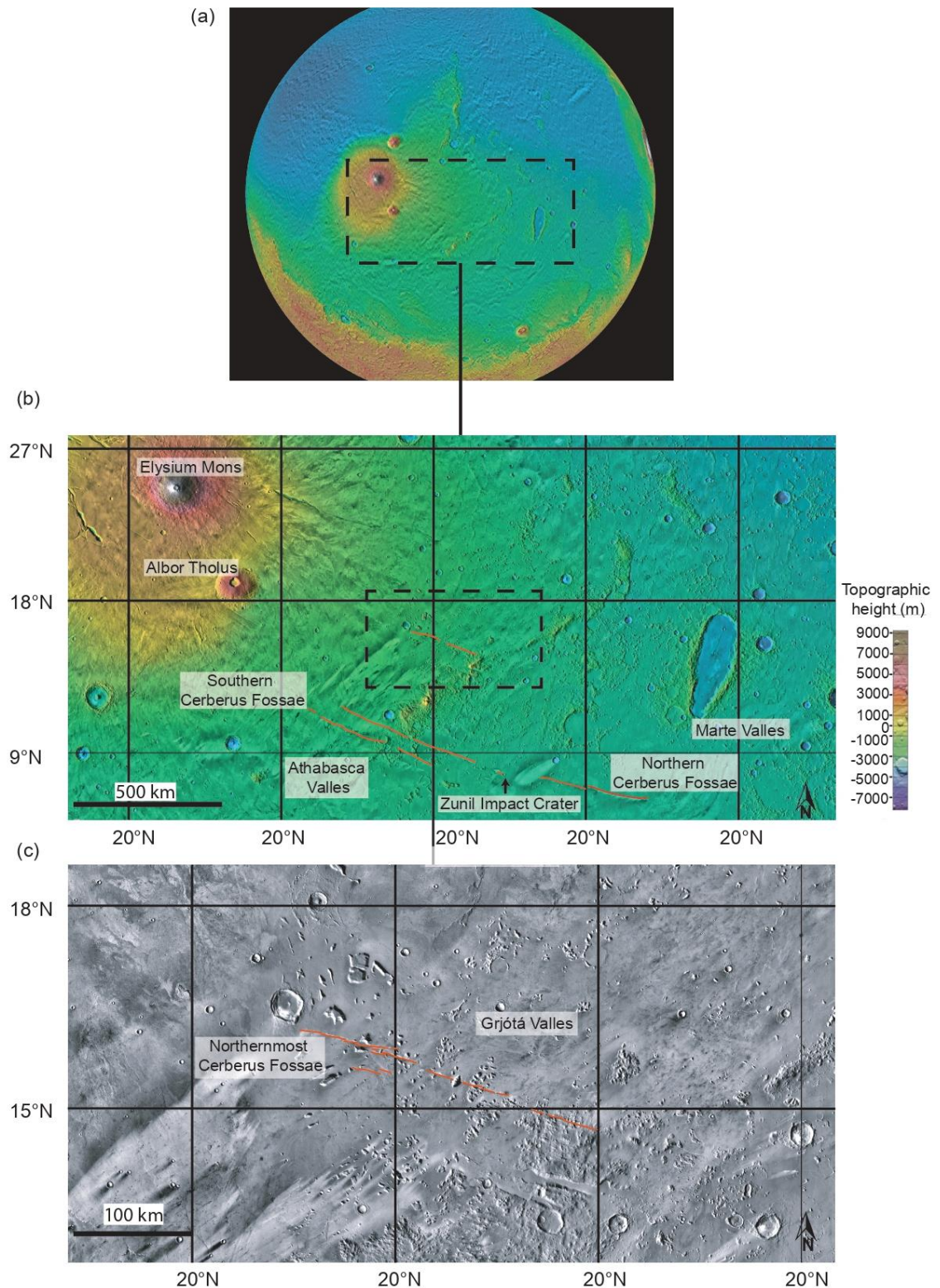


Figure 1.1. Cerberus location map (NASA/JPL-Caltech/ASU). (a) MOLA image of Mars showing the location of the study area. (b) THEMIS Day IR with coloured MOLA elevation 100 metre/pixel Global Mosaic version 13.4. A dashed box marks the study area. Note that the Northernmost Cerberus Fossae in the box is marked with red lines. Other key features in the area are named, namely the Northern and Southern Cerberus Fossae, marked by red lines. (NASA/JPL-Caltech/ASU). (c) THEMIS Day IR 100 metre/pixel global mosaic version 13.4. The study area of the Northernmost Cerberus Fossae, marked by red lines, with the Grjóta Valles channel system to the northeast of the fossae. (NASA/JPL-Caltech/ASU).

The Cerberus Fossae region of Mars (6–16N° and 154–174E°) (Figure 1.1 b and c) is located southeast of Elysium Mons, part of the Elysium volcanic complex. The region has numerous sets of segmented fractures (Figure 1.1 b). The four main fossae trend southeast away from the Elysium volcanic complex, with the northernmost Cerberus Fossae trending southeast from Albor Tholus, a 150 km across and 4 km high volcano within the Elysium volcanic complex (Carr, 2007). The four major fractures cross-cut most other features, such as impact craters and channel landforms (Figure 1.2 and Figure 1.3).

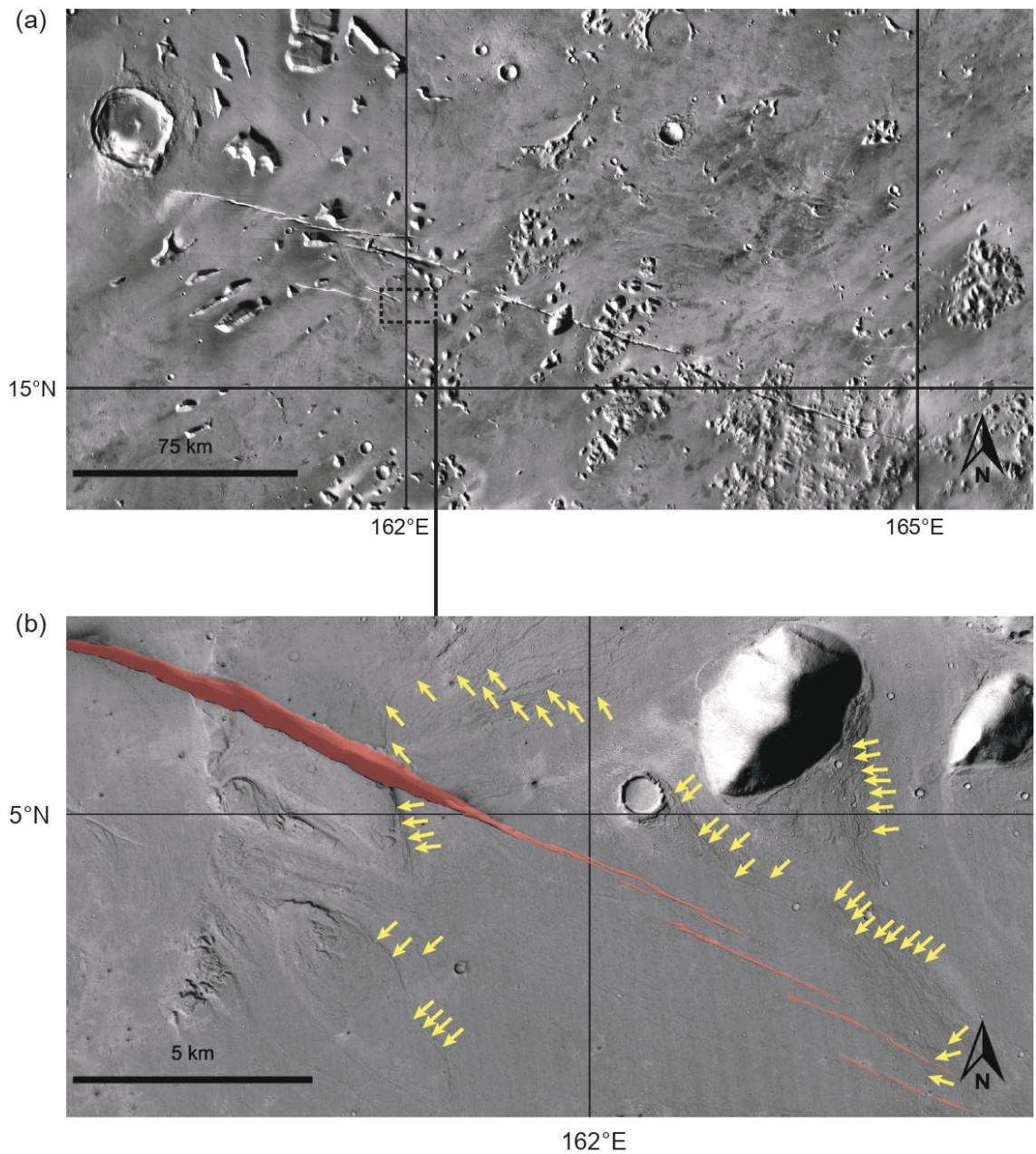


Figure 1.2. (a) Location map of the Northernmost Cerberus Fossae. THEMIS Day IR 100 metre/pixel Global Mosaic version 13.4. The dashed-line box identifies Figure 1.2 (b). (b) Seam-corrected and seam-mapped mosaic of Mars rendered at 5.0 m/px using Context Camera

(CTX) data from the Mars Reconnaissance Orbiter (MRO), centred at 15.489°N 161.985°E (CTX product ID: DIO_O31169_1958_XN_15N198W). The section shows parts of the Northernmost Cerberus Fossae coloured red, with the newer, smaller segments of the possibly still forming fossae to the lower-right of the image. The fossae cross-cut two channel features (the upper-left portion of the image where the large fossae cross-cut recessional terraces, and the lower-right of the image where the younger fossae have begun to cross-cut the terrace marks). Yellow arrows mark the terrace markings from the flow events. Not all terrace markings have been highlighted, only the key ones. The impact crater in the near centre of the image has flow marks around it, indicating the flow direction (to the southeast) and that the flow occurred after the impact crater was formed. (NASA/JPL-Caltech/ASU).

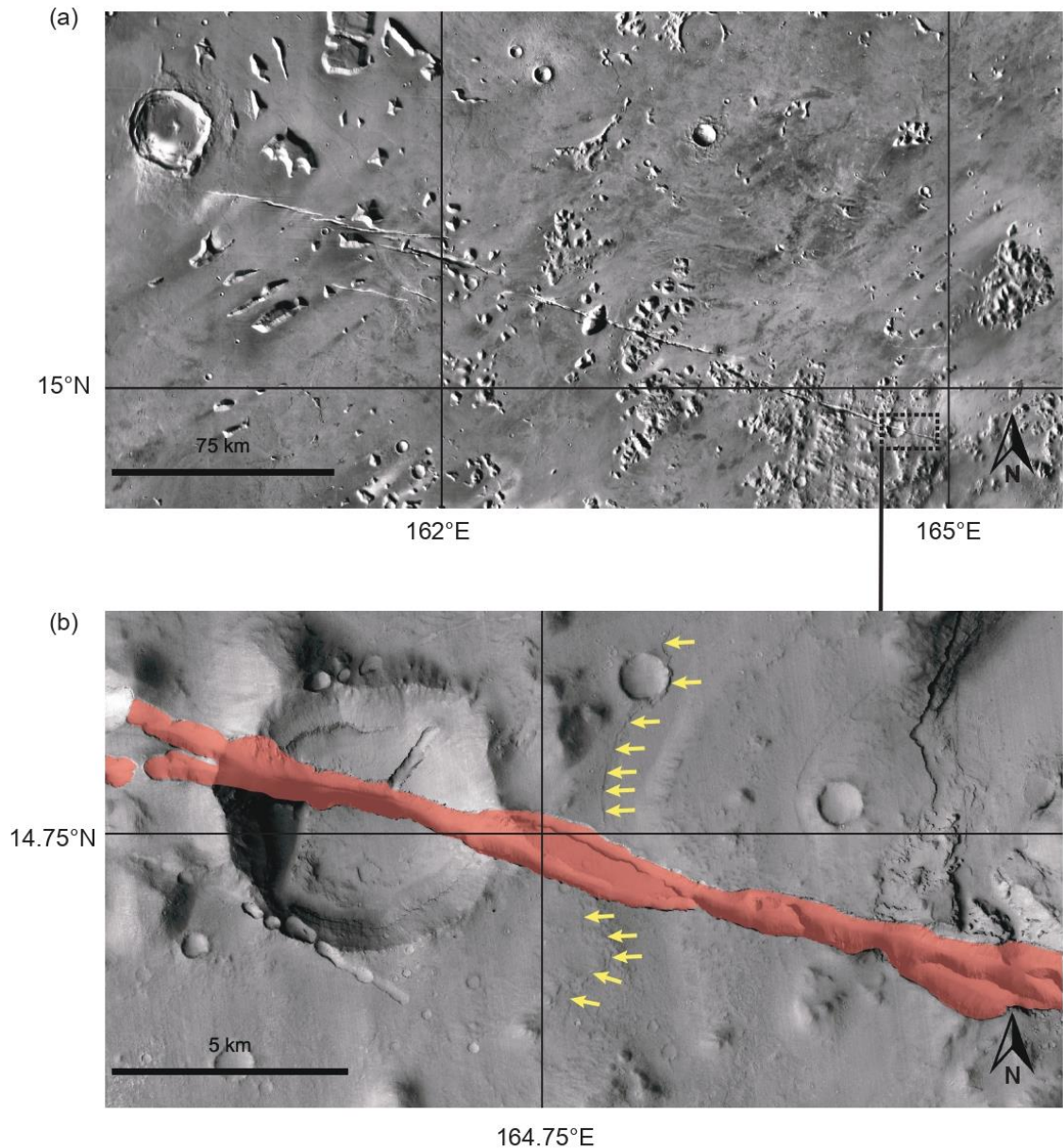


Figure 1.3. (a) Location map of the northernmost Cerberus Fossae. THEMIS Day IR 100 metre/pixel Global Mosaic version 13.4. The dashed-line box identifies Figure 1.2 (b). (b) Seam-corrected and seam-mapped mosaic of Mars rendered at 5.0 m/px using Context Camera (CTX) data from the Mars Reconnaissance Orbiter (MRO), centred at 14.743°N 164.765°E. The section shows part of the far eastern segment of the Northernmost Cerberus Fossae, coloured red, that has cross-cut a large impact crater, and a flow channel, the recessional terraces of which are marked by yellow arrows. (NASA/JPL-Caltech/ASU).

1.2. Channels and their Formation

Athabasca Valles is a major channel system that extends approximately 300 km to the southwest of the primary Cerberus Fossae fissures and appears to emanate from the location of the fissures (Figures 1.4 a and b). The outflow channels themselves were most probably carved by aqueous floods (rather than lava) (Burr et al., 2002), but the channel was later covered in flood lava, including its banks (Jaeger et al., 2007). The channel is considered to be one of the youngest outflow channel systems on Mars (Tanaka et al., 1986; Burr et al., 2002; McEwen et al., 2005) because the absence of large impact craters on the surface of Athabasca Valles indicates that the flood lava is very young. Smaller craters (approximately less than 125 m in diameter) are visible, and counts of craters on striated portions of the western channel floor, representing the fluvially eroded floor, according to Burr and McEwen (2002), give an age of 20 million years. Counts on the central part of the floor give a younger age (Berman and Hartmann, 2002). Later studies produced an estimated age of between 3 and 7 million years (Murray et al., 2005). The Zunil impact crater, located at the midway point between two segments of the Northern Cerberus Fossae (Figure 1.1. b), is a 10 km diameter impact crater. The secondaries of the Zunil impact suggest that the lava was emplaced prior to the impact, with the impact thought to be 500 ka in age (Kreslavsky, 2008).

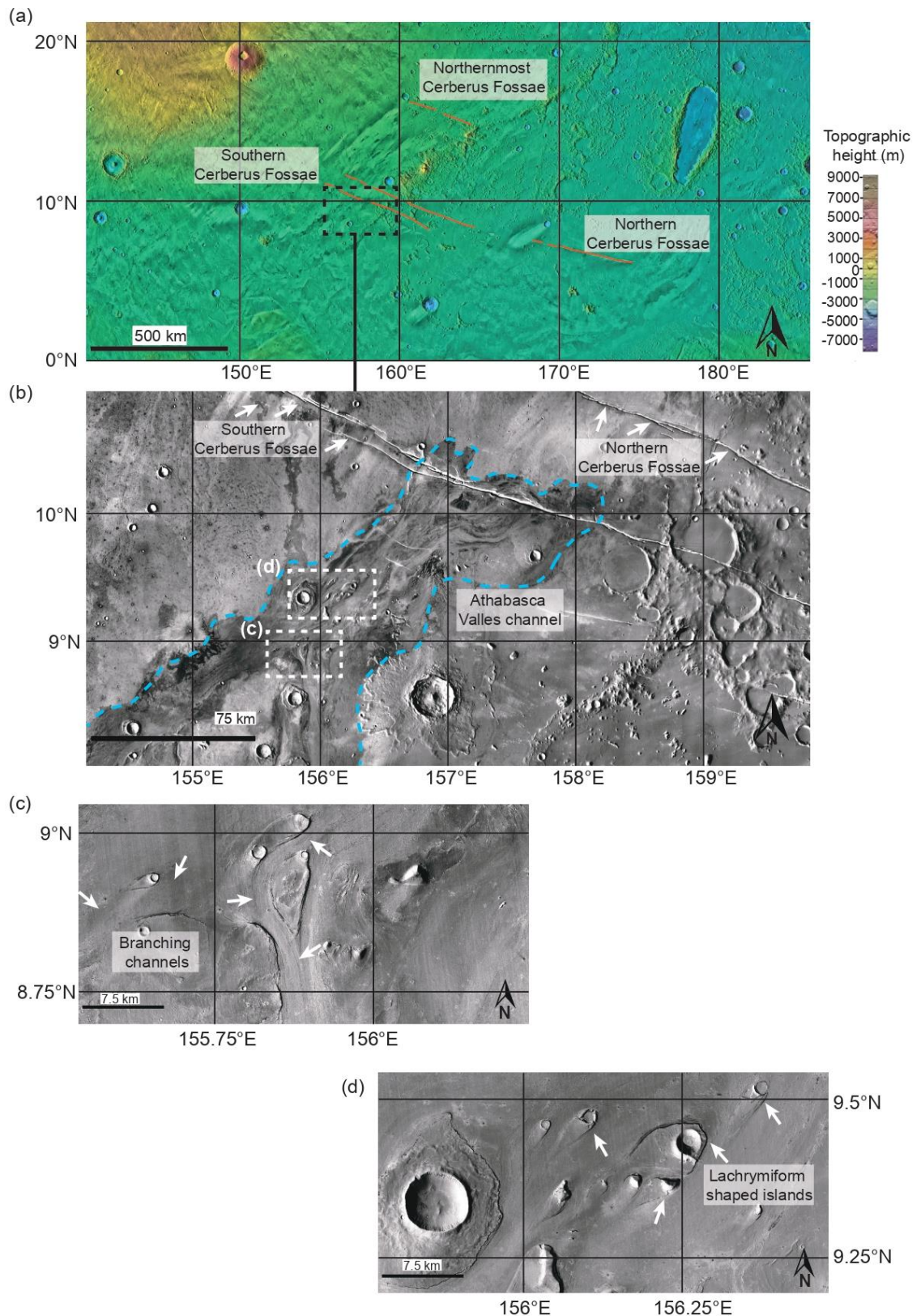


Figure 1.4. a. Location map THEMIS Day IR with coloured MOLA elevation 100 metre/pixel Global Mosaic version 13.4. A dashed box marks the approximate emanation area for flows that created the Athabasca Valles channel. Red lines mark the Northernmost Cerberus Fossae and the Southern Cerberus Fossae. (NASA/JPL-Caltech/ASU). b. Seam-corrected and seam-mapped mosaic of Mars rendered at 5.0 m/px using Context Camera (CTX) data from the Mars Reconnaissance Orbiter (MRO), centred at 9.402°N 157.023°E, showing parts of both the Northern and Southern Cerberus Fossae. The blue dashed line marks the lateral extent of the Athabasca Valles flow channel. The two dashed boxes show where images (c) and

(d) are located. c and d. Seam-corrected and seam-mapped mosaic of Mars rendered at 5.0 m/px using Context Camera (CTX) data from the Mars Reconnaissance Orbiter (MRO), centred at 8.901°N 155.889°E (c) and 9.369°N 156.125°E (d). Image c. highlights the branching channels within the Athabasca Valles, indicative of catastrophic floods. Image d. highlights the lachrymiform-shaped islands within the Athabasca Valles channel, features commonly associated with landscapes carved by aqueous flows.

Athabasca Valles bears all the hallmarks of a catastrophic flood-carved landscape because it contains branching channels, streamlined and lachrymiform-shaped islands (Burr et al., 2002) (Figure 1.4 b, c and d). Features within the channel show evidence for channel-forming erosion and channel-filling processes, for example, by flood lavas' flow. The channel may have been carved by aqueous means, but the floor of the channel and the banks were later draped with lava (Jaeger et al. (2007). The northern (upslope) side of the source for the Athabasca Valles displays thin, arcuate fronts of lava, concentric to the source region. After being formed by fluvial means, the channel was draped in lava (Figure 1.5).

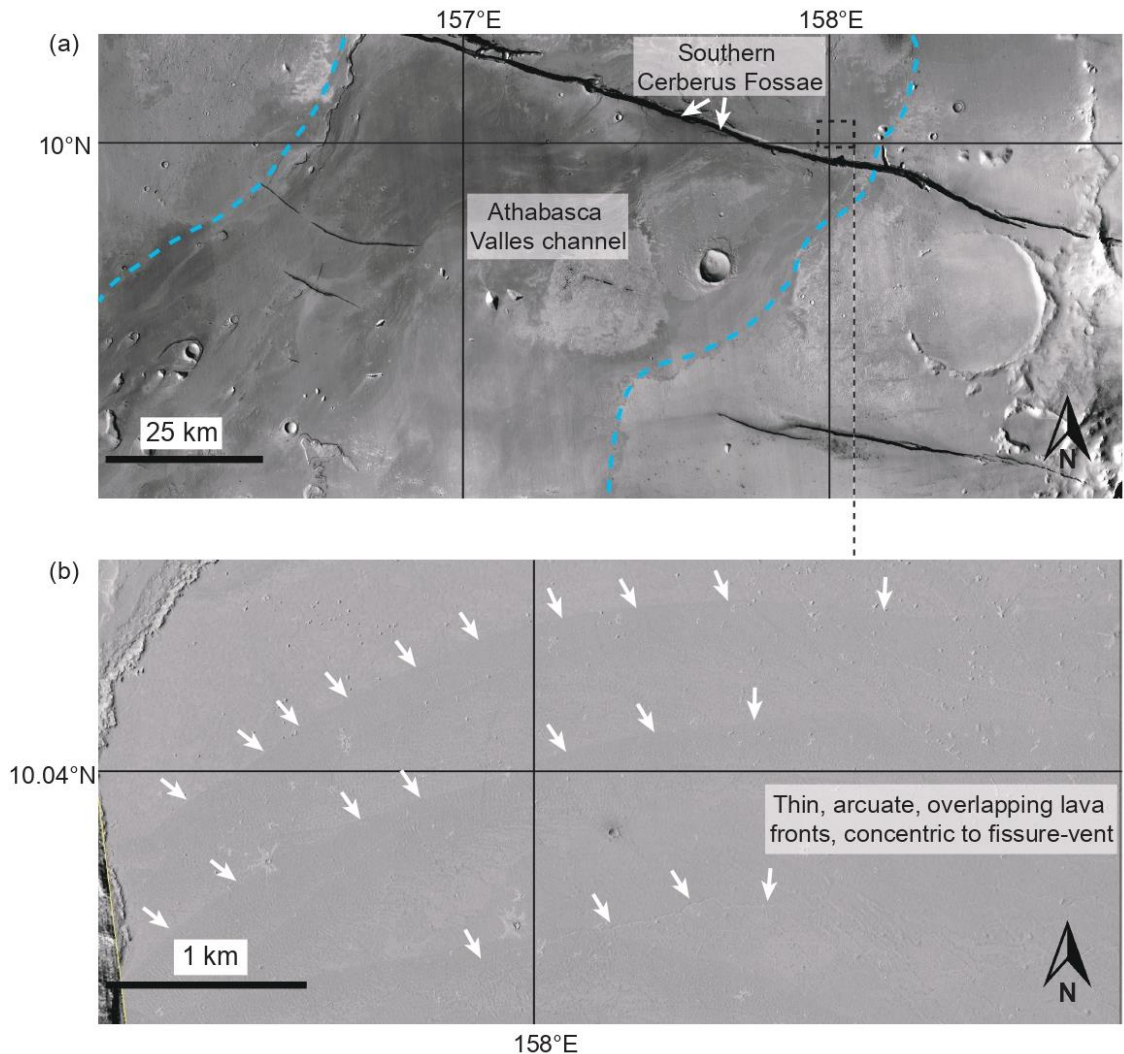


Figure 1.5. a. Location map. THEMIS Day IR 100 metre/pixel Global Mosaic version 13.4. of the Southern Cerberus Fossae, and the lateral extent of the Athabasca Valles flow channel

(marked by a dashed blue line) that emanates from the fossae and flows south, although flows have also covered a small part of the northern side of the Southern Cerberus Fossae. The dashed box marks the location of Figure 1.5 b. (NASA/JPL-Caltech/ASU). b. Detail from HiRISE image (PSP_001408_1900RED) of the north (upslope) side of the source region of flows, with fine, thin, arcuate and overlapping fronts visible (marked by white arrows). Note that the fronts are concentric to the fissure vent to the south.

Work by Jaeger et al. (2007) showed the existence of ring-mound landforms (RMLs) on the surface of parts of the channel, some with wakes that trail downstream (Figure 1.6 a and b). From several hypotheses suggested for the genesis of the RMLs, it is thought that their presence is consistent with the idea that the RMLs are hydrovolcanic, or rootless cones, that formed when groundwater, heated by the lava flow, vented, releasing steam, possibly explosively (Jaeger et al. (2007)). They are considered late-stage structures within a very fluid lava sheet flow that deflated and draped the pre-existing flood-carved landscape in Athabasca Valles (Figure 1.6 b).

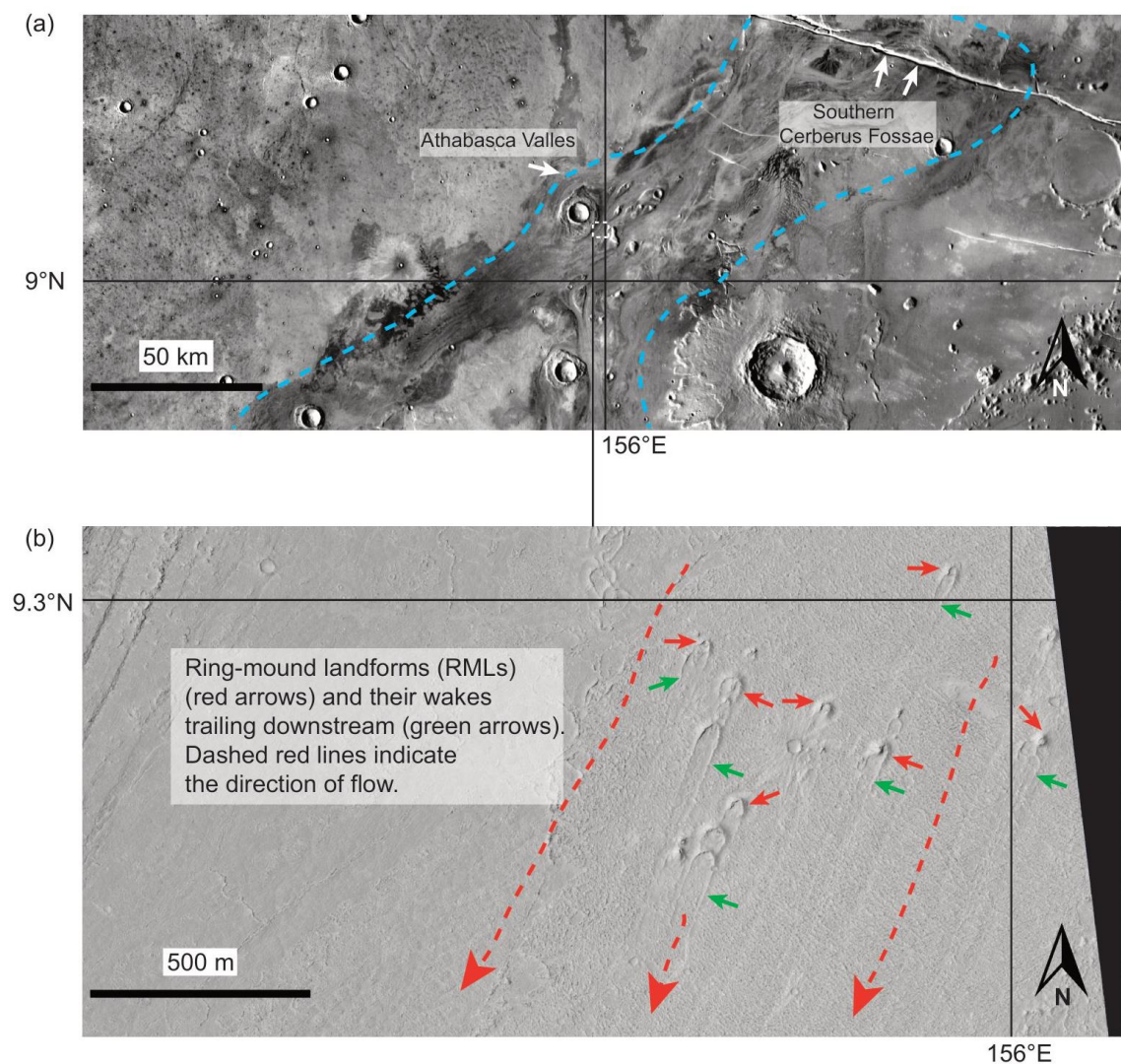


Figure 1.6. a. Location map. THEMIS Day IR 100 metre/pixel Global Mosaic version 13.4. of the Southern Cerberus Fossae and a section of the Athabasca Valles (both marked) (9.293°N 155.984°E). b. A section of HiRISE image PSP_007408_1895, centred at 9.293°N / E155.84°.

shows a section of the Athabasca Valles channel. Ring-mound landforms (RMLs) (pointed out by the red arrows) and their wakes trailing downstream (pointed out by the green arrows). Also of note is the smooth, clean appearance of the surface of the flow. The lack of impact craters on its surface suggests that the lava flow is relatively young. The dashed red lines indicate the direction of flow. The resolution is 25 cm/pixel.

The Cerberus plains (Figure 1.7 a), an area between Elysium Planitia to the west and Amazonia Planitia to the east, is the location of the Cerberus Fossae. It also has swathes of lavas and outflow channels with low crater density that are home to the Athabasca Valles flow channel in the southeast, which flows southeast and northwest through the Marte Vallis channel into Amazonis Planitia. A third flow channel, the Grjótá Valles, the smallest of the three flow channels within the Cerberus plains and the least well-studied, emanates from the northernmost Cerberus Fossae and flows southeast, then south.

Figure 1.7 a illustrates the general flow directions within the channels. Nearly the entire area has been covered by young lava (Berman and Hartmann (2002)). Research conducted by Plescia in 1990 and 2003, as well as Scott and Chapman in 1991, indicates that there have been instances of lava and water flowing periodically. Still, the specific details regarding the timing and duration of these volcanic and fluvial activities remain unknown. An example of the interplay between volcanic and fluvial releases can be observed in Marte Vallis, discussed by Berman and Hartmann (2002). In Figure 1.7 b, streamlined features within the Marte Vallis channel bear the hallmarks of having been formed by fluvial activity. Figure 1.7 c shows a close-up of a streamlined feature's eastern side. The channel floor is covered with a dark, rough material that appears to be lava. However, the channel edge of the streamlined island has been preserved, replete with recessional terrace markings. A gap exists between the lava flow and the lower terrace of the channel wall, indicating that the lava flow post-dates the fluvial flow but has flowed down a channel that fluvial releases also flowed down. Therefore, this area exhibits features created by both lava and water, indicating a close and sequential relationship. The focus of the work lies in the sequential release of flows across the Grjótá Valles. Five flow episodes in this area have been detailed, potentially fluvial, with each successive flow episode occurring farther eastward. Later, an examination will be made regarding the identification of the sequential flow episodes and the implications of the sequential release of flows in Grjótá Valles for the evolution of Cerberus Fossae and Cerberus plains. All three flow channels within the Cerberus plains exhibit commonalities concerning the interplay of fluvial and lava releases that have contributed to the formation and shaping of the channels.

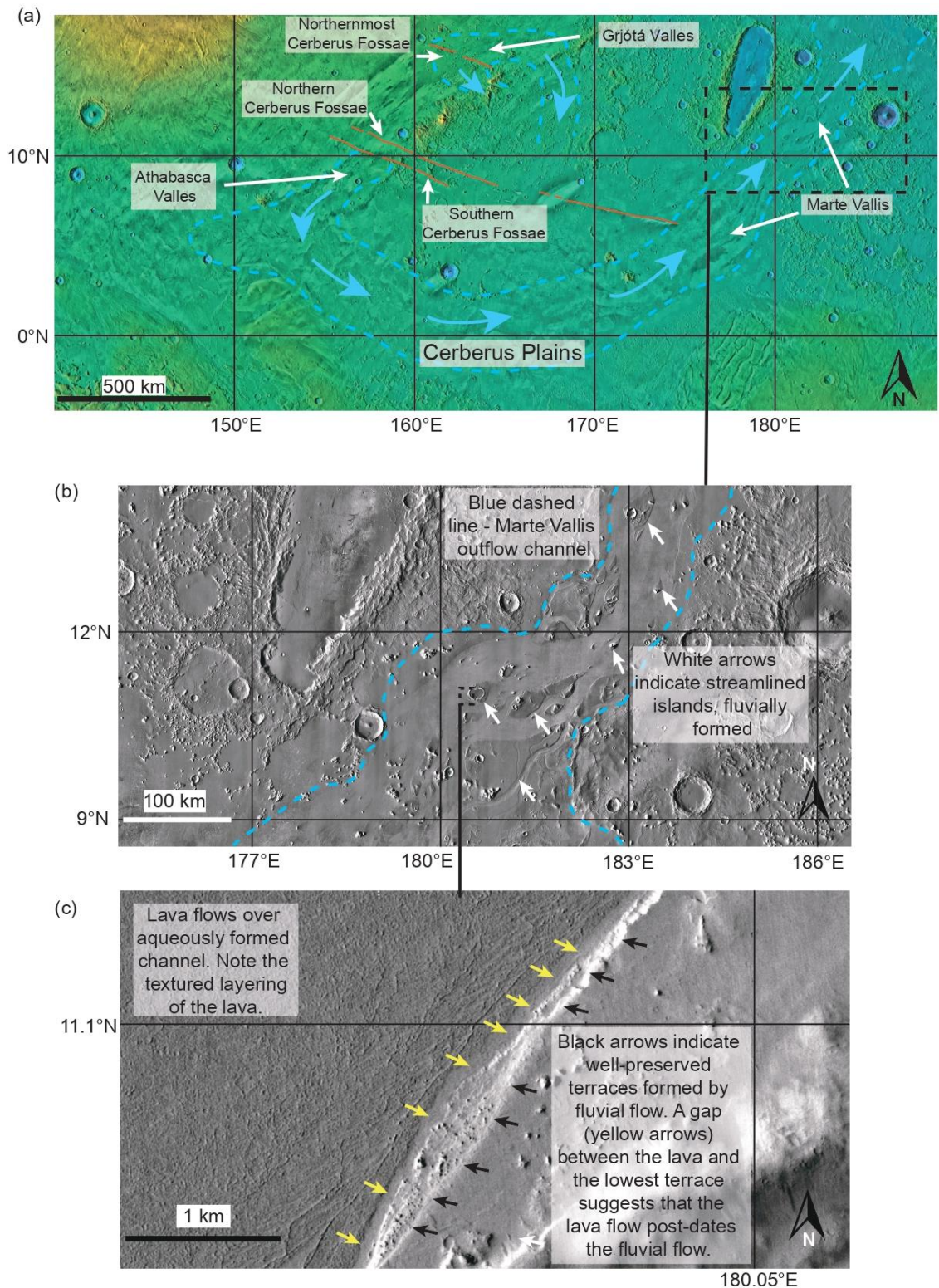


Figure 1.7. a. Location map THEMIS Day IR with coloured MOLA elevation 100 metre/pixel Global Mosaic version 13.4 of the Cerberus plains (6.281°N 164.562°E), highlighting the three main flow channels in the region: Athabasca Valles, Marte Vallis and Grjóta Valles and the flow channels' flow direction, indicated by blue arrows. Red lines mark the Cerberus Fossae. The black dashed-line box marked the area of Figure 1.7 b. Figures b and c. Seam-corrected and seam-mapped mosaic of Mars rendered at 5.0 m/px using Context Camera (CTX) data from the Mars Reconnaissance Orbiter (MRO), centred at 10.82°N 182.023°E (b) and 11.094°N 180.47°E (c). Figure b highlights an area of Marte Vallis, with apparent streamlined formations in the channel, most likely formed through fluvial means. Figure c. is a close-up of the eastern

edge of one of the streamlined islands. It looks at the channel floor and the edge of the streamlined formation. The channel floor is rough, dark and is lava. The streamlined island has recessional terraces, likely formed by fluvial activity. There is a gap between the lava and the lowest terrace of the streamlined island, and this would indicate that the lava flow post-dates the fluvial flow and the formation of the streamlined island. It also indicates that lava and aqueous processes share the same Cerberus plains conduits.

The channel features have been interpreted as potentially arising from one of the following options:

1. Magma-induced melting of the cryosphere and fluvial outflow (Berman and Hartmann, 2002; Burr et al., 2002; Head et al., 2003), such as the outflow of water from a breached aquifer (Carr, 1979; Burr et al., 2002; Plescia, 2003) above an intruding dike beneath the fossae.
2. The release of water from a sub-cryosphere aquifer a few kilometres thick and tens of kilometres in lateral extent (Manga, 2004) or from another subsurface origin (Jones et al., 2011).
3. Many studies have held that large megafloods occurred (Kattenhorn and Meyer, 2010; Burr et al., 2002, 2009) across parts of the Cerberus Fossae, flowing through the three Amazonian-aged flood channels within the region (Grjótá Valles, Marte Valles, and Athabasca Valles) (Figure 1.7 a), with the emanation points of these floods not conclusively known, although generally thought to be the fossae themselves (Burr et al. 2002, 2009).
4. Others have interpreted the outflow channels in the study region to show a predominance of landforms that resemble those produced by aqueous flows on the Earth, such as streamlined forms, scour marks and longitudinal lineations (Figure 1.4 c and d, Figure 1.7 c, and 1.8 b). However, an alternative view is that the channel formation may be associated with the flow of turbulent lavas, with turbulent lavas being suggested as a possible mechanism for cutting channels (Jaeger et al., 2010).
5. An alternate formation hypothesis is that lavas formed the channels (Leverington, 2004, 2006, 2011, 2018). The similarities between features found on the Moon and Venus and those in the channels on Mars have been observed. These features include sinuous channels, inner channels, anastomosing reaches, streamlined erosional residuals, branching channel patterns, and reaches that indicate lateral or vertical erosion (Leverington, 2011). Lavas do not require sizeable hydrological flow rates, sub-surface permeabilities, hydrologic head considerations, or implied water abundances implied by an aqueous model that do not concur with geochemical and mineralogical observations. Additionally, there are no comparable examples on Earth. (Leverington, 2011).

Considerable speculation surrounds the origin of the channels. Is the channel-forming process concluded, or are we experiencing merely a hiatus period? Are the flows released as megafloods or as discrete episodes? Is there a connection between flow episodes, seismicity, and the Cerberus Fossae's growth? The thesis will investigate the lesser-studied Grjótá Valles flow channel and the northernmost Cerberus Fossae to determine whether fluvial, volcanic processes or both formed the flow channels in Grjótá Valles. It will examine whether the flows were mega-events, encompassing large-scale occurrences that covered extensive parts of the Cerberus plains or smaller events. The study will endeavour to establish relative and absolute dating of flow events, aiming to establish connections between these events and seismic activity in the region, the eastward expansion of the Cerberus Fossae, and the gradual eastward release of flows over time. The analysis will seek to elucidate the implications of these findings for the region as a whole.

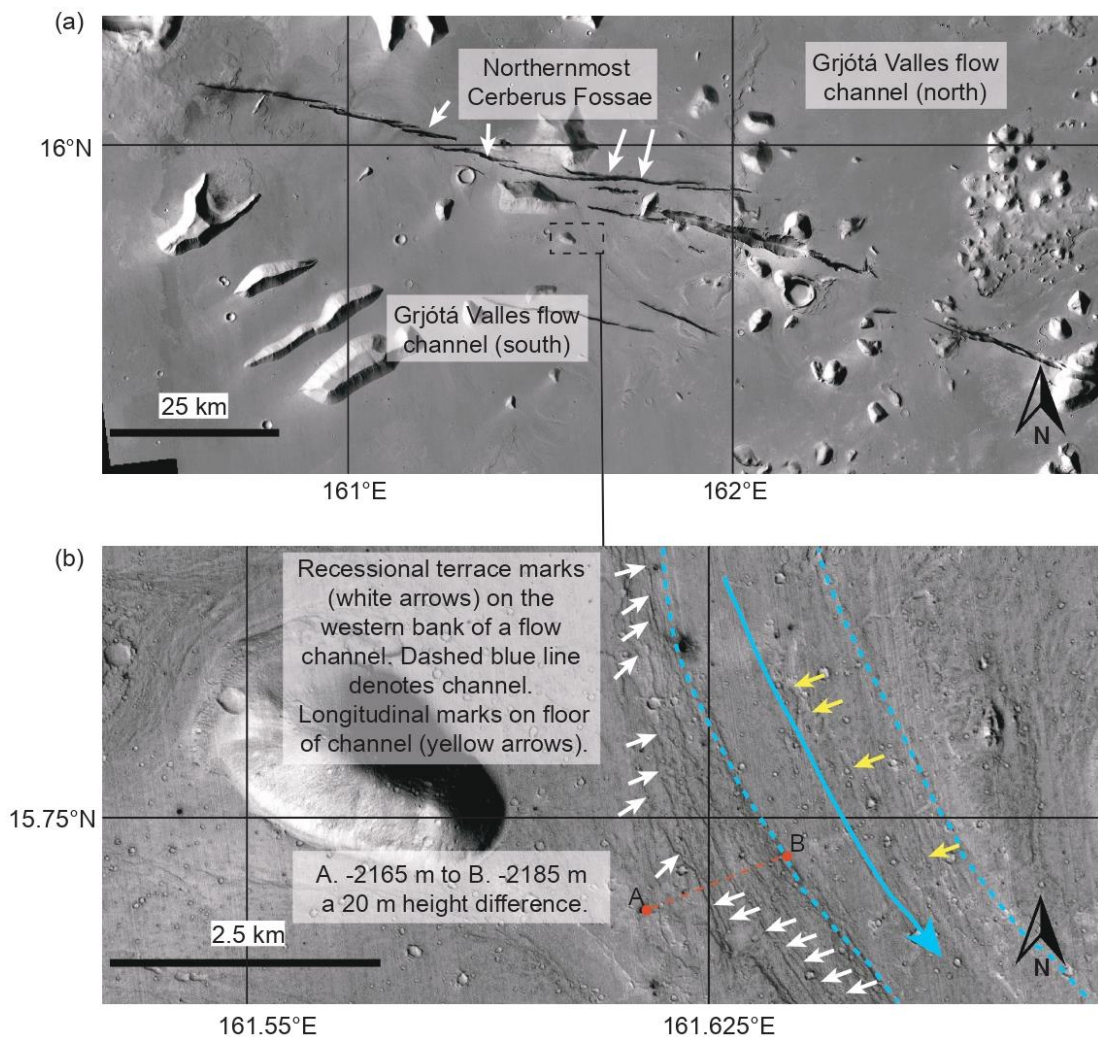


Figure 1.8. Figures a and b. Seam-corrected and seam-mapped mosaic of Mars rendered at 5.0 m/px using Context Camera (CTX) data from the Mars Reconnaissance Orbiter (MRO), centred at 15.74°N 161.656°E (a) and 15.757°N 161.607°E (a). Location map of Northernmost

Cerberus Fossae and the Grjótá Valles channels (north and south). Of note are the smooth channel floors and the streamlined features within the channel. The black-dashed box denotes the area of Figure 1.8 b. b. Close-up of a fluvial channel heading south, with the western bank of the channel covered by recessional terrace marks (white arrows). The height difference from position A (red dot) at the top of the terrace markings to position B (red dot) on the base of the channel is 20 m (-2165 m to -2185 m). This indicates that the flow channel that cut this channel incised down by at least 20 m. The existence of recessional terrace markings is a possible indicator that the channel was carved by fluvial activity. Yellow arrows on the channel floor highlight the lineation marks and scour marks on the flow channel.

As mentioned above, other nearby channel systems, such as the Athabasca Valles, have been discussed in terms of their formation through aqueous flow, but also exhibit clear signs of post-aqueous flow lava infills to the pre-existing channels (Jaeger et al., 2007; Jaeger et al., 2010) (Figure 1.6). In contrast, Grjótá Valles outflow channels lack this later lava infill, and this absence has been taken to indicate that the channels therein are possibly the result of aqueous flows (Baker and Milton, 1974; Burr et al., 2002; Head et al., 2003; Morgan et al., 2013; Plescia, 2003). This would set Grjótá Valles apart from Athabasca Valles and Marte Vallis if this were the case. However, a lack of high-resolution imagery of this area until recently has meant that it has not been thoroughly studied, meaning the results are inconclusive and speculative. My work in this area has revealed more about the channels' formation, which will be discussed in Chapter Five. It has been suggested that the flows that formed such channels were extremely large, with very high discharge rates (e.g. $1-8 \times 10^6 \text{ m}^3 \text{ s}^{-1}$ for the nearby Athabasca Valles channel system; Keszthelyi et al., 2007) because, for example, the Grjótá Valles channels cover a region of $\sim 90,000 \text{ km}^2$. However, it is debated whether or not these channels formed during single or repeated flow events (Burr et al., 2002), introducing uncertainty about flow volumes and discharge rates. This lack of certainty is due to the area of Grjótá Valles not having been fully analysed, particularly in terms of creating high-resolution topographic profiles. The available imagery and data were not of sufficient quality to identify key features necessary for determining whether the channels were formed by singular or multiple events. My work has sought to rectify this by using the highest resolution imagery available to facilitate the construction of detailed maps of the channel systems in Grjótá Valles, using topographic profiles to verify my results.

This uncertainty gives rise to several questions: If the channel formed in a single large episode, how were the implied large volumes of water/lava required for such flows to be released, and where could such volumes of water be stored?

Carr (1979, 1996) suggested that the catastrophic outflow channels, as he believed they were, were evidence that liquid water was held within the crust, but noted in a

later paper (Carr, 2000) that the role of the cryosphere must be important, in generating pressurised aquifer confinement because how else could such immense discharges be released from the Martian subsurface. Clifford (1993) expanded on Carr's work, proposing that if Mars's inventory of water exceeds the pore volume of the cryosphere, then a global sub-permafrost system would form. If this were the case, then this would allow for the subsurface transport of water. Work by Brass (1980) noted that the average global of -53°C is well below the melting temperature of ice and lower than the eutectic freezing temperature of many salt-rich brines. Even though surface temperatures rise above -0.15°C in areas near the equator, liquid water remains unstable. It could be a transient phase quickly evaporating into the dry atmosphere, freezing at the colder high latitudes. However, Mellon and Phillips's (2001) calculations showed that liquid water is stable in the crust. Clifford (1993) also suggested that climate change and geothermal gradients could periodically melt ground ice, thus replenishing subsurface water. This ties in with work by Jakosky and Phillips (2001), who point out that a reservoir of crustal liquid water has existed on the planet and that this reservoir has, at various times and to various degrees, exchanged with water at the surface and in the atmosphere. They note that although they do not know how much water is in the reservoir, they conclude that it is sizeable, global, and, intriguingly, readily accessible to the surface in some places. Carr (1996) notes that the enormous volume of water that caused catastrophic floods would mean the water released, even in the present cold climate, could flow significant distances before freezing. Tanaka (1999) and Hoffman (2000) indicate that liquid water was present in the crust, but they also consider other eroding agents, such as liquid CO_2 , SO_2 , volcanic lava, debris flows, and aeolian processes. Malin and Edgett's (2000) work studying pristine gullies on exposed walls of impact craters and valleys has led them to conclude that these gullies are identical in shape and size and possibly formation process to those on Earth—those on Earth were carved by liquid water seeping out of aquifers on exposed scarps. Interestingly, they note that the gully debris overlies features like dunes that are extremely young. If their interpretations are correct, liquid water has been present within a few hundred metres of the surface over the past few million years and may still be there today. However, recent studies (Dundas et al., 2022) note that the gullies are possibly the result of 'dry processes' (e.g., the seasonal activity of CO_2 frost, namely sublimation of CO_2 frost) and not liquid water flow. This work has helped to move consensus away from the formation of gullies via aqueous means.

Dike emplacement and penetration of the ice-rich cryosphere (Head and Wilson, 2001), pressurised volcanic influences on fracture systems (Tanaka and Chapman, 1990), and the decompression of gas hydrates deep in the crust (Max and Clifford,

2001) are other possible factors in the cataclysmic release of outburst floods. The ice-rich ground may have been melted (Zimbelman et al., 1992), perhaps following dike intrusion (Head et al., 2003), contributing water and sediment to the flood discharge. Nevertheless, melting by dike intrusion alone would not have been enough to release floodwater at the volumetric rate modelled from surface channel size and slope (McKenzie and Nimmo, 1999). Short-term ponding may have occurred in the fossae before breaching or overflowing the fossae rim (Ghatan et al., 2005; Keszthelyi et al., 2007), contributing to high instantaneous discharges.

Burr (2010) notes that four of Mars' flood channels are Amazonian in age (3.0 Ga to present) and that the channels originate at the fossae. The fossae have differing morphologies, which could indicate different mechanisms for the release of floodwater. Fossae with a graben morphology reflect the presence of subsurface dikes (Wilson and Head, 2002; Head et al., 2003a; Ghatan et al., 2005; Leask et al., 2006), suggesting that dike-induced cracking of a confining cryosphere and release of pressurised groundwater.

The fossae may be the result of magmatic extensional tectonics. Based on the hydrological properties of the Martian crust (Hanna and Phillips, 2005), modelling shows that extensional stress relief can produce sufficient excess pore pressures to drive the catastrophic release of groundwater (Hanna and Phillips, 2006). This mechanism may have acted with other factors, like aquifer pressurisation due to cryosphere growth (Clifford and Parker, 2001).

On a separate, possibly linked point, it has been suggested that the fault system running through Grjótá Valles, which forms part of Cerberus Fossae, is formed due to dike emplacement, and this contributed to flow formation (e.g. Head et al., 2003). Several authors have conducted numerical modelling to calculate the main channel discharge for the Athabasca Valles and Marte Vallis channels. Due to possible poor image quality, no estimate of the channel discharge for the Grjótá Valles (referred to in earlier literature as the 'unnamed northern channel system' (cf. Burr et al., 2000, 2002) has been calculated. Estimates by Burr et al. (2002) for Athabasca Valles, using MOLA data and a modified version of Manning's equation (modified by Carr (1979) to account for Martian gravity), an empirical formula for estimating the average velocity of a liquid flowing in a conduit that does not completely enclose the liquid were 1–2 million m³/s. Burr et al. (2002) used a different method for Marte Vallis—the U.S. Army Corps of Engineers hydraulic model HEC-RAS (U.S. Army Corps of Engineers 1998), estimating ~5 million m³/s.

Work by Head et al. (2003) on the Athabasca Valles focused on producing a model for magmatic dike emplacement that produces the following: a. surface fractures and localised volcanic eruptions, b. cryospheric cracking to fracture the surface and release pressurised groundwater within the cryosphere, c. effusion of water along an ~ 3000 km-long segment to form Athabasca Valles and d. heating of the regions adjacent to the dike to cause melting and surface subsidence, creating the observed late-stage pits and linear depressions. The model produced showed that Burr et al.'s. (2002) estimate for discharge fluxes into Athabasca Valles (1–2 million m³/s) is possible through a dike-related cryospheric fracture ~2 m wide, at water rise speeds of ~60 m/s. However, one key issue with Head et al.'s. (2003) model is that aquifer permeability on Mars must be far greater than that seen on Earth.

Manga and Wright's (2021) work compared seismic velocity readings measured by the InSIGHT mission seismometer in Elysium Planitia with seismic velocity modelled for ice-filled porous basalt, liquid water, and gas. The study found that the Martian upper crust (8–11 km) had seismic velocity readings of 1.7–2.1 km/s (Lognonné et al., 2020), similar to or lower than standard pure ice seismic velocity readings (2.0 km/s) (Gagnon et al., 1988). Based on these low velocities, it seems that the crust is not full of ice. However, as we go deeper, there appears to be an increase in seismic velocity, indicating the existence of some mineral cement-like carbonates that could have been formed from groundwater. This indirectly points towards the possibility of significant amounts of groundwater in the past. However, the study has found that if there is no ice-cemented cryosphere present, it can be concluded that there is no aquifer below, as evaporation from an aquifer would lead to ice condensation in the overlying crust. Estimates that a global layer of water >400 m existed (Carr, 1996), an estimate based on the volume of water required to produce the Martian surface's erosional features, such as the large outflow channels in Elysium Planitia, the eastern part of the Hellas basin, and the western and southern margins of Amazonia Planitia may be the case. Studies of kaersutite from an olivine-hosted melt inclusion in the Chassigny meteorite were used to predict the water content in the Chassigny source region. Results showed that the necessary abundance of water needed to agree with Carr's estimates would have existed (McCubbin et al., 2010), "...these results indicate the possibility of relatively young (early–mid-Amazonian) water-rich magmatic–hydrothermal activity at the Martian surface and subsurface, which could have been responsible for intermittent replenishment of water to these regions following the onset of the cold, dry climate that exists today." (McCubbin et al., 2010).

As mentioned previously, some authors (Tanaka, 1999 and Hoffman, 2000) have indicated that liquid water was present in the crust. However, they also consider other eroding agents, such as liquid CO₂, SO₂, volcanic lava, debris flows, and aeolian processes, feasible too. Given that lava flows are observed on channel floors in Athabasca Valles and Marte Vallis, lava is a possible candidate for being the dominant process in channel formation in the Grjótá Valles (Leverington, 2004, 2006, 2011, 2018). This hypothesis is supported by observations of geomorphic/geologic features on the Moon and Venus (Leverington, 2011). These features are similar to those reported from channels on Mars, such as sinuous channels, inner channels, anastomosing reaches, streamlined erosional residuals, branching channel patterns, and reaches suggestive of lateral or vertical erosion (Leverington, 2011).

Furthermore, the formation of channels by lavas does not rely on the very large hydrological flow rates, sub-surface permeabilities, hydrologic head considerations, implied water abundances implied by an aqueous model that do not concur with geochemical and mineralogical observations, and the lack of terrestrial analogues (Leverington, 2011). However, it is implied that if lavas did dominate channel formation, lava morphologies would be prevalent, such as lobate flow fronts, upstanding flows, platy-ridges, knobs, break-outs or rootless cones that characterise lava-infilled channels described nearby on Mars, such as for Athabasca Valles. They do not resemble sinuous rilles commonly associated with lava processes (Jaeger et al., 2007).

The Grjótá Valles, the lesser-studied outflow channel in the Cerberus plains, must be thoroughly analysed using high-resolution imagery. By doing this and analysing and studying the resultant map of Grjótá Valles outflow channels, including the use of MOLA data to produce topographic profiles across sections of channels that display possible cross-cutting relationships, a clearer picture will emerge of this channel's history and development and how this relates to the other channels in the Cerberus plains. Is there a commonality between the three channels' evolution, or do they function independently? Chapter Five of this thesis attempts to map channel formation within Grjótá Valles and to test channel formation hypotheses.

1.3. Recent seismicity and palaeoseismicity of Cerberus Fossae

Whether Mars is currently a geologically active planet or whether it is now dormant is an essential question. If the planet is still active, if there is ongoing subsurface activity, this could hint at the presence of liquid water. Based on the geomorphic features observed on the planet and likely formed by fluvial processes, liquid water was once

found on Mars. Liquid water could suggest the presence of life, so if the planet is geologically active, it could mean that liquid water is present. The implications of such a discovery would be enormous.

The arrival of the Interior Exploration using Seismic Investigations, Geodesy, and Heat Transport (InSIGHT) lander on Mars in 2018 and the deployment of its seismometer, the Seismic Experiment for Interior Structure (SEIS), in February 2019 finally allowed for conclusive proof that Mars is still a seismically active planet. Since the landing on Mars, SEIS (D. Giardini et al., 2020), and the Marsquake Service (MQS), the team that reviews seismic data recorded by SEIS, have recorded from the start of the mission through September 2021, 951 marsquakes, thought to occur at regional distances and 1,062 short duration events, considered to be caused by local thermal stresses (InSIGHT Marsquake Service 2022). The landing sight of InSIGHT was in western Elysium Planitia, to the southwest of Cerberus Fossae. The source regions of two large marsquakes were located across the Cerberus Fossae (D. Giardini et al., 2020), hinting at the possibility of still more seismic activity in this region. Stähler et al., 2022, studying seismic data from InSight, posit that low-frequency (LF) and high-frequency (HF) marsquakes could be connected to tectonic activity within the Cerberus Fossae. The LF marsquakes are extremely interesting because they occur at depths of between 15 and 50 km, which would point to a weak, possibly warm source region that is linked to extensional tectonics. Such a setting would suggest that dike intrusions, most likely from Elysium Mons, are responsible.

Investigations into possible seismicity on Mars began long before the arrival of the Interior Exploration using the Seismic Investigations, Geodesy and Heat Transport (InSIGHT) lander on Mars in 2018 and the deployment of its seismometer, the Seismic Experiment for Interior Structure (SEIS) in February 2019. The PhD work presented herein began as a search for possible geomorphic evidence for palaeoseismicity. We now know that marsquakes occur on Mars and close to the study region of Grjóta Valles, based upon the location of marsquake S0235b's epicentre, which was approximately 250 km south of the northernmost Cerberus Fossae (Clinton et al., 2021, the Marsquake Catalog from InSight). The text in this section reports how knowledge evolved before the InSIGHT data acquisition and summarises how some questions remain unanswered about the seismicity that, like on the Earth, can only be addressed by studying the earthquake geology through observations of geomorphic features.

Evidence for a once seismically active Mars exists in the numerous tectonic faults that may be observed across the Martian surface (Carr, 1974; Carr, 1981; Banerdt et al., 1992). Imaging volcanic and tectonic landforms on Mars suggested that Mars was a seismically active planet (Phillips et al., 1991). Some authors have estimated seismicity levels by analysing surface faulting. Golombek et al. (1992) measured the total slip on all major faults and calculated the total seismic moment release. They then distributed this total moment using a moment magnitude/frequency relationship. Banerdt et al. (1992) observed that radial graben systems are formed through various methods of tectonic lithospheric deformation. Knapmeyer et al. (2006) created a synthetic catalogue of seismic events. To assign a distribution of events to each observed fault, the team first calculated an annual global budget of seismic moment release caused by the contraction cooling of the planet. Then, they assumed a relationship between the measured fault length and the seismic moment release. For example, the number and size of Martian seismic events per year had been predicted prior to the InSight data, and models produced predicted an annual moment release of between 3.42×10^{16} Nm and 4.78×10^{18} Nm, with up to 572 events with magnitudes greater than four (Knapmeyer et al., 2006).

Taylor et al. (2013) estimated the seismicity of the Cerberus Fossae, namely four graben within the Northern and Southern Cerberus Fossae. The team first used crater counting to determine the age of the units around the fossae (10 Ma—Late Amazonian). Next, the fossae's motion rates were calculated using measurements of the observed throw. Digital Terrain Models (DTMs) were then used to calculate the maximum throws on the fossae. The measured throws were then used to estimate the length-averaged slip. Calculating annual moment release, the team determined that between 1.5 and 190,000 seismic events per year would be detectable by InSIGHT. That InSIGHT detected 174 marsquakes in ten months would suggest that Taylor et al.'s work was accurate.

However, seismicity modelling of Mars dates back much further, with the suggestion that Martian seismicity is at a level between the Earth's and the Moon's, based on seismic data we have for both bodies (Anderson et al., 1972). More recent seismicity modelling suggests that the source of seismicity could be thermoelastic cooling and regional loading of the surface (Phillips et al., 1991). Before the InSIGHT mission, the only seismic data from Mars was recorded by instruments aboard the Viking-2 lander in Utopia Planitia. Only one seismic signal was recorded on sol 80. It was regarded as "suspicious" due to simultaneous anemometer readings that suggested the "event" possibly being caused by a strong gust of wind (Anderson et al., 1979). Later studies

on the data collected by the Viking-2 lander looked at the meteorological and seismic data to understand the correlation between data being interpreted and to what extent meteorological events (such as winds and gusts on the surface) may have been erroneously interpreted as seismic events. These later studies support the hypothesis that the event detected on sol 80 was seismic and not caused by meteorological phenomena (Lorenz et al., 2017). The event occurred at 03.00 hours. The surface winds at the Viking sites had a consistent diurnal cycle (Nakamura and Anderson, 1979), with wind speeds being lowest in the early hours. A 16m/s windspeed would have been required to generate a seismic signal. However, on sol 80, 20 minutes before the seismic reading and 45 minutes after, the recorded windspeed was 2.6m/s and 3.6m/s, respectively, suggesting that the windspeed at 03.00 hours was also low. Although night-time gusts are possible, as dust devils can occur at night, they are much less common than in the early afternoon (Ordonez-Etxeberri et al., 2018); therefore, it seems this was a seismic event.

The advent of HiRISE imagery (High-Resolution Imaging Science Experiment onboard the Mars Reconnaissance Orbiter) in 2006, whose high resolution (~25-cm pixel sizes) allowed, for the first time, observations of boulders and boulder trails from orbit, in particular the largest boulders and trails, and hence the ability to map the characteristics of boulder populations along the strike of fault systems (Figure 1.9). Work by Roberts et al. (2012), using HiRISE images and an understanding of natural seismometers on Earth (mobilised boulders), suggested that large-magnitude marsquakes may have occurred in the recent past along Cerberus Fossae. This suggestion was evidenced by observations close to faults of anomalies in the density of trails left by mobilised boulders and boulder trail widths. Roberts et al. (2012) showed, for a section of the Southern Cerberus Fossae, that boulder trail densities per kilometre and boulder trail widths increased systematically from background values along the strike of part of the fault system, interpreting this as possible evidence that a marsquake had produced ground shaking responsible for mobilisation of the boulders. As part of the PhD studies presented herein, an investigation into possible Martian seismicity in the region of the northernmost Cerberus Fossae focused on identifying and measuring examples of boulder trails and boulder trail width on the sides of the fossae. As will be explained in Chapter Four, measurements of these trails showed that the along strike the profile “display(s) the classic pattern associated with earthquakes where both the frequency of boulder falls, and boulder sizes decrease away from the epicentre and the location of coseismic surface faulting, due to localised ground shaking” (Keefer, 1984) and that the zone of mobilised boulders measured along northernmost Cerberus Fossae might be consistent with a marsquake of moment

magnitude \sim M7.9 (Wells and Coppersmith, 1994). This work was presented in a paper by the author of this PhD, which is included in Appendix C of this thesis (Appendix C: Brown, J. R., and Roberts, G. P. (2019). Possible evidence for variation in magnitude for marsquakes from fallen boulder populations, Grjota Valles, Mars. *Journal of Geophysical Research: Planets*, 124. <https://doi.org/10.1029/2018JE005622>).

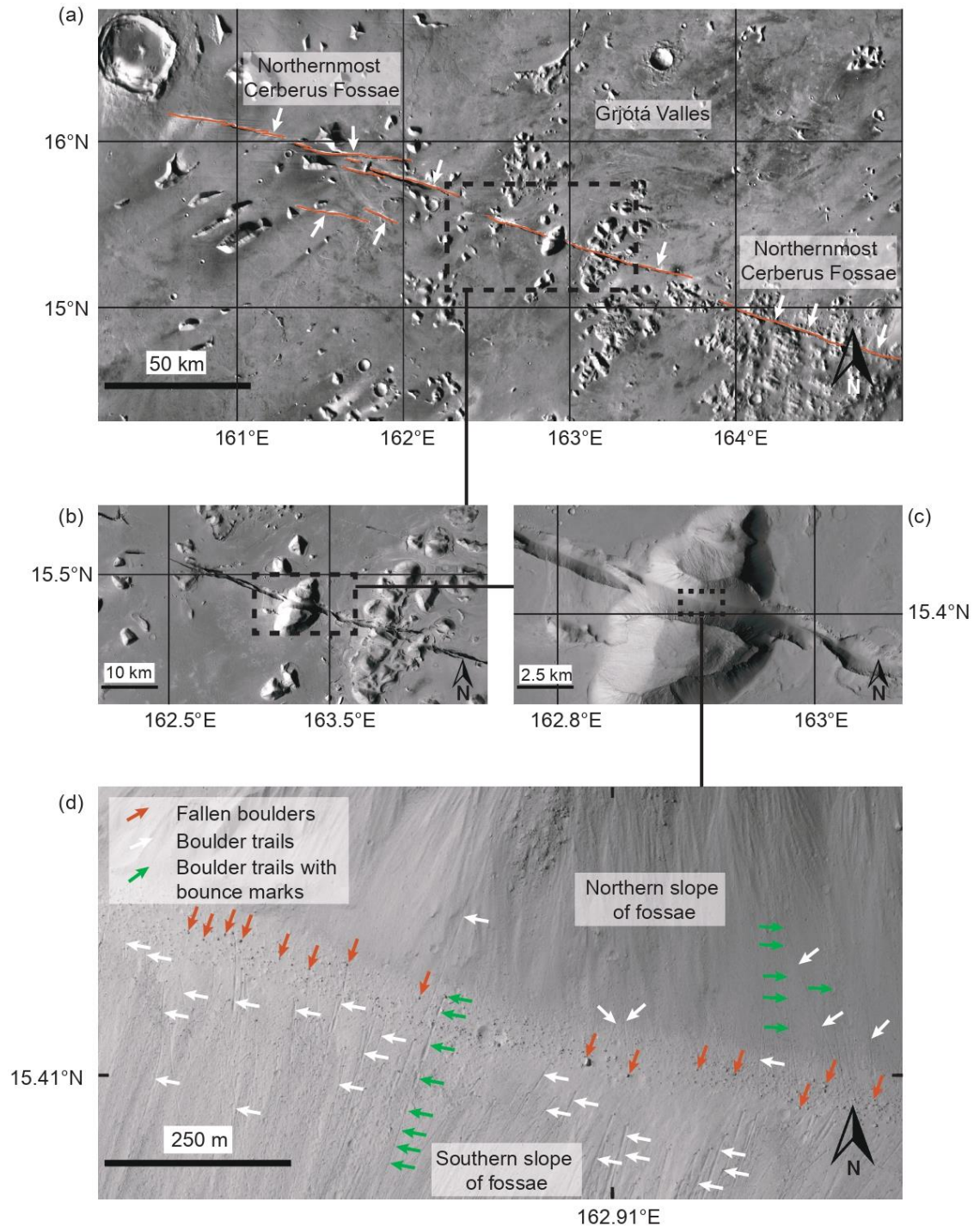


Figure 1.9. Figures a, b and c. Seam-corrected and seam-mapped mosaic of Mars rendered at 5.0 m/px using Context Camera (CTX) data from the Mars Reconnaissance Orbiter (MRO), centred at (a) 15.555°N 162.582°E, (b) 15.406°N 162.885°E, and (c) 15.407°N 162.917°E. (a). Location map of Northernmost Cerberus Fossae (red and with white arrows pointing to it) and

the Grjótá Valles channels. A black dashed-lined box highlights the area of interest, a hill split by the growth of the fossae (b) and (c). (d) A section of HiRISE image ESP_018075_1955, centred at 15.4°N 162.9°E, shows the northern and southern slopes of the fossae. Fallen boulder trails (white arrows) can be seen on both slopes, with a predominance of trails on the southern slopes. Some trails exhibit clear bounce marks (green arrows). Fallen boulders litter the floor of the fossae (red arrows), some of which have the boulder at their terminus.

As mentioned above, this initial phase of the PhD studies presented herein was completed prior to the deployment of InSIGHT's seismometer SEIS. Despite SEIS being on the surface of Mars, it cannot study the palaeoseismicity evidenced by geomorphic features on the surface of Mars. SEIS has revealed that Mars is seismically active (D. Giardini et al., 2020), and the Marsquake Service (MQS), the team that reviews seismic data recorded by SEIS from the start of the mission through September 2021, recorded 951 marsquakes and 1,062 short duration events, considered to be caused by local thermal stresses (InSIGHT Marsquake Service 2022). The landing sight of InSIGHT is in western Elysium Planitia, to the southwest of Cerberus Fossae and the sources of two large marsquakes were located across the Cerberus Fossae (D. Giardini et al., 2020), hinting at the possibility of still more seismic activity in this region.

This thesis develops ideas that suggest that channel formation, palaeoseismicity, and active seismicity may be linked. Work by Perrin et al. (2022) measured fossae widths and vertical throws from west to east along the Northern and Southern Cerberus Fossae and noted that there are systematic changes from west to east. The implication is that cumulative displacement accommodated by the Cerberus Fossae decreases from the west(-northwest) to the east(-southeast). The team believe that deformation has propagated over the long term toward the east(-southeast) away from Elysium Mons, suggesting that igneous activity beneath Elysium Mons was both the source for melts and regional tectonics stresses that were responsible for dike development and stress propagation toward the east(-southeast) at Cerberus Fossae. Perrin et al.'s (2022) research aligns with the hypothesis presented in this thesis that the connection between seismicity and channel formation may be connected by dike development, with the fossae in Grjótá Valles becoming smaller in size the further southeast the fossae are followed. The fact that fossae cross-cut even the most recent geomorphic features in Grjótá Valles suggests that dike development is ongoing. This suggests seismicity is also ongoing, and with dike development and extension, the possibility of further flow episodes occurring is a distinct possibility. Locating the most recent flow channels in Grjótá Valles may help narrow down the area where the next flow event might occur.

To help investigate these ideas, detailed mapping was conducted to allow observations of the geometries, cross-sectional profiles, cross-cutting relationships for geomorphic features, and identification and measurement of fallen boulders, boulder trails and widths. To facilitate this study, the geomorphology of the channel system and fractures was studied using Context Camera (CTX) and High-Resolution Imaging Science Experiment (HiRISE) images from the Mars Reconnaissance Orbiter (MRO), and with the use of measured cross-sectional profiles of landforms using Mars Orbiter Laser Altimeter (MOLA) data.

1.4. Aims

This thesis aims to draw together observations constraining channel formation, boulder mobilisation, and active seismicity along the northernmost Cerberus Fossae to provide more significant insights into processes in the area of Cerberus Fossae. Hence, following reviews of the background knowledge of the Cerberus Fossae region (Chapter 2) and methodology utilised in this thesis (Chapter 3), the work in this thesis is divided into two main parts, namely looking for evidence of palaeoseismicity (Chapter 4) and evidence of channel forming events in this section of the Cerberus Fossae. (Chapter 5). These observations are brought together in the final discussion, alongside InSight seismicity data, to provide a view of the processes operating and operating in the past for this part of Mars (Chapter 6). The possibility that Mars may have been tectonically active in the recent past and that liquid water may have existed, albeit as floodwater, is of significant cross-disciplinary interest, including the search for non-Earth-based life. More tantalising is the possibility that activity is ongoing today.

This thesis will draw the evidence from these studies to formulate a hypothesis regarding the structural, geomorphic and geological evolution of this section of the Cerberus Fossae.

1.5. Objectives and Methodologies

In order to test the hypotheses outlined in Sections 1.2, 1.3 and 1.4. the following objectives and methodologies are stated:

- Objective (1): To investigate palaeoseismicity in the region of the northernmost Cerberus Fossae and to determine whether it (a) existed in the past, and if so, how recently and (b) to use the results of (a) to help further understand the likelihood and character of ongoing seismicity. Note that the work for (b) was conducted

before the results from the InSIGHT mission arrived. However, questions remain about likely maximum marsquake magnitudes and whether palaeoseismicity can be established, features that are challenging or impossible to investigate solely with seismometer data.

Methodology (1): The methodology was to use images taken from NASA's Mars Reconnaissance Orbiter (MRO), including HiRISE (High-Resolution Imaging Science Experiment onboard the Mars Reconnaissance Orbiter) images and Context Camera (CTX) images of the northernmost Cerberus Fossae. These images were then imported into Google Earth as georeferenced image overlays to enable the search for and analysis of fallen boulders and boulder trails. Such data allows the calculation of the density of boulder trails and the trails' widths per kilometre. With this data, it is possible to study the pattern of boulder trails and then ascertain the plausible mechanism for boulder mobilisation. Following Roberts et al. (2012), it is concluded that the boulder data suggest large magnitude paleo-marsquakes, placing constraints on the minimum values for the largest marsquake magnitudes to be expected.

- Objective (2): To investigate channel formation in this region of Mars to determine if the well-known extensive channel systems mapped by others (Carr, 1979; Baker, 1982; Tanaka, 1986; Scott and Tanaka, 1986; Tanaka et al., 1992; Edgett and Rice, 1995; Burr et al., 2002; Berman and Hartmann, 2002) were fluvial or from another mechanism such as turbulent lava or mudflows, whether the flows were episodic or was there just one mega flow event, and to identify the source regions for the flows.

Methodology (2): To construct a large, high-resolution regional map of the study area, ~70,000 km², using available imagery with suitable coverage of the area from NASA Mars Reconnaissance Orbiter (MRO). Analysis of the image involves identifying features such as fissures, impact craters, streamlined islands, etc. and then using the image to identify channel-to-source and channel-to-channel relationships by identifying cross-cutting relationships and to use this to determine the relative ages of identified channels. Younger channels cut across and incise into older channels, so finding evidence of this from the high-resolution regional map of the study area will be essential. In the absence of extensive topographic data from photogrammetry that is both high-resolution and covers sizeable areas within the study location, Mars Orbiter Laser Altimeter (MOLA) Precision Experiment Data Records (PEDRs) are used to facilitate the construction of topographic profiles (distance/elevation) across channels. These topographic

profiles are subsequently analysed in conjunction with location-specific images to discern cross-cutting relationships between different channels by determining whether younger features incised down into and, therefore, post-dated older features while also measuring the depth of such channels and gaining elevation information for geomorphic features. This assists in identifying possible emanation points/source locations of the floods/extent of floods.

- Objective (3): To consider whether there is a connection between seismic activity and the history of channel formation.

Methodology (3): To use data acquired from palaeoseismicity studies, channel studies and the InSight seismometer data to investigate possible inter-relationships and assess ongoing processes and processes in the relatively recent past. For example, it may be possible to obtain relative ages for the channel-forming episode(s) and how this relates to the formation of the fossae. Evidence that the source of the channels has moved east over time is studied, including the study of fissures on the Martian surface. Data will be drawn together to investigate and scrutinise the possibility of a connection between seismicity and channel activity and how this may relate to active seismicity.

1.6. Thesis Structure

Chapter 2 reviews the geological background of the Cerberus Fossae and discusses current theories regarding i. the formation of the fissures—the fossae—across the Cerberus plains, ii. what is thought to have carved the channels we see across the region, and iii. subsurface mechanisms that may have both released water/lava to the surface.

Chapter 3 discusses the methods used to acquire the data. Also, a literature review on the formation of long-lived channel systems on Earth and paleoseismic observations can be derived from satellite images and geomorphology.

Chapters 4 and 5 present the thesis results, which will satisfy the objectives outlined in Section 1.5. Chapter 4 presents the discovery of evidence for paleoseismicity in the region of the northernmost Cerberus Fossae. Using HiRISE imagery to observe and analyse mobilised boulder populations and their trails reveals that palaeo-marsquakes occurred in this area. The boulder trails, seen as a whole, “display the classic pattern associated with earthquakes where both the frequency of boulder falls, and boulder

sizes decrease away from the epicentre and the location of coseismic surface faulting, due to localised ground shaking” (Keefer, 1984). The findings, as outlined by Brown and Roberts (2019), were published prior to the arrival of the Interior Exploration using Seismic Investigations, Geodesy, and Heat Transport (InSIGHT) lander on Mars.

Chapter 5 presents work on the channel-forming history of the northernmost Cerberus Fossae and surrounding areas to the north and south of the fossae. The work identifies a relative chronology for channel formation, revealing that channels have propagated further to the east through time. Analysis of cross-cutting relationships by studying HiRISE and CTX imagery reveals younger channels cross-cut and incise down across older channels. The source of five flow emanation points is also identified and discussed. The channels were asynchronous, although they could only be dated relative to each other. However, an approximate age can be given for when the episodic channel formation occurred.

Chapter 6 is the Discussion chapter. Here, observations are synthesised and discussed in the broader context of the Cerberus Fossae’s history and other studies.

1.7. Portions Included from or Based on First Author Publications

This thesis builds upon and extends the research published in two peer-reviewed journal articles. Chapter 4, which comprises most of this work, mirrors the findings presented in Brown and Roberts (2019) published as a peer-reviewed journal article in the *Journal of Geophysical Research: Planets* (Brown and Roberts, 2019) as Brown, J. R., and Roberts, G. P. (2019). Possible evidence for variation in magnitude for marsquakes from fallen boulder populations, Grjota Valles, Mars. *Journal of Geophysical Research: Planets*, 124. <https://doi.org/10.1029/2018JE005622>

Additionally, Chapter 5, largely based on the work by Brown and Roberts (2023), was published as a peer-reviewed journal article in the *Journal of Geophysical Research: Planets* (Brown and Roberts, 2023) as Brown, J. R., and Roberts, G. P. (2023). Repeated, cross-cutting and spatially migrating outflow channel formation, Grjótá Valles, Mars. *Journal of Geophysical Research: Planets*, 128, e2022JE007247. <https://doi.org/10.1029/2022JE007247> delves into the phenomenon of repeated, cross-cutting, and spatially migrating outflow channel formation within the same region. Despite the significant overlap with the content of these papers, the chapters in this thesis diverge by further exploring nuanced aspects not extensively covered in the original publications.

CHAPTER 2.

LITERATURE REVIEW

2.1. Introduction

The literature review offers an overview of our understanding of Mars, in particular with regard to the themes central to this thesis. The planet's geological history is explored, as is the role of water throughout its evolution, volcanic activity, seismicity, internal dynamics, and finally, a review of the most recent papers that discuss Mars' ongoing activity. While this chapter offers a broad perspective, more detailed discussions of specific literature relevant to the research can be found in the Results sections of Chapters 4 and 5 and in the published papers that form the core of this work.

2.2. Geological History of Mars

2.2.1. Introduction

In understanding a region like Cerberus Fossae, one must first have a broader understanding of the entire geological history of Mars. By doing so, one can contextualise an area like the Cerberus Fossae, putting into place Mars' long and complex history and then understand the planet's potential, past and present, to support life. Looking at the Cerberus Fossae in isolation does not allow this. Hence, a review of Mars' ~4.6 billion-year history is reviewed. Its history may be broken into four main epochs, with each having a set of unique geological processes and environmental conditions. The chronological overview below follows Mars' evolution from its formation right up to the present day. Each epoch will be looked at in turn in an attempt to present a clear picture of how Mars has evolved and what key developments occurred during each period.

This review aligns with Ehlmann et al. (2016), who discuss the sustainability of habitability on terrestrial planets, with particular insights into Mars' potential for supporting life. Ehlmann et al. highlights the importance of understanding Mars' early geological and atmospheric evolution, noting that Mars' formation retained primordial heterogeneity in its mantle due to limited mixing. Such early processes, including Mars' rapid accretion and differentiation, set the foundation for its later geological and climatic evolution.

2.2.2. Pre-Noachian Epoch (4.6–4.1 Ga)

Mars's early evolution and formation involved a series of events that shaped the planet in a way that set the course for its later geological evolution. Key events from this period are as follows:

- a. ~4.6–4.5 Ga. Mars was formed from the solar nebula (Bouvier and Wadhwa, 2010) and accreted from planetesimals and planetary embryos in the proto-planetary disk (Chambers, 2004; Morbidelli et al., 2012). Energy from accretion and decay of short-lived radioisotopes led to melting and the beginning of planetary differentiation (Elkins-Tanton, 2012; Kleine et al., 2009; Debaille et al., 2007; Borg et al., 2003).
- b. ~4.5 Ga. The planet's rapid core formation was completed in ~1–15 million years after the formation of the solar system (Kruijer et al., 2017). The differentiation of metal from silicates resulted in the planet's core being formed. The existence of a core helped to create implications for Mars' later thermal and magnetic evolution (Breuer and Moore, 2015), with Ehlmann et al. (2016) noting the possible implications of Mars' core regarding the generation of the planet's early magnetic field—it may have helped to protect the atmosphere from solar wind erosion.
- c. ~4.4–4.3 Ga. The creation of the Martian crustal dichotomy—the difference in the two hemispheres of the planet, with the northern hemisphere lower in elevation and less cratered; the southern hemisphere being higher in elevation and heavily cratered compared to the northern hemisphere—possibly due to a giant impact or internal processes (Marinova et al., 2008; Andrews-Hanna et al., 2008; Ehlmann et al., 2016). This event has subsequently played a huge part in Martian geology (Watters et al., 2007).
- d. d. ~4.2–4.1 Ga. The heavy bombardment period, which saw the planet be heavily cratered, was responsible for the formation of large impact basins on the surface, such as Hellas and Argyre Planitia (Werner, 2008), which began at the end of the epoch. This period created many of the large topographic features visible today (Frey, 2008). This period also saw the decline in Mars' magnetic field, which would have led to changes in surface conditions and atmospheric loss, and ultimately was the beginning of Mars' move to becoming a cold, dry planet (Ehlmann et al., 2016).

Mars would have probably had a magnetic field generated by its liquid core, which protected its early atmosphere from solar wind erosion (Acuna et al., 1999). The loss of Mars' magnetic field had huge implications regarding its atmosphere and surface conditions (Jakosky et al., 2015).

2.2.3. Noachian Epoch (4.1–3.7 Ga)

Continuing where the pre-Noachian had left off, heavy bombardment continued to shape the planet's surface. The end of the heavy bombardment saw volcanic activity and liquid water on Mars's surface, with both shaping the surface geomorphology, likely creating conditions conducive for life to emerge.

- a. Early Noachian (~4.1–3.95 Ga): Heavy bombardment of Mars continued into the Noachian from the Pre-Noachian epoch, subsequently contributing to the formation of some of the oldest surfaces on the planet (Fassett and Head, 2011). Many of Mars' large impact basins of the southern highlands, such as Isidis, were formed during this epoch (Nimmo and Tanaka, 2005).
- b. Middle Noachian (~3.95–3.8 Ga): The formation of dendritic valley systems during the Middle Noachian would suggest significant surface runoff (Fassett and Head, 2008) and the existence of a hydrological cycle on Mars, further suggesting that the planet's climate was warmer and wetter than today (Craddock and Howard, 2002).
- c. Late Noachian (~3.8–3.7 Ga): Considered the most volcanic period in the planet's history, the enormous Tharsis Rise (5,000 km across and 10 km above the surrounding terrain) (Phillips et al., 2001). The evolution of the Tharsis Rise had huge implications for the planet's geology and geography (Johnson and Phillips, 2005).

Throughout the Noachian—due to the presence of water—phyllosilicates were formed. This is important because this indicates that **a.** there were long-term water–rock interactions, suggesting that environments existed long enough to provide possible habitable conditions (Carter et al., 2013), and **b.** that the types of phyllosilicates formed were formed in environments where the pH was neutral (pH 7) to slightly alkaline (pH above 7) (Poulet et al., 2005; Ehlmann et al., 2011). This is of vital importance as such pH conditions are favourable for the emergence of life, and the neutral to slightly alkaline pH is in stark contrast to Mars' later more acidic conditions.

The formation of early sedimentary basins created environments that were ideal for the accumulation of layered deposits that could preserve a record of these early conditions on Mars (Grotzinger et al., 2015; Malin and Edgett, 2000).

2.2.4. Hesperian Epoch (3.7–3.0 Ga)

The Early Hesperian (~3.7–3.4 Ga) saw the formation of many large outflow channels. Suggested means of formation include the release of groundwater, most likely a catastrophic release(s) (Baker, 2001). These enormous channels, such as the channels that flow from Chryse Planitia (Maja Valles, Kasei Vallis, and Ares Vallis), indicate episodic flooding events that may have been caused by tectonic and/or volcanic activity (Wilson et al., 2004). The Late Hesperian (~3.4–3.0 Ga) saw plains-style volcanism, especially in regions such as Elysium and Tharis (Greeley and Spudis, 1981). The volcanism resurfaced large parts of the planet, subsequently creating large lava plains. This volcanism resurfaced large areas of Mars (Grott et al., 2013).

There were four key events during this epoch that are looked at in a little more detail below.

- a. Valles Marineris—(~4,000 km long and up to ~7 km deep)—formed due to tectonic rifting and later erosion (Andrews-Hanna, 2012). Investigation of the huge canyon system has shed further light on the crust's composition, thus revealing information about Mars' geological history (Lucchitta et al., 1992).
- b. Sulphate minerals were deposited during this epoch. This suggests a shift to more acidic conditions during the Late Hesperian (Bibring et al., 2006). This indicates a major shift in the planet's geochemistry, possibly linked to increased volcanic activity and/or the loss of atmospheric density (McLennan, 2012).
- c. A 'northern ocean' may have existed (Carr and Head, 2003). If such a body of water did exist, it would have had important ramifications regarding Mars' climate and the potential for habitability (Clifford and Parker, 2001).
- d. During the Hesperian, chaos terrain such as Hydraotes Chaos formed. Such landforms are thought to have formed as a result of the catastrophic release of groundwater (Rodríguez et al., 2005). Perinatally, such features offer evidence that there existed substantial subsurface water at this time (Zegers et al., 2010).

2.2.5. Amazonian Epoch (3.0 Ga–Present)

The Amazonian epoch, from 3.0 billion years ago to the present, marks a period of continued volcanic activity and dynamic climate changes. From the persistent volcanism in regions like Elysium and Tharsis to the geological phenomena in the Cerberus Fossae, this section explores the transformative impacts on the Martian landscape and climate.

- a. The Early Amazonian (3.0–1.0 Ga) witnessed a continuation of volcanism in Elysium and Tharis, albeit at lower levels than in previous epochs (Werner, 2009). The continued volcanic activity would have contributed to the growth of the enormous shield volcanoes on Mars (Olympus Mons—~22 km in height with a base diameter of ~600 km; Ascraeus Mons—~18 km in height with a base diameter of ~480 km) (Robbins et al., 2011).
- b. The Middle Amazonian (1.0–0.3 Ga) saw young volcanic plains in Amazonis Planitia (Vaucher et al., 2009). This is evidence of the planet's extensive volcanism continuing late into Mars' geological history (Tanaka et al., 2014).
- c. The Late Amazonian (0.3 Ga–Present) is an enigma. Despite the dry and cold conditions, Mars shows evidence of low-level geological activity (Hauber et al., 2011), namely, and most pertinently to this thesis, the formation of the Cerberus Fossae (Vetterlein and Roberts, 2010). Activity within the Cerberus Fossae is considered ongoing today (Broquet et al., 2020; Horvath et al., 2021), suggesting that the Cerberus Fossae may be a somewhat anomalous area of Mars.

It is also important to mention that throughout the Amazonian, orbital forcing has led to cyclical climate changes (Mischna et al., 2003; Laskar et al., 2004). Head et al., 2003, noted that changes in the planet's obliquity resulted in the periodic redistribution of ice from Mars' poles to the mid-latitude regions, which have left behind a record of glacial landforms (Forget et al., 2006). Head and Marchant (2003) identified recent glacial activity (within the last several hundred million years) in the tropical mountain region of Tharsis. This would suggest that the planet's climate has remained dynamic into the very recent past.

2.3. Water on Mars—Evolution and Evidence

The Italian astronomer Giovanni Schiaparelli's 1877 observations of a series of channels on the Martian surface subsequently sparked fascination because their existence was thought to be due to water. Since these early observations through to modern missions, Mars's aqueous history is a source of continued because by understanding its history, one is able to piece together the planet's climatic evolution and from there to learn if the planet was or is potentially habitable.

While modern Mars is dry and cold, there exists much evidence to suggest that liquid water existed on the planet's surface, having profound effects on Martian geology and environmental conditions.

2.3.1. Early Martian Water Discoveries

When the Viking landers detected water vapour in the Martian Atmosphere in 1976 (Nakamura and Anderson, 1979), interest in the scientific community set the stage for further investigations into Mars's hydrological history. The existence of water vapour, coupled with the existence of ancient channels suggested that liquid water once flowed on the planet, supporting theories that Mars once possessed a wetter climate (Milton, 1973; Masursky, 1973).

2.3.2. Martian Channels and Water Flow—Key Early Findings

High-resolution images taken by the Mariner 9 orbiter in 1971 effectively discovered Valles Marineris, the enormous canyon system on Mars (~4,000 km in length and up to 7 km deep). The discovery of Valles Marineris presented strong evidence of geological processes on Mars that hitherto had not been considered and suggested that the planet was far more dynamic than had originally been thought. Other channels imaged included Ares Vallis, Tiu Vallis, Simud Vallis, and Kasei Valles. Analysis of these channels led Baker and Milton (1974) to conclude they were likely formed by catastrophic floods in a way comparable to the Channelled Scablands of Washington State and Antarctica's Wright Valley.

Carr (1979, 1996) suggested that water released from confined aquifers may have caused episodic floods on Mars. Work by McKenzie and Nemo (1999) pointed to evidence of groundwater seepage as being the cause behind features like channels and valleys and that this seepage was gradual. Malin and Edgett (2000), using images

from the Mars Global Surveyor, identified gullies on steep crater walls that looked to have been formed by liquid water. The authors considered these gullies to be indicative of groundwater seepage. Clearly, Mars exhibits a complex interplay of tectonic activity, cryospheric cracking, volcanic processes, and aqueous processes that have played roles in shaping Mars's surface (Burr et al., 2002; Head et al., 2002; Plescia, 2003).

2.3.3. Water Evolution on Mars: Three Mineralogical Eras

Bibring et al.'s (2006) groundbreaking study, which used data from the Observatoire pour la Minéralogie, l'Eau, les Glaces et l'Activité (OMEGA) spectrometre on the Mars Express to suggest three key mineralogical eras on Mars enables researchers to understand Mars in a new way. A brief summary of the three eras is given below:

- **Phyllosian Era (>4.0–3.8 Ga):** During this early era, Mars experienced a persistently wet and neutral-pH environment, forming clay minerals like phyllosilicates (Poulet et al., 2005). Stable bodies of water could have existed, potentially providing conditions favourable for life. While some studies, such as Ojha et al. (2020), suggest alternating wet and dry periods, this era likely represents Mars' most habitable phase.
- **Theiikian Era (~3.8–3.5 Ga):** This era marked a transition toward more acidic conditions, possibly driven by volcanic activity and the loss of Mars' magnetic field, which led to atmospheric thinning. Sulfate minerals, such as jarosite and gypsum, began forming during this time, indicating more briny, acidic waters (Tosca et al., 2018; Bibring et al., 2006).
- **Siderikian Era (<3.5 Ga):** The Siderikian era saw the formation of ferric oxide, marking the planet's transition to its current cold, dry state. However, Stillman et al. (2020) provided evidence of recurring slope lineae (RSL), suggesting that transient liquid water may still exist today in limited, localised conditions.

2.3.4. Modern Discoveries and Current Martian Water

In the Siderikian Era, it became a cold and dry planet. Dundas et al. (2018), however, have identified exposures of ice in the mid-latitude areas of Mars. Using high-resolution imagery from the MRO, the team was able to locate areas where ice is exposed at or near the surface. This was generally in scarp areas. The ice is located just a few metres below the surface, suggesting that Mars has large reserves of water ice. The

fact that these were discovered in mid-latitude regions is intriguing because such regions were considered to be too warm or dry to sustain such ice. Ice deposits have also been found at the poles (Morgan et al., 2022). Whilst at first sight this does not seem a noteworthy discovery, it is when looked at together with the work of Dundas et al., 2018, because it gives credence to the idea that whilst dry today, Mars does, in fact, hold considerable quantities of water in the form of ice. In 2018, Orosei et al. (2018), using radar from the Mars Express mission, detected subsurface liquid water under Mars's southern polar ice cap. The research posited that liquid water exists there due to salts and pressure. Later work by Ojha et al. (2015) identified recurring slope lineae (RSL)—seasonal flows of briny water on Martian slopes—that are formed by liquid water containing salts that cause freezing point depression. These findings tally with those of Dundas et al. (2018). Certainly, all of the evidence points to there being water on Mars (both in ice and briny liquid form), ultimately showing that the history of water on Mars is far more complex and dynamic than had originally been thought. Liquid water is not stable on the surface under current conditions, but these discoveries suggest that localised and transient water activity could persist today.

2.3.5. Geological Features Shaped by Water and Ice

Ancient Martian landscapes exhibit extensive signs of past hydrological activity, such as valley networks (Hynek et al., 2010), outflow channels (Baker and Milton, 1974), and sedimentary deposits (Goudge et al., 2017). Glacial features, studied by Head et al. (2006, 2003), demonstrate that ice has also played a significant role in shaping the Martian surface. Notably, Galofre et al. (2020) suggested that some valley networks may have originated from subglacial drainage rather than surface runoff.

Regions like Cerberus Fossae and Athabasca Valles reveal evidence of both volcanic and aqueous processes (Jaeger et al., 2007; Voigt and Hamilton, 2021). Investigations by Burr et al. (2002) and Hanna and Phillips (2005, 2006) focused on the hydrological properties of these areas, offering detailed reconstructions of flood events and insights into channel morphology.

2.3.6. Implications for Habitability and Future Exploration

Understanding Mars' hydrological evolution is essential for assessing the planet's habitability potential. The early Phyllosian era likely represented the most favourable period for life to develop, with stable bodies of water and moderate pH conditions. As

Mars transitioned to the Theiikian era, the possibilities regarding potential habitability declined due to increasing acidification and atmospheric loss.

Modern exploration efforts, such as NASA's Perseverance rover and ESA's ExoMars mission, continue to investigate ancient water-bearing minerals and the potential for past life. These missions aim to uncover Mars' hydrological history through sample return missions and advanced data collection, building on the foundation of previous discoveries.

2.3.7. Conclusion

The evolution of water on Mars transformed the planet from a wet, neutral-pH environment into a dry, frozen world. Through investigations of ancient hydrological features, mineralogical evidence, and ongoing missions a complex picture of Mars' aqueous history has emerged. While liquid water is scarce today, the data strongly indicates that water once played a central role in shaping the planet's surface and may still influence localised processes. Lauro et al. (2021) provided compelling evidence for subglacial lakes beneath Mars' southern ice cap, indicating environments where liquid water could exist. Further exploration, including missions like NASA's Perseverance rover and ESA's ExoMars, will reveal Mars's potential for harbouring life, be it in the past or present.

2.4. Vulcanicity

2.4.1. Introduction

Mars exhibits a rich volcanic history characterised by a diverse array of volcanic landforms and features. Understanding the nature and implications of Martian vulcanicity is crucial for unravelling the planet's geological evolution and assessing its potential for past and present habitability. By examining various aspects of Martian volcanism, including lava flows, flood lavas, volcanic channels, and magma–water interactions, this section aims to review papers that have elucidated the diverse volcanic processes shaping the Martian surface.

2.4.2. Key Findings

Baker (1982) provided a comprehensive overview of Martian channels, highlighting the role of volcanic processes in channel formation. Notably, volcanic channels on Mars

exhibit distinctive morphological characteristics indicative of lava flow emplacement and erosion processes. Examples such as Valles Marineris and Elysium Mons underscore the influence of volcanic activity on Martian surface features. Plescia (1990) investigated recent flood lavas in the Elysium region of Mars, offering insights into the dynamics of volcanic eruptions and lava flow emplacement. Additionally, crater counts were pivotal in determining the age of the lava flows. By cataloguing and analysing impact craters within and around the lava flow deposits, Plescia established a chronological framework for the volcanic activity in the Elysium region. The abundance, distribution, and state of degradation of impact craters provided important indicators of the relative ages of the lava flows, allowing Plescia to discern periods of volcanic activity and quiescence.

Edgett and Rice (1995) examined very young volcanic, lacustrine, and fluvial features in the Cerberus and Elysium basin region, emphasising the interplay between volcanic processes and surface water interactions. Their findings suggested a complex history of volcanic activity and hydrological processes in the region, with implications for the planet's climatic evolution. Carr (1996) proposed that channels and valleys on Mars are cold climate features formed due to a thickening cryosphere, challenging earlier interpretations of fluvial activity. While acknowledging the role of water in shaping Martian landscapes, Carr emphasised the significance of cryospheric processes in channel formation and modification. Recent work by Horvath et al. (2021), using crater counting to determine the age of lava flows in the Cerberus Fossae region, suggests that the last lava flows occurred between 2 and 10 million years ago. McKenzie and Nimmo (1999) investigated the generation of Martian floods by the melting of ground ice above dykes, highlighting the potential link between volcanic activity and hydrological processes on Mars. Their study suggested that magma-induced melting of subsurface ice could trigger catastrophic flooding events, shaping the planet's surface morphology. Hartmann and Berman (2000) conducted crater count chronology studies of Elysium Planitia lava flows, providing insights into the region's timing and duration of volcanic activity. By correlating crater densities with geological units, they established a chronological framework for volcanic events, elucidating the volcanic history of Elysium Planitia. Keszthelyi et al. (2000) explored terrestrial analogues and thermal models for Martian flood lavas, offering comparative insights into volcanic processes and landform development. By simulating lava flow dynamics and thermal evolution, they provided a framework for interpreting Martian volcanic landforms and assessing their formation mechanisms. Burr et al. (2002) investigated recent fluvial, volcanic, and tectonic activity on the Cerberus plains of Mars, emphasising the role of volcanic processes in shaping surface morphology. Their findings highlighted the complex interplay between

the region's volcanic activity, tectonics, and surface water interactions. Head and Wilson (2002) synthesised general environments and geological settings of magma–water interactions on Mars, elucidating the role of water in modifying volcanic landforms. Their study underscored the significance of hydrothermal processes and magma–water interactions in shaping Martian surface features. Leverington (2004, 2006) proposed volcanic processes as alternative mechanisms of landform development on Mars, challenging conventional interpretations of outflow channel formation. By examining volcanic rilles and landforms near candidate crater-lake sites, Leverington provided alternative explanations for Martian landforms, highlighting the complexity of surface processes on Mars.

2.4.3. Aqueous or Lava?

In the debate surrounding the formation of channels on Mars, two prominent researchers, David Leverington and Devon Burr, have presented contrasting interpretations based on their analyses of Martian surface features. Leverington's research (Leverington, 2008) and Burr's findings (Burr, 2002; Burr, 2007) offer divergent perspectives on whether these channels are primarily the result of volcanic activity or fluvial processes.

Leverington's investigations have emphasised the role of volcanic activity in shaping Martian landscapes. Leverington (2008) conducted extensive analyses of channels in volcanic regions of Mars, particularly in areas such as the Tharsis and Elysium volcanic provinces. He contends that the morphology and distribution of these channels align more closely with features produced by lava flows rather than water-driven processes. Leverington (2008) highlights characteristics such as sinuous channels with levees, streamlined islands, and the absence of extensive sedimentary deposits as evidence of volcanic channel formation. He argues that the low viscosity of Martian lavas and the planet's low atmospheric pressure facilitated lava flows' rapid and extensive carving of channels.

In contrast, Burr's (2002, 2007) research has advocated for a fluvial origin for Martian channels, challenging the prevailing interpretation of volcanic formation. Central to Burr's argument is the detailed examination of Martian valley networks, which she contends bear striking similarities to terrestrial river systems in terms of morphology and distribution. Through analysis of high-resolution imaging data from Mars orbiters such as the Mars Reconnaissance Orbiter (MRO), Burr has identified key morphological features within these valley networks that are characteristic of fluvial

erosion and deposition. She points to dendritic drainage patterns, meandering channels, and evidence of erosion and sediment deposition indicative of past fluvial activity. Burr's approach relies on geomorphological analogies with Earth's river systems, suggesting that similar processes of erosion and sediment transport operated on Mars, albeit under different environmental conditions.

The key differences between Leverington's and Burr's interpretations lie in their underlying assumptions about the dominant geological processes operating on Mars and the analogies they draw with terrestrial landscapes. Leverington emphasises the erosional effects of volcanic activity, drawing parallels with features produced by lava flows to interpret Martian channels as the product of ancient volcanic activity. In contrast, Burr favours a fluvial explanation, citing the geomorphological similarities between Martian valley networks and terrestrial river systems as evidence of water-driven channel formation.

By juxtaposing Leverington's focus on volcanic processes and Burr's emphasis on fluvial processes, the debate over the origins of Martian channels underscores the complexity of interpreting planetary surface features and the importance of interdisciplinary approaches in unravelling the geological history of Mars. While Leverington's volcanic interpretation challenges conventional assumptions about the role of water in shaping the Martian landscape, Burr's emphasis on fluvial processes highlights the potential influence of water in sculpting Martian terrain. Reconciling these contrasting viewpoints may require further empirical data and integrated analyses from future Mars missions.

2.4.4. Concluding Remarks

Studies investigating Martian volcanicity, such as those by Baker (1982) and Edgett and Rice (1995), have significantly enhanced our understanding of the planet's volcanic history. However, a lack of comprehensive analysis of the interplay between volcanism and tectonics remains. While some studies, like Burr et al. (2009), review Amazonian-aged extensional-tectonic megaflood channels on Mars, they may not fully integrate seismic data into their volcanic models. Brown and Roberts' work in 2019 and 2023 focuses on flow channels and repeated, cross-cutting, and spatially migrating outflow channel formation in Grjótá Valles, Mars, respectively, highlighting the dynamic nature of Martian volcanic activity. Future research should aim to incorporate seismic observations into volcanic models, allowing for a more holistic understanding of the processes driving Martian volcanism and tectonics.

2.5. Seismicity

2.5.1. Introduction

Seismic activity on Mars offers valuable insights into the planet's internal structure, tectonic processes, and geological evolution. This brief literature review attempts to trace the history of our understanding and knowledge of Martian seismicity, drawing upon the work of seminal studies.

2.5.2. Key Findings

Nakamura and Anderson (1979) made ground-breaking observations of Martian wind activity using a seismometer deployed at the Viking lander 2 site. Their findings provided the first direct evidence of atmospheric disturbances on Mars, shedding light on the planet's atmospheric dynamics and surface interactions. However, there is still ongoing debate as to whether the observations and signals detected were, in fact, seismic in origin. Hall et al. (1986) conducted tests of lithospheric loading models for the formation of tectonic features in the Elysium region of Mars. Analysing surface topography and crustal deformation patterns offered valuable insights into the role of lithospheric stresses in shaping Martian tectonic landscapes, advancing our understanding of the planet's geodynamic processes. Golombek et al. (1992) predicted Mars' seismicity from surface faulting, proposing a correlation between surface fault patterns and potential seismic activity. Their study laid the foundation for subsequent seismic investigations on Mars, providing a framework for identifying seismically active regions and fault networks. McKenzie and Nimmo (1999) proposed that Martian floods could be generated by the melting of ground ice above dykes, highlighting the potential role of subsurface hydrological processes in inducing seismic activity. Their study offered new insights into the interconnected nature of Martian geophysical phenomena, linking seismicity to surface–water interactions and volcanic activity. Hanna and Phillips (2006) investigated the tectonic pressurisation of aquifers in the formation of Mangala and Athabasca Valles on Mars. By modelling aquifer pressurisation dynamics, they elucidated the mechanisms driving catastrophic outflow events and associated seismicity, enhancing our understanding of hydrological processes and their seismic implications on Mars. Knapmeyer et al. (2006) developed working models for the spatial distribution and level of Mars' seismicity, providing valuable insights into the distribution of seismic activity across the planet's surface. Their study contributed to the refinement of Martian seismological models, guiding the selection of target regions for future seismic investigations. Burr et al. (2009) conducted a review of extensional–

tectonic megaflood channels on Mars, highlighting the role of tectonic processes in generating catastrophic floods and associated seismic events. Their analysis underscored the dynamic interplay between tectonics, hydrology, and seismicity in shaping Martian landscapes. Giardini et al. (2020) presented a comprehensive overview of Martian seismicity, synthesising data from seismological observations and numerical models. Their study provided key insights into marsquakes' frequency, magnitude, and distribution, advancing our understanding of Martian interior dynamics and crustal properties. Perrin et al. (2022) investigated the geometry and segmentation of Cerberus Fossae on Mars, elucidating the structural complexities and seismic implications of fault systems in the region. Analysing fault patterns and subsurface geometry provided valuable constraints on the occurrence and properties of marsquakes in the Cerberus Fossae region.

2.5.3. Concluding Remarks

While previous studies by Nakamura and Anderson (1979) and Phillips and Grimm (1991) have shed light on Martian seismicity, there remain gaps in understanding the spatial and temporal variations in marsquake magnitude across different regions of the planet. Although some research, such as that conducted by Knapmeyer et al. (2006) and Taylor et al. (2013), has attempted to address this issue, these studies may not fully capture the nuances of Martian seismic activity. The work of Brown and Roberts (2019) focuses on flow channels, while their 2023 paper concentrates on the repeated, cross-cutting, and spatially migrating formation of outflow channels in Grjótá Valles, Mars. Though indirect, their research underscores the need for a deeper understanding of the geological processes driving seismic activity. Future studies should aim to integrate seismic observations with high-resolution geological mapping to elucidate the relationship between tectonics, surface features, and seismicity on Mars, thus filling critical gaps in our knowledge of Martian geophysics.

2.6. Surface and Subsurface Geological Processes on Mars

2.6.1. Introduction

Mars' similarity to Earth and its potential for harbouring signs of past or present life is intriguing. While much attention has been devoted to Mars' surface features, such as its polar ice caps, canyons, and ancient river valleys, understanding its internal structure is essential for unravelling its geological history. Numerous studies have contributed to our understanding of Mars' internal composition, shedding light on its

formation and evolution. Of particular interest is the Cerberus Fossae region, which has emerged as a pivotal area for understanding Mars' geology and seismic activity.

2.6.2. Evidence from Geological and Seismic Activity

Early missions, like the Viking landers of the 1970s, provided the first glimpses of the Martian atmosphere and surface. Mass spectrometry analysis revealed organic compounds, water, and volatile constituents, sparking intrigue about Mars' potential habitability. However, it was not until subsequent missions and studies that the understanding of Mars' internal dynamics began to take shape. Carr (1979) provided insights into the formation of Martian flood features, suggesting the release of water from confined aquifers as a mechanism. Baker and Milton (1974) highlighted erosion by catastrophic floods as a significant geological process on Mars and Earth.

The detection of Martian wind activity by a seismometer at the Viking lander 2 site, as reported by Nakamura and Anderson (1979), offered valuable insights into the planet's geological dynamics. Brass (1980) further explored the stability of brines on Mars, shedding light on the potential presence of liquid water beneath the surface. Over the years, advancements in technology and the accumulation of data from various missions allowed for more detailed investigations. Tanaka (1986) provided a comprehensive stratigraphy of Mars, offering insights into its geological history. Plescia (1990) identified recent flood lavas in the Elysium region, indicating dynamic geological processes. The notion of Martian seismicity gained traction with studies like Phillips and Grimm (1991) and Golombek et al. (1992), which predicted and detected Mars' seismic activity. This seismicity was further explored by Banerdt et al. (1992) and Zuber et al. (1992), laying the groundwork for understanding Mars' interior structure. The Cerberus Fossae region emerged as a focal point for research, with studies like Vetterlein and Roberts (2009) and Burr et al. (2009) providing insights into its structural evolution and geological activity. Pendleton (2015) and Nahm et al. (2016) contributed to understanding dike intrusion-related processes in this area. Advancements in remote sensing technology, such as those used by Dundas et al. (2018) and Horvath et al. (2021), revealed widespread exposures of ice in the mid-latitudes and evidence of geologically recent explosive volcanism. Meanwhile, Magee and Jackson (2021) explored the surface expression of dike-induced faults, offering clues about subsurface dike geometry.

2.6.3. Geological Significance of Cerberus Fossae

Recent studies have focused on the Cerberus Fossae region, a prominent tectonic feature on Mars. Burr and Parker (2006) provided insights into flood sediment deposition in the area, highlighting its geological significance. Pendleton (2015) proposed a link between Cerberus Fossae and recent groundwater flow, shedding light on the region's hydrological history. Nahm et al. (2016) further supported the notion of dike intrusion-related formation and modification in Cerberus Fossae, emphasising its role in Mars' volcanic activity.

2.6.4. Concluding Remarks

From early glimpses provided by the Viking landers to recent advancements in remote sensing technology, our understanding of Mars' geological evolution and seismic activity has grown exponentially. The Cerberus Fossae region stands as a testament to the complexity of Martian geology, offering valuable insights into the planet's past and present dynamics. As exploration continues, further discoveries are poised to deepen our understanding of Mars' internal workings and place it in the broader context of planetary science.

2.7. Recent and Ongoing Activity on Mars

2.7.1. Introduction

Recent findings have shown that Mars, contrary to being a dead planet, has areas that could well be still volcanically, tectonically, and hydrologically active. This section of the chapter looks at recent research work that investigates ongoing geological processes and how such work is reconfiguring the established view that Mars is dormant, showing instead that there are pockets on the Martian surface that suggest geological processes are still active.

2.7.2. Volcanism and Tectonic Activity in Elysium Planitia

The volcanic plains in Elysium Plains have been dated to between 53 ± 47 and 210 ± 12 million years (Horvath et al., 2021). Such young ages suggest that the planet is still volcanically active, supporting Neukum et al.'s (2004) hypothesis that there has been recent volcanic activity on the planet.

2.7.3. Seismic Activity Detected by InSight

Giardini et al. (2020) and Banerdt et al. (2020) studied data recorded by the InSight seismograph and proposed that the seismic signals recorded are due to stress adjustments within Mars's crust, either from tectonic shifts or volcanic activity. The fact that seismicity appears to be ongoing in a region like Cerberus Fossae only serves to bolster the idea that certain pockets on the Martian surface, in particular in Elysium Plaitia, are not only active but still evolving (Jacob et al., 2022).

2.7.4. Impact Cratering and Martian Subsurface Probing

Research has shown the importance of using fresh impact craters to understand Martian geology and environmental history, as each impact crater 'peels' back layers of the subsurface that were hitherto inaccessible (Daubar et al., 2013; Malin et al., 2006). Given the information that impact craters can reveal about the planet's history, it is all the more intriguing that recent work by Daubar et al. (2024), studying InSight data, suggests that a significant amount of seismic events detected by InSight, especially those in the very high-frequency category, are in fact due to impact events. This is extremely important because **a.** it would suggest that the Martian surface is being modified by impact events at a greater rate than originally thought, and **b.** "Knowledge of the recent impact rate, even if only over a narrow window in time, can be applied to chronology systems to help calibrate crater count-based estimates of surface ages." (Daubar et al., 2024). In short, how scientists understand the age of the planet's surface may need to be revised.

2.7.5. Evidence of Water Activity

The possibility of there being liquid water on Mars is intriguing. Research on Mars's water history has shown that it is more complex and dynamic than previously thought. Dundas et al. (2018) identified significant subsurface ice in mid-latitudes and the southern polar regions, respectively. Lauro et al. (2021) showed evidence of subglacial lakes under the southern polar ice cap, while Ojha et al. (2015) noted seasonal briny water flows. Localised liquid water may exist on Mars, with the emphasis being on the adjective 'localised'. The idea that localised liquid water may exist in certain pockets on the Martian surface lends weight to part of the work in this thesis, that liquid water may have recently carved channels on the Martian surface in the Cerberus Fossae region. Much more research is required in the search for liquid water on Mars.

2.7.6. Cerberus Fossae: A Key Region for Understanding Recent Geological Activity

The Cerberus Fossae is a particularly important region for understanding Mars' recent geological evolution. Formed in the Late Amazonian, possibly within the last 10 million years, the Cerberus Fossae represent a tectonically active area. These fissures are thought to have been associated with both volcanic and aqueous processes, such as the sourcing of both lava and water that carved out features like Athabasca Valles (Burr et al., 2002). The discovery of ongoing seismic activity in this region by InSight further emphasises its significance in the study of Martian geology (Jacob et al., 2022).

The Cerberus Fossae's relatively young age and recent seismic activity raise important questions about the current state of Mars' subsurface. Could volcanic or tectonic activity drive subsurface heating, potentially sustaining habitable conditions? The potential presence of subsurface liquid water, combined with ongoing tectonic shifts, suggests that Mars may not only be geologically active but could also harbour environments suitable for microbial life.

2.7.7. Mars' Geological History and Its Broader Implications

Mars has undergone profound changes over the last 4.6 billion years. It transitioned from a potentially warm and wet planet with conditions that might have supported life to the cold, dry, and largely inactive world we see today. However, recent findings indicate that Mars is not entirely static. Studies of its volcanic plains, seismic activity, and impact craters show that the planet continues to evolve geologically.

The ongoing research from missions like InSight and the study of features like the Cerberus Fossae provide crucial insights into the planet's recent geological activity. These findings help researchers to refine their understanding of planetary evolution and to assess the potential for habitable environments on Mars, both in the past and present. As new data continues to be collected, our understanding of Mars' geological activity will only deepen, potentially opening new chapters in the exploration of this enigmatic planet.

2.7.8. Conclusion

In summary, recent literature, including work from the InSight mission (Jacob et al., 2022), has shed light on Mars' ongoing activity, particularly in regions like Elysium

Planitia and Cerberus Fossae. Mars once considered a geologically dead planet, now appears to have a dynamic interior that continues to shape its surface, offering insights into both the planet's past and the potential for future exploration.

CHAPTER 3.

METHODS

3.1. Introduction

The research presented in this thesis examines the evidence for two seemingly unrelated but potentially interconnected geological processes that have taken place along the northernmost Cerberus Fossae, close to Grjótá Valles in Elysium Planitia. One is the recent seismic activity in the northernmost Cerberus Fossae identified through the observation and measurement of mobilised boulders, and the other is the flow episodes that formed channels in the late-Amazonian period. These flow episodes originate from the northernmost Cerberus Fossae and flow towards the northeast, east, and southeast. The region's proximity to the Elysium Mons and the smaller Albor Tholus volcanoes and the possibility of ongoing subsurface volcanic activity in these areas create a nexus between the two topics.

However, to identify the connection, both geological processes had to be measured to allow quantitative data collection on both processes that could be repeated. As discussed in this Chapter, qualitative research was also needed. Once data measurements had been collected for both geological processes, the next step was to use a series of steps that involved using data from the two aforementioned geological processes, published data on crater counts within the flow channels, published SEIS seismic data, and the use of a package of MATLAB tools called FiSH (Fissile Earthquake Seismology) to iterate the slip rate of the northernmost Cerberus Fossae (seismicity: boulder trail populations as a proxy seismograph used in conjunction with SEIS data; flow channels: geomorphological analyses that reveal multiple flow channels of decreasing age west–east combined with crater count ages; FiSH code to iterate slip rates of faults based on Mw estimates/data). Chapters 4, 5, and 6 discuss the research findings. However, this chapter focuses on how the data was collected and why each specific method was chosen over another. The equipment and software used will also be discussed, along with any difficulties encountered during data collection and analysis.

3.2. Identifying Boulder Trails and Fallen Boulders—High-Resolution Imaging Science Experiment (HiRISE) Images

A study of the northernmost Cerberus Fossae, an approximately 200 km long set of en echelon graben segments located within the Grjótá Valles channel system, using Google Earth Pro using the CTX Mosaic feature (a mosaic composite of all the Mars Reconnaissance Orbiter (MRO) Context Camera (CTX) images available) revealed that both sides of the fault and the base were littered with boulder trails, some with a boulder at the terminus of the trail; with others many trails without a boulder at the terminus. The width of the trails varied, as did their lengths. However, the resolution of the CTX imagery (5–6m/pixel) (Malin et al., 2007) does not have the sufficient resolution required to discern details and to make measurements. To have imagery of a quality that is high resolution enough, images captured by the High-Resolution Imaging Science Experiment (HiRISE) camera on the NASA Mars Reconnaissance Orbiter spacecraft were used. The resolution of HiRISE images is ~25cm–30cm/pixel, which is essential for the data collection required in this research. However, whilst CTX imagery covers nearly 100% of the Martian surface (Malin et al., 2007), its resolution prevents it from being a suitable tool for detailed analysis of boulder trails. HiRISE images, whilst of excellent resolution, have limited ‘footprints’ or coverage of Mars, with approximately only 4% coverage of the surface and highly non-uniform coverage (McEwen et al., 2007). Given the limited coverage, it was fortuitous that across the study region, a sufficient number of HiRISE footprints existed to cover a significant portion of the required study area. (Figure 3.1c). Table 3.1. shows the HiRISE images used in the research and identifies images with stereo pairs. Figure 3.2a–b compares CTX mosaic imagery resolution of location area 10 (corresponding with HiRISE footprint ESP_018075_1955) with that of the HiRISE image footprint ESP_018075_1955.

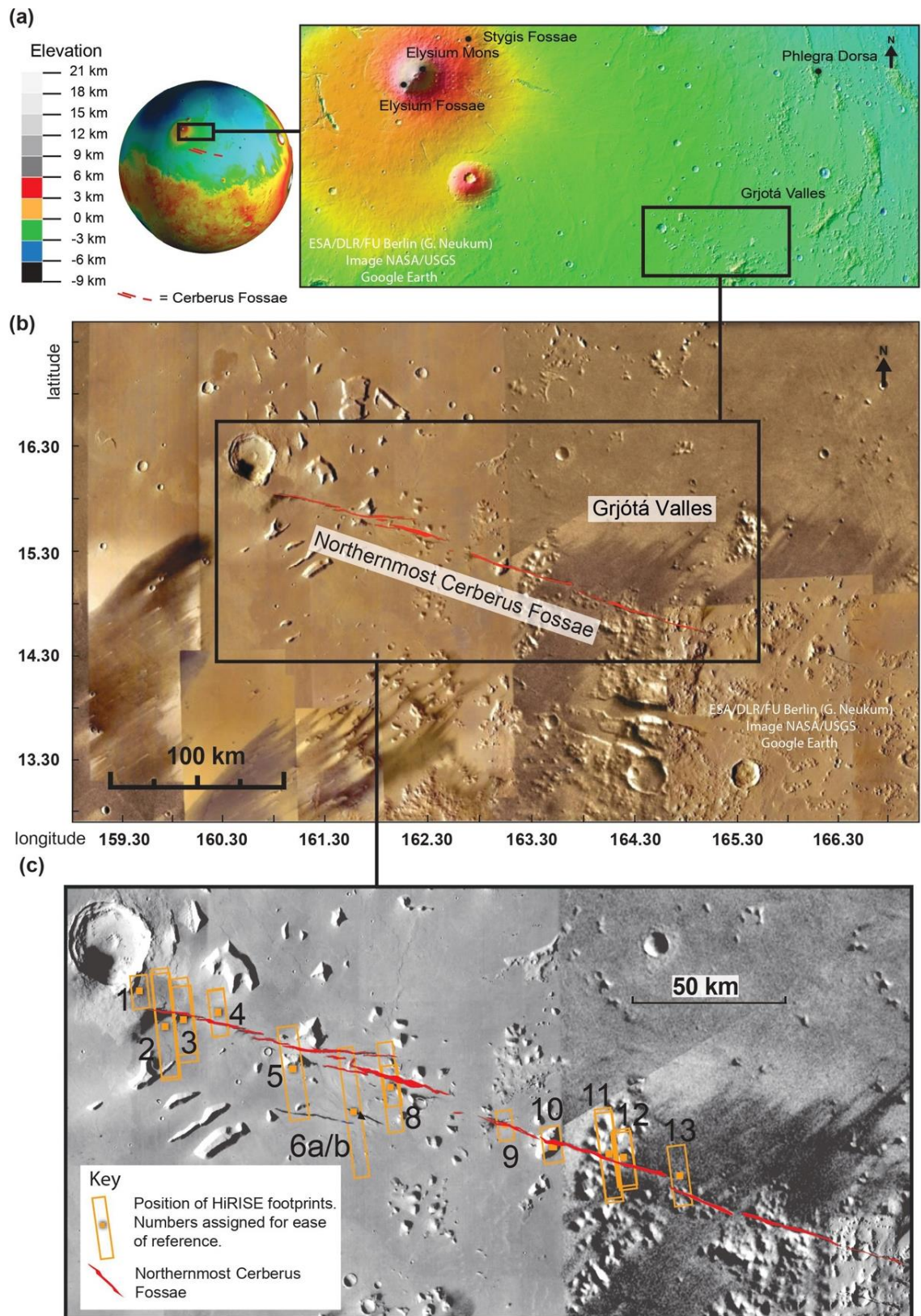


Figure 3.1. a. and b. Location map for the northernmost Cerberus Fossae c. The exact position of the HiRISE footprints (orange rectangles) along the northernmost Cerberus Fossae (red).

Table 3.1. Shows the HiRISE images used in the research, the number assigned to each number by the author, and the latitude and longitude together with the map projected scale.

Number Assigned to Image in the Research	HiRISE image name	Stereo Pair (Yes/No)	Latitude (centred)	Longitude (east)	Map projected scale
1	PSP_008502_1965	N	16.250°	160.575°	25 cm/pixel
2	ESP_018774_1965	Y ESP_018141_1965	16.085°	160.723°	50 cm/pixel
3	PSP_006999_1965	Y PSP_006709_1965	16.100°	160.828°	25 cm/pixel
4	ESP_025011_1965	Y ESP_025156_1965	16.141°	161.011°	25 cm/pixel
5	ESP_018708_1960	N	15.819°	161.448°	50 cm/pixel
6a	ESP_027345_1955	N	15.571°	161.792°	50 cm/pixel
6b	ESP_027345_1955	N	15.571°	161.792°	50 cm/pixel
8	ESP_026712_1960	Y ESP_026356_1960	15.715°	162.013°	25 cm/pixel
9	PSP_006287_1955	N	15.479°	162.677°	25 cm/pixel
10	ESP_018075_1955	N	15.386°	162.928°	25 cm/pixel
11	ESP_028400_1955	Y ESP_033371_1955	15.329°	163.242°	25 cm/pixel
12	PSP_010361_1955	Y PSP_006788_1955	15.311°	163.336°	25 cm/pixel
13	PSP_007790_1955	N	15.209°	163.657°	25 cm/pixel

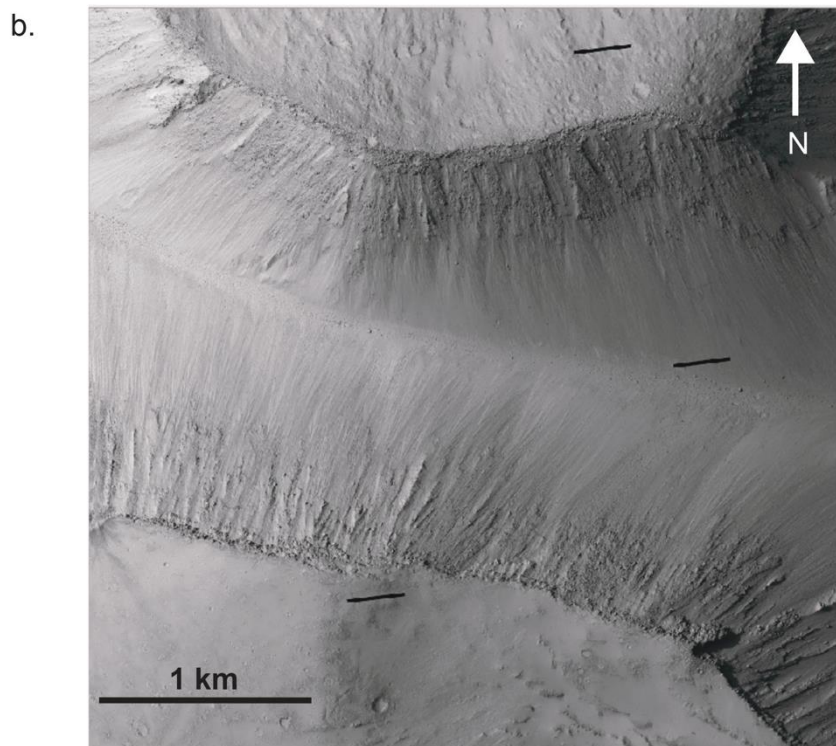
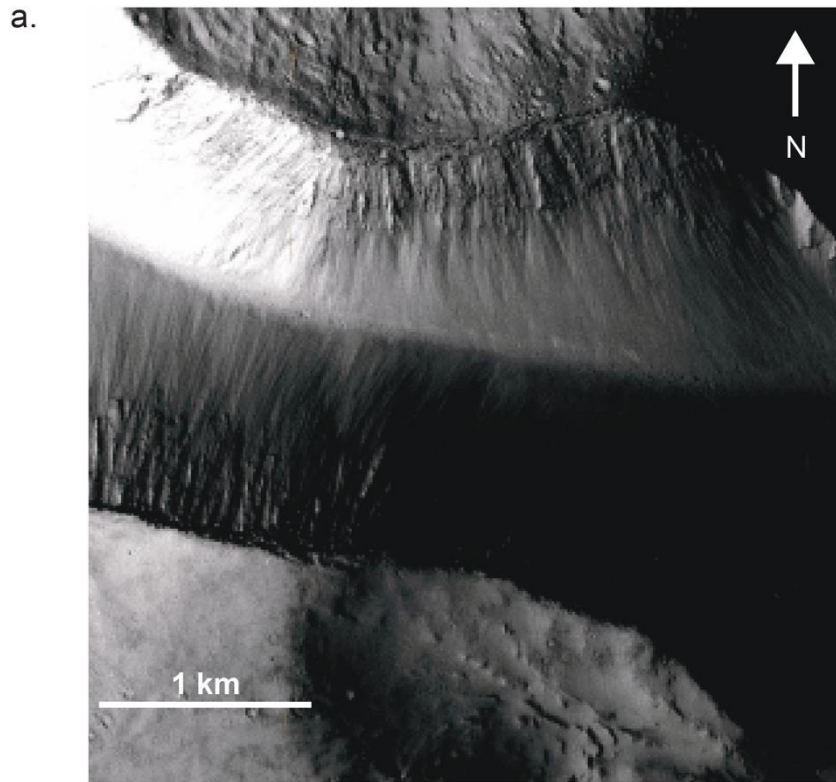


Figure 3.2. a. Seam-corrected and seam-mapped mosaic of Mars rendered at 5.0 m/px using Context Camera (CTX) data from the Mars Reconnaissance Orbiter (MRO), centred at 15.40°N / 162.923°E, the approximate location of the HiRISE footprint ESP_018075_1955. Of note is that boulder trails can be seen, but the resolution is not of sufficient quality to be sure whether these are boulder trails or something else. b. A detail from HiRISE footprint ESP_018075_1955 was resolved using HiVIEW (version 1.5.0), the image viewer and data explorer for very large JP2 files. With a resolution of ~25cm/px, the resolution is excellent and allows for a much clearer and more detailed examination of the Martian surface. Note that in comparison to the CTX mosaic image, the details are much clearer to resolve.

HiRISE images of Mars were used in this research because there were a sufficient number of clear HiRISE footprints across the northernmost Cerberus Fossae (Figure 3.1 c; Table 3.1). The HiRISE camera's high-resolution capability provides an unprecedented resolution of the Martian surface. National Aeronautics and Space Administration (NASA) HiRISE images were accessed using the Planetary Data System (PDS) node at the University of Arizona (<http://hirise.lpl.arizona.edu/>). They were then opened in HiVIEW (<https://www.uahirise.org/hiview/>), a data explorer and image viewing application supporting the JPEG2000 image format of images taken by HiRISE. A JPEG2000 contains the metadata that describes the image, stored as compressed codestreams. The JPEG2000 codestream is based on a Discrete Wavelet Transformation (DWT) of the original image pixel values. This codestream has characteristics that enable it to be selectively decoded for all or part of the entire image area at less than the original image resolution and less than the full quality level of the original image while maintaining high-quality viewing fidelity. HiVIEW uses the JPEG2000 codestream's characteristics by only rendering the area of the image needed at excellent resolution. This means that the whole images are not stored on the computer, which would have been prohibitive given the sizes of the images, with individual HiRISE images typically ranging from tens of megabytes to a few gigabytes. JPEG (Joint Photographic Experts Group) is a commonly used image format that applies lossy compression (Wallace, 1991), meaning that some data is discarded to reduce the file size. However, the compression process can cause a slight loss in image quality, especially when repeatedly saved. As such, during this research, the JPEG format (Skodras et al., 2001; Taubman and Marcellin, 2002) was used carefully to ensure that images were saved with minimal compression settings. Accordingly, this preserved the image quality, essential to analysing boulder trails, as confirmed by the resolution remaining sufficient for measurement and comparison with HiRISE data. Using JPEG with maximum quality settings made no noticeable impact on the resolution or clarity necessary for the study. An example of the excellent resolution of HiRISE images is shown in Figure 3.3 a–c. A section of the HiRISE stamp (footprint) ESP_018075_1955_RED (footprint number 10, Figure 3.1; Table 3.1.) image is shown at different magnifications. Getting 'closer' to the surface and the resolution of the imagery remains excellent. As Figure 3.3 a–c shows, boulder trails and boulders are discernible in a. In b and c, details are visible, such as the shapes of boulders, whether the boulder trails have gaps, an indication of whether a boulder bounced, and whether boulder trails have a boulder at their terminus. Such detail was essential as it permitted measurements of boulder trail density, boulder trail width, and size of boulders to be measured.

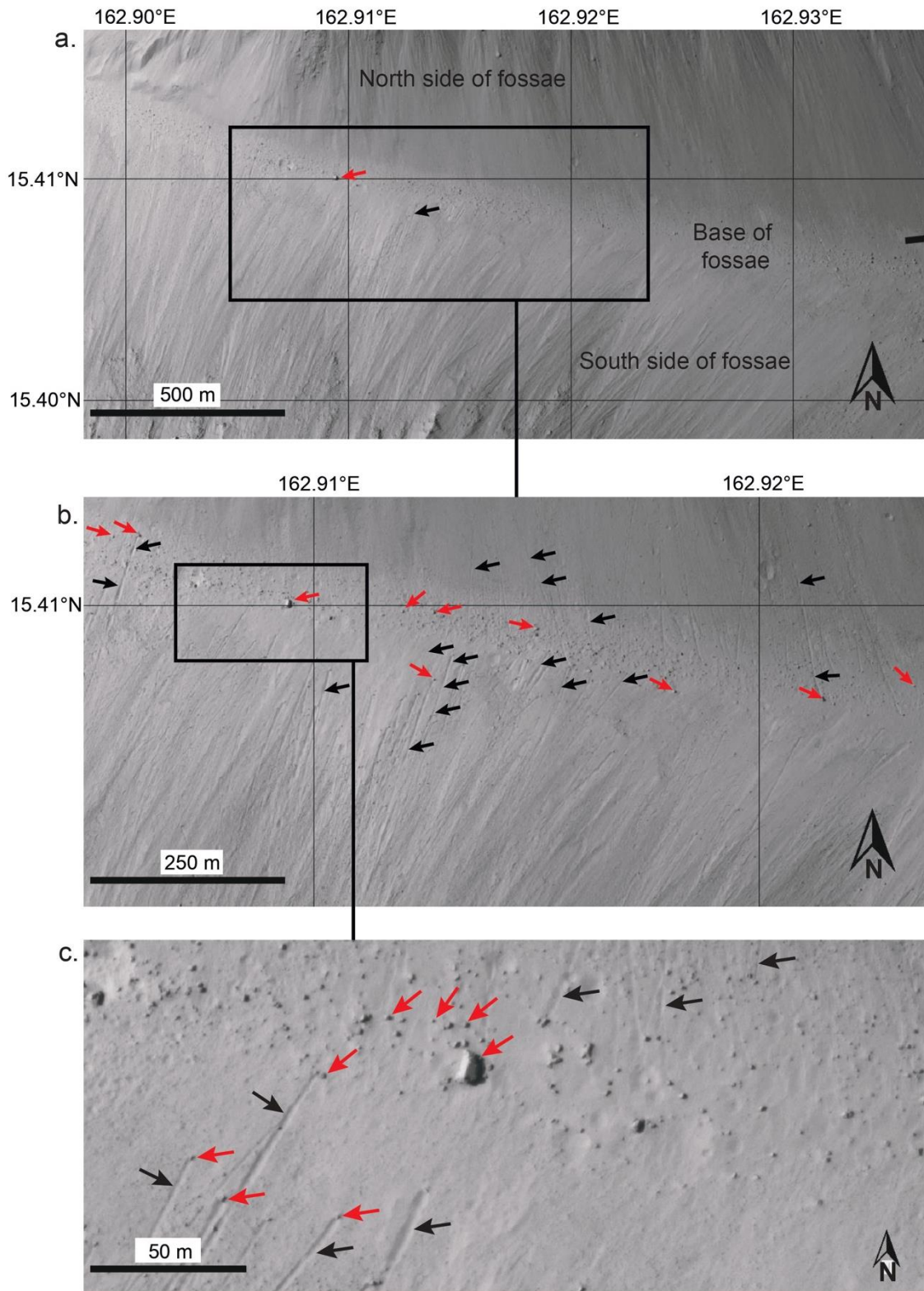


Figure 3.3. Three images of full-resolution HiRISE stamp (footprint) ESP_018075_1955_RED (footprint number 10, Figure 3.2.1. and Table 3.2.1.) The images were resolved in HiVIEW (version 1.5.0), the image viewer and data explorer for very large JP2 files at a ~25cm/px resolution. a. A view of the fossae base and northern and southern inner-slopes of the fossae. Note that few boulders and boulder trails can be fully discerned. b. A close-up image of the black box from a. The excellent resolution of the HiRISE image allows for more boulders and boulder trails to be clearly identified. c. A close-up image of the black box from b. The excellent resolution provides for a full investigation into boulders and boulder trails, with the size and

shape of boulders clear. It is also possible to identify if boulder trails have their boulders at the terminus and whether boulders have bounced down the slopes. It even allows for an analysis of the degree of degradation of the boulder trails. Black arrows indicate boulder trails; red arrows indicate fallen boulders.

Once the locations of the HiRISE images were identified, the images were analysed sequentially using HiVIEW (as discussed previously) to locate clear boulder trails and fallen boulders inside the northernmost Cerberus Fossae. Once this was completed for a particular location using HiVIEW, an image of the area was saved, ensuring that the image size scale was 1.0 to ensure that each image was saved at full resolution. Progressively, each HiRISE image was studied, boulder trails and fallen boulders were identified, and each 'close-up' image from HiVIEW was saved. Each image from each location was then, where necessary, merged with the other images from a location in Adobe Illustrator. The final images were saved as JPEGs.

3.2.1. Measuring Features Identified in HiRISE Images Using Google Earth

The HiRISE images as JPEGs were imported into Google Earth Pro (version 7.3) as georeferenced image overlays. This was carried out so that the range of measuring tools available in Google, such as the ruler tool, could be utilised. The georeferencing process involved selecting between 5 and 10 control points for each HiRISE image, matching identifiable features in both the HiRISE images and Google Earth Pro. A linear transformation was then applied to ensure accurate placement of the images. This method allowed for basic fitting of the image overlays with minimal distortion. While more complex transformations, such as polynomial or spline, were not required, careful control point selection minimised potential positional errors, ensuring that measurements of boulder trails and fractures were accurate. It was important to easily and accurately measure many features, including boulder trail length, width, and distances across the northernmost Cerberus Fossae. Another software application was considered (JMARS, developed by Arizona State University's Mars Space Flight Facility) but was not used for reasons discussed in Section 3.2.2. There were 19 areas covered by HiRISE imagery along the study area of the northernmost Cerberus Fossae (Table 3.1). Six of the locations are stereo pair-HiRISE images. One of the images (ESP_027345_1955) covers an area that has six fractures, two of which were required for this study, with one (ESP_027345_1955) split into two images (6a and 6b), meaning 13 images were used in total. Once each of the merged HiVIEW images for each HiRISE image was saved as JPEGs and imported into Google Earth as georeferenced image overlays, systematic measurements were undertaken for each image.

3.2.2. Potential Problems and Alternative Software Options

After selecting HiRISE as the preferred format for the images to be studied, due to HiRISE's high resolution (approximately 25cm per pixel), it was crucial to confirm that the HiRISE map projections and image overlay process in Google Earth Pro did not distort the images to an extent that would cause inaccuracies in any measurements taken in Google Earth Pro. Such inaccuracies would render the research findings/data flawed.

HiRISE images are processed using a local equiarectangular projection that is specific to the central latitude of each image. As such, the projection is adjusted for each individual image based on its latitude, ensuring minimal distortion. This is important to ensure an accurate representation of features between latitudes 65°S and 65°N, meaning that measurements taken during this research were accurate. Given that the images used in this research are well within this range and are relatively close to the equator, it was considered that the shape distortion of the images used in this research would be minor and not affect measurements. However, it was important to double-check this by checking measurements taken using Google Earth Pro against ArcGIS Pro (versions 2.1 and 2.2). The values were similar to those from Google Earth Pro to the extent that results were unaffected, with a <1% difference in distance between ArcGIS and Google Earth Pro at the latitudes studied. Once each of the merged HiVIEW images for each HiRISE image was saved as JPEGs and imported into Google Earth Pro as georeferenced image overlays, systematic measurements were undertaken for each image.

Java Mission-planning and Analysis for Remote Sensing (JMARS) is a geospatial information system (GIS) developed by Arizona State University's (ASU) Mars Space Flight Facility. One of its functions is to provide data-analysis tools to scientists and the general public. It provides a platform for visualising and analysing data from different Mars missions, including images and other scientific data (Christensen et al., 2009). HiRISE and CTX images are available through the platform. It was considered for use to assist in data collection and image analysis. However, the user interface proved to be slow, cumbersome, awkward, and prone to frequent glitches, such as causing the screen to freeze. As such, JMARS was not used for image analysis and measurements. However, the current version of JMARS (version 5.3.15.2) is an improvement on earlier versions and is far more user-friendly than earlier versions, albeit still prone to freezing. As such, if the research were to have begun this year, it is

possible that JMARS would have been used in conjunction with HiVIEW and Google Earth.

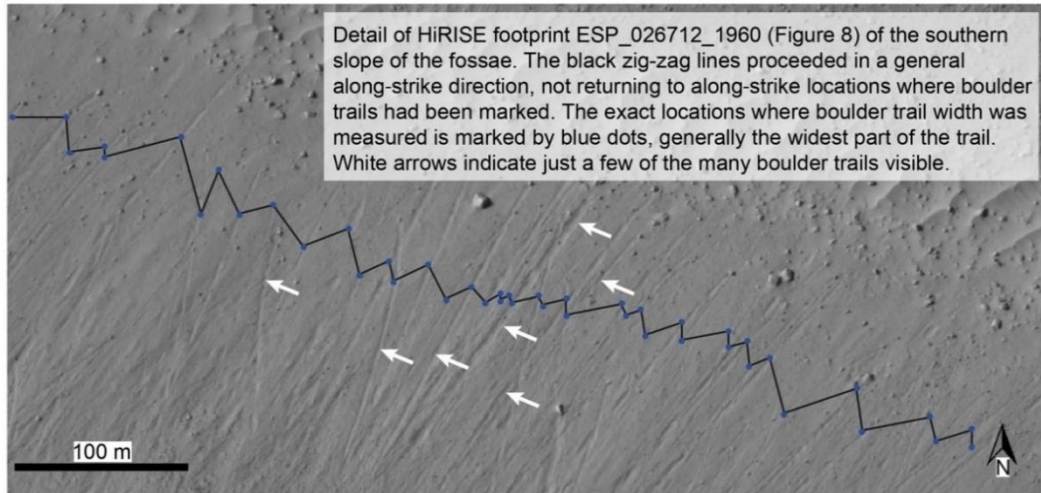
3.2.3. Measurements, Data Collection, and Analysis

3.2.3.1. Boulder Trails Measurement

For each of the 13 HiRISE images, the location of every boulder trail that could be identified in each of the 13 areas along approximately 1.5- to 6.5-km-long transects along the slopes immediately adjacent to the floors of the graben was recorded. These transects were chosen because (a) they existed at the bases of steep slopes along fault-controlled cliffs and (b) fine-grained deposits (probably aeolian sand and dust) were present that preserved boulder trails. Measurements were not made where the surface appeared too coarse to preserve boulder trails as the resolution (~25 cm/px) limits the ability to reliably distinguish boulder/rock sizes smaller than ~1 m.

An example of this procedure is shown in Figure 3.4.a. The zig-zag lines in this figure show how measurements of the boulder trails proceeded in a general along-strike direction. Some locations had a great density of boulder trail populations, and this zig-zag counting method helped to ensure accuracy whilst counting and avoid double-counting. The exact locations where boulder trail width (blue dots) were measured were generally the widest part of the trail. These locations were marked to allow revisits of the locations to measure boulder trail width. The along-strike distance was recorded as the longitude of each blue dot (Figure 3.4 a) for conversion into the values of boulder trails per kilometre using trigonometry and a conversion factor for degrees longitude into kilometres. The results of this conversion procedure are shown and explained in Chapter 4 (Section 4.3.1).

a.



b.

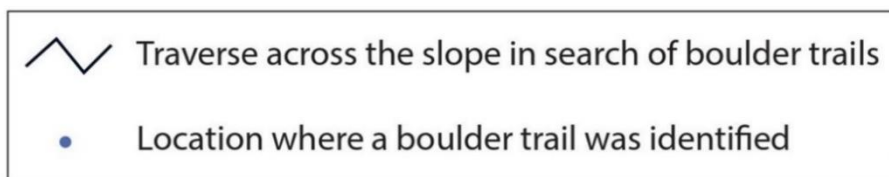
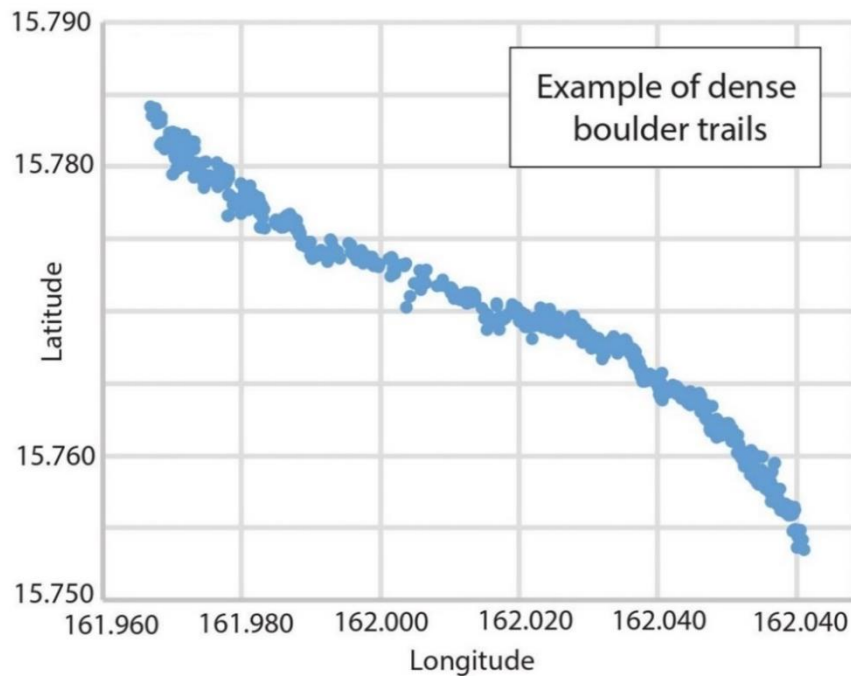


Figure 3.4. An example of a boulder trail density measurement for Image 8 (HiRISE footprint ESP_026712_1960) is centred at 15.766°N / 162.033°E. a. A HiRISE image detail showing the fossae's base and southern slope. Vertical lines of varying widths and orientations mark the slope. These are the boulder trails (some are highlighted with white arrows). There are also many fallen boulders on the lower section of the slope and at the base of the fossae. The black zig-zag line that connects the boulder trails was the method used to count boulder trails across HiRISE images. The blue dots at the apex of the zig-zags are the widest sections of that particular boulder trail. This was important as boulder trail width measurements were collected after the boulder trail measurements were taken. b. Graph showing location and density of boulder trails found along a WNW–WSE transect traversing 0.03° of longitude. The boulder trail density measurements are discussed in section 3.2.3 of this chapter.

In summary, the along-track lengths of the zig-zag tracks were not used in any calculation but served to record exactly how boulder trail populations were traversed and where measurements were made. The system employed here was reliable, and there exists a high level of confidence that in areas where boulder trail densities were relatively low ($\lesssim 45$ boulder trails per kilometre), all trails were counted. In areas where boulder trail density was greater ($\gtrsim 45$ boulder trails per kilometre), it was difficult to recognise every boulder trail because some boulder trails coalesce. Also, it is important to note that boulder trails of $\lesssim 95$ cm width were probably not resolved, leading to an underestimation of the boulder trail density. This being the case, the hypothesis depends on the largest mobilised and, therefore, the widest boulders trails.

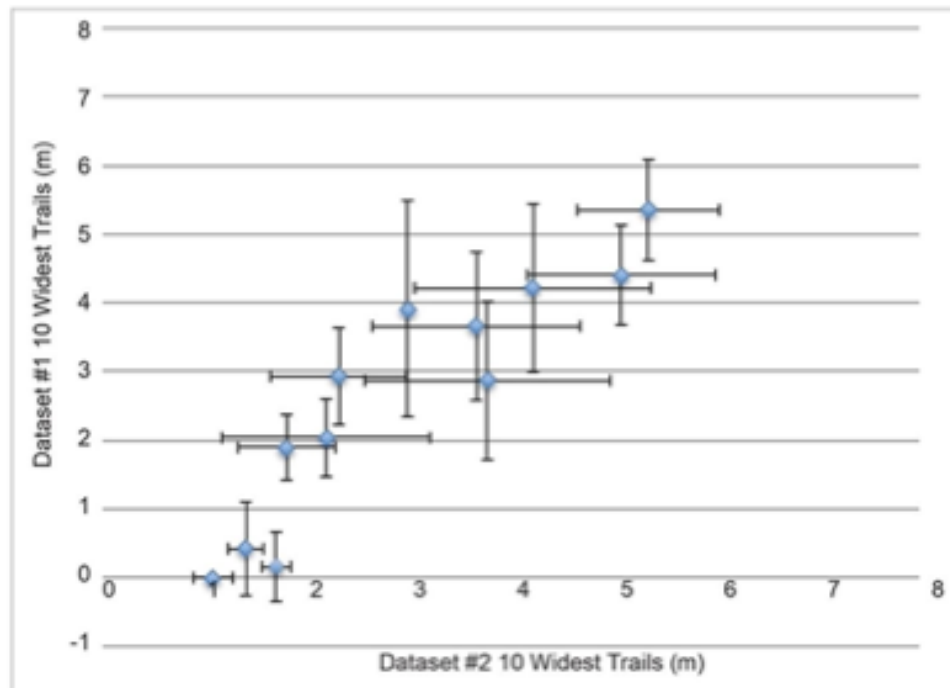
3.2.3.2. Boulder Trail Width Measurement

Boulder trail widths were defined as the width between the raised levees or sharp edges that formed on the underlying substrate as the boulder traversed across it. All boulder trails were measured, including those without an identified boulder at the trail's terminus. The widths were measured at their widest point to exclude measurements where the boulder bounces and leaves a narrower trail. There is cross-image variation in boulder trail density on HiRISE images. Where one can see that the substrate is coarse-grained, with visible boulders, no trails exist. Thus, measurements of the distance across areas where one could gain continuous records on regions where the substrate appeared fine-grained were made, and the values were converted into numbers per kilometre.

The ten widest boulder trails' widths from each of the thirteen images were used to find a mean width value to estimate the dimensions of mobilised boulders. To ensure accuracy when measuring distances using the ruler tool in Google Earth Pro on pixelated images, the co-author for the published paper (Brown, J. R., & Roberts, G. P. (2019). Possible evidence for variation in magnitude for marsquakes from fallen boulder populations, Grjótá Valles, Mars. *Journal of Geophysical Research: Planets*, p. 124. <https://doi.org/10.1029/2018JE005622>), Gerald P. Roberts and the present author independently measured the same images and compared results. Figure 3.2.5 a–b shows the comparisons between the results. The sets of results proved to be broadly comparable within error, with the differences between results (<1 m for the mean value for the ten widest boulder trails and <10 – 20 boulder trail counts per kilometre) being far smaller than the signals that were measured (between 1 m and 5.5 m for the mean value for the ten widest boulder trails and between 0 and 100 for the

boulder trail counts per kilometre). Overall, using the ruler tool in Google Earth Pro, measuring the number of boulder trails and their widths proved robust and repeatable.

(a) Calibration – 10 Widest Trails



(b) Calibration – Boulder Trail Counts per Kilometre

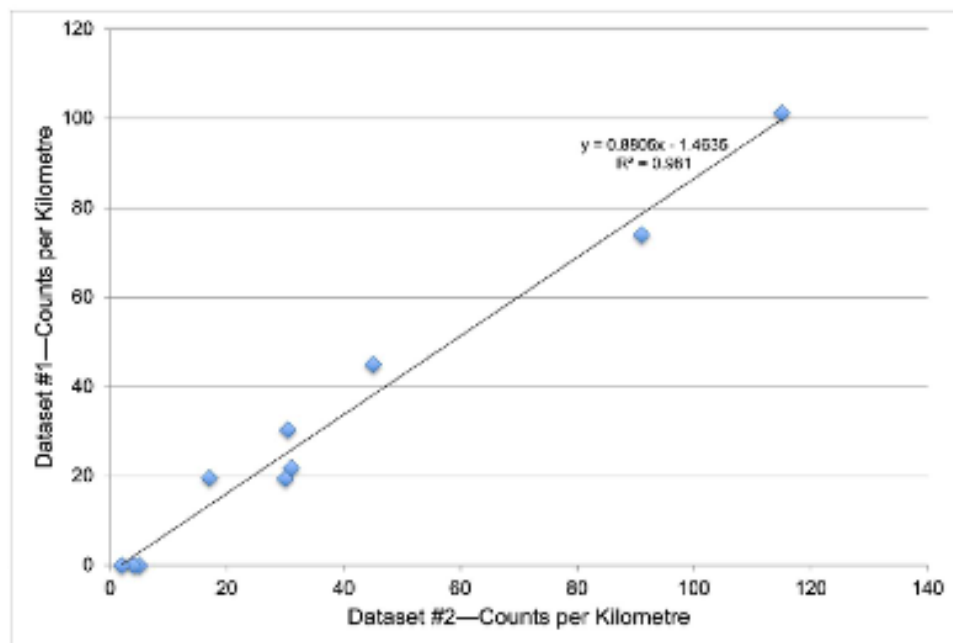


Figure 3.5. Boulder trail lengths and widths were counted and re-counted by the authors Brown, J. R., and Roberts, G. P. (2019). Possible evidence for variation in magnitude for marsquakes from fallen boulder populations, Grjótá Valles, Mars. *Journal of Geophysical Research: Planets*, p. 124. <https://doi.org/10.1029/2018JE005622>. (a) Calibration graph for the 10 widest boulder trails, showing the comparison between Dataset #1 and Dataset #2. These results demonstrate repeatability, as the results from both surveys are broadly comparable.

(b) Calibration graph for boulder trail counts per kilometre, showing a very strong correlation between the two datasets. The R^2 value for this regression is 0.981, indicating a very strong correlation. An F-test was performed, yielding an F-statistic of 258.16, which exceeds the critical F-value of 6.61 at a 95% confidence level, confirming that the correlation is statistically significant (p-value: < 0.00001).

3.2.3.3. Measuring Throw Across the Graben

The vertical displacement, or throw, across the northernmost Cerberus Fossae graben was measured using data from the Mars Orbiter Laser Altimeter (MOLA) aboard the Mars Global Surveyor (MGS) spacecraft. MOLA's high-resolution altitude data, with a vertical accuracy of approximately 1.5 meters (Smith et al., 1999), allowed for calculating the vertical offsets along the graben.

Selection of MOLA Data Points: MOLA Precision Experiment Data Records (PEDRs) were used to select transects that cross the graben. These data points are spaced approximately 300 meters apart along the MGS orbital track. The selected transects provided elevation profiles that spanned both the footwall and hanging wall of the graben, offering a comprehensive view of the vertical displacement across different sections.

Calculation of Throw: Throw was calculated as the difference in elevation between the plains adjacent to the graben (representing the footwall) and the lowest point on the graben floor (the hanging wall). The throw was determined by measuring the vertical distance between the highest point on the graben's margin and the lowest point on the floor across several cross-sections where MOLA transects intersected the graben. The following formula was used to compute throw at each transect:

$$\text{Throw} = \text{Elevation of Footwall} - \text{Elevation of Graben Floor}$$

The measurements showed vertical displacement increases from near zero at the graben tips to approximately 900 meters at longitude E162°. This distribution of throw is consistent with typical fault geometries, where displacement peaks near the centre and tapers off towards the fault tips (Schlische et al., 1996).

Verification and Error Mitigation: To ensure the accuracy of the throw measurements, MOLA data and imagery from the High-Resolution Imaging Science Experiment (HiRISE) and Context Camera (CTX) were cross-referenced. This visual comparison helped verify the graben's morphology and rule out significant sedimentary infill that could obscure its true depth.

One potential source of error in the throw measurements is the horizontal resolution of MOLA data, as data points are spaced 300 meters apart, which could lead to missed small-scale features. However, given the overall consistency of the MOLA profiles and the clear visibility of the graben's structure in HiRISE images, the measured throw values are considered to accurately reflect the vertical displacement across the graben.

Furthermore, any graben infilling by aeolian or sedimentary processes was carefully assessed using the HiRISE imagery, and no significant infilling was observed at the locations of the MOLA transects used for throw measurement.

3.2.3.4. Methods Used to Substantiate the Hypothesis

The hypothesis suggests that the boulder trails and fallen boulder populations in the northernmost Cerberus Fossae were formed due to seismic shaking. However, to validate this hypothesis, it was crucial to examine other possible theories for boulder mobilisation. Chapter 4 discusses these alternate theories and results in greater detail.

3.2.4. Identifying Outflow Channels in Grjótá Valles—Context Camera (CTX) and High-Resolution Imaging Science Experiment (HiRISE) with Mars Orbiter Laser Altimetre (MOLA) Point Data

The objective of this part of the research was to study the area of the northernmost Cerberus Fossae and the outflow channel in Grjótá Valles, a region of approximately 70,000 km², to identify cross-cutting relationships across the flow channels of this region. Given that younger flow channels would incise down into older channels (cross-cutting relationships), it was important to find a method of not only visually observing the features of cross-cutting but also finding a method whereby the elevations of channels and various markings along the sides of the channels or on the base of the channels could be measured, to enable estimates regarding a flow channel's size and depth of incision. Earlier work studying fallen boulder trails in the Cerberus Fossae (Roberts et al., 2012) had shown that High-Resolution Imaging Science Experiment (HiRISE) images would be the most useful in the search for these features, given the excellent resolution of the images (~30 cm per pixel). The HiRISE images were analysed in HiView (which uses equirectangular projection map projections). However, the limited number of HiRISE footprints in the study region (Figure 3.6 a) meant that relying wholly on HiRISE images would not be possible. However, with the majority of HiRISE footprints being located along the extent of the northernmost Cerberus Fossae, this proved to be enormously helpful as the research progressed. Context Camera

(CTX) image mosaics for Mars viewed in Google Earth Pro (which uses a spherical normal (equatorial) variant of the Mercator projection for its maps) were used in this research due to the wide extent of coverage across the study region (Figure 3.6 b), with over 90% of the study area covered by the imagery. The mosaic is a composite of images taken by cameras on board the Mars Reconnaissance Orbiter (MRO), namely the Context Camera (CTX) (with a resolution of approximately 6 m per pixel).

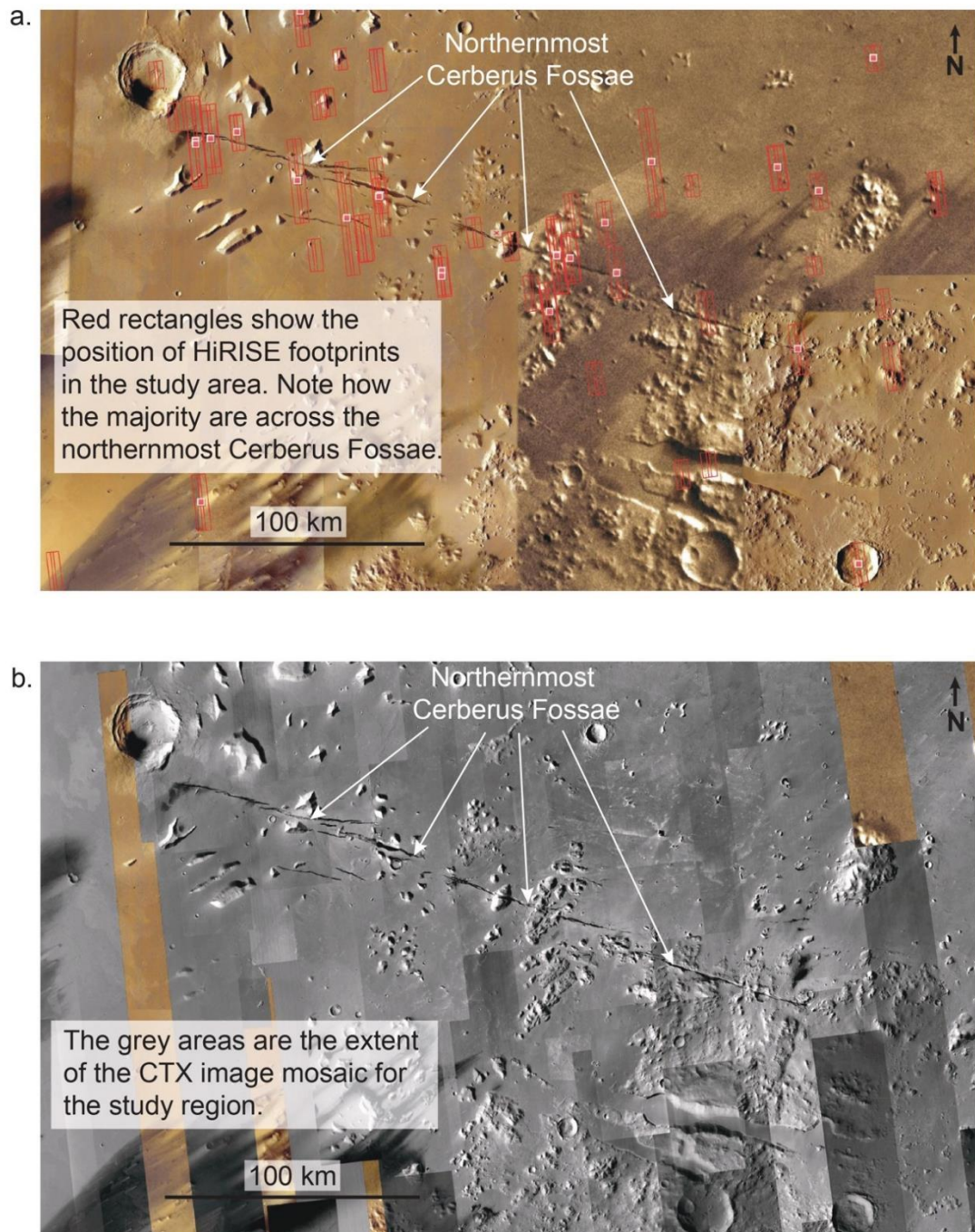


Figure 3.6. a–b Regional Map (centred at 15.25° N, 162.85° E) of the study area marking, a. HiRSIE footprints available (red rectangles) and b. CTX image mosaic coverage (grey areas). The northernmost Cerberus Fossae is marked in both images. The areas to the north and south of the fossae are the areas where flow channels can be identified, the results of which are discussed at length in Chapter 5.

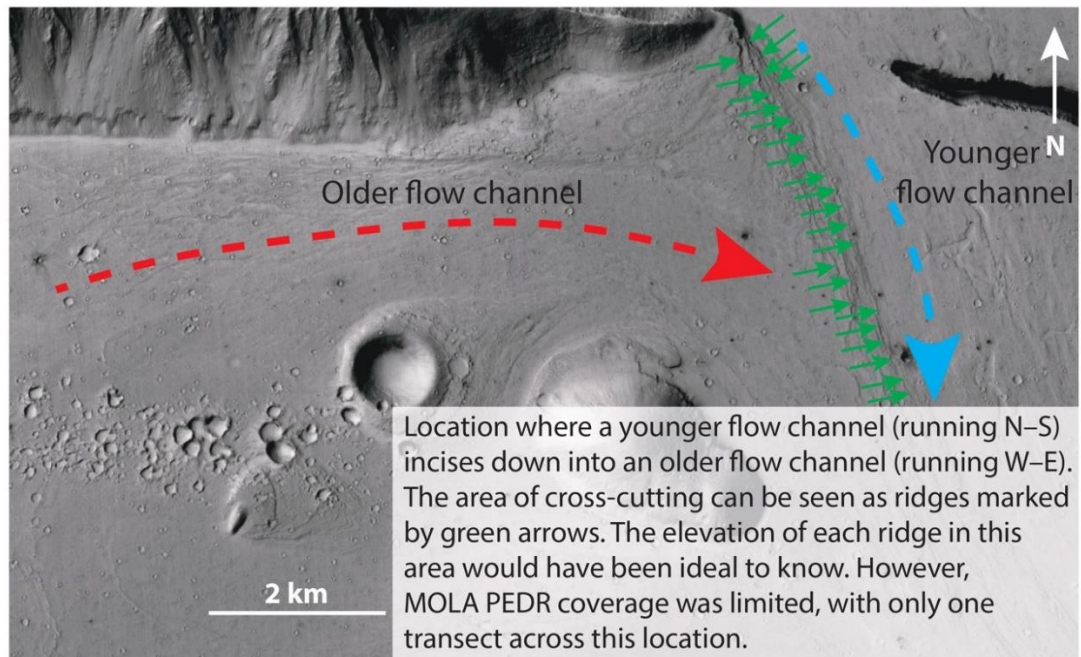
Through visual analysis of the imagery, areas that exhibited clear cross-cutting, i.e. a younger flow channel incising into an older flow channel, were identified. The next step was to then study Mars Orbiter Laser Altimetre (MOLA) data (an instrument that was part of the Mars Global Surveyor (MGS) mission), namely MOLA Precision Experiment Data Records (PEDR). MOLA PEDRs are individual altimetry readings along the MGS's orbit track, which flew in a near-polar, elliptical orbit around Mars. These individual readings are spaced 300m apart (Zuber. et al., 1992). MOLA operates by firing ten laser pulses a second towards the surface. The pulse bounces back off the surface, and the receiver measures the two-way time of light. The time taken for the pulse to travel back and forth is noted, which measures the distance between the spacecraft and the surface. Atmospheric effects are considered, and the spacecraft's position is accurately tracked to estimate the surface altitude (Smith. et al., 1999; Neumann. et al., 2001). MOLA data were used to study the vertical disposition and geometries of channels in cross-section. The MOLA PEDRs laser spots cover an area of approximately 160 m in diameter, spaced approximately every 300 m. The range measurements are quantised with a 1.5-m vertical resolution before correction for orbit and pointing errors. The relative error in altitude along profiles is 1–10 m (Albee et al., 2001). Consequently, only considering results with vertical variances exceeding 10 metres was crucial. To mitigate these issues, MOLA data from areas with elevation changes occurring over less than a 160-metre horizontal distance were disregarded, and this was ensured by analysing shadow lengths in CTX and HiRISE images, where applicable.

Given that MGS orbited Mars many times, a significant number of MGS MOLA PEDR transects offer exact altimetric data about the surface. It was important to identify MGS MOLA PEDR transects that traversed particular features that warranted close investigation. Despite a multitude of MGS MOLA PEDRs across the study area, not all locations and points of interest were covered. The research, therefore, had to be adapted to ensure that MOLA PEDRs could be used.

Figure 3.7. a–b shows an area of Mars from Location 1 that was used in the research, showing the extent of MOLA transects in the area. The area shows an older flow channel (red dashed line) cross-cut by a younger flow channel (blue dashed line). The area of interest is the ridge-like area that marks the flow channel wall of the younger flow and runs approximately N–S (marked by green arrows) in Figure 3.7.a. The 'wall' has many ridges (marked by the green arrows), likely of different elevations. A complete catalogue of these elevations would have been ideal to build a comprehensive picture of the elevation and, subsequently, the flow channel. Whilst

coverage by MOLA PEDRs was good, it was not excellent (3.7.b), and many areas of interest could not be studied due to no MOLA PEDR data across a given area, a case in point being the full extent of the ‘wall’ of the younger flow channel, indicated by green arrows in Figure 3.7a. Only 11 individual MOLA PEDRs were used for this section, marked by the orange ellipse in Figure 3.7b. MOLA data were used to study the vertical disposition and geometries of channels in cross-section.

a.



b.

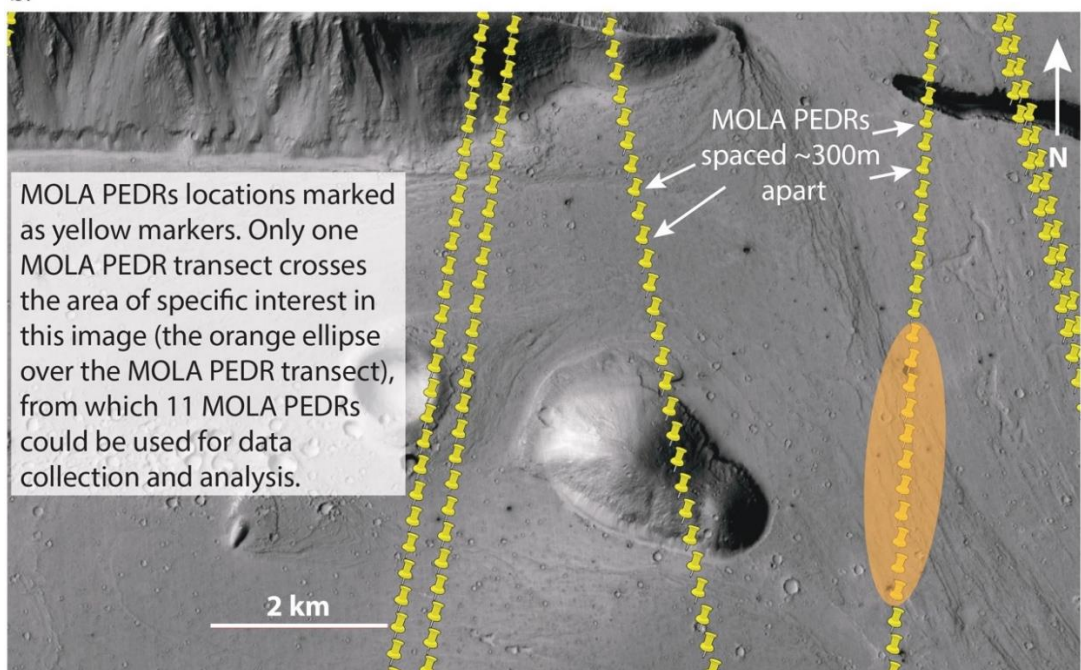


Figure 3.7. a–b. CTX image mosaic detail of a section from Location 1 from the study of flow channels in Grjóta Valles (centred at 15.78° N, 161.54° E) highlighting the locations of MOLA

PEDRs across a segment of the study region. a. An area that shows an older flow channel (red dashed arrow) being cross-cut by a younger flow channel (blue dashed arrow). Of interest is the section indicated by green arrows, the inner wall of the younger flow channel. This area is ridged, with the ridges corresponding to different elevations. b. The same location, but now the MOLA PEDR transects (yellow markers) are visible. Note that the inner wall of the younger flow channel only has one MOLA transect across it, with 11 MOLA PEDRs of use to the study, marked by an orange ellipse.

3.2.5. Construction of a Regional Map and Location Maps and Cross-Sectional Profiles using CTX, HiRISE, and MOLA PEDR Data

After a rigorous analysis of the study location, seven key locations (and four supplementary locations) were selected for more detailed analysis. The locations were selected based on the following criteria:

- i. That there exists in each location clear evidence of cross-cutting channels.
- ii. The channels visible in each location could be mapped back to their source. Some of the observed cross-cutting relationships could have been between distributary channels, where the main channel divides into multiple channels downstream. This meant it was essential to map channels back to their source to avoid an exaggerated number of outflow channel formation phases
- iii. Sufficient and pertinent MOLA PEDR coverage exists (at least five or six MOLA transects per location) to facilitate the construction of cross-sectional profiles of areas that highlight cross-cutting relationships and enable the construction of topographic profiles across the width of the flow channels.
- iv. A vertical difference greater than 10 m, meaning that the range in elevations in each location had to be more than 10 m. Less than 10 m vertical difference is the relative error in altitude profiles, as noted by Albee et al. (2001). However, this filter on features to be studied is not considered to bias the study. All the main channels observed on the HiRISE images that required study had vertical extents in excess of 10 m, so none were omitted from the study.
- v. Finding locations located along the entire length of the northernmost Cerberus Fossae and close to the northernmost Cerberus Fossae was also important, i.e. locations had to be representative of sections of the northernmost Cerberus Fossae from west to east.

The flow channels in the four supplementary locations could not be mapped back to their sources. Nonetheless, the locations were valuable because they assisted in delineating the entire research area in terms of each flow's lateral extent, thus assisting in marking each flow's boundary. Figure 3.8 shows the final location map, with the key study locations and supplementary locations marked by white rectangles.

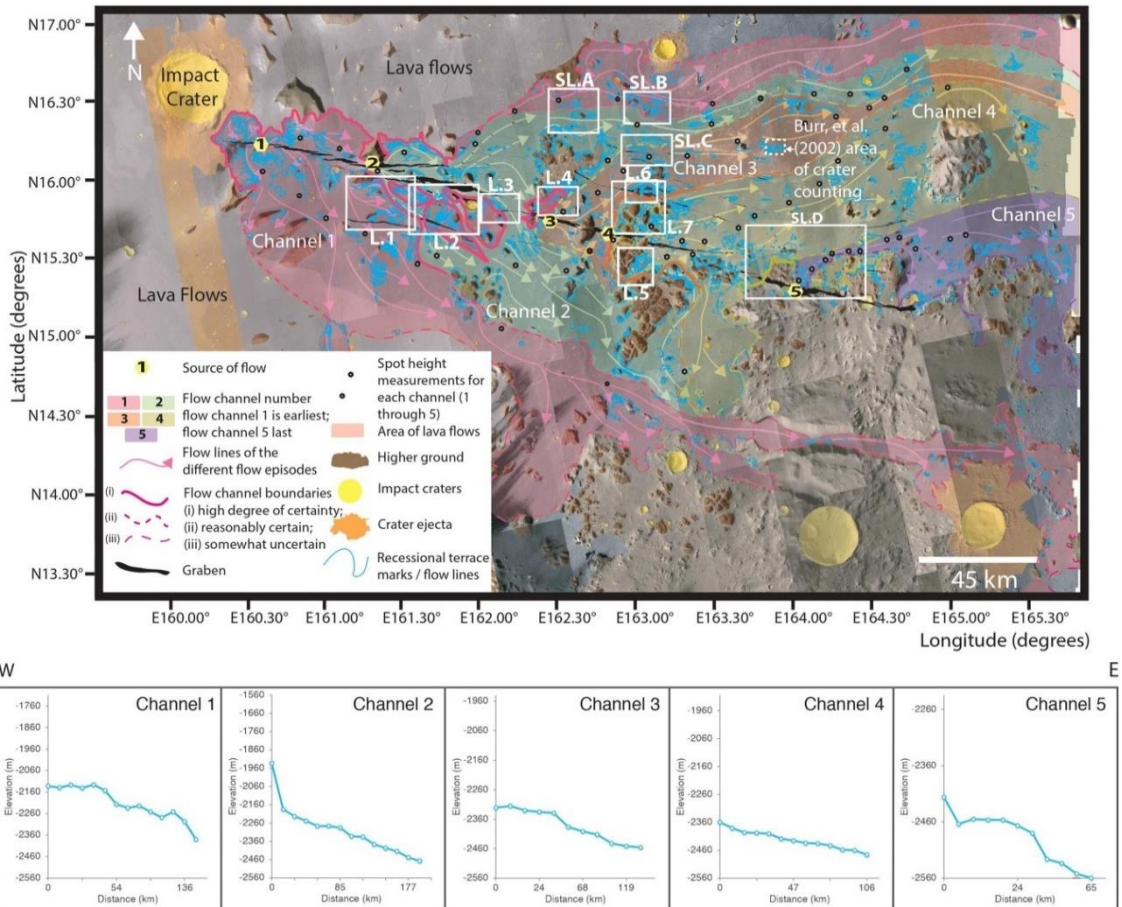


Figure 3.8. Regional Map (centred at 15.25° N, 162.85° E) of the study area marking the source areas of the five flows and the extent of each flow. The key study locations, 1 through 7 (Figures 5.4 through 5.11, respectively), are shown with white rectangles with L.1, L.2 and so on next to the boxes. Supplementary Locations A through D are shown with white rectangles with SL.A, SL.B, and so on next to the boxes. Below the Regional Map are five spot height topographic profiles for the extent of each flow area 1 through 5 (kilometres/elevation) showing the downward-east sloping topography of the Regional Map area. The vertical exaggeration for each topographic profile is x200.

Once the locations were finally selected, MOLA data was used to construct topographic profiles (distance/elevation) across the 11 locations.

Each section of a MOLA PEDR transect that highlighted a cross-cutting relationship was identified in each image, with the chosen transects marked a'-a, b'-b, c'-c, etc. within each image. Once this had been completed, the topographic profiles were constructed by plotting the MOLA PEDR elevation values across the transect against

the MOLA PEDR locations. The location coordinates were then converted into kilometres (x-axis). All topographic profiles were created in Microsoft Excel (16.0). Once each profile had been completed, they were exported as JPEGs to Adobe Illustrator (version 27.0), together with the CTX mosaic image of the study area (Location 1, Location 2, etc.) and, where possible, the HiRISE image of a particular feature.

Having already scrutinised each location image looking for geomorphological clues regarding cross-cutting relationships, it was then important to use the topographic profiles to mark where recessional terrace marks were observed, from what flow (Flow 1, Flow 2, etc.) and to work out the base elevation of the older flow(s) channel. By establishing the elevation of the base of the older flow channel, it was then possible to calculate the incision of the younger flow(s) and whether or not the incision became larger, remained the same, or varied. Concomitantly, the exported JPEG images—now in Adobe Illustrator—had clear terrace markings, longitudinal grooves, and flow channels and flow direction added using the pen and pencil tools. Different colours were assigned to each flow episode (Flow 1: red; Flow 2; green; Flow 3: orange; Flow 4: gold; Flow 5: purple), and by repeating this procedure, slowly, a picture emerged of the geomorphological history of each Location regarding the sequence of channel forming flow events. Figure 3.9 is Location 1 from the Regional Map (white rectangle—L1) and shows the final view of each Location: a. the CTX mosaic image of the target area; b. the annotated image, with the flow channels and terrace markings added; c. and d. specific details related to cross-cutting geomorphology that aided in understanding and analysing the features; e. topographic profiles replete with markings from the different flows, that allowed for an assessment of the base elevation of the older flow (here, Flow 1), thereby allowing for calculation of the incision of the younger flow (here, Flow 2).

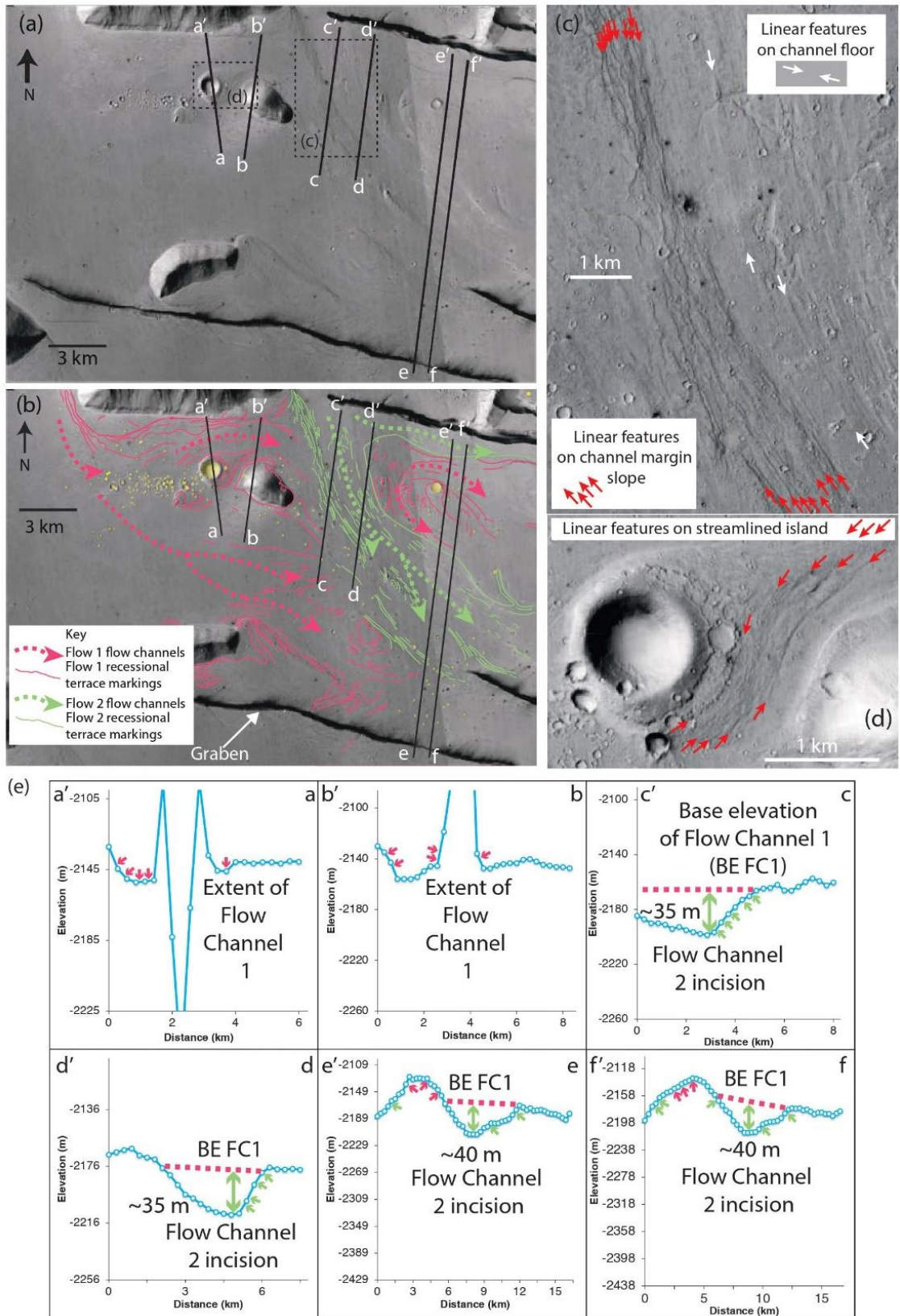


Figure 3.9. Maps and topographic profiles of Location 1 centred at 15.70° N, 161.61° E showing details of channels and cross-cutting relationships (see Figure 3.2.7 for location). (a) Map with CTX mosaic with MOLA transects; (b) Map with CTX mosaic with MOLA transects (black lines a'- a through f'- f) and interpreted channel markings/flow directions/recessional terrace markings. Topographic profiles a'- a through f'- f for each of the six transects, with the blue line in each graph representing the MOLA transects. (c) The inset from CTX shows details of the

channel floor. Linear features on the channel margin slope and the linear features on the channel floor do not resemble lava flow landforms, such as thin, concentric, and lobate flow fronts that indicate overlapping lavas or rootless cones. The interpretation is that they resemble “longitudinal grooves” or “longitudinal lineations” that have been used to infer catastrophic flow terrain on Earth and Mars (Baker, 1978; Burr et al., 2002) and/or turbulent lava (Jaeger et al., 2010), and resemble “bathtub rings” that are cut by high flow velocities and vortices, and left by lowering fluid levels during waning flows (Baker 1973, 1978); (d) Map showing similar linear features around a streamlined island. (e) Topographic profiles from MOLA spot heights (labelled a'- a through f'- f and located on (a) and (b)) showing the morphologies of channels and craters and locating linear features on channel margins. The vertical exaggeration for each topographic profile is x50. Overall, for Location 1, the interpretation is that Flow 1 (that flowed from west to east/southeast) is cross-cut by channels formed by a later flow, Flow 2 (that flowed towards the SE).

Once the locations were complete, the larger Regional Map was constructed (Figure 3.8), which shows the channels, fissures and faults, impact craters and, ultimately, the chronology. Based upon the detailed work of the 11 locations, flow lines were added to all maps (regional and the 11 locational maps), using the orientation and position of channels and geomorphic markers (tear-drop shaped features, linear features on the slopes of the depression margins, linear features on streamlined hills, and depressions) to determine the most likely flow direction of each channel.

In some cases, boundary lines between channels were challenging to identify, with the process being more straightforward, nearer to the source of the flows and more equivocal at distal locations. The Regional Map (Figure 3.8) shows three types of boundaries between channels: (a) a high degree of certainty, (b) reasonably certain, and (c) somewhat uncertain. Finally, using MOLA data, five topographic profiles (Figure 3.8) were constructed along the five main channels. This was conducted to see that each channel flowed downhill, an essential facet in understanding the flow movement of the channels studied. Creating topographic profiles, mapping, and illustration was a highly intricate and time-consuming process that required multiple double-checks to ensure no errors had been made.

3.3. FiSH Code

3.3.1. Introduction

The relevance of the Fissile Earthquake Seismology (FiSH) code in this research is discussed at length in Chapter 6—Discussion. However, for the sake of clarity its importance to the research and in helping to connect the two branches of research presented in this thesis, Chapters 4 and 5, a brief overview of FiSH code’s place within this research will be presented along with methods of use. However, to summarise, FiSH allows earthquake/marsquake magnitude distributions to be computed given

information on fault slip rate. Given that (a) the boulder study provided information on possible palaeomarsquake magnitudes for relatively large events, (b) the InSight mission provided information on the frequency and magnitudes of relatively small events, and (c) the channel study and published crater counting revealed channel source migration, and migration rates that may imply rates of sub-surface dike propagation linked to dike opening/slip-rates, FiSH allowed a study of the possible links between (a), (b) and (c).

3.3.2. What Is FiSH Code?

FiSH is a package of MATLAB tools designed to help seismic-hazard modellers analyse fault data. It enables the derivation of expected earthquake rates and helps test the consistency between magnitude–frequency distributions (MFD) and observations. The tools developed by Pace et al. (2016) can convert fault geometry and slip rates into a so-called global budget for each fault, compute recurrence parameters from historical data, and output earthquake rates for different MFD models. The source codes are open, and the aim is to help researchers identify inconsistencies and obtain reliable fault-based seismic-hazard evaluations. FiSH code is commonly used in Europe to calculate seismic hazards, as the frequency–magnitude distribution is needed to do this. FiSH is written in MATLAB (v.R2011B), a MathWorks software.

3.3.3. FiSH Code Relevancy and Usage in the Chapter 4 Research—Seismicity

Using data drawn from the research in Chapters 4 and 5 and data from the Seismic Experiment for Interior Structure (SEIS), it is possible to construct a frequency–magnitude distribution graph (boulder trail density as a proxy for maximum moment magnitude (Roberts et al., 2012)). FiSH code produced frequency–magnitude distributions for input slip rates that allow the boulder data to be compared with the InSight data using slip rates from dike propagation inferred from the channel data. This then allows for the identification of the magnitude of completeness (M_c)—the minimum magnitude of an earthquake that can be detected and recorded by a particular seismic network. Estimating the M_c involves using the Gutenberg–Richter Law (Gutenberg et al., 1944; Utsu, 1965), categorising earthquakes into ‘bins’ based on the number of events with magnitudes greater than a reference magnitude. The count of marsquakes in each bin is then plotted on a logarithmic scale. Ideally, the data should approximate a straight line, but statistically perfect datasets rarely exist. Figure 3.10 illustrates this.

Frequency–magnitude distribution for marsquakes estimated using the FiSH code.

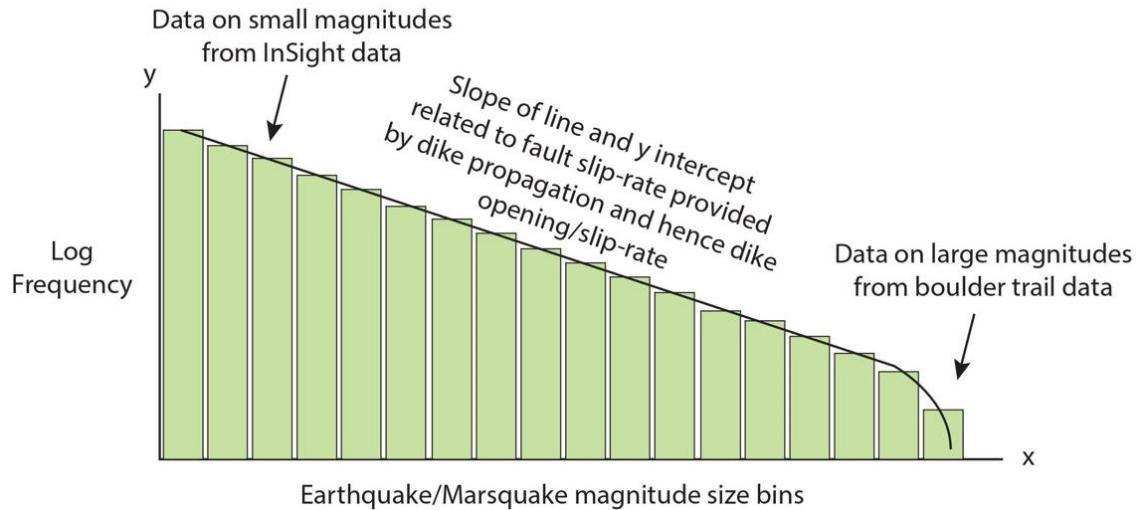


Figure 3.10. Idealised frequency–magnitude graph showing the earthquake/marsquake magnitude bin sizes on the x-axis, with magnitude increasing to the right. The y-axis measures log frequency.

The given relationship can be utilised to calculate the M_c (Wiemer & Wyss, 2000). By fitting a straight line to the data, the point at which the data diverges from the line represents the magnitude of completeness. In the given scenario, the magnitude of completeness is ~ 2.25 (as shown in Figure 3.11).

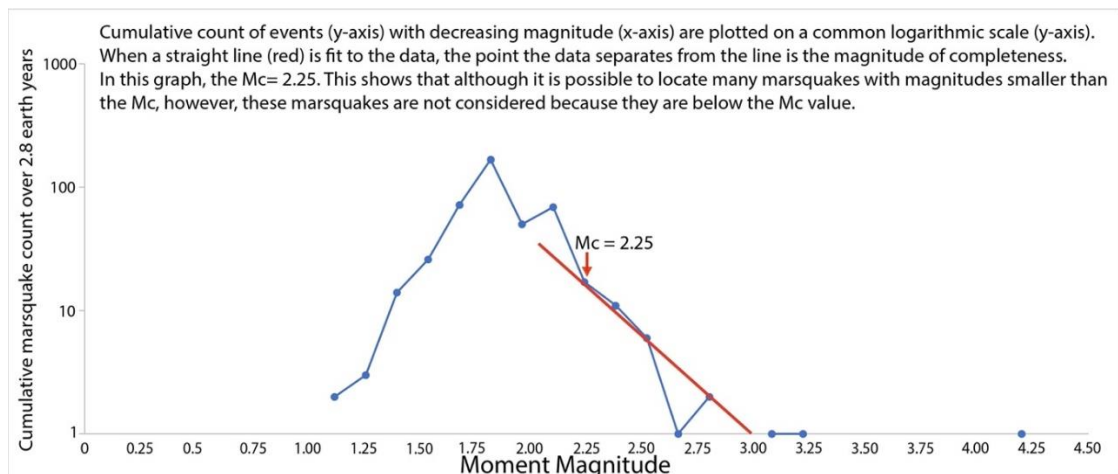


Figure 3.11. A logarithmic plot illustrating seismic event data, specifically Marsquakes, based on findings from Ceylan et al. (2002). On the y-axis, the cumulative count of events is displayed logarithmically, while on the x-axis, the magnitude of the events decreases. A straight red line denotes the magnitude of completeness (M_c), set at 2.25 in this context. The M_c value indicates the threshold below which seismic events, though they may exist, are not considered due to their magnitude falling below the designated completeness threshold.

With the M_c for marsquakes in the northernmost Cerberus Fossae now known, and with data from SEIS revealing that 16 M_w 2.25 events took place over a 2.8-year timescale means that approximately five M_w 2.5 events should occur yearly, the data from Chapter 4 revealing the largest possible marsquakes in northernmost Cerberus Fossae (M_w 7.3-7.8) could now be brought into use. Quantitative and qualitative data in the form of geomorphic evidence presented in Chapter 4 suggest that such large-magnitude marsquakes are thought to take place over tens to hundreds of thousands of years.

With a known lower value (M_w 2.25) and a higher value (M_w 7.0—chosen as the lower end of estimates), the upper and lower limits exist for marsquake magnitudes. Now, introducing FiSH code and iterating the slip rate, it was possible to produce a frequency–magnitude curve for events in Cerberus Fossae using SEIS and Chapter 4 data (Figure 3.12).

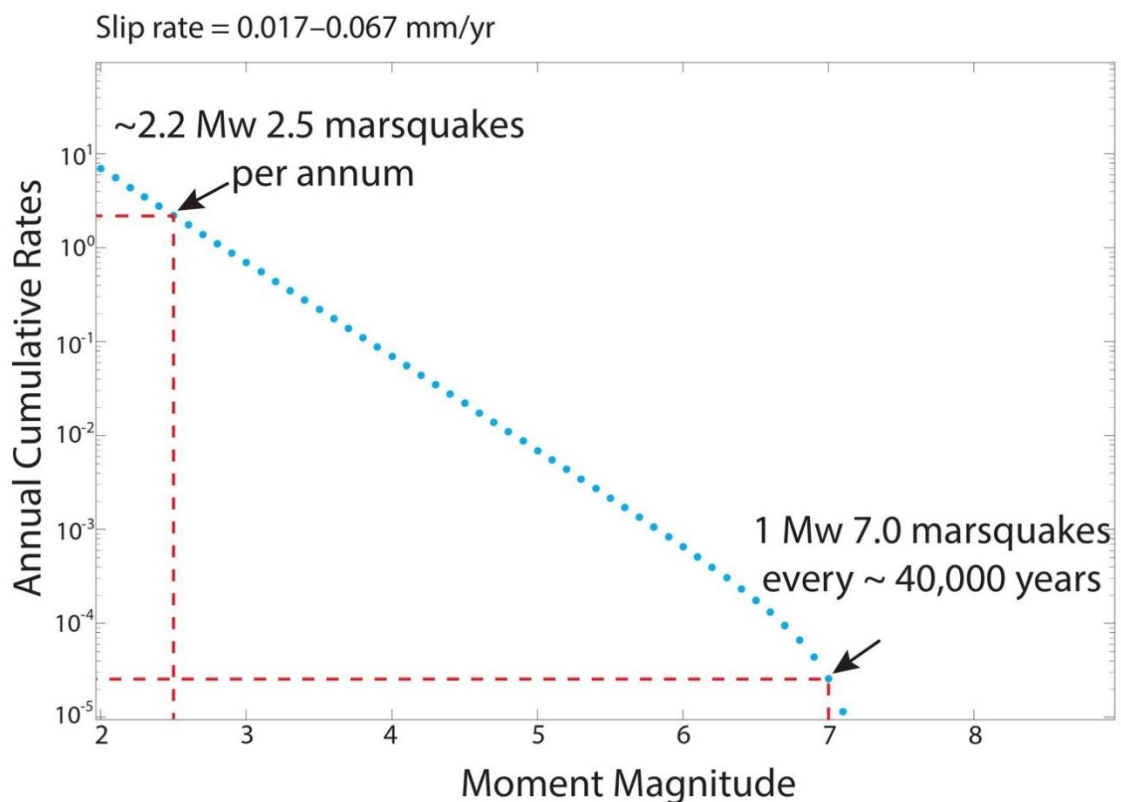


Figure 3.12. Truncated Gutenberg–Richter (GR) frequency–magnitude graph produced using FiSH code in MATLAB (v.R2011B) to create a frequency–magnitude curve of seismic events annually against moment magnitude. The graph’s y-axis is the annual cumulative rates (logarithmic), and the x-axis is the moment magnitude. Based on SEIS data that allowed the magnitude of completeness to be calculated ($M_c = 2.25$), the approximate annual rate for marsquakes of that magnitude is 5. Slip-rate adjustment to allow the estimates from SEIS and Chapter 4 boulder data to fit on the frequency–magnitude curve means that the annual rate of M_w 2.25 marsquakes, using FiSH code, is 2.2. Data from research on boulder trail populations as a proxy seismometer to estimate the magnitude of marsquakes (M_w 7.3–7.8) and the annual

cumulative rate to be in the tens of thousands of years. A Mw 7.0 marsquake, the more conservative estimate based on data, was used to fit this model, with the occurrence rate being one event every 39,019 years, in keeping with predicated timescales. Indeed, the timescales for the events are within an order of magnitude of estimates. By iterating the slip rate, the two sets of data were melded together to produce the frequency–magnitude curve that was true to SEIS data and data from research on boulder trail populations as a proxy seismometer (Chapter 4), accommodating the SEIS timescales very neatly (2.19 versus 5) and the predicted dates for marsquakes over Mw 7.0. within one order of magnitude.

The frequency–magnitude curve in Figure 3.12 shows that approximately 2.2 Mw 2.5 marsquakes occur each year (within range of the readings from SEIS) and that large marsquakes of Mw 7.0 plus occur in the tens of thousands of years (~40,000 years), correlating to the order of magnitude that had been suggested for larger marsquakes within Cerberus Fossae in Chapter 4. However, Mw 7.0 is towards the lower end of estimates for larger marsquakes. The *b*-value was set at 1 given that SEIS data is limited in terms of identifying smaller marsquakes and the length of the SEIS mission (2.8 Earth years), not to mention a limited seismic catalogue of larger marsquakes from the region. The smallest variations in slip rates dramatically changed the results in the frequency–magnitude curve. Accordingly, iteration of the slip rate was extremely important. Figure 3.13a–f shows six graphs where minute differences in slip rates are input into the FiSH code. As the six graphs reveal, frequency–magnitude curves do not align with data from SEIS (lower Mw) and estimates proposed in Chapter 4 (higher Mw). For instance, Figure 3.13c depicts a frequency–magnitude graph using a slip rate of 2.00–3.00 mm. Despite the seemingly minor difference, this variation profoundly affects the calculated readings of marsquakes per year. In this scenario, Figure 3.13c displays approximately 13 Mw 2.5 marsquakes annually and predicts a 1 Mw 7 marsquake every ~6,500 years. These values starkly contrast with the readings in Figure 3.13, which suggests approximately 2.2 Mw 2.5 marsquakes annually and a 1 Mw 7 marsquake approximately every ~40,000 years—figures that fit SEIS data and research data. The high sensitivity observed in the calculations when slip rates are adjusted implies that the FiSH code is precise when using input data to compute frequency–magnitude curves. This sensitivity is critical to the code's accuracy, demonstrating its ability to capture nuanced variations in slip rates and their subsequent impact on seismic activity predictions.

This finding reinforces the importance of meticulous consideration and calibration of input parameters in seismic modelling, as even small discrepancies can lead to significant variations in the predicted outcomes.

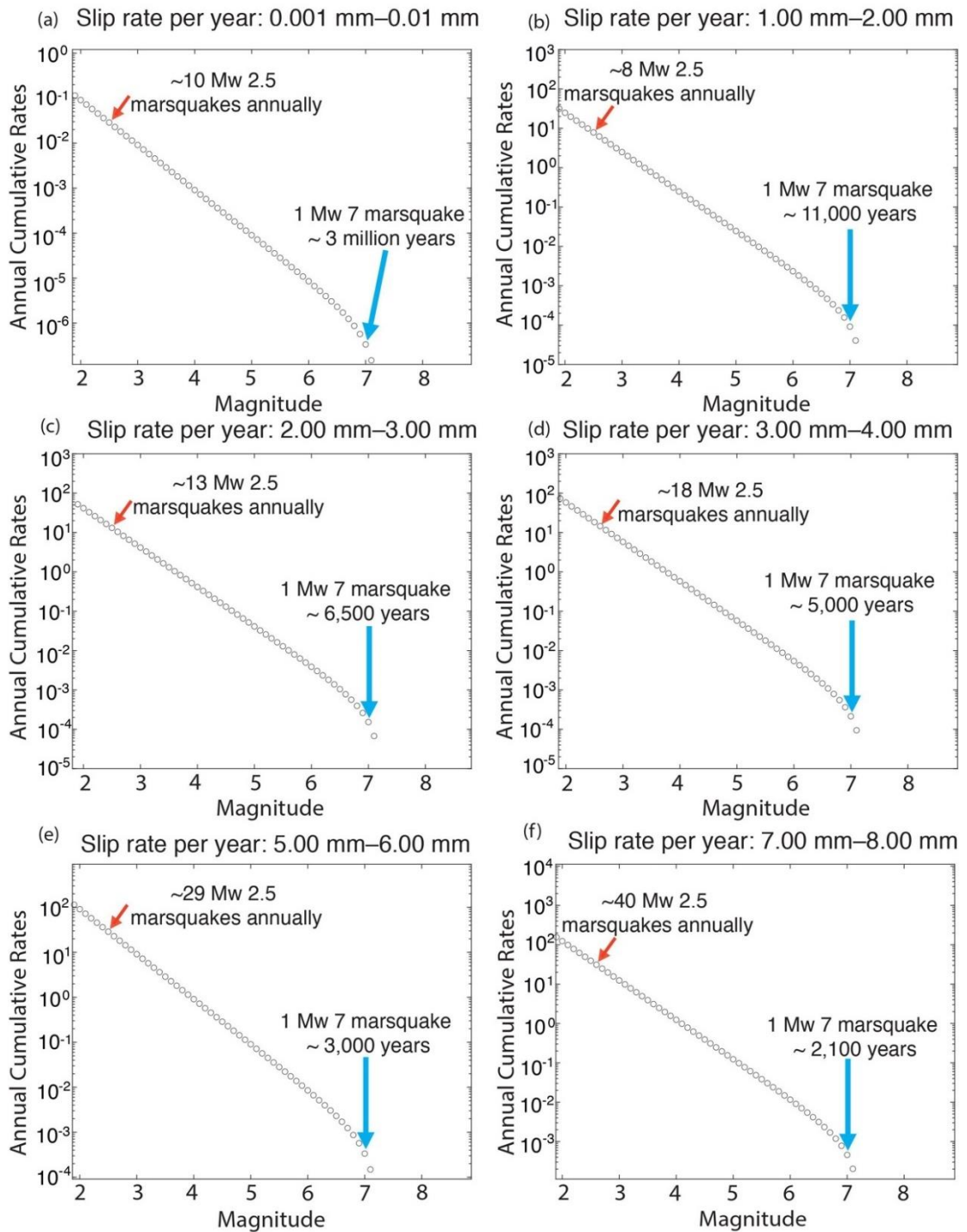


Figure 3.13. a–f: Truncated Gutenberg–Richter (GR) frequency–magnitude graphs produced using FiSH code in MATLAB (v.R2011B) to create frequency–magnitude curves of seismic events annually against moment magnitude. All graphs’ y-axis is the annual cumulative rates (logarithmic), and the x-axis is the moment magnitude. The slip rate for each graph differs from the 0.017–0.067 mm iteration of the slip rate used in Figure 3.3.4, matching the SEIS data with the data from boulder trail research explained in Chapter 4. The red arrows highlight the Mw 2.25 marsquake (magnitude of completeness) and the frequency of such a magnitude marsquake per annum. Likewise, the blue arrows highlight the Mw 7.0 marsquake and the frequency of such a magnitude marsquake. The slip rates per year for each graph are as follows: (a) 0.001–0.010 mm; (b) 1.00–2.00 mm; (c) 2.00–3.00 mm; (d) 3.00–4.00 mm; (e) 5.00–6.00 mm; (f) 7.00–8.00 mm.

3.3.4. FiSH Code Relevancy and Usage in the Chapter 5 Research—Dike Propagation

The FiSH code was used to iterate the slip rates until the Mw 2.25 marsquake occurring at a rate of approximately 2.2 events per year was connected to an Mw 7 marsquake that takes place approximately every 40,000 years. The resulting frequency-magnitude curve (Figure 3.12) closely matches the model, with the frequency and magnitude points aligning closely with data from SEIS (which was used to calculate the magnitude of completeness) and data from Chapter 4 based on three datasets that use boulder trail populations as natural seismometers to determine the possible magnitude of marsquakes.

After calculating the slip rate using seismic data and FiSH code, it is possible to test the slip rate against the known displacement (d) and length (L) relationships for faults. This can be conducted with the help of data on the age of flow channels from Chapter 5.

An empirical rule of thumb for estimating the displacement, d , in faults and dikes based on their length, L , is simplified and approximate but helpful. For faults, $d=L \times 0.03$. This implies that the displacement, d , along a fault is approximately 3% of the fault length (L). For dikes, $d=L \times 0.003$. This suggests that the displacement (d) is approximately 0.3% of the dike length (L) (Vermilye and Scholz, 1995).

The research outlined in Chapter 5 suggests that the formation of flow channels in Grjótá Valles occurs asynchronously due to melted flow released to the surface, forming channels through dike intrusions progressing eastward over time, potentially originating from a sub-surface volcanic source. Golder et al. (2020) provide crater count ages indicating younger ages from west to east: 53 Ma, 33 Ma, and 31 Ma, respectively. These ages correspond to different flow channels, constraining their formation times and dike propagation rates (Figure 3.14). By employing slip rate calculations and displacement–length relations, the dike propagation rate and fault opening rate across various flow channel areas can be determined. For instance, the dike propagation rate for Flow 1 and Flow 3, occurring over 20 Ma, is calculated at 5.75 mm/yr, with an opening rate of 0.0172 mm/yr and an estimated fault opening of ~344 m. However, caution is advised when comparing results across different flow channels due to significant timescale variations, emphasising the importance of temporal considerations in geological analyses to avoid misinterpretations.

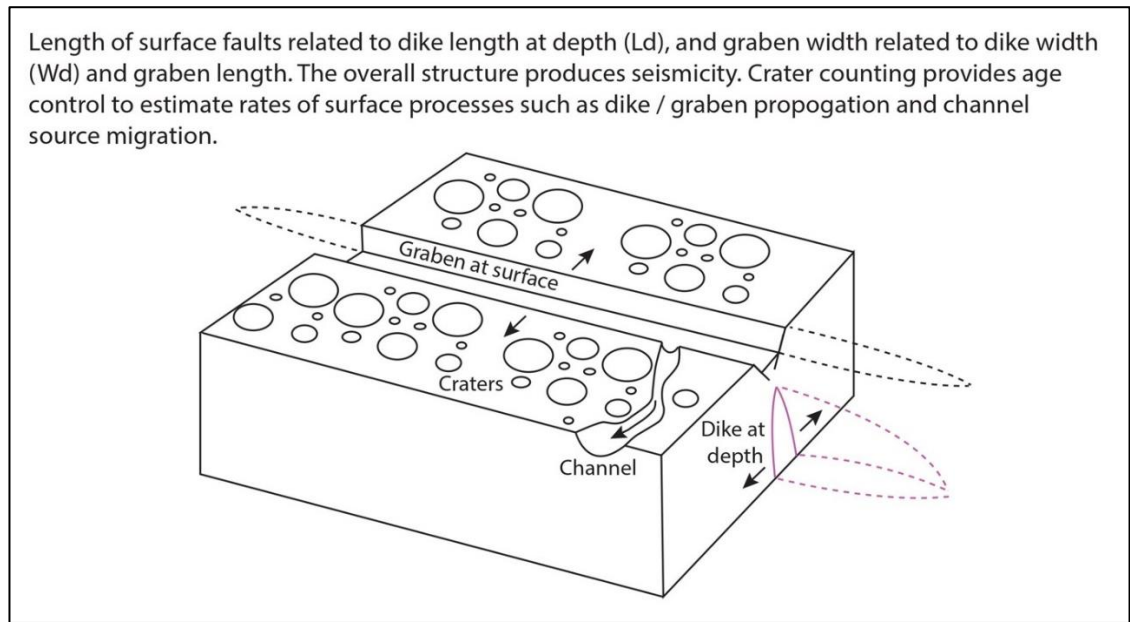


Figure 3.14. Illustration to show how crater counting provides an age control to allow for estimates of surface processes such as dike/graben propagation and channel source migration.

3.4. Concluding Remarks

Various software programs were used to conduct the research presented in this thesis. Images from the MRO cameras (HiRISE, CTX) were pivotal to the entire research. Being able to readily access these images was vital, too. To this end, HiVIEW and Google Earth Pro were used, with the latter being extremely useful in making measurements of the surface of Mars. Adobe Illustrator and Windows Excel packages were used to annotate images of the Martian surface and produce topographic profiles and graphs that allowed data gleaned from the research to be presented in a clear fashion, respectively. Finally, FiSH code was used to draw the data together and to produce reliable information regarding the connection between boulder mobilisation and flow channel formation along the northernmost Cerberus Fossae, close to Grjótá Valles in Elysium Planitia.

CHAPTER 4.

POSSIBLE EVIDENCE FOR VARIATION IN MAGNITUDE FOR MARSQUAKES FROM FALLEN BOULDER POPULATIONS, GRJÓTÁ VALLES, MARS

4.1. Introduction

This chapter is based on research originally published in the *Journal of Geophysical Research: Planets* in March 2019, co-authored by J. R. Brown and G. P. Roberts, titled *Possible Evidence for Variation in Magnitude for Marsquakes from Fallen Boulder Populations, Grjótá Valles, Mars*. The core findings remain consistent with the original publication; however, this chapter includes significant updates and additional analysis derived from the SEIS data collected by the InSight mission, which were not available at the time of the initial research. These new insights further support Brown's hypothesis regarding ongoing seismic activity on Mars.

The majority of the research, data analysis, and manuscript drafting was led by J. R. Brown, who was also responsible for the conceptualisation of the study. G. P. Roberts provided supplementary insights on Martian seismicity. The new material, including the analysis of SEIS data and expanded discussion, was exclusively contributed by J. R. Brown following the publication.

Recent studies have suggested very young or ongoing volcanic and tectonic activity on Mars (Golombek et al., 1992; Plesica, 1993; Berman and Hartmann, 2002; Vaucher et al., 2009; Antoine et al., 2010; Voigt and Hamilton, 2018; Golder et al., 2020).

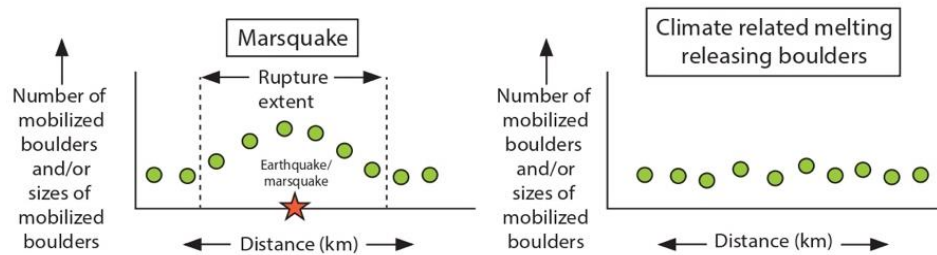
However, given Mars' smaller size, with a diameter of 6,790 km compared to Earth's 12,750 km, it has been considered less geologically active than the Earth. Zuber (2001) also notes that, given the smaller size of Mars than Earth, Mars not only heated up more quickly than Earth but also cooled off more quickly than Earth. By extension, geological activity would have occurred earlier on Mars than on Earth. Hamilton (2015) points out that as Earth and Mars were forming, they were partially melted by radiogenic heating. Both planets developed thick crusts early on that contained most of their radioactivity near the surface. However, Mars cooled down quickly and became immobile internally, remaining passive for over four billion years.

In contrast, Earth had enough radioactivity to continue evolving and experiencing different stages of internal mobility, eventually leading to plate tectonics. However,

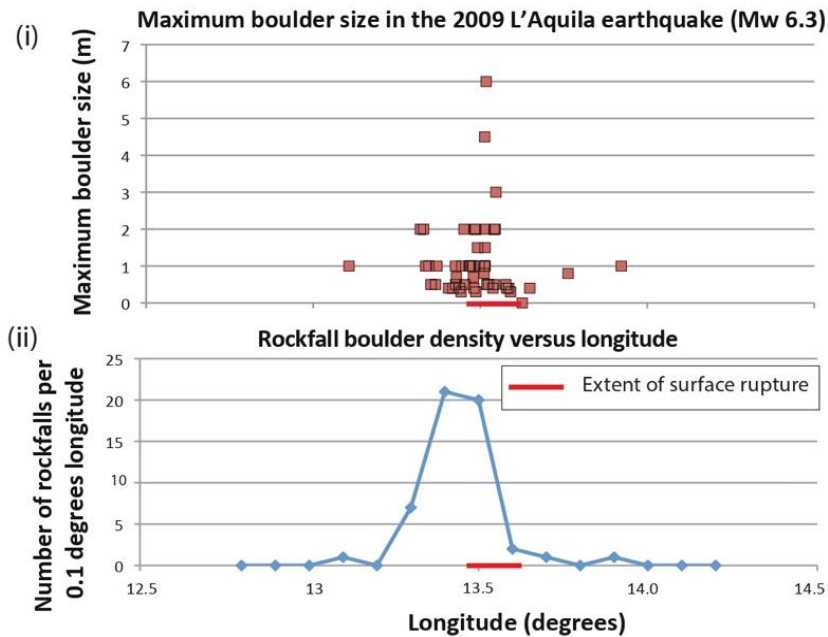
crater age dating indicates that the youngest lava flows in Elysium Planitia have ages <20 Ma (Berman and Hartmann, 2002; Vaucher et al., 2009; Voigt and Hamilton, 2018), with lava flows in Athabasca Valles being emplaced as recently as ~2.5 Ma (Vaucher et al., 2009; Golder et al., 2020). Work by Antoine et al. (2010) suggests that endogenic heat sources are present within Mars and are associated with the Cerberus Fossae fault system. This suggests that Mars was still geologically active in the very recent past.

Volcanism, faulting, and associated seismicity (marsquakes) could, theoretically, be identified without the need for an artificial seismometer to be placed on Mars. An example of 'natural seismometers' are precariously perched boulders that have toppled near an earthquake. A free-standing boulder will fall when its centre of mass moves sideways beyond the points supporting it unless the base upon which it rests displaces to return its centre of mass to a safe position (Bell et al., 1998; Brune et al., 2007). For a boulder to fall, the ground must accelerate in one direction for some time, thus allowing velocity and overall displacement to build up, even if peak ground acceleration (PGA) is small (Brune et al., 2007). However, if an earthquake event has a large PGA, this does not necessarily mean that a boulder will topple. If the direction of motion switches back and forth so rapidly that velocity and displacement never grow large, the boulder will remain in place (Brune and Whitney, 1992). This understanding of natural seismometers was used by Roberts et al. (2012) in a study of the Southern Cerberus Fossae, where analysis of anomalies in the density of boulder trails and boulder trail widths left by mobilised boulders close to faults showed that boulder trail densities per kilometre and boulder trail widths increased systematically from background values along the strike of part of the fault system. These findings suggested that a marsquake had produced ground shaking responsible for mobilising the boulders (Figure 4.1).

a) Hypothesis



b) Terrestrial dataset - 2009 Mw 6.3 Earthquake, L'Aquila, Italy



c) Martian dataset - Cerberus Fossae, Roberts et al. (2012)

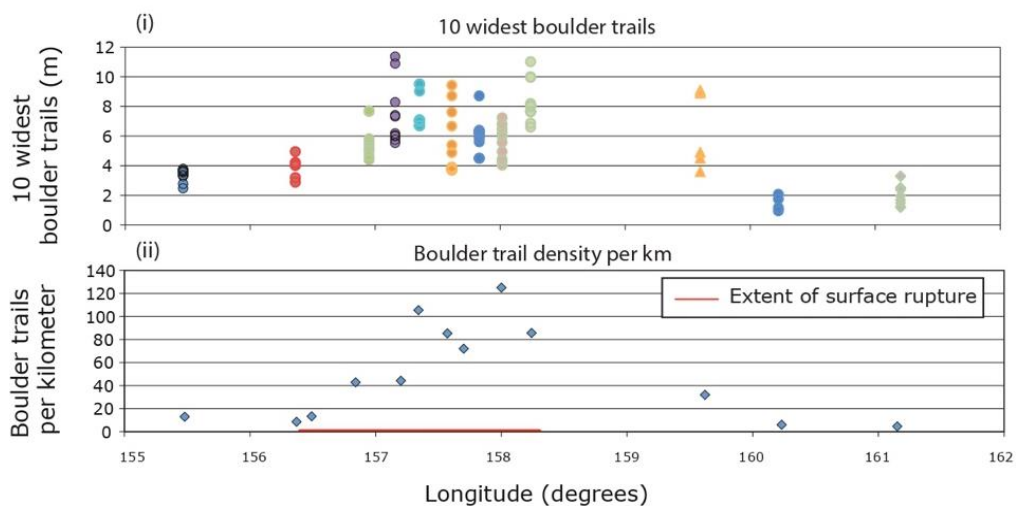


Figure 4.1. Hypotheses to explain the characteristics of the widest examples of boulder trails formed by the mobilised boulder populations due to seismic shaking and boulders' release from cliffs by ice melting. (a) Alternative hypotheses explored by Roberts et al. (2012). (b) Terrestrial rockfalls triggered by an earthquake. (c) Data from Roberts et al. (2012) for comparison with data presented in this chapter.

This study used the same approach to analyse the northernmost Cerberus Fossae in the Grjótá Valles, approximately 400 km north of the southern Cerberus Fossae. This chapter analyses fallen boulder trail populations along the northernmost Cerberus Fossae. It investigates the hypothesis that led to the conclusion that marsquakes have occurred in this region in the recent past and, hence, whether seismicity exists within this region of Mars (Figure 4.2).

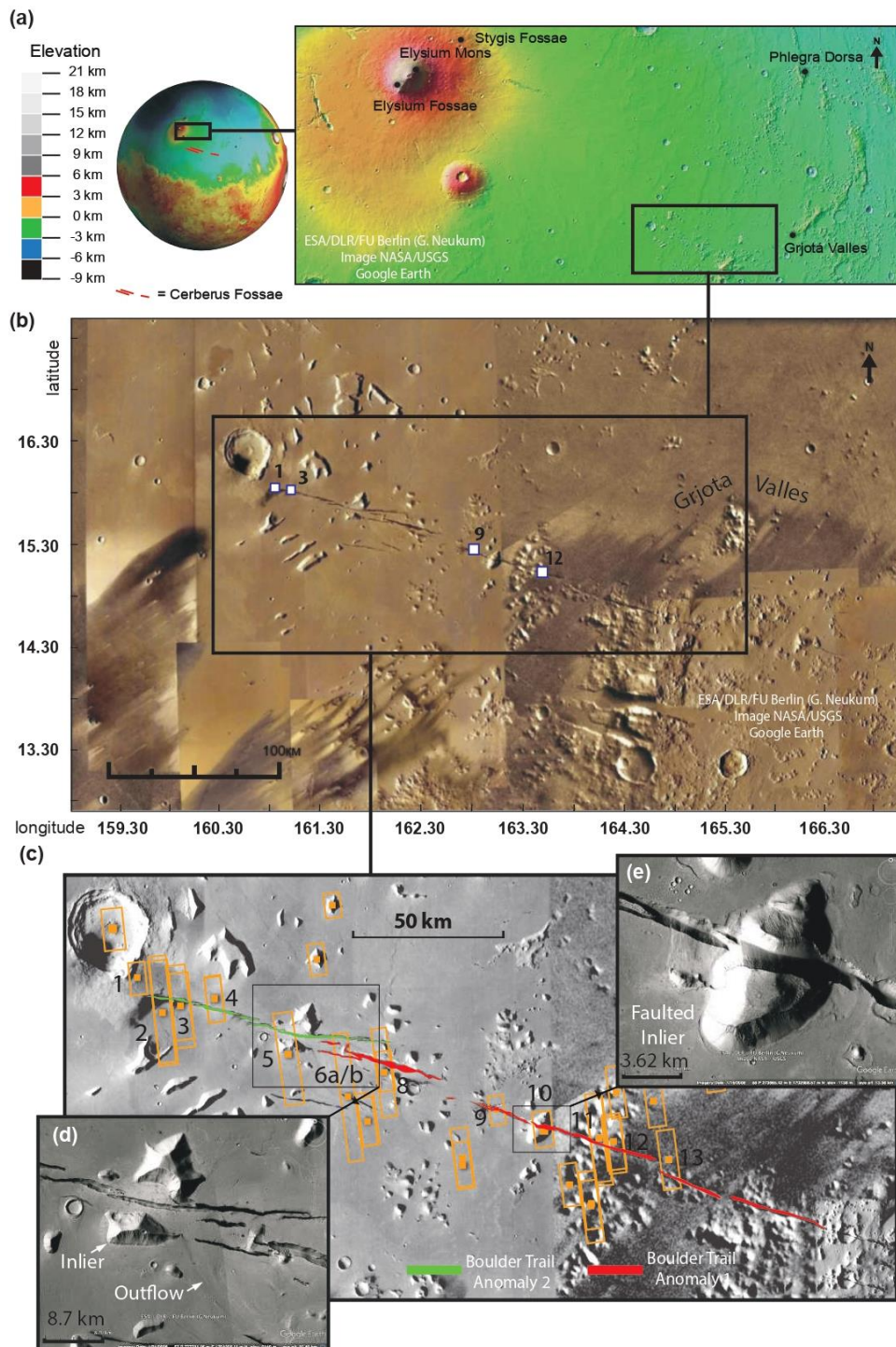


Figure 4.2. Location maps. (a) Mars Orbiter Laser Altimeter (MOLA) images of Mars show the location of the study area. (b) National Aeronautics and Space Administration (NASA) image

mosaic (visible imagery) with the location of the study area shown. The four white squares show the locations of the four geological and geomorphological interpretations for Images 1, 3, 9 and 12 (see Figures 4.3a–4.3d). (c) Seam-corrected and seam-mapped mosaic of Mars rendered at 5.0 m/px using Context Camera (CTX) data from the Mars Reconnaissance Orbiter (MRO) showing the location of the studied boulder trail anomalies. Boulder Trail Anomaly 1 (red) and Boulder Trail Anomaly 2 (green) and the location of High-Resolution Imaging Science Experiment (HiRISE) image footprints across the study area, numbered following the numbering scheme used in this study. HiRISE images 1 through 13 were used in this study. (d and e) Details of the fault geometries and geomorphology are located in (c).

The work detailed in this chapter was published in JGR: Planets in March 2019 by Brown, J. R., and Roberts, G. P. (2019). Possible evidence for variation in magnitude for marsquakes from fallen boulder populations, Grjótá Valles, Mars. *Journal of Geophysical Research: Planets*, p. 124. <https://doi.org/10.1029/2018JE005622>.

Since the publication of the paper, this hypothesis has since been borne out, with the placement of the InSIGHT (Interior Exploration using Seismic Investigations, Geodesy and Heat Transport) seismometer that reveals that marsquakes are indeed still ongoing, as presented in Giardini, D. et al. (2020).

4.2. Background

4.2.1. Cerberus Fossae

The fault system studied is the northernmost Cerberus Fossae. The Cerberus Fossae are a set of near parallel fissures, fractures and graben in the Cerberus region of Mars that trend WNW–ESE, crosscutting terrain of different ages (Tanaka et al., 2005). The two largest and better-studied fossae, the Northern Cerberus Fossae and the Southern Cerberus Fossae, are the southernmost of the fossae in the region. They are both approximately 500 km in length and are graben. The northernmost Cerberus Fossae is an approximately 200 km *en echelon* graben and fissure system. It is located between latitude N16°10'33", longitude E160°33'48", and latitude N15°12'10"/longitude E163°40'00". Its WNW–ESE orientation is sub-radial to Elysium Mons volcano, possibly a surface expression of subsurface dikes (Burr et al. 2002; Head et al. 2003). The faults are relatively recent because mapping as part of this thesis shows that they crosscut pre-existing features of known, relatively young age (Figures 4.2 and 4.3) Berman & Hartmann, 2002; Tanaka et al., 2005.

Figure 4.3 (a)
Image 1.
PSP_008502_1965 HIRISE IMAGE

Top right corner of image
16° 10' 14" + 80° N
160° 35' 24" + 20° E

- Key:
- 10 ○ Impact craters.
 - 9 Scree slopes, predominantly on the southern side of the depression.
 - 8 Southern cliff slope (dots denote presence of boulder). Colluvial deposits. Some bedrock lavas exposed?
 - 7 Edge of northern cliff area with dark material forming cliff slope face (dots denote presence of boulders). Colluvial deposits.
 - 6 Mixed area of material from scree slopes and dunes.
 - 5 Aeolian dunes (Transverse) of North to South orientation. Also, complex aeolian ripple structures (megaripple structures).
 - 4 Lighter coloured areas found only in four locations outside the depression. Possibly terrain (1) that has been cleaned of dust.
 - 3 Line marking the edge of the depression.
 - 2 Smoother, less rugged terrain with aeolian dust deposits.
 - 1 Oldest Terrain. Rugged, upstanding ridges. Circular depressions indicate poorly-preserved craters. Cratered lava surface?

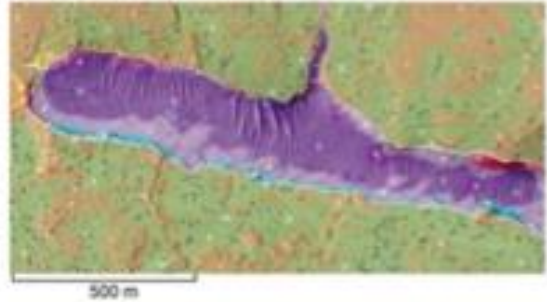
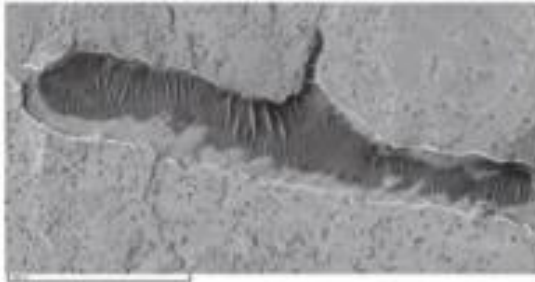


Figure 4.3 (b)
Image 3.
PSP_006999_1965 HIRISE IMAGE

Top right corner of image
16° 9' 27" + 60° N
160° 52' 41" + 90° E

- Key:
- 23 Dunes
 - 22 Denotes divide between coarser and finer grained areas.
 - 21 ○ Impact craters.
 - 20 ⊕ Impact crater with pedestal crater.
 - 19 Inner edge of northern cliff area with dark material forming cliff slope face. The edge appears sharp and lacks boulders / debris.
 - 18 Scree slope on southern side of depression.
 - 17 Area denoting darker material found towards edge of depression (3 locations). May be a lava surface cleared of dust.
 - 16 Defined slope face / cliff face along southern edge of depression, leading to rougher scree slopes down-slope. Some bedrock lava?
 - 15 w / boulders / various sizes of metre-scale.
 - 14 Aeolian dunes (Transverse) of North to South orientation. Also, complex aeolian ripple structures (megaripple structures).
 - 13 Scree slopes, predominantly on the southern side of the depression.
 - 12 Denotes edge of depression area.
 - 11 Possible edge of adjoining depression area.
 - 10 Colluvial deposits. Coarse-grained / darker material.
 - 9 Colluvial deposits. Coarser grained / darker material with evidence of aeolian influence (dune formations).
 - 8 Colluvial deposits, that appear coarse-grained.
 - 7 Denotes presence of boulders.
 - 6 Fine grained aeolian dust/sand featuring megaripple structures/transverse dunes in NE-SW orientation + N-S orientation.
 - 5 Complex dune patterns.
 - 4 Oldest Terrain. Rugged, upstanding ridges. Circular depressions indicate poorly-preserved craters. Possibly a cratered lava surface.
 - 3 Area to lower left of image appear to display an echelon form. (Also middle left of image) Note presence of aeolian dunes still visible in some higher rugged areas.
 - 2 Mixture of rougher/coarser material, s with more rugged presence of aeolian transverse dunes. Mix of terrains (4), (5) and (6).
 - 1 Outline of more obviously defined terrain (4)



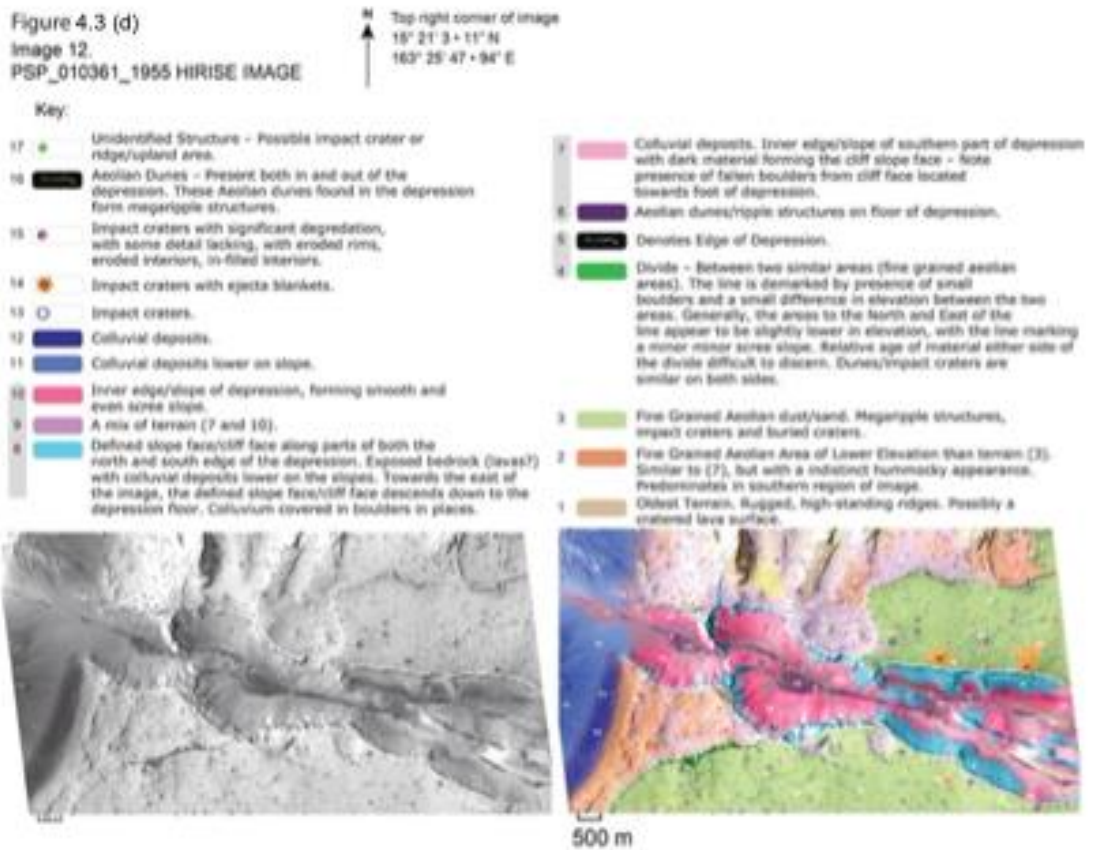
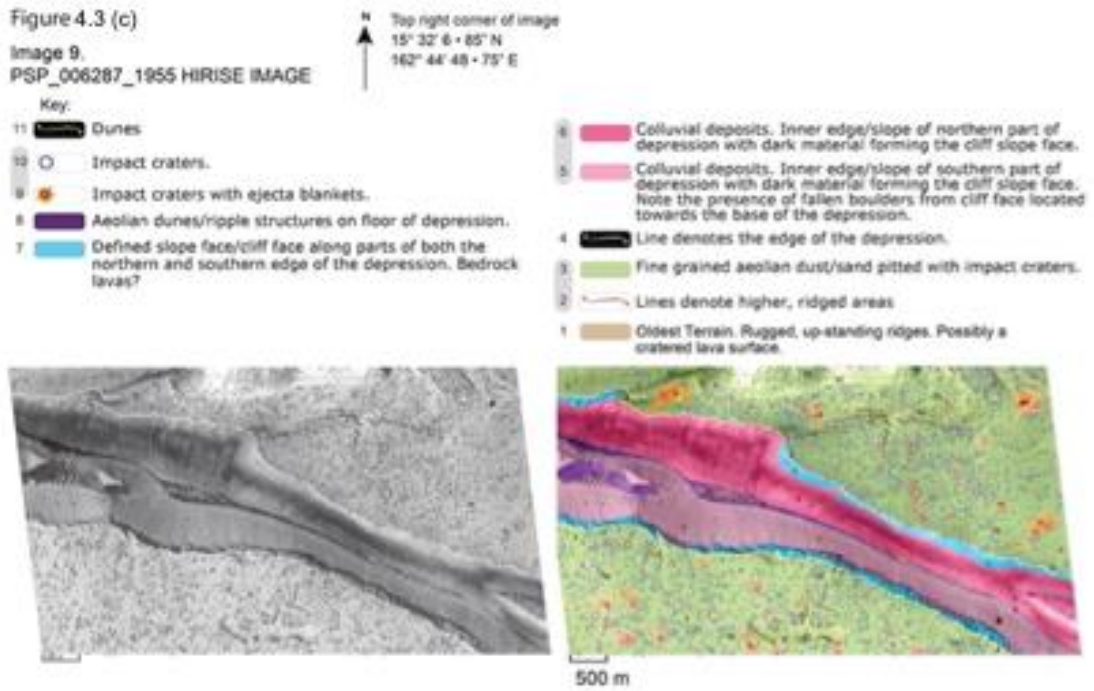


Figure 4.3. (a to d): Geological and geomorphological interpretations of Images 1, 3, 9 and 12, taken from HiRISE images (for footprint locations, please see Figure 2). The geology/

geomorphology of the fossae is that of a low-relief plain that has been faulted by graben structures and down-dropping central blocks covered by colluvium and aeolian material.

The fossae offset Late-Amazonian Cerberus lavas and older inliers (Tanaka et al., 2005; Figures 4.2 and 4.3). It is believed that the ages of the youngest lavas offset on the nearby Cerberus Fossae, assessed by crater counting methods, are <10 Ma (Hartmann and Berman, 2000; Head et al., 2003; Vaucher et al., 2009), implying that the fossae if they are all approximately the same age, are even younger. The ~900-m offset revealed by MOLA data (Figure 4.4 (a) to (d)), if developed since 10 Ma as implied by crater-count ages, implies a rate of vertical offset of ~0.09 mm/year. This value is similar to those documented rift systems on Earth (Vetterlein and Roberts, 2010). The faults also offset geomorphic features such as lava plains, older inliers, and outflow channels with streamlined islands (Figure 4.2, (c), (d), and (e); Burr, McEwen et al., 2002; Jaeger et al., 2010; Plescia, 2003). Similar features were reported for the faults along Cerberus Fossae (Roberts et al., 2012).

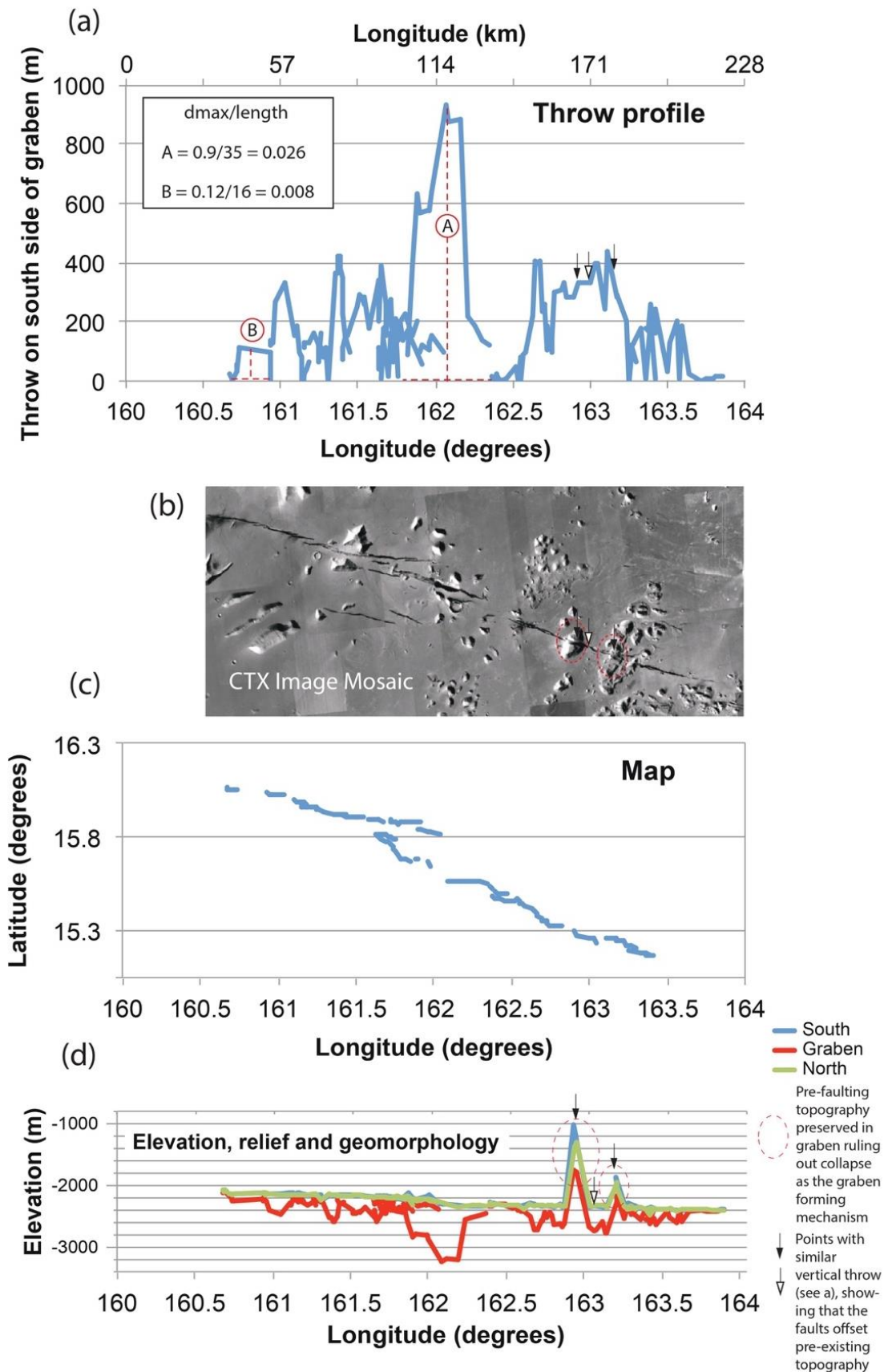


Figure 4.4. The relationship between the map trace of the graben and vertical offsets constrained by Mars Orbiter Laser Altimeter (MOLA) data. The MOLA data were processed and analysed in collaboration with the co-author of the published paper, Prof. Gerald Roberts,

who contributed to the methodology for measuring vertical offsets (see Brown and Roberts, 2019). The analysis of the MOLA data, including the plotting of longitude against vertical offset and the integration of these measurements with Context Camera (CTX) imagery, was conducted by Brown as part of this research. The vertical displacement (throw) across the graben was measured using MOLA data points spaced approximately 300 meters apart, providing high-resolution elevation profiles. The throw was calculated as the difference between the elevation of the plains adjacent to the graben (the footwall) and the lowest point of the graben floor (the hanging wall) at multiple locations, as demonstrated in plot (a). The MOLA data reveal that the throw increases from zero at the tips of the graben to a maximum of approximately 900 meters at longitude E162°, confirming a typical fault subsidence profile. **Plot (a)** illustrates the vertical offset measured across the southern side of the graben, plotted against longitude. **Figure (b)** shows the CTX mosaic, which correlates these vertical offsets with the graben's map geometry. The latitude and longitude positions of the MOLA data points used for the measurements are displayed in (c). In **plot (d)**, the absolute elevation values for the plains to the north and south of the graben, as well as the graben floor, are plotted against longitude. This shows how the vertical offsets are distributed across the graben.

Detailed geological and geomorphological mapping was undertaken to ascertain the geometry and evolution of the graben. The data reveal that the geometry of the faults of the northernmost Cerberus Fossae is consistent with that of graben: fault-controlled cliffs adjacent to flat-bottomed depressions (Figures 4.3, 4.4, and 4.5). MOLA data (Mars Orbiter Laser Altimeter on the Mars Global Surveyor (MGS) spacecraft) reveal that the vertical offset across the graben, which are exposed on a surface that slopes from -2,100 m elevation to -2,400 m elevation from west to east, increases from zero at the tips of the graben to approximately 900 m at longitude E162° (Figure 4.4). This shows an offset/subsidence profile that is typical of faults, with vertical offsets as high as approximately 900 m and a maximum displacement (d_{max})/length ratio (with d_{max} measured as a vertical offset for this example) for the whole structure of 0.005 within the range measured for terrestrial faults and those on Mars (Schlische et al., 1996; Vetterlein and Roberts, 2010). In detail, the MOLA data constrain the vertical offset across the graben at 180 locations and reveal displacement gradients and d_{max} /length ratios associated with individual distal and medial fault segments of 0.008–0.026, again similar to values measured on Earth (Vetterlein and Roberts, 2010); (Figure 4.4). The similarity in d_{max} /length values between faults in Grjótá Valles and the Earth suggests that the material strength is similar in the two regions (Gomez-Rivas et al., 2015). If the material strength is similar, the relationships between rupture length, d_{max} , stress drop, and moment magnitude are also likely to be similar (Ali and Shieh, 2013). Therefore, d_{max} /length observations suggest that these are faults formed by similar deformation processes to those on Earth. As such, it may be possible to infer some aspects of seismicity, such as moment magnitude, from observations of surface deformation.

4.2.2. Cerberus Fossae—Recent seismic activity and natural seismometers

The subsurface region underlying the Cerberus Fossae is likely still geologically active. Antoine et al. (2011), analysing THEMIS-IR (Thermal Emission Imaging System – Infrared) images, revealed high night-time temperatures with the Cerberus Fossae, with the walls and floors of the fossae up to 40 K warmer than the surrounding areas. The team concluded that the temperature variation was caused by geothermal heat transported by air convection through the porous debris aprons. The possibility of endogenic heat beneath the fossae suggests that geological activity is ongoing in this region. With outflow channels such as Athabasca Valles dated to “... a few million years” (Keszthelyi et al., 2007; Hartmann and Berman, 2000; Burr et al., 2002; Murray et al., 2005), although “... an age of several tens of millions of years is considered more likely,” (Plescia, 2003; McEwen et al., 2005), the fact that the Southern Cerberus Fossae cross-cuts the Athabasca Valles outflow channel would indicate that the fossae are younger features. If these estimates are correct, the vertical offset of Athabasca Valles across Cerberus occurred within the last 2.5 Ma (Vaucher et al., 2009).

Studies of the lesser-studied fossa and associated flow channels from the Cerberus Fossae in Grjótá Valles, the northernmost area of the Cerberus Fossae region, have revealed that the region is younger from west to east. The northernmost Cerberus Fossae cross-cuts a series of outflow channels across the area of Grjótá Valles, with the source of each younger channel being progressively further eastward (please see Chapter 5 for a more detailed discussion). Golder et al.’s (2020) work provides crater count ages within the study region that are younger from west to east (53 Ma, then 33 Ma, then 31 Ma). Golder et al. (2020) suggest this change in age is due to changes in the rheological properties of the lavas during emplacement, such as material strength and porosity. This could be the case, but the ages obtained by Golder et al. (2020) are from areas that partially overlap flow deposits (please see Chapter 5 for further details). The 53 Ma age happens to coincide with the proximal regions for the two oldest flow episodes, Flow 1 and Flow 2; the 33 Ma age coincides with the area occupied by the distal parts of later flow episodes, Flow 3 and Flow 4; the 31 Ma age coincides with an area to the east of the region occupied by the latest flow episode, Flow 5.

Research looking at fallen boulder trails within the Southern Cerberus Fossae, a more extensive set of fractures to the south of the northernmost Cerberus Fossae, revealed that the most plausible explanation for the fallen boulders was seismicity and that seismicity is not only recent along the Southern Cerberus Fossae but possibly putative in nature and ongoing, too. Work on the Southern Cerberus Fossae, using HiRISE

imagery (High-Resolution Imaging Science Experiment onboard the Mars Reconnaissance Orbiter) of excellent resolution (~25-cm pixel sizes) allowed for a thorough study of boulders and boulder trails from orbit. Roberts et al. (2012) showed that boulder trail densities per kilometre and boulder trail widths increased systematically from background values along the strike of part of the Southern Cerberus Fossae fault system by being able to measure the widths of boulder trails and counting boulder trail populations across the study area. The team's findings were interpreted as possible evidence that a marsquake had produced ground-shaking that was responsible for mobilising the boulders. The team suggested that boulder populations mobilised by seismic shaking, in particular the widest boulder trails, would show decreases in mobilised boulder frequency and boulder size over tens of kilometres or more away from putative epicentres if produced by single large events as observed on the Earth (Figure 4.1) as evidenced on Mars by the widths of trails in the dust left by mobilised boulders. In contrast, boulder populations mobilised by processes facilitating the release of boulders from steep cliffs, such as the melting of ground ice on steep slopes, would produce spatially uniform boulder trail populations, lacking anomalies with dimensions of tens of kilometres or more. Measurements presented by Roberts et al. (2012) were consistent only with the hypothesis of mobilisation by seismic shaking (Figure 4.1).

Furthermore, the trails in the underlying sediment left by boulders as they rolled and bounced downslopes suggest relatively recent boulder mobilisation and, hence, possible ongoing marsquake activity. This is because tracks produced by the rovers Spirit and Opportunity were erased over timescales of only days to months (Geissler et al., 2010) due to the passage of dust storms during the perihelion season, although evidence exists of track preservation for more extended periods in locations sheltered from the wind; thus, tracks left by boulders would also be erased, suggesting that preserved examples must be relatively young if the material is fine enough to be mobilised by the wind. Tracks produced by boulders at Cerberus Fossae are wider and deeper (several metres and several decimetres) than trails left by rovers (centimetres to millimetres), so presumably, it would take longer to erase them with aeolian processes. However, the same arguments apply, and it is difficult to envisage an age as old as, for example, 10^6 – 10^7 years for the boulder trails. Roberts et al. (2012) also pointed out that the geographic dimension of the boulder trail width/frequency anomaly along the fault system's strike might indicate the marsquake's magnitude, as is the case on Earth (Keefer, 1984). The ~200 km-wide zone of mobilised boulders measured along the northernmost Cerberus Fossae might be consistent with a marsquake of moment magnitude ~M7.9 (see Wells and Coppersmith, 1994). A marsquake of this

magnitude is not inconsistent with the along-strike extent of the faults of Cerberus Fossae because Vetterlein and Roberts (2009) showed that these faults exhibit continuous along-strike displacement profiles constraining a fault length of ~325 km, longer than the implied rupture extent. However, Knapmeyer et al. (2006) suggested a maximum magnitude of 7.6. Vetterlein and Roberts (2010) showed that the d_{\max}/length (measured as vertical offset, throw, in this example) of the Cerberus Fossae faults was ~0.1 to 0.001, similar to those measured on Earth, suggesting that the relationships between slip dimensions and marsquake magnitude might also be similar to the Earth.

Using the concept of precariously positioned boulders serving as natural seismometers (Brune and Whitney, 1992; Bell et al., 1998; Brune et al., 2007) similar to Roberts et al. (2012), in this thesis an examination of the northernmost Cerberus Fossae looking for boulder trails and fallen boulders along the fossae was undertaken. The exact details of how this process worked will be elucidated in the Methods section of this chapter (4.3). At the commencement of the studies for this thesis, there was no functioning seismometer on Mars. The paper by Brown and Roberts was published in March 2019, shortly after the InSIGHT (Interior Exploration using Seismic Investigations, Geodesy and Heat Transport) seismometer SEIS (Seismic Experiment for Interior Structure) was deployed on western Elysium Planitia, Mars on February 12, 2019. In April 2019, NASA announced that SEIS had detected its first marsquake. This reference is crucial to highlight, as it underscores the significance of prior research on the northernmost Cerberus Fossae. This work revealed the existence of ancient seismic events on Mars, suggesting that seismic activity might persist even today. This finding is particularly noteworthy as it predates the detection of Marsquakes by SEIS, indicating the potential continuation of seismic activity on the planet.

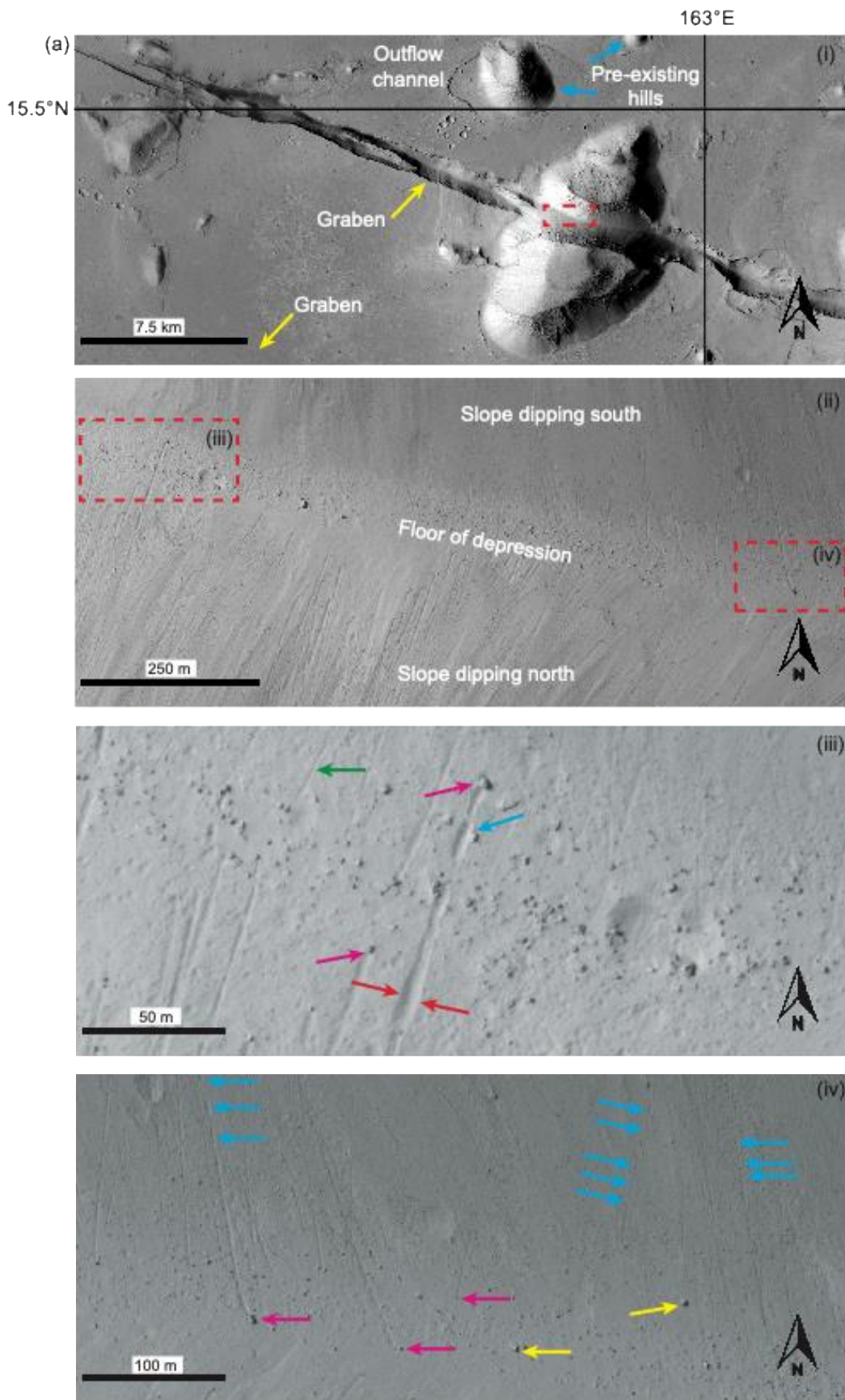
At the outset, the work in this thesis studying the northern Cerberus Fossae was to find the following:

- (a) Possible examples of boulder trail anomalies, with evidence ruling out causes other than marsquakes for their formation.
- (b) Whether marsquakes of different magnitudes and, hence, different epicentral shaking intensities to mobilise boulders can be inferred.

Faults close to Grjótá Valles offset planar surfaces that are probably lava flows, inliers of older terrain such as hills that protrude upward through the lava flows, and outflow

channels that may be of aqueous or volcanic origin associated with volcanism (e.g., Burr, Grier, et al., 2002; Hamilton, 2013; Jaeger et al., 2010; Morgan et al., 2013; Plescia, 2003, for associated examples).

This means the Grjótá Valles faults are morphologically similar to those along Cerberus Fossae studied by Roberts et al. (2012). As for the examples from Cerberus Fossae described by Roberts et al. (2012), initial inspection of down-faulted regions in Grjótá Valles revealed many thousands of boulder trails made by mobilised boulders that have fallen from fault-controlled cliffs (Fig 5 (a) – (d)). However, it is evident from inspection of imagery that the faults associated with Grjótá Valles are segmented (Figure 4.2 (b) and (c)), with shorter segments (maximum of 60–80 km) than those associated with larger graben on the Northern and Southern Cerberus Fossae (Taylor et al., 2013; Vetterlein and Roberts, 2009, 2010). Such a combination of features allowed for testing whether anomalies in boulder trail densities and dimensions occur along the faults and are best explained by marsquakes. If marsquakes best explain them, whether their dimensions correlate with the dimensions of fault segments.








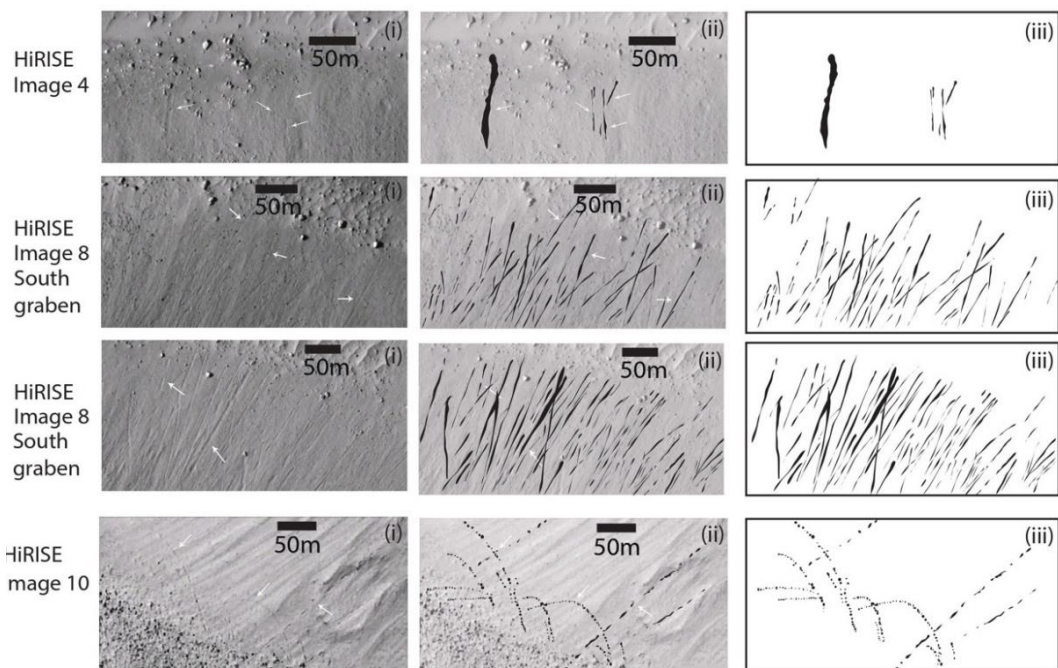
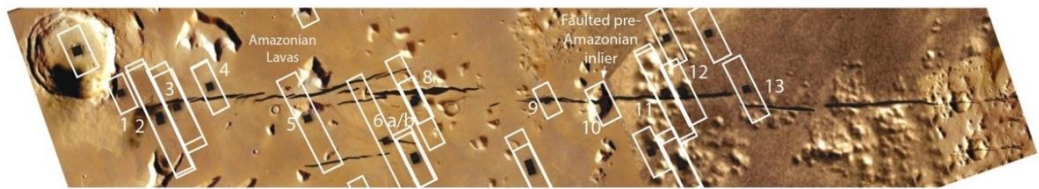
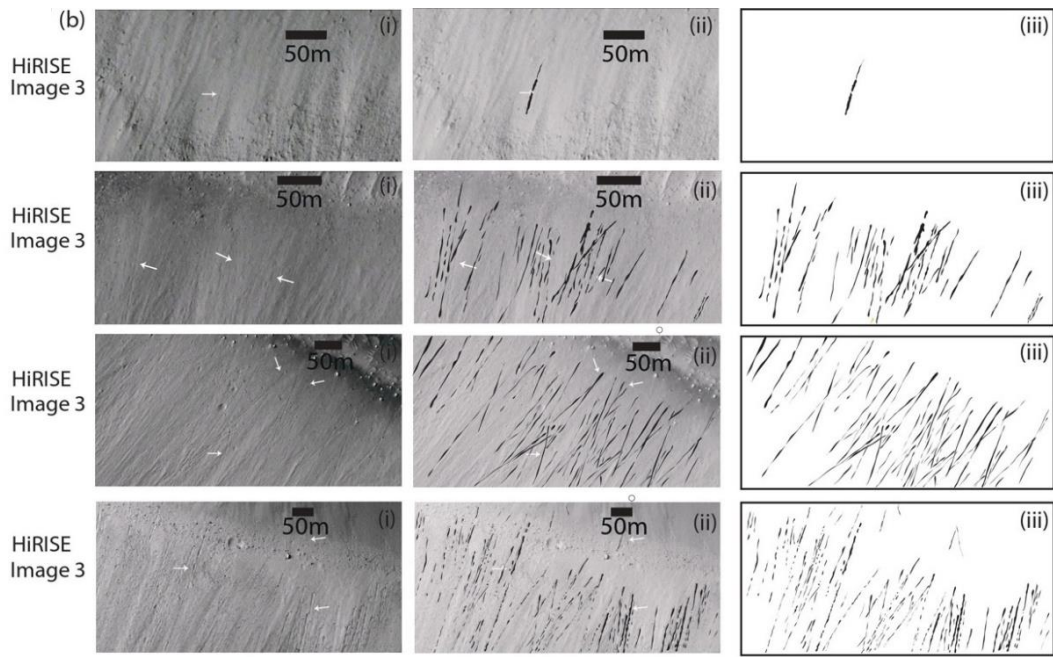
-  = Trail measured at widest point on trail defined by raised levees and sharp edges to trails
-  = elliptical depressions indicate bouncing  = boulder with no trail not included in count
-  = clear boulder that produced a trail  = trail with no clear boulder included in count

Figure 4.5a. (a): (i) Location map of the area - Seam-corrected and seam-mapped mosaic of Mars rendered at 5.0 m/px using Context Camera (CTX) data from the Mars Reconnaissance Orbiter (MRO). (ii) Detail from HiRISE image (ESP_018075_1955) of the area within the red-dashed rectangle in (i), which shows the floor of the depression and the north and south slopes. Note the abundance of boulder trails on both slopes, some with a boulder at their terminus. (iii) and (iv) are details from the HiRISE image (ESP_018075_1955) of the area within the red-dashed rectangles in (ii). Both images allow for the identification of a range of boulder trail features, including elliptical depressions (blue arrows) that indicate bouncing boulders, clear boulders at the end of a boulder trail (pink arrows), and boulders with no trail (yellow arrows). These trails were not included in boulder trail counts. Trails with no boulders (green arrows). These were included in the boulder trail counts.



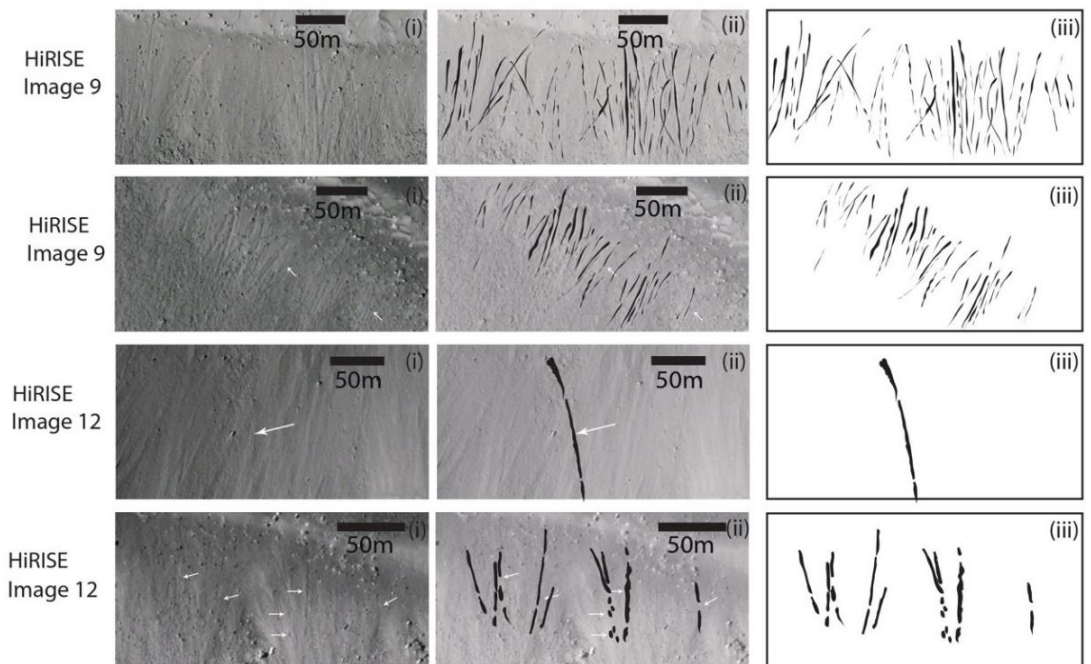
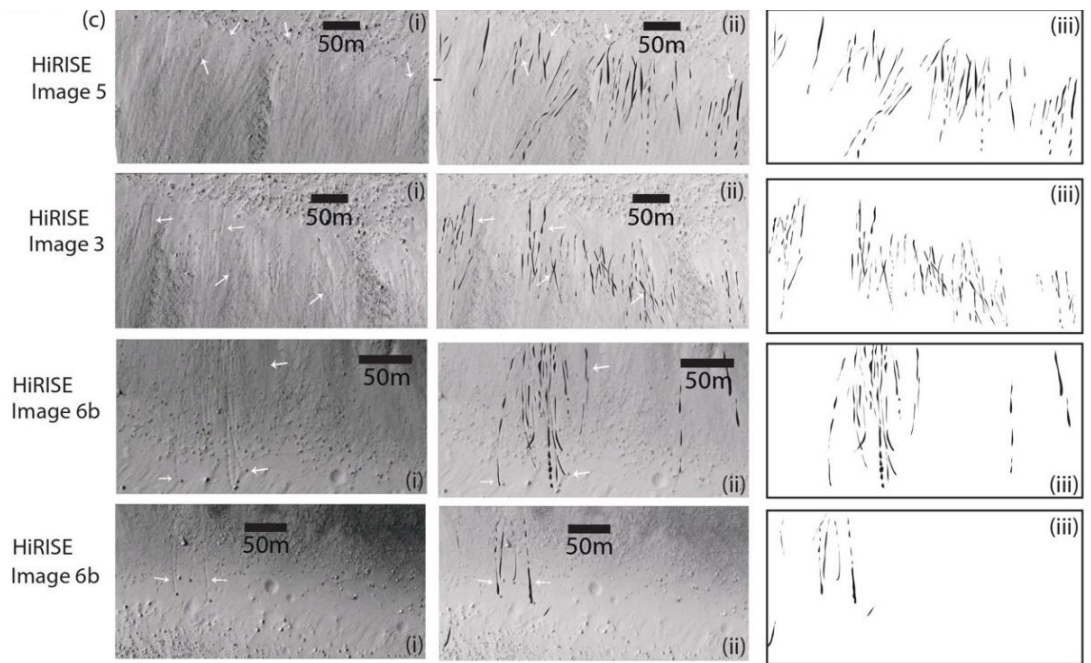
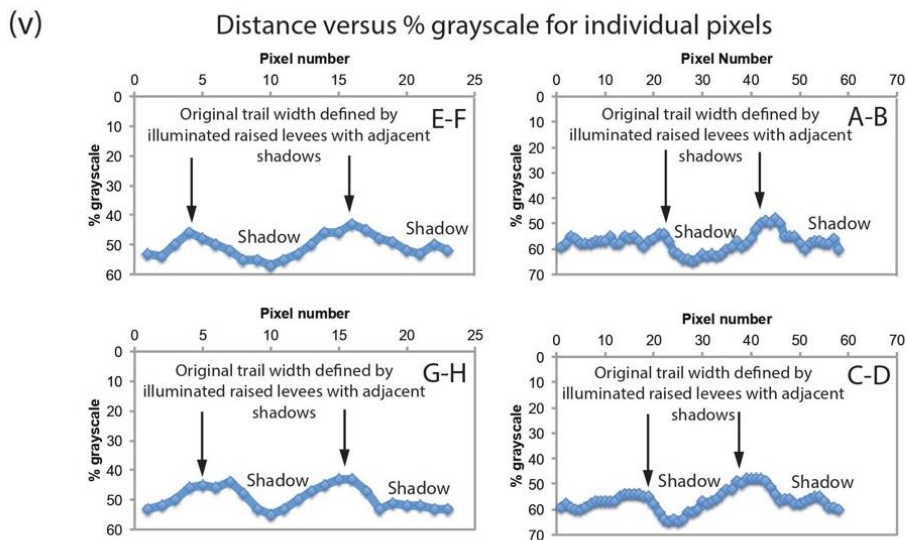
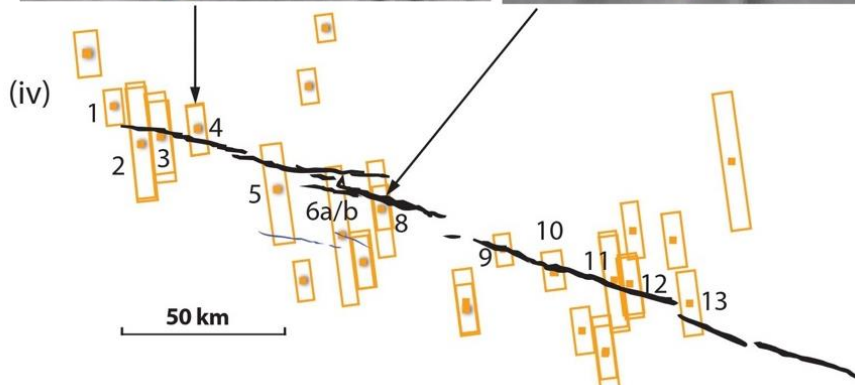
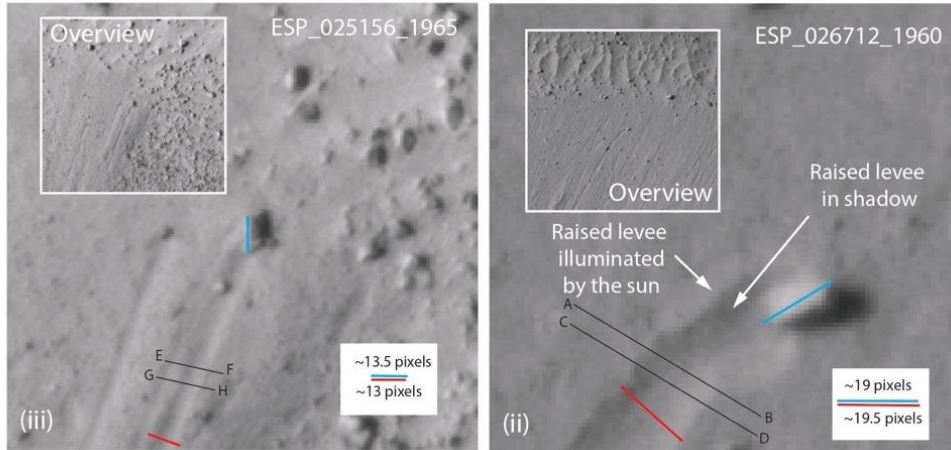
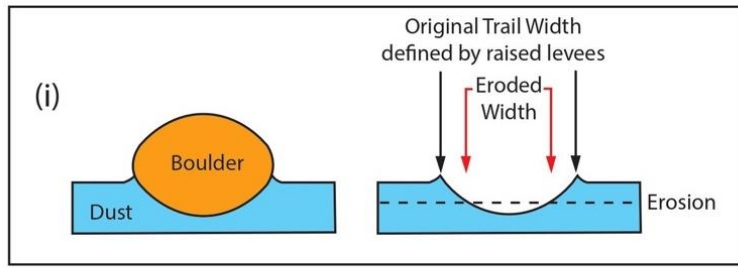


Figure 4.5.b,c. (b) and (c): A selection of images showing the variation in boulder trails between different High-Resolution Imaging Science Experiment (HiRISE) images used (please see Figure 4.2 for HiRISE footprint locations) and different parts of the same HiRISE images: (i) original image with added white arrows pointing out a selection of boulder trails/bounce marks; (ii) the image with the boulder trail/bounce marks drawn in black, and (iii) with only the black infill. The figures illustrate only a small proportion of the boulder trails in each image.



Lower % grayscale values indicate raised, illuminated levees, with higher values indicating shadows produced by the levees

Figure 4.5d. (d): Observations of boulder trails and boulder dimensions. The similarity between the dimensions of boulders and boulder trails suggests that boulder trails have not been significantly affected by erosion. (i) A possible hypothesis is that boulder trails may be degraded

by erosion and that degradation may vary spatially, influencing the number of trails preserved and the measured widths. (ii and iii) Comparison of boulder trail widths with the dimensions of the boulders that formed them from HiRISE images ESP_026712_1960 and ESP_025156_1965). (iv) Location map showing the position of HiRISE images ESP_026712_1960 and ESP_025156_1965. (v) That the trails have not been significantly degraded by wind erosion is consistent with the preservation of raised levees produced by the motion of boulders, evidenced by variation in percentage grayscale for individual pixels in the images. This is evidenced by visual inspection of many examples and also evidenced by the percentage grayscale measurements made that show systematic variation in percentage grayscale on the floors of the tracks, not constant values as would be expected for a flat, depositional surface illuminated by the Sun. If the levees are made of sand, and their preservation potential is low, then the ages of the boulder trails whose widths are defined by the levees are likely to be similar and relatively young. In other words, the widespread preservation of levee crests in the images suggests that the boulder trails are similar in age because they have not been eroded/degraded. Moreover, it is suggested that the population of boulder trails is primarily composed of individual trails of similar age; therefore, this does not rule out the possibility that the trails were formed during single, widespread events, such as marsquakes.

4.3. Method

Chapter 3 provided an overview of the methods used in this thesis. This section provides more detail specific to the study of mobilised boulders in this chapter. In order to be able to search for boulder trails and fallen boulders and to be able to measure the lengths and widths of the boulder trails in an attempt to constrain the extent of boulder trail anomalies (Figure 4.2 (b), (c), and (d)), it was essential first to identify HiRISE footprints that covered sections of the northernmost Cerberus Fossae within Grjóta Valles. HiRISE images were the only ones that offered the resolution needed to discern and measure these features. (Figure 4.5 (b), (c), and (d)). National Aeronautics and Space Administration (NASA) HiRISE images were accessed using the Planetary Data System (PDS) node at the University of Arizona (<http://hirise.lpl.arizona.edu/>; Table 4.1).

Table 4.1. HiRISE images used in the study of the northernmost Cerberus Fossae. Exact footprint locations may be seen in Figure 4.2 (c) and Figure 4.5 (b) and (c).

Image numbers used in this chapter	HiRISE image name	Latitude (centred)	Longitude (east)	Map projected scale
1	PSP_008502_1965	16.250°	160.575°	25 cm/pixel
2	ESP_018774_1965	16.085°	160.723°	50 cm/pixel
3	PSP_006999_1965	16.100°	160.828°	25 cm/pixel
4	ESP_025011_1965	16.141°	161.011°	25 cm/pixel
5	ESP_018708_1960	15.819°	161.448°	50 cm/pixel
6a	ESP_027345_1955	15.571°	161.792°	50 cm/pixel
6b	ESP_027345_1955	15.571°	161.792°	50 cm/pixel
8	ESP_026712_1960	15.715°	162.013°	25 cm/pixel
9	PSP_006287_195	15.479°	162.677°	25 cm/pixel
10	ESP_018075_1955	15.386°	162.928°	25 cm/pixel
11	ESP_028400_1955	15.329°	163.242°	25 cm/pixel
12	PSP_010361_1955	15.311°	163.336°	25 cm/pixel
13	PSP_007790_1955	15.209°	163.657°	25 cm/pixel

The images were downloaded at their highest resolution (JPEG2000 black and white) map-projected images. They were then opened in HiVIEW, a *data explorer and image viewing application supporting the JPEG2000 image format of images taken by HiRISE*. A JPEG2000 contains the metadata that describes the image, stored as compressed codestreams. The JPEG2000 codestream is based on a Discrete Wavelet Transformation (DWT) of the original image pixel values. This codestream has characteristics that enable it to be selectively decoded for all or part of the entire image area at less than the original image resolution and less than the full quality level of the original image while maintaining high-quality viewing fidelity. HiVIEW uses the JPEG2000 codestream's characteristics by only rendering the area of the image needed at excellent resolution. This means that the whole images are not stored on the computer, which would have been prohibitive given the enormous sizes of the images.

The objective of analysing the HiRISE images was to locate boulder trails and fallen boulders inside the northernmost Cerberus Fossae. Once this was done for a particular location using HiVIEW, the area was saved, making sure that the image size scale was 1.0 to ensure that each image was saved at full resolution. Progressively, each HiRISE image was studied, boulder trails and fallen boulders were identified, and each 'close-up' image from HiVIEW was saved. Each image from each location was then, where necessary, merged with the other images from a location in Adobe Illustrator. The final

merged images were saved as JPEGs and imported into Google Earth as georeferenced image overlays. This enabled the use of the measurement tools in Google to accurately measure features such as the length of boulder trails, widths of boulder trails, and distances across the northernmost Cerberus Fossae. There were 18 areas covered by HiRISE imagery along the study area of the northernmost Cerberus Fossae (Figure 4.2 (c)). However, six of the locations are covered by two HiRISE images. One of the images (ESP_027345_1955) covers an area that has six fractures, two of which were required for this study, with one (ESP_027345_1955) split into two images (6a and 6b), meaning 13 images were used in total—the number of images available provided sufficient along-strike coverage of the structures for measurement. The ruler tool in Google Earth was used to measure distances and boulder trail lengths and widths, allowing for boulder trail density to be calculated. Distance measurements were then checked in ArcGIS to ensure accuracy. The values were similar to those from Google Earth to the extent that results were unaffected, with a <1% difference in distance between ArcGIS and Google Earth at the latitudes studied. Once each of the merged HiVIEW images for each HiRISE image was saved as JPEGs and imported into Google Earth as georeferenced image overlays, systematic measurements were undertaken for each image.

Boulder trail widths were defined as the width between the raised levees or sharp edges that formed on the underlying substrate as the boulder traversed across it (Figure 4.5 (a), (b), (c), and (d)). All boulder trails were measured, including those without an identified boulder at the trail's terminus. The widths were measured at their widest point to exclude measurements where the boulder bounces and leaves a narrower trail. There is cross-image variation in boulder trail density on HiRISE images. Where one can see that the substrate is coarse-grained, with visible boulders, no trails exist. Examples of cross-trail variations are shown in (Figure 4.5 (a), (b), (c), and (d)). Thus, measurements of the distance across areas where one could gain continuous records on regions where the substrate appeared fine-grained were made, and the values were converted into numbers per kilometre.

4.3.1. Identifying, counting, and measuring boulder trails

The position of every bolder trail was identified in each of the 13 locations along approximately 1.5 km to 6.5 km-long transects along the slopes immediately adjacent to the floors of the graben (Figure 4.2 (c), Figure 4.6, and Table 4.1).

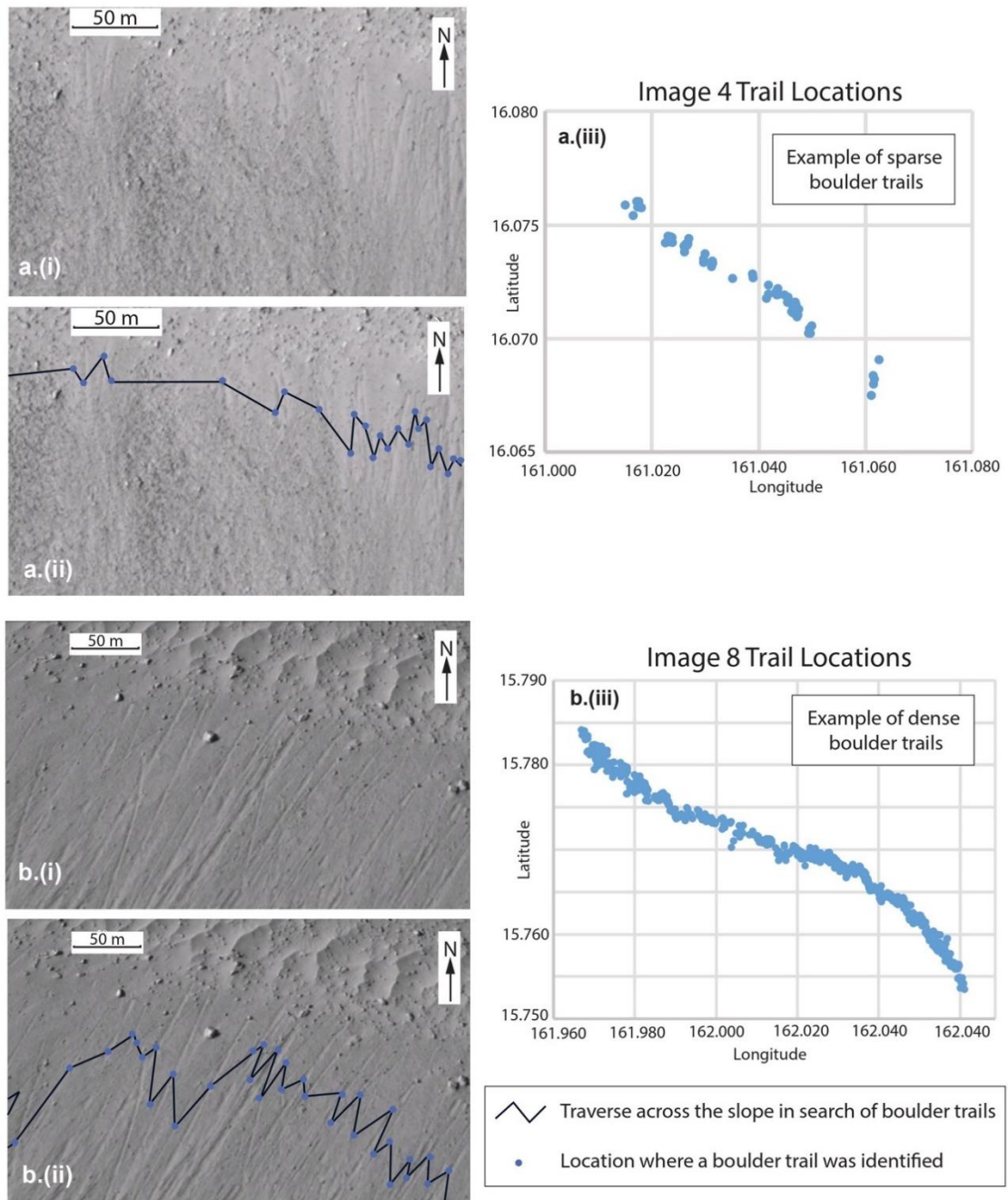


Figure 4.6. Example of a boulder trail density measurement for two images: (a) Image 4 (HiRISE Image ESP_025011_1965) and (b) Image 8 (HiRISE Image ESP_026712_1960). (a) Image 4 (i) shows a sparse concentration of narrow trails, all of similar width and length. (ii) The blue dots at the apex of the dark lines indicate boulder trails along a transect shown in dark blue. (iii) Graph showing location and density of boulder trails found along a WNW–WSE transect traversing 0.03° of longitude, showing the locations of trails. (b) Image 8 (i) shows a dense concentration of both narrow and some wider trails. The lengths of the trails in the image are comparable. Some trails exhibit bounce marks. (ii) The dots at the apex of the dark lines indicate boulder trails along a transect shown in dark blue. (iii) Graph showing location and density of boulder trails found along a WNW–WSE transect traversing 0.05° of longitude, showing the locations of trails.

The transects were chosen according to two criteria: (a) they existed at the bases of steep slopes along fault-controlled cliffs, and (b) fine-grained deposits (probably aeolian sand and dust) were present that preserved boulder trails. It was not possible

to take measurements where the surface was formed of coarse-grained sediments (≥ 20 to 50 cm particle size) or on solid rock. In such locations, it is unlikely that boulder trails would be preserved.

Figure 4.6 shows how the boulder trails were measured—the zig-zag orientation of the lines in a. (ii) and b. (ii) resulted from accurately counting the boulder trails and ensuring that double counts did not occur. Some locations had vast numbers of boulder trails, and this method of counting many close-together trails, with some trails cross-cutting others, ensured accuracy in that trails were not double-counted or missed. The blue dots visible on each boulder trail were the widest part of each trail, and later width measurements of boulder trails were taken at these points. Counting was done along-strike direction. The along-strike distance was recorded as the longitude of each blue dot in Figure 4.6 for conversion into boulder trails per kilometre values in Figure 4.7 (b) using trigonometry and a conversion factor for degrees longitude into kilometres. The along-track lengths of the zig-zag tracks were not used in any calculation but served only to record precisely how the boulder trail populations were traversed and where the measurements were made. In areas where boulder trail densities were relatively low ($\lesssim 45$ boulder trails per kilometre), and the trails were clear on the analysed images, there is a high degree of certainty that all boulder trails were measured. In areas with high boulder trail density (≥ 45 boulder trails per kilometre), identifying each boulder trail became challenging as boulder trails coalesced. There may have been an underestimation of the number of boulder trails per kilometre. However, this would not have affected the overall conclusions (e.g., Figure 4.6, with results in Figures 4.7 and 4.8, respectively). Another consideration is the existence of boulder trails $\lesssim 95$ cm in width. Such trails would not have been resolved with HiRISE imagery; therefore, boulder trail density would have been underestimated. That said, the hypothesis depends on the largest mobilised boulders (widest boulder trails), so the absence of data on boulder trails $\lesssim 95$ cm in width would not affect the conclusions.

The ten widest boulder trails' widths from each of the thirteen images were used to find a mean width value to estimate the dimensions of mobilised boulders. To ensure accuracy when measuring distances using the ruler tool in Google Earth on pixelated images, the co-author for the published paper (Gerald Roberts) and the present author independently measured the same images and then compared results. Figures 4.8 (a) and 8 (b) show the comparisons between the results. The sets of results proved to be broadly comparable within error, with the differences between results (<1 m for the mean value for the ten widest boulder trails and <10 – 20 boulder trail counts per

kilometre) being far smaller than the signals that were measured (between 1 m and 5.5 m for the mean value for the ten widest boulder trails and between 0 and 100 for the boulder trail counts per kilometre). Overall, the method for measuring the number of boulder trails and their widths using the ruler tool in Google Earth proved robust and repeatable should others choose to make measurements from the same images.

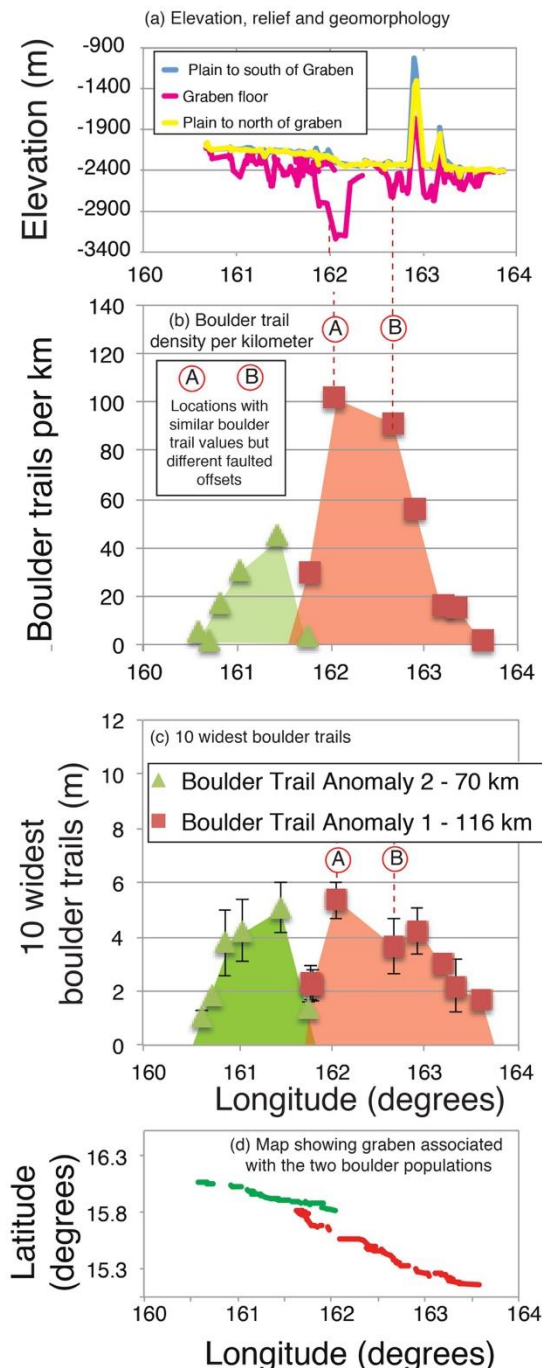
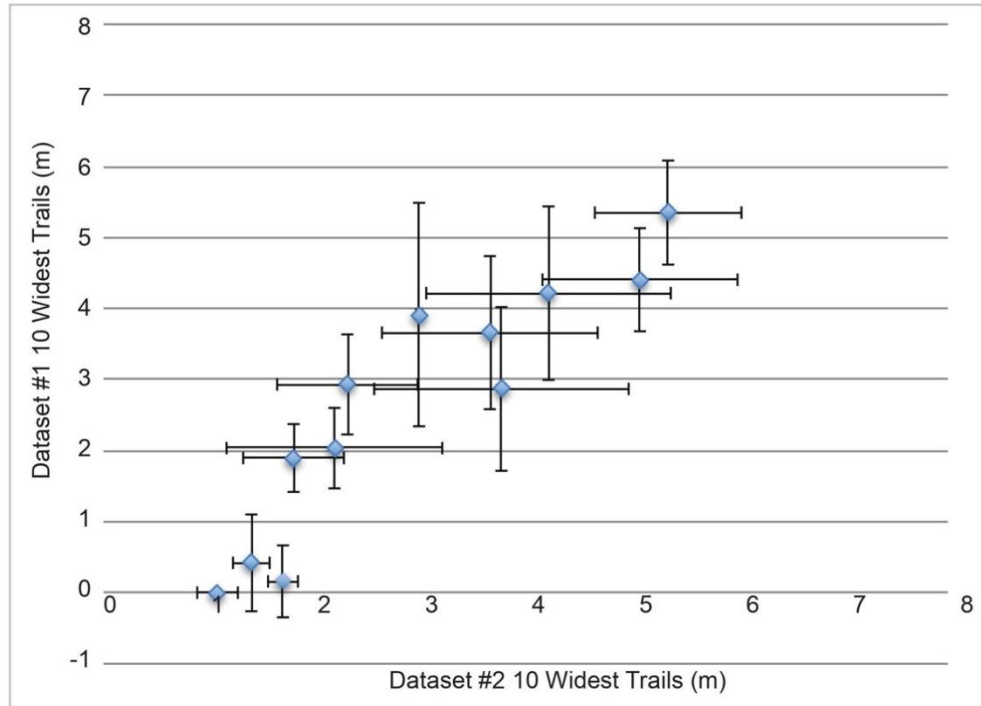


Figure 4.7. (a) Plot showing absolute elevation values for the plain to the south of the graben, the plain north of the graben, and the floor of the graben versus longitude. (b) Graph of longitude versus boulder trails per kilometre. (c) Graph of longitude versus boulder trail widths. (d) The location of the graben is associated with the two sets of boulder populations.

(a) Calibration - 10 Widest Trails



(b) Calibration - Boulder Trail Counts per Kilometre

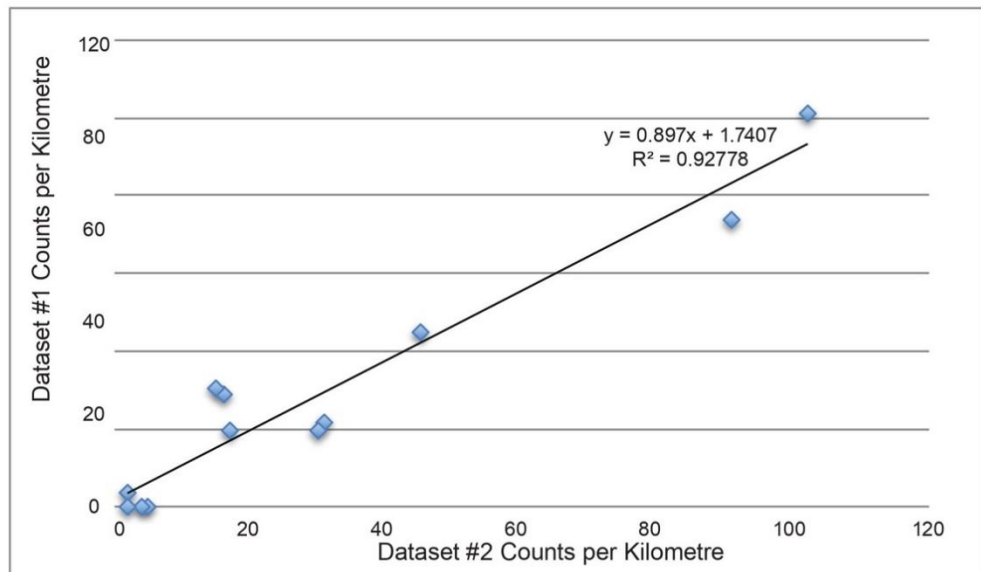


Figure 4.8. Boulder trail lengths and widths were counted and re-counted along Boulder Trail Anomaly 1 and Boulder Trail Anomaly 2. (a) Calibration graph for boulder trail counts. (b) Calibration graph for boulder width counts. These results show that the results are repeatable, with results from the two surveys being broadly comparable.

Once each of the thirteen images had been analysed, with the number of boulder trails per kilometre and mean boulder trail widths recorded, these data were then used to construct a variety of graphs, with the x-axis as the longitude, and the y-axis variable (boulder trails per kilometre/widest boulder trails per HiRISE image location/mean ten

widest boulder trails) and boulder trails per kilometre against the ten widest trails. Comparative data from studies of the Southern Cerberus Fossae regarding boulder trails per kilometre against longitude were also constructed. This was to compare and analyse boulder trail populations along the northernmost Cerberus Fossae.

4.3.1.1. Results

Once the data from each location had been collected, the information was used to construct graphs whose x-axis was the longitude along the strike of the northernmost Cerberus Fossae. Boulder trail density per kilometre was recorded against longitude, and the ten widest boulder trails per location were recorded against longitude.

Figure 4.9 a, b, and c below show the results of the boulder trail per kilometre calculations once collected, analysed, and put into graphic form. Boulder Trail Anomaly 1 (green) and Boulder Trail Anomaly 2 (red) (Figure 4.9 b) show the northernmost Cerberus Fossae and where the measurements were made. Two graphs were constructed for each segment of the northernmost Cerberus Fossae, the longer of the two Boulder Trail Anomaly 1 and the shorter Boulder Trail Anomaly 2. The two graphs are merged and discussed later in this chapter. There are 13 points in total on both graphs: seven on the Boulder Trail Anomaly 1 graph and six on the Boulder Trail Anomaly 2 graph, each point corresponding to each of the 13 HiRISE images used to identify boulder trails and fallen boulders. The location of every boulder trail that was identifiable in each of the 13 areas along approximately 1.5- to 6.5-km-long transects along the slopes immediately adjacent to the floors of the graben was recorded. The widest boulder trails for each location were also measured. Once all data was collected, the results for each location were converted into values of boulder trails per kilometre using trigonometry and a conversion factor for degrees longitude into kilometres.

Data from graphs Figure 9 a and c show an increase in boulder trails approaching 161°E. With Boulder Trail Anomaly 2, the number of observed boulder trails tails off further to the west. With Boulder Trail Anomaly 1, the number of observed boulder trails tails off further to the east, suggesting that the peak values for boulder trails per kilometre are between 161.5°E and 162°E in the northernmost Cerberus Fossae. Of the two graphs, Boulder Trail Anomaly 1 records many more boulder trails than Boulder Trail Anomaly 2, despite the general shape of both graphs being strikingly similar.

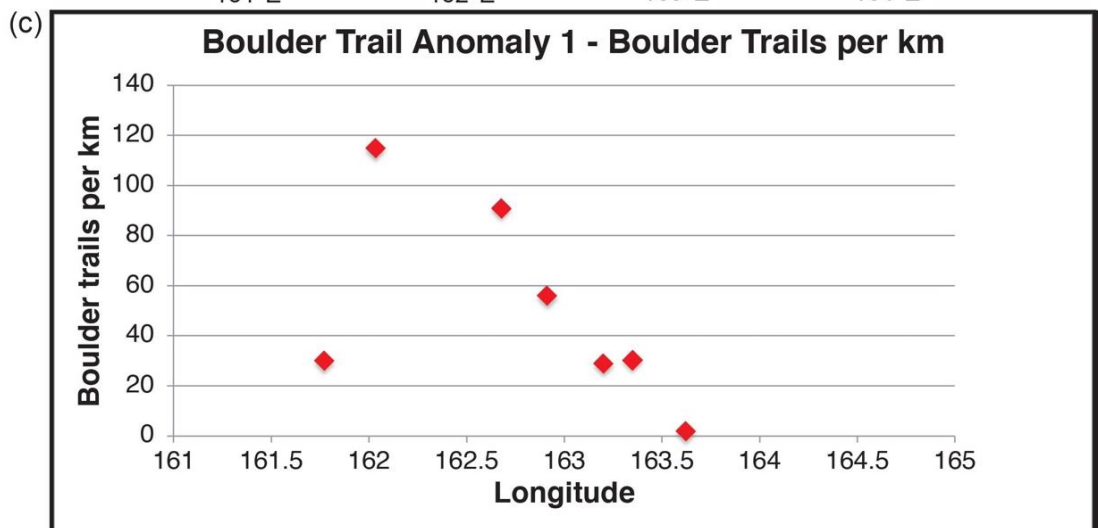
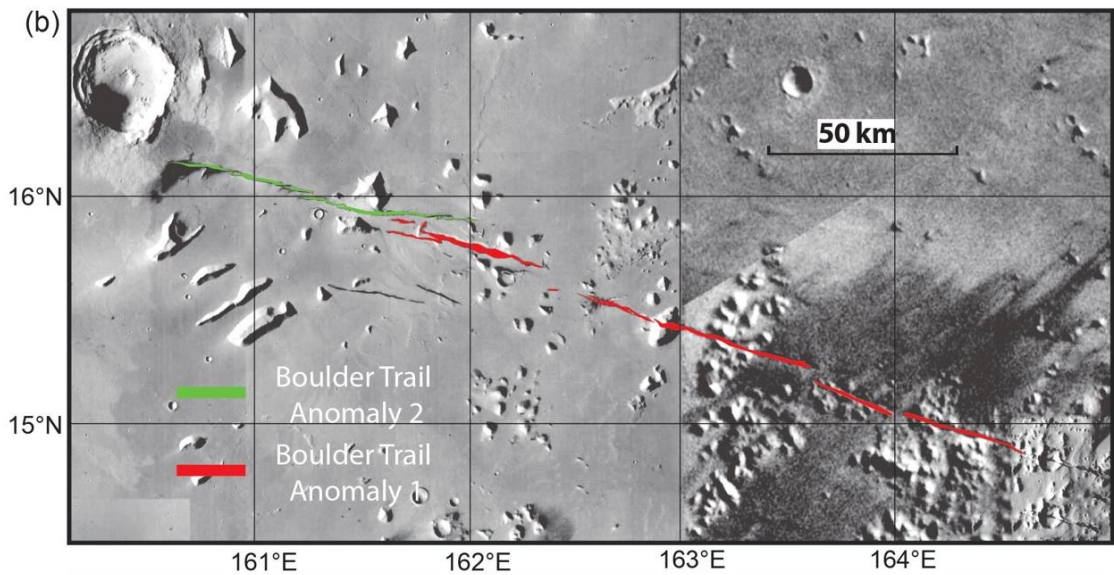
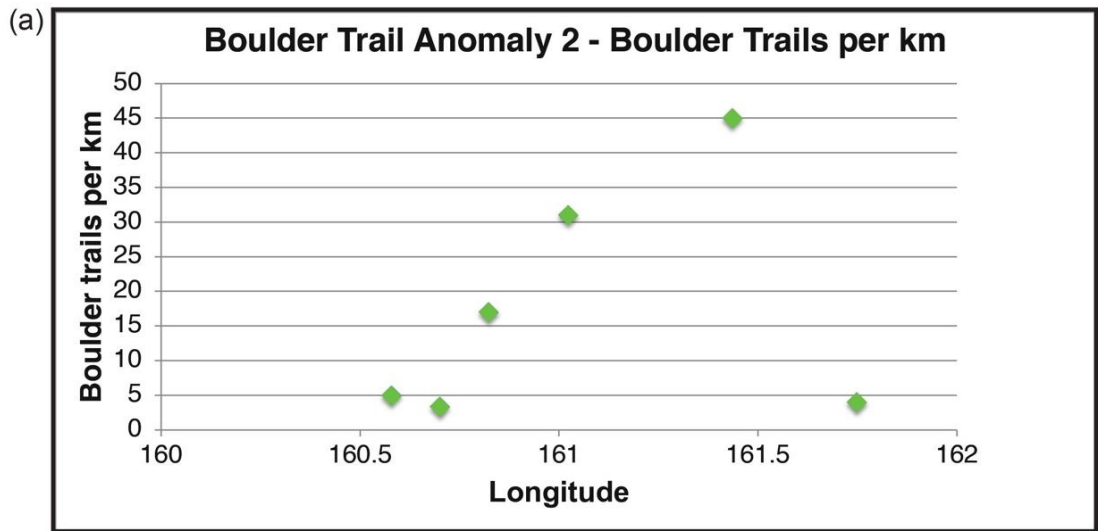


Figure 4.9. b. Location map of the northernmost Cerberus Fossae with Boulder Trail Anomalies 1 and 2 marked. The larger of the two Boulder Trail Anomalies is Boulder Trail Anomaly 1 (red) to the east, with the smaller being Boulder Trail Anomaly 2 (green) to the west. a. A graphic representation of the boulder trails per km found along Boulder Trail 2, with a peak of 45

boulder trails per km identified at around longitude 161.5° E. c. A graphic representation of the boulder trails per km found along Boulder Trail 1, with a peak of just under 120 boulder trails per km identified at around longitude 162° E.

Upon analysis of the data and analysis of the northernmost Cerberus Fossae, it became clear that the data from the 13 locations can be divided into two key areas based upon the *en echelon* geometry of the northernmost Cerberus Fossae: Boulder Anomaly 2, the stretch of the western section of the fossae that comprises six echelon faults, all very close to one another (between ~150 m to ~1 km) or connected, albeit very slightly; Boulder Anomaly 1 includes the remainder of the *en echelon* faults to the east (Figure 4.2 (c), Figure 4.7 (a), (b), (c), and (d), Figure 4.10 (a)). Again, the faults are very close or connected. However, a slightly more significant gap exists between the faults in Boulder Anomaly 2 of ~5 km, which is close to the centre of the northernmost Cerberus Fossae. Furthermore, very fine extensional cracks extend from the tips of the fossae towards each other (Figure 4.10 (a), (b), and (c)).

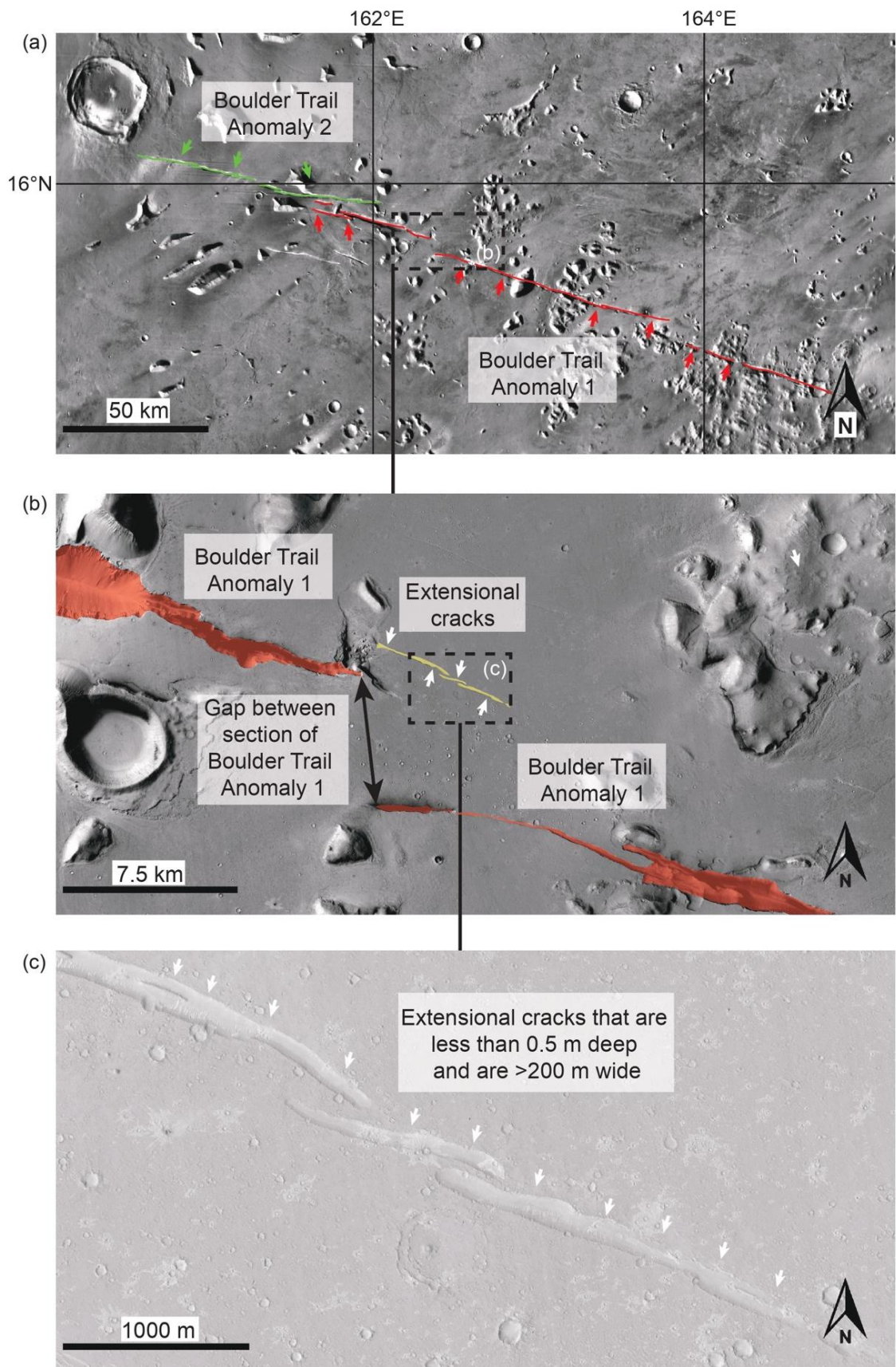


Figure 4.10. (a) Seam-corrected and seam-mapped mosaic of Mars rendered at 5.0 m/px using Context Camera (CTX) data from the Mars Reconnaissance Orbiter (MRO) showing the location of the northernmost Cerberus Fossae. The section of the northernmost Cerberus

Fossae recorded as Boulder Trail Anomaly 2 is green; Boulder Trail Anomaly 1 is red. (b) Seam-corrected and seam-mapped mosaic of Mars rendered at 5.0 m/px using Context Camera (CTX) data from the Mars Reconnaissance Orbiter (MRO) showing the 'gap' area between two sections of the northernmost Cerberus Fossae Boulder Trail Anomaly 1. The gap is ~5 km in size. Marked in yellow are small extensional cracks between the two segments of the northernmost Cerberus Fossae Boulder Trail Anomaly 1. (c) Detail from HiRISE image (ESP_059639_1960RED) of the extensional cracks. Measurements of the cracks using the profile function in JMARS (NASA/JPL-Caltech/Arizona State University) revealed depths of not more than 1 m and widths of >200 m.

Once the plots for boulders per kilometre and the ten widest boulder trails for Boulder Trail Anomaly 1 and Boulder Trail Anomaly 2 were put together (Figure 4.7 (b) and (c)), it became apparent that a coincident maxima in boulder trail density and widths along the strike of the northernmost Cerberus Fossae exists.

Regarding the spatial variations in boulder trail density along the strike of the fault system of the northernmost Cerberus Fossae, maxima in boulder trail counts exist at 161.5°E and E162.°E longitude (Figures 4.7 (b) and (c), and Figure 4.9 a, b, and c). Boulder trail count values decrease east and west from these locations along the strike of the faults toward their lateral terminations. These variations are used to define Boulder Trail Anomaly 1 and Boulder Trail Anomaly 2, as shown in Figures 4.2 (c) and 4.10 (a). For Boulder Trail Anomaly 2, a peak of 45 boulder trail counts per kilometre at 161.43°E longitude was measured (Figure 4.7 (b)), with lower values recorded closer to the east and west tips of the graben. For Boulder Trail Anomaly 1, a peak of 102 counts per kilometre at E162.03° was measured (Figure 4.7 (b)), with lower values recorded closer to the east and west tips of the graben.

Boulder trails per kilometre values exhibit an asymmetric pattern along strike (Figures 4.7 (a) and (b)). The westernmost point of Boulder Trail Anomaly 2 exhibits the smallest number of trails per kilometre (five) at 160.57°E longitude, with the number of trails increasing eastward, culminating in a peak of 45 counts per kilometre at 161.43°E longitude. This is followed by a sharp decrease in recorded trails, with four per kilometre at E161.74° longitude, giving the graph in Figure 4.8 (b) an asymmetric appearance. For Boulder Trail Anomaly 1, measurements begin at E161.76° longitude, extremely close to the tip of Boulder Trail Anomaly 2, but at a latitude of N15.81°, some 6 km to the south of the last measured point along Boulder Trail Anomaly 2. The first count along Boulder Trail Anomaly 1 records 30 counts per kilometre at E161.7° followed by a sharp increase in counts, rising to a peak of 102 counts per kilometre at E162.03° longitude, the highest count along the entire fault. Further east, the number of counts decreases, falling to two counts per kilometre at E163.63° close to the lateral

termination of Boulder Trail Anomaly 1. Again, these measurements give an asymmetric shape (Figure 4.7 (b)).

The graphs of Figure 4.7 (b) and (c) reveal that the mean maxima of boulder trails per kilometre and the ten widest boulder trails measured from the 13 HiRISE images are spatially coincident. Mean values increase from close to zero near the tips of the structures toward maximum values (Figures 4.7 (b) and (c)). This shows that the high boulder trail density areas have the widest boulder trails (compare Figures 4.7 (b) and (c)). The widest mean boulder trail width along Boulder Trail Anomaly 2 was ~5 m, and this measurement was recorded in the region exhibiting the highest number of boulder trails at longitude 161.43°E. As with boulder trails per kilometre, a sharp decrease in the mean width of boulder trails is observed further west along the fault, with a mean trail width of 1.4 m recorded in the region where only four boulder trails were located (161.76°E). Boulder Trail Anomaly 1 also exhibits the relationship mentioned above, with a maximum mean boulder trail width of ~5 m in areas of the most boulder trails per kilometre (102). From this peak, the mean width of trails drops to 1.7 m at 163.62°E, where only two boulder trails per kilometre were recorded (Figure 4.7 (c)). It is also important to note that the shape of the graphs of Figure 4.7 (b) and (c) is asymmetric, with the steepest gradients closest to the *en echelon* fault step-over, which lies between the two fault segments of Boulder Trail Anomaly 1 and Boulder Trail Anomaly 2.

Regarding Boulder Trail Anomaly 1, if extrapolated along strike, the boulder trail width and boulder counts per kilometre have maximum values near longitude 162.5°E. In this location, where the surface expression of the fault appears to be non-existent due to the presence of tips to individual graben (see Figures 4.2(c) and 4.10 (a), (b), and (c)), a flat plain separates two graben at this location with only very small extensional cracks visible between the two graben. There is no apparent correlation between the vertical offset across the graben and the number of boulder trails per km or the mean value for the size of the ten widest boulder trails.

4.3.1.2. Discussion

Analysis of the results shows geographically coincident maxima in boulder trail density per kilometre and boulder trail widths along the graben of the northernmost Cerberus Fossae. The question of the cause behind the mobilisation of boulder populations with this coincident boulder trail density and width was then investigated. Work on the Southern Cerberus Fossae by Roberts et al. (2012) investigating the cause of

mobilised boulders suggested that the mechanism behind the movement was seismic shaking associated with palaeomarsquakes (see Figure 4.1 (a) and (b)). This conclusion was drawn because boulders mobilised by seismic shaking would "...display the classic pattern associated with earthquakes where both the frequency of boulder falls, and boulder sizes decrease away from the epicentre and the location of coseismic surface faulting, due to localised ground shaking (Keefer, 1984)." Indeed, this is a possibility regarding the cause behind mobilising boulders in such a way as to create the patterns seen in Figure 4.7 (b) and (c) on the northernmost Cerberus Fossae. However, examining and explaining exactly why boulders could be mobilised was essential. There are many ways in which boulders could become mobilised, and these ways are discussed below.

4.3.2. Release of boulders by melting ice

One possible theory is that boulders are held on steep slopes and cliffs associated with the graben by water or CO₂ ice. Any diurnal, seasonal, or longer-term warming might melt the ice and release the boulders. Roberts et al. (2012) suggest that boulders mobilised in this way would show "a random spatial pattern of maximum boulder sizes" when sampled over "tens to hundreds of kilometres" (Figure 4.1 (a)). However, measurements taken along the northernmost Cerberus Fossae display clear local maxima in boulder trail widths and boulder trail density per kilometre that are geographically coincident (Figure 4.7 (b) and (c)). These results, with geographically coincident maxima in values for the two variables (Figure 4.7 (b) and (c)), are not what would be expected of the mechanism of boulder release by melting ice.

Furthermore, it is unclear how this process could control the dimensions of boulders recorded by the boulder trail widths, and no evidence has been found for differing joint-spacing in the bedrock to explain the variable maximum boulder sizes implied by the variable maximum boulder trail widths. However, the restriction of image resolution means this cannot be ruled out because joint spacings cannot be mapped in sufficient detail with current imagery. Moreover, persistent CO₂ frost may not be plausible at this latitude (Piqueux et al., 2016), so expecting such frost to hold boulders on slopes may be unrealistic. For these reasons, this hypothesis is rejected.

4.3.3. Effect of local differences in lithology and weathering/erosion

Another plausible hypothesis is that different lithologies might be prone to erosion, which might control the number and sizes of boulders released from the steep slopes

and cliffs associated with the graben. Geological mapping across much of the northernmost Cerberus Fossae shows no apparent changes in the lithology of the rocks forming the walls to graben (Figure 4.3 (a), (b), (c), and (d)). Examining available THEMIS (Thermal Emission Imaging System) and CRISM (Compact Reconnaissance Imaging Spectrometer for Mars) data to determine if local lithological changes correlate with the measured maxima in boulder trail widths that are coincident with the measured maxima in boulder trails per kilometre was undertaken. CRISM is a visible–infrared imaging spectrometer with a scannable field of view. CRISM can cover wavelengths from 0.362 to 3.92 microns (362 to 3920 nanometres) at 6.55 nanometres/channel, enabling the identification of a broad range of minerals on the Martian surface (Murchie et al. (2007)). CRISM data, although having limited lateral extent and hence availability, showed no noticeable change in lithology of the rocks forming the walls to graben concerning oxidised iron minerals, mafic mineralogy, hydroxylated silicates, bound water or water ice, and CO₂ ice (Figure 4.11).

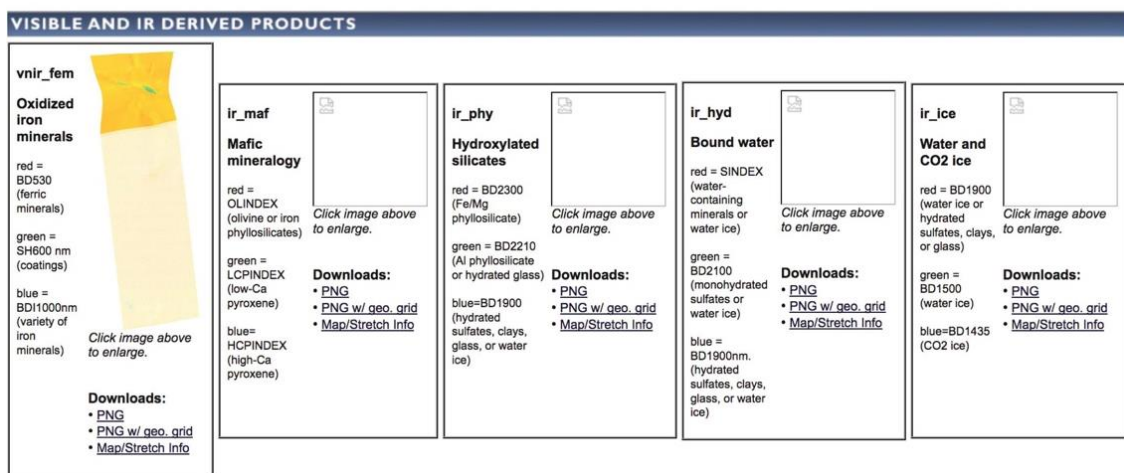
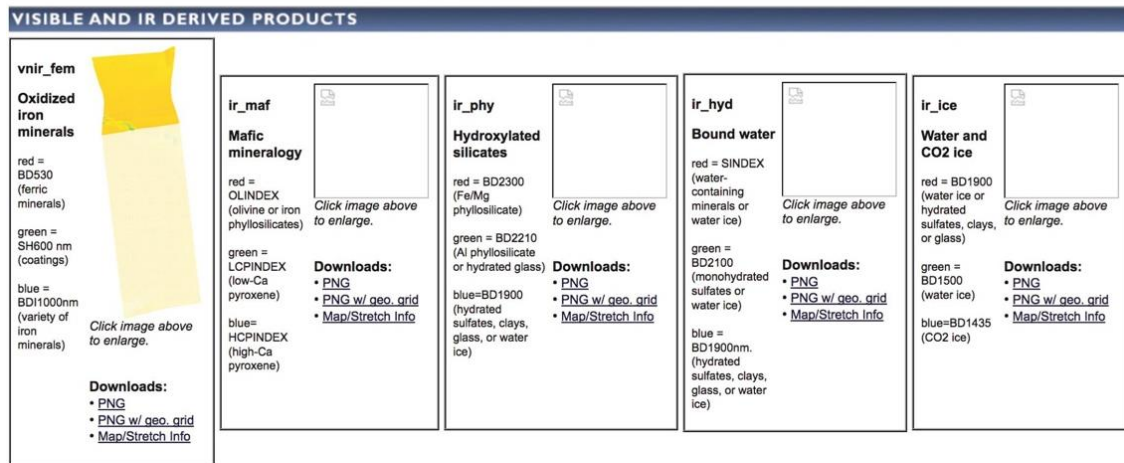
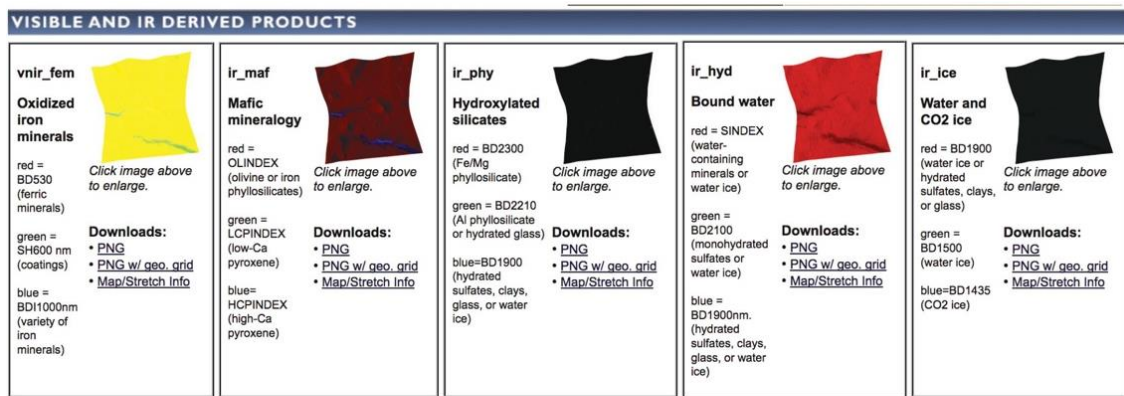


Figure 4.11. CRISM data, although having limited lateral extent and hence availability, showed no noticeable change in lithology of the rocks forming the walls to graben concerning oxidised iron minerals, mafic mineralogy, hydroxylated silicates, bound water or water ice, and CO₂ ice.

Furthermore, the Thermal Emission Imaging System (THEMIS) is a tool on the 2001 Mars Odyssey that uses multi-spectral thermal-infrared images in nine wavelengths and visible/near-infrared images in five bands to investigate Mars's surface mineralogy and physical properties. THEMIS can create Mars maps using day and night multi-spectral infrared images at a resolution of 100-m per pixel. This tool can identify geologic materials, including carbonates, silicates, sulphates, phosphates, and

hydroxides, based on their fundamental vibrational absorption bands in the thermal–infrared spectral region. By identifying a range of minerals, THEMIS can help identify key aqueous minerals such as carbonates and hydrothermal silica (Christensen et al., 2002). The THEMIS data, including both night-time and daytime infrared measurements, provided complete spatial coverage of the area studied, and, although probably saturated in the images, again show no noticeable change in lithology of the rocks forming the walls to the graben, highlighting only that the walls of the graben appear to be formed of bedrock (Figures 4.12 and 4.13), as confirmed by the clear stratigraphic layers in the HiRISE images (Figure 4.3 (a) to (d)).

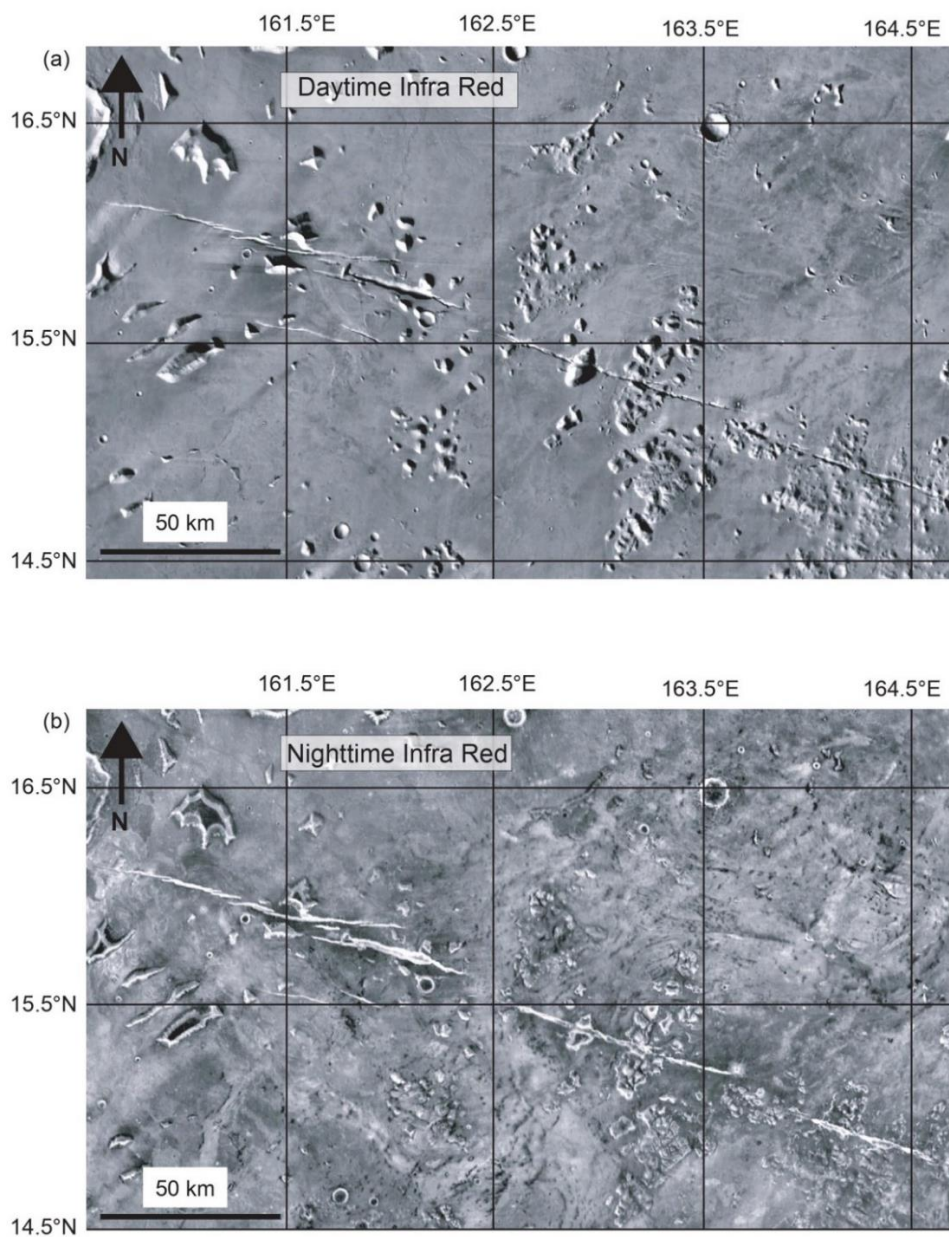


Figure 4.12. NASA Mars Odyssey spacecraft imagery of the northernmost Cerberus Fossae in (a) daytime infrared and (b) night-time infrared (NASA/JPL/Arizona State University). Note that the lithology of the rocks forming the walls to the graben does not noticeably change, highlighting only that the walls appear to be bedrock.

The HiRISE data show a layered stratigraphy in the graben walls, presumably, lava flows and possibly sedimentary layers formed by weathering erosion and aeolian processes between lava flow events. There appear to be no apparent differences in stratigraphy between different HiRISE images (Figure 4.3 (a) to (d)). As such, no changes in lithology were identified despite having a variety of data sources, and therefore, the hypothesis that different lithologies might be prone to erosion, and this might control the number and sizes of boulders released from the steep slopes and cliffs associated with the graben was rejected. Unfortunately, no evidence exists that addresses the possibility that wind helped dislodge rocks, either directly or indirectly (by forcing sand and dust into cracks and wedging them open) in a way that produces the regional variations in boulder trail frequency and size shown in Figure 4.7 (b) and (c).

4.3.4. Higher cliffs supply more boulders

The higher frequency of boulder trails measured in some HiRISE images may be due to their positions close to higher cliffs, areas with more loose boulders that could be mobilised. Taluses at the bases of the cliffs within the northernmost Cerberus Fossae are also comprised of boulders that could be mobilised because their position on the slopes is close to their angle of repose. Therefore, it is important to consider the combined height of the cliffs and the talus. The talus is also likely to be close to its angle of repose. The cliffs appear vertical, meaning variations in the taluses' angles need not be considered. Measuring the heights and slopes of all the individual cliffs and taluses was not possible because:

- (i) The Mars Orbiter Laser Altimeter (MOLA) spot spacing of ~300 m is too coarse (Figure 4.13);

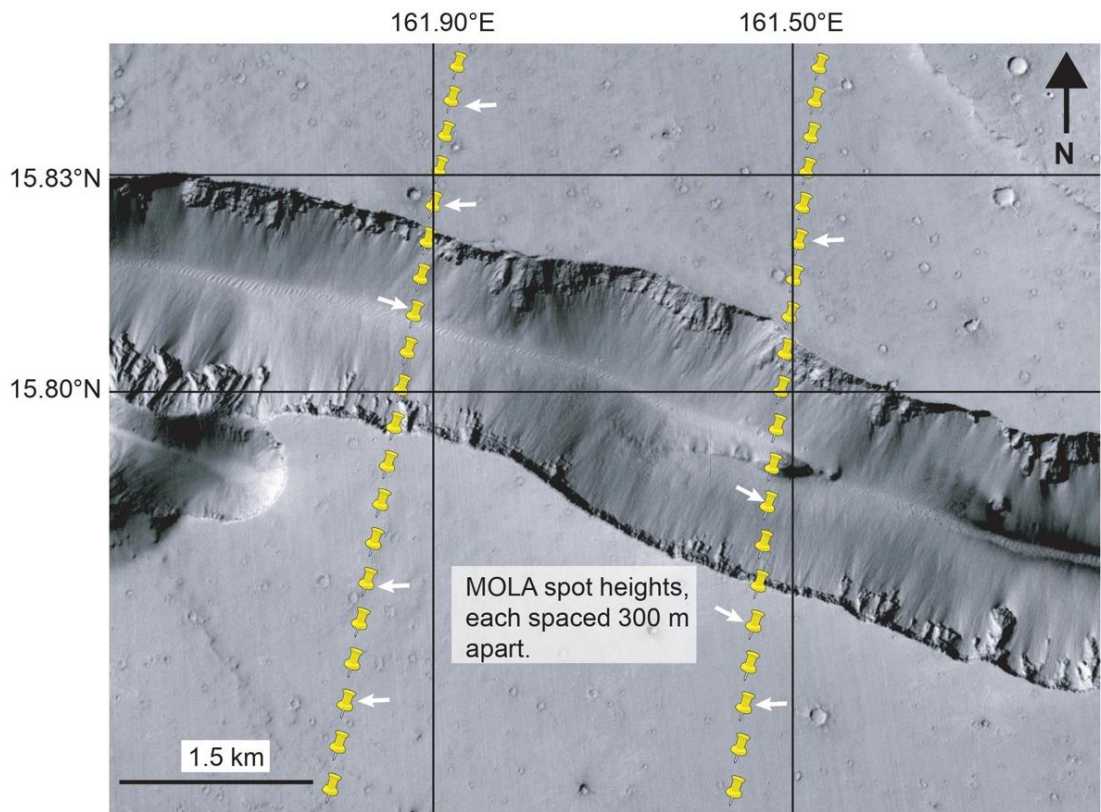
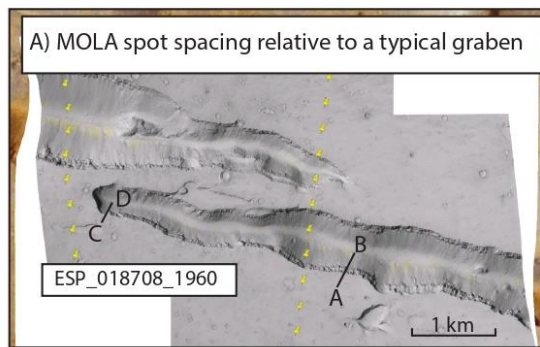


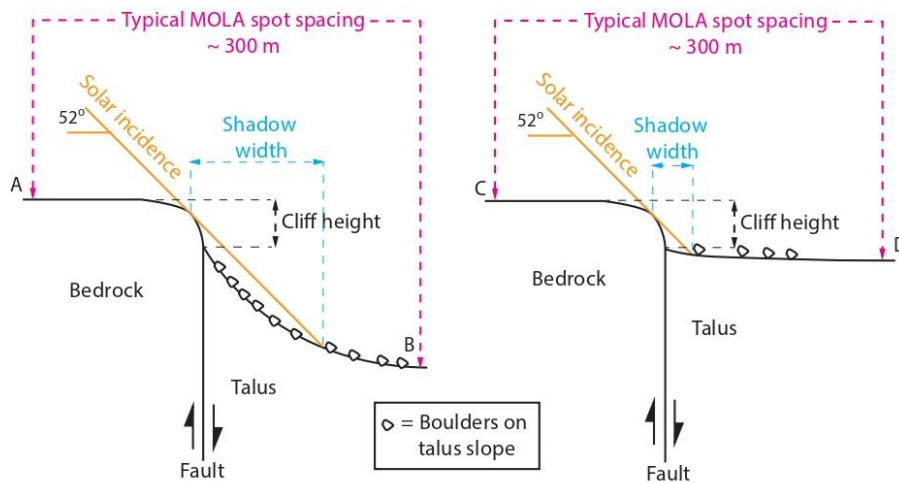
Figure 4.13. Seam-corrected and seam-mapped mosaic of Mars rendered at 5.0 m/px using Context Camera (CTX) data from the Mars Reconnaissance Orbiter (MRO) showing a section of the northernmost Cerberus Fossae. The yellow pointers indicate the location of the MOLA spot heights, with each spot height along the same transect being 300 m apart.

(ii) The shadow width and solar incidence angle cannot be used to define vertical height differences via trigonometry because the horizontal extents of taluses vary between different examples (Figure 4.14);



b) Example with a wide talus slope

c) Example with a narrow talus slope



d) Rock pinnacles attached e) Rock pinnacles toppling f) Perched Boulders thrown upwards g) Perched boulders rolling and interacting h) Boulders detach from rock-mass

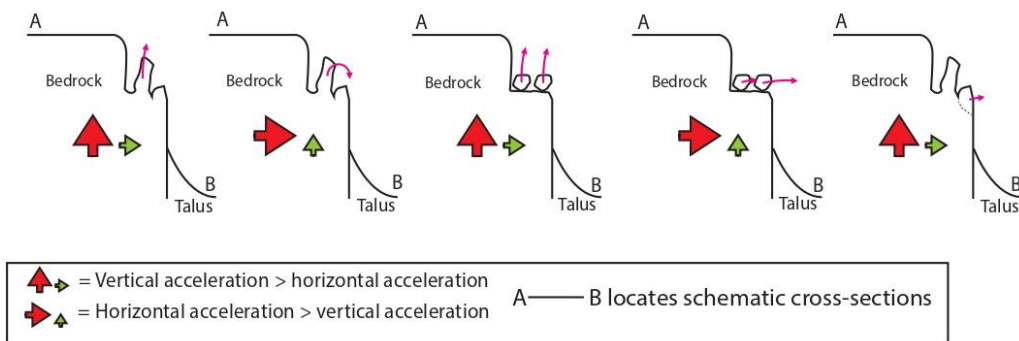


Figure 4.14. The geological setting and modes of ground acceleration for mobilised boulders. (a) The detail from the HiRISE image (ESP_018708_1960RED) shows a section of the northernmost Cerberus Fossae and the MOLA spot height locations. Two transects, C-D and A-B, are marked on the image. (b) This is a schematic representation, and the fault orientation should not be taken as a literal depiction of its dip angle. (c) Note that these are simplified schematics that illustrate the general structure and are not exact representations of the fault's geometry or orientation. (d) to (h) illustrate the possible mechanisms by which boulders can be mobilised depending on the vertical and horizontal acceleration relationship.

(iii) Stereo HiRISE pairs to make local digital elevation models are only available for some HiRISE locations in the study area. However, measuring the total offset across the faults controlling the graben walls is possible using MOLA data (Figures 4.4 and 4.7). For example, locations A and B in Figure 4.7 (a), (b), and (c) show similar values for boulder trails per kilometre and boulder trail widths but very different combined heights of the fault-controlled cliffs plus talus slope height defined by the total offset measured with MOLA data. Thus, if the vertical extent of cliffs plus associated taluses provide more candidate boulders for mobilisation, this does not tally with measurements of maxima in boulder trail frequency. Also, this hypothesis does not explain why the size of the boulders, and by extension, the widths of boulder trails, correlate with the frequency of boulder trails. For these two reasons, this hypothesis is rejected.

4.3.5. Boulder mobilisation caused by nearby impacts

The formation of nearby impact craters could have produced ground shaking that mobilised the boulders. An examination of all impact craters within approximately 50 km across the strike of the graben was studied. A crater of approximately 4 km diameter is located at latitude 15.618° N and longitude 162.183° E. It is close to the area with the maxima in boulder trail frequency and width. Inspection of the crater and its ejecta blanket reveals that the ejecta blanket has been eroded by an outflow channel, meaning that the impact crater predates the outflow channel.

Given that the outflow channels identified in the areas adjacent to the northernmost Cerberus Fossae predate the graben, fractures and fissures and that boulder trails postdate graben formation, then the impact crater is too old to be connected to boulder mobilisation (please see Chapter 5 for further details on the relative chronology of features identified in this area). There are much smaller impact craters (~40 m diameters) within a few hundred metres from the graben, close to the area of the maxima in boulder trail frequency and width (Figure 4.15).

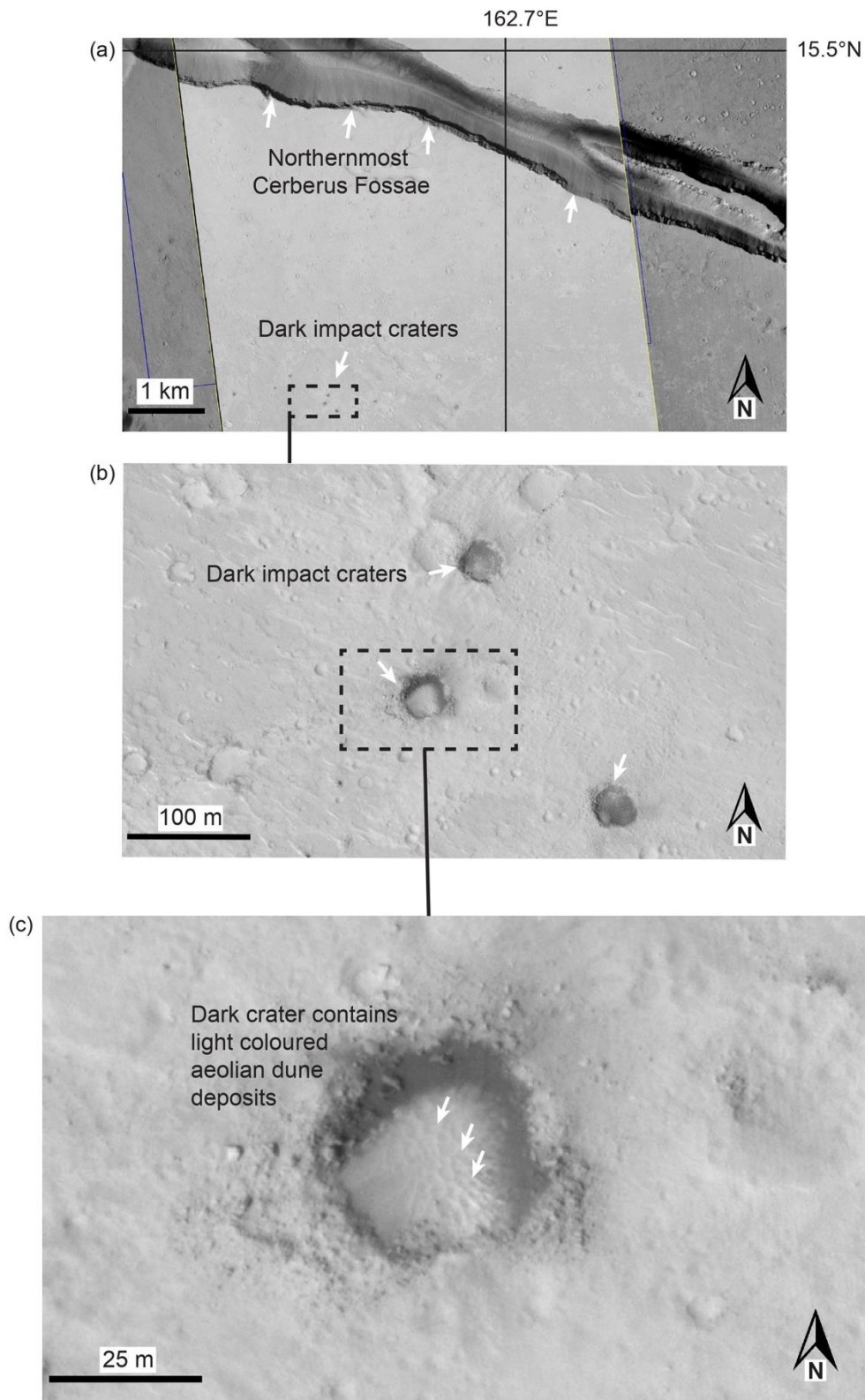


Figure 4.15. a) Detail from HiRISE image (ESP_055845_1955_RED) of part of the northernmost Cerberus Fossae and an area to the south of the northernmost Cerberus Fossae that contains three dark-coloured impact craters (b). (c) A close-up of one of the three craters. Although some craters near the anomalies of boulder trails along the northernmost Cerberus Fossae appear dark and, therefore, young, when viewed close up, dunes are visible within the impact crater (c), which suggests that significant aeolian sedimentation took place after their formation. The dunes are probably older than the boulder trails within the northernmost Cerberus Fossae, which aeolian processes have yet to obscure.

These craters, despite having a relatively young appearance at first glance, are in part due to the existence of dark, relatively dust-free material within them. However, upon closer inspection, the impact craters are partially filled with aeolian dunes. This is pertinent because aeolian processes mobilised the dunes. However, the boulder trails inside the fossae have not been destroyed by aeolian processes, suggesting that the boulder trails are younger than the dunes. Suppose the rate of aeolian processes is similar between the craters and the graben floors. In that case, these small craters may also be ruled out as the explanation for the ground shaking that mobilised the boulders.

Recent studies, including seismic predictions and data from the InSight mission, have shown that impacts can produce measurable seismic effects. For example, a nearby 1.5 m diameter impact crater was observed near InSight, and the predicted seismic amplitudes were in the range of 0.8–4 nm/s with frequencies around 1–3 Hz (Daubar et al., 2020). However, these signals often fall near or below the noise level, and detection is only possible during quiet periods, which occur around 20–30% of the time. Based on these findings, the size of the smaller craters (~40 m diameter) observed in this region is likely too small to produce the ground acceleration necessary to mobilise boulders.

No suitable candidate impact craters have been identified, so the hypothesis that impact craters caused boulder mobilisation is rejected. However, it is important to note that this depends on the assumption that the rate of aeolian processes is similar between impact craters and the graben floors.

4.3.6. The relevance of boulder track density

Boulder track density could be correlated with better preservation and/or lower degradation rather than more abundant boulder track formation. A possible hypothesis to support this is that mobilised boulder trails could be degraded by aeolian processes and that degradation varies spatially, therefore influencing the number of preserved boulder trails and the measured widths. In order to assess this, a comparison of boulder trail widths against the dimensions of the mobilised boulders that formed the trails was undertaken (Figure 4.5 (d)). Because boulders are more resistant to aeolian processes than the dust surfaces on which they lie, they may be assumed to maintain their original dimensions. Comparing the dimensions of the boulder trails and the boulders should, therefore, reveal whether or not aeolian processes have altered the boulder trails. Measurements revealed that in areas of both high and low boulder trail density, the widths of the boulder trails are almost identical to the widths of the

boulders that formed them (Figure 4.5 (d) – (ii) and (iii)), with the width of the fallen boulders in both images (blue line) corresponding to the measured width of the boulder trail (red line). The boulder trails are not eroded to an extent that drastically alters their preservation or widths. The boulder trails have not been markedly degraded by aeolian processes, and this tallies with the preservation of raised levees produced by the motion of fallen boulders, evidenced by variation in percentage grayscale for individual pixels in the images (Figure 4.5 (d) – (v)). As such, this hypothesis is rejected.

4.3.7. Variation in the incidence angle of the images

Another possibility is that boulder trails may be challenging to see because of the variation in the solar incidence angles in the HiRISE images. However, Figure 4.16 shows that the solar incidence angles are similar to the images studied across the northernmost Cerberus Fossae. After studying many examples, qualitative assessment shows that individual boulder trails are equally clear on low- and high-boulder trail frequency images. Based on this data, this hypothesis is rejected.

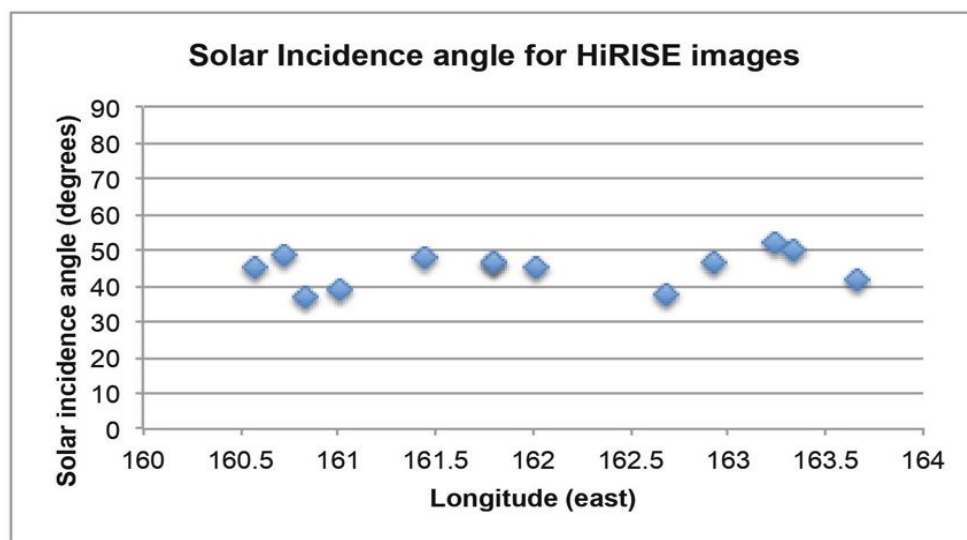


Figure 4.16. Solar incidence data show little variation along the strike of the graben.

4.3.8. Multiple single rockfalls

Another possibility to investigate is whether boulder trail populations may have grown over time due to multiple single rockfalls. Single rockfalls have been observed on repeat imagery (Figure 4.17 (a) and (b)) as demonstrated by Malin et al. (2006), who documented boulder trails forming over time in mid-latitude craters between repeated MOC image observations.

A Mars Orbiter Camera (MOC) image (MOC2-1222b) of one set of boulder tracks in a south mid-latitude crater (located near 35.8°S, 158.4°W) was taken in November 2003. Figure 4.17 shows two MOC images: one taken in November 2003 and the other in early December 2004. Contrasting the two, the latter reveals more than a dozen fresh boulder trails on the crater wall, indicating the formulation of new tracks within approximately a year. This suggests that between November 2003 and December 2004, a small collection of boulders dislodged from the crater wall, descended, and possibly bounced to the crater floor.

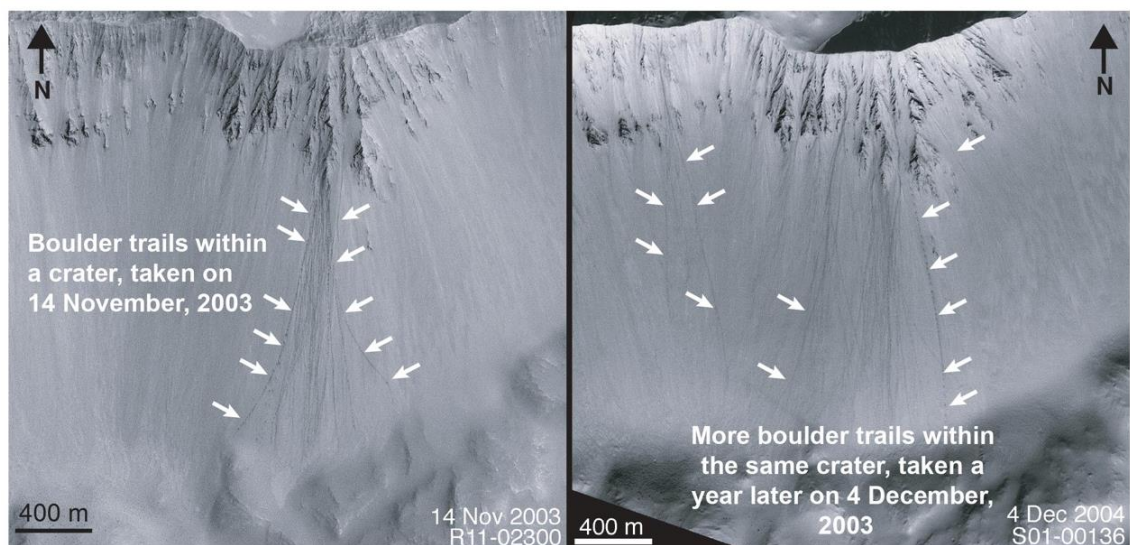


Figure 4.17. Mars Orbiter Camera (MOC) image MOC2-1222b of boulder trails within a south mid-latitude crater (located near 35.8°S, 158.4°W). The images are of the same section of the crater wall, taken 386 days apart. The first image, on the left, already displays visible boulder trails in the mid-section of the image. The later image, on the right, displays the earlier boulder trails and several other trails across the entire slope and is not limited to the same area of boulder trails as the first image.

Therefore, repeated single rockfalls, possibly triggered by many small marsquakes or the melting of ice and the other mechanisms discussed above, could create populations of boulder trails. Qualitative analysis reveals that the boulder trails' morphology in the MOC2-1222b images (Figure 4.17) is identical to the boulder trails observed along the northernmost Cerberus Fossae, with raised levees only a few decimetres across, possibly composed of dust to coarse sand (Figure 4.5 (d)). Dust to coarse sand is susceptible to being disturbed by a mobilised boulder to form a raised levee. Following this, dust to coarse sand would also be susceptible to aeolian erosion. It is unlikely that these examples on Mars are associated with gravel-grade material that would be less susceptible to wind erosion. Fieldwork in Iceland by the paper's co-author (Gerald Roberts; Brown and Roberts, 2019) showed that boulder trails have

formed in talus cones on fault scarps composed of gravel-grade material, with grain sizes between 10 cm and 15 cm. (Figure 4.18).

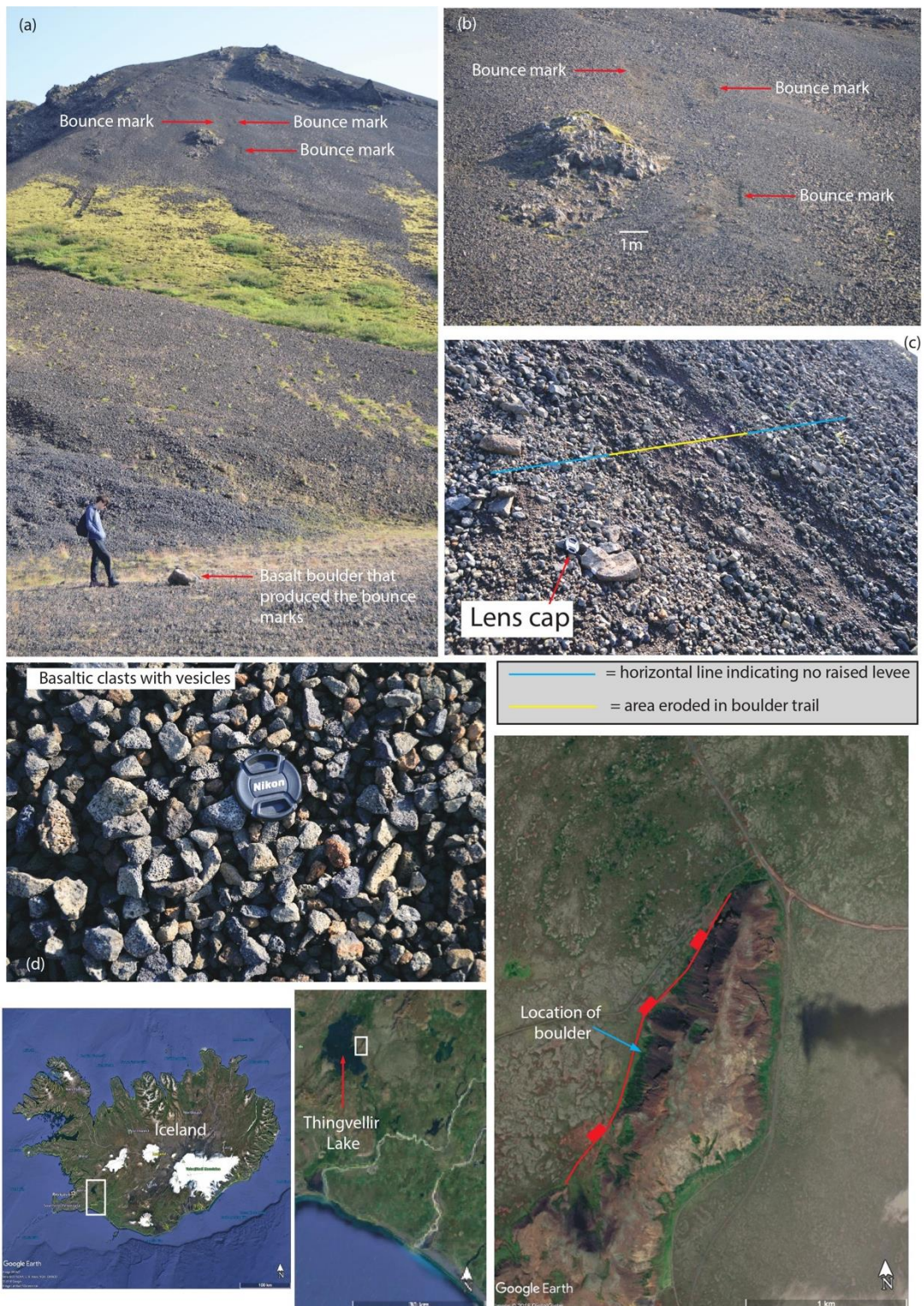


Figure 4.18. An example of a mobilised boulder from Iceland with coarse-grained talus and no raised levees, in contrast to the examples in Figure 4.5 (d).

The trails in Iceland lack raised levees, likely due to the coarse grain size. It is concluded that the examples from Mars are probably dust to coarse sand.

The raised levee examples from Mars are evidenced by variations in percentage grayscale for individual pixels in the images, with the Sun illuminating the raised levees that also produce shadows (Figure 4.5 (d) (v)). In computer-generated imagery, a grayscale image is one where the value of each pixel is a single sample representing only an amount of light. This means that it only carries intensity information. Grayscale images are shades of grey, contrasting from black (weakest) to white (strongest) (S. Johnson, 2006). The plots in (Figure 4.5 (d) (v)) show that the levees are raised and illuminated. With examples of active aeolian activity on the floors of the graben, i.e. dunes (Figure 4.3 (a) to (d)), the fact that the levees of the boulder trails are preserved in many thousands of examples suggests that the trails are both young and of a similar age. Therefore, the hypothesis of the boulder trail populations' incremental formation by adding single boulder falls is rejected. However, the above findings are supported by qualitative observations only. Two separate events are suggested by looking at the two boulder trail anomalies in Figure 4.7. Suppose the theory regarding the levees is incorrect and the boulder trail populations contain a range of different aged individual boulder trails. In that case, the boulder trail populations may have grown through many minor rockfalls. If this were the case, it would invalidate the large-magnitude marsquakes interpretation. However, evidence suggests the interpretation of large-magnitude marsquakes causing boulder mobilisation along the northernmost Cerberus Fossae.

4.3.9. Inaccurate statistical treatment of boulder trail anomalies

Another plausible hypothesis is that measurements taken are inaccurate. Perhaps the mean width of the ten widest boulder trails is not adequate to allow a comparison of boulder trail populations produced by mobilising a subset of the population of available boulders if populations of different numbers are considered and they have a power law or exponential size distribution. One schema could be that if more boulders were taken from such a population, there would be more individual large boulders. The mean would then be larger, even if the size to frequency distribution is identical. The current study has been unable to define the number, as the total number of boulders in each location was not counted because this would need to include buried boulders that are impossible to visualise in the imagery. However, the large number of candidate boulders for mobilisation at every location may mean that the population sizes are not notably different. Therefore, the results stand assuming that the number of boulders in

the population is identical between locations. Regardless, this has not been ruled out as a possibility.

4.3.10. Mobilisation of boulders due to seismic shaking

After appraising the alternative scenarios explaining the boulder trail data along the northernmost Cerberus Fossae, the most plausible explanation is suggested to be that the boulders were mobilised by seismic shaking connected to marsquakes, with the shaking and resultant boulder mobilisation decreasing with distance from the epicentre.

For the marsquake interpretation to be likely, one of the interpreted marsquake ruptures must cross an area without surface offset (Figure 4.19 (a), (b), (c), and (d), Figure 4.7 (d), and Figure 4.10 (a), (b), and (c)). On Earth, it is common for ruptures to jump between active faults that are not physically continuous in earthquakes (Livio et al., 2016). The same may apply to Mars. This is important to note because, like on Earth, estimates of maximum marsquake magnitude may be erroneously small if it is assumed that ruptures can be confined to single active fault segments.

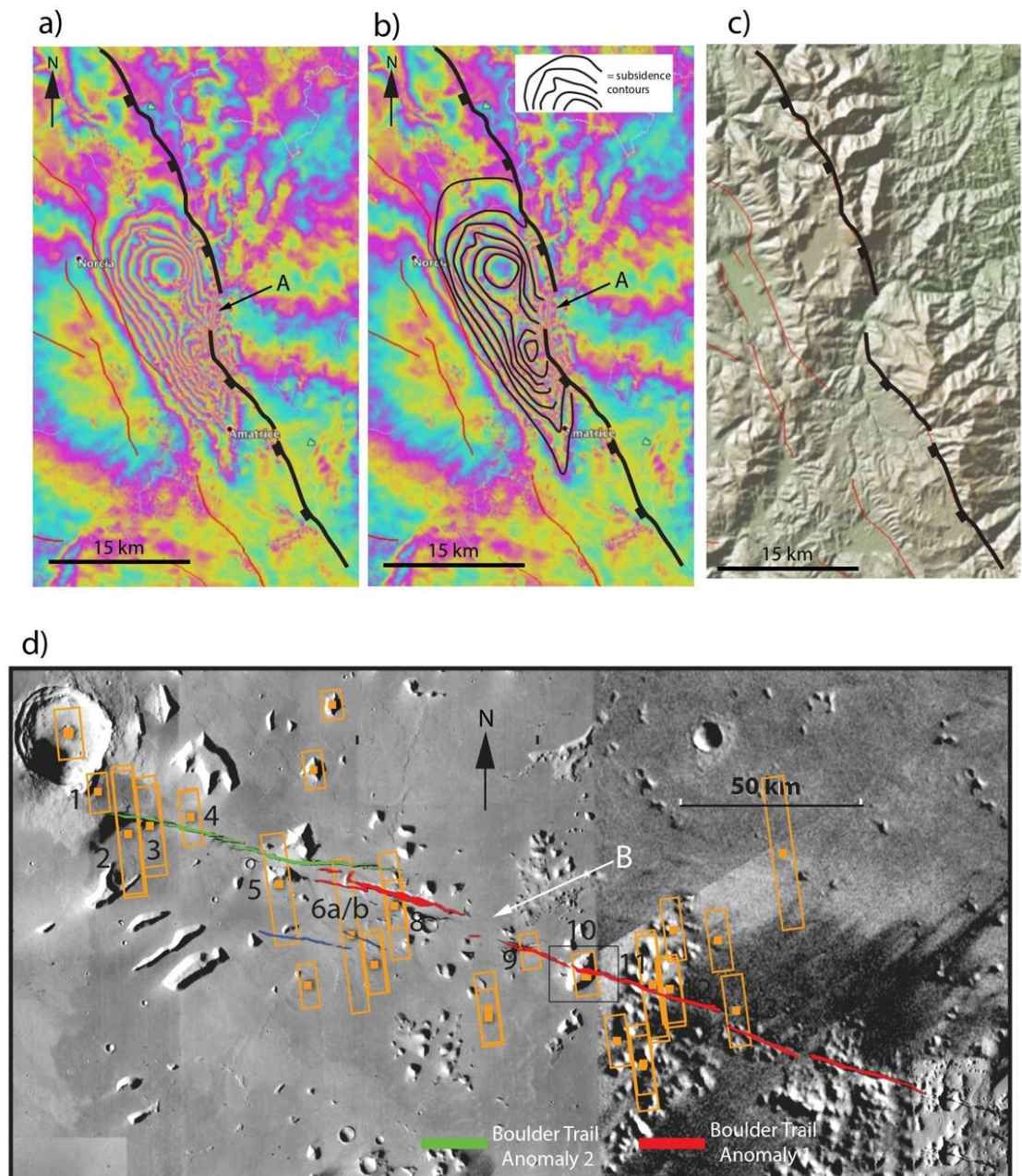


Figure 4.19. (a) and (b) are InSAR data showing the 24th August Mw 6.2 earthquake in central Italy jumping across an area where no surface faulting was reported in the earthquake or on geological maps recording longer-term deformation (marked as 'A' in both images), with image (c) showing the landscape using a Space Shuttle Radar Topography Mission Digital Elevation Model (SRTM DEM). This is analogous to the proposed scenario from the fault system in Grjota Valles, (d) where no surface faulting exists on a flat plain (marked as 'B'). InSAR data from <http://comet.nerc.ac.uk/latest-earthquakes-and-eruptions/apennines-earthquakes-aftershocks-italy/> distributed as a kmz file, with one fringe equal to 4.8 cm change in the line of sight. The colours in figures (a) and (b) represent relative ground displacement, with each full-colour cycle corresponding to 4.8 cm of deformation in the line of sight. Although the exact colour legend is not provided, a common convention is that warm colours (such as red and yellow) often indicate uplift or movement towards the satellite. In contrast, cool colours (such as blue and green) represent subsidence or movement away from the satellite.

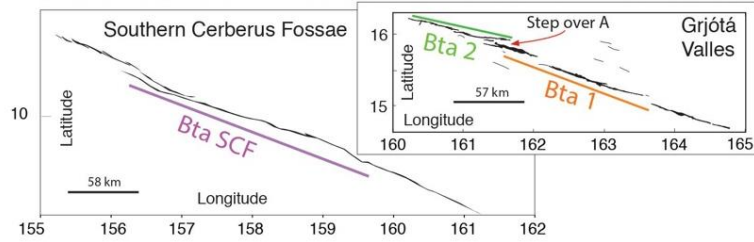
Figure 4.19 illustrates this with images (a) and (b) showing Interferometric Synthetic Aperture Radar (InSAR) data from the 24th August Mw 6.0 earthquake in central Italy

jumping across an area where no surface faulting was observed in the earthquake or on geological maps recording longer-term deformation. InSAR images measure changes in land surface altitude. Image (c) shows the landscape using a Space Shuttle Radar Topography Mission Digital Elevation Model (SRTM DEM). The sizeable surface gap between the two surface faults visible in all three images is noteworthy. This is comparable to the suggested fault system in the northernmost Cerberus Fossae, with no surface faulting, albeit only trace faulting on the flat plain between fault segments (Figure 4.1919 (d), Figure 4.10 (a), (b), and (c)).

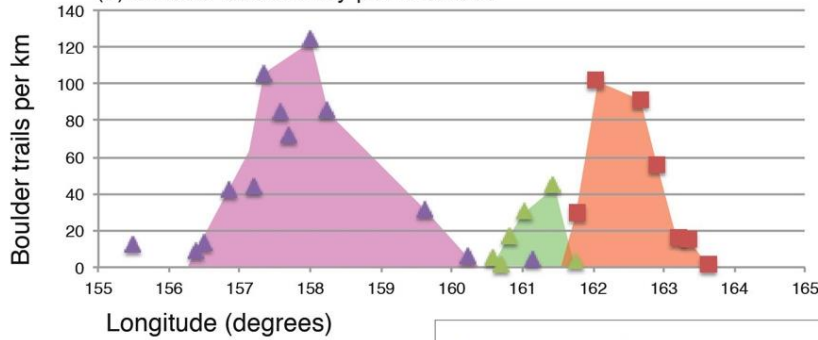
4.3.11. Comparison of mobilised boulder populations from different graben within the Cerberus Fossae

If the hypothesis that marsquakes mobilised the boulder populations is correct, then it is sensible to compare this data with similar data on boulder populations from the Southern Cerberus Fossae (Roberts et al., 2012) to help understand the significance of boulder trail populations in understanding seismicity within this region of Mars (Figure 4.20).

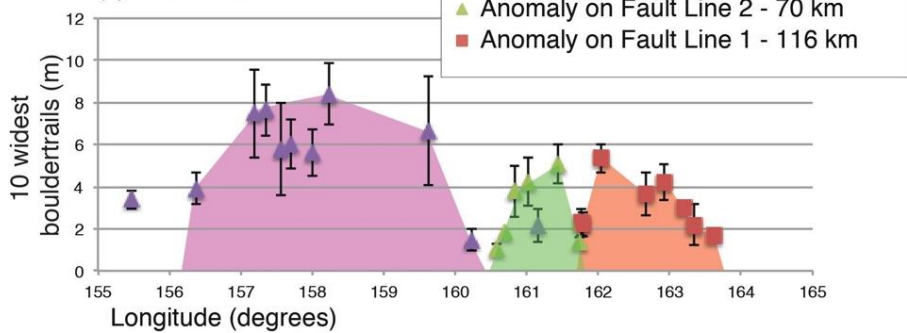
(a) Maps showing the relatively continuous fault length of Cerberus Fossae compared to Grjótá Valles and the extent of boulder trail anomalies (Bta).



(b) Boulder trail density per kilometre



(c) 10 widest boulder trails



(d) Speculative inference of marsquake magnitude from rupture length

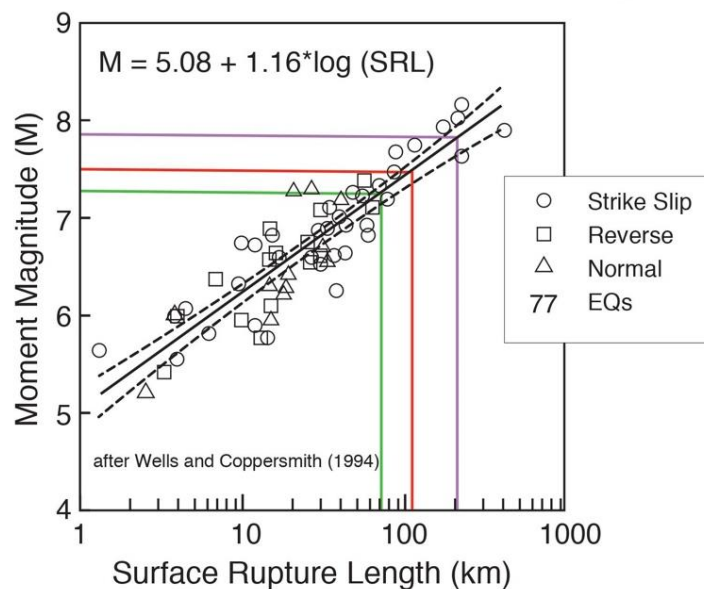


Figure 4.20. Compares the data from the northernmost Cerberus Fossae with similar data from work on the Southern Cerberus Fossae. (a) compares the continuous fault length of the Southern Cerberus Fossae (Bta SFC, purple line) with the discontinuous northern Cerberus

Fossae in Grjótá Valles (Bta 2 - green line; Bta 1, red line). The step over between the two segments of the fault is marked as 'Step over A'. (b) and (c) compare the boulder trail densities and ten widest boulders along the Southern Cerberus Fossae (purple) and the two segments of the northernmost Cerberus Fossae (boulder trail anomalies 2 (green) and 1 (red)). (d) Speculative inference of marsquake magnitude from rupture length of the three fault lines (after Wells and Coppersmith, 1994).

A critical difference between the data sets from the northernmost Cerberus Fossae and data examined by Roberts et al. (2012) on fallen boulder populations and trails on the Southern Cerberus Fossae is the difference in length of the along-strike extent of seismic shaking and the hump-shaped anomalies. Figure 4.20 b compares the boulder trails per km on the Southern Cerberus Fossae (purple) and the northernmost Cerberus Fossae (green for the western Boulder Trail Anomaly 1 and red for the eastern Boulder Trail Anomaly 2). What is noticeable is the asymmetric profiles of each of the three profiles. The range in size of each profile can be best understood by referring to Figure 4.20 d (after Wells and Coppersmith, 1994), which offers speculative inference of marsquake magnitude based upon the rupture's length. The rupture length of the Southern Cerberus Fossae (purple) is 207 km, and the northernmost Cerberus Fossae (green) for the western Boulder Trail Anomaly 1, 70 km, and (red) for the eastern Boulder Trail Anomaly 2, 116 km. Essentially, the larger the surface rupture, the larger the marsquake. Figure 4.20 c compares the ten widest boulder trails on the Southern Cerberus Fossae (purple) and the northernmost Cerberus Fossae (green for the western Boulder Trail Anomaly 1 and red for the eastern Boulder Trail Anomaly 2). The profiles here are also asymmetric, but the profiles are less pronounced. The two fault anomalies of the northernmost Cerberus Fossae show greater similarity in size, with a clear similarity in the number of widest boulder trails being apparent. The northernmost Cerberus Fossae section is approximately 120 km for Boulder Trail Anomaly 1 and approximately 70 km for Boulder Trail Anomaly 2. In comparison, the Southern Cerberus Fossae is approximately 210 km (Figure 4.20 (a), (b), and (c)). Roberts et al. (2012) suggested that the along-strike extent of seismic shaking strong enough to mobilise boulders on Earth is approximately the same as the along-strike extent of surface faulting for the earthquake ruptures following observations of the 2009 L'Aquila earthquake (see Fig. 1).

Roberts et al. (2012) tentatively mapped possible surface rupture extent using HiRISE images for Cerberus Fossae, and observations were consistent with the hypothesis. In the present study, while surface rupture could not be mapped, the 1:1 ratio between rupture length and the dimensions of areas with mobilised boulders on Earth has been assumed, with the along-strike extent of hump-shaped anomalies in boulder trail data taken as proxies for rupture extent. This suggests implied moment magnitudes for the

palaeomarsquakes in the range of \sim Mw 7.3–7.8, assuming the anomalies result from single events (Figure 4.20 (d)). These magnitudes should be considered maximum values, as the anomalies may have formed from multiple smaller events (see discussion in 4.5.7). This assumption is indirectly supported by d_{\max} /length ratios for the Martian faults examined (0.026–0.008; Figure 4.4 (a)), which are similar to those measured on Earth (0.1–0.001; see Vetterlein and Roberts, 2010, for a review). This implies that the relationships between rupture length, d_{\max} , stress drop, and moment magnitude may be similar on Mars and Earth (Ali and Shieh, 2013; Gomez-Rivas et al., 2015).

Moment magnitudes of \sim Mw 7.3–7.8 imply that such events would generate seismic shaking detectable by seismometers, such as those used in the InSIGHT mission. However, the assumption that hump-shaped anomalies in boulder trail data are proxies for rupture extent may be inaccurate, as surface rupture could not be mapped in Grjótá Valles. Additionally, Mars' lower gravity (\sim 38% of Earth's) means less force might be required to mobilise boulders, though this depends on factors like how each boulder was attached and whether it was mobilised by vertical or horizontal accelerations (see Figure 4.14 (d) to (h)). Consequently, the estimated magnitudes should be treated as maximum values, given that the along-strike extent of the anomalies may exceed the rupture extent.

Nonetheless, suppose one were to use the observation that boulder trail anomalies have similar along-strike dimensions to suggested surface ruptures for the Cerberus Fossae example (Roberts et al., 2012). In that case, the results point toward the conclusion that a variety of magnitudes of palaeomarsquakes may have been detected, with larger magnitudes on the Cerberus Fossae fault system, which displays fault segment lengths of several hundred kilometres from geomorphic observations of offset features and smaller magnitudes on the Grjótá Valles system where segmented lengths are in the range of 50–100 km, again from geomorphic observations (Figures 4.2 (c) and 4.20 (a) to (d)). This correlation between fault dimensions and dimensions of areas affected by putative seismic shaking adds further support, albeit indirect, for the interpretation of palaeomarsquakes.

Furthermore, it may be possible to infer how well the natural seismometer records seismic shaking, that is, the boulder trail population data. Figure 4.21 compares the three faults, Boulder Trail Anomaly 1, Boulder Trail Anomaly 2, from the northern Cerberus Fossae and results from Roberts et al.'s work on the Southern Cerberus Fossae, plotting boulder trails per kilometre versus boulder trail width.

A positive relationship exists between boulder trails per kilometre and the width of boulder trails, with more boulder trails corresponding to a greater width of boulder trails (Figure 4.21 (a)). However, it is interesting to note that the data appears to saturate. According to data from Roberts et al. (2012), the mean value of the ten widest boulder trails increases from zero to approximately 5–8 metres for a range of 0–50 boulder trails per kilometre. After that, the value appears to level off at larger numbers, with the mean value of the ten widest trails remaining around 5–8 metres for a range of 50–125 boulder trails per kilometre. One interpretation is that the natural seismometer is saturated and unable to record shaking that would mobilise larger boulders. It may be that boulders >5–8 m are not available in great numbers on the fault-controlled slopes, perhaps controlled by joint spacing or layer thicknesses in the rocks. Furthermore, Figure 4.21 (b) shows a positive relationship between the along-strike length of the boulder trail anomaly and the maximum value for boulder trails per kilometre recorded. This may be interpreted to suggest that maximum ground acceleration may increase with marsquake magnitude. However, from the sparse data available, and because of only constraining with three data points, the trend again flattens out, and therefore, one might expect the example from Roberts et al. (2012) to have more than ~120 boulder trails per kilometre recorded. The natural seismometer might be saturating, perhaps because once a value of ~45 boulder trails per kilometre is exceeded, it becomes difficult in some cases to identify every single boulder trail because they appear to coalesce on the images. The performance of natural seismometers is speculative. However, if correct, it implies that boulder trail populations may not be effective in measuring the effects of marsquakes at the largest magnitudes because the measurements may be saturated.

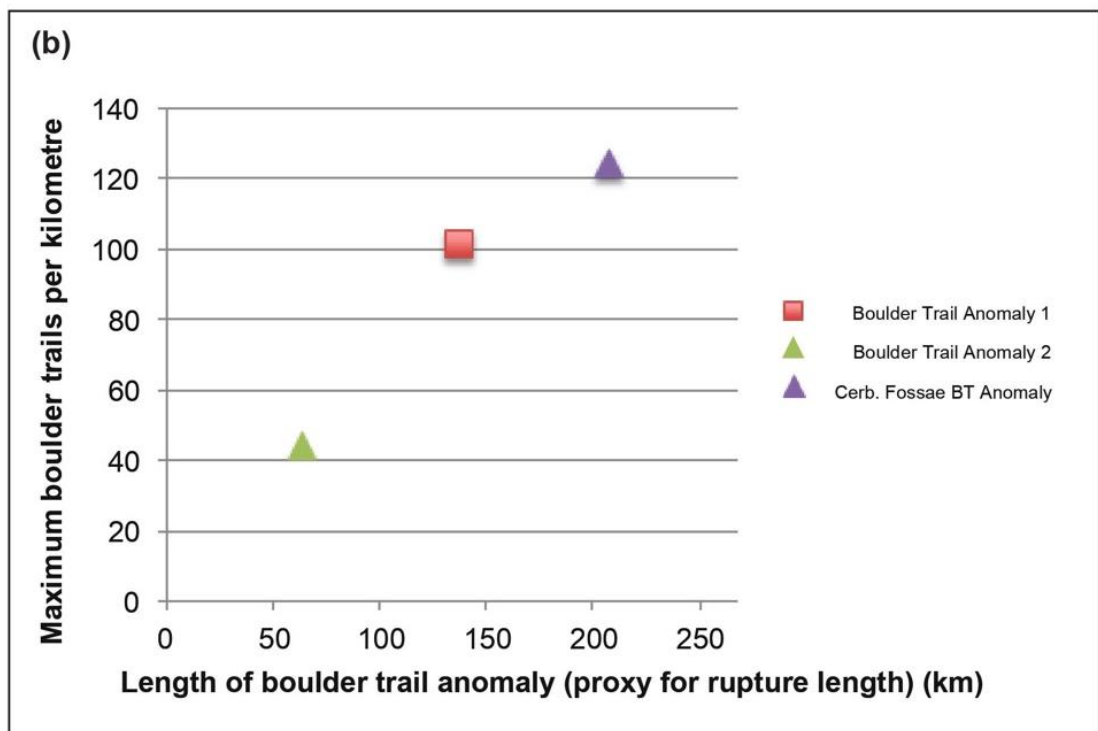
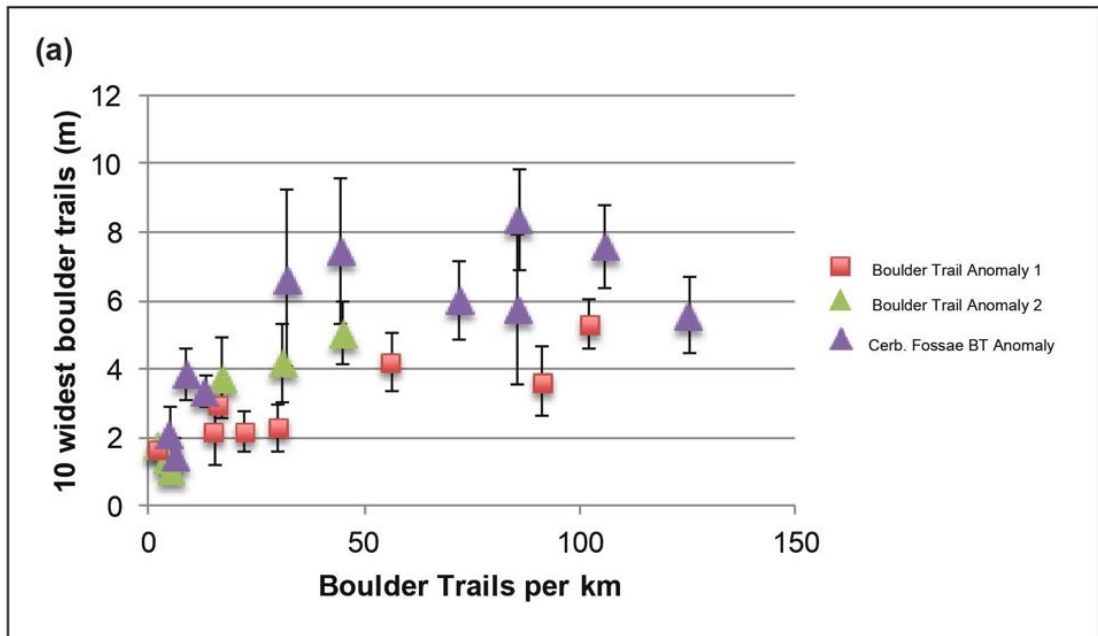


Figure 4.21. Two graphs that compare: (a) the ten widest boulder trails (m) against boulder trails per km of the Southern Cerberus Fossae (purple) with the two sections of the northernmost Cerberus Fossae, Boulder Trail Anomaly 1 (red) and Boulder Trail Anomaly 2 (green), and; (b) maximum boulder trails per km against the length of boulder trail anomaly (km) of the Southern Cerberus Fossae (purple) with the two sections of the northernmost Cerberus Fossae, Boulder Trail Anomaly 1 (red) and Boulder Trail Anomaly 2 (green).

The profiles of data for Boulder Trail Anomalies 1 and 2 are asymmetric (Figures 4.7 (b) and (c) and 20 (b) and (c)), with the steepest gradients closest to the *en echelon*

fault step-over (labelled A in Figure 4.20 (a)) between these two fault segments. For faults on the Earth, displacement gradients steepen in the step-over zones between interacting faults (Jackson et al., 2002). The asymmetry in boulder trail populations may be related to this. A speculative interpretation might be that slip-distributions for each of the individual marsquake ruptures that produced these boulder-trail anomalies were skewed toward the tips of fault segments so that the largest coseismic displacements, and hence highest levels of ground acceleration, were located close to the *en echelon* step-over between the fault segments, as occurs on the Earth (Faure Walker et al., 2009).

It is important to note that the research results presented in this chapter were presented before the deployment of the InSIGHT mission's seismometer on Mars in February 2019. Since deploying the InSIGHT mission's seismometer on Elysium Planitia, close to 4.5° N and 136° E, the seismometer has detected over 1,300 marsquakes, with over 50 having clear enough signals to determine information about their location on Mars. A large cluster of high-quality events was identified as coming from the Cerberus Fossae region, ~1,700 kilometres east of the InSight landing site. Two of the more prominent signals (S0235b and S0173a) could be determined quite accurately, and of that, another quake (S0183a), which produced fewer clear signals, with somewhat reduced accuracy (Giardini et al., 2020). Figure 4.22 shows the position of the three most prominent signals detected by the InSIGHT seismometer in relation to the northernmost Cerberus Fossae and the larger Northern and Southern Cerberus Fossae.

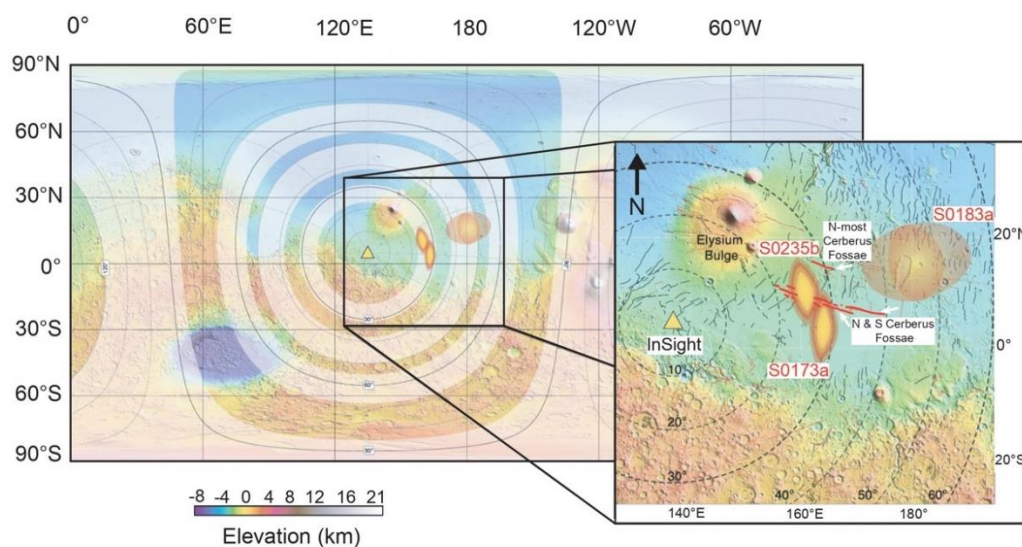


Figure 4.22. Position of the three most prominent signals detected by the InSIGHT seismometer (S0183a, S0235b, and S0173A—marked as orange ellipses) in relation to the northernmost Cerberus Fossae, which is equidistant between S0183a and S0235b, and the

larger Northern and Southern Cerberus Fossae, to the south of the northernmost Cerberus Fossae. The position of the InSIGHT lander is marked as a yellow triangle (after Giardini et al., 2020). Recent work by Stähler et al. (2022) further corroborates the presence of significant seismic activity in the Cerberus Fossae region, providing coordinates and error ellipses for 15 (+2) marsquake events, including the signals shown here. Their study suggests that the seismic events, detected between 15 km and 50 km depth, indicate an extensional regime consistent with dike intrusion processes, supporting the ongoing tectonic activity in the region.

The data within this chapter suggests relatively large events, perhaps up to Mw 7.3–7.8, have occurred within the area of the Cerberus Fossae. However, magnitudes $>Mw$ 7.6 seem improbable, given the analysis of Knapmeyer et al. (2006). However, the uncertainty indicated by the spread in the data supporting Figure 4.20 (d) allows the interpretations to be consistent with the estimate in Knapmeyer et al. (2006). Nonetheless, events as large as Mw 7.6 would have very long recurrence intervals (perhaps hundreds to thousands of years), much longer than the lifetime of a seismometer. However, if, like on the Earth, for every large event, there are hundreds to thousands of smaller events with shorter return times following Gutenberg–Richter b-value scaling (e.g., Knapmeyer et al., 2006), it may be that the smaller events recorded by the InSIGHT seismometers are these smaller events. The annual detectability of such events by the InSIGHT instruments was investigated by Taylor et al. (2013), and they concluded that between 1.5×10^0 and 1.9×10^5 events would be detected, depending on the maximum defined event size.

Since 1,300 marsquakes were detected over four years, Taylor et al. (2013) figures were reasonably accurate. Likewise, the work within this chapter looks for evidence of marsquakes in the northernmost Cerberus Fossae. It concludes that marsquakes are indeed ongoing, and numerous have been proven correct with the InSIGHT seismometer. This is a very seismically active area of Mars.

4.4. Conclusions

1. Two faulted areas near Grjótá Valles (Boulder Trail Anomaly 1 and Boulder Trail Anomaly 2) were studied, and measurements of the densities and widths of boulder trails created by boulders falling from fault-controlled cliffs were taken.
2. Data are consistent with previous results in that the most parsimonious interpretation is that boulders have been mobilised by seismic shaking associated with palaeomarsquakes in the recent past.

3. In the Grjótá Valles region, two en echelon graben/faults have similar $d_{max}/length$ ratios to those found on Earth. Boulder trail data has identified two peaks in (a) boulder trails per kilometre and (b) maximum width of boulder trails—one that is approximately 116 km long and another that is around 70 km long.
4. The maximum values for the number of trails per kilometre and width differ for the two anomalies. For the 70-km-long anomaly, the maximum values are 45 trails per kilometre and a 5-metre trail width. For the 116-km-long anomaly, the maximum values are 115 trails per kilometre and a 5.3-metre trail width. These values are higher than the background values of zero trails per kilometre and zero boulder trail widths.
5. Combined with published data from Cerberus Fossae, where an ~200-km-long anomaly in boulder trails per km (125 trails per kilometre maxima) and maximum boulder trail width (8.5-m maximum trail width), the three data sets suggest correlations between the along-strike length of boulder trail anomalies, boulder trails per kilometre and maximum boulder trail width. Implied moment magnitudes, derived by using the along strike dimensions of boulder trail anomalies as proxies for rupture extent, could be as large as M_w 7.3–7.8, values that are thought to be accompanied by much more frequent seismic activity at lower moment magnitudes.

CHAPTER 5.
OUTFLOW CHANNELS IN GRJÓTÁ VALLES.
EVIDENCE FOR REPEATED, CROSS-CUTTING AND SPATIALLY
MIGRATING OUTFLOW CHANNEL FORMATION

5.1. Introduction

This chapter describes the study of possible outflow channels in the area of the Grjótá Valles, adjacent to the northernmost Cerberus Fossae fractures, that served as conduits for aqueous flows. The age of the channels is observed to decrease from west to east, indicating a connection with the extension of the Cerberus Fossae fractures from west to east.

Outflow channels are extremely long, wide swathes of scoured ground on Mars (Carr, 2007) that extend many kilometres and usually are more than one kilometre in width. Three large outflow channel systems exist around Cerberus Planitia, Mars: Athabasca Valles, Marte Valles, and Grjótá Valles (Burr et al., 2002), with the flow that formed the channels thought to have emerged from the Cerberus Fossae fissures (Figure 5 1 a and b). Some studies (Ghatan et al., 2005; Kattenhorn and Meyer, 2010; Burr et al., 2002, 2009) suggest that the channels formed in a single event due to large megafloods across parts of the Cerberus Fossae, possibly creating the three outflow channels within the region. The emanation points or areas of these floods have not been conclusively identified, but it is most likely that the Cerberus Fossae fissures and graben were the source areas (Burr et al. 2002, 2009). If single events, then concerns regarding where the huge volumes of fluid required to form such extensive channels came from arise. However, some studies (Burr et al., 2002b, 2009; McEwen et al., 2005) have instead suggested that water flowed in the channels that originate from the Cerberus Fossae at different times during the late to very late Amazonian Epoch (Burr et al., 2002b; McEwen et al., 2005; Hanna and Phillips, 2006; Manga, 2004), suggesting that flow releases were episodic rather than a one-off megaflood.

Grjótá Valles is the lesser-studied of the three outflow channels. In this chapter, observations are presented of cross-cutting relationships between outflow channels within the Grjótá Valles, suggesting the occurrence of no fewer than five distinct channel-forming events that took place there. By tracing these intersecting channels upstream, we can identify five potential sources, each representing separate channel-forming events. The cross-cutting channels can be mapped upstream to five separate

potential channel sources along the present trace of a system of faults, fractures and fissures in Grjótá Valles that form the northernmost part of Cerberus Fossae. It is important to have evidence that cross-cutting occurred as it shows that the fault, fracture, and fissure system formed after the channels. It is, therefore, essential to date the flow episodes relatively. Observations of the channels, shown in the images within this chapter, show landforms that resemble those produced by aqueous flows on the Earth. However, it is important to stress that such landforms have been suggested by others to have been formed by the flow of turbulent lava. Observations are derived from detailed mapping, topographic profiling, and identification of cross-cutting relationships. These observations are used to discuss whether a single event or multiple events cut the channels and what processes formed these channels in Grjótá Valles.

The work detailed in this chapter has been published in JGR: Planets. Brown, J. R., and Roberts, G. P. (2023). Repeated, cross-cutting and spatially migrating outflow channel formation, Grjótá Valles, Mars. *Journal of Geophysical Research: Planets*, 128, e2022JE007247. <https://doi.org/10.1029/2022JE007247>. While the core findings of cross-cutting and spatially migrating outflow channel formation in Grjótá Valles are shared between the thesis and the publication, the thesis chapter provides additional detail on the geological context, methodology, and background literature. The published paper condenses these findings, focusing on the broader implications for Martian surface processes. In particular, this chapter offers more in-depth discussion on mapping techniques and references to previous studies, whereas the published version streamlines the presentation of results for a wider scientific audience.

5.2. Background

5.2.1. Grjótá Valles outflow channel system

The Grjótá Valles outflow channel system emanates from the vicinity of the northernmost Cerberus Fossae (Figure 5.1 a and b). The fault system of the northernmost Cerberus Fossae is a ~200 km long set of *en echelon* fissure segments located between 16.175°N / 160.563°E, and 15.202°N / 163.666°E (Brown and Roberts, 2019). The WNW–ESE orientation of the fissures would indicate that the fractures are sub-radial to Elysium Mons (Fig. 5.1 a).

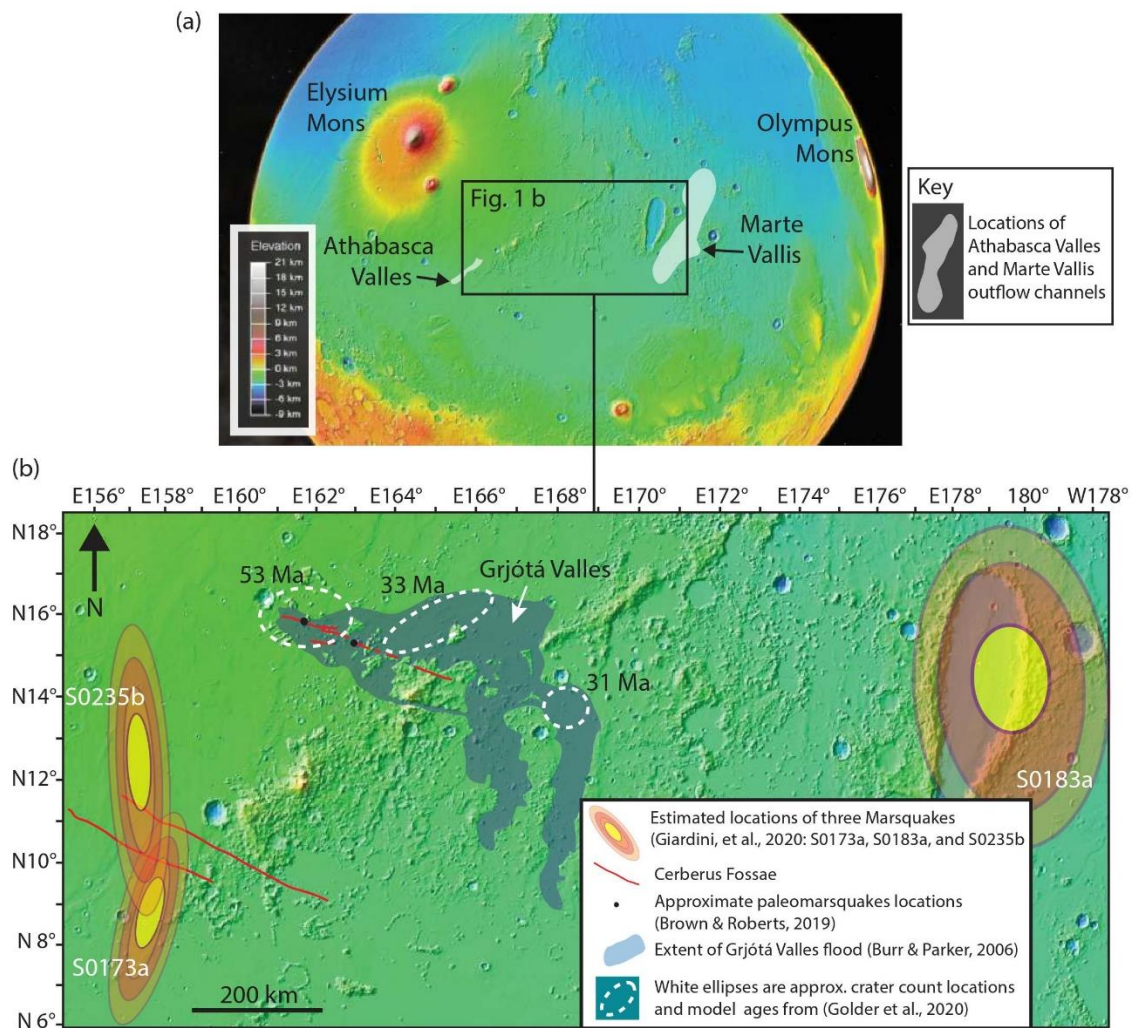


Figure 5.1. a. Regional location map of the study area with the locations of Athabasca Valles and Marte Vallis highlighted. b. The study area is marked by a black rectangle to the east of Elysium Mons. Estimated locations of three Marsquakes (Giardini et al. (2020) have been added (S0173a, S0183a, and S0235b) as coloured ellipses. The extent of the Grjótá Valles flow tract (after Burr and Parker (2006) has been added. Red lines mark the fossae, with the northernmost being the centre of the study region in this thesis and the two to the southwest being the Northern and Southern Cerberus Fossae (Vetterlein and Roberts, 2009, 2010). Black dots identify two locations that show the approximate paleomarsquakes locations along the Northern Cerberus Fossae after Brown and Roberts (2019)—see Chapter Four of this thesis. The three white ellipses are crater count locations, and their matching crater count model, ages for lava, flows in this area (Golder et al., 2020).

While this figure highlights the key marsquakes used in this analysis, recent studies by Stähler et al. (2022) and Zenhäusern et al. (2024) have identified additional marsquake events specifically within the Cerberus Fossae region, which includes the current study location. These events encompass both high-frequency (HF) and low-frequency (LF) quakes, with HF events typically associated with tectonic activity and LF quakes potentially indicative of magmatic processes. However, despite the additional seismic events noted in these studies, they do not significantly alter the conclusions of this work, as the marsquakes shown here remain the most prominent and relevant for understanding the tectonic activity in the area.

The faults in this region (Fig. 5.1 b) have been active relatively recently because they crosscut pre-existing features of a relatively young age. For example, the fossae offset

late Amazonian Cerberus lavas and older inliers (Tanaka et al., 2005). Using crater counting methods, the ages of the youngest lavas offset on the nearby Cerberus Fossae are <10 Ma (Hartmann and Berman, 2000; Head et al., 2003; Vaucher et al., 2009), implying that the fossae are very young. Work by Golder et al. (2020) using the results from studies of crater populations of (i). comets (Holsapple and Housen, 2007); (ii). adjacent cogenetic lunar geologic units (van der Bogert et al., 2010; van der Bogert et al., 2017), and (iii). platy-ridged lava flows on Mars (Murray et al., 2005; Chapman et al., 2010) show geospatial variation within geologic units in the final diameters of impact craters and crater size-frequency distributions (CSFDs), looked at how crater characteristics are affected by the material they have impacted—in the Cerberus region, this was lava flow. Of note was that the Cerberus lava flows exhibit decreasing age trends in large late-Amazonian lava flows seen in the Cerberus Fossae region, including the Grjóta Valles. Golder et al.'s (2020) work concluded that changes in the material properties of the lava during emplacement are the most likely reason why the observed crater-based age trends are as they are. In short, this means that at locations proximal to the inferred source of the lava, larger craters yield older model ages due to the weaker, more porous rock. At more distal locations from the inferred source of the lava, Golder et al. (2020) suggested that smaller craters yield younger model ages due to more substantial, non-porous rock. Within the extent of the Grjóta Valles flow tract (Fig 5.1 b.), crater counting suggests that the implied ages range from 55 Ma (proximal) to 33 Ma (distal) (see Figure 5.2 for locations of crater counts) (Golder et al., 2020). Below, these interpretations by Golder et al. (2020) are discussed in terms of whether they can, instead, be used to constrain the timing of flows that formed the channels.

The Grjóta Valles flow channel system (Fig. 5.2), referred to by earlier authors as the unnamed northern channel system (Burr et al., 2002), is at least 400 km in length (west to east), with the northernmost Cerberus Fossae serving as the main conduit for aqueous flow. The northernmost Cerberus Fossae is the central area of the flows' origins, with the distance of the flow channels northern and southern limits from the northernmost Cerberus Fossae not being more than 100 km on both sides. The flow channels' general orientation is that they extend from the northernmost Cerberus Fossae to the northeast, then head southeast before their surface expression becomes indistinct. Burr et al. (2003) described fluvial geomorphic features indicating that water emanated from the source area of the northernmost Cerberus Fossae, flowed eastward, and then flowed southeast. This chapter builds upon the work of previous studies such as Burr et al. (2002), who suggested that repeated flow events may be responsible for the channels, and Burr et al. (2002) and Plescia (2003), who suggested

that the area exhibits the typical characteristics of channels produced by the catastrophic release of water, such as a well-defined source area, low sinuosity channels, and longitudinal grooving of channel floor, and tear-drop shaped 'islands'. These ideas are described in more detail in Sections 5.2.2 and 5.2.3. However, these two points on formation via water flow and repeated flows are a source of debate (Leverington, 2011) and will be discussed later. Due to the resolution of data available to researchers prior to 2006 (the launch of the Mars Reconnaissance Orbiter, which has both the High-Resolution Imaging Science Experiment (HiRISE) and Context Camera (CTX) cameras on board), they were unable to discern cross-cutting relationships between individual channel sections or provide detailed observations of the source of flows. Only since 2006 has a catalogue of images from Mars become available, and only since January 2009 have HiRISE images of the Cerberus Fossae become available, with still large areas of the Cerberus Fossae and associated flow channels not covered by HiRISE imagery.

5.2.2. Outflow channels in Cerberus—what formed them?

Numerous theories exist regarding the mechanism that formed the outflow channels in Cerberus, namely Athabasca Valles, Marte Valles, and Grjótá Valles. Numerical modelling has been used to link dike-related heat flow and flood volume on Mars in general (Wilson and Head, 2002). It shows that such dikes would, in some cases, be able to produce heat to melt ground ice, which could produce flood water to create channels and/or landforms similar to those observed within Grjótá Valles (e.g. McKenzie and Nimmo, 1999; Wilson and Head, 2002; Plescia, 2003). Head et al. (2003) suggest for Athabasca Valles, which, like the Grjótá Valles emanates from Cerberus Fossae, that dike emplacement produces surface cracking, localised volcanic eruptions, cryospheric cracking, and release of pressurised groundwater from beneath the cryosphere, while studies by Jaeger et al. (2007, 2010) suggest that the Athabasca Valles were water carved channels that were later draped in lava. Therefore, it is not unreasonable to presume that Grjótá Valles was formed by similar mechanisms, being connected to the Cerberus Fossae. However, the distance from the northernmost Cerberus Fossae, the likely emanation area for the formation of the Grjótá Valles outflow channels, to the southern Cerberus Fossae, the emanation point for the Athabasca Valles outflow channel, is approximately 400 km, with the northernmost Cerberus Fossae and the southern Cerberus Fossae being structurally quite different. Hence, it is important for this thesis to study the former to assess whether it formed in the same way as the latter.

5.2.3. Aqueous origin

In detail, one conjecture for the origin of the channels in Grjótá Valles is that they result from aqueous flows (Baker and Milton, 1974; Burr et al., 2002; Head et al., 2003; Morgan et al., 2013; Plescia, 2003). It has been suggested that the water was formed by (a) the magma-induced melting of the cryosphere (Berman and Hartmann, 2002; Burr et al., 2002; Head et al., 2003); (b) the outflow of water from a breached aquifer above an intruding dike beneath the fossae (Carr, 1979; Burr et al., 2002; Plescia, 2003); (c) the release of water from a sub-cryosphere aquifer a few kilometres thick, and tens of kilometres in lateral extent (Manga, 2004), or; (d) from another subsurface origin (Jones et al., 2011). Some authors have suggested that large megafloods occurred (Kattenhorn and Meyer, 2010; Burr et al., 2002, 2009) within the Cerberus Fossae and were responsible for the formation of Grjótá Valles, Marte Valles, and Athabasca Valles outflow channels. The exact emanation points/areas of these floods have not been conclusively identified, although generally, it is thought to be the fossae themselves (Burr et al. 2002, 2009). To have formed these three individual channels in just three single events, the flows would have had to have been extremely large, with enormous discharge rates (e.g. $1-8 \times 10^6 \text{ m}^3 \text{ s}^{-1}$ for the nearby Athabasca Valles channel system; Keszthelyi et al., 2007), because, for example, the Grjótá Valles outflow channels cover a large region of $\sim 90,000 \text{ km}^2$. Manga's (2003) studies on determining whether subsurface aquifers can discharge water at a sufficient/required rate to explain the flood features observed suggest that a deep groundwater origin for recent floods is possible as long as subsurface aquifers are many tens of km in lateral extent, something not yet encountered on Mars.

Nevertheless, lingering questions remain: How could such large volumes of water/lava needed for such flows be released, and where could such volumes of water be stored? Are there other possible storage mechanisms for large volumes of water and are the storage methods in some way connected to the form of release? Regarding the first question, Head et al. (2003) noted that if the water emanated from an aquifer, that the required aquifer permeability is larger than commonly encountered on Earth, meaning that either water is transported through the subsurface by a highly efficient, as yet unknown mechanism, and/or the volume flux values are overestimated. Indeed, as suggested by Manga (2003), the aquifers would need to be tens of kilometres in size, and there exists no evidence for the existence of such huge bodies. Accordingly, such theories are not plausible.

Regarding the second question, sub-surface ice could be a possible source of water. Studies by Dundas et al. (2018, 2021) and Harish et al. (2020) revealed exposed shallow subsurface water ice on Mars, but the observations are currently limited to mid- and high latitudes of Mars. Piqueux et al. (2019) reported widespread shallow water ice in the high latitude and midlatitude up to 35°N/45°S of Mars based on trends of seasonal surface temperature. Observations of seismic wave velocity of the Martian crust suggest that the subsurface is not ice-saturated (Manga and Wright, 2021); however, their findings do not rule out the possibility of the existence of groundwater. Regarding specifically the region of Mars under investigation in this thesis (Cerberus Fossae), Alberti et al.'s (2012) study of the subsurface material of the Cerberus plains indicated high porosity underlying material in this region. Morgan et al.'s (2015) work noted an extensive blanket of sediments plausibly mixed with lava to the south of Cerberus Fossae. Meng et al. (2020) reported a ~40 m thick lava layer over the possible water-ice deposits to the west of Elysium Mons. Xiong et al. (2021) investigated the shallow subsurface of the central Cerberus plains and estimated a permittivity value of 3.12—a value that would suggest shallow subsurface water ice. While the consensus regarding the origin of water is far from clear, the existence of subsurface water in volumes vastly smaller than the proposed aquifer model might suggest that aqueous flow was released in discrete flows, offering an alternative to the megaflood theory. Head et al. (2003) have suggested that the fault system that runs through Grjótá Valles, the northernmost Cerberus Fossae, is formed due to dike emplacement and has somehow facilitated flow formation. Numerical modelling has been used to draw a general connection between dike-related heat flow and flow volume on Mars. Results show that such dikes would, in some cases, be able to produce enough heat to melt ground ice/subsurface ice, which could, in turn, produce flow water that could create channels and landforms similar to those described within this chapter (e.g. McKenzie and Nimmo, 1999; Wilson and Head, 2002; Plescia, 2003). Work by Head et al. (2003) on the Athabasca Valles outflow channel, which, like the outflow channels in Grjótá Valles, is thought to have emanated from Cerberus Fossae fissures and graben, revealed features suggestive of dike emplacement, including surface cracking, localised volcanic eruptions, cryospheric cracking, and release of pressurised groundwater from beneath the cryosphere. However, as explained earlier, Head et al. (2003) note that the required aquifer permeability is more significant than generally encountered on Earth. This would suggest that water is transported through the subsurface by a highly efficient but hitherto unknown mechanism, and there have been overestimates of the volume flux values. Of course, this depends on sufficient quantities of sub-surface ice, which is debatable. As for the existence of sub-surface igneous heat sources (i.e., dikes along Cerberus Fossae) that could melt sub-surface

ice, lavas have been identified in some locations (e.g. Keszthelyi et al., 2000; Burr et al., 2002; Plescia, 2003; Jaeger et al., 2007; Jaeger et al., 2010). Volcanic centres have been mapped (Plescia, 2003), and studies suggest possible dikes exposed on the floor of Cerberus Fossae (Head et al., 2003). This thesis investigates alternative hypotheses, such as small, multiple cross-cutting flows suggested by Burr et al. but not fully studied by them.

5.2.4. Lava origin

The flow of turbulent lavas has also been suggested as a possible mechanism for cutting outflow channels (Jaeger et al., 2010). The evidence that supports the idea that the outflow channels in the Athabasca Valles may have been formed by lava includes the following: (i) the presence of ring-mound landforms (RMLs) imaged with HiRISE (High-Resolution Imaging Science Experiment), which have been interpreted as volcanic (rootless) cones formed as lavas heated underlying groundwater causing steam explosions (Jaeger et al., 2007) Figure 1.6 a and b; (ii) the presence of thin, concentric, lobate flow fronts that indicate overlapping lavas (Jaeger et al., 2007), Figure 1.5 a and b and; (iii) the presence of platy-flow or platy-ridged surfaces indicating lava crusts (Chapman et al., 2009; Keszthelyi et al., 2000) (Figure 5 in Keszthelyi et al., 2000; Figure 8 b–d and Figure 10 in Chapman et al. 2009 to see examples of platy-flow from the Amazonian).

Concerning Grjótá Valles, it has been suggested that the flow of lava was the principal process in channel formation (Leverington, 2004, 2006, 2011, 2018). This hypothesis is based on observations of geomorphic features on Venus and the Moon. The features observed are suggested to be similar to those observed from the outflow channels on Mars, such as anastomosing reaches inner channels, streamlined erosional residuals, sinuous channels, branching channel patterns, and reaches that suggest lateral or vertical erosion (Leverington, 2011). Moreover, it has been suggested that channel formation by lavas does not depend on the actual hydrological flow rates, sub-surface rock permeabilities, factors regarding hydrologic head, suggested water abundances implied by an aqueous model that are not following geochemical and mineralogical observations, and the lack of terrestrial analogues (Leverington, 2011). However, in this thesis, it is suggested that if lavas were the dominant factor in channel formation, typical lava morphologies should be readily identifiable, such as upstanding flows lobate flow fronts, knobs, platy-ridges, and rootless cones that characterise lava-infilled outflow channels (Athabasca Valles) in parts of the Cerberus Fossae.

As such, prior to this thesis, there was a debate regarding possible links between aqueous and lava processes. Initial work for this thesis suggested that this uncertainty was partly due to the uncertainty regarding whether multiple or single-flow episodes produced the channels.

5.3. Methods

In order to be able to study the area of the northernmost Cerberus Fossae and the outflow channel in Grjótá Valles, a region of approximately 70,000 km² was studied, using CTX (Fig. 5.2). CTX image mosaics for Mars in Google Earth (which uses a spherical normal (equatorial) variant of the Mercator projection for its maps) were used in this thesis. The mosaic is a composite of images taken by cameras on board the Mars Reconnaissance Orbiter (MRO), namely the Context Camera (CTX) (with a resolution of approximately 6 m per pixel). High-Resolution Imaging Science Experiment (HiRISE) images (with a resolution of approximately 30 cm per pixel) were also used to focus on areas requiring a much greater resolution, where that was possible. HiRISE images were analysed in HiView (which uses equirectangular projection map projections). HiRISE coverage over the entire area is sparse, predominantly across the fissures of the northernmost Cerberus Fossae. By analysing the images, it was possible to map the geomorphology of the outflow channel system (see Section 5.4). Areas of interest that exhibited possible cross-cutting were studied with Mars Orbiter Laser Altimeter (MOLA) point data to produce cross-sectional profiles. A combination of these observations allowed a chronology of the process involved in shaping this area to be developed.

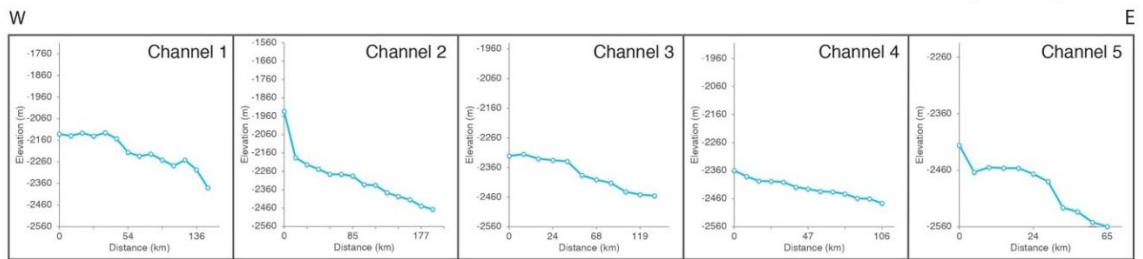
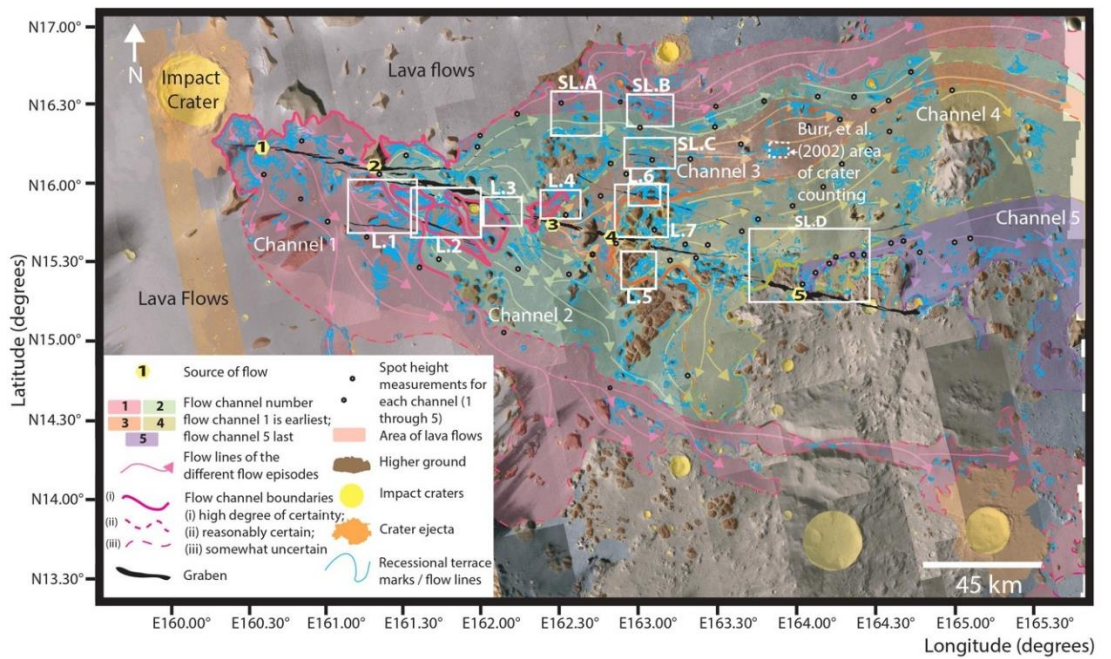


Figure 5.2. Regional Map (centred at 15.25° N, 162.85° E) of the study area marking the source areas of the five flows and the extent of each flow. The key study locations, 1 through 7 (Figures 5.4 through 5.11, respectively), are shown with white rectangles with L.1, L.2 and so on next to the boxes. Supplementary Locations A through D are shown with white rectangles with SL.A, SL.B, and so on next to the boxes. Below the Regional Map are five spot height topographic profiles for the extent of each flow area 1 through 5 (kilometres/elevation) showing the downward-east sloping topography of the Regional Map area. The vertical exaggeration for each topographic profile is x200.

Early observations and investigations revealed the existence of cross-cutting channels in several locations in the study area. These channels were mapped back to their probable sources to accurately delineate the total number of outflow channels. Some of the observed cross-cutting relationships could have been between distributary channels, where the main channel divides into multiple channels downstream (Figure 5.3), so it was essential to map channels back to their source to avoid an exaggerated number of outflow channel formation phases. As such, the focus was on mapping channels and locations that could be traced back to their source. It will be shown in the results section (Section 5.4) that there are five phases of channel formation, each of which can be mapped back to a different source along the northern Cerberus Fossae. The five clear examples located can all be mapped back to their sources without interruption by another cross-cutting channel (Figure 5.3).

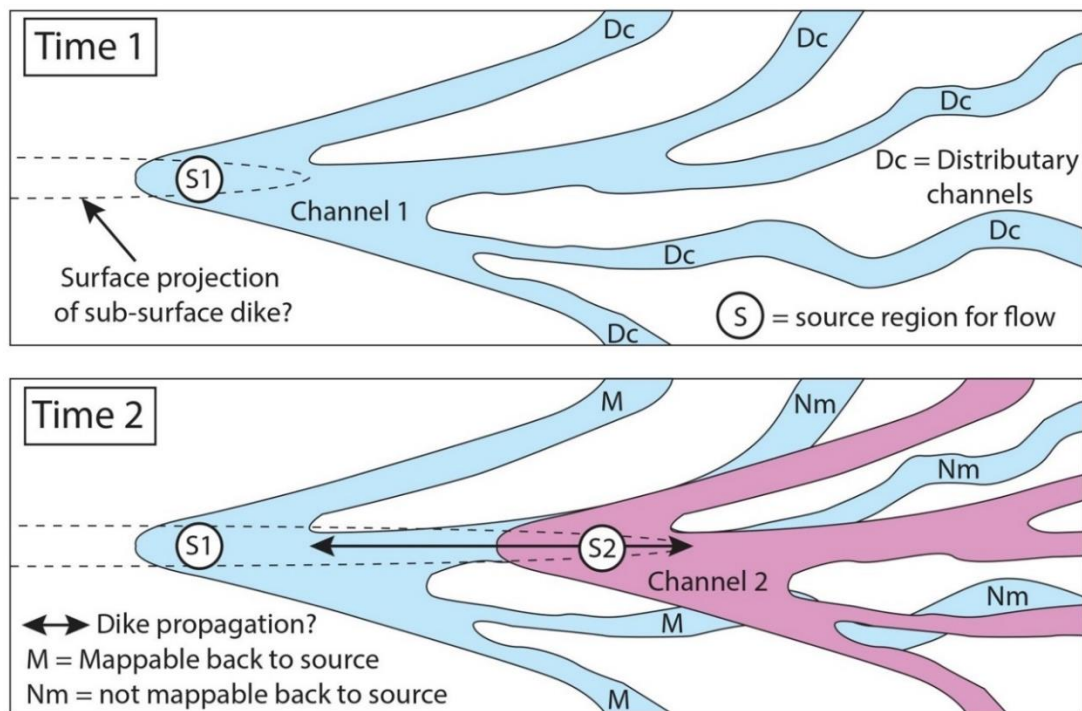


Figure 5.3. Schematic summary of cross-cutting relationships between channels. Time 1 took place before the later Time 2. In Time 1, a flow occurred that was sourced as S1, and the flow formed distributary channels (Dc) that can all be mapped back to the source of the flow, S1. In Time 2, a later flow S2 occurred, sourced further east than the earlier S1. The flow from S2 formed distributary channels, which cross-cut the earlier distributary channels formed by S1 flows. In Time 2, only three of the five S1 distributary channels can be mapped back to their S1 source. This is why it is challenging to map some distributary channels back to the source of the flows. Speculative dike geometry at depth explains the lateral migration of the source locations for the two-channel systems.

Identifying cross-cutting relationships that can be mapped back to the source was possible for seven locations (Figures 5.4 through 5.11). Other locations that displayed cross-cutting relationships were found. However, it was not possible to map these channels back to a source, primarily due to ambiguous and unclear relationships identified in the imagery. These four locations are located far from the northernmost Cerberus Fossae fissures, and they were used to help delineate possible boundaries among different flow episodes in the downstream and distal regions. As such, these locations assisted in developing and completing the regional map (Fig. 5.2 and outlying supplementary locations A through D (Figs. 5.S1 through 5.S4)).

After identifying cross-cutting areas and whether they could be traced back to the source, Mars Orbiter Laser Altimeter (MOLA) Precision Experiment Data Records (PEDRs) were used to produce transects across each location area so that a topographic profile of each location could be constructed. Unfortunately, MOLA data was only available for some locations and, in some cases, did not fully cover specific areas of note in the chosen locations. The chosen locations exhibited clear cross-cutting and had enough relevant

MOLA PEDR points to allow the construction of a usable topographic profile. This was carried out to measure the depths of channels at each location, which would be the depth of the channel incision.

In addition to studying cross-cutting channel morphologies as described above, it was envisaged that MOLA data could provide extra information because a younger channel might, presumably, incise vertically down across landforms produced by pre-existing channels, and this would confirm or deny the time sequence of channel formation. Thus, MOLA data were used to study the vertical disposition and geometries of channels in cross-section. The MOLA PEDRs laser spots cover an area of approximately 160 m in diameter, spaced approximately every 300 m.

The range measurements are quantised with a 1.5-m vertical resolution before correction for orbit and pointing errors. The relative error in altitude along profiles is 1–10 m (Albee et al., 2001). As a result, it was important only to attach significance to results where the vertical differences were greater than 10 m. To help ameliorate these problems, MOLA data from locations where the elevation dramatically changes at less than 160 m horizontal length scale was not used, and this was ensured by scrutinising shadow lengths on CTX and HiRISE images (where available).

Each of the seven study locations within this chapter was chosen and studied based on the following requirements:

- (a) clear evidence of cross-cutting channels that can be mapped back to the source;
- (b) sufficient MOLA coverage at each location to enable the construction of topographic profiles across the width of the channels;
- (c) a vertical difference greater than 10 m, meaning that the range in elevations in each location had to be more than 10 m. Less than 10 m vertical difference is the relative error in altitude profiles, as noted by Albee et al. (2001);
- (d) MOLA data were available for at least five to six transects per location. Locations with less than five or six MOLA transects meant that there was insufficient data available to construct useable topographic data. It should be noted that some areas had sufficient MOLA coverage. However, the orientation of the MOLA transects to the channels and landforms under investigation meant that the MOLA transects were not able to be used because they missed a particular feature. It was also important to find locations that were further to the east than the last and close to the Cerberus Fossae.

By adhering to these four points (a–d above), seven locations were identified with clear cross-cutting relationships between channels discernible, with channels traceable back to their respective sources. Four additional locations with clear cross-cutting relationships discernible between channels were identified. However, in these locations, point (a) was not fulfilled—it was not possible to trace the channels back to the source unambiguously. With the locations finally selected, (seven fulfilling all four criteria (a–d), and four fulfilling criteria (b–d)). MOLA data was used to construct topographic profiles (distance/elevation) across the 11 locations. Once constructed, the topographic profiles were studied, along with the location images in CTX mosaic and HiRISE (where available). A study of the topographic profiles was used to provide support for or to deny the cross-cutting relations identified in the map view studying cross-cutting relationships between the different channels by seeing and measuring if younger features had incised down into older features, i.e. if the younger channels had crosscut down across older channels. Such incisions were measured using the topographic profiles to determine the vertical extent of the incision. Analysis of the illumination of the slopes observed was also crucial in helping to determine the aspects of the slopes. Using colour coding for each channel and geomorphic feature, the chronology of geomorphic evolution was developed.

Once each location was completed, details from each were used to complete the larger regional map, which shows the channels, fissures and faults, impact craters, and ultimately the chronology (Fig. 5.2). To the regional map, based upon the detailed work of the 11 locations, flow lines were added to all maps (regional and the 11 locational maps), using the orientation and position of channels and geomorphic markers (tear-drop shaped features, linear features on the slopes of the depression margins, linear features on streamlined hills, and depressions) to best determine the most likely flow direction of each channel. In some cases, boundary lines between channels were challenging to identify, with the process being more straightforward, nearer to the source of the flows and more equivocal at distal locations. The regional map (Fig. 5.2) shows three types of boundaries between channels, these being: (a) a high degree of certainty, (b) reasonably certain, and (c) somewhat uncertain.

Finally, topographic profiles were constructed along the five main channels using MOLA data for the regional map. This was carried out to see that each channel flowed downhill, an essential facet in understanding the flow movement of the channels studied.

5.4. Results

Eleven geomorphic maps with topographic profiles were created (seven for locations that fulfilled the four essential criteria mentioned in section 5.3 and four locations that fulfilled three of the four essential criteria mentioned in section 5.3, but each not fulfilling the same criterion, that being showing clear evidence of cross-cutting channels that can be mapped back to the source). Upon completing all eleven maps and accompanying topographic profiles, it became apparent that the geomorphic features identified in the first location (Figure 5.4) are common across all locations—a commonality existed regarding geomorphic features in all locations. As such, the first location, Location 1 (Figure 5.4), was used as a ‘type’ example for the remaining locations (Location 2–7 (Figures 5.6–5.11), and the four locations that lack clear evidence of cross-cutting channels that can be mapped back to the source, SL A–D (Figures 5SLA–5SLD)). The description of observed geomorphic features from Location 1 (Figure 5.4) is used to explain how each geomorphic feature was identified and differentiated from across the entire study region. Each geomorphic feature identified was described. Any interpretation regarding a particular feature’s origin and significance came later. The type examples given regarding Location 1 (Fig. 5.4) were then used to identify and interpret features in the other locations (Location 2–7 (Figures 5.6–5.11), as well as for the four locations where the tracing of channels back to the source was not possible (SL A–D (Figures 5SLA–5SLD))).

Once all eleven locations were mapped and topographic profiles for each location produced, the larger regional map and accompanying topographic profiles (Figure 5.2) were developed and produced. Of particular focus with the regional map was the attempt to delineate each separate flow episode based on the findings from the eleven locations.

5.4.1. Location 1 (Fig. 5.4)

Location 1 (15.70° N, 161.61°E) is in the western section of the overall channel system (Figure 5.2). It is approximately 10 km south of the central system of faults, fractures and fissures that form part of the northernmost Cerberus Fossae. It is traversed by more minor fractures that trend WNW–ESE. The terrain is predominantly a flat plain with relatively low crater densities, though some areas exhibit higher topography with what appear to be relatively higher crater densities based on visual observation. While this statement is qualitative rather than quantitative, these features are of interest for further study. Below is a description of the five key features that are of note.

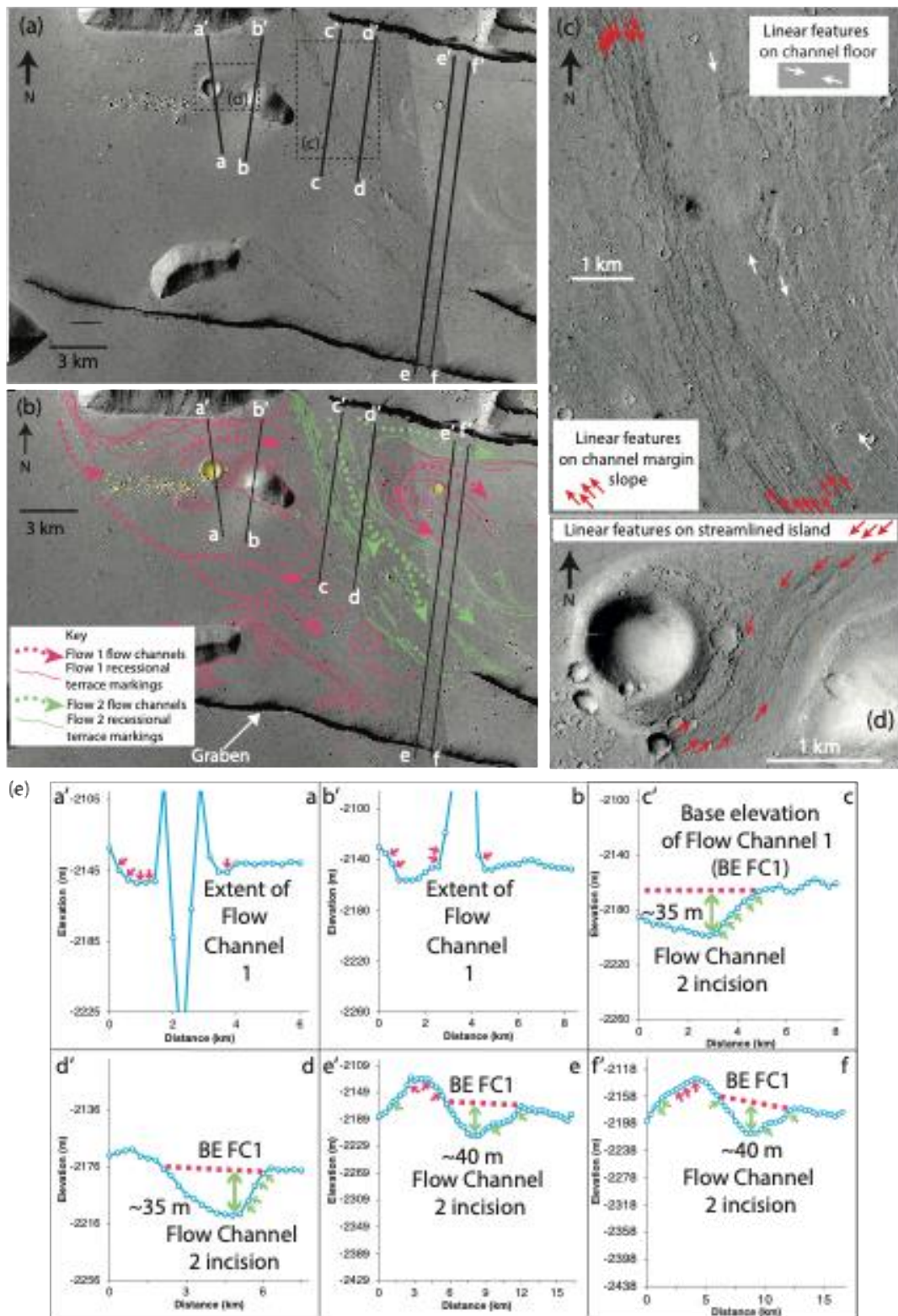


Figure 5.4. Maps and topographic profiles of Location 1 centred at 15.70° N, 161.61° E showing details of channels and cross-cutting relationships (see Figure 2 for location). (a) Map with CTX mosaic with MOLA transects; (b) Map with CTX mosaic with MOLA transects (black lines a'–a through f'–f) and interpreted channel markings/flow directions/recessional terrace markings. Topographic profiles a'–a through f'–f for each of the six transects, with the blue line in each graph representing the MOLA transects. (c) The inset from CTX shows details of the channel floor. Linear features on the channel margin slope and the linear features on the

channel floor do not resemble lava flow landforms, such as thin, concentric, and lobate flow fronts that indicate overlapping lavas or rootless cones. The interpretation is that they resemble “longitudinal grooves” or “longitudinal lineations” that have been used to infer catastrophic flow terrain on Earth and Mars (Baker, 1978; Burr et al., 2002) and/or turbulent lava (Jaeger et al., 2010), and resemble “bathtub rings” that are cut by high flow velocities and vortices, and left by lowering fluid levels during waning flows (Baker 1973, 1978). (d) Map showing similar linear features around a streamlined island. (e) Topographic profiles from MOLA spot heights (labelled a’–a through f’–f and located on (a) and (b)) showing the morphologies of channels and craters and locating linear features on channel margins. The vertical exaggeration for each topographic profile is x50. Overall, for Location 1, the interpretation is that Flow 1 (that flowed from west to east/southeast) is cross-cut by channels formed by a later flow, Flow 2 (that flowed towards the SE). Flow sources are shown in Figure 5.5.

5.4.1.1. Descriptions of landforms at Location 1

a) Depressions

Observations of Location 1 indicate the presence of depressions, visible on the Google Earth CTX mosaic images, and this is confirmed when MOLA profiles that cross these depressions are analysed. The most prominent depression follows a NW–SE orientation and is approximately three to four kilometres wide (Figs. 5.4 a, b and c) and approximately 40 metres deep. MOLA data points cross this depression, marked as profiles c’–c, d’–d, e’–e and f’–f (Figs. 5.4 a, b and 4 c and topographic profiles c’–c, d’–d, e’–e, and f’–f). The other depressions in Location 1 are all shallower than the main depression, all being less than 10 metres, with their orientations running W–E as is the case for the northern part of the MOLA profiles a’–a and b’–b, and the southern end of profile c’–c (Figs. 5.4 a and b).

Illumination from the SW produces shadows on the NE of geomorphic features, shadows that slope towards the NE and brighter areas on features that slope towards the SW.

b) Linear features on the depression floor

These are 3 to 4 km long, approximately 50 to 100 metre wide linear features with what appears to be a set of smooth ridges, known because they have shadows on their E or NE sides and relatively brightly illuminated W or SW sides (Fig 5.4 c). These ridges die out in the NNW and SSE direction, terminating with lenticular-shaped ends.

c) Linear features on the slopes of the depression margins

On the slopes that form the edges/margins of the depressions, linear features can be found. An excellent example is Figure 5.4 c, where approximately nine sub-parallel linear features can be identified. However, the features appear to have embayed traces that are, in some places, sinuous and discontinuous. MOLA data reveals that these features differ from the linear features found on the floors of the depressions because they have shadows on their NE side (Fig 5.4 c.). However, the obverse side is not brightly illuminated, thus indicating that the linear features on the slopes of the depression margins resemble steps cut into the slope. Analysis of MOLA point data shows that, in places, nine to ten of these linear features are found on the slopes of the depressions that are approximately 1 kilometre across, with a relief of approximately 40 metres. The 'steps' are only a few metres high (e.g. Fig. 5.4 c and topographic profiles c'-c, d'-d, e'-e, and f'-f).

d) Linear features on streamlined hills

Linear features also exist along the slopes of streamlined hills (e.g. Fig 5.4 d). Similar to the linear ridges found on the floors of the depression, they have shadows on their eastern sides and lack brightly illuminated western sides. Analysis of MOLA data shows that their vertical dimensions are just a few metres (e.g. Fig. 5.4 c). They also resemble the 'steps' of the linear features on the slope of the depression margins.

e) 'Tear-drop' shaped hills

There are raised features shaped like teardrops, common in Location 1 and throughout the larger study area (e.g. Fig. 5.4 a, b and d). They vary in size from a few hundred metres to several kilometres or more in area. Some features have formed around pre-existing craters (e.g. Fig. 5.4 d); others have formed around low hills (e.g. Fig. 5.4 a and b). Some of these hills contain very low-relief depressions (e.g. the hill crossed by profiles e'-e and f'-f shown in Figs. 5.4 a, b, and topographic profiles e'-e and f'-f) that were only discernible through analysis of MOLA data.

5.4.1.2. Interpretation of five geomorphic landforms at Location 1

- a) Depressions interpreted as channels

The observed depressions have been interpreted to be channels. Based on the dimensions of the channels (40 m x 3000 m), it is unlikely that glaciers cut these channels due to their depth-to-width ratios and form ratio (0.013), unlike glacially formed valleys on Earth whose form ratios, for active glacial channels, is between 0.20 and 0.58 (Harbor, 1992). Up-standing morphology types commonly associated with mudflows or lavas were not identified in Location 1. However, incised depressions were identified, and aqueous flow at high volumetric flow rates could produce these incisions. Jaeger et al. (2010) point out that the flow of turbulent lavas could produce mechanical erosion, too, and as such, turbulent lavas cannot be ruled out as having formed the channels.

- b) Linear features on the depression floor are interpreted as 'longitudinal grooves' or 'longitudinal lineations.'

The linear features observed are interpreted as 'longitudinal grooves' or 'longitudinal lineations' (Baker, 1978; Burr et al., 2002). The existence of these 'longitudinal grooves' or 'longitudinal lineations' has been used to suggest catastrophic flow terrain on Mars and Earth (Baker, 1978; Baker and Milton, 1974).

'Longitudinal grooves' or 'longitudinal lineations' are found on the channel floors with alternating high ridges and low grooves oriented parallel to the channel walls. As suggested by Burr et al. (2002), the lineations are evidence of a formation process that is sensitive to the local topography. As with streamlined forms, 'longitudinal lineations' or 'longitudinal grooves' have been used to infer catastrophic flood terrain on both Earth (Baker, 1978a, p. 70) and Mars (Baker and Milton 1974).

- c) Linear features on the slopes of the depression margins interpreted as terraces on channel margin slopes

The linear features on the slopes of the depression margins are interpreted as terraces on channel margin slopes. Burr et al. (2002) believed these to result from erosion of pre-existing layered terrain, which may be partially correct. However, in this location, the features are not dissimilar to 'bathtub rings'. These features are

cut by high volumetric flow rates and vortices and are left as the water levels lower as flows wane (Baker 1973, 1978). As with the other features, turbulent lava flows may have created these features through mechanical erosion (e.g. Jaeger et al. 2010). Jaeger et al. (2007) conducted a study on the Athabasca Valles to determine the composition of the flow that formed the outflow channels. They aimed to decide whether or not it was primarily composed of sediment, ice, or lava. They analysed the many ring-mound landforms (RMLs) in Athabasca Valles using HiRISE imagery to do this. The RMLs are believed to have originated from various sources, and each source points to a specific flow composition. For instance, if the RMLs are pingos (ice-covered mounds), the flow is a mixture of sediment and ice. If the RMLs are cryophreatic cones, the flow is sediment that was volatile-rich but has since degassed. Finally, if the RMLs are rootless cones (hydrovolcanic) formed when a flow heats the groundwater below it, causing steam explosions, then the flow is lava. Jaeger et al. (2007) analysed RMLs and found evidence of relict wakes trailing in the direction of the flow. This indicates that the wakes formed atop the active flow and that gas vented from a fixed source at depth into a moving flow. Thus, it is evident that the RMLs in Athabasca Valles are rootless cones and that the flow was lava (Figure 1.6 a and b). However, Jaeger et al. (2007, 2010) also suggest that aqueous forces most likely formed the channels themselves. Tanaka and Chapman (1990) found that the channels in Mangala Valles are similar to those in the Cerberus plains. Both originate from graben that are radial to a volcanic centre, suggest evidence of more than one aqueous flood episode, and indicate that both aqueous flooding and lava emplacement occurred concurrently. It is crucial to note that the interpretations of erosion of pre-existing layered terrain versus recessional terraces may not be mutually exclusive. This can pose a challenge, particularly in regions where sub-horizontal lava layers may be present, such as Grjótá Valles. Regarding the examples described, the interpretation is that as the fluids waned, the fluid levels dropped. This cut into the bedrock, creating the 'bathtub rings' features, or 'recessional terraces', during the recession of the fluids. Research into 'recessional terraces' has not provided any evidence that these features are produced by either mudflows or highly viscous lava flows.

- d) Linear features on streamlined hills interpreted as linear features on the streamlined hills. These are recessional terraces cut by waning rapid fluid flows.
- e) 'Tear-drop' shaped hills interpreted as streamlined islands cut by the flows. These are interpreted as streamlined islands cut by the flows, based upon earlier

interpretations of the recessional terraces cut by waning high volumetric fluid flows. These 'tear-drop' shaped features within the channels, with the rounded-end pointing upslope and the pointed-end pointing downslope, often flat-topped and topographically raised, is strong evidence for high volumetric flow rates within these channels (Burr et al., 2002). Examples of these features can be seen in Figs 5.4 a, b, and d, such as the impact crater, which has been streamlined into a tear-drop-shaped island through which transect a'-a passes. Its flat top to the east of the crater and the pointed end of the feature pointing downslope display the classic tear-drop form. The general morphology of these streamlined islands indicates that the general flow direction was northwest to southeast (Figure 5.4 b). This trend is apparent in this location, and the entire study region (Fig. 5.2). Work by Burr and Parker (2006) (Fig. 5.1 b) also estimated similar general flow direction.

5.4.1.3. Summary

Landforms identified in Location 1 appear to have been formed by aqueous flows. They were not formed by highly viscous lava flows. Evidence for this exists in several forms. Firstly, there are no RMLs considered rootless cones (Jaeger et al., 2007) seen in Athabasca Valles. Secondly, features indicative of lava flows, such as thin, concentric, lobate flow fronts that indicate overlapping lavas (Jaeger et al., 2007) or platy-flow or platy-ridged surfaces indicating lava crusts (Chapman et al., 2010; Keszthelyi et al., 2000) were not observed. The geomorphic landforms do not appear to have been formed by mudflows because features that are the result of mudflows such as (i) elongated ridges with rough surfaces, (ii) hills characterised by circular plan-map appearance with flow-like structures extending from their bases, (iii) broad plateaus with a smooth central uplifted unit, often containing a rimless pit, and (iv) an extensive and chaotic combination of overlapping landforms of points (i), (ii), and (iii) above (Brož et al., 2020; Cuřín et al., 2021).

Consequently, the five geomorphic landforms described above were not formed due to the flow of mud or highly viscous lavas, but are the result of aqueous flows or turbulent lava flows, a theory propounded by some authors (e.g. Burr et al. 2002; Jaeger et al., 2010).

5.4.1.4. Observations of the relative chronology of geomorphic features

Building a relative chronology of events was paramount to understanding the history of events at Location 1. In Location 1, the pivotal observation that allowed for the

establishment of a relative chronology is that the NW–SE trending channel cuts across and incises down across the E–W trending channels (Fig. 5.4 b). Using MOLA data to construct topographic profiles that transect the channels in Location 1 (Fig 5.4 e) allowed for the measurement of the base elevation of channels. This was important to determine and measure the depth of the cross-cutting incision.

Regarding the E–W channels, the base elevation is approximately -2156 m. However, the base elevation of the NW–SE channel is deeper, at approximately -2194 m. This suggests an approximate incision of 40 m by the NW–SE channel (Fig. 5.4 e topographic profiles a'- a through f'- f). Recessional terraces of the E–W streamlined islands and channels are at elevations of between -2130 m to -2160 m, while recessional terraces of the streamlined islands and channels of the NW-SE channel are at elevations between -2170 m to -2195 m. The recessional terraces within the E–W channels oblique to those found in the NW–SE channel and appear cross-cut by the recessional terraces from the NW–SE channel (e.g. the region between profiles b'–b and c'–c, Fig. 5.4 b).

5.4.1.5. Interpretation of the relative chronology of geomorphic features

The interpretation of the relative chronology within Location 1 is that two separate episodes of channel formation occurred. The recessional terraces from older channels are cross-cut by recessional terrace marks associated with a younger channel (also visible in Figs 5.2, 5.6, 5.7, 5.8, 5.9, 5.10, and 5.11). Such evidence suggests that the water levels from the older flow episode had fully waned and that the later channel then formed. This would indicate two separate flow episodes, with the channels from these flows not anastomosing distributary channels from one flow.

5.4.1.6. Channel sources

It is important to be able to map channels back to their source points/areas for the reasons explained in section 5.3 (Methods). The oldest flow (Flow 1, Figure 5.5 a and b) can be traced and mapped back to its source, located in the vicinity of the cracks and fissures that make up the northernmost Cerberus Fossae (Figure 5.2 and Figure 5.5 a and b).

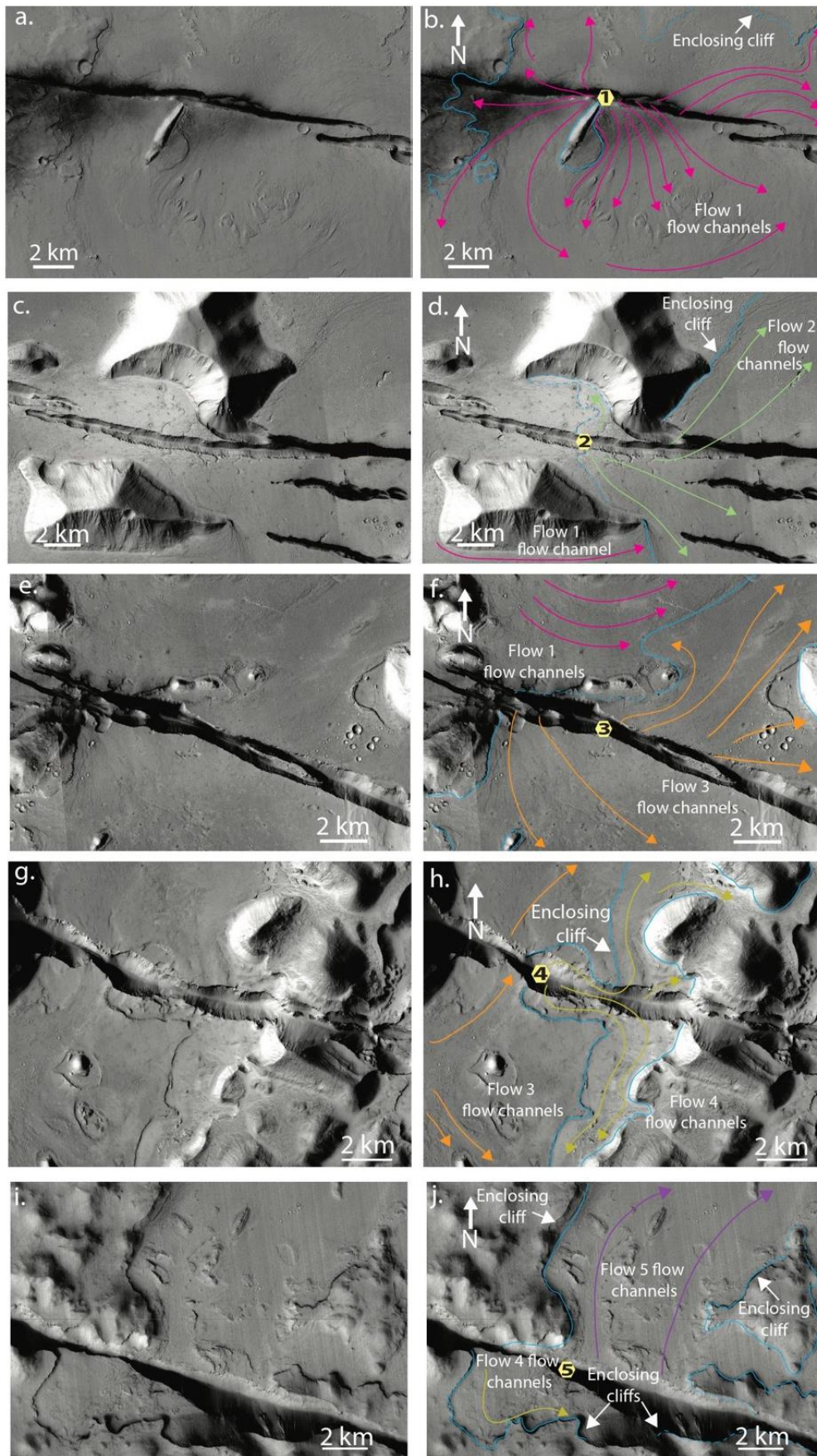


Figure 5.5. Panels a. through j. show the approximate location of the source area for each flow (marked and unmarked), marked by a number (1, 2, 3, 4 and 5, representing each flow) in a

yellow hexagon. (Panel a.; Flow 1, centred at 16.05° N, 160.48°E / panel c.; Flow 2, centred at 15.56° N, 161.33°E / panel e.; Flow 3, centred at 15.30° N, 162.41°E / panel g.; Flow 4, centred at 15.20° N, 163.05°E / panel j.; Flow 5, centred at 14.56° N, 164.17°E). The source areas have been disrupted by later faulting. Solid blue lines represent enclosing cliffs/boundaries with a high level of confidence; dashed blue lines represent enclosing cliffs/boundaries with a lower level of confidence.

Analysis of the source area reveals that it is surrounded to an extent by enclosing cliffs and that the initial flow direction, based on the orientation of the streamlined islands in the channels, was to the north and south. A faulted depression stretches west to east (Figures 5.5 a and b), and its walls are fresh and uneroded by the flow, suggesting that faulting occurred after the flow formed the channels and geomorphic features such as streamlined islands. Such an interpretation is similar to the interpretation and timing propounded by Burr, Sakimoto, and McEwen (2002) and Vetterlein and Roberts (2009) regarding the timing of flows and faulting. The younger flow can also be mapped back to its source point/area (Figure 5.2 and Figure 5.5 c and d). This source region is also surrounded to an extent by enclosing cliffs. Its walls are fresh and uneroded by the flow, suggesting faulting occurred after the flow formed the channels and geomorphic features, such as streamlined islands, much like the older flow. The source of the second flow is to the east of the source of the earlier flow. Again, the walls of the faulted depression appear fresh and un-eroded by the flow, suggesting that the faulting occurred after flow formation (Brown and Roberts, 2023).

5.4.1.7. Summary

Interpretation of Location 1 (Fig. 5.4 a, b, c, d, and e) shows two separate flow events (Flow 1 and Flow 2), with Flow 1 being older than Flow 2. Both flows can be mapped back to two separate source locations along the northernmost Cerberus Fossae fissures and cracks.

The five geomorphic features identified and discussed in detail are found across the study region. The observations and interpretations of geomorphic landforms in Location 1 are used as type examples to assist with interpreting landforms in the remaining locations (2 through 7 and the outlying supplementary locations A through D (Figs. 5.S1 through 5.S4)). Accordingly, a separate description and interpretation for every example in each location will not be included.

5.4.2. Location 2 (Fig. 5.6)

Location 2, centred at 15.60° N, 162.07° E, is east of Location 1 and has further examples of cross-cutting relationships between the two flows from Location 1 (Flow 1 and Flow 2). As with the examples in Location 1, the channels in Location 2 exhibit linear features on the channel floors and margins. These are longitudinal lineations and recessional terraces (Fig. 5.6 c).

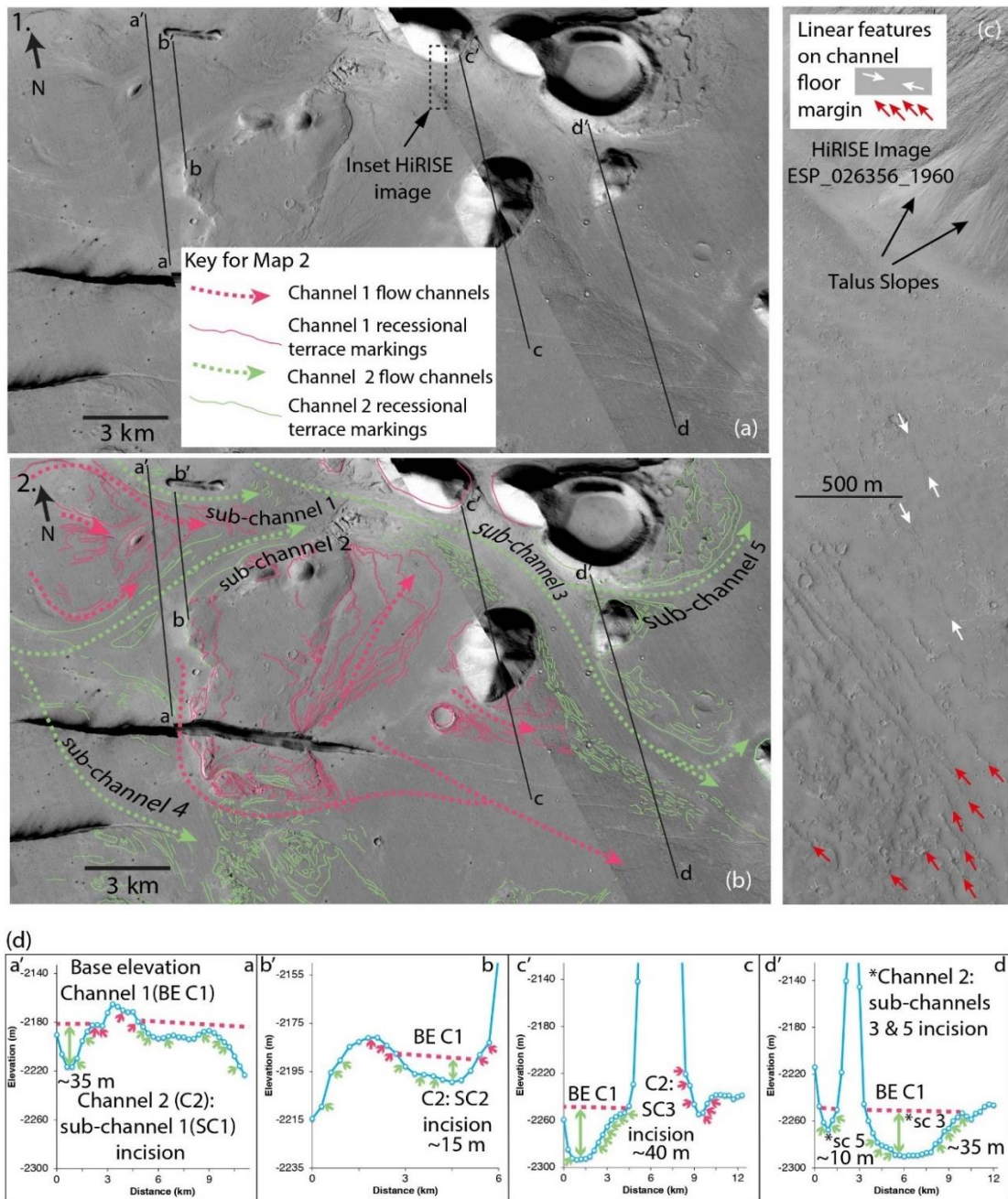


Figure 5.6. Maps and topographic profiles of Location 2 centred at 15.60° N, 162.07° E showing details of channels and cross-cutting relationships (see Figure 5.2 for location). (a) Map 1—CTX mosaic with MOLA transects. (b) Map 2—CTX with MOLA transects (black lines a'- a through d'- d) and interpreted channel markings/flow directions/recessional terrace markings. (c) Inset map

located in (a) from HiRISE Image ESP_026356_1960 showing details of a channel margin and channel floor. Talus slopes cover the channel margin in the NE. Features such as lobate flow fronts or rootless cones indicating lava flows were not identified. (d) Topographic profiles a'-a through d'-d for each of the four transects, with the blue line representing the MOLA transects in each profile. The vertical exaggeration for each topographic profile is x70. Overall, the interpretation of Location 2 is that older Flow 1 channels are cross-cut by younger Flow 2 channels. Five distinct Flow 2 channels are visible from the maps and topographic profiles. Of interest is the island-like streamlined landform in the top left of Maps 1 and 2. The channels from Flow 2 have created a streamlined 'island', but measurements and observations show that before Flow 2, this area was two or smaller 'islands' that the channels from Flow 1 had formed.

Landforms from Flow 1 are preserved on top of two streamlined islands defined by Flow 2. Flow 1, with a general flow direction of NW to SE, produced multiple channels within the bounds of the two main streamlined islands. The streamlined island in the top left of the image (Fig 5.6 a and b) is also in Location 1, and the channels have similar basal elevations (Location 1, -2180 m; Location 2, -2180 m). The later Flow 2 cross-cuts Flow 1 in several locations. Fig 5.6 b shows how Flow 2 sub-channels 1 and 2 are tributary channels, flowing north and south of a streamlined island that preserves features from Flow 1. They join to form sub-channel 3, which flows in a SW direction. Flow 2 sub-channel 4 flows SW and is a distributary channel that diverges from sub-channel 2 as they abut against a streamlined island, upon which features from Flow 1 are preserved. Flow 2 sub-channel 5 is a distributary channel that flows NW and diverges from Flow 2 sub-channel 3. At the northern end of transect c'-c (Fig. 5.6 a and b), Flow 2 sub-channel 3 flows towards the SE and cuts across a channel associated with Flow 1. The base of Flow 2 sub-channel 3 incises downwards to -2295 m, approximately 40 m beneath the basal elevation of channels associated with this portion of Flow 1 at around -2255 m and also beneath recessional terraces of Flow 1 (Fig. 5.6, topographic profile c'-c).

Flow 2 incises down below the level of Flow 1. On transect c'-c (Fig. 5.6, topographic profile c'-c), the elevation difference between the base of the second channel and the recessional terraces from Flow 1 suggests an incision of up to approximately 40 m. MOLA transect d'-d (Fig. 5.6 a and b) crosses Flow 2 sub-channels 3 and 5. Topographic data and recessional terrace markings indicate that Flow 2 channel sub-channel 3 incised down beneath the elevation of Flow 1. The incision is approximately 40 metres, from -2250 m to -2290 m, similar to those seen at transect c'-c. The distributary Flow 2 sub-channel 5 incised down into the surface produced by Flow 1. The incision is approximately 10 metres, from -2250 m to -2260 m. Topographic profiles a'-a and b'-b, with incision values of approximately 35 m and 15 m, respectively, offer further evidence that Flow 2 incised below the basal level of Flow 1.

Mapping back both flows to their sources indicates that these are the same two flows identified at Location 1.

5.4.3. Location 3 (Fig. 5.7)

Location 3 (Fig. 5.7), centred at 15.58° N, 162.37° E, shows further details of the relationship between Flows 1 and 2. The location is downstream of Location 2.

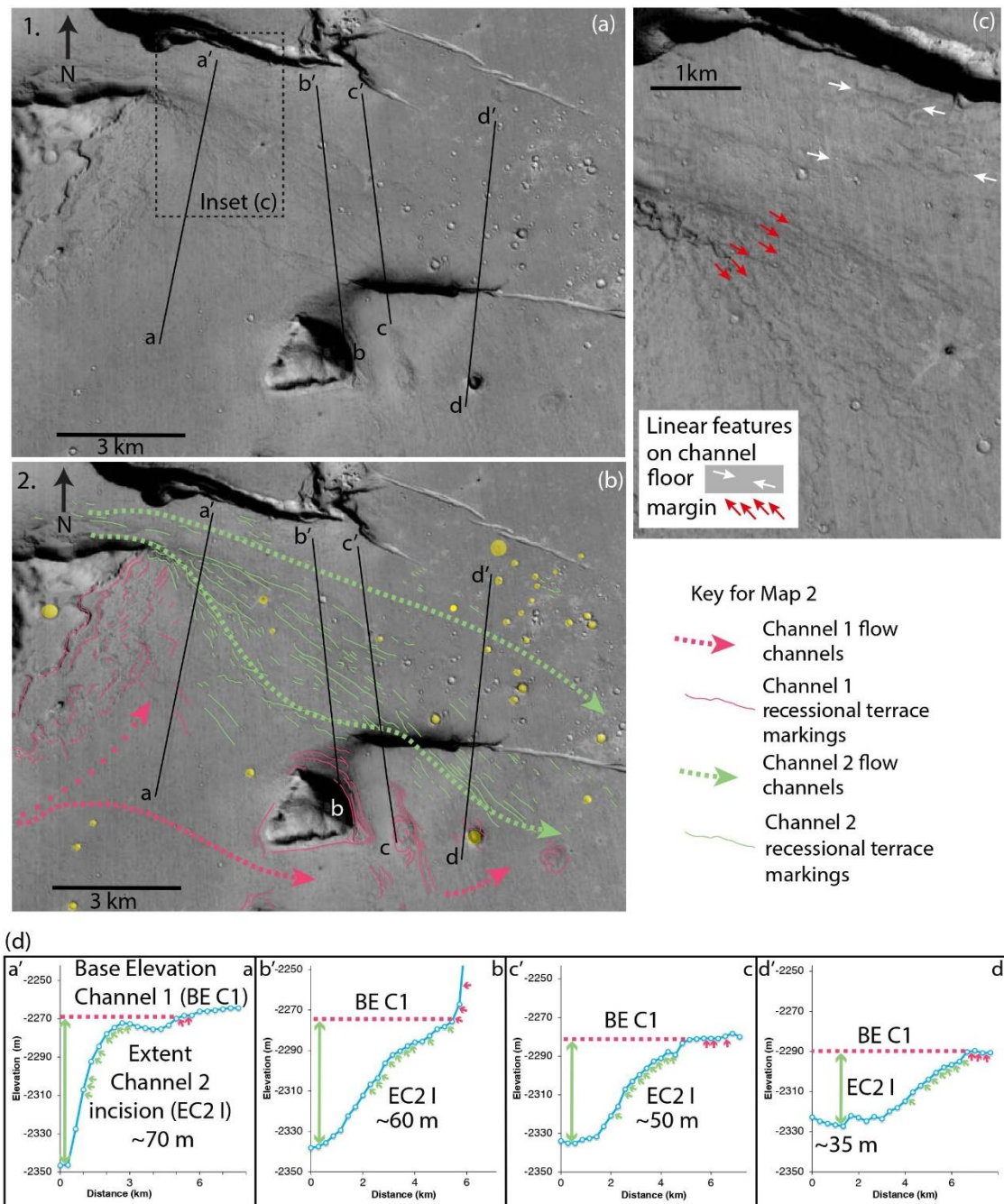


Figure 5.7. Maps and topographic profiles of Location 3 centred at 15.58° N, 162.37° E showing details of channels and cross-cutting relationships (see Figure 5.2 for location). (a) Map 1—CTX mosaic with MOLA transects. (b) Map 2—CTX with MOLA transects (black lines a'–a through d'–

d) and interpreted channel markings/flow directions/ recessional terrace markings. (c) Inset located in (a) from CTX data showing channel floor details and margin details. Longitudinal lineations and recessional terraces exist (see caption in Figure 5.4). Talus slopes cover the channel margin in the NE. Features such as lobate flow fronts or rootless cones indicating lava flows were not identified. (d) Topographic profiles a'–a through d'–d. for each of the four transects, with the blue line in each profile representing the MOLA transects. The vertical exaggeration for each topographic profile is x70. Overall, the interpretation for Location 3 is that a broad Flow 1 channel oriented to the east or NE was cross-cut by a later flow (Flow 2) that cut a channel indicating flow towards the SE.

Geomorphic Flow 1 landforms correlate with those in Location 1 and Location 2 because the basal elevation is similar at between -2270 to -2290 m. The channel floors and margins exhibit longitudinal lineations and recessional terraces (Fig. 5.7 c). On the southeastern side of a broad Flow 1 channel, a streamlined island has recessional terraces, possibly resulting from waning flow. The channel has longitudinal lineations that show the flow direction to the NE and E. Flow 2, later than Flow 1, flowed SE and cross-cut the landforms created by Flow 1. MOLA data indicated that the basal elevation for Flow 1 ranges from -2270 m in the west (MOLA transect a'–a) to -2290 m in the east (MOLA transect d'–d) (Fig. 5.7, topographic profiles a'–a and d'–d). The cross-cutting of Flow 1 by Flow 2 is clear from the recessional terrace marks of Flow 2, which are perpendicular to the flow direction of Flow 1. And its accompanying recessional terraces. There is a decrease from west to east in Flow 2's incision, with MOLA transect a'–a having a maximum incision of approximately 70 to 75 m; MOLA transect b'–b approximately 60 metres; MOLA transect c'–c approximately 50 metres; and MOLA transect d'–d approximately 35 metres. This marked decrease is in tandem with a decrease in the basal elevation of Flow 1 and accompanying channel features from west to east. Both Flow 1 and Flow 2 predate the fissures, with longitudinal lineations and recessional terrace markings from Flow 2 disrupted by later faulting.

5.4.4. Location 4 (Fig. 5.8)

Location 4, centred at 15.60° N, 162.75° E, is east of the previous three Locations. The focus of this location is the presence of the oldest flow channel, Flow 1, which is cross-cut by a third flow, Flow 3. As with the previous locations, the channels and geomorphic bodies are characterised by longitudinal lineations and recessional terraces (Fig. 5.8 c).

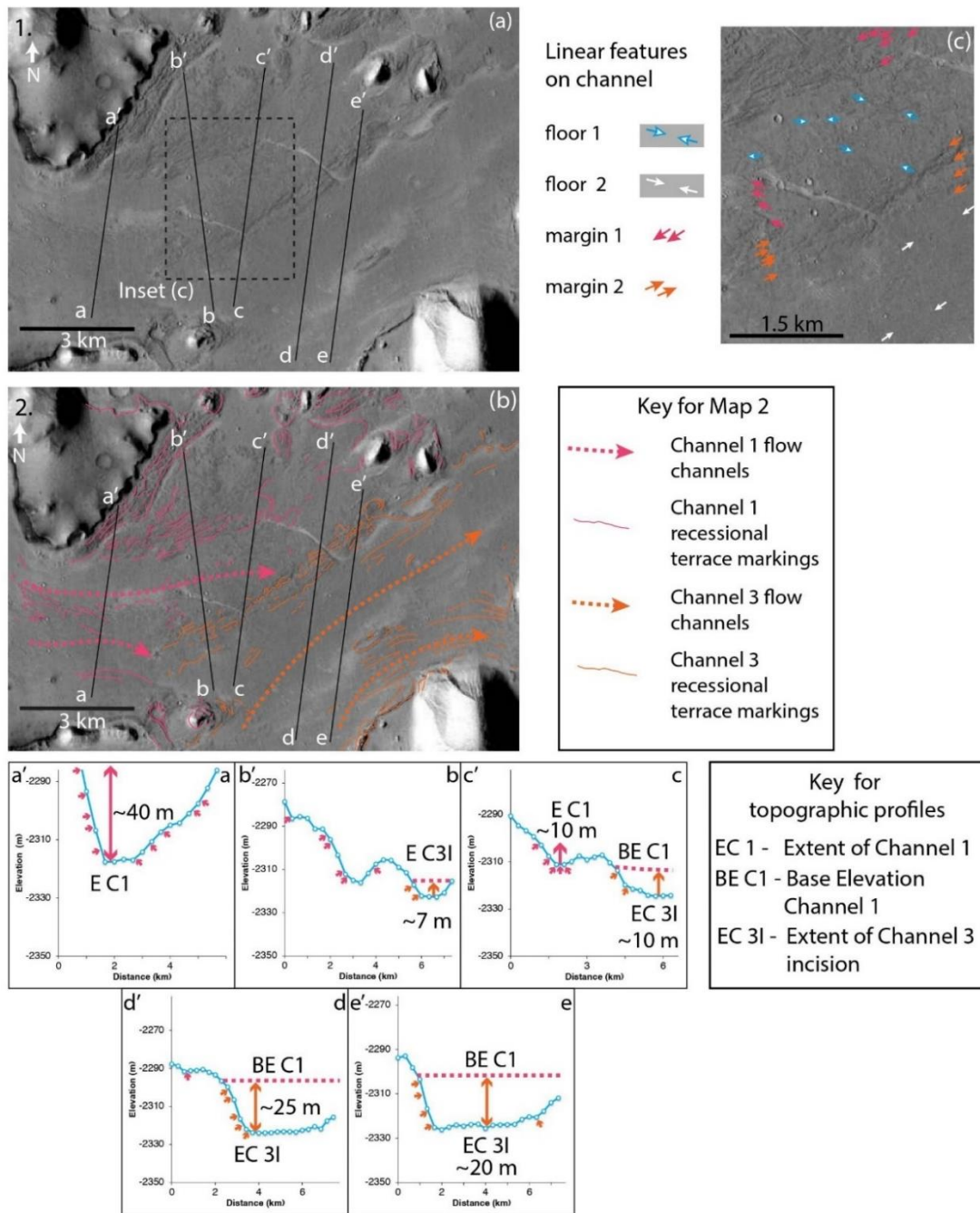


Figure 5.8. Maps and topographic profiles of Location 4 centred at 15.60° N, 162.75° E showing details of channels and cross-cutting relationships (see Figure 5.2 for location). (a) Map 1—CTX mosaic with MOLA transects. (b) Map 2—CTX with MOLA transects (black lines a'-a through e'-e) and illustrated channel markings/flow directions/ recessional terrace markings. (c) Inset located in (a) from CTX data showing channel floor details and margin details. Longitudinal lineations and recessional terraces exist (see caption in Figure 5.4). No features, such as lobate flow fronts or rootless cones indicating lava flows, were identified. (d) Topographic profiles a'-a through e'-e for each of the five transects, with the blue line in each profile representing the MOLA transects. The vertical exaggeration for each topographic profile is x80. Overall, the interpretation of Location 4 is that a Flow 3 channel cross-cuts and incises into a channel from Flow 1. The age of the Flow 1 channel is interpreted from the observation that it can be mapped back to its source (see Figures 5.2 and 5.5). The Flow 3 channel indicates flow towards the NE. As seen from topographic profiles c'-c, d'-d and e'-e, the base of the Flow 3 channel is at approximately -2325 metres elevation at its deepest. This location appears to cross-cut a Flow 1 channel, possibly a remnant channel of Flow 1 that Flow 2 channels have not covered. The fissures are younger geological features, with recessional terrace markings from the flows disrupted by them.

MOLA data from an analysis of the topographic profiles of transects a'–a, b'–b, and c'–c suggests Flow 1 may have carved the channel, with the flow W to NE and with a basal elevation of approximately -2310 to -2320 m (Fig. 5.8 a and b, and topographic profiles a'–a, b'–b, and c'–c). This may be a remnant channel not covered by the later Flow 2. The basal elevation of this channel (-2310 to -2320 m) would indicate that it is a downstream continuation of Flow 1 from Location 3 (around -2290 m) and not a continuation of those for Flow 2, which are of a lower elevation (around -2345 m) (see Figure 5.16 for a compilation of elevations).

The flow that cross-cuts Flow 1 cannot be mapped back to the Flow 2 source, and this is interpreted as a third flow, Flow 3, which can be mapped back to its source (Fig 5.2 and Fig 5.5 e and f). As with the source locations for Flow 1 and Flow 2, the source location for Flow 3 is located along the northernmost Cerberus Fossae. Faulting postdates the flow because the walls and edges of the fissure appear uneroded by the flow. The source of Flow 3 is partially surrounded by enclosing cliffs on the eastern side. MOLA measurements reveal that Flow 3 incised downwards into the earlier Flow 1 channel by between 7 m and 25 m, with incision depth increasing as the Flow 3 channel moves further to the NE.

5.4.5. Location 5 (Fig. 5.9)

Location 5, centred at 15.13° N, 163.21° E, shows an area with three possible flow channels, two exhibiting cross-cutting relationships (Fig. 5.9 a and b). A fourth flow, Flow 4, is identified here and can be located back to its source. As with the previous locations, the channels within Location 5 exhibit longitudinal lineations and recessional terraces (Fig. 5.9 c).

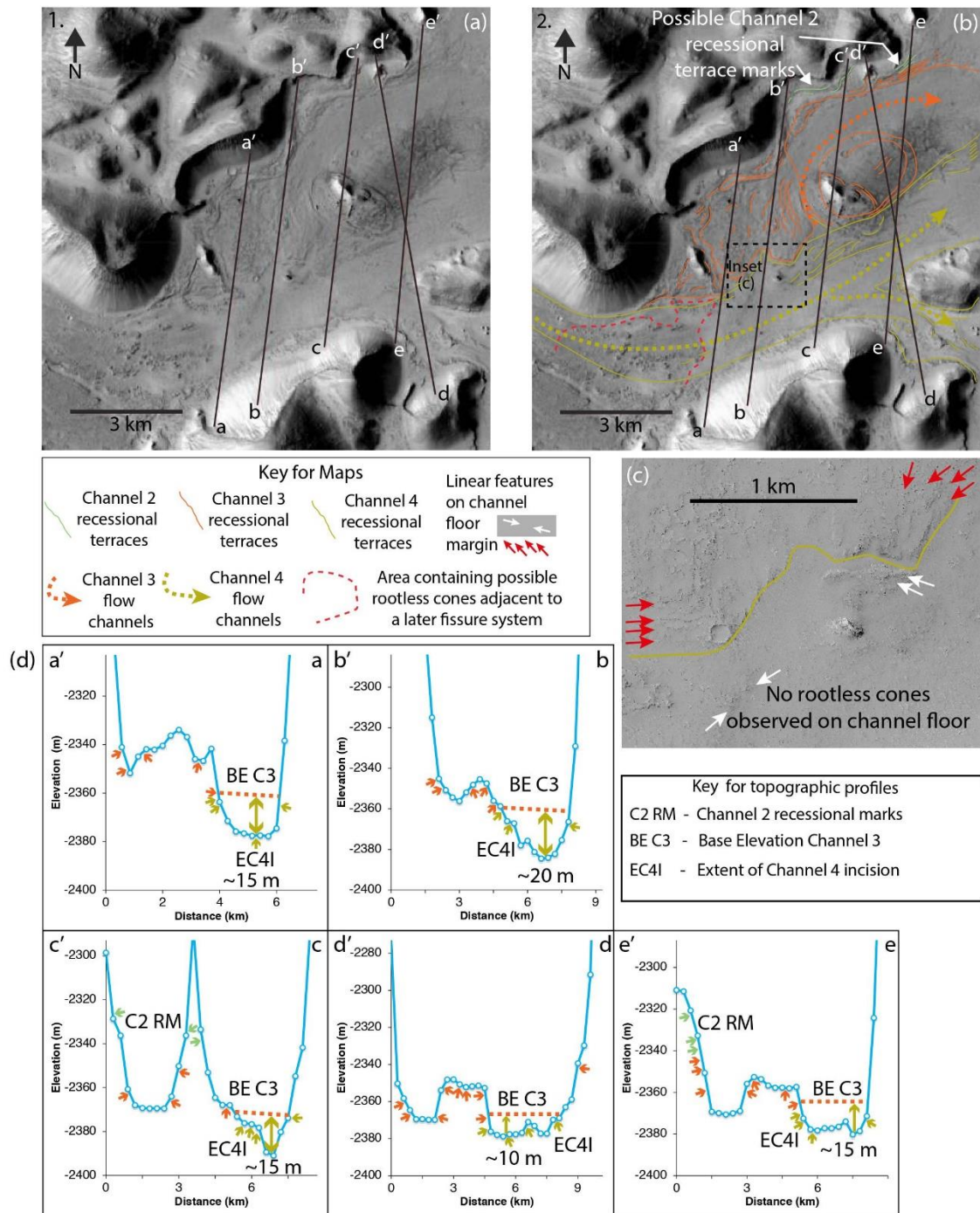


Figure 5.9. Maps and topographic profiles of Location 5 centred at 15.13° N, 163.21° E showing details of channels and cross-cutting relationships (see Figure 5.2 for location). (a) Map 1—CTX mosaic with MOLA transects. (b) Map 2—CTX with MOLA transects (black lines a'–a through e'–e) and interpreted channel markings/flow directions/ recessional terrace markings. An area containing possible rootless cones is adjacent to a later fissure system. The cones are possibly related to volcanism associated with the fissures that post-date channel formation. (c) The inset shows details of the channel floor from the HiRISE image ESP_025789_1950. No rootless cones are seen over most of the channel, for example, as shown herein. (d) Topographic profiles a'–a through e'–e for each of the five transects, with the blue line in each profile representing the MOLA transects. Location 5 maps and topographic profiles show an area of possibly three flow channels. The vertical exaggeration for each topographic profile is x80. The overall interpretation of Location 5 is that a channel from Flow 4 cross-cuts and incises into older channels.

Flow features from the older Flow 2 are seen in the imagery. MOLA transects at relatively high elevations c'–c and e'–e allowed me to construct topographic profiles (Fig. 5.9 a and b, and topographic profiles c'–c and e'–e) that show recessional terraces at elevations of -2325 m and -2340 m located high on the escarpment running SW-NE across the image (Fig 5.9 b, indicated by white arrows). A later flow incised downwards, with the incision cutting a channel down to -2370 m (Fig. 5.9, transects d'–d and e'–e). This is possibly a remnant of the Flow 3 channel, untouched by the later Flow 4. The later Flow 4 incises more deeply, with its channel base at a depth of approximately -2379 metres (transect a'–a), to a maximum of -2390 metres (transect c'–c). Recessional terrace markings indicate the incision depth for Flow 4 was approximately 20 m deep (Fig. 5.9 transect b'–b).

Flow 4 channels can be mapped back to the source, approximately 15 km to the NW (Fig. 5.2 and Fig. 5.5 g and h). The source is a depression along the trace of the northernmost Cerberus Fossae, partially enclosed and defined by surrounding cliffs. The fissures postdate the flow because the sidewalls and edges of the fissure cross-cut the enclosing cliffs, indicating that the faulting is later than the flow.

Of all the locations studied, this was the only one where possible RMLs were observed (Fig. 5.9 a, b and c). However, these are adjacent to a later fissure and are not present across the vast part of the channel floor. If these are RMLs, they are related to a possible small lava flow connected to a later fissure system. They do not indicate lava forming the Flow 4 channel because of their associated lava postdates channel formation.

5.4.6. Location 6 (Fig. 5.10)

Location 6, centred at 15.60° N, 163.30° E, focuses on a small, rounded, hummocky location just north of the main W to E fissure that cuts across the central regional map (Fig. 5.2). It is approximately 20 km NNE from the source of Flow 4 and approximately 40 km NE of the source of Flood 4 (Fig. 5.2).

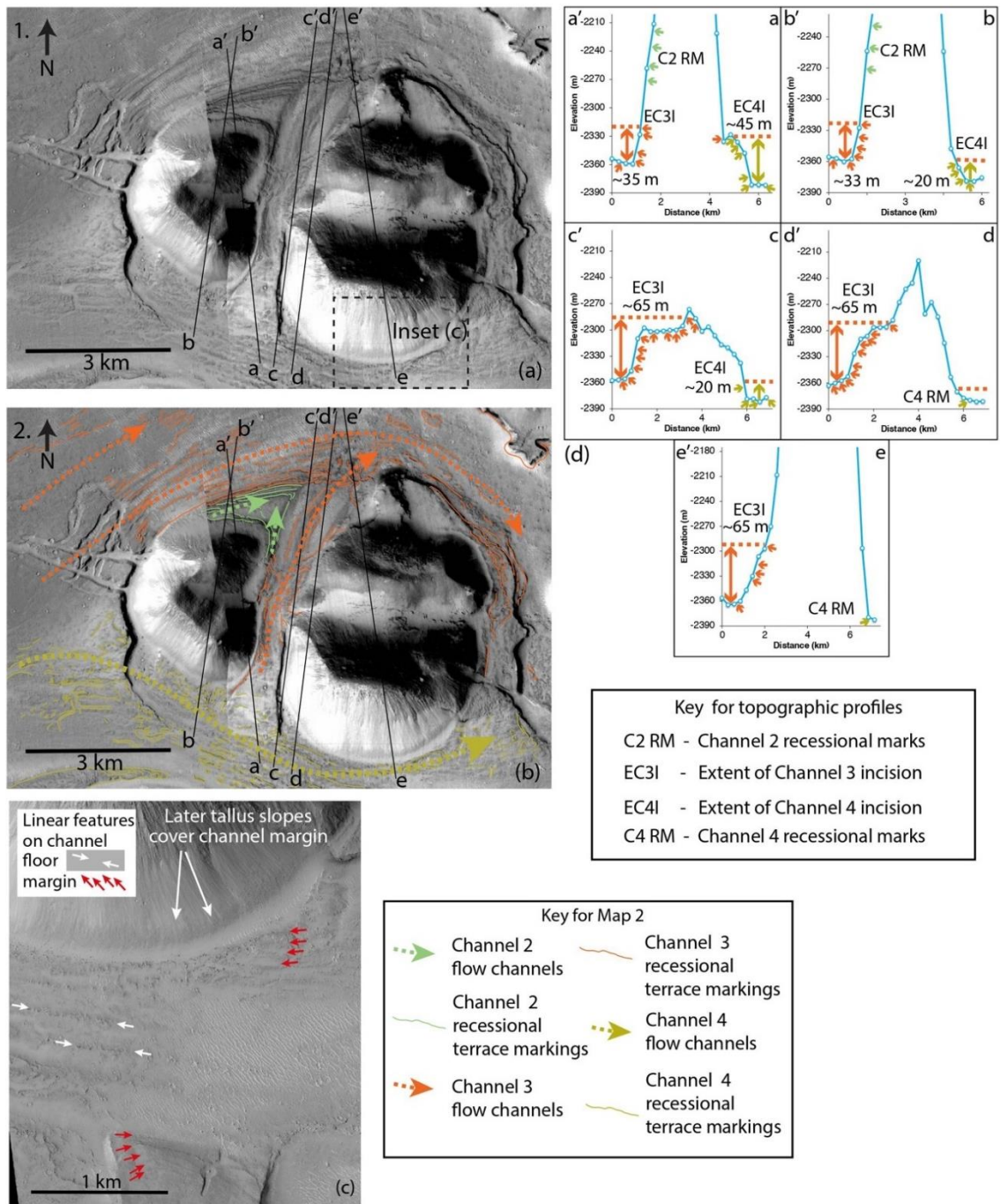


Figure 5.10. Maps and topographic profiles of Location 6 centred at 15.60° N, 163.30° E showing details of channels and cross-cutting relationships (see Figure 5.2 for location). (a) Map 1—CTX mosaic with MOLA transects. (b) Map 2—CTX with MOLA transects (black lines a'–a through e'–e) and illustrated channel markings/flow directions/ recessional terrace markings. Fissure extension took place after the flow episodes. The new fissure formations ran parallel with the major fissure running through this region, approximately 16 km southwest of the newly formed fissure. (c) Inset from HiRISE image ESP_028756_1960 showing details of a channel floor and margins. We interpret the presence of longitudinal lineations and recessional terraces (see caption to Figure 5.4). Features such as lobate flow fronts or rootless cones indicating lava flows were not identified. (d) Topographic profiles a'–a through e'–e for each of the five transects, with the blue line in each profile representing the MOLA transects. The vertical exaggeration for each topographic profile is x35. The overall interpretation of Location 6 is that Flow 4 channels cross-cut earlier Flow 3 channels. Remnant recessional terraces also exist from a possible Flow 2 channel.

The key interpretation of this location is the cross-cutting relationship between a Flow 4 channel and earlier Flow 3 channels. Observations of imagery also suggest the existence of remnant recessional terraces from a Flow 2 channel. All flow channels in this location exhibit longitudinal lineations and recessional terraces (Fig. 5.10 c).

Flow 3 channels appear to have flowed around, through and south of the two areas of higher ground central in the image (Fig. 5.10 a and b).

MOLA transects a'–a and b'–b show the base of the Flow 3 channel was approximately -2360 metres, and recessional terrace marks are visible up to about

-2320 metres, meaning that the vertical extent of this Flow 3 channel was approximately 33 m to 35 m at these locations. MOLA transects c'–c, d'–d, and e'–e are more challenging to interpret because they pass through an area that divides the two areas of high ground. Recessional terrace marks are observed, indicating that a channel from Flow 3 flowed in a south-to-north direction up between the two areas of high ground. Interpretation of MOLA transects c'–c, d'–d, and e'–e, together with a basal elevation of -2355 metres for Flow 3, suggests the maximum elevation of

Flow 3 was approximately -2290 metres. Therefore, the vertical extent of this Flow 3 channel was approximately 65 metres.

A later flow incised across the channel from Flow 3 (Figure 5.10 a and b), and this flow can be mapped back to a source (Fig. 5.2 and Fig. 5.5 g and h), identifying it as Flow 4. A Flow 4 channel runs west to east across the bottom of Figure 10 a and b, with a basal elevation of approximately -2380 metres. The channel incises below the base of Flow 3 by up to 45 m. Recessional terrace marks for the Flow 4 channel were identified on the imagery and upon the study of MOLA transects, with the depth of Flow 4 channels ranging from approximately 40 m (MOLA transect a'–a); approximately 20 m (MOLA transects b'–b and c'–c); to only being able to identify the recessional terrace marks, but not enough of them to measure incision, of Flow 4 (MOLA transects d'–d and e'–e). A possible remnant area of a Flow 2 channel was identified, with the elevation of the identified terrace marks correlated with Flow 2 features in the previous locations, with the lowest identified recessional channel for this Flow 2 channel area being about -2270 metres and the highest being about -2220 metres. The vertical extent of the flow from this Flow 2 was more than 50 metres.

Fissures cross-cut the recessional terrace markings of the flow channels, with fissure formation and orientation running parallel to the major fissure within the study region that runs 16 km to the SW of the fissure in this location. The cross-cutting of the fissures indicates that the formation of the fissures postdates the flow episodes.

5.4.7. Location 7 (Fig. 5.11)

Location 7, centred at 15.46° N, 163.28° E, includes the area of Location 6 and an area to the south of that location. The study area focuses on the relationship between the two principle flows, Flow 3 and Flow 4.

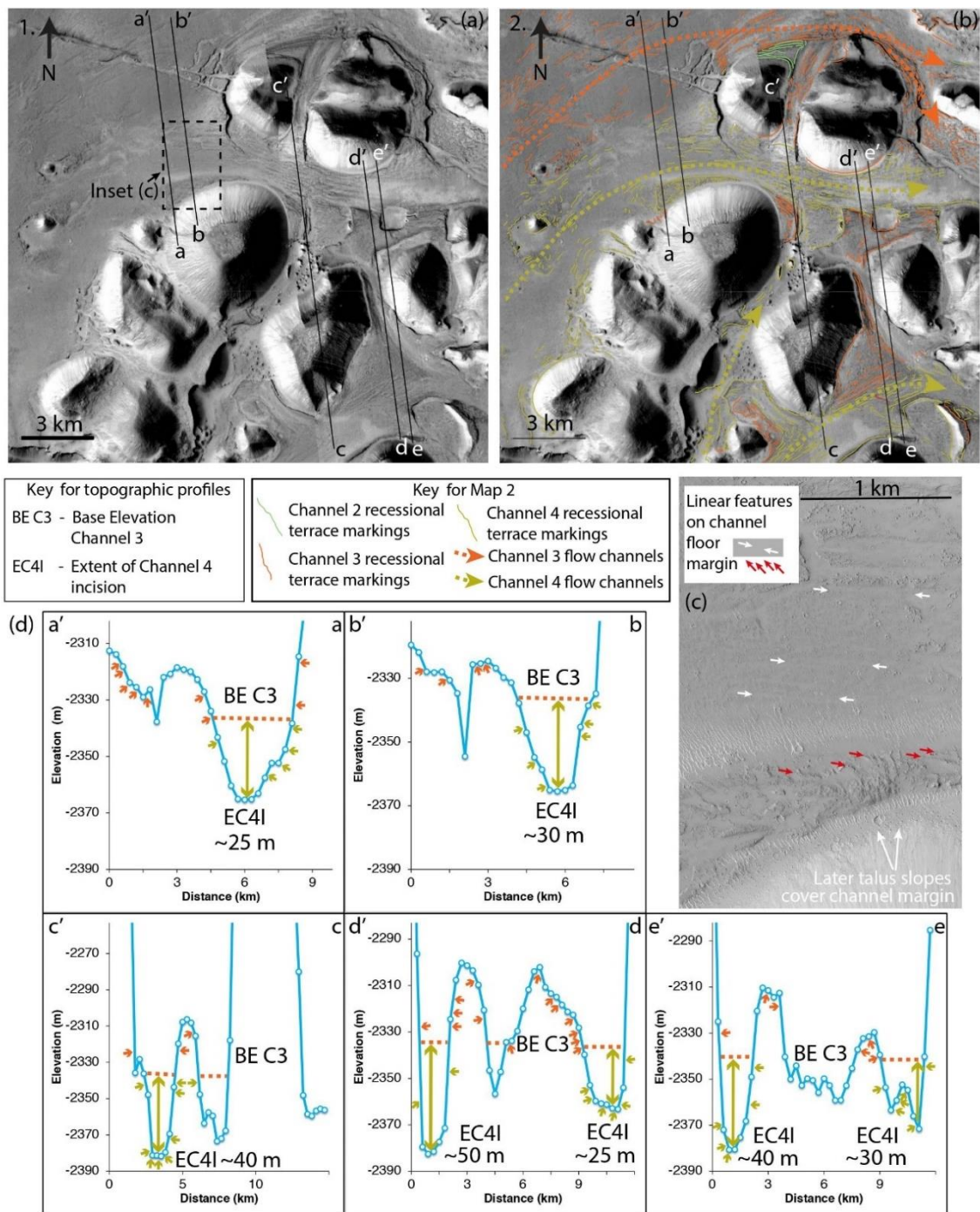


Figure 5.11. Maps and topographic profiles of Location 7 centred at 15.46° N, 163.28° E showing details of channels and cross-cutting relationships (see Figure 5.2 for location). (a) Map 1—CTX mosaic with MOLA transects. (b) Map 2—CTX with MOLA transects (black lines a'–a through e'–e) and illustrated channel markings/flow directions/ recessional terrace markings. (c) Inset from HiRISE image ESP_028400_1955 showing details of a channel floor and margins. Longitudinal lineations and recessional terraces exist (see caption in Figure 5.4). Features such as lobate flow fronts or rootless cones indicating lava flows were not identified. (d) Topographic profiles a'–a through e'–e for each of the five transects, with the blue line in each profile representing the MOLA transects. The vertical exaggeration for each topographic profile is x10. The overall interpretation of Location 7 is that channels from Flow 4 flowed to the east, cross-cutting earlier flow channels formed by Flow 3 channels.

The area comprises eleven large hummocks and several smaller, lower-elevation mounds, with a discernible that runs NE then E through the centre of the location map (Fig. 5.11 a and b). Within the hummocks in the south of the image are smaller channels, with one more significant channel with a NE orientation. The channels are characterised by recessional terraces and longitudinal lineations (Fig. 5.11 c).

Location 7 lies 15 km northeast of the estimated source area of Flow 4, with the primary Flow 4 channel's orientation being N then NE (Figure 5.11 a and b), cross-cutting earlier channels formed by Flow 3. The basal elevation of the main Flow 4 channels deepens as the channel moves eastward, with MOLA data revealing a base elevation for transects a'–a and b'–b to be approximately -2365 m, deepening to approximately -2380 m for transects c'–c, d'–d, and e'–e. Flow 4 recessional terrace marks indicate that the upper limit of Flow 4 was -2340 m to -2330 m. This means that the vertical extent of Flow 4 ranged from 25 metres in topographic profiles a'–a and b'–b to approximately 50 metres and 25 metres in topographic profiles c'–c, d'–d, and e'–e. Recessional terrace markings for an earlier flow exist and are from Flow 3, based upon MOLA data that define the base of interpreted Flow 3 channels at similar elevations in different locations, such as -2325 m in Location 4, Fig. 5.8 and -2335 m in Location 7, Fig. 5.11. The elevation of the sources for Flow 3 and Flow 4 indicates that the Flow 3 source is -2325 m, and the Flow 4 source is -2344 m (Figure 5.16). Based on this data, geomorphic features and recessional terrace markings above -2330 m are most likely a result of Flow 3. Geomorphic features and recessional terrace markings below -2344 m were most likely formed by Flow 4. The measurements are consistent with the measured Flow 4 incision depth of just over -2380 m, the basal elevation for Flow 4 in this location.

Within the location are four remnant Flow 3 areas. However, these areas do not exhibit clear evidence of cross-cutting relationships with Flow 4 channels. Determining a base elevation measurement for Flow 3 using available MOLA data proved challenging due to insufficient MOLA coverage of areas that could exhibit cross-cutting relationships.

MOLA data from Location 6 (Fig. 5.10), the northern section of the area within Location 7 (Fig. 5.11 a and b), reveals a base elevation of -2365 metres for Flow 3. However, that measurement is for the northern channel of Flow 3. It is, therefore, quite different from the Flow 3 channel to the south of the split-hill/hummock formation in the north of Location 7 maps 1 and 2 (Fig. 5.11 a and b). Regardless, the measurement is a valuable proxy. It suggests that the Flow 4 channel measured here is Flow 4, not Flow 3. However, due to a lack of coverage by MOLA data in this region, the vertical extent of Flow 4 may be overestimated.

5.4.8. Outlying Supplementary Locations A through D (Fig 5. SL A through Fig 5. SL D)

Four flows were identified in outlying locations exhibiting geomorphic landforms in downstream locations (Fig 5.2 and Figs 5. SL A, 5. SL B, 5. SL C, and 5. SL D). They provided evidence of the lateral extent of the geomorphic landforms produced by the flows in downstream locations. Defining cross-cutting relationships with distance from the flow sources is challenging because the incision generally decreases downstream, and channel courses run almost parallel to each other in a west-to-east direction. Accordingly, it was necessary to focus on locations that did not necessarily exhibit clear cross-cutting relationships but instead offered evidence through geological observation and analyses of MOLA data to possible positions of boundary lines between the different flow episodes. The observations and analyses of these four locations allowed me to construct Figure 2 and discern possible boundaries between flow episodes.

5.4.8.1. Supplementary Location A (Fig 5.12 SLA)

Supplementary Location A (centred at 16.15° N, 162.90° E) and topographic profiles (Fig. 5.12 SLA) show the possible flow boundary between the earlier Flow 1 channels and the younger Flow 2 channels. The position of observed recessional terrace marks and to what flow they belong are marked on the topographic profiles as arrows in colours corresponding to the flow colour.

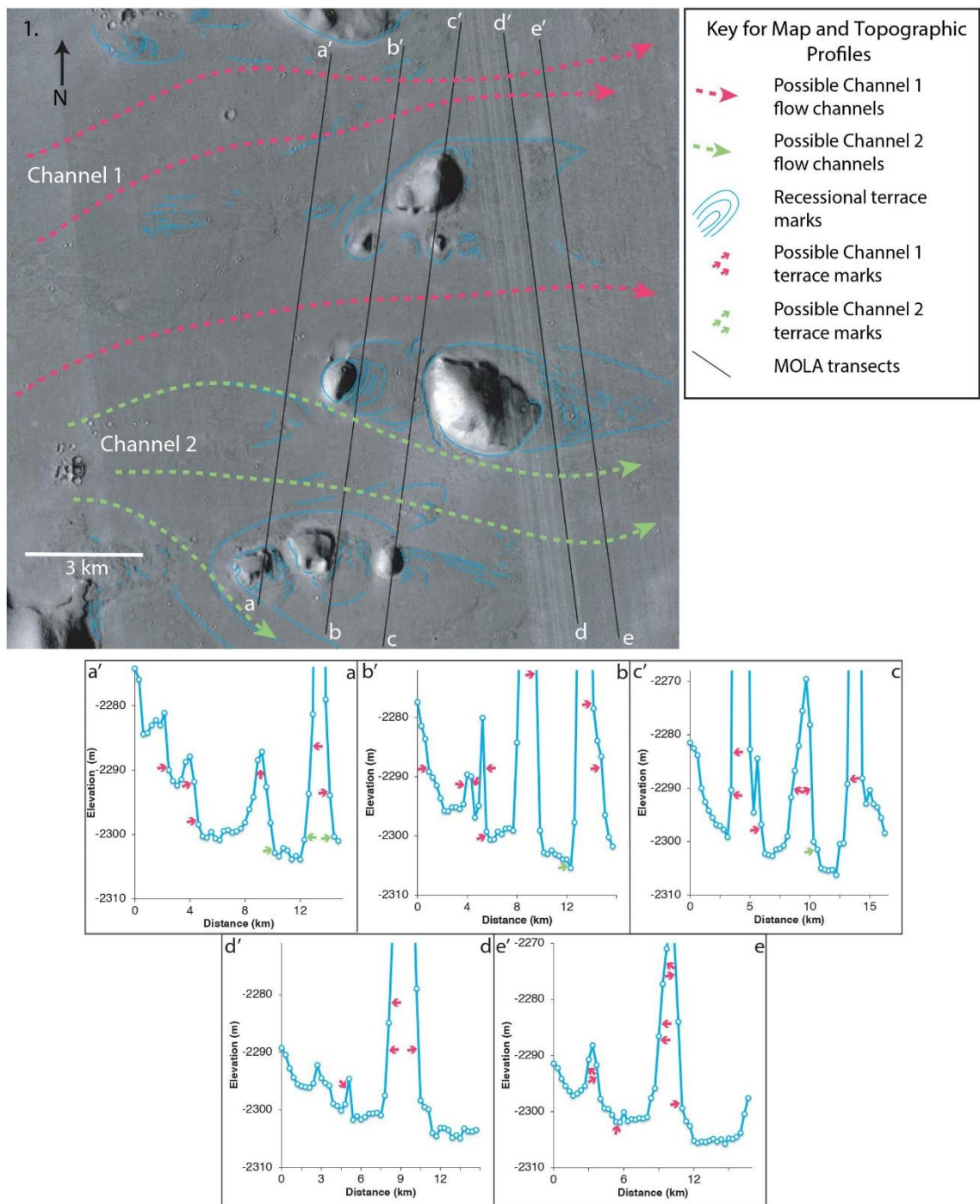


Figure 5.12. SL A:Supplementary Location A (centred at 16.15° N, 162.90° E) and topographic profiles.

5.4.8.2. Supplementary Location B (Fig. 5.13 SL B)

Supplementary Location B (centred at 16.13° N, 163.37° E) and topographic profiles (Fig. 5.13 SLB) show the possible flow boundary between the earlier Flow 1 channels and the younger Flow 2 channels. A boundary between the two flows appears to be delineated by the area of higher ground. This area of higher ground/hummocks may

have served as a natural boundary between Flow 1 and Flow 2 channels. The position of observed recessional terrace marks and to what flow they belong are marked on the topographic profiles as arrows in colours corresponding to the flow colour.

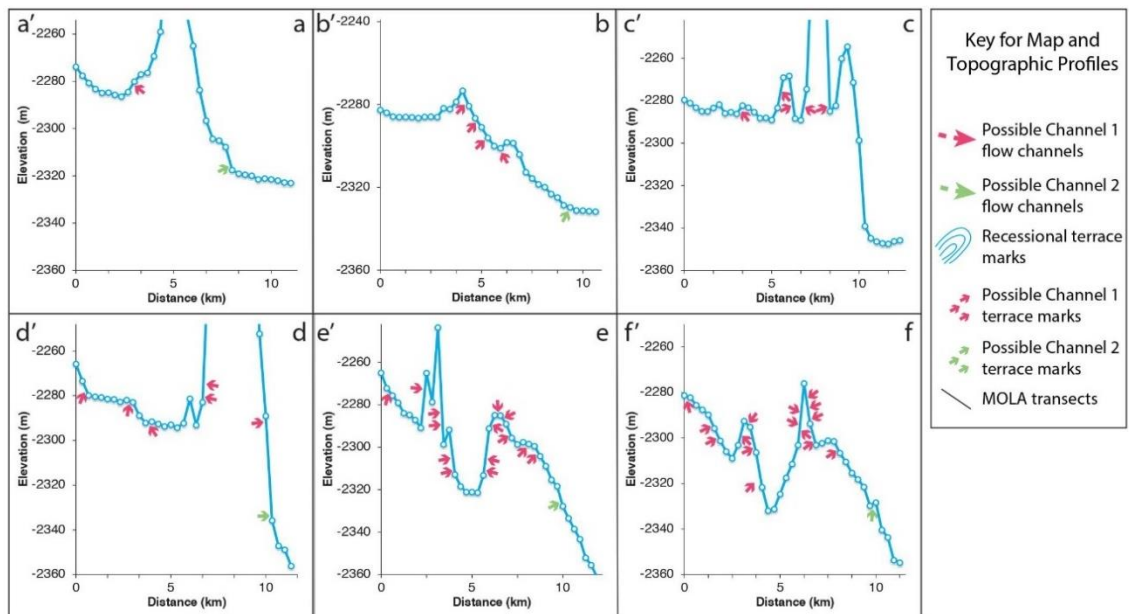
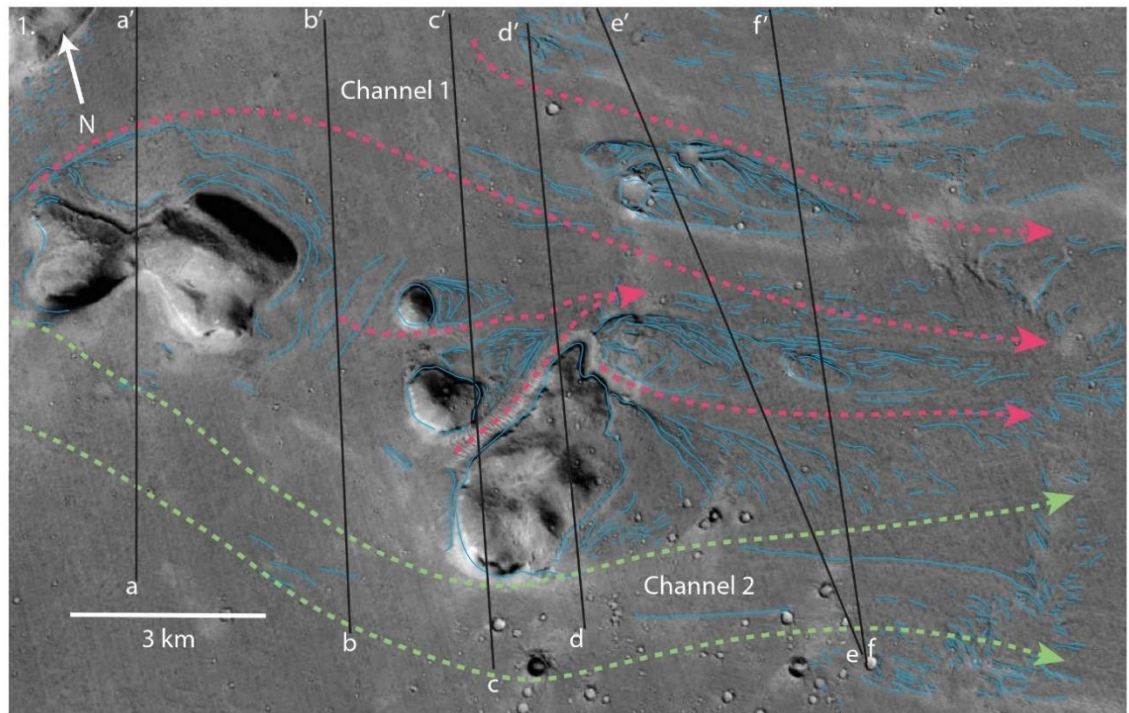


Figure 5.13. Supplementary Location A (centred at 16.15° N, 162.90° E) and topographic profiles.

5.4.8.3. Supplementary Location C (Fig 5.14 SL C)

Supplementary Location C (centred at 15.83° N, 163.36° E) and topographic profiles (Fig. 5.14SL C) show the boundary between Flow 2 and 3. As the geomorphic features within Supplementary Location 3 show, the orientation of the features shaped by Flow 2 suggests that flow movement was from the northwest and flowed southeast before reaching a depression, after which the course of the flow is in an east-by-south direction. The orientation of the features shaped by Flow 3 suggests that flow movement moved from the southwest and flowed in a direction towards the northeast/east.

This location also reveals the position of Flood 2 flow channels to the west, showing that Flow 2 channels flowed in an easterly direction. The flow pattern for Flow 3 channels in Supplementary Location 2 above ties in with the flow boundaries for Flows 2 and 3 in the Location 4 (Fig. 5.4) maps and topographic profiles. The position of observed recessional terrace marks and to what flow they belong are marked on the topographic profiles as arrows in colours corresponding to the flow colour. Fissure formations that run parallel with the significant fissure formation 34 km south are young, certainly younger than the flow episodes, clearly displacing Flow 3 flow lines and, therefore, postdate the flow episodes.

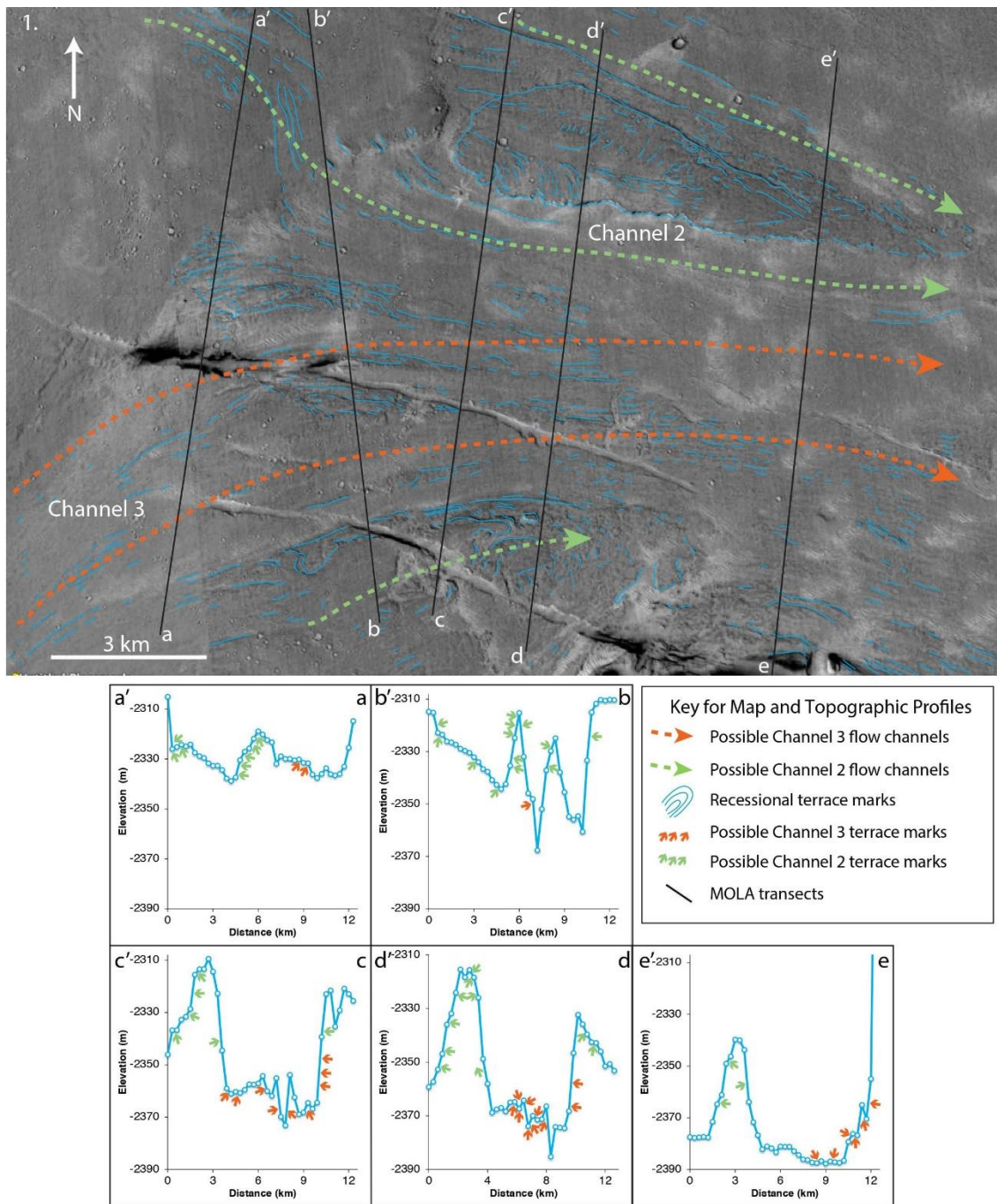


Figure 5.14. SL C: Supplementary Location A (centred at 16.15° N, 162.90° E) and topographic profiles.

5.4.8.4. Supplementary Location D (Fig 5.15 SL D)

Supplementary Location D (centred at 15.00° N, 164.35° E) and topographic profiles (Fig 5.15 SL D) show the boundaries between Flow 4 and Flow 5. The estimated emanation point for Flow 5 is marked on the lower section of Map 1 as the number 5 in a yellow hexagon. The source location is based upon MOLA data visible in topographic

profiles a'–a through f'–f. Profile a'–a clearly shows the unidirectional flow from west to east at an elevation that is in keeping with Flow 4 elevations further west, considering the sloping west-to-east topography. Profile b'–b follows a similar pattern until reaching an area close to the main fissure formation, where the elevation decreases, and visible flow lines / recessional terrace marks are observed. The orientation of the streamlined bodies in this area strongly suggests a flow channel emanated from this area and flowed northeast. The fissure that runs southeast along the bottom of the image is younger than the flow channels and has offset the recessional terrace markings of Flow 5 close to the source of Flow 5. The position of observed recessional terrace marks and to what flow they belong are marked on the topographic profiles as arrows in colours corresponding to the flow colour (Figure 5 SLD, topographic profiles a'–a through f'–f).

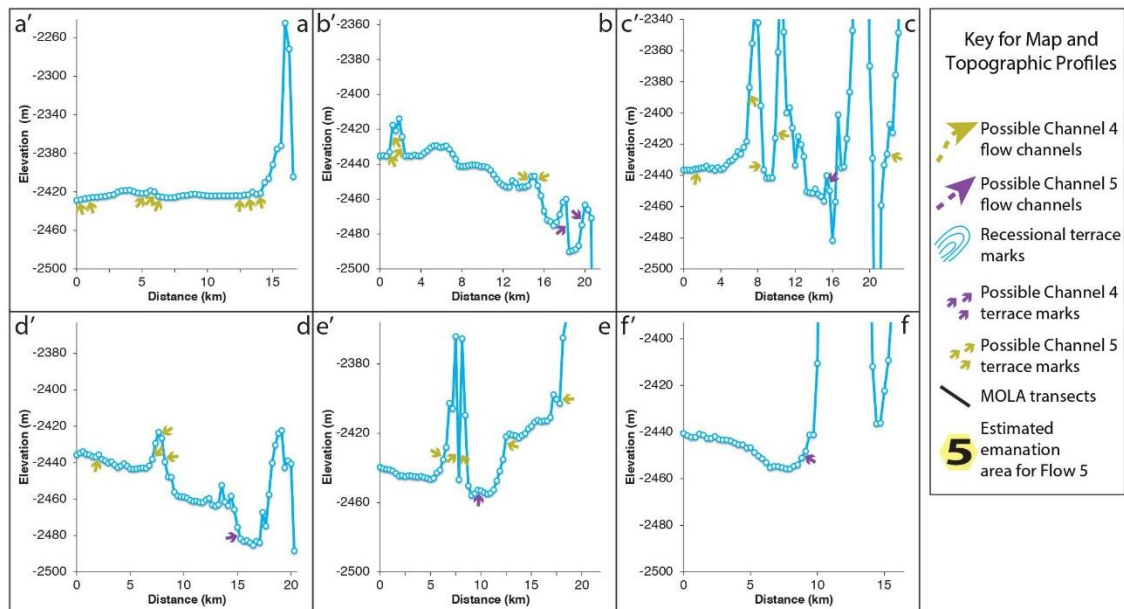
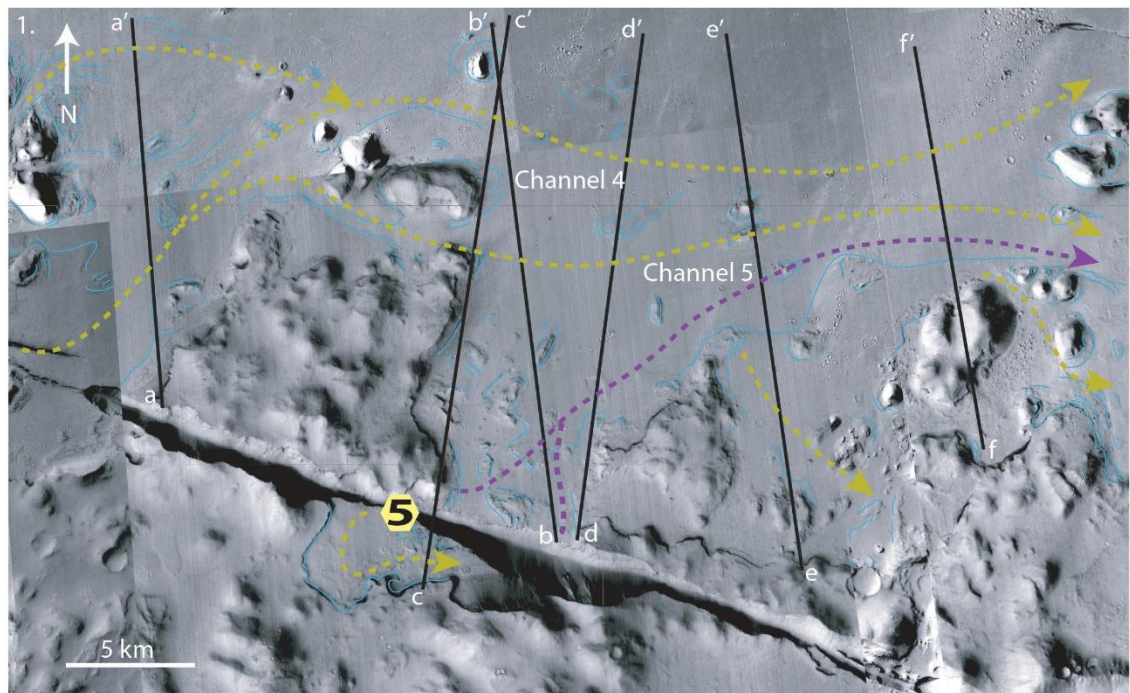
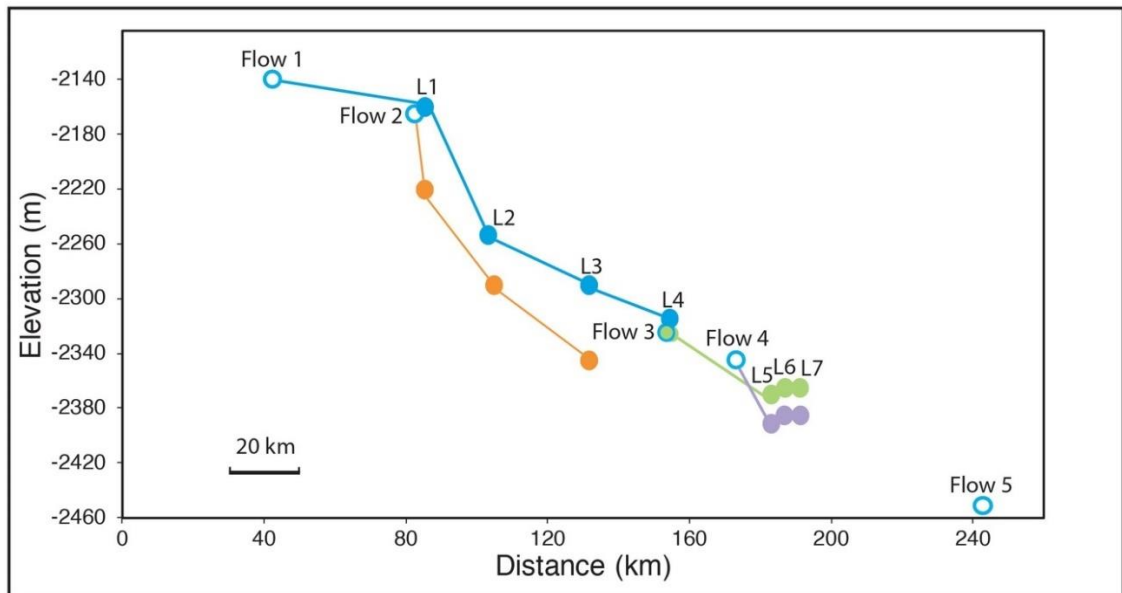


Figure 5.15. SL D: Supplementary Location A (centred at 16.15° N, 162.90° E) and topographic profiles.

5.4.9. Construction of the regional map and channel profiles

The regional map (Fig. 5.2), centred at 15.25° N, 162.85° E, and overall channel profiles (Figure 5.16) were constructed after drawing together data from the seven main study locations and the four outlying supplementary locations to understand the flow geometries across the region.



- Channel 1 base elevation
- Channel 2 base elevation
- Channel 3 base elevation
- Channel 4 base elevation
- Estimated location of each flow (1 through 5) at source
- L1 through L7 - Channel base elevations at each location

Figure 5.16. Shows the base elevations of identified flow channels in Locations 1 through 7, marked on the topographic profiles as L1, L2, L3, etc. The lowest elevation for each channel was used for each location, and the estimated elevation at the source for each flow episode (Flows 1 through 5). The last three points in Flow 3 are very close together (within ~10-20 km) and within <10 m of each other vertically, and the same is true for the last three points in Flow 4; this is less than the uncertainty on vertical measurements from MOLA (± 10 m). In this thesis, it is considered that these data points are essentially at the same elevation within error, and the likely slight downward slope cannot be measured but cannot be excluded within error. The vertical exaggeration for the topographic profile is x80.

The regional map (Figure 5.2) covers an area of the northernmost Cerberus Fossae (an approximately 200 km long set of *en echelon* fissure segments that run NW to SE), part of the unnamed northern channel system to the NE of the image, and a scoured area to the SE of the northernmost Cerberus Fossae. Five discrete flow episodes were identified within the regional map (Fig. 5.2), with evidence from the observed geomorphic features that the formation of the fissures and fractures associated with the northernmost Cerberus Fossae postdate the flow episodes.

The first (oldest) of the five flow channels studied, Flow 1's source, lies far west of the northernmost Cerberus Fossae at an approximate elevation of -2139 m. Flow 1 appears to have been the largest in terms of the area of the flow plain. The second flow, Flow 2, with its source further east along the northernmost Cerberus Fossae at an

elevation of -2165 m, occurred at an unknown time after Flow 1. Examples of cross-cutting between Flow 1 and Flow 2 channels are the clearest, with geomorphic observations and MOLA data from Locations 1, 2, and 3 (Figs. 5.4, 5.6, and 5.7) showing unequivocal evidence that two separate and distinct flow episodes occurred. Further east along the northernmost Cerberus Fossae is the source of Flow 3, at an elevation of approximately -2325 m, followed by the source of Flow 4, at an approximate elevation of -2345 m. Locations 4, 5, 6 and 7 (Figs. 5.8, 5.9, 5.10, and 5.11) focus on the area predominantly covered by Flow 3. Location 4 identifies the relationship between Flow 1 and Flow 3, while Locations 5, 6 and 7 focus on the relationship between Flow 3 and 4. The source of Flow 5, at an elevation of approximately -2451 m, is located further to the east along the northernmost Cerberus Fossae and is the last flow source identified. A study of this source location reveals that the Flow 5 (Fig. 5. SL D) channel rises by approximately 8 m before plateauing and then flowing downslope in an easterly direction. However, despite much analysis, the work for this thesis did not find an unambiguous cross-cutting relationship with Flow 4. However, based on the geomorphic indicators, there is a high degree of certainty that this is the source location of a separate, later flow, Flow 5 and that the source is geographically separate from that of other flows.

Figure 5.16 shows the locations of each flow (1 through 5) at the source. The figure shows the connection to the basal elevation of each flow (1 through 4 at each location (Location 1 through Location 7) to the location of each flow source. The five flow sources (Flow 1 through 5) appear progressively further east, with the elevation of each source lowering from west to east. Figure 5.16 shows that the flow channels running from each source all flow downhill from W to E. Where cross-cutting channels were identified in each location, the flow channels are at a lower elevation and incise downwards into the older predecessor channels.

The results would indicate that the study area (Fig. 5.2) was affected by a sequence of discrete, asynchronous flow events from source locations along the northernmost Cerberus Fossae, with each flow event located further eastward than the last and each source at progressively lower elevations. Each of the five events created flow channels that flowed downhill in a general easterly direction (Fig. 5.16).

5.5. Discussion

Before the study of this area was undertaken, discussions of this region of Grjótá Valles were primarily on the following points:

- (a) The channels and channel systems emanating from this section's fissures, fractures and faults of the northernmost Cerberus Fossae.
- (b) The possibility that multiple channels exist was very much an open question (Burr and McEwen, 2002; Burr et al., 2002; Burr et al., 2006).
- (c) The ongoing debate regarding the processes that formed the channels (Burr et al., 2002; Leverington, 2004, 2012, Jaeger et al., 2010).
- (d) Un-eroded fracture and fissure walls and edges, bi-flow directions at some sources, and fissures and fractures cross-cutting channels suggest faulting postdates channel formation (Vetterlein and Roberts, 2009).
- (e) Observations of mobilised boulder populations have been suggested to be evidence of paleoseismic marsquakes (Brown and Roberts, 2019).
- (f) InSIGHT seismometers had recorded seismicity associated with normal faulting in this region (Burr et al., 2002; Burr and Parker, 2006; Jaeger et al., 2007, 2010, Leverington 2011; Brown and Roberts, 2019; Voight and Hamilton, 2018; Giardini et al., 2020; Golder et al., 2020).

Work by Rivas-Dorado et al. (2022) identified the connection that exists between dikes and seismicity in the Cerberus Fossae and how the history of multiple intrusive phases and faulting activity fits with a chronology of tectonic and volcanic events in the Cerberus Fossae. Using the morphological evidence shown in this chapter would suggest a link between seismicity, volcanic activity, and fluvial activity is something that exists and needs to be investigated further, something that Keske et al. (2015) also noted in the team's study of outflow channels in Mangala Valles, explaining that there exists a "close interplay of fluvial and volcanic activity", which would suggest "...that fluvial activity not only played a major role during a period of volcanism, but also may be linked to, or even triggered by volcanic processes". But how does dike propagation connect with fluvial activity? Ernst et al. (2002) identified the fossae as giant fractures resulting from giant dike swarms at depth radiating from Elysium Mons. Hall et al. (1986) suggested a flexural loading model to demonstrate that the formation of the fossae may be due to the global stress field caused by the Tharsis rise. It is believed that the fossae were created as a result of regional extensional stress, caused either by the formation of graben faults (Vetterlein and Roberts, 2010) or by fracturing processes occurring above growing dike(s) at depth (e.g., Berman and

Hartmann, 2002; Burr et al., 2002; Head et al., 2003; Nahm et al., 2015, 2016; Plescia, 1990). This is a phenomenon that is commonly observed on Earth (e.g., Gudmundsson, 1984; Hjartardóttir et al., 2016; Magee and Jackson, 2021; Rowland et al., 2007; Rubin, 1992; Rubin and Pollard, 1988; Tentler, 2005). Many studies have highlighted the local impact of the combination of dike intrusion and subsurface cryospheric melting on the surface of Mars that resulted in large lava flows and catastrophic floods of meltwater on the planet's surface, which subsequently shaped the areas adjacent to the fossae regions (Burr et al. (2002), Cassanelli and Head (2018), Nahm et al. (2015, 2016), Pendleton (2015), and Plescia (2003)). According to Taylor et al. (2013), the Cerberus Fossae may still be an active tectonic structure, able to release a seismic moment of between 10^{15} and 10^{17} $\text{Nm}\cdot\text{yr}^{-1}$. They attributed this recent tectonic activity (less than 10 million years old) to the presence of young lava flows (Vaucher et al., 2009), indicative of recent volcanic activity, potentially from subsurface dikes. Horvath et al. (2021) identified a possible pyroclastic deposit in Elysium Planitia (centred at 7.9° N, 165.8° E), which bears similarity to pyroclastic deposits documented on the Moon and Mercury that is dated to less than 250,000 years old, supporting the hypothesis of ongoing geological activity in the region. Since 2018, the InSight mission has confirmed multiple seismic events, with a magnitude of approximately 3.5. in the vicinity of Cerberus Fossae (Giardini et al., 2020). The findings tally with pre-mission estimations by several authors (Böse et al., 2017; Panning et al., 2017; Brown and Roberts, 2019).

Considering the aforementioned evidence, if the eastward progression in the formation of channels in the region results from faulting and/or dike propagation, then this indicates that the distribution of seismicity would have changed over time. Results presented within this chapter provide an understanding of those mentioned above because they expound clear cross-cutting relationships between different flow channels, which can be mapped back to five separate flow sources with the source locations located further east through time. Furthermore, the findings validate that the flows responsible for forming the channels occurred before surface faulting. If igneous processes indeed played a role in initiating the flows that formed the channels, then clearly, such processes took place prior to the appearance of surface faulting. Therefore, this may or may not predate the beginning of present-day seismicity. Such a sequence is not surprising as the concept that the injection of sub-surface dikes leads to the formation of overlying graben has been modelled (Rubin, 1992) and observed (Wright et al., 2006) in terrestrial examples, with these ideas widely applied to graben on Mars. The heat produced by dike injections has been considered a possible method by which sub-surface ice melts, releasing water or melting ice to release trapped water

(McKenzie and Nimmo, 1999; Head et al., 2003). However, the issue has been that the large geographic extent of the channels, for example, associated with Grjótá Valles, has been taken to suggest huge volumes of fluid, and hence flow rates that may be implausibly high (Head et al., 2003; Leverington, 2011).

If the active channel's dimensions are smaller than that implied by a larger channel, then the flow rates may also be proportionately lower. However, a lack of knowledge of the flow duration limits the ability to state a specific flow rate. Furthermore, observations from the InSight seismometers suggest that the seismic velocity below 10 km for Elysium Planitia is too low to be ice-saturated (Manga and Wright, 2021).

Much more work is required to elucidate connections between igneous processes, seismicity, faulting, ice/water within the crust and the formation of flow channels, including the composition of the flows. However, this work suggests that multiple, relatively small flows took place, in contrast to previous estimates of a single, much larger flow. In other words, it is suggested that the total geographic extent of the Grjótá Valles channel system studied in this chapter resulted from at least five discrete and separate flow episodes and not a single flow event. Unfortunately, being able to quantify the flow volume or the flux rate of fluid discharge for each flow episode has not been possible because there is no way of knowing the duration of each flow episode. Likewise, definitively pinpointing a process or set of processes that liberated these flows and caused these flow episodes to occur is not possible. That said, the research has shown that the flow sources are located progressively further to the east through time, so there is a connection between these processes and their propagation eastward through time. One conceivable explanation is that the eastward propagation of fluid release, if caused by melting due to intrusive sub-surface dikes or the eruption of turbulent lava, is due to eastward dike propagation (Fig 5.3). Another explanation is that dike intrusions occurred progressively eastwards and emanated from a sub-surface volcanic source underlying the region (Genova et al., 2016; Golder et al., 2020).

Regarding the absolute timing of the propagation events, if that is the process that occurred, work by Golder et al. (2020) provides crater count ages within the study region that are younger from west to east (53 Ma, then 33 Ma, then 31 Ma). Golder et al. (2020) suggest this change in age is due to changes in the rheological properties of the lavas during emplacement, such as material strength and porosity. This could be the case, but the ages obtained by Golder et al. (2020) are from areas that partially overlap flow deposits (Fig. 5.1b). The 53 Ma age happens to coincide with the proximal

regions for Flow 1 and Flow 2; the 33 Ma age coincides with the area occupied by the distal parts of Flow 3 and Flow 4; the 31 Ma age coincides with an area to the east of the region mapped that is occupied by Flow 5. This means that the ages constrain the ages of channels, the times between channel formation episodes, and the timescale, hence the lateral dike propagation rate. It reveals the episodic nature of the flow episodes and, by extension, that of seismicity brought on by possible dike extension. Effectively, by being able to constrain the ages of the events, one is able to build an absolute chronology for these events. More work is warranted to understand the geological significance of the ages of craters within Grjótá Valles and to explicate the timing of the relationships between aqueous, volcanic, faulting, and seismicity processes. Crater counting and the time frame information this provides may be a key future avenue for research to constrain the rates of formation of the features mapped in Grjótá Valles.

5.6. Conclusion

Detailed analysis and examination of the northernmost Cerberus Fossae and channels within the adjacent area of Grjótá Valles were undertaken using CTX images, HiRISE images and MOLA data. The conclusions are as follows:

1. The floors and margins of channels reveal landforms that appear to have been cut by water and/or turbulent lava (channel floor longitudinal lineations, channel margin recessional terraces), with no indication that these landforms were formed by viscous lava.
2. Cross-cutting relationships and channel incision data show at least five asynchronous flow episodes, each source at a different location along an approximately 200 km long section of the northernmost Cerberus Fossae. This indicates that multiple events formed the channels.
3. Channels flow downhill away from their sources. Younger channels cross-cut older channels, with incisions ranging from 10 m to 70 m.
4. The sources of the flows are located progressively further east through time.
5. As yet, it is still unclear why there is an eastward progression of flow sources. However, some possible explanations include dike propagation from west to east (a) melted near-surface ice, (b) released turbulent lava, and (c) released magma

from an underlying regional melt zone that melted sub-surface ice farther to the east through time.

6. The mechanisms responsible for the release of fluids still need to be clarified. Whatever the process behind the release of fluids into this region is, it does not need to produce the enormous volumes of fluid suggested by other authors if the flow channels have formed in the manner presented here, i.e. asynchronously.

CHAPTER 6.

DISCUSSION

6.1. Introduction

At first sight, it would appear challenging to reconcile the data from Chapter 4 (boulder trails) with data from Chapter 5 (flow channels) and data from InSight's seismometer, SEIS, the Seismic Experiment for Interior Structure, to test that the hypotheses of this thesis—that paleoseismicity and channel-forming episodes in the area of the northernmost Cerberus Fossae and part of the Grjótá Valles channel system are connected. However, the three seemingly contrasting data sets can be combined to build a comprehensive picture of events in the northernmost Cerberus Fossae and part of the Grjótá Valles channel system that tell a story not only of seismicity and flow events but also some age information of seismic events, dike propagation, and displacement rates of faults in this region of Mars and show that paleoseismicity and channel-forming episodes are indeed connected. This chapter proposes a comparison between dike propagation and opening rates with data derived from InSight and the calculated dike propagation rate from crater counting within the channels to cross-reference the datasets.

This chapter will demonstrate the relationship between seismicity and channel source migration. This process will use the following steps: (1) Determine the dike propagation rate by using published crater counts for the channels, enabling (2) the calculation of the fossae opening rate through empirical-based equations of dike length versus opening. With this data, (3) a comparison can be drawn between the calculated opening rate and the rate implied by the InSight seismic data, achieved by calculating the opening rate using the frequency–magnitude distribution calculated by the FISH code. If step (3) proves to be successful, it establishes a connection between seismicity and channel source migration via constraints on dike propagation. This multi-faceted comparison will provide new insights into the geological processes in Grjótá Valles. By aligning the dike propagation and opening rates with the seismicity data obtained from InSight, it will be possible to assess the consistency and correlation between these different indicators of geological activity. This comparison will help validate the methods used to calculate dike propagation rates and provide additional insights into the relationship between tectonic processes and seismic events on Mars. Furthermore, incorporating crater counting within the channels adds a temporal dimension to the analysis. By calculating the dike propagation rate from the crater

counting data, a timeline of geological events can be established and compared with the seismicity records.

To carry out the analysis described above, a review of the research objectives will be presented in this chapter—to evaluate whether there is a connection between seismic activity and the history of channel formation. To achieve these objectives, as described in Chapter 4, it was necessary to investigate seismicity and channel-formation processes to test specific hypotheses. Firstly, to investigate palaeoseismicity in the region of the northernmost Cerberus Fossae to determine if there was any seismic activity in the past, and if so, how long ago. Secondly, the results will be used to better understand the likelihood and nature of ongoing seismic activity. It should be noted that the work was conducted before the results from the InSight mission arrived. Then, as described in Chapter 5, it was necessary to investigate the formation of channels in this region of Mars. Specifically, an attempt was made to determine whether the mapped extensive channel systems were formed by fluvial activity or another mechanism, such as turbulent lava or mudflows. Also, to find out if the flows were episodic or if there was just one mega flow event and to identify the source regions for the flows and what was the cause of these flow events—is it due to dike propagation from west to east and can a time-scale be attributed to this dike propagation? The methodology used for both objectives has been described in Chapters 4 and 5 and published in two papers in *JGR Planets* (Brown and Roberts 2019, 2023). Having information regarding the paleoseismicity and channel-formation processes, it was then possible to go back to the initial objective (whether there is a connection between seismic activity (Chapter 4, Brown and Roberts 2019) and the history of channel formation (Chapter 5, Brown and Roberts 2023) and develop a methodology that would work toward that objective, this being to use data acquired from palaeoseismicity studies, channel studies, and the InSight seismometer data, the Seismic Experiment for Interior Structure (SEIS) to investigate possible inter-relationships and assess ongoing processes and processes in the relatively recent past. For example, is it possible to obtain relative ages for the channel-forming episode(s) and how this relates to the formation of the fossae? Evidence that the source of the channels has moved east over time has been presented (Chapter 5), including the study of fissures on the Martian surface. Data will be drawn together to investigate and scrutinise the possibility of a connection between seismicity and channel-forming processes, how this may relate to active seismicity, and the cause of observed seismicity in the area.

This chapter will present an overview of key findings from the research and the interpretation of the results from Chapters 4 and 5, presented in Key Findings (6.2,

6.2.1, and 6.2.2). Next, the Approach and Methodology section (6.3) will look at how data from Chapters 4 and 5, together with data from InSight's seismometer, SEIS, and the use of a specialised piece of software run in Matlab (FiSH code), is used to explain the methods for comparing the datasets. This will be followed by a Results section (6.4) where the calculations that compare the datasets will be presented using the previously described methods by which the datasets will be compared. Section 6.5 presents a brief conclusion that will provide an overview of the Results section, attempt to interpret the results, and explain what the data show and mean. Finally, Future Work (6.6) offers suggestions for continued research. The implications of the results will be discussed and scrutinised in terms of what they mean in the context of current theories and models.

6.2. Key findings

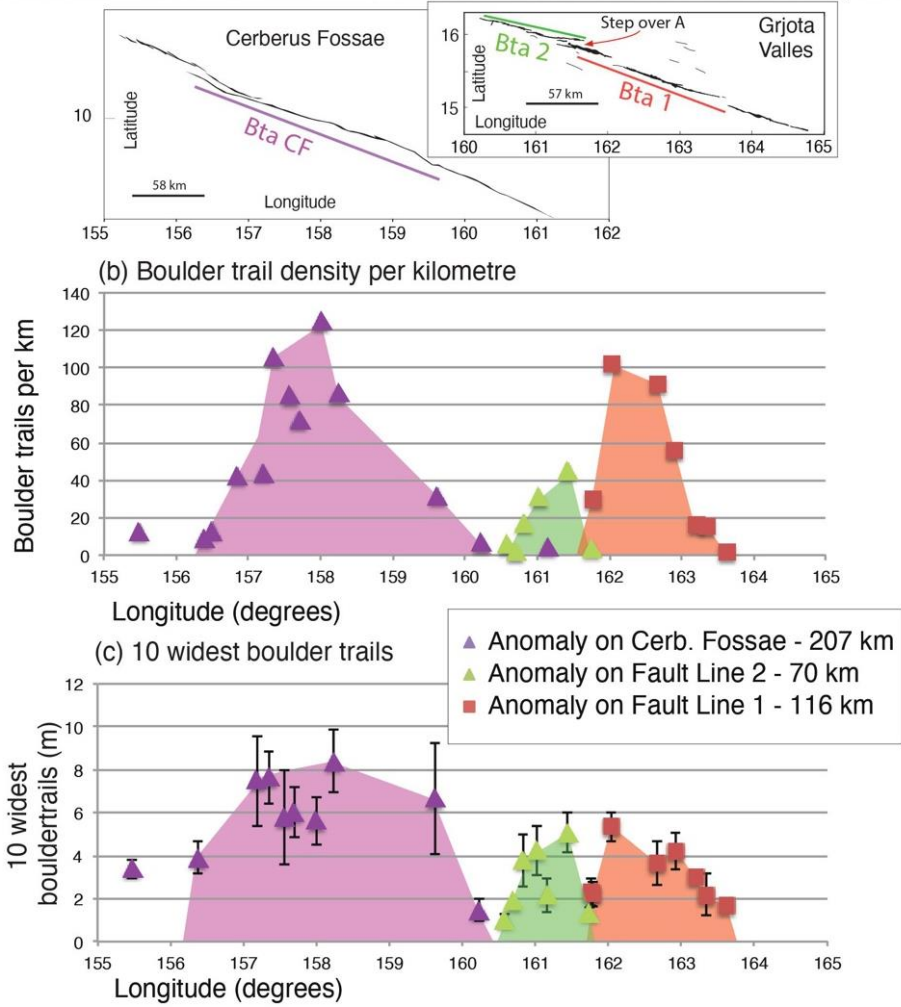
In this section, the key findings from the research that form this thesis will be highlighted briefly and concisely. Chapters 4 and 5 dealt with the results of the research. Chapter 4 dealt with fallen boulders along the inside of the northernmost Cerberus Fossae fault caused by seismic activity that can be used to calculate marsquake magnitude, and Chapter 5 investigated outflow channel formation in the area of Grjótá Valles, using evidence to show that the channels are discrete, cross-cut older channels and that younger floods occur ever to the east.

6.2.1. Using fallen boulder trail populations in the fault system of the northernmost Cerberus Fossae as a proxy seismograph

Two faulted areas that make up a section of the northernmost Cerberus Fossae in Grjótá Valles (Boulder Trail Anomaly 1 and Boulder Trail Anomaly 2) were studied due to these areas of the faults (the inside walls and floors of the faults) having multitudinous boulder trails with many of these trails also having the boulder that formed the trail at the base of the trail (Figure 6.1 a). The densities of these populations were measured, as were the individual trails' widths, so a picture of where the trails are more abundant and wider along the fault could be made. Data suggest that the boulders were mobilised by seismic shaking, which is associated with paleomarsquakes, and that these events occurred in the recent past (Figure 6.1). The data are consistent with previous results from other studies (Roberts et al. (2012)). The analysis identifies that the boulder trail data has two peaks in (i) boulder trails per kilometre (Figure 6.1 b) and (ii) maximum width of boulder trails along two en echelon faults: one ~116 km in length; the other ~70 km in length (Figure 6.1 c). The data

reveals that the maximum values for the number of trails per kilometre and trail width differ for the two faults. For the ~116 km-long fault (Boulder Trail Anomaly 1—Bta 1), the maximum values are 115 trails per kilometre and a 5.3-metre trail width. For the ~70 km-long fault (Boulder Trail Anomaly 2—Bta 2), the maximum values are 45 trails per kilometre and a 5-metre trail width. The data supports published data from Cerberus Fossae (Boulder Trail Anomaly Cerberus Fossae—Bta CF), where an ~200-km-long anomaly in boulder trails per km (125 trails per kilometre maxima) and maximum boulder trail width (8.5-m maximum trail width), the three data sets suggest correlations between the along-strike length of boulder trail anomalies, boulder trails per kilometre and maximum boulder trail width. Implied moment magnitudes, derived by using the along strike dimensions of boulder trail anomalies as proxies for rupture extent, could have been as large as Mw 7.3–7.8, values that are generally considered to be accompanied by much more frequent seismic activity at lower moment magnitudes (Figure 6.1 d) (Brown and Roberts, 2019).

(a) Relatively continuous fault length of part of the Southern Cerberus Fossae (Bta CF) compared to the Northernmost Cerberus Fossae and the extent of boulder trail anomalies (Bta 1 and 2).



(d) Speculative inference of marsquake magnitude from rupture length

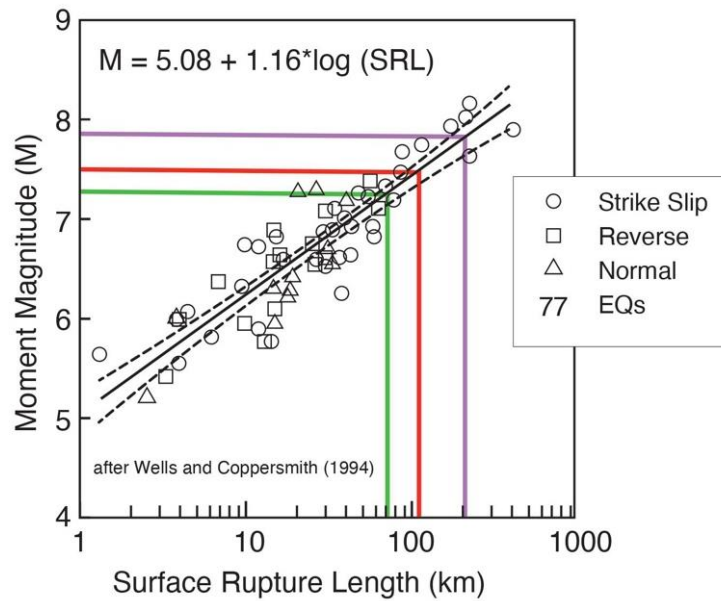


Figure 6.1. a, b, c, and d: Comparison of data from the Northernmost Cerberus Fossae (Boulder Trail Anomaly 1 and 2, red and green, respectively) with similar data from work on the

Southern Cerberus Fossae (Boulder Trail Anomaly Cerberus Fossae, purple). (a) compares the continuous fault length of the Southern Cerberus Fossae (Bta CF, purple line) with the discontinuous northern Cerberus Fossae in Grjótá Valles (Bta 2 - green line; Bta 1, red line). The step over between the two segments of the fault is marked as 'Step over A'. (b) and (c) compare the boulder trail densities and ten widest boulders along the Southern Cerberus Fossae (purple) and the two segments of the northernmost Cerberus Fossae (Boulder Trail Anomalies 2 (green) and 1 (red)). (d) Speculative inference of marsquake magnitude from rupture length of the three fault lines (Boulder Trail Anomaly 1 and 2 and Boulder Trail Anomaly Cerberus Fossae) (after Wells and Coppersmith, 1994).

Concerning the thesis's hypotheses, the findings summarised above do fulfil the original objectives, namely to determine whether or not seismicity existed in the past in the area of the Northernmost Cerberus Fossae (it did), and it is possibly still ongoing today.

6.2.2. Geomorphology of Outflow Channels in the Area of the Northernmost Cerberus Fossae, Grjótá Valles Suggests Multiple Flow Episodes

Using CTX images, HiRISE images, and MOLA data, a detailed analysis of the Northernmost Cerberus Fossae and channels within the adjacent area of Grjótá Valles was conducted to identify any cross-cutting relationships between outflow channels (Brown and Roberts, 2023).

The analyses identify that the floors and margins of channels appear to have been cut by water and/or turbulent lava (channel floor longitudinal lineations, channel margin recessional terraces). There is no indication that these landforms were formed by viscous lava. Additionally, the analyses identify cross-cutting relationships and data derived from studying channel incisions data reveal at least five asynchronous flow episodes, the source of each flow being located at a different position along an approximately 200 km long section of the northernmost Cerberus Fossae, with the younger flow source locations located further east than each successive older flow source location, which indicates that multiple events formed the channels. Analysis of MOLA data suggests that the channels flow downhill away from their sources. Younger channels cross-cut older channels, with incisions ranging from 10 m to 70 m. It is also clear that the sources of the flows are located progressively further east through time. Quite why there is an eastward progression of flow sources is open to speculation. Still, probable explanations are based on dike propagation from west to east that did (and possibly continues to do) one of the following: melted near-surface ice, released turbulent lava, and released magma from an underlying regional melt zone that melted sub-surface ice farther to the east through time. However, exactly what mechanisms were responsible for the release of fluids is also unclear. However, what is evident from

the data and the analyses of the geomorphology of the region is that whatever the process behind the release of fluids into this region is, it does not need to produce the enormous volumes of fluid suggested by other authors if the flow channels have formed in the manner presented here, i.e. asynchronously, and in small, discrete flows (Brown and Roberts, 2019).

6.3. Approach and methodology

The methodological details related to the FiSH code, which is central to this research, were introduced in Chapter 3. There, the theoretical framework for how FiSH models earthquake frequency–magnitude distributions based on fault slip rates was thoroughly discussed. In this chapter, the focus shifts to applying the FiSH code to specific datasets from Mars, including boulder trail densities and seismic data collected by InSight's SEIS instrument, to explore the tectonic activity in the northernmost Cerberus Fossae.

While the detailed explanation of the FiSH code's mechanics can be found in Chapter 3, Section 3.3, this section will concentrate on how the code was specifically employed to integrate palaeoseismic data from the boulder trails with recent marsquake observations. The goal is to link these datasets to develop a comprehensive model of seismicity and dike propagation rates in the Cerberus Fossae region.

6.3.1. FiSH Code—frequency–magnitude curve and seismicity estimates

A package of MATLAB tools called FiSH (Fissile Earthquake Seismology) has been designed to help seismic-hazard modellers analyse fault data, derive expected earthquake rates, and test the consistency between magnitude–frequency distributions (MFD) and observations. The tools developed by Pace et al. (2016) include converting fault geometry and slip rates into a global budget, computing recurrence parameters from historical data, and output earthquake rates for different MFD models. The source codes are open, aiming to help researchers identify inconsistencies and obtain reliable fault-based seismic-hazard evaluations. FiSH code is commonly used (especially in Europe) to help calculate seismic hazards, as the frequency–magnitude distribution is needed to do this (Pace et al., 2016). FiSH is written in MATLAB (v.R2011B), a MathWorks software. The results from the FiSH code are presented in the Results section (6.4.2 and 6.4.3).

To ensure the FiSH code produced reliable seismic hazard modelling for the fault systems in Cerberus Fossae, the selection and justification of key parameters were critical. These parameters were derived from existing geological and mechanical data on the Martian crust. The following section outlines and justifies the key parameters used in this analysis.

6.3.2. Parameter Selection and Justification for FiSH Code Modelling of Cerberus Fossae

6.3.2.1. Introduction

This section presents the selection and justification of the parameters used in the FiSH code for modelling fault systems in Cerberus Fossae. Key parameters such as the shear modulus and slip rate are defined, justified, and contextualised based on available data on the Martian crust's mechanical properties. These parameters are necessary for seismic hazard modelling and fault system analysis.

6.3.2.2. Shear Modulus of the Martian Crust

The shear modulus (μ) is a critical parameter representing the rigidity of materials. For the Martian crust, the shear modulus value of 10 GPa has been selected. This value falls within the range suggested by geological studies focusing on Mars' surface and subsurface materials. Several studies confirm that the shear modulus in the Martian crust typically ranges from 10 to 40 GPa, depending on depth and local geology. Using gravity and topography data from the Mars Global Surveyor, Golombek et al. (2000) and McGovern et al. (2002) estimated shear modulus values between 10 and 20 GPa, with McGovern's calculations reaching up to 40 GPa in the Tharsis region. Their estimates relied on flexural modelling of lithospheric bending observed in gravity and topography admittance spectra, allowing them to infer rigidity and other mechanical properties at various depths. A moderate value of 10 GPa is selected for Cerberus Fossae, where recent volcanic activity, faulting, and possible localised heating likely reduce crustal strength and rigidity, making this lower shear modulus more representative. Golder et al. (2020) demonstrated similar values in their studies of dike propagation in the northern hemisphere of Mars.

The selection of a moderate shear modulus value (10 GPa) is appropriate for the Cerberus Fossae region, which is characterised by tectonic activity and dike propagation.

6.3.2.3. Slip Rate and Seismic Moment

The FiSH code requires a defined slip rate to model seismic events. For Cerberus Fossae, the slip rate was iterated between 0.017 and 0.067 mm/year, chosen to match observed seismicity and frequency-magnitude data. The seismic moment (M_0) is calculated using the following equation from Pace et al. (2016):

$$M_0 = \mu \cdot D \cdot L \cdot W$$

where:

μ = shear modulus,

D = displacement,

L = fault length,

W = fault width

This equation allows for the determination of the seismic moment, helping to justify the chosen parameters for the FiSH code. Given the geological data, these values align with known properties of the Martian crust.

6.3.2.4. Recurrence Time (T_{mean})

The recurrence time (T_{mean}) of seismic events is calculated as follows:

$$T_{mean} = \frac{10^{1.5M_{max}+9.1}}{\mu \cdot V \cdot L \cdot W}$$

where:

M_{max} is the maximum observed magnitude;

μ is the shear module;

V is the average slip rate;

L and W are the fault length and width, respectively.

This equation provides the time between major seismic events based on fault characteristics, adding rigour to the seismic hazard assessments of Cerberus Fossae.

Table 6.1. A summary of the parameters used in the FiSH code for this analysis.

Parameter	Value	Unit	Justification
Shear Modulus (μ)	10 GPa	GPa	Based on studies by Golombek et al. (2000), McGovern et al. (2002), and Golder et al. (2020).
Slip Rate	0.017–0.067	mm/year	Iterated in FiSH code based on seismicity data and geomorphological estimates.
Fault Length (L)	115 km	km	Based on fault measurements in the Cerberus Fossae region.
Displacement (D)	Calculated	Metres	Derived using the FiSH code and geological data.
Magnitude of Completeness (M_c)	2.25	Moment Magnitude (M_w)	Based on SEIS data for Martian Seismicity (Pace et al., 2016).

6.3.2.5. Conclusion

The parameters used in this model are well justified based on studies of the Martian crust, and the methodology allows for reliable seismic hazard modelling. The shear modulus, slip rate, and recurrence time calculations all contribute to a robust understanding of fault behaviour in Cerberus Fossae. The FiSH code provided a frequency-magnitude curve that aligns closely with SEIS data, reinforcing the validity of the model. Future studies may explore variability in the shear modulus to refine these results further, but the current values are appropriate for this analysis.

6.4. Results

6.4.1. Magnitude of completeness

Using data presented in Appendix A: Supplementary Data: Supplementary Material 2 (Ceylan et al. (2002) and the data discussed in Chapters 4 and 5, it is possible to construct a frequency–magnitude distribution graph (boulder trail density as a proxy for maximum moment magnitude) from SEIS data that allows for the identification of the magnitude of completeness (M_c) (Figure 6.2). The magnitude of completeness (M_c) refers to the minimum magnitude of an earthquake that can be detected and recorded by a particular seismic network. Any earthquake with a magnitude below this threshold may not be detected or recorded.

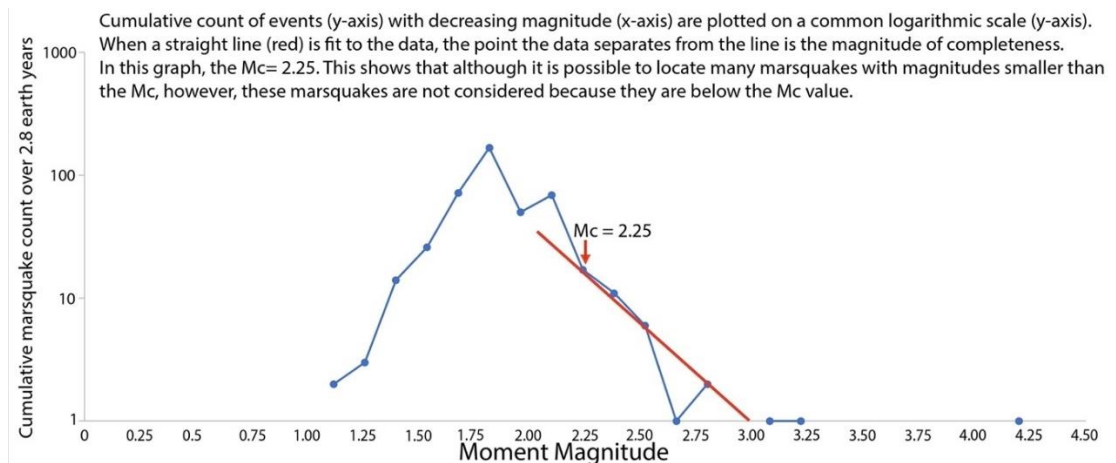


Figure 6.2. The graph displays a logarithmic plot with the cumulative count of events on the y-axis and decreasing magnitude on the x-axis after data from Ceylan et al. (2002). The straight red line represents where the data diverges from the line, indicating the magnitude of completeness, which, in this case, is $M_c = 2.25$. This means that although there may be several marsquakes with magnitudes lower than the M_c , they are not considered as they fall below the M_c value.

Data from Chapter 4 focused on the largest possible moment magnitude marsquakes based on work by Wells and Coppersmith (1994) (Figure 6.1 d) for the northernmost Cerberus Fossae, approximately 7.2–7.5 M_w . Data from SEIS, on the other hand, is limited in several ways. First, the data are from the first 1,011 sols (2.8 Earth years). Given the brevity of the entire SEIS mission (three Earth years and five days—deployment 19th December 2018—end of mission 24th December 2021), it would have been unrealistic to expect a large moment magnitude marsquake to be detected. As such, no large marsquakes (over 4.5 M_w) were detected. Equally, SEIS was not sensitive enough to detect small-moment magnitude marsquakes (0.16–1.0 M_w), as shown by the absence of detected marsquakes that fit these bins (Ceylan et al., 2022). This leaves a small range of marsquakes that SEIS was able to detect. Given the limitations of SEIS, it was important to calculate the magnitude of completeness when studying the SEIS seismic catalogue. Estimating the magnitude of completeness (M_c) involves using the Gutenberg–Richter Law (Gutenberg et al., 1944; Utsu, 1965) and categorising into ‘bins’ according to the number of events with magnitudes greater than a specified reference magnitude. The count of marsquakes in each bin is then plotted on a logarithmic scale. Ideally, the data should form a straight line, but statistically perfect datasets rarely exist. However, this relationship can be used to estimate the M_c . When a straight line is fitted to the data, the point at which the data deviates from the line is the magnitude of completeness. In this case, the magnitude of completeness is approximately 2.25 (Figure 6.2).

6.4.2. FiSH Code Results: Frequency–magnitude curve and seismicity estimates

Knowing that the M_c for marsquakes in Cerberus Fossae is 2.25 and that 16 Mw 2.25 events took place over a 2.8-year timescale means that approximately five Mw 2.5 events should occur yearly (Figure 6.2). Chapter 4 research shows that the largest possible marsquakes in Cerberus Fossae occur between Mw 7.3 and 7.8 and are thought to take place over tens to hundreds of thousands of years based on geomorphological evidence. To err on caution, an Mw 7.0 was set as the high range of marsquakes when iterating the slip rate. As such, upper and lower limits for marsquake magnitudes now exist. By using FiSH code and iterating the slip rate, it was possible to produce a frequency–magnitude curve for events in Cerberus Fossae using SEIS data and Chapter 4 data (Figure 6.3).

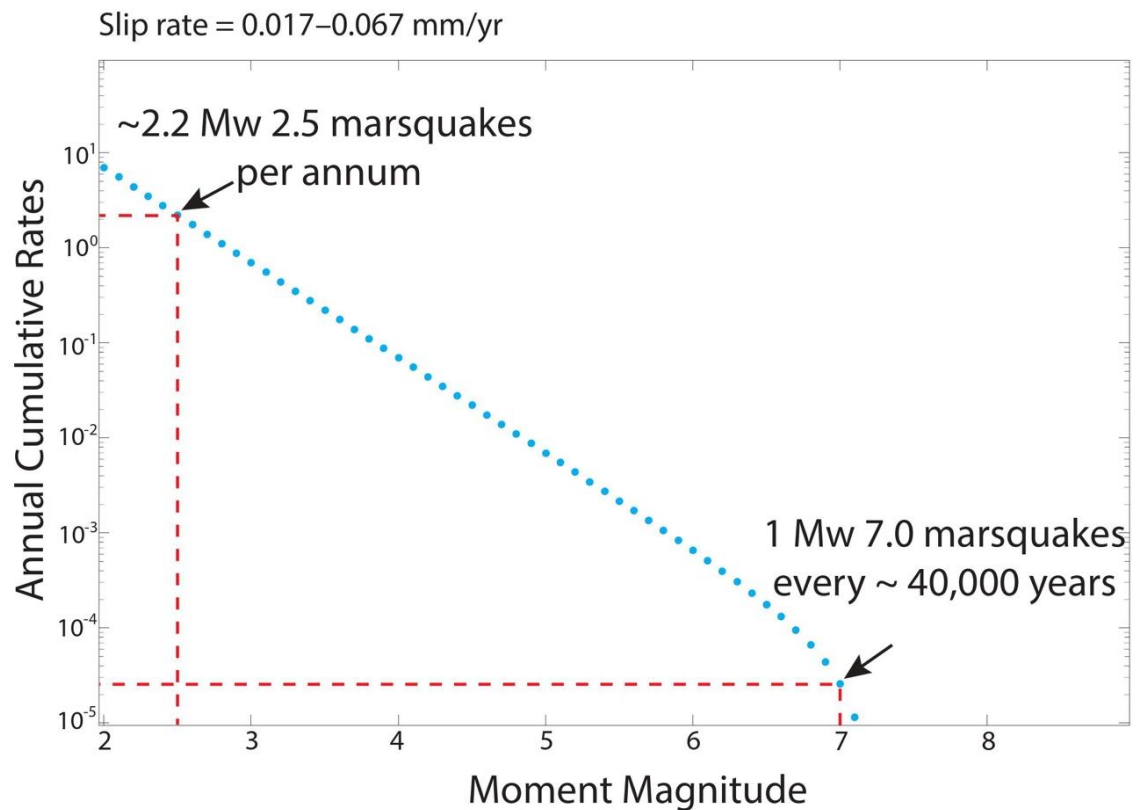


Figure 6.3. Truncated Gutenberg–Richter (GR) frequency–magnitude graph produced using FiSH code in MATLAB (v.R2011B) to create a frequency–magnitude curve of seismic events annually against moment magnitude. The graph’s y-axis is the annual cumulative rates (logarithmic), and the x-axis is the moment magnitude. Based on SEIS data that allowed the magnitude of completeness to be calculated ($M_c = 2.25$), the approximate annual rate for marsquakes of that magnitude is 5. Slip-rate adjustment to allow the estimates from SEIS and Chapter 4 boulder data to fit on the frequency–magnitude curve means that the annual rate of Mw 2.25 marsquakes, using FiSH code, is 2.2. Data from research on boulder trail populations as a proxy seismometer to estimate the magnitude of marsquakes (Mw 7.3–7.8) and the annual cumulative rate to be in the tens of thousands of years. A Mw 7.0 marsquake, the more conservative estimate based on data, was used to fit this model, with the occurrence rate being one event every 39,019 years, in keeping with predicated timescales. Indeed, the timescales for

the events are within an order of magnitude of estimates. By iterating the slip rate, the two sets of data were melded together to produce the frequency–magnitude curve that was true to SEIS data and data from research on boulder trail populations as a proxy seismometer (Chapter 4), accommodating the SEIS timescales very neatly (2.19 versus 5) and the predicted dates for marsquakes over Mw 7.0. within one order of magnitude.

The frequency–magnitude curve shows that approximately 2.2 Mw 2.5 marsquakes occur each year, within range of the readings from SEIS, given that the SEIS readings spanned just under three years and that large marsquakes of Mw 7.0 plus occur in the tens of thousands of years (~40,000 years), correlating to the order of magnitude that had been suggested for larger marsquakes within Cerberus Fossae in Chapter 4. However, Mw 7.0 is towards the lower end of estimates for larger marsquakes. The slip rate used for the FiSH code to produce the curve in Figure 6.3.1 was 0.017–0.067 mm per year, and the *b*-value was set at 1.

Iteration of the slip rate was important because slight changes resulted in the frequency–magnitude curve being significantly off the SEIS reading correlating with data from Chapter 4, as the six example graphs in Figure 6.4 a–f show.

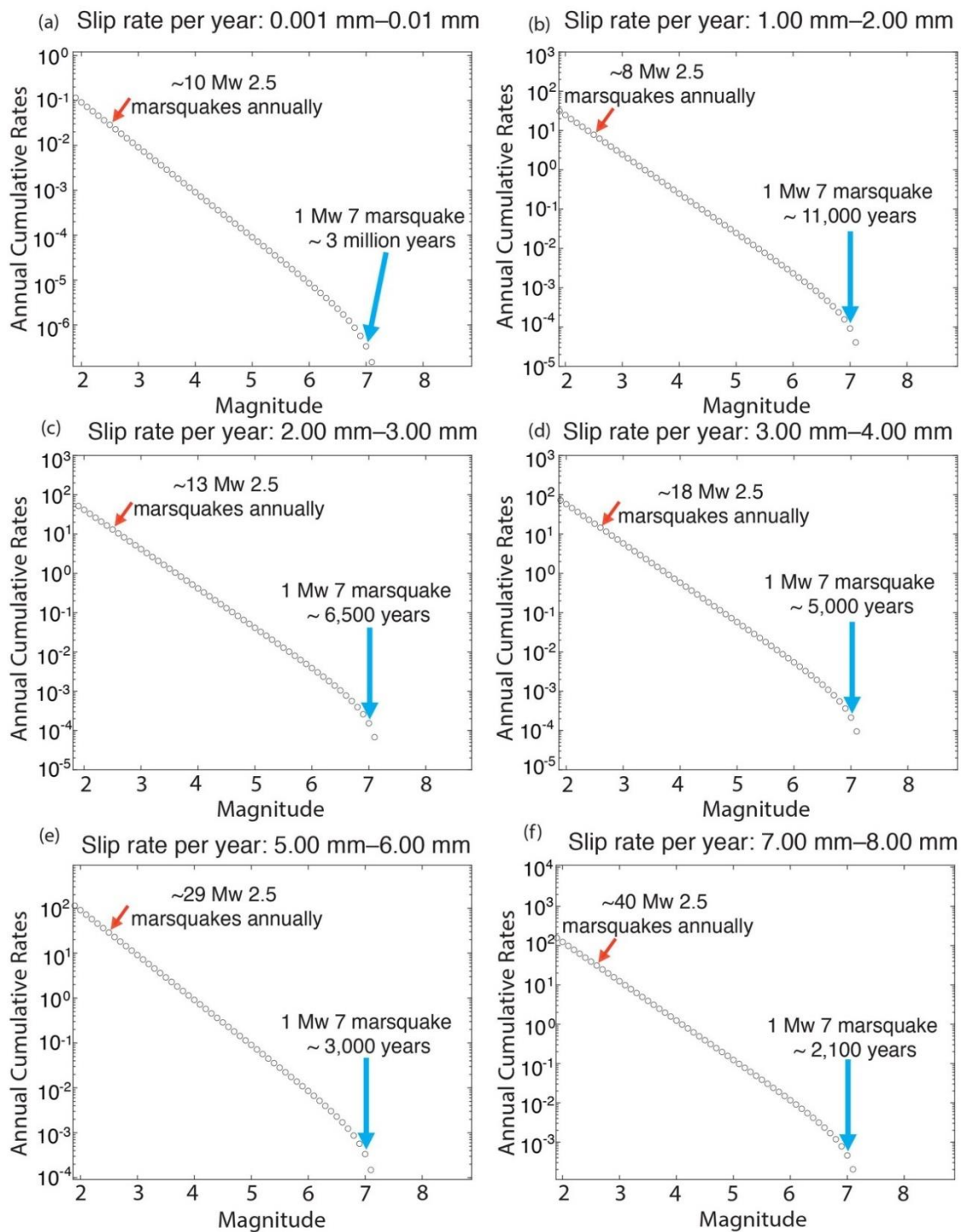


Figure 6.4. a–f: Truncated Gutenberg–Richter (GR) frequency–magnitude graphs produced using FiSH code in MATLAB (v.R2011B) to create frequency–magnitude curves of seismic events annually against moment magnitude. All graphs’ y-axis is the annual cumulative rates (logarithmic), and the x-axis is the moment magnitude. The slip rate for each graph differs from the 0.017–0.067 mm iteration of the slip rate used in Figure 6.4.2, which matches the SEIS data with the data from boulder trail research explained in Chapter 4. The red arrows highlight the $M_w 2.5$ marsquake (magnitude of completeness) and the frequency of such a magnitude marsquake per annum. Likewise, the blue arrows highlight the $M_w 7.0$ marsquake and the frequency of such a magnitude marsquake. The slip rates per year for each graph are as follows: (a) 0.001–0.010 mm; (b) 1.00–2.00 mm; (c) 2.00–3.00 mm; (d) 3.00–4.00 mm; (e) 5.00–6.00 mm; (f) 7.00–8.00 mm.

Figure 6.4 a–f underscores the remarkable sensitivity of the calculations in response to small variations in slip rates. The graphs reveal that even a minute difference of half a millimetre in slip rates can significantly impact the frequency–magnitude curves, resulting in curves that do not align with data from SEIS (lower Mw) and estimates proposed in Chapter 4 (higher Mw). For instance, Figure 6.4c depicts a frequency–magnitude graph using a slip rate of 2.00–3.00 mm. Despite the seemingly minor difference, this variation profoundly affects the calculated readings of marsquakes per year. In this scenario, Figure 6.4c displays approximately 13 Mw 2.5 marsquakes annually and predicts a 1 Mw 7 marsquake every ~6,500 years. These values starkly contrast with the readings in Figure 6.3, which suggests approximately 2.2 Mw 2.5 marsquakes annually and a 1 Mw 7 marsquake approximately every ~40,000 years. The high sensitivity observed in the calculations when slip rates are adjusted implies that the FiSH code is precise when using input data to compute frequency–magnitude curves. This sensitivity is critical to the code's accuracy, demonstrating its ability to capture nuanced variations in slip rates and their subsequent impact on seismic activity predictions.

This finding reinforces the importance of meticulous consideration and calibration of input parameters in seismic modelling, as even small discrepancies can lead to significant variations in the predicted outcomes.

6.4.3. FiSH Code: Slip rates and dike propagation

The slip rates were iterated in FiSH code until the frequency–magnitude curve connected the Mw 2.25 marsquake at ~2.2 events a year with an Mw 7 marsquake that occurs every ~40,000 years, within the order of magnitude predicted. This curve (Figure 6.4) then ‘fits’ the model with the frequency and magnitude points corresponding very closely with data from SEIS (the calculation of the magnitude of completeness) and data from Chapter 4 on the possible magnitude of marsquakes based upon three data sets that used boulder trail populations as natural seismometers (Figure 6.1a–d). The frequency of events was predicted to be within the tens or hundreds of thousands of years. Such an estimate used knowledge of the extremely slow erosion rates on the Martian surface since the Hesperian (10^{-2} nm/yr), as noted by Golombek et al. (2000) studying erosion rates at the Pathfinder landing site, together with evidence for almost imperceptible erosion of boulder trails on the Martian surface to arrive at these figures. As such, a slip rate (0.017–0.067 mm/yr) has now been calculated, and this slip rate can now be tested for veracity using data from Chapter 5. From the research that comprises Chapter 5, the proposed explanation for the

eastward progression of flow sources is the eastward movement of a dike. The propagation of the dike releases the following: (i) melted near-surface ice, (ii) turbulent lava, and (iii) released magma from an underlying regional melt zone that melted sub-surface ice farther to the east through time. Now that a slip rate has been calculated using available seismic data and FiSH code, the slip rate may also be tested against knowledge of displacement, d , and length, L , relationships for faults in conjunction with data on the age of flow channels from Chapter 5.

An empirical rule of thumb for estimating the displacement, d , in faults and dikes based on their length, L , is simplified and approximate but useful for estimating. For faults, $d=L \times 0.03$. This implies that the displacement, d , along a fault, is approximately 3% of the fault length (L). For dikes, $d=L \times 0.003$. This suggests that the displacement, d , is approximately 0.3% of the dike length (L) (Vermilye and Scholz, 1995).

Research data presented in Chapter 5 suggests that the asynchronous formation of the flow channels in Grjótá Valles is caused by melted flow released to the surface, forming the observed channels due to dike intrusions that occur progressively eastward over time, possibly emanating from a sub-surface volcanic source underlying the region (Genova et al., 2016; Golder et al., 2020). Golder et al.'s (2020) work provides crater count ages within the study region that are younger from west to east: 53 Ma, 33 Ma, and 31 Ma, respectively. They suggest this change in age is due to changes in the rheological properties of the lavas during emplacement, such as material strength and porosity (Golder et al., 2020). This is a possibility, but the ages obtained by Golder et al. (2020) are from areas that partially overlap flow deposits (Fig. 6.5). The 53 Ma age happens to coincide with the proximal regions for Flow 1 and Flow 2; the 33 Ma age coincides with the area occupied by the distal parts of Flow 3 and Flow 4; the 31 Ma age coincides with an area to the east of the region mapped that is occupied by Flow 5. This means that the ages constrain the ages of channels, the times between channel formation episodes, and the timescale, hence the lateral dike propagation rate.

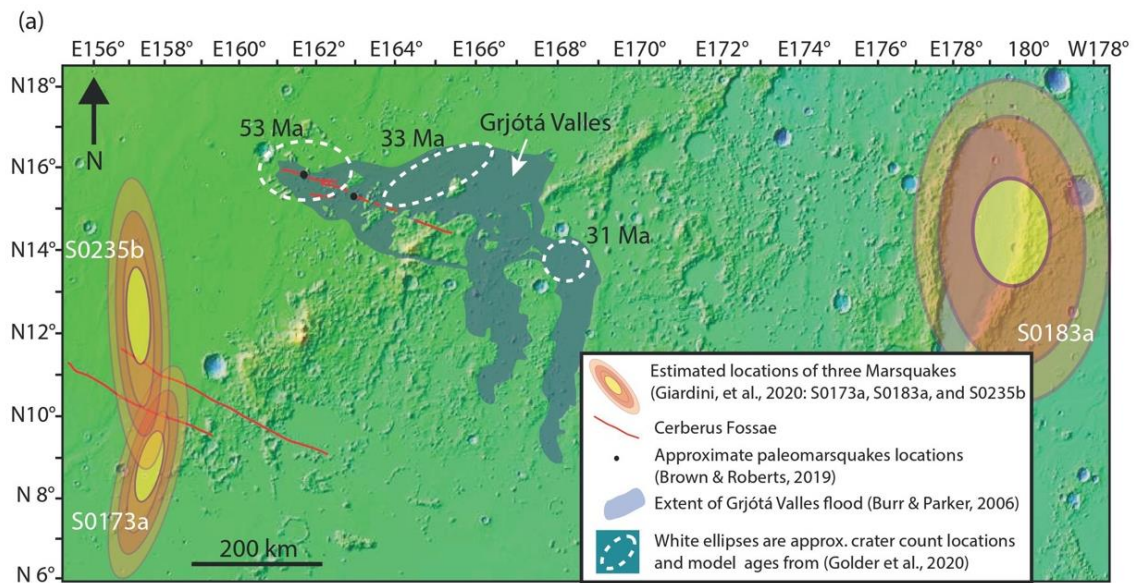


Figure 6.5. The extent of the Grjótá Valles flow tract (after Burr and Parker (2006) is the dark green area in the centre of the image. Red lines mark the fossae, with the Northernmost Cerberus Fossae running WNW–ESE across the centre of the Grjótá Valles flow tract area. The larger Northern and Southern Cerberus Fossae are marked by two red lines to the SW of the image. Black dots identify two locations showing the approximate paleomarsquakes locations along the northern Cerberus Fossae after Brown and Roberts (2019)—see Chapter Four of this thesis. The three white ellipses are crater count locations, and their matching crater count model ages for lava flows in this area (Golder et al., 2020).

Using the slip rate calculated from FiSH code, with the age of the flow channels and the displacement–length relation equation for dikes, it is possible to calculate the dike propagation rate and the opening rate of the fault across different flow channel areas. In short, the speed of dike propagation and whether such a figure is reasonable.

According to crater counts, Flow 1 occurred at ~53Ma and Flow 3 at 33Ma. Their source locations are ~115 km apart (115,000,000 mm in 20,000,000 years), meaning a dike propagation rate of 5.75 mm/yr, averaged over 20 Ma. Using the $d=L \times 0.003$ equation, it is possible to calculate the opening rate of the fault: 0.0172 mm/yr and the amount of dike opening: ~344 m in 20 Ma. The opening rate of the fault tallies well with the slip rate range iterated using FiSH code and the data from SEIS and Chapter 4 estimates. However, the age of different flow channels varies across the area. Flow 4 and 5 occurred at approximately 33 Ma and 31 Ma, respectively, with their respective source locations approximately 75 km apart. The age difference between the two flows is 2 million years. Calculations similar to those used for the Flow 1–Flow 3 comparison are applied to determine dike propagation and fault opening rates. The dike propagation over 2 million years is calculated as 37.5 mm/yr, and using the $d = L \times$

0.003 equation, the opening rate of the fault along this section is determined to be 0.11 mm/yr.

Table 6.2. A summary of dike propagation and fault opening rates for Flows 1, 3, 4, and 5

Flow Comparison	Age (Ma)	Source Location Distance (km)	Dike Propagation Rate (mm/yr)	Fault Opening Rate (mm/yr)	Total Dike Opening (m)
Flow 1– Flow 3	53–33	115	5.75	0.0172	344
Flow 4– Flow 5	33–31	75	37.5	0.11	225

Additionally, the dike opening is estimated to be approximately 220 metres over the 2 million years. The analysis rightly points out the potential pitfalls of comparing these results directly with the Flow 1–Flow 3 data due to the significant difference in timescales. Given the two million-year age gap between Flow 4 and Flow 5, the calculated rates and values are specific to this timeframe and should not be directly compared with those derived from the earlier flows. This cautious approach highlights the importance of considering temporal variations when analysing geological processes. Comparing data from events with vastly different timescales can lead to misinterpretations; therefore, prudence is needed.

From seemingly disparate data sets, it has been possible to use information about boulder trail populations (Chapter 4), SEIS seismological data, and research data about asynchronous flow channels and each flow channel age (Chapter 5) to build a picture of what is happening in the northernmost Cerberus Fossae and part of the Grjótá Valles channel system, to what degree, and when.

Chapter 4 research into using boulders as natural seismometers allowed a maximum Mw to be estimated (Mw 7.3–7.8). Using SEIS data from the first 1,011 sols on Mars, it was then possible to calculate the magnitude of completeness for the data set, essentially the lowest Mw (Mw 2.5). By using FiSH code to iterate the slip rate for faults and dike propagation rates, a frequency–magnitude curve was produced using a slip rate (per year) iteration that matched very closely with the number of estimated marsquakes that would be detected per year at the magnitude of completeness against the actual number of marsquakes detected by SEIS per year at the magnitude of completeness (2.196 events vs. 5) with the estimated time scales for Mw 7

marsquakes (conservatively choosing the lower end of the original estimates discussed in Chapter 4), these being one event every 39,019 years. Minor changes to the slip rate produced frequency–magnitude curves that did not tally with the marsquake date (magnitude/frequency). The fact that the data used to produce the frequency–magnitude curve (Figure 6.3) matches so well suggests that the FiSH code calculation for the slip rate is reliable and that SEIS measurements and estimates of Mw from Chapter 4 are correct. Using the calculated slip rate and the data regarding the ages of flow channels (Chapter 5), it was then possible to calculate the rate of dike opening (assuming dike opening is a proxy for slip rate) for the northernmost Cerberus Fossae and, thereby, the rate of fault opening per year:

Flow 1 occurred at ~53Ma and Flow 3 at 33Ma, meaning a dike propagation rate of 5.75 mm/yr, averaged over 20 Ma. The opening rate of the fault was 0.0172 mm/yr (~344 m in 20 Ma). Flow 4 occurred at ~33 Ma; Flow 5 occurred at 31 Ma, meaning a dike propagation of 37.5 mm/yr averaged over 2 Ma. The opening rate of the fault was 0.11 mm/yr (~220 m in 2 Ma).

6.5. Conclusion

Three seemingly contrastive data sets (boulder trail populations as a proxy seismograph used in conjunction with SEIS data; FiSH code to iterate slip rates of faults based on Mw estimates/data; geomorphological analyses that reveal multiple flow channels of decreasing age west–east combined with crater count ages) have been combined that enable a further level of understanding to be gleaned regarding the recent geological history of the northernmost Cerberus Fossae and part of the Grjótá Valles channel system. The processes behind the observed seismicity in the northernmost Cerberus Fossae and the series of discrete flow channels that progress west–east in areas adjacent to the Grjótá Valles channel system are connected. Dike propagation west–east, the rate of which has been calculated, is responsible for the marsquakes observed in this region. This is relevant because it shows that the two processes are connected. More importantly, it indicates that dike propagation was, until recently, occurring and is possibly ongoing. This suggests that other flow events may occur in the future. Given that the flow events are likely aqueous, the possibility that liquid water may flow over the Martian surface in the future and in an area that can be predicted, namely a location to the east of the last flow source, offers a tantalising opportunity for future researchers to study surface process on Mars and to know where to look.

6.6. Future work

Reducing the uncertainty in calculations related to geomorphology and seismicity on Mars requires a focused and multidisciplinary approach. Two key points that future researchers should consider are as follows:

6.6.1. Extended seismicity record and improved seismograph sensitivity

A longer seismic record is necessary to build a more comprehensive understanding of Mars' geological activity. A more extended period of observations allows for detecting a broader range of seismic events, including small-magnitude marsquakes. This extended record contributes to a more robust dataset for analysis.

A focus on small-magnitude marsquakes is of great importance. Future researchers should emphasise the importance of capturing data on small-magnitude marsquakes. Improving the sensitivity of seismographs can help detect and record these smaller events, providing valuable information for understanding the full spectrum of Martian seismicity. This approach is essential for refining models and calculations related to tectonic and seismic processes.

6.6.2. Enhanced crater counting for accurate age determination

A refined approach to crater counting is necessary to reduce uncertainties in age determinations of flow channels. While crater counting is inherently integrated into the process of identifying units for dating, focusing on more targeted and systematic methods can help improve accuracy. This involves a detailed analysis of craters specifically associated with the flow channels, allowing for more precise age estimates and reducing the margin of error in dating these geological features.

Integration with geomorphological analyses is also an area that needs development. Combining crater counting with geomorphological analyses strengthens the dating process. Integrating these methods will allow future researchers to cross-verify and refine age estimates, leading to a more precise understanding of the chronological sequence of geological events. The area of Cerberus Fossae is of key relevance, and research should be focused on this area. However, other regions of Mars should also be considered candidates for research, including the Tharis volcanic plateau and the eastern edge of the Valles Marineris canyon system.

6.6.3. Importance of future work

The quantitative link between geomorphology and seismicity—the demonstrated method within this thesis underscores the need for future work, allowing researchers to link geomorphology with seismicity quantitatively. Establishing empirical relationships between dike propagation rates and seismicity is a significant advancement. This linkage provides a powerful tool for understanding the dynamic processes occurring on Mars.

Future research is essential for a deeper understanding of Martian geological processes. The ability to quantitatively link geomorphological features with seismic events offers insights into the interactions between tectonic activities, dike propagation, and surface morphology. This knowledge is crucial for unravelling the geological history of Mars and predicting future events.

6.6.4. Summary

In summary, future researchers can reduce uncertainty in calculations by extending the seismicity record, improving seismograph sensitivity, focusing on small-magnitude marsquakes, adopting a targeted approach to crater counting for age determination, and recognising the significance of the quantitative link established between geomorphology and seismicity. Collectively, these efforts will contribute to advancing our understanding of Mars' geological evolution.

LIST OF REFERENCES

- Albee, A. L., Arvidson, R. E., Palluconi, F., & Thorpe, T. (2001). Overview of the Mars global surveyor mission. *Journal of Geophysical Research*, 106(E10), 23291–23316.
<https://doi.org/10.1029/2000je001306>
- Acuna, M. H., Connerney, J. E. P., Ness, N. F., Lin, R. P., Mitchell, D. L., Carlson, C. W., ... & Rème, H. (1999). Global distribution of crustal magnetization discovered by the Mars Global Surveyor MAG/ER experiment. *Science*, 284(5415), 790-793.
- Alberti, G., Castaldo, L., Orosei, R., Frigeri, A., & Cirillo, G. (2012). Permittivity estimation over Mars by using SHARAD data: the Cerberus Palus area. *Journal of Geophysical Research: Planets*, 117(E9).
- Ali, W., & Shieh, S. (2013). Earthquake repeat time, stress drop, type of slip and earthquake magnitude. *Journal of Geology and Geophysics*, 2, 118.
<https://doi.org/10.4172/2329-6755.1000118>
- Anderson, D. M., Biemann, K., Orgel, L. E., Oro, J., Owen, T., Shulman, G. P., ... & Urey, H. C. (1972). Mass spectrometric analysis of organic compounds, water and volatile constituents in the atmosphere and surface of Mars: the Viking Mars lander. *Icarus*, 16(1), 111-138.
- Andrews-Hanna, J. C., Zuber, M. T., & Banerdt, W. B. (2008). The Borealis basin and the origin of the Martian crustal dichotomy. *Nature*, 453(7199), 1212-1215.
- Andrews-Hanna, J. C. (2012). The formation of Valles Marineris: 3. Trough formation through super-isostasy, stress, sedimentation, and subsidence. *Journal of Geophysical Research: Planets*, 117(E6).
- Antoine, R., Lopez, T., Baratoux, D., Rabinowicz, M., & Kurita, K. (2011). Thermal analysis of fractures at Cerberus Fossae, Mars: Detection of air convection in the porous debris apron. *Icarus*, 214(2), 433–446.
- Baker, V. R. (1973). 144: Paleohydrology and sedimentology of Lake Missoula flooding in eastern Washington. Geological Society of America, Special Papers. Preprint
<https://doi.org/10.1130/spe144>

- Baker, V. R. (1982). *The channels of Mars*. Bristol: Hilger.
- Baker, V. R., & Milton, D. J. (1974). Erosion by catastrophic floods on Mars and Earth. *Icarus*, 23(1), 27–41. [https://doi.org/10.1016/00191035\(74\)90101-8](https://doi.org/10.1016/00191035(74)90101-8)
- Baker, V. R., & Patton, P. C. (1978). New evidence for pre-Wisconsin flooding in the channeled scabland of Eastern Washington. *Geology*, 6(9), 567. [https://doi.org/10.1130/0091-7613\(1978\)6<567:nepfi>2.0.co;2](https://doi.org/10.1130/0091-7613(1978)6<567:nepfi>2.0.co;2)
- Baker, V. R. (2001). Water and the Martian landscape. *Nature*, 412(6843), 228-236.
- Balme, M., Berman, D. C., Bourke, M. C., & Zimbelman, J. R. (2008). Transverse aeolian ridges (TARs) on Mars. *Geomorphology*, 101(4), 703-720.
- Banerdt, W. B., Golombek, M. P., & Tanaka, K. L. (1992). Stress and tectonics on Mars. *Mars*, 249-297.
- Banerdt, W. B., Smrekar, S. E., Lognonné, P., Spohn, T., Asmar, S. W., Banfield, D., ... & Antonangeli, D. (2020). Initial results from the InSight mission on Mars. *Nature Geoscience*, 13(3), 183-189.
- Bell, J. W., Brune, J. N., Liu, T., Zreda, M., & Yount, J. C. (1998). Dating precariously balanced rocks in seismically active parts of California and Nevada. *Geology*, 26(6), 495-498.
- Berman, D. C., & Hartmann, W. K. (2002). Recent fluvial, volcanic, and tectonic activity on the Cerberus Plains of Mars. *Icarus*, 159(1), 1–17. <https://doi.org/10.1006/icar.2002.6920>
- Bibring, J. P., Langevin, Y., Mustard, J. F., Poulet, F., Arvidson, R., Gendrin, A., ... & Neukum, G. (2006). Global mineralogical and aqueous Mars history derived from OMEGA/Mars Express data. *science*, 312(5772), 400-404.
- Borg, L. E., Connelly, J. N., Boyet, M., & Carlson, R. W. (2003). Chronological evidence that the Moon is either young or did not have a global magma ocean. *Nature*, 423(6939), 322-324.

- Borg, L. E., Brennecka, G. A., & Symes, S. J. (2016). Accretion timescale and impact history of Mars deduced from the isotopic systematics of martian meteorites. *Geochimica et Cosmochimica Acta*, 175, 150-167.
- Böse, M., Clinton, J. F., Ceylan, S., Euchner, F., van Driel, M., Khan, A., ... & Banerdt, W. B. (2017). A probabilistic framework for single-station location of seismicity on Earth and Mars. *Physics of the Earth and Planetary Interiors*, 262, 48-65.
- Brass, G. W. (1980). Stability of brines on Mars. *Icarus*, 42(1), 20-28.
- Breuer, D., & Moore, W. B. (2015). Dynamics and thermal history of the terrestrial planets, the Moon, and Io. In G. Schubert (Ed.), *Treatise on Geophysics* (2nd ed., pp. 255–305). Elsevier. <https://doi.org/10.1016/B978-0-444-53802-4.00173-1>
- Broquet, A., Massé, M., Bourgeois, O., & Lecomte, A. (2020). Geological constraints on the origin of the Cerberus Fossae: Fractures, dikes, or grabens?. *Journal of Geophysical Research: Planets*, 125(9), e2020JE006403.
- Brown, J. R., & Roberts, G. P. (2019). Possible evidence for variation in magnitude for marsquakes from fallen boulder populations, Grjota Valles, Mars. *Journal of Geophysical Research: Planets*, 124(3), 801–822. <https://doi.org/10.1029/2018je005622>
- Brown, J. R., & Roberts, G. P. (2023). Repeated, Cross-Cutting, and Spatially Migrating Outflow Channel Formation, Grjótá Valles, Mars. *Journal of Geophysical Research: Planets*, 128(2), e2022JE007247. <https://doi.org/10.1029/2022JE007247>
- Brož, P., Kryza, O., Wilson, L., Conway, S. J., Hauber, E., Mazzini, A., et al. (2020). Experimental evidence for lava-like mud flows under Martian surface conditions. *Nature Geoscience*, 13(6), 403–407. <https://doi.org/10.1038/s41561-020-0577-2>
- Brune, J. N. (1993). Precariously balanced rocks in Nevada and California: implications for earthquake hazard in Nevada, particularly at Yucca Mtn. *Geological Society of America, Abstracts with Programs;(United States)*, 25(CONF-9305259-).
- Brune, J. N., and Whitney, J., 1992, Precariously balanced rocks with rock varnish: Paleoindicators of maximum ground acceleration? [abs.]: *Seismological Research Letters*, v. 63, p. 351.

Brune, J. N., Purvance, M. D., & Anooshehpour, A. (2007). Gauging Earthquake Hazards with Precariously Balanced Rocks: Finding easily toppled boulders that are still standing provides a way to test models of seismic hazard. *American Scientist*, 95(1), 36-43.

Burr, D. M. (2003). Hydraulic modelling of Athabasca Vallis, Mars. *Hydrological Sciences Journal*, 48(4), 655–664. <https://doi.org/10.1623/hysj.48.4.655.51407>

Burr, D. M. (2010). Palaeoflood-generating mechanisms on Earth, Mars, and Titan. *Global and Planetary Change*, 70(1-4), 5-13.

Burr, D. M., & McEwen, A. S. (2002). The extremes of the extremes: Extraordinary floods: Proceedings of an international symposium on extraordinary floods held at Reykjavik, Iceland. In July 2000. Wallingford: International association of hydrological sciences. Recent extreme floods on Mars (p. 101).

Burr, D. M., & Parker, A. H. (2006). Grjotá Valles and implications for flood sediment deposition on Mars. *Geophysical Research Letters*, 33(22), L22201. <https://doi.org/10.1029/2006gl028011>

Burr, D. M., Grier, J. A., McEwen, A. S., & Keszthelyi, L. P. (2002). Repeated aqueous flooding from the Cerberus Fossae: Evidence for very recently extant, deep groundwater on Mars. *Icarus*, 159(1), 53–73. <https://doi.org/10.1006/icar.2002.6921>

Burr, D. M., McEwen, A. S., & Sakimoto, S. E. H. (2002). Recent aqueous floods from the Cerberus Fossae, Mars. *Geophysical Research Letters*, 29(1), 1013. <https://doi.org/10.1029/2001GL013345>

Burr, D. M., Wilson, L., & Bargery, A. S. (2009). Floods from fossae: A review of Amazonian-aged extensional–tectonic megaflood channels on Mars,” *Megaflooding on Earth and Mars* (pp. 194–208). <https://doi.org/10.1017/cbo9780511635632.010>

Carr, M. H. (1974). Tectonism and volcanism of the Tharsis region of Mars. *Journal of Geophysical Research*, 79(26), 3943-3949.

Carr, M. H. (1979). Formation of Martian flood features by release of water from confined aquifers. *Journal of Geophysical Research*, 84(B6), 2995. <https://doi.org/10.1029/jb084ib06p02995>

- Carr, M. H. (1996). Channels and valleys on Mars: Cold climate features formed as a result of a thickening cryosphere. *Planetary and Space Science*, 44(11), 1411-1423.
- Carr, M. H. (2000). Martian oceans, valleys and climate. *Astronomy & Geophysics*, 41(3), 3-20.
- Carr, M. H. (2007). *The surface of Mars* (Vol. 6). Cambridge University Press.
- Carr, M. H., & Clow, G. D. (1981). Martian channels and valleys: Their characteristics, distribution, and age. *Icarus*, 48(1), 91-117.
- Carr, M. H., & Head III, J. W. (2003). Oceans on Mars: An assessment of the observational evidence and possible fate. *Journal of Geophysical Research: Planets*, 108(E5).
- Carr, M. H., & Head, J. W. (2010). "Geologic history of Mars." *Earth and Planetary Science Letters*, 294(3-4), 185-203.
- Carter, J., & Poulet, F. (2013). Ancient plutonic processes on Mars inferred from the detection of possible anorthositic terrains. *Nature Geoscience*, 6(12), 1008-1012.
- Cassanelli, J. P., & Head, J. W. (2018). Large-scale lava-ice interactions on Mars: Investigating its role during Late Amazonian Central Elysium Planitia volcanism and the formation of Athabasca Valles. *Planetary and Space Science*, 158, 96-109.
- Ceylan, S., Clinton, J. F., Giardini, D., Stähler, S. C., Horleston, A., Kawamura, T., ... & Banerdt, W. B. (2022). The marsquake catalogue from insight, sols 0–1011. *Physics of the Earth and Planetary Interiors*, 333, 106943.
- Chambers, J. E. (2004). Planetary accretion in the inner Solar System. *Earth and Planetary Science Letters*, 223(3-4), 241-252.
- Chapman, M. G., Neukum, G., Dumke, A., Michael, G., van Gasselt, S., Kneissl, T., et al. (2010). Amazonian geologic history of the Echus Chasma and Kasei Valles system on Mars: New data and interpretations. *Earth and Planetary Science Letters*, 294(3–4), 238–255. <https://doi.org/10.1016/j.epsl.2009.11.034>

Christensen, P. R., Engle, E., Anwar, S., Dickenshied, S., Noss, D., Gorelick, N., & Weiss-Malik, M. (2009, December). JMARS-a planetary GIS. In AGU fall meeting Abstracts (Vol. 2009, pp. IN22A-06).

Clifford, S. M. (1993). A model for the hydrologic and climatic behavior of water on Mars. *Journal of Geophysical Research: Planets*, 98(E6), 10973-11016.

Clifford, S. M., & Parker, T. J. (2001). The evolution of the Martian hydrosphere: Implications for the fate of a primordial ocean and the current state of the northern plains. *Icarus*, 154(1), 40-79.

Clinton, J. F., Ceylan, S., van Driel, M., Giardini, D., Stähler, S. C., Böse, M., et al. (2021). The Marsquake catalogue from InSight, sols 0–478. *Physics of the Earth and Planetary Interiors*, 310, 106595. <https://doi.org/10.1016/j.pepi.2020.106595>.

Craddock, R. A., & Howard, A. D. (2002). The case for rainfall on a warm, wet early Mars. *Journal of Geophysical Research: Planets*, 107(E11), 21-1.

Cuřín, V., Brož, P., Hauber, E., & Markonis, Y. (2021). Mud flows in the southwestern Utopia Planitia, Mars. <https://doi.org/10.5194/epsc2021-382>

Daubar, I. J., Garcia, R. F., Stott, A. E., Fernando, B., Collins, G. S., Dundas, C. M., ... & Banerdt, W. B. (2024). Seismically detected cratering on Mars: Enhanced recent impact flux? *Science Advances*, 10(26).

Daubar, I. J., Lognonné, P., Teanby, N. A., Collins, G. S., Clinton, J., Stähler, S., ... & Banerdt, B. (2020). A new crater near InSight: Implications for seismic impact detectability on Mars. *Journal of Geophysical Research: Planets*, 125(8), e2020JE006382.

Daubar, I. J., McEwen, A. S., Byrne, S., Kennedy, M. R., & Ivanov, B. (2013). The current Martian cratering rate. *Icarus*, 225(1), 506-516.

Debaille, V., Brandon, A. D., Yin, Q. Z., & Jacobsen, B. (2007). Coupled ¹⁴²Nd–¹⁴³Nd evidence for a protracted magma ocean in Mars. *Nature*, 450(7169), 525-528.

Dundas, C. M., Bramson, A. M., Ojha, L., Wray, J. J., Mellon, M. T., Byrne, S., ... & Holt, J. W. (2018). Exposed subsurface ice sheets in the Martian mid-latitudes. *Science*, 359(6372), 199-201.

Dundas, C. M., Byrne, S., McEwen, A. S., Mellon, M. T., Kennedy, M. R., Herkenhoff, K. E., & Thomas, N. (2018). Exposed subsurface ice sheets in the Martian mid-latitudes. *Science*, 359(6372), 199-201.

Dundas, C. M., Mellon, M. T., Conway, S. J., Daubar, I. J., Williams, K. E., Ojha, L., ... & Pathare, A. V. (2021). Widespread exposures of extensive clean shallow ice in the midlatitudes of Mars. *Journal of Geophysical Research: Planets*, 126(3), e2020JE006617.

Dundas, C. M., Conway, S. J., & Cushing, G. E. (2022). Martian gully activity and the gully sediment transport system. *Icarus*, 386, 115133.

Edgett, K. S., & Rice, J. W. (1995, March). Very young volcanic, lacustrine, and fluvial features of the Cerberus and Elysium basin region, Mars: Where to send the 1999 Mars Surveyor Lander. In *Abstracts of the Lunar and Planetary Science Conference*, volume 26, page 357,(1995) (Vol. 26).

Ehlmann, B. L., Anderson, F. S., Andrews-Hanna, J., Catling, D. C., Christensen, P. R., Cohen, B. A., ... & Zahnle, K. J. (2016). The sustainability of habitability on terrestrial planets: Insights, questions, and needed measurements from Mars for understanding the evolution of Earth-like worlds. *Journal of Geophysical Research: Planets*, 121(10), 1927-1961.

Ehlmann, B. L., Mustard, J. F., Murchie, S. L., Poulet, F., Bishop, J. L., Brown, A. J., ... & Bibring, J. P. (2011). Subsurface water and clay mineral formation during the early history of Mars. *Nature*, 479(7371), 53-60.

Elkins-Tanton, L. T. (2012). Magma oceans in the inner solar system. *Annual Review of Earth and Planetary Sciences*, 40(1), 113-139.

Ernst, R., Grosfils, E., & Mège, D. (2002). Giant Dike Swarms: Earth, Venus, and Mars. *Annual Review of Earth and Planetary Sciences*, 29(1), 489–534.

<https://doi.org/10.1146/annurev.earth.29.1.489>

- Fassett, C. I., & Head III, J. W. (2008). Valley network-fed, open-basin lakes on Mars: Distribution and implications for Noachian surface and subsurface hydrology. *Icarus*, 198(1), 37-56.
- Fassett, C. I., & Head, J. W. (2011). Sequence and timing of conditions on early Mars. *Icarus*, 211(2), 1204-1214.
- Faure Walker, J., Roberts, G. P., Cowie, P. A., Papanikolaou, I., Michetti, A. M., Sammonds, P., & Phillips, R. (2009). Horizontal strain-rates and throw-rates across breached relay-zones, central Italy: Implications for the preservation of throw deficits at points of normal fault linkage. *Journal of Structural Geology*, 31(10), 1145–1160. <https://doi.org/10.1016/j.jsg.2009.06.01>
- Forget, F., Haberle, R. M., Montmessin, F., Levrard, B., & Head, J. W. (2006). Formation of glaciers on Mars by atmospheric precipitation at high obliquity. *science*, 311(5759), 368-371.
- Frey, H. V. (2008). Ages of very large impact basins on Mars: Implications for the late heavy bombardment in the inner Solar System. *Geophysical Research Letters*, 35(13), L13203.
- Gagnon, R. E., Kieft, H., Clouter, M. J., & Whalley, E. (1988). Pressure dependence of the elastic constants of ice Ih to 2.8 kbar by Brillouin spectroscopy. *The Journal of Chemical Physics*, 89(8), 4522–4528. <https://doi.org/10.1063/1.454792>
- Galofre, A. G., Bahia, R. S., Jellinek, A. M., Whipple, K. X., & Gallo, R. (2020). Did Martian valley networks substantially modify the landscape?. *Earth and Planetary Science Letters*, 547, 116482.
- Geissler, P. E., Sullivan, R., Golombek, M., Johnson, J. R., Herkenhoff, K., Bridges, N., et al. (2010). Gone with the wind: Eolian erasure of the Mars Rover tracks. *Journal of Geophysical Research*, 115, E00F11. <https://doi.org/10.1029/2010JE003674>
- Geissler, P. E., Sullivan, R., Golombek, M., Johnson, J. R., Herkenhoff, K., Bridges, N., ... & Bell, J. (2010). Gone with the wind: Eolian erasure of the Mars Rover tracks. *Journal of Geophysical Research: Planets*, 115(E7).

Genova, A., Goossens, S., Lemoine, F. G., Mazarico, E., Neumann, G. A., Smith, D. E., & Zuber, M. T. (2016). Seasonal and static gravity field of Mars from MGS, Mars Odyssey and MRO Radio Science. *Icarus*, 272, 228–245.

<https://doi.org/10.1016/j.icarus.2016.02.050>

Ghatan, G. J., Head, J. W., & Wilson, L. (2005). Mangala Valles, Mars: assessment of early stages of flooding and downstream flood evolution. *Earth, Moon, and Planets*, 96(1-2), 1-57.

Giardini, D., Lognonne, P., Banerdt, B., Boese, M., Ceylan, S., Clinton, J., et al. (2020). Seismicity of Mars. *Nature Geoscience*(13), 205–212.

<https://doi.org/10.5194/egusphere-egu2020-20437>

Golder, K. B., Burr, D. M., & Kattenhorn, S. A. (2020). Investigation of target property effects on crater populations in long lava flows: A study in the Cerberus region, Mars, with implications for magma source identification. *Icarus*, 335, 113388.

<https://doi.org/10.1016/j.icarus.2019.113388>

Golombek, M. P., Banerdt, W. B., Tanaka, K. L., & Tralli, D. M. (1992). A prediction of Mars seismicity from surface faulting. *Science*, 258(5084), 979-981.

Golombek, M. P., & Phillips, R. J. (2010). Mars tectonics. *Planetary tectonics*, 11, 183-232.

Gomez-Rivas, E., Griera, A., & Llorens, M.-G. (2015). Fracturing of ductile anisotropic multilayers: influence of material strength. *Solid Earth*, 6, 497–514.

<https://doi.org/10.5194/se-6-497-2015>

Goudge, T. A., Ehlmann, B. L., Fassett, C. I., Head, J. W., Mustard, J. F., Mangold, N., ... & Brown, A. J. (2017, March). Jezero Crater, Mars as a Compelling Site for Future In Situ Exploration. In 48th Annual Lunar and Planetary Science Conference (No. 1964, p. 1197).

Greeley, R., & Spudis, P. D. (1981). Volcanism on Mars. *Reviews of Geophysics*, 19(1), 13-41.

Greeley, R., & Guest, J. (1987). Geological Survey (US), Geologic map of the eastern equatorial region of Mars (Vol. 1). The Survey.

- Grott, M., Baratoux, D., Hauber, E., Sautter, V., Mustard, J., Gasnault, O., ... & Toplis, M. J. (2013). Long-term evolution of the Martian crust-mantle system. *Space Science Reviews*, 174, 49-111.
- Grotzinger, J. P., Sumner, D. Y., Kah, L. C., Stack, K., Gupta, S., Edgar, L., ... & Waters, L. S. (2015). Deposition, exhumation, and paleoclimate of an ancient lake deposit, Gale crater, Mars. *Science*, 350(6257).
- Gudmundsson, A. (1984). Formation of dykes, feeder-dykes, and the intrusion of dykes from magma chambers. *Bulletin Volcanologique*, 47(3), 537-550.
- Gutenberg, B. (1944). Energy ratio of reflected and refracted seismic waves. *Bulletin of the Seismological Society of America*, 34(2), 85-102.
- Hall, J. L., Solomon, S. C., & Head, J. W. (1986). Elysium region, Mars: Tests of lithospheric loading models for the formation of tectonic features. *Journal of Geophysical Research: Solid Earth*, 91(B11), 11377-11392.
- Hamilton, C. W. (2013). Flood lavas associated with the Cerberus Fossae 2 unit in Elysium. *Lunar and Planetary Institute Science Conference Abstracts*, 44, 3070.
Retrieved from
https://www.researchgate.net/publication/258804346_Flood_Lavas_Associated_with_the_Cerberus_Fossae_2_unit_in_Elysium_Planitia_Mars
- Hamilton, W. B. (2015). Terrestrial planets fractionated synchronously with accretion, but Earth progressed through subsequent internally dynamic stages whereas Venus and Mars have been inert for more than 4 billion years. *The Interdisciplinary Earth: A Volume in Honor of Don L. Anderson: Geological Society of America Special Paper*, 514, 123-156.
- Hanna, J. C., & Phillips, R. J. (2005). Hydrological modeling of the Martian crust with application to the pressurization of aquifers. *Journal of Geophysical Research: Planets*, 110(E1).
- Hanna, J. C., & Phillips, R. J. (2006). Tectonic pressurization of aquifers in the formation of Mangala and Athabasca Valles, Mars. *Journal of Geophysical Research: Planets*, 111(E3).

Harbor, J. M. (1992). Numerical modeling of the development of U-shaped valleys by glacial erosion. *The Geological Society of America Bulletin*, 104(10), 1364–1375. [https://doi.org/10.1130/0016-7606\(1992\)104<1364:nmotdo>2.3.co;2](https://doi.org/10.1130/0016-7606(1992)104<1364:nmotdo>2.3.co;2)

Harish, Vijayan, S., Mangold, N., & Bhardwaj, A. (2020). Water-Ice Exposing Scarps Within the Northern Midlatitude Craters on Mars. *Geophysical Research Letters*, 47(14), e2020GL089057.

Hartmann, W. K., & Berman, D. C. (2000). Elysium Planitia Lava flows: Crater count chronology and geological implications. *Journal of Geophysical Research*, 105(E6), 15011–15025. <https://doi.org/10.1029/1999je001189>

Hartmann, W. K., & Berman, D. C. (2000). Elysium Planitia lava flows: Crater count chronology and geological implications. *Journal of Geophysical Research*, 105(E6), 15,011–15,025. <https://doi.org/10.1029/1999JE001189>

Hauber, E., Brož, P., Jagert, F., Jodłowski, P., & Platz, T. (2011). Very recent and wide-spread basaltic volcanism on Mars. *Geophysical Research Letters*, 38(10).

Head, J. W., & Marchant, D. R. (2003). Cold-based mountain glaciers on Mars: Western Arsia Mons. *Geology*, 31(7), 641-644.

Head, J. W., Marchant, D. R., Agnew, M. C., Fassett, C. I., & Kreslavsky, M. A. (2006). Extensive valley glacier deposits in the northern mid-latitudes of Mars: Evidence for Late Amazonian obliquity-driven climate change. *Earth and Planetary Science Letters*, 241(3-4), 663-671.

Head, J. W., III., & Wilson, L. (2002). Mars: A review and synthesis of general environments and geological settings of magma-H₂O interactions. Geological Society, London, Special Publications, 202(1), 27–57. <https://doi.org/10.1144/GSL.SP.2002.202.01.03>

Head, J. W., Wilson, L., & Mitchel, K. L. (2003). Generation of recent massive water floods at Cerberus Fossae, Mars by dike emplacement, cryospheric cracking, and confined aquifer groundwater release. *Geophysical Research Letters*, 30(11), 1577. <https://doi.org/10.1029/2003GL017135>

Hjartardóttir, Á. R., Einarsson, P., Gudmundsson, M. T., & Högnadóttir, T. (2016). Fracture movements and graben subsidence during the 2014 Bárðarbunga dike intrusion in Iceland. *Journal of Volcanology and Geothermal Research*, 310, 242-252.

Hoffman, N. (2000). White Mars: A new model for Mars' surface and atmosphere based on CO₂. *Icarus*, 146(2), 326-342.

Holsapple, K. A., & Housen, K. R. (2007). A crater and its ejecta: An interpretation of Deep Impact. *Icarus*, 191(2), 586-597.

Horvath, D. G., Moitra, P., Hamilton, C. W., Craddock, R. A., & Andrews-Hanna, J. C. (2021). Evidence for geologically recent explosive volcanism in Elysium Planitia, Mars. *Icarus*, 365, 114499. <https://doi.org/10.1016/j.icarus.2009.09.011>

Hynek, B. M., Beach, M., & Hoke, M. R. (2010). Updated global map of Martian valley networks and implications for climate and hydrologic processes. *Journal of Geophysical Research: Planets*, 115(E9).

Jackson, C. A. L., Gawthorpe, R. L., & Sharp, I. R. (2002). Growth and linkage of the East Tanka fault zone, Suez rift: structural style and syn-rift stratigraphic response. *Journal of the Geological Society*, 159, 175–187.

Jacob, A., Plasman, M., Perrin, C., Fuji, N., Lognonné, P., Xu, Z., ... & Banerdt, W. B. (2022). Seismic sources of InSight marsquakes and seismotectonic context of Elysium Planitia, Mars. *Tectonophysics*, 837, 229434.

Jaeger, W. L., Keszthelyi, L. P., McEwen, A. S., Dundas, C. M., & Russell, P. S. (2007). Athabasca Valles, Mars: A lava-draped channel system. *Science*, 317(5845), 1709–1711. <https://doi.org/10.1126/science.1143315>

Jaeger, W. L., Keszthelyi, L., Skinner, J., Milazzo, M., McEwen, A., Titus, T., et al. (2010). Emplacement of the youngest flood lava on Mars: A short, turbulent story. *Icarus*, 205(1), 230–243. <https://doi.org/10.1016/j.icarus.2009.09.011>

Jakosky, B. M., & Phillips, R. J. (2001). Mars' volatile and climate history. *nature*, 412(6843), 237-244.

Jakosky, B. M., Lin, R. P., Grebowsky, J. M., Luhmann, J. G., Mitchell, D. L., Andersson, L., ... & Yelle, R. (2015). MAVEN observations of the response of Mars to an interplanetary coronal mass ejection. *Science*, 350(6261).

Johnson, S. (2006). *Stephen Johnson on Digital Photography*. O'Reilly Media, Inc.

Johnson, C. L., & Phillips, R. J. (2005). Evolution of the Tharsis region of Mars: Insights from magnetic field observations. *Earth and Planetary Science Letters*, 230(3-4), 241-254.

Jones, A. P., McEwen, A. S., Tornabene, L. L., Baker, V. R., Melosh, H. J., & Berman, D. C. (2011). A geomorphic analysis of Hale crater, Mars: The effects of impact into ice-rich crust. *Icarus*, 211(1), 259-272.

Jones, A. P., McEwen, A., Tornabene, L., Baker, V., Melosh, H., & Berman, D. (2011). A geomorphic analysis of Hale Crater, Mars: The effects of impact into ice-rich crust. *Icarus*, 211(1), 259–272. <https://doi.org/10.1016/j.icarus.2010.10.014>

Kattenhorn, S. A., & Meyer, J. A. (2010). Magmatic dikes and megafloods: A protracted history of interactions. Retrieved from https://www.researchgate.net/publication/270572954_Magmatic_dikes_and_megafloods_a_protracted_history_of_interactions_between_magma_and_subsurface_ice_Cerberus_Fossae_Mars

Kedar, S., Panning, M. P., Smrekar, S. E., Stähler, S. C., King, S. D., Golombek, M. P., ... & Banerdt, W. B. (2021). Analyzing low frequency seismic events at Cerberus Fossae as long period volcanic quakes. *Journal of Geophysical Research: Planets*, 126(4), e2020JE006518.

Keefer, D. K. (1984). Landslides caused by earthquakes. *Geological Society of America Bulletin*, 95(4), 406–421. [https://doi.org/10.1130/0016-7606\(1984\)95<406:LCBE>2.0.CO;2](https://doi.org/10.1130/0016-7606(1984)95<406:LCBE>2.0.CO;2)

Keske, A. L., Hamilton, C. W., McEwen, A. S., & Daubar, I. J. (2015). Episodes of fluvial and volcanic activity in Mangala Valles, Mars. *Icarus*, 245, 333–347. <https://doi.org/10.1016/j.icarus.2014.09.040>

- Keszthelyi, L. P., Denlinger, R. P., O'Connell, D. R. H., & Burr, D. M. (2007). Initial insights from 2.5D hydraulic modeling of floods in Athabasca Valles, Mars. *Geophysical Research Letters*, 34(21), L21206. <https://doi.org/10.1029/2007gl031776>
- Keszthelyi, L. P., R. P. Denlinger, D. R. H. O'Connell, and D. M. Burr (2007), Initial insights from 2.5D hydraulic modeling of floods in Athabasca Valles, Mars, *Geophys. Res. Lett.*, 34, L21206, doi:10.1029/2007GL031776.
- Keszthelyi, L., McEwen, A. S., & Thordarson, T. (2000). Terrestrial analogs and thermal models for Martian flood lavas. *Journal of Geophysical Research*, 105(E6), 15027–15049. <https://doi.org/10.1029/1999je001191>
- Kleine, T., Touboul, M., Bourdon, B., Nimmo, F., Mezger, K., Palme, H., ... & Halliday, A. N. (2009). Hf–W chronology of the accretion and early evolution of asteroids and terrestrial planets. *Geochimica et Cosmochimica Acta*, 73(17), 5150-5188.
- Knapmeyer, M., Oberst, J., Hauber, E., Wahlisch, M., Deuchler, C., & Wagner, R. (2006). Working models for spatial distribution and level of Mars' seismicity. *Journal of Geophysical Research*, 111, E11006. <https://doi.org/10.1029/2006JE002708>
- Kreslavsky, M. (2008, September). Young populations of small craters on Mars: A case study. In *European Planetary Science Congress 2008* (p. 237).
- Kruijer, T. S., Kleine, T., Borg, L. E., Brennecka, G. A., & Fisher-Gödde, M. (2017). The early differentiation of Mars inferred from Hf–W chronometry. *Earth and Planetary Science Letters*, 474, 345-354.
- Laskar, J., Correia, A. C., Gastineau, M., Joutel, F., Levrard, B., & Robutel, P. (2004). Long term evolution and chaotic diffusion of the insolation quantities of Mars. *Icarus*, 170(2), 343-364.
- Lauro, S. E., Pettinelli, E., Caprarelli, G., Guallini, L., Rossi, A. P., Mattei, E., ... & Orosei, R. (2021). Multiple subglacial water bodies below the south pole of Mars unveiled by new MARSIS data. *Nature Astronomy*, 5(1), 63-70.
- Leask, H. J., Wilson, L., & Mitchell, K. L. (2006). Formation of Ravi Vallis outflow channel, Mars: Morphological development, water discharge, and duration estimates. *Journal of Geophysical Research: Planets*, 111(E8).

Leverington, D. W. (2004). Volcanic rilles, streamlined islands, and the origin of outflow channels on Mars. *Journal of Geophysical Research*, 109(E10), E10011.

<https://doi.org/10.1029/2004je002311>

Leverington, D. W. (2006). Volcanic processes as alternative mechanisms of landform development at a candidate Crater-Lake site near Tyrrhena Patera, Mars. *Journal of Geophysical Research*, 111(E11), E11002. <https://doi.org/10.1029/2004je002382>

Leverington, D. W. (2011). A volcanic origin for the outflow channels of Mars: Key evidence and major implications. *Geomorphology*, 132(3–4), 51–75.

<https://doi.org/10.1016/j.geomorph.2011.05.022>

Leverington, D. W. (2018). Is Kasei Valles (Mars) the largest volcanic channel in the solar system? *Icarus*, 301, 37–57. <https://doi.org/10.1016/j.icarus.2017.10.007>

Livio, F., Michetti, A. M., Vittori, E., Gregory, L., Wedmore, L., Piccardi, L., et al. (2016). Surface faulting during the August 24, 2016, central Italy earthquake (Mw 6.0): Preliminary results. *Annals of Geophysics*, 59. <https://doi.org/10.4401/ag-7197>

<https://doi.org/10.4401/ag-7197>

Lognonné, P., Banerdt, W. B., Pike, W. T., Giardini, D., Christensen, U., Garcia, R. F., ... & Zweifel, P. (2020). Constraints on the shallow elastic and anelastic structure of Mars from InSight seismic data. *Nature Geoscience*, 13(3), 213-220.

Lorenz, R. D., Nakamura, Y., & Murphy, J. R. (2017). Viking-2 seismometer measurements on Mars: PDS data archive and meteorological applications. *Earth and Space Science*, 4, 681–688. <https://doi.org/10.1002/2017EA000306>

Lucchitta, B. K. (1999). Geologic map of Ophir and central Candor Chasmata (MTM-05072) of Mars (Vol. 1). US Geological Survey.

Malin, M. C., & Edgett, K. S. (2000). Evidence for recent groundwater seepage and surface runoff on Mars. *Science*, 288(5475), 2330-2335.

Malin, M. C., & Edgett, K. S. (2000). Sedimentary rocks of early Mars. *Science*, 290(5498), 1927-1937.

- Malin, M. C., Edgett, K. S., Posiolova, L. V., McColley, S. M., & Dobrea, E. Z. N. (2006). Present-day impact cratering rate and contemporary gully activity on Mars. *science*, 314(5805), 1573-1577.
- Magee, C., & Jackson, C. A. L. (2021). Can we relate the surface expression of dike-induced normal faults to subsurface dike geometry?. *Geology*, 49(4), 366-371.
- Malin, M. C., et al. (2007), Context Camera Investigation on board the Mars Reconnaissance Orbiter, *J. Geophys. Res.*, 112, E05S04, doi:10.1029/2006JE002808.
- Manga, M. (2004). Martian floods at Cerberus Fossae can be produced by groundwater discharge. *Geophysical Research Letters*, 31(2), L02702.
<https://doi.org/10.1029/2003gl018958>
- Manga, M., & Wright, V. (2021). No cryosphere-confined aquifer below insight on Mars. *Geophysical Research Letters*, 48(8), e2021GL093127.
<https://doi.org/10.1029/2021gl093127>
- Marinova, M. M., Aharonson, O., & Asphaug, E. (2008). Mega-impact formation of the Mars hemispheric dichotomy. *Nature*, 453(7199), 1216-1219.
- Masursky, H. (1973). An overview of geological results from Mariner 9. *Journal of Geophysical Research*, 78(20), 4009-4030.
- Max, M. D., & Clifford, S. M. (2001). Initiation of Martian outflow channels: Related to the dissociation of gas hydrate?. *Geophysical Research Letters*, 28(9), 1787-1790.
- McCubbin, F. M., Smirnov, A., Nekvasil, H., Wang, J., Hauri, E., & Lindsley, D. H. (2010). Hydrous magmatism on Mars: A source of water for the surface and subsurface during the Amazonian. *Earth and Planetary Science Letters*, 292(1-2), 132-138.
- McEwen, A. S., Byrne, S., Hansen, C., Daubar, I. J., Sutton, S., Dundas, C. M., ... & Wilson, S. A. (2023). The high-resolution imaging science experiment (HiRISE) in the MRO extended science phases (2009–2023). *Icarus*, 115795.
- McEwen, A. S., Eliason, E. M., Bergstrom, J. W., Bridges, N. T., Hansen, C. J., Delamere, W. A., ... & Weitz, C. M. (2007). Mars reconnaissance orbiter's high

resolution imaging science experiment (HiRISE). *Journal of Geophysical Research: Planets*, 112(E5).

McEwen, A. S., Preblich, B. S., Turtle, E. P., Artemieva, N. A., Golombek, M. P., Hurst, M., ... & Christensen, P. R. (2005). The rayed crater Zunil and interpretations of small impact craters on Mars. *Icarus*, 176(2), 351-381.

McGovern, P. J., Solomon, S. C., Smith, D. E., Zuber, M. T., Simons, M., Wieczorek, M. A., ... & Head, J. W. (2002). Localized gravity/topography admittance and correlation spectra on Mars: Implications for regional and global evolution. *Journal of Geophysical Research: Planets*, 107(E12), 19-1.

McKenzie, D., & Nimmo, F. (1999). The generation of Martian floods by the melting of ground ice above Dykes. *Nature*, 397(6716), 231–233. <https://doi.org/10.1038/16649>

McLennan, S. M. (2012). Geochemistry of Sedimentary Processes on Mars. *Sedimentary Geology of Mars*, 119-138.

Mellon, M. T., & Phillips, R. J. (2001). Recent gullies on Mars and the source of liquid water. *Journal of Geophysical Research: Planets*, 106(E10), 23165-23179.

Meng, X., Xu, Y., Xiao, L., & Xiao, Z. (2020). Permittivity estimation of subsurface deposits in the Elysium–utopia region on Mars with MRO shallow radar sounder data. *The Astronomical Journal*, 159(4), 156.

Milton, D. J. (1973). Water and processes of degradation in the Martian landscape. *Journal of Geophysical Research*, 78(20), 4037-4047.

Mischna, M. A., Baker, V., Milliken, R., Richardson, M., & Forget, F. (2003). Orbital forcing of Martian water and CO₂ cycles: A general circulation model study with geologic implications. *Icarus*, 170(2), 479-487.

Morbidelli, A., Lunine, J. I., O'Brien, D. P., Raymond, S. N., & Walsh, K. J. (2012). Building terrestrial planets. *Annual Review of Earth and Planetary Sciences*, 40(1), 251-275.

Morgan, D. D., Dieval, C., Gurnett, D. A., Duru, F., Dubinin, E. M., Fraenz, M., ... & Plaut, J. J. (2014). Effects of a strong ICME on the Martian ionosphere as detected by

Mars Express and Mars Odyssey. *Journal of Geophysical Research: Space Physics*, 119(7), 5891-5908.

Morgan, G. A., Campbell, B. A., Carter, L. M., Plaut, J. J., & Phillips, R. J. (2013). 3D reconstruction of the source and scale of buried young flood channels on Mars. *Science*, 340(6132), 607–610. <https://doi.org/10.1126/science.1234787>

Morgan, G. A., Dundas, C., Chojnacki, M., Russell, M., Baker, D. M. H., Putzig, N. E., & the Mars SWIM Team. (2022). Searching for the shallowest Martian midlatitude ice: Thermal contraction crack polygon mapping. 53rd Lunar and Planetary Science Conference.

Mouginis-Mark, P. J., Harris, A. J., & Rowland, S. K. (2007). Terrestrial analogs to the calderas of the Tharsis volcanoes on Mars. *Environments on Earth: Clues to the Geology of Mars*. Cambridge University Press, New York, 71-94.

Murchie, S., Arvidson, R., Bedini, P., Beisser, K., Bibring, J. P., Bishop, J., ... & Wolff, M. (2007). Compact reconnaissance imaging spectrometer for Mars (CRISM) on Mars reconnaissance orbiter (MRO). *Journal of Geophysical Research: Planets*, 112(E5).

Murray, J. B.; Balme, M. R.; Muller, J-P. A. L. and Kim, J-R. (2007). Stratigraphical evidence of Elysium sea ice from HiRISE images. In: 38th Lunar and Planetary Science Conference, 12-16 Mar 2007, League City, Texas. <https://oro.open.ac.uk/12583/>

Murray, J. B., Muller, J. P., Neukum, G., Werner, S. C., van Gasselt, S., Hauber, E., ... & HRSC Co-Investigator Team. (2005). Evidence from the Mars Express High Resolution Stereo Camera for a frozen sea close to Mars' equator. *Nature*, 434(7031), 352-356.

Nahm, A. L., Kattenhorn, S. A., & Pendleton, M. W. (2015). *Unraveling the formation mechanism(s) of the Cerberus Fossae, Mars: Evacuated dikes, graben, or both?* Department of Geological Sciences, University of Idaho.

Nahm, A. L., Pendleton, M. W., & Kattenhorn, S. A. (2016). Cerberus Fossae, Mars: The Case for Dike Intrusion-related Formation and Modification. *Acta Geologica Sinica*, 90, 173-174.

- Nakamura, Y., & Anderson, D. L. (1979). Martian wind activity detected by a seismometer at Viking lander 2 site. *Geophysical Research Letters*, 6(6), 499-502.
- Neukum, G., Jaumann, R., Hoffmann, H., Hauber, E., Head, J. W., Basilevsky, A. T., ... & HRSC Co-Investigator Team. (2004). Recent and episodic volcanic and glacial activity on Mars revealed by the High Resolution Stereo Camera. *Nature*, 432(7020), 971-979.
- Neumann, G. A., Rowlands, D. D., Lemoine, F. G., Smith, D. E., & Zuber, M. T. (2001). Crossover analysis of Mars orbiter laser altimeter data. *Journal of Geophysical Research: Planets*, 106(E10), 23753-23768.
- Nimmo, F., & Tanaka, K. (2005). Early crustal evolution of Mars. *Annu. Rev. Earth Planet. Sci.*, 33(1), 133-161.
- Ojha, L., Buffo, J., Karunatillake, S., & Siegler, M. (2020). Groundwater production from geothermal heating on early Mars and implication for early martian habitability. *Science advances*, 6(49).
- Ojha, L., Wilhelm, M. B., Murchie, S. L., McEwen, A. S., Wray, J. J., Hanley, J., ... & Chojnacki, M. (2015). Spectral evidence for hydrated salts in recurring slope lineae on Mars. *Nature Geoscience*, 8(11), 829-832.
- Ordóñez-Etxeberria, I., Hueso, R., and Sánchez-Lavega, A (2018) A systematic search of sudden pressure drops on Gale crater during two Martian years derived from MSL/REMS data. *Icarus*, Volume 299, Pages 308-330, ISSN 0019-1035, <https://doi.org/10.1016/j.icarus.2017.07.032>.
- Orosei, R., Lauro, S. E., Pettinelli, E., Cicchetti, A. N. D. R. E. A., Coradini, M., Cosciotti, B., ... & Seu, R. (2018). Radar evidence of subglacial liquid water on Mars. *Science*, 361(6401), 490-493.
- Pace, B., Visini, F., & Peruzza, L. (2016). FiSH: MATLAB tools to turn fault data into seismic-hazard models. *Seismological Research Letters*, 87(2A), 374-386.
- Panning, M. P., Lognonné, P., Bruce Banerdt, W., Garcia, R., Golombek, M., Kedar, S., ... & Wookey, J. (2017). Planned products of the Mars structure service for the InSight mission to Mars. *Space Science Reviews*, 211, 611-650.

Pendleton, M. W. (2015). Geomorphic evidence for geologically recent groundwater flow associated with the Cerberus Fossae magmatic and volcanic system, Mars. University of Idaho ProQuest Dissertations & Theses, 2015. 1595198.

Perrin, C., Jacob, A., Lucas, A., Myhill, R., Hauber, E., Batov, A., ... & Fuji, N. (2022). Geometry and segmentation of Cerberus Fossae, Mars: Implications for marsquake properties. *Journal of Geophysical Research: Planets*, 127(1), e2021JE007118.

Phillips, R. J., & Grimm, R. E. (1991). Martian seismicity. In *Proceedings of the 22nd Lunar and Planetary Science Conference* (p. 1061).

<https://ui.adsabs.harvard.edu/abs/1991LPI....22.1061P>

Phillips, R. J., Zuber, M. T., Solomon, S. C., Golombek, M. P., Jakosky, B. M., Banerdt, W. B., ... & Hauck II, S. A. (2001). Ancient geodynamics and global-scale hydrology on Mars. *Science*, 291(5513), 2587-2591.

Piqueux, S., Kleinböhl, A., Hayne, P. O., Heavens, N. G., Kass, D. M., McCleese, D. J., et al. (2016). Discovery of a widespread low-latitude diurnal CO₂ frost cycle on Mars. *Journal of Geophysical Research: Planets*, 121, 1174–1189.

<https://doi.org/10.1002/2016JE005034>

Piqueux, S., Kleinböhl, A., Hayne, P. O., Heavens, N. G., Kass, D. M., McCleese, D. J., ... & Shirley, J. H. (2016). Discovery of a widespread low-latitude diurnal CO₂ frost cycle on Mars. *Journal of Geophysical Research: Planets*, 1

Plescia, J. B. (1990). Recent flood lavas in the Elysium region of Mars. *Icarus*, 88(2), 465-490.

Plescia, J. B. (2003). Cerberus fossae, Elysium, Mars: A source for lava and water. *Icarus*, 164(1), 79–95. [https://doi.org/10.1016/s0019-1035\(03\)00139-8](https://doi.org/10.1016/s0019-1035(03)00139-8)

Plescia, J. B. (2003). Cerberus Fossae, Elysium, Mars: a source for lava and water. *Icarus*, 164(1), 79-95.

Poulet, F., Bibring, J. P., Mustard, J. F., Gendrin, A., Mangold, N., Langevin, Y., ... & Gondet, B. (2005). Phyllosilicates on Mars and implications for early Martian climate. *Nature*, 438(7068), 623-627.

Rivas-Dorado, S., Ruíz, J., & Romeo, I. (2022). Giant dikes and dike-induced seismicity in a weak crust underneath Cerberus Fossae, Mars. *Earth and Planetary Science Letters*, 594, 117692. <https://doi.org/10.1016/j.epsl.2022.117692>

Robbins, S. J. (2023). Mars Global Surveyor's Mars Orbiter Camera (MOC) Wide-Angle Images (1999–2006): 2. Data Investigation Into North Polar Hood Formation, Broad Brightness Changes in Acidalia, and Seasonal Frost in Hellas. *Journal of Geophysical Research: Planets*, 128(8), e2022JE007621.

Robbins, S. J., Di Achille, G., & Hynek, B. M. (2011). The volcanic history of Mars: High-resolution crater-based studies of the calderas of 20 volcanoes. *Icarus*, 211(2), 1179-1203.

Roberts, G. P., Matthews, B., Bristow, C., Guerrieri, L., & Vetterlein, J. (2012). Possible evidence of paleomarsquakes from fallen boulder populations, Cerberus Fossae, Mars. *Journal of Geophysical Research*, 117, E02009.

Rodriguez, J. A., Sasaki, S., Kuzmin, R. O., Dohm, J. M., Tanaka, K. L., Miyamoto, H., ... & Ferris, J. C. (2005). Outflow channel sources, reactivation, and chaos formation, Xanthe Terra, Mars. *Icarus*, 175(1), 36-57.

Rubin, A. M. (1992). Dike-induced faulting and graben subsidence in volcanic rift zones. *Journal of Geophysical Research*, 97(B2), 1839–1858. <https://doi.org/10.1029/91jb02170>

Rubin, A. M., & Pollard, D. D. (1988). Dike-induced faulting in rift zones of Iceland and Afar. *Geology*, 16(5), 413-417.

Sakimoto, S. E. H. (2005). Martian Polar Craters: Possible Polar Materials Apparent Effects and Post-Impact Modification by Apparent Perennial Permafrost Mound (Pingo) Formation. In *Workshop on the Role of Volatiles and Atmospheres on Martian Impact Craters* (Vol. 1273, pp. 94-95).

Schlische, R. W., Young, S. S., Ackermann, R. V., & Gupta, A. (1996). Geometry and scaling relations of a population of very small rift-related normal faults. *Geology*, 24, 683–686.

Scott, D. H., & Chapman, M. G. (1991). Mars Elysium Basin: Geologic/volumetric analyses of a young lake and exobiologic implications. In IN: Lunar and Planetary Science Conference, 21st, Houston, TX, Mar. 12-16, 1990, Proceedings (A91-42332 17-91). Houston, TX, Lunar and Planetary Institute, 1991, p. 669-677 (Vol. 21, pp. 669-677).

Scott, D. H., & Tanaka, K. L. (1986). Geologic map of the western equatorial region of Mars (Vol. 1). Geological Survey (US).

Skodras, A., Christopoulos, C., & Ebrahimi, T. (2001). "The JPEG 2000 Still Image Compression Standard." *IEEE Signal Processing Magazine*, 18(5), 36-58.

Smith, D. E., Sjogren, W. L., Tyler, G. L., Balmino, G., Lemoine, F. G., & Konopliv, A. S. (1999). The gravity field of Mars: results from Mars Global Surveyor. *Science*, 286(5437), 94-97.

Smith, D. E., Zuber, M. T., Solomon, S. C., Phillips, R. J., Head, J. W., Garvin, J. B., ... & Duxbury, T. C. (1999). The global topography of Mars and implications for surface evolution. *science*, 284(5419), 1495-1503.

Smith, D., Zuber, M. T., Neumann, G. A., & Jester, P. (2003). Mars Global Surveyor Laser Altimeter Precision Experiment Data Record (NASA Planetary Data System, MGS-M-MOLA-3-PEDR-L1A-V1.0). NASA.

Stähler, S. C., Mittelholz, A., Perrin, C., Kawamura, T., Kim, D., Knapmeyer, M., ... & Banerdt, W. B. (2022). Tectonics of Cerberus Fossae unveiled by marsquakes. *Nature Astronomy*, 6(12), 1376-1386.

Stillman, D. E., Bue, B. D., Wagstaff, K. L., Primm, K. M., Michaels, T. I., & Grimm, R. E. (2020). Evaluation of wet and dry recurring slope lineae (RSL) formation mechanisms based on quantitative mapping of RSL in Garni Crater, Valles Marineris, Mars. *Icarus*, 335, 113420.

Tanaka, K. L. (1986), The stratigraphy of Mars, *J. Geophys. Res.*, 91(B13), E139–E158, doi:10.1029/JB091iB13p0E139.

Tanaka, K. L. (1999). Debris-flow origin for the Simud/Tiu deposit on Mars. *Journal of Geophysical Research: Planets*, 104(E4), 8637-8652.

Tanaka, K. L., & Chapman, M. G. (1990). The relation of catastrophic flooding of Mangala Valles, Mars, to faulting of Memnonia Fossae and Tharsis volcanism. *Journal of Geophysical Research: Solid Earth*, 95(B9), 14315-14323.

Tanaka, K.L., Chapman, M.G. and Scott, D.H. (1992) 19920101, Geologic map of the Elysium region of Mars: <https://doi.org/10.5066/P97NUOKK>.

Tanaka, K. L., Robbins, S. J., Fortezzo, C. M., Skinner Jr, J. A., & Hare, T. M. (2014). The digital global geologic map of Mars: Chronostratigraphic ages, topographic and crater morphologic characteristics, and updated resurfacing history. *Planetary and Space Science*, 95, 11-24.

Tanaka, K. L., Skinner, J. A., & Hare, T. M. (2005). "Geologic map of the northern plains of Mars," scientific investigations map. Preprint. <https://doi.org/10.3133/sim2888>

Tanaka, K. L., Skinner, J. A., & Hare, T. M. (2005). Geologic map of the Northern Plains of Mars. Pamphlet to accompany Scientific Investigations Map 2888, USGS for NASA. <https://pubs.usgs.gov/sim/2005/2888/>

Taubman, D., & Marcellin, M. (2002). JPEG2000: Image Compression Fundamentals, Standards and Practice.

Taylor, J., Teanby, N. A., & Wookey, J. (2013). Estimates of seismic activity in the Cerberus Fossae region of Mars. *Journal of Geophysical Research: Planets*, 118, 2570–2581. <https://doi.org/10.1002/2013JE004469>

Tentler, T. (2005). Propagation of brittle failure triggered by magma in Iceland. *Tectonophysics*, 406(1-2), 17-38.

Tosca, N. J., Ahmed, I. A., Tutolo, B. M., Ashpitel, A., & Hurowitz, J. A. (2018). Magnetite authigenesis and the warming of early Mars. *Nature geoscience*, 11(9), 635-639

Utsu, T. (1965). A method for determining the value of b in a formula $\log n = a - bM$ showing the magnitude frequency relation for earthquakes. *Geophys. Bull. Hokkaido Univ.*, 13, 99-103.

van der Bogert, C. H., Hiesinger, H., Dundas, C. M., Krüger, T., McEwen, A. S., Zanetti, M., & Robinson, M. S. (2017). Origin of discrepancies between crater size-frequency distributions of coeval lunar geologic units via target property contrasts. *Icarus*, 298, 49-63. <https://doi.org/10.1016/j.icarus.2016.11.040>

van der Bogert, C. H., Hiesinger, H., McEwen, A. S., Dundas, C., Bray, V., Robinson, M. S., Plescia, J. B., Reiss, D., Klemm, K., & LROC Team. (2010). Discrepancies Between Crater Size-Frequency Distributions on Ejecta and Impact Melt Pools at Lunar Craters: An Effect of Differing Target Properties? In 41st Lunar and Planetary Science Conference, held March 1-5, 2010 in The Woodlands, Texas (LPI Contribution No. 1533, p. 2165).

Vaucher, J., Baratoux, D., Mangold, N., Pinet, P., Kurita, K., & Gregoire, M. (2009). The volcanic history of central Elysium Planitia: Implications for Martian magmatism. *Icarus*, 204(2), 418–442. <https://doi.org/10.1016/j.icarus.2009.06.032>

Vermilye, J. M., & Scholz, C. H. (1995). Relation between vein length and aperture. *Journal of structural geology*, 17(3), 423-434.

Vetterlein, J., & Roberts, G. P. (2009). Postdating of flow in Athabasca Valles by faulting of the Cerberus Fossae, Elysium Planitia, Mars. *Journal of Geophysics Research*, 114, E07003. <https://doi.org/10.1029/2009JE003356>

Vetterlein, J., & Roberts, G. P. (2010). Structural evolution of the northern Cerberus Fossae graben system, Elysium Planitia, Mars. *Journal of Structural Geology*, 32(4), 394–406. <https://doi.org/10.1016/j.jsg.2009.11.004>

Vittori, E., Di Manna, P., Blumetti, A. M., Comerci, V., Guerrieri, L., Esposito, E., ... & Cowie, P. A. (2011). Surface faulting of the 6 April 2009 M w 6.3 L'Aquila earthquake in central Italy. *Bulletin of the Seismological Society of America*, 101(4), 1507-1530.

Voigt, J. R. C., & Hamilton, C. W. (2018). Investigating the volcanic versus aqueous origin of the surficial deposits in eastern Elysium Planitia, Mars. *Icarus*, 309, 389–410. <https://doi.org/10.1016/j.icarus.2018.03.009>

Voigt, J. R. C., Hamilton, C. W., Scheidt, S. P., Munzer, U., Hoskuldsson, A., Jonsdottir, I., & Thordarson, T. (2021). Geomorphological characterization of the 2014–

2015 Holuhraun lava flow-field in Iceland. *Journal of Volcanology and Geothermal Research*, 419, 107278. <https://doi.org/10.1016/j.jvolgeores.2021.107278>

Voigt, J. R., Hamilton, C. W., Steinbrügge, G., Christoffersen, M. S., Nerozzi, S., Kerber, L., ... & Carter, L. M. (2023). Revealing Elysium Planitia's young geologic history: Constraints on lava emplacement, areas, and volumes. *Journal of Geophysical Research: Planets*, 128(12), e2023JE007947.

Wallace, G. K. (1991). "The JPEG Still Picture Compression Standard." *Communications of the ACM*, 34(4), 30-44.

Watters, T. R., Campbell, B., Carter, L., Leuschen, C. J., Plaut, J. J., Picardi, G., ... & Stofan, E. R. (2007). Radar sounding of the Medusae Fossae Formation Mars: equatorial ice or dry, low-density deposits?. *Science*, 318(5853), 1125-1128.

Watters, T. R., McGovern, P. J., & Irwin, R. P. (2007). Hemispheres apart: The crustal dichotomy on Mars. *Annu. Rev. Earth Planet. Sci.*, 35(1), 621-652.

Wells, D. L., & Coppersmith, K. J. (1994). New empirical relationships among magnitude, rupture length, rupture width, rupture area, and surface displacement. *Bulletin of the Seismological Society of America*, 84(4), 974–1002.

Werner, S. C. (2008). The early Martian evolution—Constraints from basin formation ages. *Icarus*, 195(1), 45-60.

Werner, S. C., Ivanov, B. A., & Neukum, G. (2009). Theoretical analysis of secondary cratering on Mars and an image-based study on the Cerberus Plains. *Icarus*, 200(2), 406-417.

Wiemer, S., & Wyss, M. (2000). Minimum Magnitude of Completeness in Earthquake Catalogs: Examples from Alaska, the Western United States, and Japan. *Bulletin of the Seismological Society of America*, 90(4), 859-869.

Wilson, L., Ghatan, G. J., Head, J. W., & Mitchell, K. L. (2004). Mars outflow channels: A reappraisal of the estimation of water flow velocities from water depths, regional slopes, and channel floor properties. *Journal of Geophysical Research: Planets*, 109(E9).

Xiong, S., Tao, Y., Persaud, D. M., Campbell, J. D., Putri, A. R. D., & Muller, J. P. (2021). Subsurface reflectors detected by SHARAD reveal stratigraphy and buried channels over central Elysium Planitia, Mars. *Earth and Space Science*, 8(1), e2019EA000968.

Zegers, T. E., Oosthoek, J. H., Rossi, A. P., Blom, J. K., & Schumacher, S. (2010). Melt and collapse of buried water ice: An alternative hypothesis for the formation of chaotic terrains on Mars. *Earth and Planetary Science Letters*, 297(3-4), 496-504.

Zenhäusern, G., Wójcicka, N., Stähler, S. C., Collins, G. S., Daubar, I. J., Knapmeyer, M., ... & Giardini, D. (2024). An estimate of the impact rate on Mars from statistics of very-high-frequency marsquakes. *Nature Astronomy*, 1-10.

Zimbelman, J. R., Craddock, R. A., Greeley, R., & Kuzmin, R. O. (1992). Volatile history of Mangala Valles, Mars. *Journal of Geophysical Research: Planets*, 97(E11), 18309-18317.

Zuber, M. T., Smith, D., Solomon, S. C., Muhleman, D. O., Head, J. W., Garvin, J. B., ... & Bufton, J. L. (1992). The Mars Observer laser altimeter investigation. *Journal of Geophysical Research: Planets*, 97(E5), 7781-7797.

APPENDICES

Appendix A.

The Mars Global Surveyor's Mars Orbiter Laser Altimeter (MOLA) Precision Experiment

The Mars Global Surveyor's Mars Orbiter Laser Altimeter (MOLA) Precision Experiment. Data Record (PEDR) accessed through https://ode.rsl.wustl.edu/mars/pagehelp/Content/Missions_Instruments/MGS/MOLA/Intro.htm. The accompanying Excel chart graphically denotes the exact location of each MOLA PEDR. The extent of the MOLA PEDR was chosen to cover the entire study area for both the work within Chapter 4 and Chapter 5 of this thesis. Given the file size, the data is available at the following link: <https://figshare.com/s/7e2f0093ef33bb6599fb>

Appendix B.

Boulder trail length and width data

Image data used in the calculation of the number of boulder trails per kilometre per image and the calculation of the 10 widest boulder trails for each image, with standard deviation.

Image number	HiRISE image name	Latitude (centered)	Longitude (east)	Map projected	Boulder trails count	Fault Line 1 Count per	Fault Line 2 Count per	10 Widest boulder	σ
1	PSP_008502_1965	16.250°	160.575°	25 cm/pixel	5		5	0	0
2	ESP_018774_1965	16.085°	160.723°	50 cm/pixel	3.4		3.4	1.896	0.47728864
3	PSP_006999_1965	16.100°	160.828°	25 cm/pixel	17		17	2.868	1.15206867
4	ESP_025011_1965	16.141°	161.011°	25 cm/pixel	31		31	4.216	1.22099413
5	ESP_018708_1960	15.819°	161.448°	50 cm/pixel	45		45	2.38	0.72541176
6a	ESP_027345_1955	15.571°	161.792°	50 cm/pixel	4		4	0.42	0.68117545
6b	ESP_027345_1955	15.571°	161.792°	50 cm/pixel	30	30		2.931	0.70457946
8	ESP_026712_1960	15.715°	162.013°	25 cm/pixel	115	115		5.35	0.73219609
9	PSP_006287_1955	15.479°	162.677°	25 cm/pixel	91	91		3.66	1.07723927
10	ESP_018075_1955	15.386°	162.928°	25 cm/pixel	56	56		7.103	2.84332376
11	ESP_028400_1955	15.329°	163.242°	25 cm/pixel	28.9	28.9		3.915	1.57233196
12	PSP_010361_1955	15.311°	163.336°	25 cm/pixel	91	30.41		2.035	0.56598488
13	PSP_007790_1955	15.209°	163.657°	25 cm/pixel	2	2		0.16	0.50596443

10 widest boulder trails for each image	Image 1	Image 2	Image 3	Image 4	Image 5	Image 6a	Image 6b	Image 8	Image 9	Image 10	Image 11	Image 12	Image 13
1	0	1.82	4.09	5.22	1.4	1.5	3.22	4.5	2.4	8.23	2.25	2.15	0
2	0	1.49	2.19	2.34	1.9	1.5	3.81	4.3	2.8	5.52	2.99	1.69	1.6
3	0	1.75	1.83	5.1	3.4	1.2	1.52	5.3	3.1	4.23	6.84	1.73	0
4	0	2.39	1.86	5.3	2.8	0	3.16	5.8	5.2	5.49	3.88	2.55	0
5	0	2.04	1.69	6	1.8	0	2.77	5.6	5.6	9.02	3.59	2.47	0
6	0	1.84	2.32	4.2	3.1	0	2.41	5.9	3.4	13.71	3.6	3.15	0
7	0	2.96	3.46	4.6	3.1	0	2.21	5.2	3.9	4.08	6.53	1.73	0
8	0	1.83	4.02	3.2	2.1	0	3.53	6.8	2.7	5.92	4.01	1.35	0
9	0	1.44	2.3	3.3	2.7	0	3.17	5.3	4.3	7.6	3.05	2.12	0
10	0	1.4	4.92	2.9	1.5	0	3.51	4.8	3.2	7.23	2.41	1.41	0
Mean	0	1.896	2.868	4.216	2.38	0.42	2.931	5.35	3.66	7.103	3.915	2.035	0.16
σ	0	0.47728864	1.15206867	1.22099413	0.72541176	0.68117545	0.70457946	0.73219609	1.07723927	2.84332376	1.57233196	0.56598488	0.50596443

Appendix C.

Brown, J. R., and Roberts, G. P. (2019). Possible evidence for variation in magnitude for marsquakes from fallen boulder populations, Grjota Valles, Mars. *Journal of Geophysical Research: Planets*

Brown, J. R., and Roberts, G. P. (2019). Possible evidence for variation in magnitude for marsquakes from fallen boulder populations, Grjota Valles, Mars. *Journal of Geophysical Research: Planets*, 124. <https://doi.org/10.1029/2018JE005622>.

[Check for updates](#)

AGU100 ADVANCING EARTH AND SPACE SCIENCE

JGR Planets

RESEARCH ARTICLE
10.1029/2018JE005622

Key Points:

- We use natural seismometers' to show that the regions of Cerberus Fossae and Grjota Valles are possibly seismically active areas on Mars
- Evidence through boulder trails shows that the seismic activity is relatively recent and possibly ongoing
- Data suggest that relatively large events (up to Mw 7–8) have occurred

Supporting Information:

- Supporting Information S1
- Figure S1
- Figure S2
- Figure S3
- Figure S4
- Figure S5
- Figure S6
- Figure S7
- Figure S8
- Figure S9

Correspondence to:
J. R. Brown,
123jrb.jason@gmail.com

Citation:
Brown, J. R., & Roberts, G. P. (2019). Possible evidence for variation in magnitude for marsquakes from fallen boulder populations, Grjota Valles, Mars. *Journal of Geophysical Research: Planets*, 124, 801–822. <https://doi.org/10.1029/2018JE005622>

Received 21 MAR 2018
Accepted 30 JAN 2019
Accepted article online 6 FEB 2019
Published online 18 MAR 2019

©2019. American Geophysical Union.
All Rights Reserved.

Possible Evidence for Variation in Magnitude for Marsquakes From Fallen Boulder Populations, Grjota Valles, Mars

Jason R. Brown¹ and Gerald P. Roberts¹

¹Department of Earth and Planetary Sciences, Birkbeck, University of London, London, UK

Abstract Following observations of mobilized boulder trail populations from Cerberus Fossae, Mars, that have been interpreted as possible evidence of large-magnitude marsquakes rupturing for distances of ~207 km along exposed active faults, additional boulder trail populations were measured along shorter faults within the region of Grjota Valles (50- to 150-km length) to test the hypotheses that (1) these faults are also candidate locations for marsquakes and (2) that marsquake magnitude might be smaller, limited by fault dimensions available for rupture. For a region containing two en echelon graben, boulder trail data define two anomalies with maxima in (a) boulder trails per kilometer and (b) maximum width of boulder trails, one that is ~116 km in length along strike and the other ~70 km in length along strike. Values for the maxima are 45 trails per kilometer and 5-m mean trail width for the 70-km-long anomaly and 115 trails per kilometer with 5.3-m mean trail width for the 116-km-long anomaly, above background values measured elsewhere along these faults of zero trails per kilometer with zero boulder trail widths. If combined with published data from Cerberus Fossae with an ~207-km-long anomaly in boulder trails per km (125 trails per kilometer maxima) and maximum mean boulder trail width (8.5-m maximum trail width), the three data sets suggest correlations between the (a) along-strike length of boulder trail anomalies, (b) boulder trails per kilometer, and (c) maximum boulder trail width. If interpreted as due to single marsquakes, and if the dimensions of these anomalies are a proxy for rupture length, when combined, one interpretation of this is that boulders have been mobilized by marsquakes and that the marsquake magnitude is proportional to the along-strike length of the anomalies. In other words, the data suggest that marsquake magnitude, if that is the cause of the anomalies, is limited by fault length as expected for terrestrial seismically active faults. Such findings suggest that the Martian surface may have been shaken, in the very recent past, by large-magnitude marsquakes. We discuss this in terms of the seismicity of Mars.

Plain Language Summary Boulder trail populations were measured along faults on Grjota Valles, Mars, to test the hypotheses that these faults are locations for possible marsquakes. If the boulder trail populations are due to single marsquakes, one theory is that the boulders were moved in the very recent past by large-magnitude marsquakes. The area we studied showed that there are coincident maxima in boulder trail density and boulder trail widths along the strike of the faults in Grjota Valles, Mars. We also saw that the boulder count values decrease away from the locations of most boulder trails. Our results show us that geographically coincident maxima in boulder trail density per kilometer and boulder trail widths along the fault exist. This suggests that a plausible mechanism to mobilize such populations of boulders is through seismic shaking associated with palaeomarsquakes. Our results point to this possibility because boulders mobilized by seismic shaking display a particular pattern: the number of boulder falls and boulder sizes decrease away from the epicenter. Such research suggests that marsquakes not only occurred on Mars but maybe occurred in the recent past, too. With the Interior Exploration using Seismic Investigations, Geodesy and Heat Transport (InSIGHT) mission now on Mars, its seismometer may well pick up seismic vibrations.

1. Introduction

Given that the diameter of Mars (6,790 km) is much smaller than that of the Earth (12,750 km), it has long been considered that Mars is less geologically active than the Earth because the internal heat source for volcanism and associated faulting would have been lost more quickly (see Roberts et al., 2012, for a discussion). However, studies by Antoine et al. (2010) suggest that endogenic heat sources might well be present within Mars associated with the Cerberus Fossae fault system. Roberts et al. (2012), using

BROWN AND ROBERTS801

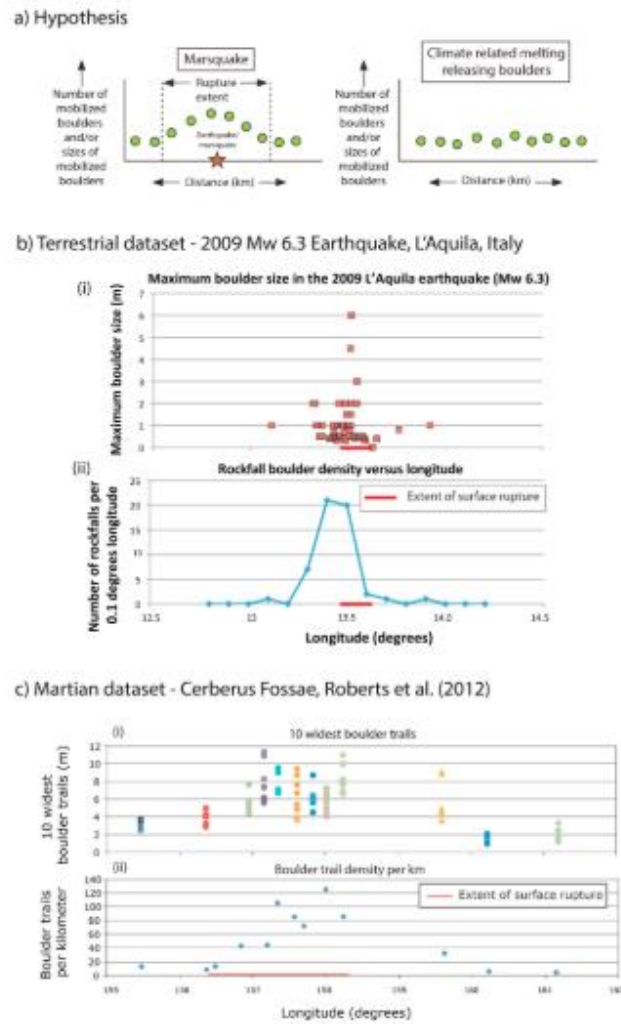


Figure 1. Hypotheses to explain the characteristics of the widest examples of boulder trails formed by the mobilized boulder populations due to seismic shaking and release of boulders from cliffs by melting of ice. (a) Alternative hypotheses explored by Roberts et al. (2012). (b) Terrestrial rockfalls triggered by an earthquake. (c) Data from Roberts et al. (2012) for comparison with data presented in this paper.

understanding of natural seismometers on Earth, suggested that large-magnitude marsquakes may have occurred in the recent past along Cerberus Fossae, evidenced by observations close to faults of anomalies in the density of trails left by mobilized boulders and boulder trail widths (Figures 1 and 2). Roberts et al. (2012) showed, for Cerberus Fossae, that boulder trail densities per kilometer and boulder trail widths increased systematically from background values along the strike of part of the fault system, interpreting

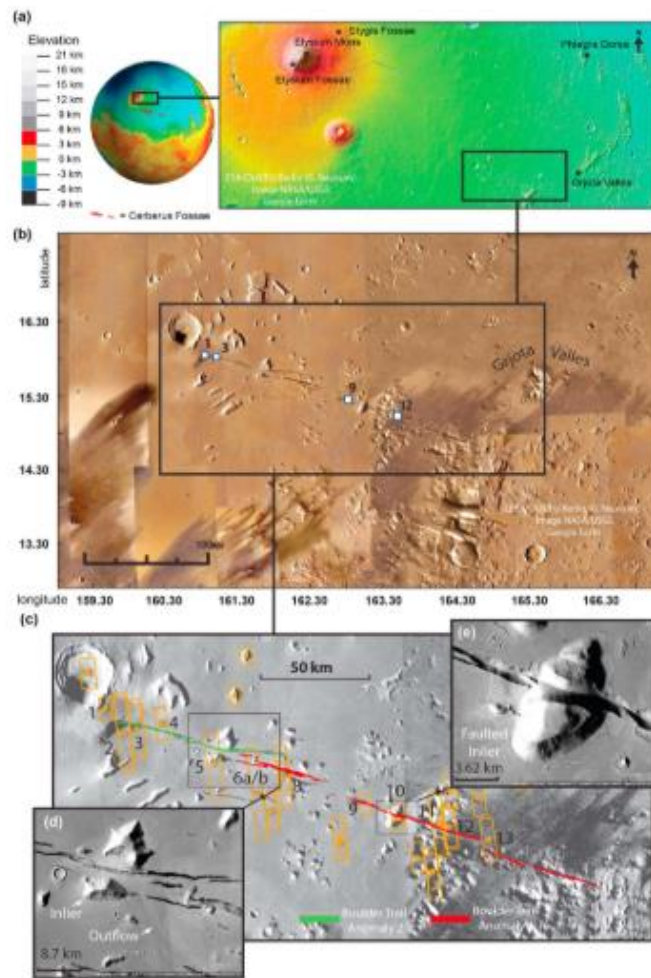


Figure 2. Location maps. (a) Mars Orbiter Laser Altimeter (MOLA) images of Mars showing the location of the study area. (b) National Aeronautics and Space Administration (NASA) image mosaic (visible imagery) with the location of the study area shown. The four white squares show the locations of the four geological and geomorphological interpretations for Images 1, 3, 9 and 12 (see Figures 4a–4d). (c) Map showing location of the studied boulder trail anomalies. Boulder Trail Anomaly 1 (red) and Boulder Trail Anomaly 2 (green) and location of High Resolution Imaging Science Experiment (HiRISE) image footprints across the study area, numbered in accordance with number scheme used in this study. HiRISE images 1 through 13 were used in this study. (d and e) Details of the fault geometries and geomorphology and are located in (c).

this as possible evidence that a marsquake had produced ground shaking responsible for mobilization of the boulders. This study was facilitated by the advent of HiRISE imagery (High Resolution Imaging Science Experiment onboard the Mars Reconnaissance Orbiter) whose high resolution (~25 cm pixel sizes) allowed, for the first time, observations of boulders and boulder trails from orbit, in particular the largest boulders and trails, and hence the ability to map the characteristics of boulder populations along the strike of fault systems. Roberts et al. (2012) suggested that boulder populations mobilized by seismic shaking, in particular the widest boulder trails, would show decreases in mobilized boulder frequency and boulder size over tens of kilometers or more away from putative epicenters if produced by single large events, as observed on the Earth (Figure 1), and evidenced on Mars by the widths of trails in dust left by mobilized boulders. In contrast, boulder populations mobilized by processes facilitating release of boulders from steep cliffs, such as melting of ground ice on steep slopes, would produce spatially uniform boulder trail populations, lacking anomalies with dimensions of tens of kilometers or more. Measurements presented by Roberts et al. (2012) were consistent only with the hypothesis of mobilization by seismic shaking (Figure 1). Furthermore, the trails in the underlying sediment left by boulders as they rolled and bounced downslopes suggest relatively recent boulder mobilization and hence possible ongoing marsquake activity. This is because tracks produced by the rovers Spirit and Opportunity were erased over timescales of only days to months (Geissler et al., 2010), due to the passage of dust storms during the perihelion season, although evidence exists of track preservation for longer periods of time in locations sheltered from the wind; thus, tracks left by boulders would also be erased, suggesting that preserved examples must be relatively young if the material is fine enough to be mobilized by the wind. Tracks produced by boulders at Cerberus Fossae are wider and deeper (several meters and several decimeters) than trails left by rovers (centimeters, centimeters to millimeters) so presumably it would take longer to erase them with eolian processes, but the same arguments apply and it is difficult to envisage an age as old as, for example, 10^6 – 10^7 years for the boulder trails. Roberts et al. (2012) also pointed out that the geographic dimension of the boulder trail width/frequency anomaly, along the strike of the fault system, might be indicative of the magnitude of the marsquake, as is the case on Earth (Keefer, 1984). The ~207-km-wide zone of mobilized boulders measured along Cerberus Fossae might be consistent with a marsquake of moment magnitude ~M7.9 (see Wells & Coppersmith, 1994). A marsquake of this magnitude is not inconsistent with the along-strike extent of the faults of Cerberus Fossae because Vetterlein and Roberts (2009) showed that these faults exhibit continuous along-strike displacement profiles constraining a fault length of ~325 km, longer than the implied rupture extent, although Knapmeyer et al. (2006) suggested a maximum magnitude of 7.6. Vetterlein and Roberts (2010) showed that the $d_{max}/length$ (measured as vertical offset, throw, in this example) of the Cerberus Fossae faults was ~0.1–0.001, similar to those measured on Earth, suggesting that the relationships between slip dimensions and marsquake magnitude might also be similar to the Earth. The question that arises is whether other examples exist on Mars where shorter fault lengths are associated with smaller along-strike extents of boulder trail anomalies, implying smaller moment magnitudes.

In this paper we seek to extend our knowledge of possible marsquakes by investigating whether: (a) other possible examples of boulder trail anomalies can be identified, with evidence ruling out causes other than marsquakes for their formation, and (b) whether marsquakes of different magnitudes and hence different epicentral shaking intensities to mobilize boulders can be inferred. To this end, we have studied another set of faults that are parallel to the southern Cerberus Fossae faults located in the region of Grjota Valles (Figure 2). Faults in the vicinity of Grjota Valles offset (i) planar surfaces that are probably lava flows, (ii) inliers of older terrain such as hills that protrude upward through the lava flows, and (iii) outflow channels that may be of aqueous or volcanic origin associated with volcanism (e.g., Burr, Grier, et al., 2002; Hamilton, 2013; Jaeger et al., 2010; Morgan et al., 2013; Plescia, 2003, for associated examples). This means that the Grjota Valles faults are very similar morphologically to those along Cerberus Fossae studied by Roberts et al. (2012). Like the examples from Cerberus Fossae described by Roberts et al. (2012), initial inspection of down faulted regions in Grjota Valles examples revealed many thousands of boulder trails made by mobilized boulders that have fallen from fault controlled cliffs (Figure 3). However, it is clear from inspection of imagery that the faults associated with Grjota Valles are segmented (Figure 2), with segments that are shorter (maximum of 60–80 km) than those associated with Cerberus Fossae (Taylor et al., 2013; Vetterlein & Roberts, 2009, 2010). This combination of features allows us to test (a) whether anomalies in boulder trail densities and dimensions occur along the faults and are best explained by marsquakes and

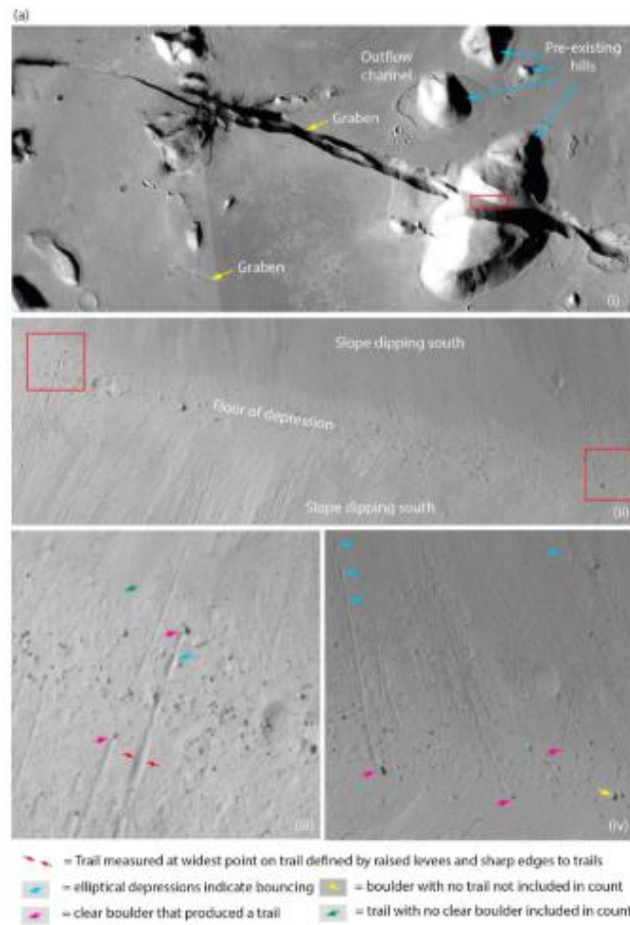


Figure 3. (a) Images showing typical locations and attributes of the boulder trails counted in this study. (b and c) A selection of images showing the variation in boulder trails between different High Resolution Imaging Science Experiment (HiRISE) images and different parts of the same HiRISE images: (i) original image with added white arrows pointing out a selection of boulder trails/bounce marks; (ii) the image with the boulder trail/bounce marks drawn in black, and (iii) with only the black infill. The figures illustrate only a small proportion of the total number of boulder trails in each image. (d) Observations of boulder trails and boulder dimensions. The similarity between the dimensions of boulders and boulder trails suggests that boulder trails have not been significantly affected by erosion. (i) A possible hypothesis is that boulder trails may be degraded by erosion, and that degradation may vary spatially, influencing the number of trails that are preserved, and the widths that are measured. (ii and iii) Comparison of boulder trail widths with the dimensions of the boulders that formed them from ESP_026712_1960 and from ESP_025156_1965. (iv) Location map showing the position of ESP_026712_1960 and ESP_025156_1965. (v) That the trails have not been significantly degraded by wind erosion is consistent with the preservation of raised levees produced by the motion of boulders, evidenced by variation in percentage gray scale for individual pixels in the images. This is evidenced by visual inspection of many examples and also evidenced by the percentage gray scale measurements we have made that show systematic variation in percentage gray scale on the floors of the tracks, not constant values as would be expected for a flat, depositional surface illuminated by the Sun. If the levees are made of sand, and their preservation potential is low, then the ages of the boulder trails whose widths are defined by the levees are likely to be similar, and relatively young. In other words, the widespread preservation of levee crests in the images suggests the

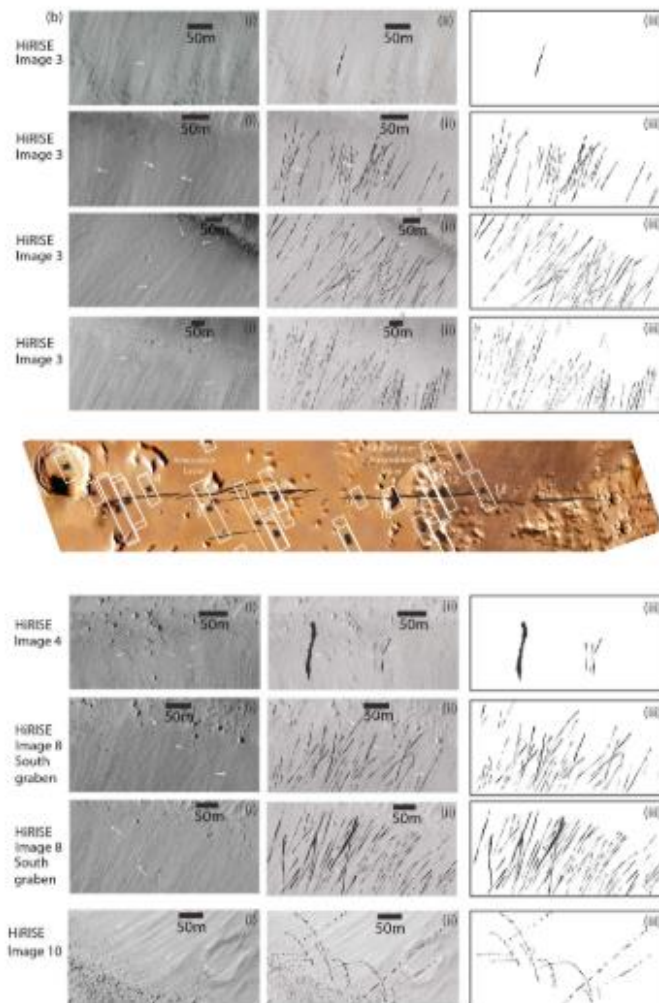


Figure 3b.

(b) if they are best explained by marsquakes, whether their dimensions correlate with the dimensions of fault segments. To this end, we examined all the HiRISE images (Figures 2 and 3) that were available at the time of the study to constrain the extent of boulder trail anomalies (see Figures 2b and 2c and 2a). We explain in detail why we have separated the faults into Boulder Trail Anomaly 1 and Boulder Trail Anomaly 2, based on

boulder trails are similar in age, because they have not been eroded/degraded. And that is what we use to suggest the population of boulder trails is mostly composed of individual trails of similar age, hence possibly produced in single, widespread events, that is, marsquakes.

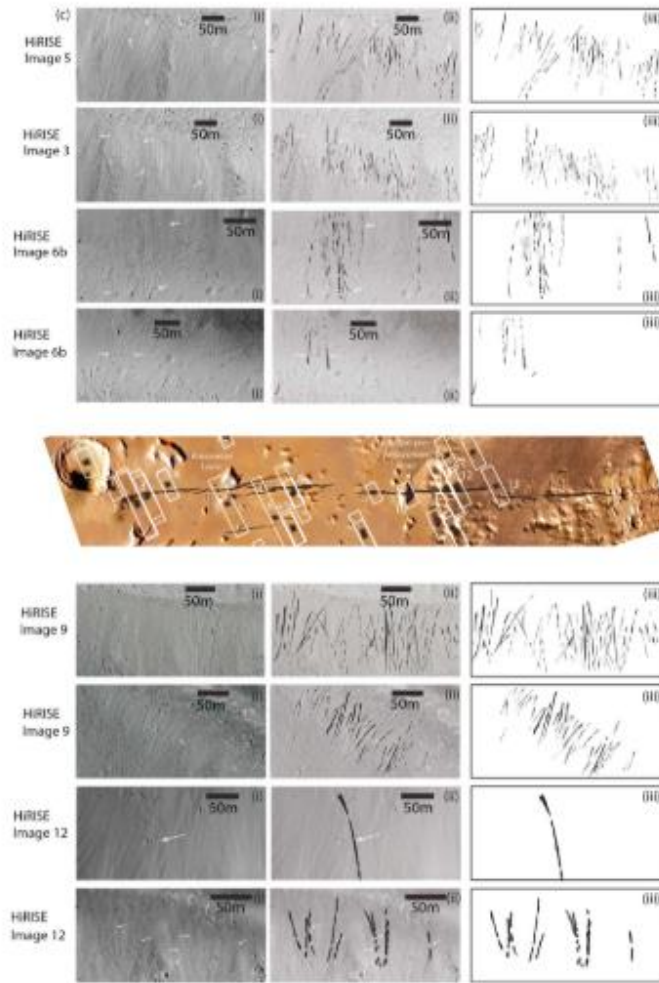


Figure 3c.

boulder trail data, below. We have identified two local maxima in boulder trail densities (that also correlate with boulder trail width) — one associated with each fault line. We discuss these in terms of their most likely mode of formation, concluding that marsquakes may be the most likely cause. We then discuss the results in terms of the possible occurrence of marsquakes with magnitudes controlled by fault dimensions, while also considering that the marsquake activity may well be relatively recent.

First, we present maps of the fault system containing two en echelon graben/faults, one which is ~115-km length along strike and the other ~82 km length along strike (Figures 2–4). Second, we present data concerning the density of boulder trails per kilometer and boulder trail widths. After discussing the cause of the

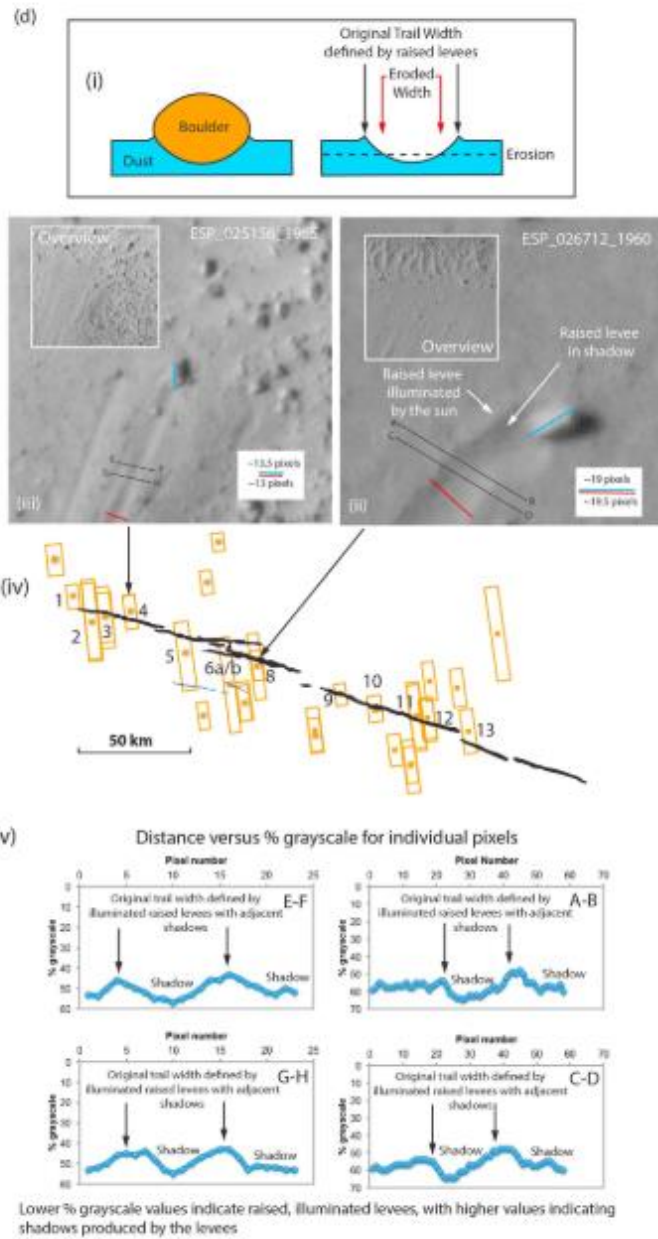


Figure 3d.

boulder trail anomalies, concluding that marsquakes may be the most likely cause of the boulder trail results, and explaining why other causes are unlikely, we conclude that with the two new boulder trail data sets presented in this paper, and the example from Roberts et al. (2012), we have three examples where boulder trail anomaly dimensions correlate with fault lengths and by analogy maximum along-strike rupture extent. Thus, the boulder trail data appear to be consistent with the interpretation that the boulders were mobilized by seismic shaking produced by marsquakes and that boulder-trail data may help reveal the magnitudes of the marsquakes.

2. Geological Background

The fault system we study is located in the vicinity of Grjota Valles and comprises an ~197-km-long set of en echelon graben segments located between latitude N16°10'33", longitude E160°33'48", and latitude N15°12'10"/longitude E163°40'00". The WNW-ESE orientation of the graben means that the fractures are subradial to the Elysium Mons volcano (Figure 2a) and may be the surface expression of subsurface dikes. Detailed geological and geomorphological mapping reveals that the geometry of the faults is consistent with that of graben, with fault controlled cliffs adjacent to flat-bottomed depressions (Figures 3–5). MOLA data (Mars Orbiter Laser Altimeter on the Mars Global Surveyor [MGS] spacecraft) reveal that the vertical offset across the graben, which are exposed on a surface that slopes from ~2,100-m elevation to ~2,400-m elevation from west to east, increases from zero at the tips of the graben to ~900 m at latitude E162° (Figure 5). This reveals an offset/subsidence profile that is typical of faults, with vertical offsets as high as ~900 m, and a d_{\max}/length ratio (with d_{\max} measured as vertical offset for this example) for the whole structure of 0.005, within the range measured for terrestrial faults and those on Mars (Schlische et al., 1996; Vetterlein & Roberts, 2010). In detail, the MOLA data constrain the vertical offset across the graben at 180 locations and reveal displacement gradients and d_{\max}/length ratios associated with individual distal and medial fault segments of 0.008–0.026, again similar to values measured on Earth (Vetterlein & Roberts, 2010; Figure 5). The similarity in d_{\max}/length values between faults in Grjota Valles and the Earth suggests that the material strength is similar in the two regions (Gomez-Rivas et al., 2015). If the material strength is similar, then the relationships between rupture length, d_{\max} , stress drop, and moment magnitude are also likely to be similar (Ali & Shieh, 2013). Thus, our d_{\max}/length observations support the suggestion that these are faults formed by similar deformation processes to those on the Earth and it may be possible to infer some aspects of the seismicity, such as moment magnitude, from observations of surface deformation.

The faults can be shown to be relatively recent in that they crosscut preexisting features of known, relatively young age (Figures 2 and 4). The fossae offset Late Amazonian Cerberus lavas and older inliers (Tanaka et al., 2005). It is believed that the ages of the youngest lavas offset on the nearby Cerberus Fossae, assessed by crater counting methods, are <10 Ma (Hartmann & Berman, 2000; Head et al., 2003; Vaucher et al., 2009), implying that the fossae, if they are all approximately the same age, are even younger. The ~900-m offset revealed by MOLA data (Figure 5), if developed since 10 Ma as implied by crater-count ages, implies a rate of vertical offset of ~0.09 mm/year, a value that is similar to well-documented rift systems on the Earth (Vetterlein & Roberts, 2010). The faults also offset a variety of geomorphic features such as lava plains, older inliers, and outflow channels with streamlined islands (Figure 2; Burr, McEwen, et al., 2002; Jaeger et al., 2010; Plescia, 2003). The similar features were reported for the faults along Cerberus Fossae (Roberts et al., 2012), so we suggest a similar mode and age of formation for the faults in Grjota Valles.

3. Method

We mapped parts of the Grjota Valles fault system in detail to ascertain the nature of the geology of the region and gain an overview of the geomorphic features that the boulders were associated with (Figure 4).

National Aeronautics and Space Administration (NASA) HiRISE images have been accessed using the Planetary Data System (PDS) node at the University of Arizona (<http://hirise.lpl.arizona.edu/>; Table 1). They were downloaded at their highest resolution. The images were imported into Google Earth as georeferenced image overlays. At the time of writing, there were 18 areas covered by HiRISE imagery within the

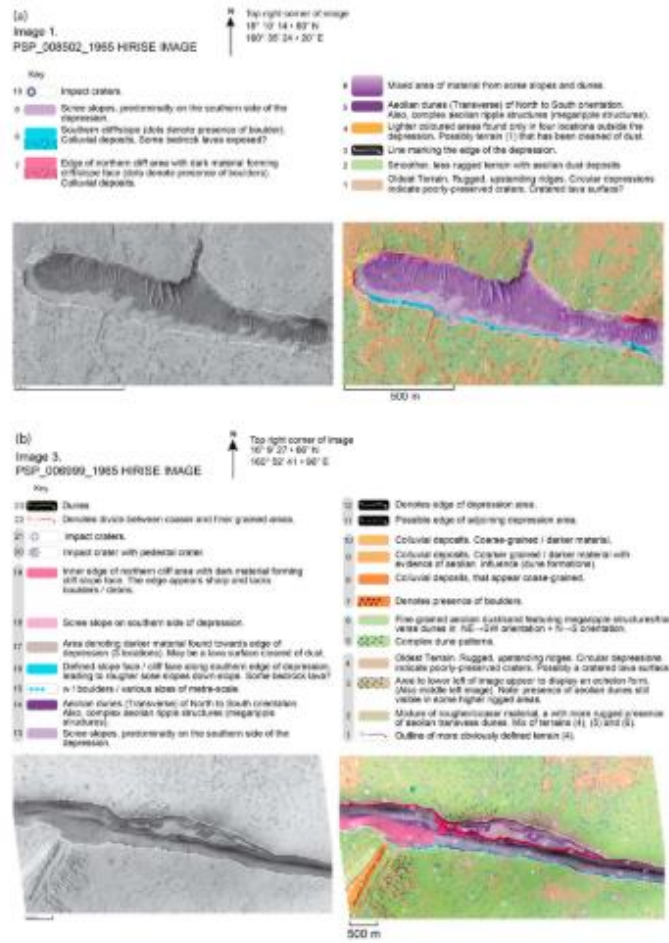


Figure 4. (a-d) Geological and geomorphological interpretations of Images 1, 3, 9, and 12. The geology/geomorphology on the fossae is that of a low-relief plain that has been faulted by graben structures, down-dropping central blocks that have been covered by colluvium and eolian material.

study area of the Grjota Valles (Figure 2). However, six of the locations are covered by two HIRISE images, and one of the images (ESP_027345_1955) covers an area which has six fractures, two of which were required for this study—meaning 12 images were used in total, with one (ESP_027345_1955) split into two images: 6a and 6b. We believe that the number of images available provide sufficient along-strike coverage of the structures for our purposes. The ruler tool in Google Earth was used to measure distances and hence boulder trail lengths and widths, allowing for boulder trail density to be calculated. Roberts et al. (2012) showed that such measurements reproduce the dimensions of ground truthed terrestrial boulders to an extent that is adequate for our purposes. We also checked distance measurements in

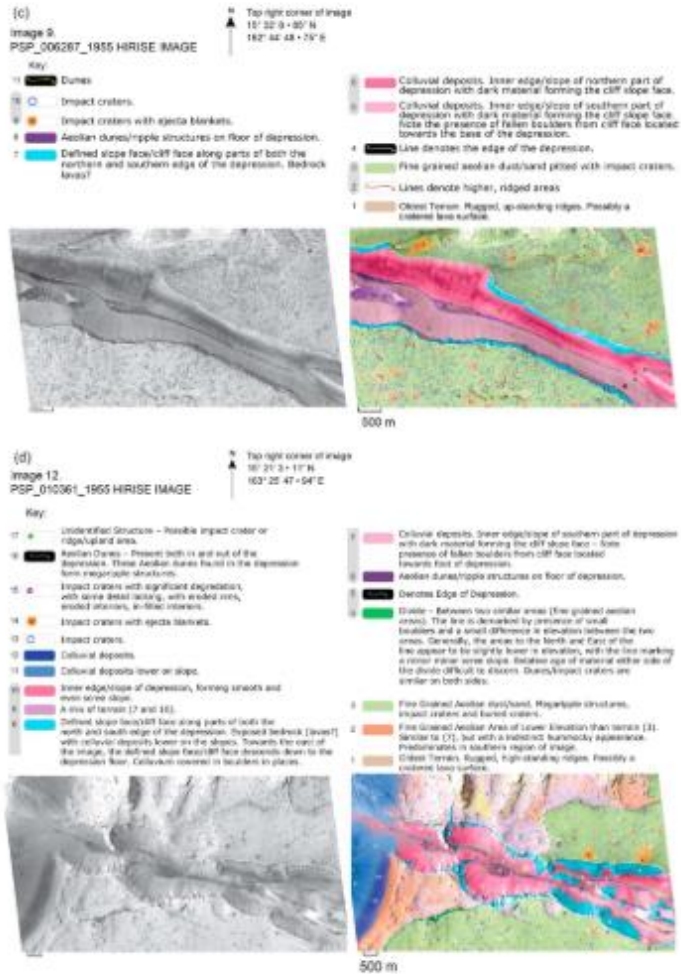


Figure 4b.

ArcGIS and found that this provides values that are similar to the values from Google Earth to an extent that does not affect our conclusions (<1% difference between ArcGIS and Google Earth at the latitudes we are interested in).

We defined the width of boulder trails as the width between what we term *raised levees* or *sharp edges* that formed as the boulder traversed across the underlying substrate (Figures 3a–3d). We included boulder trails without terminal boulders. We measure the width of the trail where the trail is widest to exclude measurements where the boulder was bouncing and leaving a narrower trail. There is cross-image variation in boulder trail density on HIRISE images. Where one can see that the substrate is coarse grained, with visible boulders, no trails exist. Examples of cross trail variations are shown in Figures 3b and 3c. Thus, we

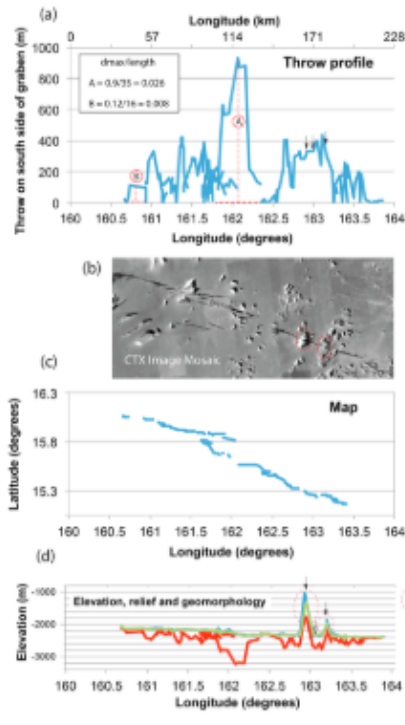


Figure 5. The relationship between the map trace of the graben and vertical offsets constrained by Mars Orbiter Laser Altimeter (MOLA) data. (a) Plot of longitude against vertical offset measured across the south side of the graben from MOLA data. (b) Context Camera (CTX) mosaic showing how the vertical offsets in (a) relate to the map geometry of the graben. (c) The location of MOLA data in latitude and longitude, showing how the vertical offsets in (a) relate to the map geometry of the graben. (d) Plot showing absolute values of elevation for the plain to the south of the graben, the plain north of the graben, and the floor of the graben, versus longitude.

measured the distance across areas where we could gain continuous records on regions where the substrate appeared fine-grained, converting the values into number per kilometer.

For each HiRISE image we measured the following:

1. We recorded the location of every boulder trail that we were able to identify in each of the 13 areas along approximately 1.5- to 6.5-km-long transects along the slopes immediately adjacent to the floors of the graben (e.g., Figure 6). These transects were chosen because (i) they existed at the bases of steep slopes along fault-controlled cliffs and (ii) fine grained deposits (probably eolian sand and dust) were present that preserved boulder trails. We did not make measurements where the surface was formed of coarse-grained sediments (≥ 20 - to 50-cm particle size) or on solid rock because such locations would be unlikely to preserve the passage of mobilized boulders if such motion had occurred. The zigzag lines in Figure 6 show (a) that we proceeded in a general along-strike direction, not returning to along-strike locations where we had already noted boulder trails, because we were concerned that this could result in erroneous double-counting of boulder trails in our inventory, and (b) the exact locations where we measured boulder trail width (blue dots), in general the widest part of the trail, so we could revisit the locations of measurements at a later date if needed. Along-strike distance was recorded as the longitude of each blue dot in Figure 6, for conversion into the values of boulder trails per kilometer in Figure 8 using trigonometry and a conversion factor for degrees longitude into kilometers. In summary, the along track lengths of the zigzag tracks were not used in any calculation but serve to record exactly how we traversed the boulder trail population and exactly where we made measurements. We are confident that we have measured every boulder trail where densities were relatively low (≤ 45 boulder trails per kilometer) because they were clear on the imagery. However, in places it was difficult to recognize every individual boulder trail at higher densities because some boulder trails coalesce; in these locations (≥ 45 boulder trails per kilometer) we think we may have underestimated the number of boulder trails per kilometer, but this does not affect our overall conclusions (e.g., Figure 6, with results in Figures 7 and 8). We also note that if the boulder trails were ≤ 95 cm in width, they would not have been resolved on current imagery, so again this may have led us to underestimate the boulder trail density, but again, this does not affect our conclusions as our hypothesis depends on the largest mobilized and hence the widest boulders trails (Figure 1).

2. We measured the width of the 10 widest boulder trails we could identify in each image, reporting the mean value, to provide an estimate of the dimensions of mobilized boulders.

We were aware that measuring distances using a ruler tool in software on pixelated images can be subjective so the two authors made independent measurements of the same images, with Figure 7a and 7b showing comparisons between results from the two authors. These results show that the results are repeatable with results from the two surveys being broadly comparable within error. The differences between results from the two authors (< 1 m for the mean value for the 10 widest boulder trails and < 10 - 20 boulder trail counts per kilometer) are far smaller than the signals that were measured (between 1 and 5.5 m for the mean value for the 10 widest boulder trails and between 0 and 100 for the boulder trail counts per kilometer). Overall, we are confident that our method for measuring the number of boulder trails and their widths using the ruler tool in Google Earth is robust and repeatable if others were to make measurements from the same images.

Table 1
HiRISE Image Observations Used

Image number used in this paper	HiRISE image name	Latitude (centered)	Longitude (east)	Map projected scale
1	PSP_008502_1965	16.250 ^o	160.575 ^o	25 cm/pixel
2	ESP_018774_1965	16.085 ^o	160.723 ^o	50 cm/pixel
3	PSP_006999_1965	16.100 ^o	160.828 ^o	25 cm/pixel
4	ESP_025011_1965	16.141 ^o	161.011 ^o	25 cm/pixel
5	ESP_018708_1960	15.819 ^o	161.448 ^o	50 cm/pixel
6a	ESP_027345_1955	15.571 ^o	161.792 ^o	50 cm/pixel
6b	ESP_027345_1955	15.571 ^o	161.792 ^o	50 cm/pixel
8	ESP_026712_1960	15.715 ^o	162.013 ^o	25 cm/pixel
9	PSP_006287_1955	15.479 ^o	162.677 ^o	25 cm/pixel
10	ESP_018075_1955	15.386 ^o	162.928 ^o	25 cm/pixel
11	ESP_028400_1955	15.329 ^o	163.242 ^o	25 cm/pixel
12	PSP_010361_1955	15.311 ^o	163.336 ^o	25 cm/pixel
13	PSP_007790_1955	15.209 ^o	163.657 ^o	25 cm/pixel

Note. HiRISE, High Resolution Imaging Science Experiment.

4. Results

The data in Figure 8 show that there are coincident maxima in boulder trail density and boulder trail widths along the strike of the faults in Grjota Valles.

In terms of the spatial variations in boulder trail density along the strike of the fault system, maxima in boulder trail counts exist at around E161.5 and E162.5° longitude. Boulder trail count values decrease both east and west from these locations along the strike of the faults toward their lateral terminations. We use these variations to define Boulder Trail Anomaly 1 and Boulder Trail Anomaly 2 mentioned above and shown in Figure 2c. For Boulder Trail Anomaly 2 we measured a peak of 45 boulder trail counts per kilometer at E161.43° longitude, with lower values recorded closer to the east and west tips of the graben. For Boulder Trail Anomaly 1, a peak of 102 counts per kilometer at E162.03° was measured, again with lower values recorded closer to the east and west tips of the graben.

We note that values for boulder trails per kilometer exhibit an asymmetric pattern along strike (Figures 8a and 8b). The westernmost point of Boulder Trail Anomaly 2 exhibits the smallest number of trails per kilometer at 5 trails per kilometer at E160.57° longitude, with the number of trails increasing as we follow the fault east, culminating in a peak of 45 counts per kilometer at E161.43° longitude. This is followed by a sharp decrease in the number of recorded trails, with 4 per kilometer at E161.74° longitude, giving the graph in Figure 8 an asymmetric appearance. For Boulder Trail Anomaly 1, measurements begin at E161.76° longitude, extremely close to the tip of Boulder Trail Anomaly 2, but at a latitude of N15.81°, some 6 km to the south of the last measured point along Boulder Trail Anomaly 2. The first count along Boulder Trail Anomaly 1 records 30 counts per kilometer at E161.7° followed by a sharp increase in counts, rising to a peak of 102 counts per kilometer at E162.03° longitude, the highest count along the entire fault. Further east the number of counts decreases, dropping to 2 counts per kilometer at E163.63° close to the lateral termination of Boulder Trail Anomaly 1. Again, these measurements give an asymmetric shape (Figure 8b).

Coincident with boulder trail counts per kilometer, there are maxima in boulder trail widths, with mean values again increasing from close to zero near tips of the structures toward maximum values (Figures 8a and 8c). This shows that the areas of high boulder trail density also have the widest boulder trails (compare Figures 8b and 8c). Again, we note an asymmetry along strike of the graben for the boulder trail width data. The widest mean boulder trail width along Boulder Trail Anomaly 2 was ~5 m, and this measurement was recorded in the region exhibiting the highest number of boulder trails at E161.43° longitude. As with boulder trails per kilometer, a sharp decrease in the mean width of boulder trails is observed as we progress west along the fault, with a mean trail width of 1.4 m being recorded in the region where only four boulder trails were located (E161.76°). Boulder Trail Anomaly 1 also clearly exhibits the aforementioned relationship, with a maximum mean boulder trail width of ~5 m located

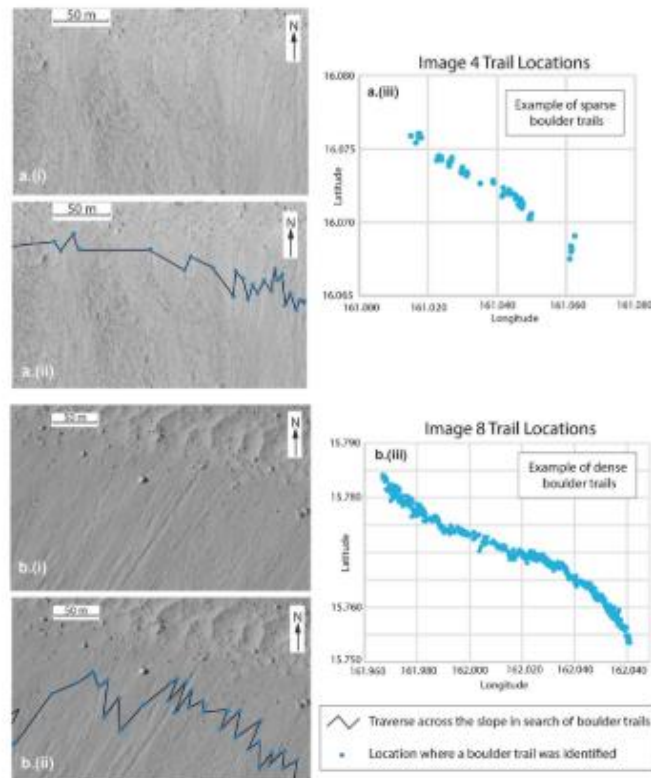


Figure 6. Example of a boulder trail density measurement for two images: (a) Image 4 (HiRISE Image ESP_025011_1965) and (b) Image 8 (HiRISE Image ESP_026712_1960). (a) Image 4 (i) shows a sparse concentration of narrow trails, all of similar width and similar length. (ii) The blue dots at the apex of the dark lines indicate boulder trails along a transect shown in dark blue. (ii) Graph showing location and density of boulder trails found along a WNW-WSE transect traversing 0.03° of longitude, showing the locations of trails. (b) Image 8 (i) shows a dense concentration of both narrow and some wider trails. The lengths of the trails in the image are comparable. Some trails exhibit bounce marks. (ii) The dots at the apex of the dark lines indicate boulder trails along a transect shown in dark blue. (ii) Graph showing location and density of boulder trails found along a WNW-WSE transect traversing 0.05° of longitude, showing the locations of trails.

in the area of most boulder trails per kilometer (102), and from this peak the mean width of trails drops to 1.7 m at E163.62°, an area where only 2 boulder trails per kilometer were recorded (Figure 8d). Note that for Boulder Trail Anomaly 1, both the boulder trail width and boulder counts per kilometer, if extrapolated along strike, have maximum values near to longitude E162.5°, a location where the surface expression of the fault appears to be nonexistent due to the presence of tips to individual graben (see Figures 2b and 2c); a flat plain separates two graben at this location, and we discuss the possible reasons for this later in the paper. We also note that there does not appear to be an obvious correlation between the vertical offset across the graben and the number of boulder trails per km or the mean value for the size of the 10 widest boulder trails (see locations A and B in Figure 8); again, this is discussed later in the paper.

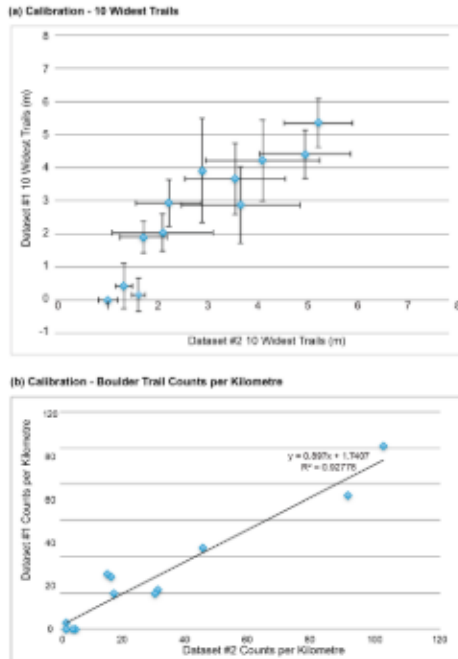


Figure 7. Both authors counted boulder trails and boulder widths along Boulder Trail Anomaly 1 and Boulder Trail Anomaly 2. (a) Calibration graph for boulder trail counts. (b) Calibration graph for boulder width counts. Both of these results show that the results are repeatable with results from the two surveys being broadly comparable.

5. Discussion

Results from Grjota Valles show geographically coincident maxima in boulder trail density per kilometer and boulder trail widths along the graben. This type of observation was used by Roberts et al. (2012) to suggest that the most plausible mechanism to mobilize such populations of boulders is seismic shaking associated with palaeomarsquakes (see Figure 1). They concluded that this because boulders mobilized by seismic shaking would “display the classic pattern associated with earthquakes where both the frequency of boulder falls and boulder sizes decrease away from the epicenter and the location of coseismic surface faulting, due to localized ground shaking (Keefer, 1984)” (Figure 1). However, there are other possible mechanisms that may have mobilized the boulders, and we discuss each of them in turn below.

1. *Release of boulders by melting ice.* A plausible hypothesis is that boulders are held on the steep slopes and cliffs associated with the graben by water or CO₂ ice. Any diurnal, seasonal, or longer term warming might melt the ice and release the boulders. Roberts et al. (2012) suggest that boulders mobilized in this way would show “a random spatial pattern of maximum boulder sizes when sampled over tens to hundreds of kilometers” (Figure 1). However, our measurements show clear local maxima in boulder trail widths and boulder trail density per kilometer that are geographically coincident (Figure 8). Note that the actual mean value for the widest boulder trail may be larger if measured from a larger population of trails, so there is an element of circular reasoning here. However, even with this caveat, these results, with geographically coincident maxima in values for the two variables (Figure 8), are not what would be expected of the mechanism of boulder release by melting ice. Furthermore, it is unclear how this process could control the dimensions of boulders recorded by the boulder trail widths, and, like Roberts et al. (2012; their Figure 10), we have found no evidence for differing joint spacing in the bedrock to explain the variable maximum boulder sizes implied by the variable maximum boulder trail widths, although the restriction of image resolution means we cannot rule it out. Furthermore, persistent CO₂ frost may not be plausible at this latitude (Piqueux et al., 2016), so it may be unrealistic to expect such frost to hold boulders on slopes. For these reasons so we reject this hypothesis.

2. *The effect of local differences lithology and hence weathering/erosion.* A plausible hypothesis is that different lithologies might be more or less prone to erosion and this might control the number and sizes of boulders released from the steep slopes and cliffs associated with the graben. Our geological mapping shows no obvious changes in lithology of the rocks forming the walls to graben (Figure 4). We have also examined available THEMIS (Thermal Emission Imaging System) and CRISM (Compact Reconnaissance Imaging Spectrometer for Mars) data to try to ascertain if local lithological changes correlate with the measured maxima in boulder trail widths that are coincident with the measured maxima in boulder trails per kilometer. The CRISM data, although having limited lateral extent and hence availability, appear to show no obvious change in lithology of the rocks forming the walls to graben with regard to oxidized iron minerals, mafic mineralogy, hydroxylated silicates, bound water or water ice, and CO₂ ice (Figure S1 in the supporting information). The THEMIS data, including both nighttime and daytime infrared measurements, provide complete spatial coverage of the area studied, and, although probably saturated in the images we show, again show no obvious change in lithology of the rocks forming the walls to the graben, highlighting only that the walls of the graben appear to formed of bedrock (Figures S2 and S3), as confirmed by the clear stratigraphic layers in the HiRISE images (Figure 4). The HiRISE data show a layered stratigraphy in the graben walls that are presumably lava flows and possibly sedimentary layers formed by weathering erosion and eolian processes between

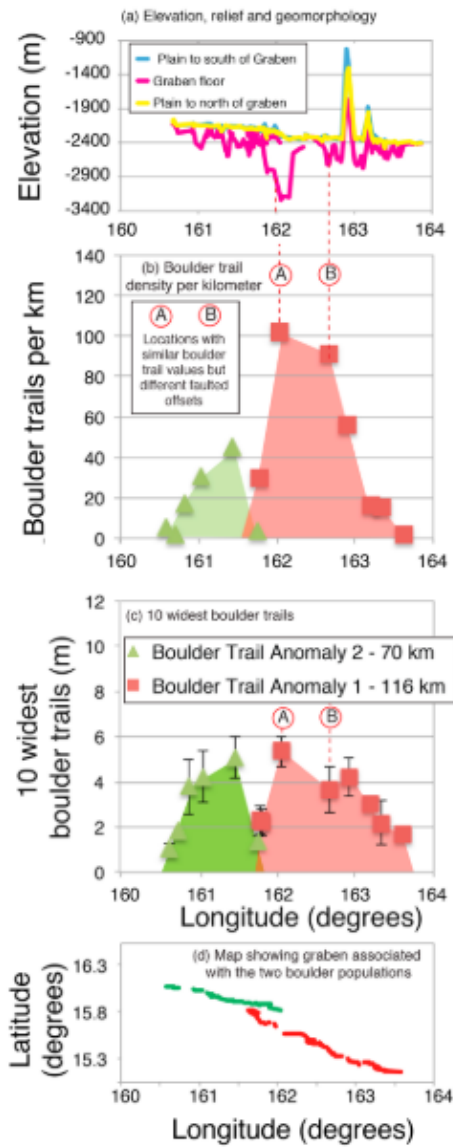


Figure 8. (a) Plot showing absolute values of elevation for the plain to the south of the graben, the plain north of the graben, and the floor of the graben, versus longitude. (b) Graph of longitude versus boulder trails per kilometer. (c) Graph of longitude versus boulder trails widths. (d) Map showing graben associated with the two boulder populations.

lava flow events. There appears to be little if any obvious differences in stratigraphy between different HiRISE images (Figure 4). Thus, as we have not identified any changes in lithology, despite having a variety of data sources, we reject the hypothesis that different lithologies might be more or less prone to erosion and this might control the number and sizes of boulders released from the steep slopes and cliffs associated with the graben. We also have no evidence to address the possibility that that wind helps dislodge rocks, either directly or by forcing sand and dust into cracks, wedging them open, in a way that produces the regional variations in boulder trail frequency and size shown in Figure 8.

3. *Higher cliffs could supply more boulders.* A plausible hypothesis is that the higher frequency of boulder trails we have measured in some HiRISE images might be explained by proximity to higher cliffs that have a greater number of loose boulders available for mobilization. However, it is not just the cliffs that supply boulders. The talus at the bases of the cliffs also contains boulders that could be mobilized as they are likely to be sitting on slopes that are close to their angle of repose. Thus, the combined height of the cliffs and the talus should be taken into account. Also, the talus slopes are all likely to be close to their angle of repose, and the cliffs appear to be close to vertical, so variations in local slope is probably not a variable that needs to be considered. Although it is not possible to measure the heights and slopes of all the individual cliffs or individual talus cones, because (a) MOLA spot spacing of ~300 m is too coarse (Figure S4); (b) shadow width and solar incidence angle cannot be used to define vertical height differences via trigonometry, because the horizontal extents of talus slopes vary between different examples (Figure S5); and (c) stereo HiRISE pairs to make local digital elevation models are not available for the majority of HiRISE locations in the study area, it is possible to measure the total offset across the faults controlling the graben walls using the MOLA data (Figures 5 and 8). For example, locations A and B in Figure 8 show similar values for boulder trails per kilometer and boulder trail widths, but very different combined heights of the fault-controlled cliffs plus talus slope height defined by the total offset measured with MOLA data. Thus, if the vertical extent of cliffs plus associated talus slopes provides more candidate boulders for mobilization, this does not tally with our measurements of maxima in boulder trail frequency. Also, this hypothesis does not explain why the widths of boulder trails correlate with the frequency of boulder trails. Thus, for these two reasons we reject this hypothesis.
4. *Boulder mobilization caused by nearby impacts.* A plausible hypothesis is that formation of nearby impact craters could have produced ground shaking that mobilized the boulders. We have examined all impact craters within ~50 km across strike of the graben we have studied. An ~4-km diameter crater is located at latitude 15.618° and longitude 162.183°, close to the area with maxima in boulder trail frequency and boulder trail width. However, the ejecta blanket from this crater has been eroded by an outflow channel, so the crater predates the outflow. The outflow channels predate the graben evidenced by cross cutting relationships (see Vetterlein & Roberts, 2009, for a description of how cross cutting relationships are ascertained), and the boulder trails postdate graben formation. Hence, this crater is too old to have been involved in boulder mobilization. Smaller craters (~40 m

diameter) exist within a few hundred meters of the graben in the vicinity of the maxima in boulder trail frequency and width (Figure S6). However, these craters, although having a relatively young appearance at first sight, due to the existence of dark, presumably relatively dust free material within them, are in fact partially filled with eolian dunes. The dunes were mobilized by the wind, yet the boulder trails have not been destroyed by the action of wind, suggesting that they are younger than the dunes. Thus, if the rate of eolian processes is similar between these craters and the graben floors, these small craters are also ruled out as candidates for producing the ground shaking that mobilized the boulders. Thus, as no candidate craters have been identified we rule out this hypothesis, but note that this is dependent on our assumption that the rate of eolian processes is similar between craters and the graben floors.

5. *Track density may correlate with better preservation and/or lower degradation rather than more abundant formation.* A plausible hypothesis is that the boulder trails may be degraded by erosion and that degradation may vary spatially influencing the number of trails that are preserved and the widths that are measured. To assess this, we have compared boulder trail widths with the dimensions of the boulders that formed them (Figure 3d). We assume that the boulders are more resistant to wind erosion than the underlying dust surfaces that they have rolled over and will maintain their original dimensions. Thus, a comparison between the dimensions of the boulders and the trails should reveal whether trail widths have been altered by wind erosion. We have found that in areas of both high and low boulder trail density and width, the widths of the boulder trails are indistinguishable in width from the width of the boulders that formed them. This suggests that the trails are not eroded to an extent that radically alters their widths or preservation. That the trails have not been significantly degraded by wind erosion is consistent with the preservation of raised levees produced by the motion of boulders, evidenced by variation in percentage gray scale for individual pixels in the images (Figure 3d (v)). Thus, we reject this hypothesis.
6. *Variation in incidence angle of the images makes trails difficult to see.* A plausible hypothesis is that recognition of trails may be hindered by, for example, the solar incidence angles in the HiRISE images. Figure S7 shows that solar incidence angles are very similar for the images we have studied. Also, our qualitative assessment after studying many examples is that individual boulder trails are as clear on images with low boulder trail frequency and width as they are on images with high boulder trail frequency and width. For these reasons we reject this hypothesis.
7. *The accumulation of boulder trail populations may have developed from multiple single rockfalls through time.* As single rockfalls have been observed on repeat imagery (for example, see https://www.msss.com/mars_images/moc/2005/09/20/bouldertracks/), which appears to show possible bounce marks and longer lived debris flow channels), then a plausible hypothesis is that repeated single rockfalls could be responsible for the populations of boulder trails, perhaps triggered by many small marsquakes or many releases of boulder by melting ice or other processes. Our qualitative observation on this point is that the morphology of the boulder trails appears to be identical across the many thousands of boulder trails we have observed. They appear to have raised levees only a few decimeters across that are presumably made of dust to coarse sand (Figure 3d). We think it is dust to coarse sand because it is susceptible to subsequent wind erosion (Figure 3d). We do not think these examples on Mars are associated with gravel-grade material that would be less susceptible to wind erosion. This is because we have conducted fieldwork in Iceland where boulder trails have formed in talus cones on fault scarps made of gravel-grade material (grain size of up to 10–15 cm; Figure S8). The examples in Iceland lack raised levees, and we think this is due to the relatively coarse grain size, and hence interpret the grain size for the examples from Mars as dust to coarse sand. The raised levees in the examples from Mars are, as described above, evidenced by variation in percentage gray scale for individual pixels in the images with the Sun illuminating the raised levees that also produce shadows (Figure 3d). The key point is that with clear examples of active eolian processes on the graben floors in the form dunes (e.g., Figure 4a), and the interpreted dust to coarse sand grain size, the fact that raised levees are preserved in many thousands of examples suggests that they are young and hence of very similar age. For this reason we reject the hypothesis of incremental formation of the boulder trail populations by addition of single boulder falls, although we admit that this is supported only by qualitative observations. Rather, we suggest that two events have formed the two boulder trail populations shown in Figure 8. Note that if we are incorrect about the levees, and in fact the population of boulder trails contains examples of individual boulder trails with very different ages, then the population could have accumulated through many smaller rockfalls,

invalidating our large magnitude marsquake interpretations, but we suggest that our evidence appears to point to the opposite interpretation, consistent with large magnitude marsquakes.

8. *Measurements used to define boulder trail anomalies.* A plausible hypothesis is that there may be a problem with our measurements. It may be that the mean width of the 10 widest trails is inadequate to allow comparison of boulder trail populations produced by mobilization of a subset of the population of available boulders, if populations of different number are considered and they have a power law or exponential size distribution. One scenario could be that if more boulders are drawn from such a population, there will be more individual large boulders and the mean will be larger, even if the size frequency distribution is identical. We have been unable to define the number, as we have not counted the total number of boulders in each location, but it is perhaps likely that the extremely large numbers of candidate boulders for mobilization at every location means that the population sizes are not significantly different. Our results stand if we assume that the number of boulders in the population is identical between locations, but clearly we have not been able to rule out this possibility.

After consideration of the alternative scenarios described above, we conclude, following Roberts et al. (2012), that a plausible explanation for the boulder trail data we present herein may be that the boulders were mobilized by seismic shaking associated with palaeomarsquakes, with shaking, and hence boulder mobilization, decreasing with distance from the epicenters. Thus, although, perhaps not completely proven, as we have not ruled out some alternative hypotheses, we think it worthwhile to explore the implications that arise if this marsquake hypothesis is correct.

We note that the marsquake interpretation requires one of our interpreted marsquake ruptures to cross an area where there is no surface offset. We note that it is common for ruptures to jump between active faults that are not physically continuous in terrestrial earthquakes and provide an example of this in Figure S9 (see Livio et al., 2016). The same may apply on Mars. This is important to note, because, like on the Earth, estimates of maximum marsquake magnitude may be erroneously small if it is assumed that ruptures can be confined to single active faults.

If our conclusion that the boulder populations were mobilized by marsquakes is correct, the observation that the results of this study are similar to those of Roberts et al. (2012) suggests that we should discuss data from that paper alongside those in this paper to broaden our understanding of the potential significance of the boulder trail populations (Figure 9). An obvious difference between the data sets is that the hump shaped anomalies extend over ~207 km for Cerberus Fossae (Roberts et al. (2012), while those that emerge from this paper extend over ~116 km for Boulder Trail Anomaly 1, and ~70 km for Boulder Trail Anomaly 2 (Figure 9). Roberts et al. (2012) suggested that the along-strike extent of seismic shaking great enough to mobilize boulders on Earth is approximately the same as the along-strike extent of surface faulting for the earthquake ruptures, consistent with observations from the 2009 Mw 6.3 earthquake near L'Aquila, Italy. Roberts et al. (2012) also tentatively mapped possible surface rupture extent using HiRISE images for Cerberus Fossae, and observations were consistent with the hypothesis. Following this, although we have not been able to map rupture extent in the present example, and the 1:1 ratio between rupture length and the dimensions of areas with mobilized boulders on Earth is only approximate, if the along-strike extent of the hump-shaped anomalies in boulder trail data are taken as proxies for along-strike rupture extent, the implied moment magnitudes for the palaeomarsquakes, assuming that the humps result from single events, may be in the range of ~Mw 7.3–7.8 (Figure 9d). It should be noted that our assumption that the anomalies formed in single events and not multiple small events (see the discussion in Point 7 above), mean that these magnitudes should be considered as maximum values. However, our assumptions are supported indirectly by the observation that $d_{max}/length$ ratios for the Martian faults examined herein (0.026–0.008; Figure 5) are similar to those measured on the Earth (0.1–0.001; see Vetterlein & Roberts, 2010, for a review). In turn, this implies that material strength and the relationships between rupture length, d_{max} , stress drop, and moment magnitude are also likely to be similar to those on the Earth (Ali & Shieh, 2013; Gomez-Rivas et al., 2015). Moment magnitudes in the range of ~Mw 7.3–7.8 imply events whose seismic shaking would be widely felt/detected on the Martian surface by seismometers such as those associated with the Interior Exploration using Seismic Investigations, Geodesy and Heat Transport (InSIGHT) mission. However, also note that we may be mistaken in our assumption that along-strike extent of the hump-shaped anomalies in boulder trail data is a proxy for along strike rupture extent, as unfortunately, unlike Roberts et al. (2012), we have been unable to map surface rupture for example in Grjota Valles. Gravity on Mars is ~38% compared to that of the Earth so

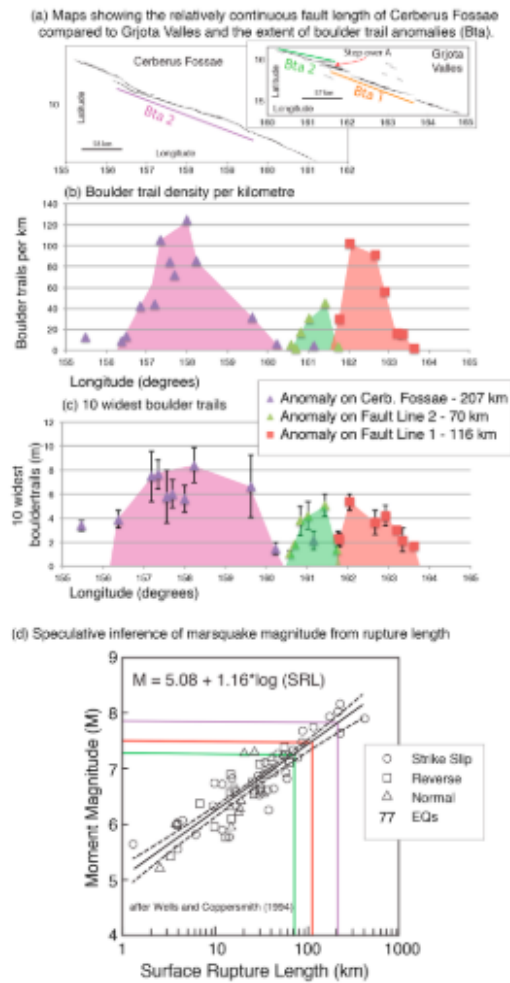


Figure 9. (a) Comparison of three data sets of boulder trails per kilometer against longitude for Boulder Trail Anomaly 1, Boulder Trail Anomaly 2 and data from Cerberus Fossae (Roberts et al. (2012)). Roberts et al. (2012) suggested that if the along-strike extent of seismic shaking great enough to mobilize boulders on Earth is approximately the same as the along-strike extent of surface faulting for the earthquake ruptures, it may be possible to infer the magnitude of seismic events. Following this, if the long strike extent of the hump-shaped anomalies in boulder trail data is taken as proxies for along-strike rupture extent, the implied moment magnitudes for the palaeomarsquakes, assuming that the humps result from single events, is in the range of Mw 7.3–7.8. (b) Comparison of three data sets of boulder trail density per kilometer against longitude for Boulder Trail Anomaly 1, Boulder Trail Anomaly 2 and data from Cerberus Fossae (Roberts et al. (2012)). (c) Comparison of three data sets of 10 widest boulder trails per kilometer against longitude for Boulder Trail Anomaly 1, Boulder Trail Anomaly 2, and data from Cerberus Fossae (Roberts et al. (2012)). (d) Graph of surface rupture length versus moment magnitude adapted from Wells and Coppersmith (1994). If the long strike extent of the hump shaped anomalies seen in Figures 9a–9c in boulder trail data is taken as proxies for along strike rupture extent, the implied moment magnitudes for the palaeomarsquakes, assuming that the humps result from single events, is in the range of Mw 7.3–7.8.

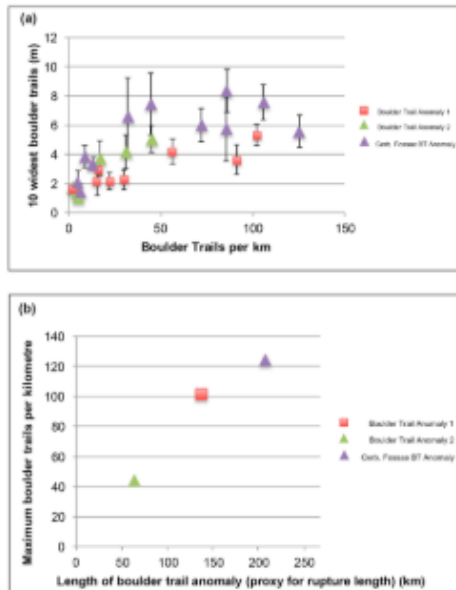


Figure 10. (a) Comparison of three data sets of the 10 widest boulder trails against boulder trails per kilometer for Boulder Trail Anomaly 1, Boulder Trail Anomaly 2 and data from Cerberus Fossae (Roberts et al., 2012). (b) Comparison of three data sets of the maximum number of boulder trails per kilometer against length of boulder trail anomaly for Boulder Trail Anomaly 1, Boulder Trail Anomaly 2 and data from Cerberus Fossae (Roberts et al., 2012). Note the positive correlation between the along-strike length of the boulder trail anomaly and the maximum value for boulder trails per kilometer recorded. This may be interpreted to suggest that maximum ground acceleration may increase with earthquake magnitude.

less force might be needed to mobilize boulders, but it is hard to be precise as this depends on how each boulder was attached and detached, and whether each boulder was mobilized by vertical or horizontal accelerations (see Figures S5c–S5h for an explanation). However, it is possible that the along-strike extent of the hump-shaped anomalies in boulder trail data may be greater than along-strike rupture extent, so this is another reason why the estimates of M_w 7.3–7.8 should be considered maximum values. Nonetheless, if we use the observation that boulder trail anomalies have similar along-strike dimensions to suggested surface ruptures for the Cerberus Fossae example (Roberts et al., 2012), the results point toward the conclusion that a variety of magnitudes of palaeomarsquake may have been detected, with larger magnitudes on the Cerberus Fossae fault system, which displays fault segments lengths of several hundred kilometers from geomorphic observations of offset features, and smaller magnitudes on the Grjota Valles system where segmented lengths are in the range of 50–100 km, again from geomorphic observations (Figures 2 and 9). This correlation between fault dimensions and dimensions of areas affected by putative seismic shaking adds further support, albeit indirect, for our interpretation of palaeomarsquakes.

Furthermore, we suggest that it may be possible to infer details of how well seismic shaking is recorded by our natural seismometer, that is, the boulder trail population data. Figure 10a compares the three faults; Boulder Trail Anomaly 1, Boulder Trail Anomaly 2 and Roberts et al.'s (2012) fault, plotting boulder trails per kilometer versus boulder trail width. A positive relationship exists between boulder trails per kilometer and the width of boulder trails, with a greater number of boulder trails corresponding to a greater width of boulder trails. However, it is interesting to note that the data appear to saturate. Data from Roberts et al. (2012) increase from zero to \sim 5–8 m for the mean value of the 10 widest boulder trails over the range of \sim 0–50 boulder trails per kilometer, and then appear to flatten out at larger values with the value of \sim 5–8 m for the mean value of the 10 widest boulder trails maintained over the range of \sim 50–125 boulder trails per km. One interpretation of this is that the natural seismometer is saturating and unable to record shaking that would mobilize larger boulders. It may be that boulders $>$ 5–8 m are not available in great

numbers on the fault controlled slopes, perhaps controlled by joint spacing or layer thicknesses in the rocks. Furthermore, we note that the Figure 10b shows a positive relationship between the along-strike length of the boulder trail anomaly and the maximum value for boulder trails per kilometer recorded. This may be interpreted to suggest that maximum ground acceleration may increase with marsquake magnitude. However, we note that from the sparse data we have, constrained with only 3 data points, that the trend again flattens out, and that we might expect the example from Roberts et al. (2012) to have more than the \sim 120 boulder trails per kilometer recorded. We suggest that again the natural seismometer might be saturating, perhaps because once a value of \sim 45 boulder trails per kilometer is exceeded it becomes difficult in some cases to identify every single boulder trail because they appear to coalesce on the images. The preceding text pertaining to performance of our natural seismometer is speculative. However, we note that if correct, it implies that boulder trail populations may not be effective in measuring the effects of marsquakes at the largest magnitudes because the measurements may be saturated.

As a final point of discussion we note that profiles of data for boulder trail anomalies 1 and 2 are asymmetric (Figures 8 and 9), with the steepest gradients closest to the en echelon fault step-over (labeled A in Figure 9a) between these two fault segments. For faults on the Earth we note that displacement gradients steepen in the step over zones between interacting faults (Jackson et al., 2002). The asymmetry in boulder trails populations may, perhaps, be related to this. A speculative interpretation might be that slip-distributions for each of the individual marsquake ruptures that produced these boulder trail anomalies were skewed toward the

tips of fault segments, so that the largest coseismic displacements, and hence highest levels of ground acceleration, were located close to the en echelon step-over between the fault segments, as occurs on the Earth (Faure Walker et al., 2009).

Overall, the boulder trail data presented in this paper are intriguing, but not conclusive. Clearly, what is needed is for a seismometer placed on the surface of Mars to actually record a marsquake before we can conclude that seismicity is present (see Lorenz et al., 2017, who suggest that seismometer data from the Viking missions may have already detected seismic shaking, and data acquisition planned for the InSIGHT seismometer mission to Mars of 2018–2019). The data herein may suggest relatively large events, perhaps up to Mw 7.3–7.8. However, magnitudes >Mw 7.6 seems improbable given the analysis of Knapmeyer et al. (2006). We point out that the uncertainty indicated by the spread in the data supporting Figure 9d allow our interpretation to be consistent with the estimate in Knapmeyer et al. (2006). Nonetheless, events as large as Mw 7.6 would have recurrence intervals that are very long (perhaps hundreds to thousands of years), much longer than the lifetime of a seismometer. The likelihood of measuring such an event with the InSIGHT seismometers is, of course, very small. However, if like on the Earth, for every large event there are hundreds to thousands of smaller events with shorter return times following Gutenberg-Richter b-value scaling (e.g., Knapmeyer et al., 2006), it may be that one of these smaller events is more likely to be recorded by the InSIGHT seismometers. The annual detectability of such events by the InSIGHT instruments was investigated by Taylor et al. (2013), and they conclude that between 1.5×10^9 and 1.9×10^5 events would be detected, depending on the maximum defined event size; our results provide new information on the possible maximum event sizes. The ideas in this paper can and should be tested by data provided by the InSIGHT mission. The data in this paper suggest that the Martian surface is not completely still; instead, they hint that the Martian surface may well have been shaken by large-magnitude marsquakes in the very recent past.

6. Conclusions

We have studied two faulted areas in the vicinity of Grjota Valles (Boulder Trail Anomaly 1 and Boulder Trail Anomaly 2), measuring the densities and widths of boulder trails created by boulders falling from fault-controlled cliffs. These data are consistent with previous results (Roberts et al., 2012) in that the most parsimonious interpretation is that boulders have been mobilized by seismic shaking associated with palaeo-marsquakes in the recent past. Our conclusions can be tested with data from the InSIGHT mission that is on the Martian surface at the time of writing. For now, we report that a region containing two en echelon graben/faults with similar d_{\max}/length ratios to those from the Earth, boulder trail data define two maxima in (a) boulder trails per kilometer and (b) maximum width of boulder trails, one which is ~116-km length and the other ~70-km length. Values for the maxima are 45 trails per kilometer and 5-m maximum trail width for the 70-km-long anomaly, and 115 trails per kilometer with 5.3-m maximum trail widths for the 116-km-long anomaly, above background values of zero trails per kilometer with zero boulder trail widths. Combined with published data from Cerberus Fossae where an ~207 km long anomaly in boulder trails per km (125 trails per kilometer maxima) and maximum boulder trail width (8.5-m maximum trail width), the three data sets suggest correlations between the along-strike length of boulder trail anomalies, boulder trails per kilometer and maximum boulder trail width. Implied moment magnitudes, derived by using the along-strike dimensions of boulder trail anomalies as proxies for rupture extent, could be as large as Mw 7.3–7.8, values that we expect to be accompanied by much more frequent seismic activity at lower moment magnitudes.

Acknowledgments

We acknowledge STFC grant ST/K006037/1 that funded some of this work. We acknowledge the HiRISE teams (NASA/JPL/University of Arizona) for providing images and the MOLA team for topographic data. We thank Jonny Roberts for his help with the fieldwork in Iceland. The data used in this paper are appropriately cited in the references section of this paper. We thank the reviewers and Associate Editor for their detailed and constructive comments.

References



- Ali, W., & Shieh, S. (2013). Earthquake repeat time, stress drop, type of slip and earthquake magnitude. *Journal of Geology and Geophysics*, 2, 118. <https://doi.org/10.4172/2329-6755.1000118>
- Antoine, R., Lopez, T., Baratoux, D., Rabinowicz, M., & Kurita, K. (2010). Thermal analysis of fractures at Cerberus Fossae, Mars: Detection of air convection in the peroxyl debris apron. *Icarus*, 214(2), 433–446.
- Barr, D. M., Grier, J. A., McEwen, A. S., & Keszihegyi, L. P. (2002). Repeated aqueous flooding from the Cerberus Fossae: Evidence for very recently extant, deep groundwater on Mars. *Jarus*, 159(1), 53–75. <https://doi.org/10.1006/icar.2002.6921>
- Barr, D. M., McEwen, A. S., & Sakimoto, S. E. H. (2002). Recent aqueous floods from the Cerberus Fossae, Mars. *Geophysical Research Letters*, 29(1), 1013. <https://doi.org/10.1029/2001GL013345>
- Faure Walker, J., Roberts, G. P., Cowie, P. A., Papanikolaou, I., Michetti, A. M., Sammonds, P., & Phillips, R. (2009). Horizontal strain-rates and throw-rates across breached relay-zones, central Italy: Implications for the preservation of throw deficits at points of normal fault linkage. *Journal of Structural Geology*, 31(10), 1145–1160. <https://doi.org/10.1016/j.jsg.2009.06.011>

- Geissler, P. E., Sullivan, R., Golombek, M., Johnson, J. R., Herkenhoff, K., Bridges, N., et al. (2010). Gone with the wind: Eolian erasure of the Mars Rover tracks. *Journal of Geophysical Research*, *115*, E00F11. <https://doi.org/10.1029/2010JE003674>
- Gomez-Rivas, E., Griera, A., & Llorens, M.-G. (2015). Fracturing of ductile anisotropic multilayers: influence of material strength. *Solid Earth*, *6*, 497–514. <https://doi.org/10.5194/se-6-497-2015>
- Hamilton, C. W., (2013) Flood lavas associated with the Cerberus Fossa 2 unit in Elysium Planitia, Mars. Abstract for the 44th Lunar and Planetary Science Conference.
- Hartmann, W. K., & Berman, D. C. (2000). Elysium Planitia lava flows: Crater count chronology and geological implications. *Journal of Geophysical Research*, *105*(E6), 15,011–15,025. <https://doi.org/10.1029/1999JE001189>
- Head, J. W., Wilson, L., & Mitchell, K. L. (2003). Generation of recent massive water floods at Cerberus Fossae, Mars by dike emplacement, cryospheric cracking, and confined aquifer groundwater release. *Geophysical Research Letters*, *30*(11), 1577. <https://doi.org/10.1029/2003GL017135>
- Jackson, C. A. L., Gowthorpe, R. L., & Sharp, I. R. (2002). Growth and linkage of the East Tanka fault zone, Suez rift: structural style and syn-rift stratigraphic response. *Journal of the Geological Society*, *159*, 175–187.
- Jaeger, W. L., Kesathelyi, K. P., Skinner, J. A., Milazzo, M. P., McEwen, A. S., Titus, T. N., et al., & HiRISE Team (2010). Emplacement of the youngest flood lava on Mars: A short turbulent story. *Icarus*, *205*, 230–243. <https://doi.org/10.1016/j.icarus.2009.09.011>
- Keefer, D. K. (1984). Landslides caused by earthquakes. *Geological Society of America Bulletin*, *95*(4), 406–421. [https://doi.org/10.1130/0016-7606\(1984\)95<406:LCBE>2.0.CO;2](https://doi.org/10.1130/0016-7606(1984)95<406:LCBE>2.0.CO;2)
- Knäuper, M., Oberst, J., Hauber, E., Wählisch, M., Deuchler, C., & Wagner, R. (2006). Working models for spatial distribution and level of Mars' seismicity. *Journal of Geophysical Research*, *111*, E11006. <https://doi.org/10.1029/2006JE002708>
- Livio, F., Michetti, A. M., Vittori, E., Gregory, L., Wedmore, L., Piccardi, L., et al. (2016). Surface faulting during the August 24, 2016, central Italy earthquake (Mw 6.0): Preliminary results. *Annals of Geophysics*, *59*. <https://doi.org/10.4401/ag-7197>
- Lorenz, R. D., Nakamura, Y., & Murphy, J. R. (2017). Viking-2 seismometer measurements on Mars: PDS data archive and meteorological applications. *Earth and Space Science*, *4*, 681–688. <https://doi.org/10.1002/2017EA000306>
- Morgan, G., Campbell, B. A., Carter, L. M., Plant, J. J., & Phillips, R. J. (2013). 3D reconstruction of the source and scale of buried young flood channels on Mars. *Science*, *340*. <https://doi.org/10.1126/science.1234787>
- Piqueux, S., Kleinböhl, A., Hayne, P. O., Heavens, N. G., Kass, D. M., McCleese, D. J., et al. (2016). Discovery of a widespread low latitude diurnal CO₂ frost cycle on Mars. *Journal of Geophysical Research: Planets*, *121*, 1174–1189. <https://doi.org/10.1002/2016JE005034>
- Plescia, J. B. (2005). Cerberus Fossae, Elysium, Mars: A source for lava and water. *Icarus*, *164*, 79–95.
- Roberts, G. P., Matthews, B., Bristow, C., Guerrieri, L., & Vetterlein, J. (2012). Possible evidence of paleoearthquakes from fallen boulder populations, Cerberus Fossae, Mars. *Journal of Geophysical Research*, *117*, E02009. <https://doi.org/10.1029/2011JE003816>
- Schlichte, R. W., Young, S. S., Ackermann, R. V., & Gupta, A. (1996). Geometry and scaling relations of a population of very small rift-related normal faults. *Geology*, *24*, 683–686.
- Tanaka, K. L., Skinner, J. A., & Hare, T. M. (2005). Geologic map of the Northern Plains of Mars. Pamphlet to accompany Scientific Investigations Map 2888, USGS for NASA. <https://pubs.usgs.gov/sim/2005/2888/>
- Taylor, J., Teanby, N. A., & Wooley, J. (2013). Estimates of seismic activity in the Cerberus Fossae region of Mars. *Journal of Geophysical Research: Planets*, *118*, 2570–2581. <https://doi.org/10.1002/2013JE004469>
- Vaucher, J., Baratoux, D., Mangold, N., Pinet, P., Kurita, K., & Gregoire, M. (2009). The volcanic history of central Elysium Planitia: Implications for Martian magmatism. *Icarus*, *204*(2), 418–442. <https://doi.org/10.1016/j.icarus.2009.06.032>
- Vetterlein, J., & Roberts, G. P. (2009). Postdating of flow in Athabasca Valles by faulting of the Cerberus Fossae, Elysium Planitia, Mars. *Journal of Geophysical Research*, *114*, E07005. <https://doi.org/10.1029/2009JE003356>
- Vetterlein, J., & Roberts, G. P. (2010). Structural evolution of the northern Cerberus Fossae graben system, Elysium Planitia, Mars. *Journal of Structural Geology*, *32*(4), 394–406. <https://doi.org/10.1016/j.jsg.2009.11.004>
- Wells, D. L., & Coppersmith, K. J. (1994). New empirical relationships among magnitude, rupture length, rupture width, rupture area, and surface displacement. *Bulletin of the Seismological Society of America*, *84*(4), 974–1002.

Appendix D.

Brown, J. R., and Roberts, G. P. (2023). Repeated, cross-cutting and spatially migrating outflow channel formation, Grjótá Valles, Mars

Brown, J. R., and Roberts, G. P. (2023). Repeated, cross-cutting and spatially migrating outflow channel formation, Grjótá Valles, Mars. *Journal of Geophysical Research: Planets*, 128, e2022JE007247. <https://doi.org/10.1029/2022JE007247>





JGR Planets

RESEARCH ARTICLE

10.1029/2022JE007247

Repeated, Cross-Cutting, and Spatially Migrating Outflow Channel Formation, Grjótá Valles, Mars

Jason R. Brown¹  and Gerald P. Roberts¹ 

¹Department of Earth and Planetary Sciences, Birkbeck, University of London, London, UK

Key Points:

- Cross-cutting relationships and channel incision reveal that at least five asynchronous flow episodes have taken place in Grjótá Valles, Mars
- At least five asynchronous flow episodes have taken place at different locations along a section of the northernmost Cerberus Fossae

Supporting Information:
Supporting Information may be found in the online version of this article.

Correspondence to:
J. R. Brown,
123jb.jason@gmail.com

Citation:
Brown, J. R., & Roberts, G. P. (2023). Repeated, cross-cutting and spatially migrating outflow channel formation, Grjótá Valles, Mars. *Journal of Geophysical Research: Planets*, 128, e2022JE007247. <https://doi.org/10.1029/2022JE007247>

Received 14 FEB 2022
Accepted 22 JAN 2023

© 2023. The Authors.
This is an open access article under the terms of the [Creative Commons Attribution-NonCommercial-NoDerivs License](https://creativecommons.org/licenses/by/4.0/), which permits use and distribution in any medium, provided the original work is properly cited, the use is non-commercial and no modifications or adaptations are made.

Abstract Cross-cutting relationships and the incision history for multiple outflow channels have been mapped and studied to establish their relative chronology in Grjótá Valles, Mars, in order to establish whether observed geomorphic channels were formed in a single event or multiple events. The relative chronology can be established by mapping cross-cutting relationships between channel margins and successive incisions, where later channels incise downward into older channels. We show that the source areas of five distinct channels can be established, with younger channels progressively sourced further to the east along the Grjótá Valles fault system, and incising downwards into older channels. The channels resemble examples interpreted elsewhere as cut using catastrophic aqueous flow processes (diluvial) due to their regional morphology, the presence of streamlined islands surrounded by anabranching channels marked by incisions, recessional terraces and longitudinal erosional grooves; however, turbulent lava flows may have also been involved. Those five distinct flows occur progressively further to the east may indicate the progressive propagation from west to east of the processes at depth that released the fluid responsible for cutting the channels, such as dike propagation and associated seismicity. Our observation of multiple flows and channel formation episodes implies instantaneous volumes of fluid that are smaller than that for a single flow interpretation.

Plain Language Summary Channels attributed to catastrophic aqueous flows have been suggested to exist on Mars, but debate surrounds the relative roles of water versus lavas in forming the channel morphologies, and the large volumes of fluid required to form the channels if they formed during single events. Our study of a channel system associated with Grjótá Valles, where channels emerge in the vicinity of faults, fissures and fractures, demonstrates cross-cutting relationships between channels that can be mapped back to five distinct channel sources. This suggests at least five separate channels forming events. The channels show geomorphic features that resemble those formed by catastrophic aqueous flows on the Earth, and lack features suggesting the filling of channels by lava; however, we cannot rule out that turbulent lava flows may also have helped to cut the channels. We use these observations to discuss the processes that led to the formation of the channels for this portion of Mars.

1. Introduction

Three large channel systems exist around Cerberus Planitia, Mars (Athabasca Valles, Marte Valles, Grjótá Valles; Burr, Grier, et al., 2002), but uncertainty exists with regard to whether the channels formed during single events of multiple events, with the former leading to concerns about the very large volumes of fluid required. In this paper, we describe new observations of cross-cutting relationships between channels in Grjótá Valles that imply at least five separate channels forming events. We show that the cross-cutting channels can be mapped upstream to five separate channel sources along the present trace of a system of faults, fractures and fissures in Grjótá Valles that forms part of Cerberus Fossae. Cross-cutting relationships show that the fault, fracture and fissure system formed after the channels. Our observations of the channels show landforms that resemble those produced by aqueous flows on the Earth, but the flow of turbulent lava flows may also have played a role in their formation. Other nearby channel systems (e.g., Athabasca Valles) have been shown to exhibit clear signs of lava infills in their pre-existing channels (e.g., Jaeger et al., 2007, 2010). We report our observations derived from detailed mapping, topographic profiling, and identification of cross-cutting relationships and use this to discuss whether the channels were cut by a single event or multiple events and what processes formed these channels.

It is unclear whether these channels formed during single or repeated flow events (Burr, Grier, et al., 2002), and this therefore introduces uncertainty with regard to estimated flow volumes and discharge rates. As to what

BROWN AND ROBERTS

1 of 26

process formed the channels, three hypotheses (aqueous, lava, mudflow) have been considered and we look at each in turn.

The hypothesis that the channels in Grjótá Valles result from aqueous flows that have existed for some time (Burr, Grier, et al., 2002; Baker & Milton, 1974; Head et al., 2003; Morgan et al., 2013; Plescia, 2003). The cause of the channel formation has been interpreted as either the result of magma-induced melting of the cryosphere (Burr, Grier, et al., 2002; Berman & Hartmann, 2002; Head et al., 2003), the outflow of water from a breached aquifer above an intruding dike beneath the fossae (Burr, Sakimoto, & McEwen, 2002; Carr, 1979; Plescia, 2003), release of water from a sub-cryosphere aquifer a few kilometres thick, and tens of kilometres in lateral extent (Manga, 2004), or from another subsurface origin (Jones et al., 2011). A number of researchers have suggested that large mega floods occurred (Burr, Grier, et al., 2002, 2009; Kattenhorn and Meyer, 2010) across parts of the Cerberus Fossae, flowing through the three Amazonian aged flood channels within the region (Grjótá Valles, Marte Valles, and Athabasca Valles), with the emanation points of these floods not conclusively identified, although generally thought to be the fossae themselves (Burr, Sakimoto, & McEwen, 2002, 2009). It has been suggested that the flows that formed such channels were very large, with very high discharge rates (e.g., $1-8 \times 10^8 \text{ m}^3 \text{ s}^{-1}$ for the nearby Athabasca Valles channel system; Keszthelyi et al., 2007) because, for example, the Grjótá Valles channels cover a region of $\sim 90,000 \text{ km}^2$. An alternate hypothesis is that the flow of turbulent lava is a possible mechanism for cutting channels (Jaeger et al., 2010). This uncertainty gives rise to a number of questions including how could the implied large volumes of water/lava needed for such flows be released, and where such volumes of water could be stored. It has been suggested that the fault system running through Grjótá Valles, that forms part of Cerberus Fossae, is formed due to dike emplacement and this facilitated flow formation (e.g., Head et al., 2003). Numerical modeling has been used to link dike-related heat flow and flow volume on Mars in general, and shows that such dikes would in some cases be able to produce heat to melt ground ice, which could produce flow water to create channels and/or landforms similar to those described herein (e.g., Head & Wilson, 2002; McKenzie and Nimmo, 1999; Plescia, 2003). Head et al. (2003) suggest for Athabasca Valles, which like the Grjótá Valles emanates from Cerberus Fossae, that dike emplacement produces surface cracking, localized volcanic eruptions, cryospheric cracking, and release of pressurized groundwater from beneath the cryosphere. However, Head et al. (2003) note that the required aquifer permeability is larger than commonly encountered on Earth, meaning that either water is transported through the subsurface by a highly efficient, as yet unknown mechanism, and/or the volume flux values are overestimated. Furthermore, the existence of voluminous sub-surface ice is debateable. Observations of seismic wave velocity of the Martian crust suggest that the subsurface is not ice-saturated (Manga and Wright, 2021); however, their findings do not rule out the possibility of the existence of groundwater. However, support exists for sub-surface igneous heat sources (i.e., dikes along Cerberus Fossae) as lavas have been identified in some locations infilling the channels emanating from it (e.g., Burr, Sakimoto, & McEwen, 2002; Jaeger et al., 2007, 2010; Keszthelyi et al., 2000; Plescia, 2003). Volcanic centers have been mapped (Plescia, 2003), and observations suggest possible dikes exposed on the floor of Cerberus Fossae (Head et al., 2003). Observations supporting the existence of lava infilling channels include (a) the presence of so-called ring-mound landforms imaged with HiRISE (High Resolution Imaging Science Experiment), which have been interpreted as volcanic (rootless) cones formed as lavas heated underlying groundwater causing steam explosions (Jaeger et al., 2007), (b) the presence of thin, concentric, lobate flow fronts that indicate overlapping lavas (Jaeger et al., 2007), and (c) the presence of platy-flow or platy-ridged surfaces indicating lava crusts (Chapman et al., 2010; Keszthelyi et al., 2000). However, the links between aqueous and lava processes, if they exist, remain elusive partly due to the uncertainty with regard to flow-rates and durations of flow, which are ultimately connected to whether multiple or single flow episodes produced the channels.

An alternate hypothesis is that lavas formed the Grjótá Valles, with the action of lavas as the dominant process in the channel formation (Leverington, 2004, 2006, 2011, 2018). This hypothesis was supported by observations of geomorphic/geologic features on the Moon and Venus. These features are similar to those reported from channels on Mars, such as sinuous channels, inner channels, anastomosing reaches, streamlined erosional residuals, branching channel patterns, and reaches suggestive of lateral or vertical erosion (Leverington, 2011). Furthermore, the formation of channels by lavas does not rely on the very large hydrological flow rates, sub-surface permeabilities, hydrologic head considerations, implied water abundances implied by an aqueous model, that do not concur with geochemical and mineralogical observations, and the lack of terrestrial analogs (Leverington, 2011). However, it is implied that if lavas did dominate channel formation, lava morphologies should be identifiable, such as lobate flow fronts, upstanding flows, platy-ridges, knobs, break-outs or rootless cones that characterize lava-infilled

channels described nearby on Mars, such as for Athabasca Valles, and they do not resemble sinuous rilles that are commonly associated with lava processes (Jaeger et al., 2007).

A third possibility is that channels formed during the passage of mudflows. Studies by Brož et al. (2020) looking at how the instability of water within a mud flow changes the mud behavior showed that mud exposed to atmospheric pressure and temperatures as low as that on Mars could propagate in a similar way to some terrestrial lava flows, notably pahoehoe flows. They showed that experimental mud flows in a low pressure/temperature chamber propagate like terrestrial pahoehoe lava flows, with liquid mud spilling from ruptures and then refreezing to form a new flow lobe. The channels would exhibit features characteristic of such mud flows, such as upstanding rubbly chaotic mudflow deposits with lobate fronts or distributary aprons.

We made detailed observations of the geometries, cross-sectional profiles, and cross-cutting relationships for geomorphic features. We also mapped the landforms to investigate whether the channels formed in single or repeated events. We mapped the geomorphology of the channel system and fractures using Context Camera (CTX) and HiRISE images from the Mars Reconnaissance Orbiter (MRO), measured cross-sectional profiles of landforms using Mars Orbiter Laser Altimeter (MOLA) data and assessed the timeline of events. Our interpretation is that at least five distinct channel-forming events occurred in Grjótá Valles. The channels are dominated by landforms cut by high rates of water/turbulent-lava flow, with these flows pre-dating the development of vertical offsets across the faults and fractures that are present. We consider this as evidence of at least five asynchronous fluvial flow episodes that occurred in this region of Mars.

1.1. Background

The Grjótá Valles outflow channel system emanates from the northernmost Cerberus Fossae (Figures 1a and 1b). The fault system of the northernmost Cerberus Fossae is a ~200 km long set of *en echelon* fissure segments located between 16.175°N/160.563°E, and 15.202°N/163.666°E (Brown & Roberts, 2019). The WNW-ESE orientation of the fissures would indicate that the fractures are sub-radial to Elysium Mons (Figure 1).

The faults in this region (Figure 1b) are relatively recent in that they crosscut pre-existing features of known, relatively young age with the fossae also offsetting late Amazonian Cerberus lavas and older inliers (Tanaka et al., 2005). Using crater counting methods, the ages of the youngest lava offset on the nearby Cerberus Fossae are <10 Ma (Hartmann & Berman, 2000; Head et al., 2003; Vaucher et al., 2009), which would imply that the fossae are even younger. However, studies by Golder et al. (2020) show that discrepancies in the ages of craters could be due to rheological changes produced during lava emplacement, meaning that at locations proximal to the inferred source of the lava, larger craters yield older model ages due to the weaker, more porous rock. At more distal locations from the inferred source of the lava, smaller craters yield younger model ages due to stronger, non-porous rock. Within the extent of the Grjótá Valles flow tract (Figure 1b), crater counting suggests that the implied ages range from 55 Ma (proximal) to 33 Ma (distal) (see Figure 2 for locations of crater counts) (Golder et al., 2020). Although uncertainty exists regarding how to interpret these ages, the fact that faults cross-cut and offset the surface would confirm the relatively young age of the faulting. The lavas in Grjótá Valles have been interpreted as lava emplaced as single flow units due to their morphologies and mapped extents (Hamilton, 2013; Jaeger et al., 2010).

Burr, Sakimoto, and McEwen (2002), Burr, Grier, et al. (2002) note that the Cerberus Plains show three spatially and temporally distinct, young aqueous flow channel systems (Figures 1a and 1b). One of these flow channel systems that we study herein, the unnamed northern channel system, has been suggested to be a ~100 km wide channel for water emanating from the northernmost Cerberus Fossae. It extends for a few hundred kilometres from the northernmost Cerberus Fossae to the north-east, then heading south-east before its surface expression becomes indistinct. Burr (2003) described fluvial geomorphic features indicating that water emanated from the source area of the northernmost Cerberus Fossae, flowed eastward, and then flowed south-east. Our study draws upon the work of previous studies such as Burr, Sakimoto, and McEwen (2002), Burr, Grier, et al. (2002) who suggested that repeated flow events may be responsible for the channels, and Burr, Sakimoto, and McEwen (2002), Burr, Grier, et al. (2002), and Plescia (2003) who suggested that the area exhibits the typical characteristics of channels produced by the catastrophic release of water, such as a well-defined source area, low sinuosity channels, and longitudinal grooving of channel floor, but this is a source of debate as described above (Leverington, 2011). Due to the resolution of data available to them at the time, they were unable to demonstrate cross-cutting relationships between individual channel sections or provide detailed observations of the source of flows.

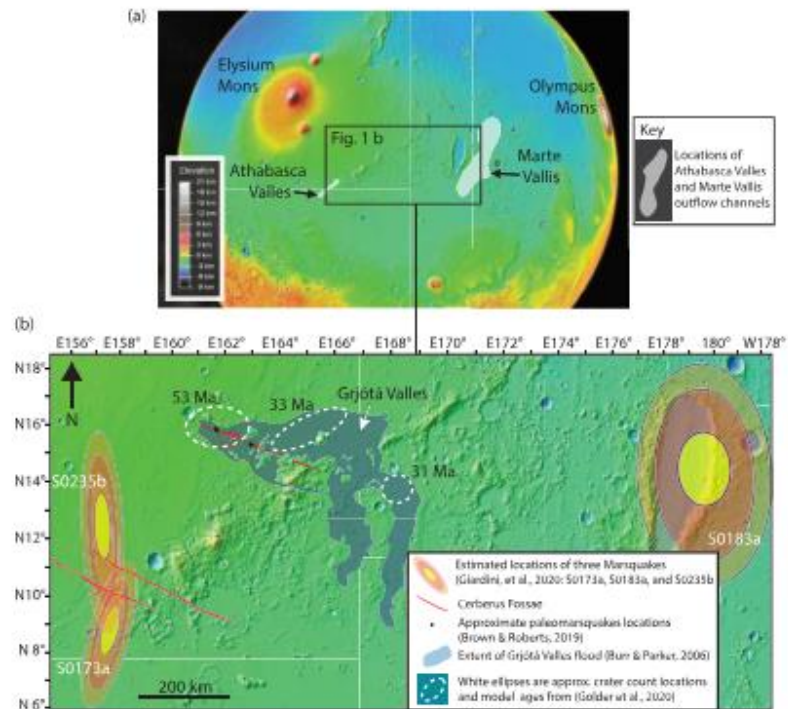


Figure 1. (a) Regional location map of the study area, with the locations of Athabasca Valles, and Marte Vallis highlighted. (b) The study area marked by a black rectangle to the east of the Elysium Rise. Estimated locations of three Marsquakes (Giardini et al., 2020) have been added (S0173a, S0183a, and S0235b) as colored ellipses. The extent of the Grjótá Valles flow tract (after Burr and Parker (2006)) has been added. Red lines mark the fossae, with the northernmost being the center of our study region, and the two to the south-west being the Northern and Southern Cerberus Fossae. Black dots identify two locations that show the approximate paleomarsquakes locations along the Northern Cerberus Fossae after Brown and Roberts (2019). The three white ellipses are crater count locations and their matching crater count model ages for lava flows in this area (Golder et al., 2020).

2. Method

We used the CTX image mosaic for Mars, a mosaic composite of all the Mars Reconnaissance Orbiter (MRO) Context Camera (CTX) images available (~6 m per pixel) and HiRISE images (~30 cm per pixel) from two instruments on the MRO to study an area of ~70,000 km² (Figure 2). We mapped the geomorphology of the channel system and fractures using a combination of CTX and HiRISE images, constrained the cross-sectional profiles of landforms using MOLA point data, and combined these observations to gain a chronology of the processes involved. We used Google Earth (which uses spherical normal (equatorial) variant of the Mercator projection for its maps) and HiView (which uses equirectangular projection map projections) to study and analyze the images.

Initial observations highlighted the presence of cross-cutting channels in several locations. Initially, we concentrated on mapping these locations and also attempted to map them back to sources where channels emanated from Cerberus Fossae (Figure 3). Mapping the channels back to their sources was found to be very important in delineating the total number of channels that could be identified because some cross-cutting relationships may be between distributary channels where the initial channel separates into multiple courses downstream. We were careful to make sure this did not lead to an exaggeration of the number of separate channels because the five

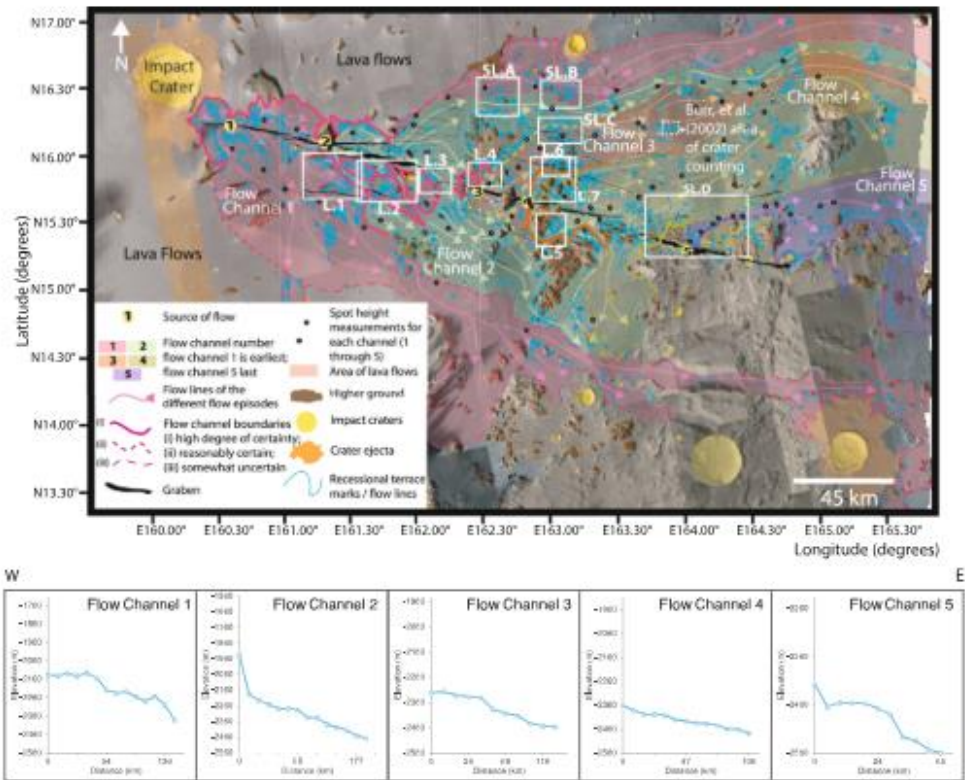


Figure 2. Regional Map (centered at 15.25°N, 162.85°E) of the study area marking the source areas of the five flows and the extent of each flow. The key study locations, 1 through 7 (Figures 4–10 respectively) are shown with white rectangles with L.1, L.2 and so on next to the boxes. Supplementary Locations A through D are shown with white rectangles with SL.A, SL.B and so on next to the boxes. Below the Regional Map are five spot height topographic profiles for the extent of each of the Flow areas 1 through 5 (kilometres/elevation) showing the downward-east sloping topography of the Regional Map area. The vertical exaggeration for each topographic profile is $\times 200$.

examples we have identified can all be mapped back to separate sources without interruption by a cross-cutting channel (Figure 12). Identification of cross-cutting relationships that can be mapped back to the channel sources was possible for some locations (Figures 4–10), but for others we were unable to map back to the sources due to ambiguous relationships on the imagery, and we include these as Figures S1–S4 in Supporting Information S1. In other words, Supplementary Locations (A through D) (Figure 2 and Figure S1–S4 in Supporting Information S1) were constructed in an identical manner to Locations (1 through 7) (Figures 2 and 4–10) except that their purpose was to assist in delineating the possible boundaries between two different flow areas in the downstream region, and thereby helped us develop our regional map (Figure 2).

Once the areas exhibiting cross-cutting relationships were identified, we then used MOLA Precision Experiment Data Records (PEDRs) to produce transects across the location areas. We did this to measure channel depths and hence amounts of channel incision. The laser spots cover an area of ~ 160 m diameter, spaced every ~ 300 m, and this introduces uncertainty in the elevation values estimated to be 1–10 m (Albee et al., 2001). Thus, we only report observations based on MOLA data if the vertical differences were > 10 m. We were also careful not to use laser returns from locations where the elevation changes dramatically at < 160 m horizontal length-scale,

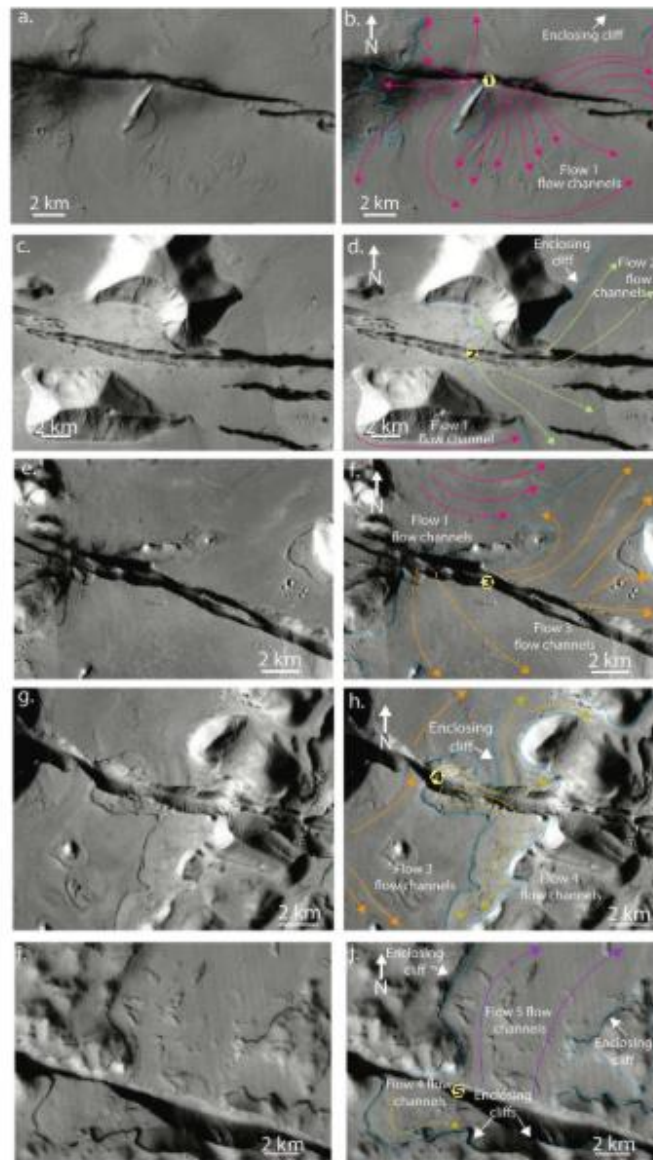


Figure 3.

excluding such locations by examining shadow lengths on CTX and HiRISE images. For individual locations, we found that MOLA data were available from about five to six transects for each location studied, and we used all available data points. From these data, we constructed topographic profiles (distance/elevation) across each of the areas of interest (11 locations). These topographic profiles were then studied in conjunction with the location images and our mapping to assess cross-cutting relationships between different channels by determining whether younger features incised down into and hence post-dated older features, as well as to measure the depth of such channels, and to gain elevation information for geomorphic features. We also studied the illumination of images as these helped us understand the aspects of slopes.

We then color coded geomorphic features separated by cross-cutting relationships to indicate a chronology for the geomorphic evolution. We then mapped between locations to produce a regional map of the channels, faults and their chronology (Figure 2). Once the location maps and topographic profiles were completed, and the regional map constructed, we then began to add flow lines to all maps, based upon the position and orientation of the different channels and the orientation of any geomorphic markers (such as depressions, linear features on the depression floor, linear features on the slopes of the depression margins, linear features on streamlined hills, and “tear-drop” shaped hills) within the channels.

We then constructed topographic profiles along channels from MOLA data. These profiles were used to assess whether individual channels flowed downhill, a key criterion in any interpretation.

3. Results

We created geomorphic maps of seven locations. We start by describing how we differentiate and identify key geomorphic features that are widespread across the region, using Location 1 as a type location (Figure 4). For each feature, we initially describe it before interpreting its significance. Following this, we use these type examples to interpret features in Locations 2 through to 7 (Figures 5–10; Figures S1–S4 in Supporting Information S1).

4. Location 1 (Figure 4)

Location 1 is centered at 15.70°N, 161.61°E, in the western portion of the overall channel system (Figure 2). It lies ~10 km south of the main system of faults, fractures and fissures that form part of Cerberus Fossae, but is crossed by smaller fractures that trend WNW-ESE. The area is a relatively flat plain with relatively low crater densities and several areas of higher topography with relatively high crater densities (see topographic profiles). The area also contains features that resemble channels and a streamlined island, and below we describe the five main features of note.

4.1. Descriptions of Five Geomorphic Landforms at Location 1

(i) *Depressions*: Our observations suggest the presence of depressions that are visible on the CTX images and are apparent in the MOLA profiles that cross their traces. The main depression runs NW-SE, is 3–4 km wide (Figures 4a–4c), and is in the order of 35–40 m deep; it is crossed by profiles c'-c, d'-d, e'-e, and f'-f (Figures 4a–4c and topographic profiles c'-c, d'-d, e'-e, and f'-f). Other depressions are shallower (<~10 m) and in places run W-E, such as the examples that are crossed by the northern end of profiles a'-a and b'-b, and the southern end of profile c'-c. The depressions are visible due to illumination from the SW that produces shadows on the NE of features that slope toward the NE and brighter areas on features that slope toward the SW.

(ii) *Linear features on depression floor*: These are 3–4 km long, ~50–100 m wide, defined by what appears to be a set of relatively smooth ridges because they have shadows on their E or NE sides and relatively brightly illuminated W or SW sides (Figure 4c). These ridges die out in both the north-northwest and south-southeast directions, terminating in places with lenticular-shaped ends.

(iii) *Linear features on the slopes of the depression margins*: Linear features also exist on the slopes forming the margins of the depressions. We identify up to 9 sub-parallel examples in Figure 4 c, but note that they have

Figure 3. Panels a. through j. show the approximate location of the source area for each flow (marked and unmarked), marked by a number (1, 2, 3, 4 and 5, representing each flow) in a yellow hexagon. (Panel a.—Flow 1, centered at 16.05°N, 160.48°E/panel c.—Flow 2, centered at 15.56°N, 161.33°E/panel e.—Flow 3, centered at 15.30°N, 162.41°E/panel g.—Flow 4, centered at 15.20°N, 163.05°E/panel j.—Flow 5, centered at 14.56°N, 164.17°E). The source areas have been disrupted by later faulting. Solid blue lines represent enclosing cliffs/boundaries which we are fairly certain about; dashed blue lines represent enclosing cliffs/boundaries which we are less certain about.

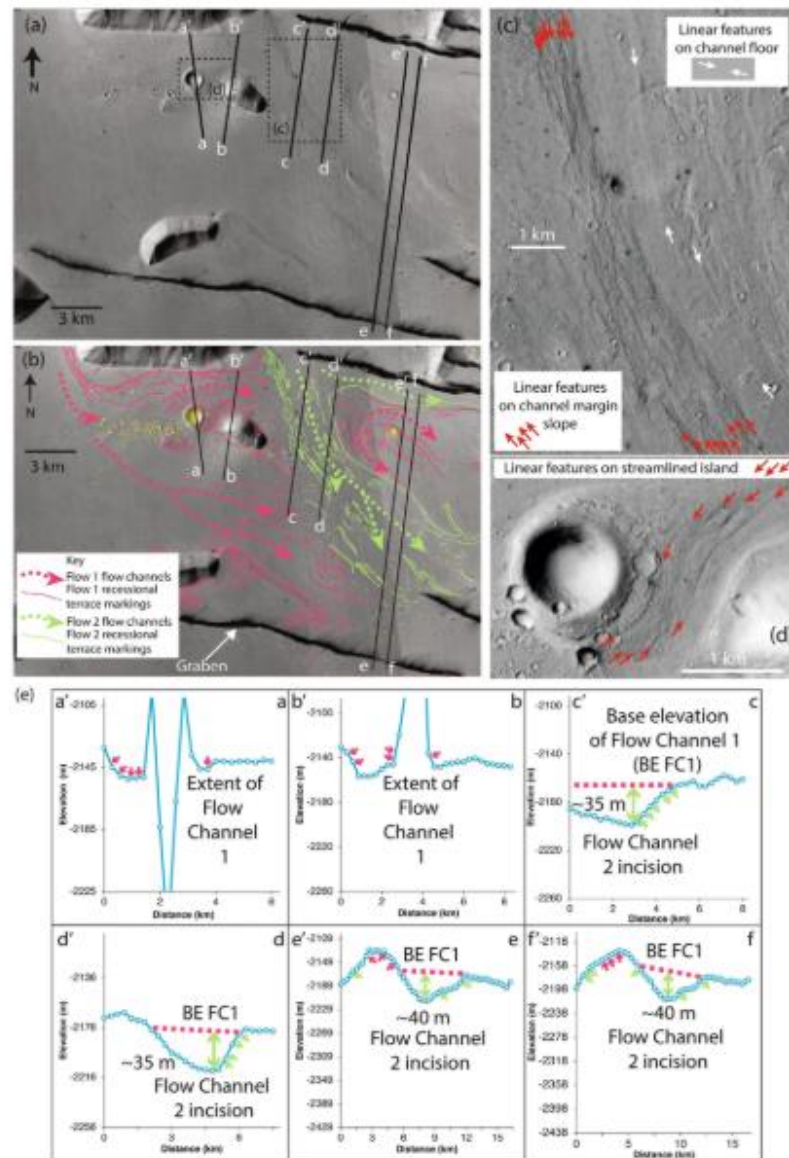


Figure 4.

embayed traces that are in places sinuous and discontinuous. They differ from the linear features that exist on the depression floors because MOLA data show they exist on the depression margin slopes and hence they have shadows on one side (the NE side in Figure 4c) but no relatively brightly illuminated opposite side. This implies that they resemble a set of steps cut into the slope on the margin of the depressions. MOLA data reveal that in places up to 9–10 of these linear features exist on slopes that are ~1 km across with relief of ~35–40 m, revealing that the individual steps are no more than a few meters high (e.g., Figure 4c and topographic profiles e'-e, d'-d, e'-e, and f'-f).

(iv) *Linear features on streamlined hills:* Linear features exist on the slopes of streamlined hills (e.g., Figure 4d). Like the linear ridges on the depression floors, they have shadows on their E sides but lack relatively brightly illuminated W sides. MOLA data reveal that they have vertical dimensions that are at most only a few meters (e.g., Figure 4c). They resemble the sets of steps similar to the linear features on the slopes of the depression margins.

(v) *"Tear-drop" shaped hills:* Hills shaped like tear-drops are common in the study area (e.g., Figures 4a, 4b, and 4c). These cover areas of a few hundred meters to several kilometres or more. Some have formed around pre-existing craters (e.g., Figure 4d) whereas others, with less obvious shapes, have formed around low hills (e.g., Figures 4a and 4b). Some of these low hills contain low-relief depressions (e.g., the hill crossed by profiles e'-e and f'-f shown in Figures 4a and 4b, and topographic profiles e'-e and f'-f).

4.2. Interpretation of Five Geomorphic Landforms at Location 1

(i) We interpret the depressions visible on the CTX images, and apparent in the MOLA profiles as channels. We do not think these depressions are cut by the passage of glaciers because their depth to width ratios ($40 \times 3,000$ m) have a form ratio of 0.013 and do not resemble terrestrial examples whose form ratios for active glacial channels are between 0.20 and 0.58 (Harbor, 1992). The fact that we have not observed up-standing morphologies like those associated with lavas or mudflow deposits, but instead incised depressions, does not support formation by flowing viscous lava or the passage of mudflows. Aqueous flow at relatively high velocity could produce such incision, but we concede that this does not rule out the flow of turbulent lavas that may also produce mechanical erosion (Jaeger et al., 2010).

(ii) We interpret linear features on the channel floor as so-called "longitudinal grooves" or "longitudinal lineations" (Baker & Patton, 1978; Burr, Sakimoto, & McEwen, 2002), that have been used to infer catastrophic flow terrain on Earth and Mars (Baker & Milton, 1974; Baker & Patton, 1978). They form due to high flow velocities associated with flowing water, perhaps with some entrained sediment, but turbulent lavas may have also been involved (e.g., Jaeger et al., 2010). In summary, observations imply that the channel-floor landforms were formed by rapid flow by water or turbulent lava.

(iii) We interpret the linear features on the depression margin slopes as terraces on channel margin slopes. Burr, Sakimoto, and McEwen (2002) interpreted similar terraces as the result of erosion of a pre-existing layered terrain, which may be correct in places. However, here we suggest that they also resemble "bathtub rings" that are cut by high flow velocities and vortices, and left by lowering water levels during waning flows (Baker, 1973; Baker & Patton, 1978). The flow of turbulent lava may also have caused the mechanical erosion (e.g., Jaeger et al., 2010). Note that the interpretations of erosion of pre-existing layered terrain vs. recessional terraces may not be mutually exclusive and hence challenging in regions where sub-horizontal lava layers may be present, such as Grjóta Valles. For the particular examples we describe, our interpretation is that as the fluids that formed

Figure 4. Maps and topographic profiles of Location 1 centered at 15.70°N, 161.61°E showing details of channels and cross-cutting relationships (see Figure 2 for location). (a) Map with CTX mosaic with Mars Orbiter Laser Altimeter (MOLA) transects; (b) Map with CTX mosaic with MOLA transects (black lines a'-a through f'-f) and interpreted channel markings/flow directions/recessional terrace markings. Topographic profiles a'-a through f'-f for each of the six transects with the blue line in each graph representing the MOLA transects. (c) Inset from CTX shows the detail of the channel floor. Linear features seen on the channel margin slope and the linear features observed on the channel floor do not resemble lava flow landforms, such as the presence of thin, concentric, lobate flow fronts that indicate overlapping lava or rootless cones. Our interpretation is that they resemble "longitudinal grooves" or "longitudinal lineations" that have been used to infer catastrophic flow terrain on Earth and Mars (Baker & Patton, 1978; Burr, Sakimoto, & McEwen, 2002), and/or turbulent lava (Jaeger et al., 2010) and resemble "bathtub rings" that are cut by high flow velocities and vortices, and left by lowering fluid levels during waning flows (Baker, 1973; Baker & Milton, 1974); we term the latter "recessional terraces." (d) Map showing similar linear features around a streamlined island. (e) Topographic profiles from MOLA spot heights (labeled a'-a through f'-f and located on (a, b)) showing the morphologies of channels and craters, and locating linear features on channel margins. The vertical exaggeration for each topographic profile is $\times 50$. Overall, for Location 1 our interpretation is that Flow 1 (that flowed from west to east/south-east) is cross-cut by channels formed by a later flow, Flow 2 (that flowed toward the SE). Flow sources are shown in Figure 3.

the channels waned, the fluid level dropped cutting terraces into bedrock so they formed during the recession of fluids leaving features that resemble bath-tub rings. We use the term “recessional terraces” for these features. We also note that we are unaware of any examples where terraces such as those we have observed are produced by flowing highly viscous lava or mudflows.

(iv) We interpret the linear features on the streamlined hills in the same way that we interpret the linear features on the depression margin slopes. We suggest that these are recessional terraces cut by waning rapid fluid flows.

(v) Due to the existence of what we interpret as recessional terraces cut by waning rapid fluid flows, we interpret the hills shaped like airfoils as streamlined islands cut by the flows. The most distinctive evidence for rapid fluid flows is the presence in the channels of streamlined mesas, that is, flat-topped, topographically higher landforms that have a “tear-drop” shape in plan view in which their rounded ends point up slope and their pointed ends down slope (Burr, Grier, et al., 2002). Such features are clearly visible in Figures 4a, 4b, and 4d notably the impact crater, which is a streamlined island through which transect A passes. It displays a classic tear-drop shape, with a generally flat top east of the impact crater with the pointed end of the “tear-drop” pointing downstream. The morphology of the streamlined islands suggests a general flow direction of NW to SE for the example shown in Figure 4b. Our estimated flow direction is the same in this location, and in fact across our entire study region, as Burr and Parker’s (2006) estimates (Figure 1b).

In summary, we note that Location 1 does not contain landforms reminiscent of highly viscous lava flows or mudflows. We see no examples of (a) ring-mound landforms that some have interpreted as volcanic (rootless) cones (Jaeger et al., 2007), (b) thin, concentric, lobate flow fronts that indicate overlapping lavas (Jaeger et al., 2007), or (c) platy-flow or platy-ridged surfaces indicating lava crusts (Chapman et al., 2010; Keszthelyi et al., 2000). This suggests to us that the channels and streamlined island were not cut by the passage of highly viscous lava. Instead, as suggested by a number of other authors (e.g., Burr, Grier, et al., 2002; Jaeger et al., 2010), we interpret the five geomorphic landforms described and interpreted above as evidence for aqueous flow or the flow of turbulent lavas. We also see no landforms reminiscent of other mudflow products such as (a) hills characterized by circular plan-map appearance with flow like structures extending from their bases, (b) elongated ridges with rough surfaces, (c) wide plateaus with a smooth central uplifted unit, often containing a rimless pit, and (d) an extensive and chaotic combination of overlapping landforms of points (a), (b), and (c) above (Brož et al., 2020; Cufin et al., 2021).

4.3. Observations of the Relative Chronology of Geomorphic Features

The key observation that provides evidence of relative chronology is that the channel that NW-SE cuts across and incises down across other channels that run E-W (Figure 4b). The base elevation of the E-W channels is about $-2,156$ m, while the base elevation of the NW-SE channel is deeper, at about $-2,194$ m, implying ~ 40 m of incision (Figure 4c topographic profiles a' - a through f' - f). Also, recessional terraces associated with the E-W channels and streamlined islands exist at elevations of $-2,130$ m to $-2,160$ m, above those for the NW-SE channel ($-2,170$ to $-2,195$ m). The recessional terraces from the E-W channels are oblique to and appear to be cross-cut by recessional terraces from the NW-SE channel (e.g., the region between profiles b' - b and c' - c, Figure 4b).

4.4. Interpretation of the Relative Chronology of Geomorphic Features

Our interpretation is that two distinct periods of channel formation are visible in Figure 4. The observation that our interpreted recessional terraces from the earlier channels are cross-cut by those associated with the later channel (as is also visible in Figures 2 and 5-9) suggests that water levels from an initial flow had fully waned before the later channel started to form. Thus, our interpretations suggest two separate flow events, and the separate channels are not simply anastomosing distributary channels from a single flow.

4.5. Channel Sources

We mapped the channels back to their sources. The earliest flow can be mapped back to a source located in the current location of the faults, fractures and fissures that form part of Cerberus Fossae (Figures 2, 3a, and 3b). The source region is partly surrounded by enclosing cliffs, and flow directions from the streamlined islands

suggest initial flow toward both the north and the south of the present position of Cerberus Fossae. The walls of the faulted depression appear fresh and un-eroded by the flow, suggesting that the faulting occurred after flow formation, similar to the interpretation of the timing of flows and faulting advanced by Burr, Sakimoto, and McEwen (2002) and Vetterlein and Roberts (2009). The later flow can be mapped back to a source, again partly constrained by enclosing cliffs (Figures 2, 3c, and 3d). The source of the second flow is to the east of the source of the earlier flow. Again, the walls of the faulted depression appear fresh and un-eroded by the flow, suggesting that the faulting occurred after flow formation.

5. Summary

Observations from Location 1 (Figure 4) have been interpreted to indicate the existence of two separate flow events (Flow 1 and Flow 2) that can be mapped back to two separate sources.

Note that we mapped a large number of geomorphic features for the other locations described in this paper. Space does not allow us to separate description and interpretation for every example in the rest of the paper, but we will show that the five types of geomorphic features described above are widespread across the region in Figure 2. We use our observations and interpretations of Location 1 as type examples to guide interpretations of the landforms in Locations 2 through 7 and Supplementary Locations A through D.

6. Location 2 (Figure 5)

Location 2, centered at 15.60°N and 162.07°E, is east of Location 1 and shows more examples of cross-cutting relationships between Flow 1 and Flow 2. The channels are characterized by linear features on the channel floors and on the channel margins that we interpret as longitudinal lineations and recessional terraces, respectively (Figure 5c). Landforms from Flow 1 are preserved on top of two streamlined islands defined by Flow 2, and we describe five inter-connected channels that we assign to Flow 2.

Flow 1 has produced multiple channels confined within the bounds of two streamlined islands. Flow directions during Flow 1 were generally to the NE and SE. We assign them to Flow 1, correlated with the features mapped at Location 1 because one of the streamlined islands exists in both Location 1 and Location 2, and the channels have a similar basal elevation (Location 1, -2,180 m; Location 2, -2,180 m).

Flow 2 cross-cuts Flow 1 in the following locations. For Flow 2, sub-channels 1 and 2 are tributary channels flowing north and south of a streamlined island that preserves features from Flow 1; they join to form sub-channel 3. Sub-channel 4 is a distributary channel that diverges from sub-channel 2 as they abut against a streamlined island, upon which features from Flow 1 are preserved. Sub-channel 5 is a distributary channel that diverges from sub-channel 3. At the northern end of transect c'-c (Figure 5 map 1 and 2) one of the Flow 2 channels, sub-channel 3, flows toward the SE and cuts across a channel associated with Flow 1. The base of sub-channel 3 incises downwards to -2,295 m, ~40 m beneath the basal elevation of channels associated with this portion of Flow 1 at around -2,255 m and also beneath recessional terraces of Flow 1 (Figure 5, topographic profile c'-c).

Flow 2 also incises down below the level of Flow 1. On transect c'-c (Figure 5, topographic profile c'-c), the elevation difference between the base of the second channel and the recessional terraces from Flow 1 suggest incision of up to ~40 m. MOLA transect D (Figure 5, maps A and B) crosses sub-channels 3 and 5 from Flow 2. Both topographic data and recessional terrace markings show that the Flow 2 channel (sub-channel 3) has incised beneath the elevation of Flow 1. The incision is approximately 40 m, from -2,250 m to -2,290 m, and these values are similar to those derived from transect c'-c. The distributary Flow 2 channel (sub-channel 5) has incised down into the surface produced by Flow 1. The incision is approximately 10 m, from -2,250 m to -2,260 m. Evidence that Flow 2 incises beneath the level of Flow 1 can also be seen in topographic profiles a'-a and b'-b, with values for incision of ~35 and ~15 m respectively.

In summary, Location 2 contains evidence for the two separate flows. Mapping back to the sources of the flows indicates that these are the same two flows identified at Location 1.

7. Location 3 (Figure 6)

Location 3 (Figure 6), centered at 15.58°N and 162.37°E, again reveals more details of the relationship between Flows 1 and 2, and is downstream of Location 2, where we might expect incision from Flow 2 to be greater. Flow

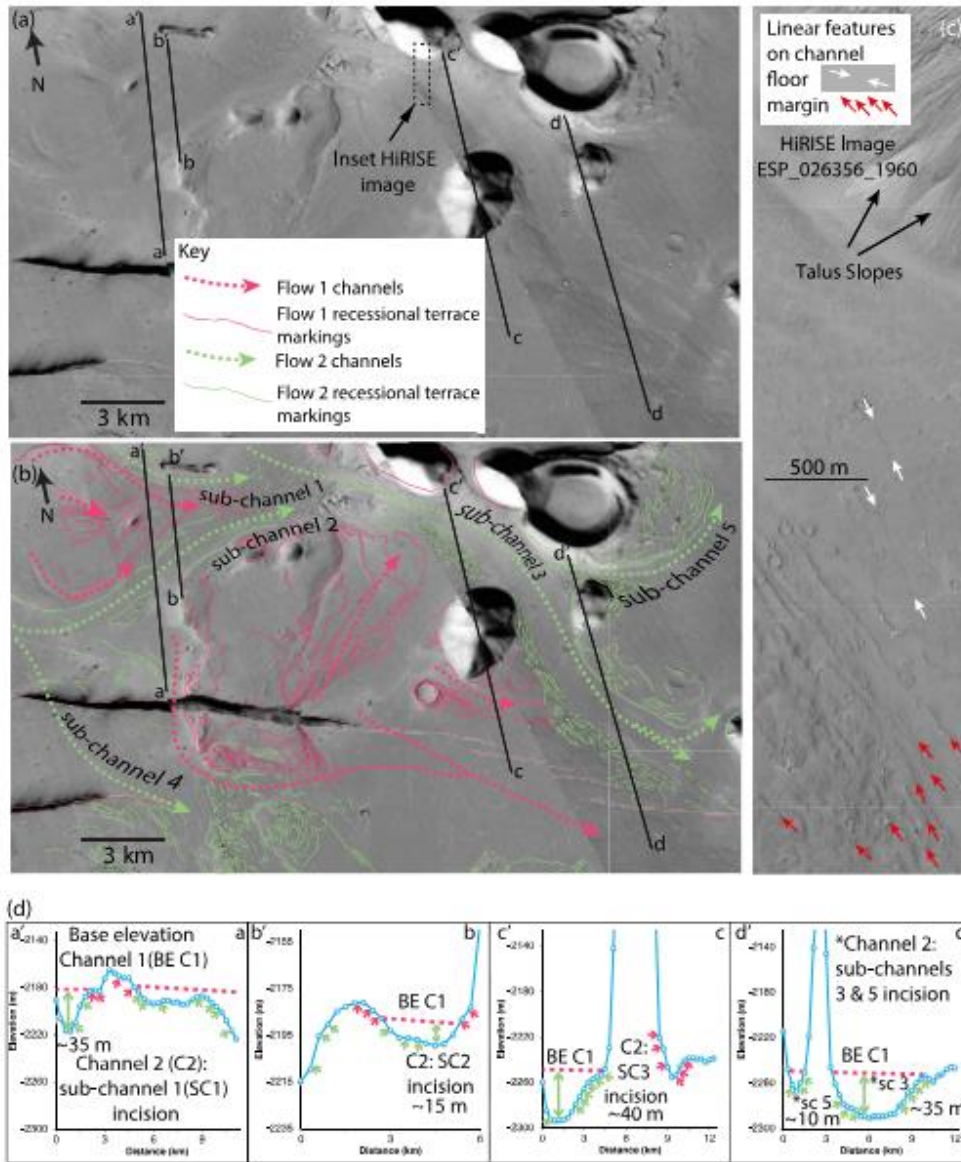


Figure 5.

1 landforms are correlated with those in Locations 1 and 2 because its base elevation is similar to that in those areas ($-2,270$ to $-2,290$ m) and a streamlined island upon which Flow 1 landforms exist is continuous between Locations 2 and 3. Similar to Locations 1 and 2, the floors and margins of channels are characterized by longitudinal lineations and recessional terraces (Figure 6c).

Within a streamlined island, a broad Flow 1 channel shows longitudinal lineations and streamline features indicating flow toward the east and NE, with evidence for waning flow in the form of recessional terraces. A later flow (Flow 2) channel flowed toward the SE, and in so doing cross-cut the Flow 1 channel landforms. The base elevation for the Flow 1 channel ranges from $-2,270$ m in the west (MOLA transect a'-a), to $-2,290$ m in the east (MOLA transect d'-d) (Figure 6, topographic profiles a'-a and d'-d). Flow 2 cross-cuts Flow 1 and a series of clear recessional terraces are found across the area of cross-cut. The orientation of these Flow 2 recessional terrace marks is perpendicular to the flow direction of Flow 1 and its recessional terraces. The extent of the Flow 2 incision decreases from west to east, with a maximum incision of approximately 70 – 75 m at MOLA transect a'-a, ~ 60 m at MOLA transect b'-b, ~ 50 m at MOLA transect c'-c, and ~ 35 m at MOLA transect d'-d, in tandem with the decreasing basal elevation of the Flow 1 channel features. The fissures are clearly younger geological features, as flow from Flow 2 is to the SE on both sides of the fissure, appearing to have been cut by the fissure, so the recessional terrace markings from the flows were disrupted by later faulting.

In summary, Location 3 contains evidence for the two separate flows. Mapping back to the sources of the flows indicates that these are the same two flows identified at Location 1.

8. Location 4 (Figure 7)

Location 4, centered at 15.60°N , 162.75°E , is located to the east of the previous three Locations, and focuses on a relatively early channel, possibly from Flow 1, that is cross-cut by a third flow, Flow 3. Again, these channels are characterized by longitudinal lineations and recessional terraces (Figure 7c).

Recessional terrace marks from a relatively early channel, together with MOLA data from transects a'-a, b'-b and c'-c, suggest that a flow channel, possibly Flow 1, flowed from the west to the north-east, with the base elevation for this channel being approximately $-2,310$ to $-2,320$ m (Figure 7 maps 1 and 2, and topographic profiles a'-a, b'-b and c'-c). We believe this may be a remnant of Flow 1 that was not covered by Flow 2 because the base levels of the channels at $-2,315$ m appear to be the downward continuation of those for Flow 1 at Location 3 (around $-2,290$ m), rather than a continuation of those for Flow 2, which are lower in elevation (around $-2,345$ m) (see Figure 11 for a compilation of elevations).

At Location 4, the later flow cannot be mapped back to flow source 2. Instead, the later flow is interpreted to be a third flow, Flow 3 because it can be mapped back to a source shown in Figures 2, 3c, and 3f. This source is again located along the trace of Cerberus Fossae, and faulting appears to post-date the flow because the walls of the subsided fault, fracture and fissure system appear un-eroded by the flow. The source is again partially surrounded by enclosing cliffs. Flow 3 incises downwards into the earlier flow by between ~ 7 and 25 m.

9. Location 5 (Figure 8)

Location 5, centered at 15.13°N and 163.21°E , is located further to the east and shows an area with three possible flow channels, two exhibiting cross-cutting relationships (Figure 8 maps 1 and 2). We suggest that a fourth flow, Flow 4, can be identified at this location because it can be mapped back to a separate source (Figures 2 and 3g and 3h). Again, these channels are characterized by longitudinal lineations and recessional terraces (Figure 8c).

Figure 5. Maps and topographic profiles of Location 2 centered at 15.60°N , 162.07°E showing details of channels and cross-cutting relationships (see Figure 2 for location). (a) Map 1—CTX mosaic with Mars Orbiter Laser Altimeter (MOLA) transects. (b) Map 2—CTX with MOLA transects (black lines a'-a through d'-d) and interpreted channel markings/flow directions/recessional terrace markings. (c) Inset map located in (a) from HiRISE Image ESP_026356_1960 showing details of a channel margin and channel floor. We interpret the presence of longitudinal lineations and recessional terraces (see caption of Figure 4). Talus slopes cover the channel margin in the NE. We have not identified features that would indicate lava flows such as lobate flow fronts or rootless cones. (d) Topographic profiles a'-a through d'-d for each of the four transects with the blue line in each profile representing the MOLA transects. The vertical exaggeration for each topographic profile is $\times 70$. Our overall interpretation of Location 2 is that older Flow 1 channels are cross-cut by later Flow 2 channels. Five distinct Flow 2 channels are visible from the maps and topographic profiles. Of interest is the island-like streamlined landform in the top left of Maps 1 and 2. The channels from Flow 2 have created a streamlined "island," but measurements and observations show that prior to Flow 2, this area was two or more smaller "islands" that the channels from Flow 1 had formed.

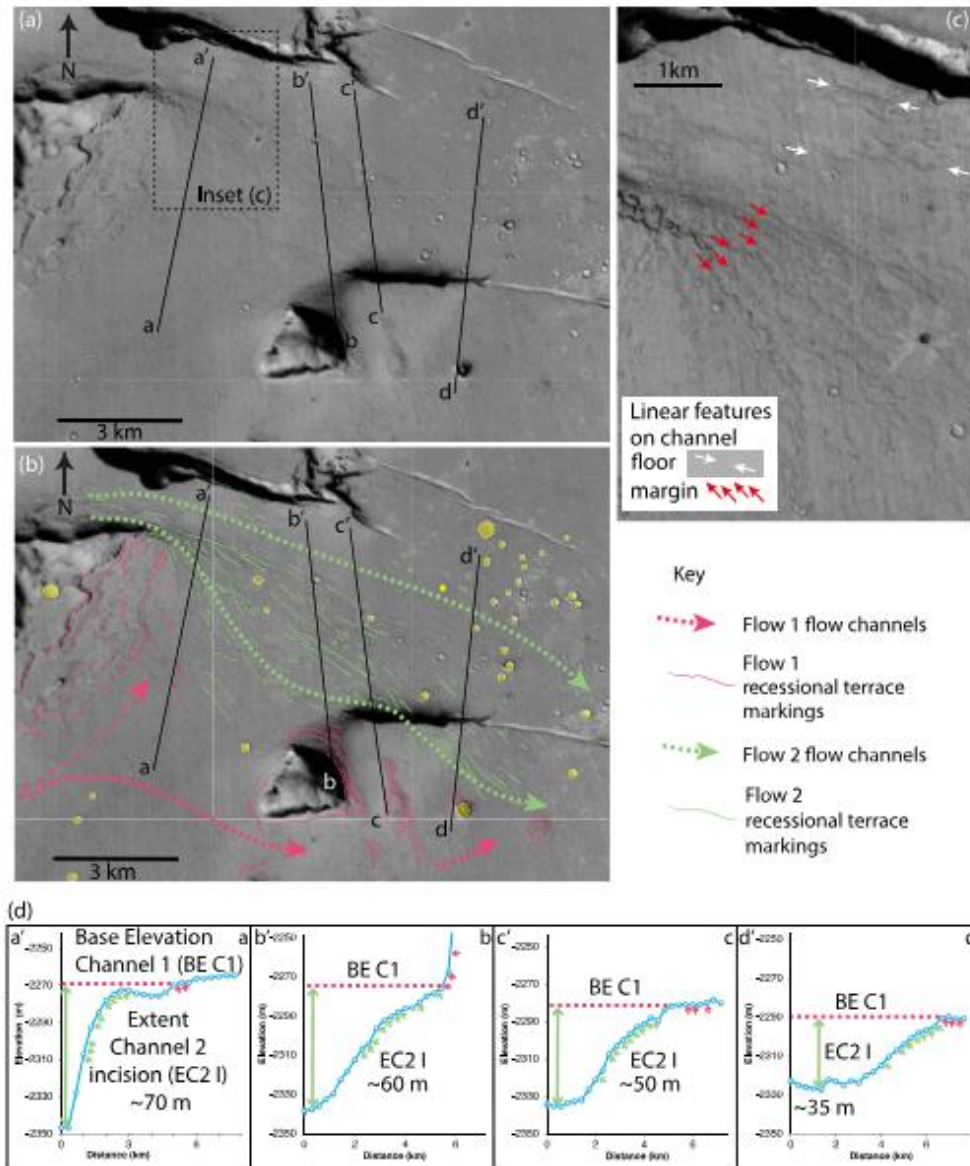


Figure 6.

Beginning with the oldest flow features, we find recessional terrace markings along two of the MOLA transects at relatively high elevations: $c'-c$ and $e'-e$. The topographic profiles for these transects (Figure 8 maps 1 and 2, and topographic profiles $c'-c$ and $e'-e$) indicate that recessional terraces at elevations of $-2,325$ m and $-2,340$ m are located high on the escarpment running SW-NE across the image (Figure 8, map 2, indicated by white arrows). We attribute these terrace markings to Flow 2. A later flow incised downwards, and this incision cut a channel down to $-2,370$ m (Figure 8, transects $d'-d$ and $e'-e$) and we suggest this is a remnant of the Flow 3 channel, untouched by the later Flow 4. Flow 4 incises more deeply, with the base of its channel at a depth of approximately $-2,379$ m (transect $a'-a$) to a maximum of $-2,390$ m (transect $c'-c$). Recessional terrace markings indicate that the flow for Flow 4 was ~ 20 m deep (Figure 8 transect $b'-b$).

We interpret the existence of Flow 4 because the channels we attribute to it can be mapped back to a source ~ 15 km to the NW (see Figures 2, 3g, and 3h). The source is a depression along the trace of Cerberus Fossae that is partially enclosed and defined by surrounding cliffs. The sidewalls of the fossae cross-cut the enclosing cliffs, indicating that the faulting is later than the flowing.

This location is the only one where we have identified possible examples of rootless cones (Figure 9b). However, these are adjacent to a later fissure and are not present over most of the channel floor. Our interpretation is that the rootless cones, if that is what they are, are related to a relatively small lava flow associated with the later fissure system, and hence were not responsible for channel formation because their associated lava post-dates channel formation.

10. Location 6 (Figure 9)

Location 6, centered at 15.60°N , 163.30°E , focuses on a small hummocky location just to the north of the main W to E fissure that cuts across the central Regional Map (Figure 2). The location is 20 km to the north-northeast of the source of Flow 4, and approximately 40 km to the NE of the source of Flow 3 (Figure 2). We interpret this area to show a cross-cutting relationship between a Flow 4 channel and earlier Flow 3 channels. There may also be remnant recessional terraces from a Flow 2 channel. Again, these channels are characterized by longitudinal lineations and recessional terraces (Figure 9c).

Location 6 illustrates how Flow 3 channels flowed around, through and possibly to the south of the two areas of higher ground (Figure 9). MOLA transects $a'-a$ and $b'-b$ show that what is probably the base of the Flow 3 channel was at approximately $-2,360$ m, and recessional terrace marks are visible up to about $-2,320$ m, indicating that the vertical extent of this Flow 3 channel was in the region of 33–35 m at these locations. MOLA transects $c'-c$, $d'-d$ and $e'-e$ are challenging to interpret because they pass through an area that divides the two areas of high ground. The presence of recessional terrace marks suggests that a channel from Flow 3 may have flowed in a south to north direction between the two areas of high ground. If this were the case, we can measure the height of Flow 3 using the base elevation of the channel as $-2,355$ m. Interpretation of the MOLA transects $c'-c$, $d'-d$ and $e'-e$ suggests that the maximum elevation of Flow 3 was about $-2,290$ m, meaning that the vertical extent of this Flow 3 channel at this location was ~ 65 m.

We believe a later flow incised across the channel from Flow 3 as shown in Figure 9, maps 1 and 2). This flow can be mapped back to a source (Figures 2, 3g, and 3h), identifying it as from Flow 4. A Flow 4 channel runs west to east at the bottom of Figure 9 map 2 with a base elevation of approximately $-2,380$ m, incising below the base of Flow 3 by up to ~ 45 m. Recessional terrace marks for the Flow 4 channel were identified on all MOLA transects, with the depth of the Flow 4 channels ranging from ~ 40 m ($a'-a$), ~ 20 m ($b'-b$ and $c'-c$) to only being able to identify the recessional terrace marks of Flow 4 ($d'-d$ and $e'-e$). A small area in Figure 9, map 2 shows a possible remnant area of a Flow 2 channel. The lowest identified recessional channel for this possible Flow 2 channel area was at about $-2,270$ m, and the highest identified recessional channel for this possible Flow 2 channel area was

Figure 6. Maps and topographic profiles of Location 3 centered at 15.58°N , 162.37°E showing details of channels and cross-cutting relationships (see Figure 2 for location). (a) Map 1—CTX mosaic with Mars Orbiter Laser Altimeter (MOLA) transects. (b) Map 2—CTX with MOLA transects (black lines $a'-a$ through $d'-d$) and interpreted channel markings/flow directions/recessional terrace markings. (c) Inset located in (a) from CTX data showing details of a channel floor and margin. We interpret the presence of longitudinal lineations and recessional terraces (see caption to Figure 4). Talus slopes cover the channel margin in the NE. We have not identified features that would indicate lava flows such as lobate flow fronts or rootless cones. (d) Topographic profiles $a'-a$ through $d'-d$. For each of the four transects with the blue line in each profile representing the MOLA transects. The vertical exaggeration for each topographic profile is $\times 70$. Overall our interpretation for Location 3 is that a broad Flow 1 channel oriented to the east or NE was cross-cut by a later flow (Flow 2) that cut a channel indicating flow toward the SE.

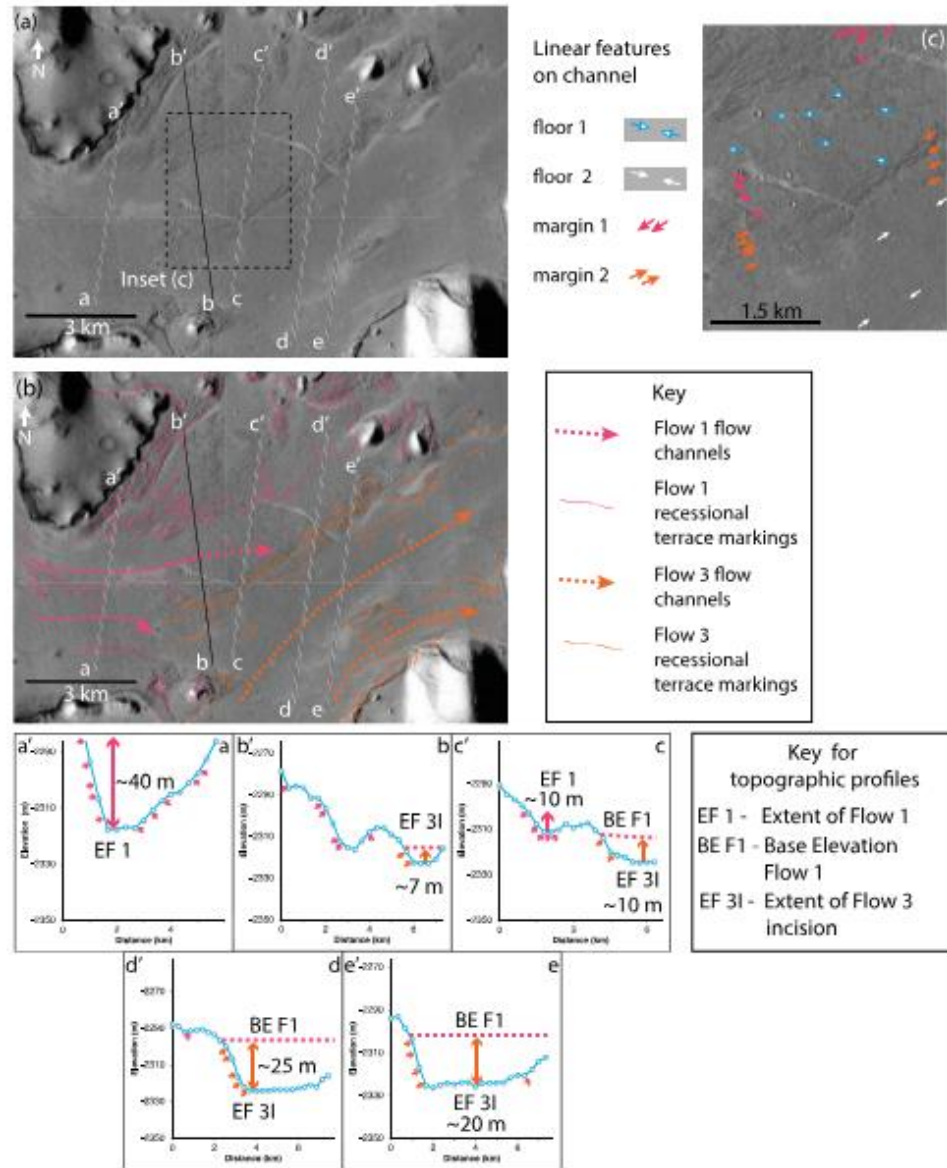


Figure 7.

at about $-2,220$ m. If this is indeed a Flow 2 channel remnant, the vertical extent of the flow would have been well in excess of 50 m.

Formation of the fossae took place after the flow episodes, with the fissures cross-cutting the recessional terrace markings of the flows, with the new fissure formations running parallel with the major fissure running through this region, approximately 16 km to the south-west of the newly formed fissure.

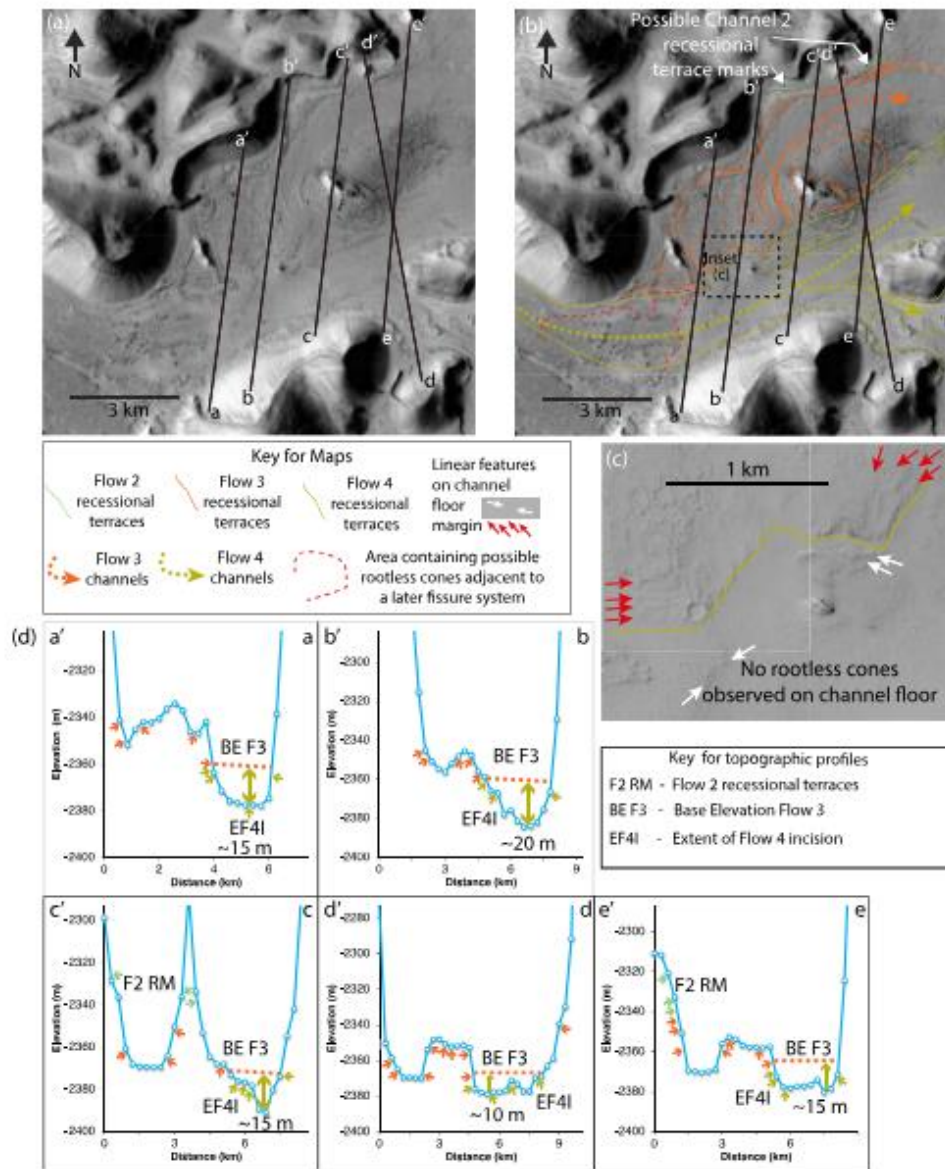
11. Location 7 (Figure 10)

Location 7, centered at 15.46°N , 163.28°E , is an extension of Location 6 (Figure 9) to the south and focuses on the relationship between Flows 3 and 4. As with Location 6 (Figure 9), Location 7 is a hummocky area with one clear and discernible flow channel running north-east and then east through the middle of the location map. There are smaller channels to the south of the map, notably a clear channel flowing in a north-easterly direction. Again, these channels are characterized by longitudinal lineations and recessional terraces (Figure 10c).

The center of Location 7 is just 15 km to the north-east of the estimated source area of Flow 4. The main channel from Flow 4 traces a path north-east across Figure 10 maps 1 and 2, cross-cutting earlier flow channels formed by Flow 3. The base elevation of the main Flow 4 channel appears to deepen as it moves west to east. Topographic profiles a'-a and b'-b reveal a base elevation of approximately $-2,365$ m, which deepens to approximately $-2,380$ m in topographic profiles c'-c, d'-d and e'-e. Recessional terrace marks for Flow 4 suggest that the upper limit for Flow 4 in this area was between $-2,330$ m and $-2,340$ m, meaning that the vertical extent of Flow 4 ranged from approximately 25 m (topographic profiles a'-a and b'-b) to between ~ 50 and ~ 25 m (topographic profiles c'-c, d'-d, and e'-e). Recessional terrace markings for an earlier flow are visible and are suggested to be Flow 3 recessional terraces based on the MOLA data that define the base of interpreted Flow 3 channels at similar elevations in different locations (e.g., $-2,325$ m in Location 4, Figure 7; $-2,335$ m in Location 7, Figure 10). Data regarding the possible source elevation of Flows 3 and 4 (Figure 11) show the Flow 3 source to be at $-2,325$ m and the Flow 4 source to be at $-2,344$ m. These measurements suggest that the recessional terrace markings and geomorphic features observed in Location 7 maps 1 and 2 (Figure 10) and accompanying topographic profiles, above $-2,330$ m are very likely Flow 3 markings and formations. The Flow 4 source elevation is $-2,344$ m, and therefore recessional marks at this elevation and below are most likely formed by Flow 4. Measurements are consistent with the incision depth of Flow 4 (just over $-2,380$ m), which we have calculated is the base elevation for Flow 4 in this location.

There are possibly four remnant Flow 3 areas within the Flow 4 areas, but they do not show clear cross-cutting relationships with Flow 4 and ascertaining a base elevation for Flow 3 in this region is challenging using available MOLA data because the coverage is sparse and does not include the locations that would possibly show clear cross-cutting relationships. MOLA data from Location 6 (Figure 9), on the northern section of the area within Location 7 (Figure 10), reveals a base elevation of Flow 3 as $-2,365$ m. However, that measurement is for the northern channel of Flow 3 and is distinct from the Flow 3 channel we are focused on in this image, that is, the channel to the south of the split-hill formation in the north of Location 7 maps 1 and 2 (Figure 10). Nevertheless, the measurement can be used as a useful proxy and does suggest that the Flow 4 channel measured here is in fact Flow 4 and not Flow 3 although the possibility does exist that we may have overestimated the vertical extent of Flow 4 in this region because the region is not comprehensively covered by MOLA transects.

Figure 7. Maps and topographic profiles of Location 4 centered at 15.60°N , 162.75°E showing details of channels and cross-cutting relationships (see Figure 2 for location). (a) Map 1—CTX mosaic with Mars Orbiter Laser Altimeter (MOLA) transects. (b) Map 2—CTX with MOLA transects (black lines a'-a through e'-e) and illustrated channel markings/flow directions/recessional terrace markings. (c) Inset located in (a) from CTX data showing details of a channel floor and margin. We interpret the presence of longitudinal lineations and recessional terraces (see caption to Figure 4). We have not identified features that would indicate lava flows such as lobate flow fronts or rootless cones. (d) Topographic profiles a'-a through e'-e for each of the five transects with the blue line in each profile representing the MOLA transects. The vertical exaggeration for each topographic profile is $\times 80$. Our overall interpretation of Location 4 is that a Flow 3 channel cross-cuts and incises into a channel from Flow 1. The age of the Flow 1 channel is interpreted from the observation that it can be mapped back to its source (see Figures 2 and 3). The Flow 3 channel indicates flow toward the NE. As seen from the topographic profiles c'-c, d'-d, and e'-e, the base of the Flow 3 channel is at approximately $-2,325$ m elevation at its deepest. This location appears to cross-cut a Flow 1 channel, possibly a remnant channel of Flow 1 that has not been covered by Flow 2 channels. The fissures are younger geological features, with recessional terrace markings from the flows disrupted by them.



12. Supplementary Locations A Through D (Figures S1–S4 in Supporting Information S1)

A further four locations were identified that provided further evidence and examples of landforms in downstream locations that may have been produced by flows. The four location figures and landforms are discussed in greater detail in the Supporting Information S1, Supplementary Locations A through D (Figures S1–S4 in Supporting Information S1) and these locations are also highlighted on Figure 2 as SL. A, SL. B, SL. C, and SL. D.

12.1. Construction of a Regional Map and Channel Profiles

The Regional Map (Figure 2), centered at 15.25°N, 162.85°E, and overall channel profiles (Figure 11) attempt to draw all the data gleaned from locations and supplementary locations into a whole to gain a regional overview of the flow geometries. The regional map covers the area of the northernmost Cerberus Fossae, a ~197 km long set of *en echelon* fissure segments that run west by north to east by south, as well as part of the unnamed northern channel system to the north and east, and the scoured area to the south and east of the northernmost Cerberus Fossae.

We believe that five separate flow episodes can be identified in our regional map (Figure 2). The cross-cutting relationships identified indicate that the fissures and fractures associated with Cerberus Fossae appear to have formed after the flow episodes.

The first, Flow 1, with its source at the far west of the northernmost Cerberus Fossae at an approximate elevation of -2,139 m, appears to be the largest in terms of area covered. This was followed, after an unknown period of time, by Flow 2, with its source further east and at an approximate elevation of -2,165 m. The cross-cutting relationships between Flow 1 and Flow 2 are the clearest, with Locations 1, 2, and 3 showing unambiguous evidence of the existence of two distinct flow episodes in this area. Moving further east, we find the source of Flow 3 at an approximate elevation of -2,325 m, with the source of Flow 4 at an approximate elevation of -2,345 m. Locations 4, 5, 6 and 7 (Figures 7–10) cover the Flow 3 region, with Location 4 looking at the Flow 1/Flow 3 relationship, and Locations 5, 6, and 7 (Figures 8–10) looking at the Flow 3/Flow 4 relationship. The source of Flow 5 is at an approximate elevation of -2,451 m, and is the final flow source we have identified. We observe that the channel rises very slightly by approximately 8 m before plateauing out and then flowing downward eastward. We have been unable to unambiguously define a cross-cutting relationship with Flow 4; hence, we chose to put this location in our Supplementary Locations files (Supplementary Location D (Figure S4 in Supporting Information S1)). However, as explained in regard to Supplementary Location D (Figure S4 in Supporting Information S1), we are confident that this is the source area of a separate flow (Flow 5), primarily due to geomorphic indicators that reveal the flow direction and the geomorphology of the source with enclosing cliffs.

Figure 11 shows the location (elevation and longitude) of each flow (Flow 1 through 5) at the source. We then connected the base elevation of each channel (1 through 4) at each location (L1 through L7) to the location of each flow source. Each of the five flow sources (Flow 1 through 5) occurs progressively further to the east, with the elevation of each source progressively lower from west to east. A key observation is that the channels from these five sources all flow downhill from west to east. Where cross-cutting relationships have been identified and described above, each channel is at a lower elevation and hence incises downwards into its predecessor channel.

In summary, our results indicate that the study area was affected by a sequence of multiple flows emanating from at least five sources that appear to be located progressively further to the east along the direction of the northernmost Cerberus Fossae. Each flow event flowed downhill and each flow source occurred at progressively lower elevations (Figures 11a and 11b).

Figure 8. Maps and topographic profiles of Location 5 centered at 15.13°N, 163.21°E showing details of channels and cross-cutting relationships (see Figure 2 for location). (a) Map 1—CTX mosaic with Mars Orbiter Laser Altimeter (MOLA) transects. (b) Map 2—CTX with MOLA transects (black lines a'–a through e'–e) and interpreted channel markings/flow directions/recessional terrace markings. An area containing possible rootless cones is adjacent to a later fissure system, and we interpret the cones to be related to volcanism associated with the fissures that post-date channel formation. (c) Inset showing details of the channel floor from HiRISE image ESP_025789_1950. No rootless cones are seen over most of the channel, for example, as shown herein. (d) Topographic profiles a'–a through e'–e for each of the five transects with the blue line in each profile representing the MOLA transects. Location 5 maps (centered at) and topographic profiles show an area of possibly three flow channels. The vertical exaggeration for each topographic profile is $\times 80$. Our overall interpretation of Location 5 is that a channel from Flow 4 cross-cuts and incises into older channels.

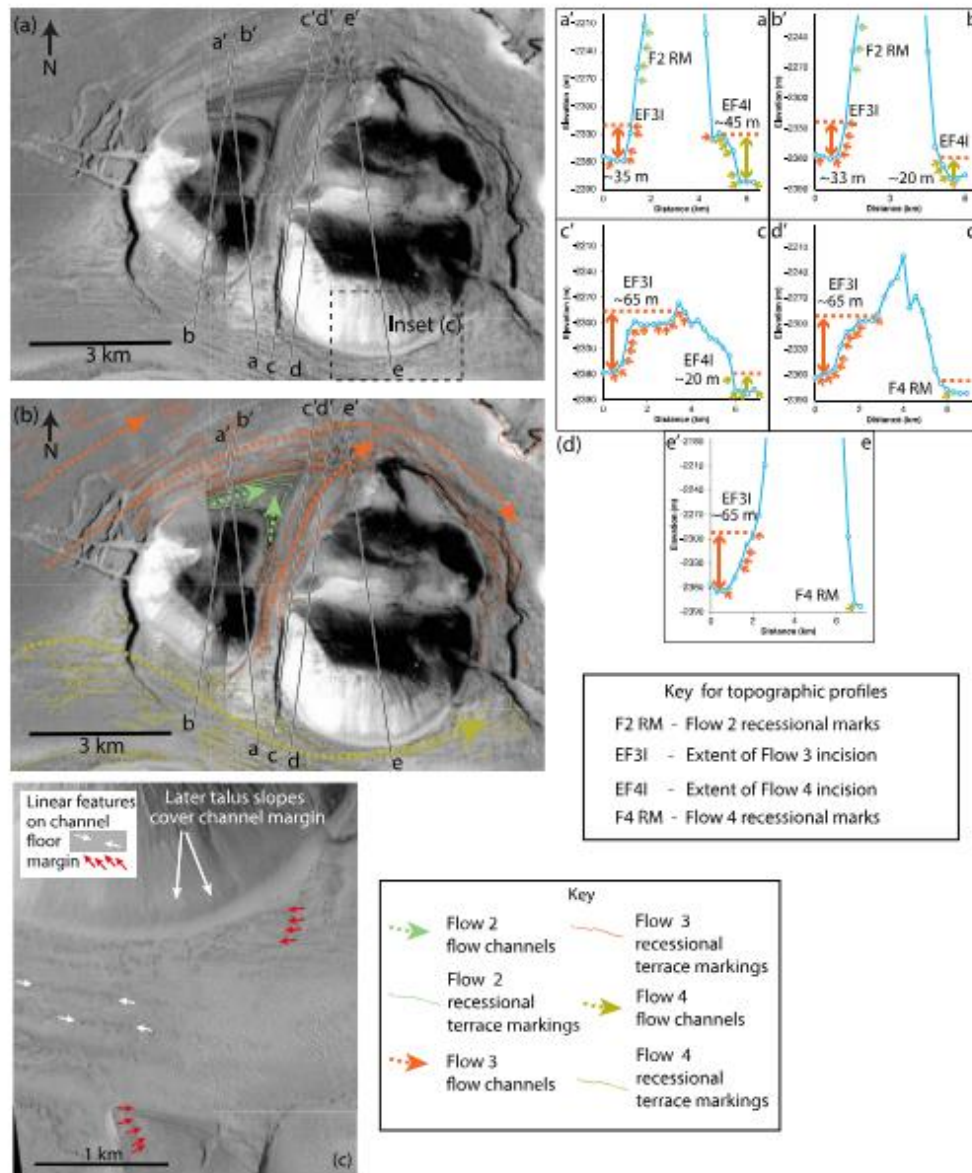


Figure 9.

13. Discussion

Prior to our study, discussions of the geology of the region of Grjótá Valles were focused on the following: (a) Extensive channels exist that emanate from the vicinity of faults, fractures and fissures that form part of Cerberus Fossae. (b) There had been some suggestions that multiple channels may exist, this was still an open question (Burr, Grier, et al., 2002; Burr & McEwen, 2002; Burr & Parker, 2006). (c) Channel formation processes had not been conclusively determined, with the debate still open (Burr, Sakimoto, & McEwen, 2002; Jaeger et al., 2010; Leverington, 2004, 2011). (d) Faulting post-dates channel formation evidenced by the un-eroded fracture walls, bi-directional flow directions at some flow sources, and fractures cross-cutting channels (Vetterlein and Roberts, 2009). (e) Evidence for palaeoseismic marsquakes has been gathered using observations of mobilized boulder populations (Brown & Roberts, 2019). (f) Seismicity associated with normal faulting marsquakes had been recorded in the vicinity by the InSight seismometers (Burr, Grier, et al., 2002; Brown & Roberts, 2019; Burr & Parker, 2006; Giardini et al., 2020; Golder et al., 2020; Jaeger et al., 2007, 2010; Leverington, 2011; Voight & Hamilton, 2018). Furthermore, Keske et al. (2015), studying outflow channels elsewhere on Mars noted that there exists a “close interplay of fluvial and volcanic activity” which would suggest “...that fluvial activity not only played a major role during a period of volcanism, but also may be linked to, or even triggered by, volcanic processes.” We note that if the eastward progression in channel formation is due to fault or dike propagation then in the past the distribution of seismicity would have changed through time, and this should be considered when developing models to explain the present-day seismicity.

Our results provide insights into the above because they document clear cross-cutting relationships between flow channels which can be mapped back to five distinct flow sources, with the locations of sources progressively located further to the east through time. Our observations confirm that the flows that formed the channels pre-dates surface faulting. If igneous processes are responsible for triggering the flows, then these processes acted before faulting appeared at the surface, and hence, this may or may not predate the onset of the present-day seismicity. This sequence is not unexpected, as the idea that injection of sub-surface dikes leads to the formation of overlying graben has been modeled (Rubin, 1992) and observed in terrestrial examples, with these ideas widely applied to graben on Mars. Indeed, the heating produced by dike injection has been suggested to provide the possibility of melting sub-surface ice, or releasing water trapped by ice (Head et al., 2003; McKenzie & Nimmo, 1999). However, the issue has been that the large geographic extent of the channels, for example, associated with Grjótá Valles, have been taken to suggest very large volumes of fluid, and hence flow-rates that may be implausibly high (Head et al., 2003; Leverington, 2011). If the dimensions of the active channel are smaller than that implied by a single larger channel, then the flow rates may also be proportionately lower. However, our lack of knowledge on the flow duration and composition of the flow limit our ability to state a specific flow rate. Furthermore, observations from the InSight seismometers suggest that the seismic velocity below 10 km for Elysium Planitia is too low to be ice-saturated (Manga & Wright, 2021).

Although It is clear that more work is needed to explain the links between igneous processes, faulting, seismicity, water/ice in the crust and formation of flow channels by water and/or turbulent lava, it is interesting that our results imply relatively small flows compared to previous estimates. This is because the total geographic extent of the channel system associated with Grjótá Valles was formed by at least five distinct flows and not a single event. Despite this conclusion, unfortunately, we have no way to quantify the volume or the flux rate of fluid discharge due to a lack of knowledge regarding the duration of each single flow event. Another interesting aspect is that the flow sources are located progressively further to the east through time. We have been unable to provide more data that constrain the process or processes that liberated the fluids, but we do provide the insight that those processes propagate to the east through time. One possibility is that eastward propagation of fluid release, if produced by melting due to the intrusion of sub-surface dikes, or eruption of turbulent lava, may suggest eastward dike propagation as is speculatively shown in Figure 12. Another alternative is that the intrusion of dikes occurred

Figure 9. Maps and topographic profiles of Location 6 centered at 15.60°N, 163.30°E showing details of channels and cross-cutting relationships (see Figure 2 for location). (a) Map 1—CTX mosaic with Mars Orbiter Laser Altimeter (MOLA) transects. (b) Map 2—CTX with MOLA transects (black lines a'–a through e'–e) and illustrated channel markings/flow directions/recessional terrace markings. Fissure extension took place after the flow episodes, with the new fissure formations running parallel with the major fissure running through this region, approximately 16 km to the south-west of the newly formed fissure. (c) Inset from HiRISE image ESP_028756_1960 showing details of the channel floor and margins. We interpret the presence of longitudinal lineations and recessional terraces (see caption to Figure 4). We have not identified features that would indicate lava flows such as lobate flow fronts or rootless cones. (d) Topographic profiles a'–a through e'–e for each of the five transects with the blue line in each profile representing the MOLA transects. The vertical exaggeration for each topographic profile is $\times 35$. Our overall interpretation of Location 6 is that Flow 4 channels cross-cut earlier Flow 3 channels. There also exist remnant recessional terraces from a possible Flow 2 channel.

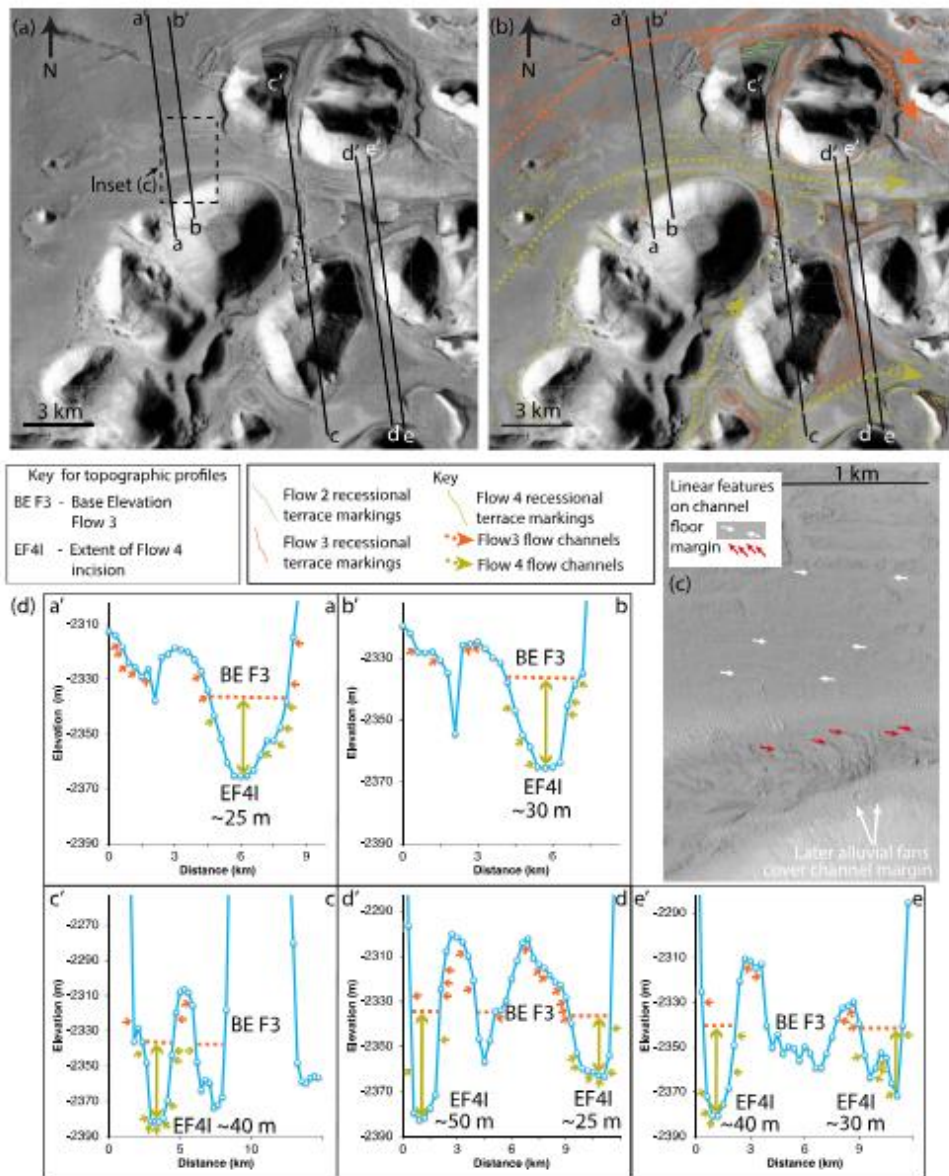


Figure 10.

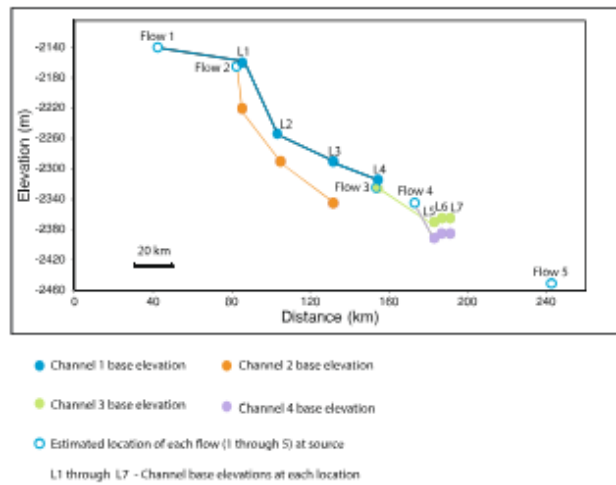


Figure 11. Shows the base elevations of identified flow channels in Locations 1 through 7 marked on the topographic profiles as L1, L2, L3, etc. The lowest elevation for each channel was used for each location and the estimated elevation at the source for each flow episode (Flows 1 through 5). The last three points on Flow 3 are very close together (within ~10–20 km) and within <10 m of each other vertically, and the same is true for the last three points in Flow 4; this is less than the uncertainty on vertical measurements from Mars Orbiter Laser Altimeter (± 10 m). We consider them to be at the same height within error and the likely slight downward slope cannot be measured but also cannot be excluded within error. The vertical exaggeration for the topographic profile is $\times 80$.

progressively further east but emanated from a sub-surface volcanic source that already underlay the region (Genova et al., 2016; Golder et al., 2020). Although we have no direct constraints on the time scale of this propagation, we note that Golder et al. (2020) provide crater count ages that become progressively younger toward the east (53 Ma, then 33 Ma, then 31 Ma) in the region we study. They suggest that the change in apparent age is caused by changes in the rheological properties of the lavas during emplacement, such as material strength and porosity. Although we have no grounds to dispute this explanation, we note that the ages are obtained from areas that partially overlap the flow deposits (Figure 1b), and the age of 53 Ma coincides within the proximal regions for Flow 1 and Flow 2, the 33 Ma age coincides with the region occupied by the distal parts of our Flow 3 and Flow 4, and the 31 Ma age coincides with a region to the east of the area we have mapped that may be occupied by Flow 5. We suggest that more work may be warranted to clarify the geological significance of crater counts in Grjótá Valles as this may help elucidate the timing of the relationships between volcanic, aqueous, faulting and seismicity processes in this enigmatic region.

14. Conclusions

We conducted a detailed analysis of the northernmost Cerberus Fossae and the surrounding area using CTX images, HiRISE images and MOLA data. Our conclusions are as follows.

Figure 10. Maps and topographic profiles of Location 7 centered at 15.46°N, 163.28°E showing details of channels and cross-cutting relationships (see Figure 2 for location). (a) Map 1—CTX mosaic with Mars Orbiter Laser Altimeter (MOLA) transects. (b) Map 2—CTX with MOLA transects (black lines a'–a through e'–e) and illustrated channel markings/flow directions/recessional terrace markings. (c) Inset from HiRISE image ESP_028400_1955 showing details of a channel floor and margins. We interpret the presence of longitudinal lineations and recessional terraces (see caption to Figure 4). We have not identified features that would indicate lava flows such as lobate flow fronts or rootless cones. (d) Topographic profiles a'–a through e'–e for each of the five transects with the blue line in each profile representing the MOLA transects. The vertical exaggeration for each topographic profile is $\times 110$. Our overall interpretation of Location 7 is that channels from Flow 4 flowed to the east, cross-cutting earlier flow channels formed by Flow 3 channels.

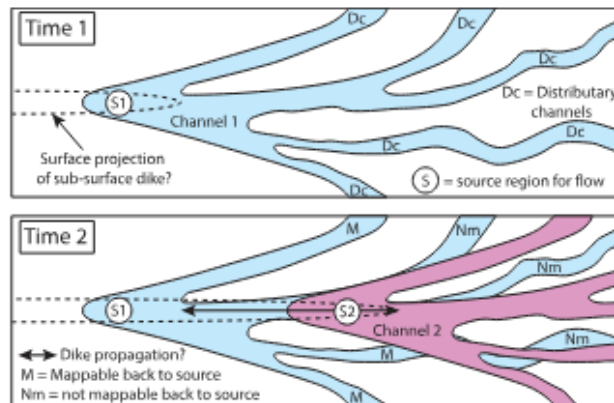


Figure 12. Schematic summary of cross-cutting relationships between channels. Time 1 took place before the later Time 2. In Time 1, a flow occurred at S1, and the flow formed distributary channels (Dc) that can all be mapped back to the source of the flow, S1. In Time 2, a later flow S2 occurred further east than the earlier S1. The flow from S2 formed distributary channels which cross cut the earlier distributary channels formed by S1 flows. In Time 2, we now see that only three of the five S1 distributary channels can be mapped back to their S1 source. This is why it is challenging to map some distributary channels back to the source of the flows. Speculative dike geometry at depth.

1. Examination of the floors and margins of prominent channels reveals the presence of landforms such as channel floor longitudinal lineations and channel margin recessional terraces that appear to have been cut by water and/or turbulent lava, with no signs of landforms that would suggest that the channels have been cut by viscous lava or mudflows.
2. Cross-cutting relationships and channel incision reveal that at least five asynchronous flow episodes have taken place, sourced at different locations along a 180 km section of the main northernmost Cerberus Fossae, demonstrating that the channels were formed by multiple events.
3. Channels flow downhill away from the sources we have identified, with younger channels cross-cutting older channels, incising downwards by 25–70 m.
4. The source areas for the flows are located progressively further to the east through time.
5. We have been unable to explain the eastward progression of flow sources, but we suggest that possibilities may include either dike propagation from west to east, which melted near-surface ice or released turbulent lava, or that magma from an underlying regional melt zone-influenced melting of ice near the surface further to the east through time.
6. Further work is required to elucidate the mechanisms responsible for the release of fluids; however, our observations show that regardless of the explanation, the mechanism does not need to produce the large volumes of fluid implied if the channels are all interpreted to have formed asynchronously.

Data Availability Statement

We acknowledge the use of imagery provided by services from NASA's Mars Reconnaissance Orbiter (MRO), and MOLA Precision Experiment Data Records (PEDRs). We acknowledge the use of Google Earth in our research. All data are available in Brown and Roberts (2022).

References

- Albee, A. L., Arvidson, R. E., Pallacini, F., & Thorpe, T. (2001). Overview of the Mars global surveyor mission. *Journal of Geophysical Research*, 106(E10), 23291–23316. <https://doi.org/10.1029/2000je001306>
- Baker, V. R. (1973). 144. *Paleohydrology and sedimentology of Lake Missoula flooding in eastern Washington*. Geological Society of America Special Papers. Preprint <https://doi.org/10.1130/spc144>

Acknowledgments

This work was part of a self-funded PhD study by Brown. Roberts acknowledges STFC Grant ST/R016037/1 in the initial part of this work. A Data Availability Statement is available for this paper, with all data used being available through Figshare. We thank the Editors, Susan Conway and several anonymous reviewers for comments that improved the paper.

- Baker, V. R., & Milton, D. J. (1974). Erosion by catastrophic floods on Mars and Earth. *Icarus*, 23(1), 27–41. [https://doi.org/10.1016/0019-1035\(74\)90101-8](https://doi.org/10.1016/0019-1035(74)90101-8)
- Baker, V. R., & Patton, P. C. (1978). New evidence for pre-Wisconsin flooding in the channeled scabland of Eastern Washington. *Geology*, 6(9), 567. [https://doi.org/10.1130/0091-7613\(1978\)6<567::aeflgi>2.0.co;2](https://doi.org/10.1130/0091-7613(1978)6<567::aeflgi>2.0.co;2)
- Berman, D. C., & Hartmann, W. K. (2002). Recent fluvial, volcanic, and tectonic activity on the Cerberus Plains of Mars. *Icarus*, 159(1), 1–17. <https://doi.org/10.1006/icar.2002.6920>
- Brown, J. R., & Roberts, G. P. (2019). Possible evidence for variation in magnitude for meanderbank from fallen boulder populations, Crjota Valles, Mars. *Journal of Geophysical Research: Planets*, 124(3), 801–822. <https://doi.org/10.1029/2018je005622>
- Brown, J. R., & Roberts, G. P. (2022). Repeated, cross-cutting and spatially migrating outflow channel formation, Grijota Valles, Mars, figshare. Figshare. Retrieved from https://figshare.com/collections/Repeated_cross-cutting_and_spatially_migrating_outflow_channel_formation_Grijota_Valles_Mars/5794766
- Broß, P., Kryza, O., Wilson, L., Conway, S. J., Hauber, E., Mazzini, A., et al. (2020). Experimental evidence for lava-like mud flows under Martian surface conditions. *Nature Geoscience*, 13(6), 403–407. <https://doi.org/10.1038/s41561-020-0577-2>
- Burr, D. M., & Parker, A. H. (2006). Grijota Valles and implications for flood sediment deposition on Mars. *Geophysical Research Letters*, 33(22), L22201. <https://doi.org/10.1029/2006gl028011>
- Burr, D. M. (2003). Hydraulic modelling of Athabasca Vallis, Mars. *Hydrological Sciences Journal*, 48(4), 655–664. <https://doi.org/10.1623/hysj.48.4.655.51407>
- Burr, D. M., Grier, J. A., McEwen, A. S., & Keszeihelyi, L. P. (2002). Repeated aqueous flooding from the Cerberus Fossae: Evidence for very recently extant, deep groundwater on Mars. *Icarus*, 159(1), 53–73. <https://doi.org/10.1006/icar.2002.6921>
- Burr, D. M., & McEwen, A. S. (2002). The extremes of the extremes: Extraordinary floods: Proceedings of an international symposium on extraordinary floods held at Reykjavik, Iceland. In July 2000. *Wallfingford: International association of hydrological sciences. Recent extreme floods on Mars* (p. 101).
- Burr, D. M., Sakimoto, E. H., & McEwen, A. S. (2002). Recent aqueous floods from the Cerberus fossae, Mars. *Geophysical Research Letters*, 29(1), 1013. <https://doi.org/10.1029/2001gl013345>
- Burr, D. M., Wilson, L., & Bangery, A. S. (2009). Floods from fossae: A review of Amazonian-aged extensional-tectonic megaflood channels on Mars. *Megaflooding on Earth and Mars* (pp. 194–208). <https://doi.org/10.1017/9780511635632.010>
- Car, M. H. (1979). Formation of Martian flood features by release of water from confined aquifers. *Journal of Geophysical Research*, 84(B6), 2995. <https://doi.org/10.1029/jb084i06p02995>
- Chapman, M. G., Neukum, G., Durrke, A., Michael, G., van Gansell, S., Kneissl, T., et al. (2010). Amazonian geologic history of the Echus Chasma and Kasei Valles system on Mars: New data and interpretations. *Earth and Planetary Science Letters*, 294(3–4), 238–255. <https://doi.org/10.1016/j.epsl.2009.11.034>
- Cufin, V., Broß, P., Hauber, E., & Markonis, Y. (2021). Mud flows in the southwestern Utopia Planitia, Mars. <https://doi.org/10.5194/eps2021-1-382>
- Genova, A., Goossens, S., Lemoine, F. G., Mazarico, E., Neumann, G. A., Smith, D. E., & Zuber, M. T. (2016). Seasonal and static gravity field of Mars from MGS, Mars Odyssey and MRO Radio Science. *Icarus*, 272, 228–245. <https://doi.org/10.1016/j.icarus.2016.02.050>
- Giardini, D., Lognonne, P., Banerdt, B., Boese, M., Ceylan, S., Clinton, J., et al. (2020). Seismicity of Mars. *Nature Geoscience*(13), 205–212. <https://doi.org/10.5194/egusphere-egu2020-20437>
- Golter, K. B., Burr, D. M., & Kattenhorn, S. A. (2020). Investigation of target property effects on crater populations in long lava flows: A study in the Cerberus region, Mars, with implications for magma source identification. *Icarus*, 335, 113388. <https://doi.org/10.1016/j.icarus.2019.113388>
- Hamilton, C. W. (2013). Floodlavas associated with the Cerberus Fossae 2 unit in Elysium. *Lunar and Planetary Institute Science Conference Abstracts*, 44, 3070. Retrieved from https://www.researchgate.net/publication/258804346_Flood_Lavas_Associated_with_the_Cerberus_Fossae_2_unit_in_Elysium_Planitia_Mars
- Harbor, J. M. (1992). Numerical modeling of the development of U-shaped valleys by glacial erosion. *The Geological Society of America Bulletin*, 104(10), 1364–1375. [https://doi.org/10.1130/0016-7606\(1992\)104<1364::mtdco>2.3.co;2](https://doi.org/10.1130/0016-7606(1992)104<1364::mtdco>2.3.co;2)
- Hartmann, W. K., & Berman, D. C. (2000). Elysium Planitia Lava flows: Crater count chronology and geological implications. *Journal of Geophysical Research*, 105(E6), 15011–15025. <https://doi.org/10.1029/1999je001189>
- Head, J. W., III., & Wilson, L. (2002). Mars: A review and synthesis of general environments and geological settings of magma-H₂O interactions. *Geological Society, London, Special Publications*, 202(1), 27–57. <https://doi.org/10.1144/GSL.SP.2002.202.01.03>
- Head, J. W., Mitchell, L. K., & Wilson, L. (2003). Generation of recent massive water floods at Cerberus Fossae, Mars by dike emplacement, cryospheric cracking, and confined aquifer groundwater release. *Geophysical Research Letters*, 30(11), 1577. <https://doi.org/10.1029/2003gl017135>
- Jaeger, W. L., Keszeihelyi, L., Skinner, J., Milazzo, M., McEwen, A., Titus, T., et al. (2010). Emplacement of the youngest flood lava on Mars: A short, turbulent story. *Icarus*, 205(1), 230–243. <https://doi.org/10.1016/j.icarus.2009.09.011>
- Jaeger, W. L., Keszeihelyi, L. P., McEwen, A. S., Dundke, C. M., & Russell, P. S. (2007). Athabasca Valles, Mars: A lava-draped channel system. *Science*, 317(5845), 1709–1711. <https://doi.org/10.1126/science.1143315>
- Jones, A. P., McEwen, A., Tornabene, L., Baker, V., Melosh, H., & Berman, D. (2011). A geomorphic analysis of Hale Crater, Mars: The effects of impact into ice-rich crust. *Icarus*, 211(1), 259–272. <https://doi.org/10.1016/j.icarus.2010.10.014>
- Kattenhorn, S. A., & Meyer, J. A. (2010). Magmatic dikes and megafloods: A protracted history of interactions. Retrieved from https://www.researchgate.net/publication/270572954_Magmatic_dikes_and_megafloods_a_protracted_history_of_interactions_between_magma_and_subsurface_ice_Cerberus_Fossae_Mars
- Keske, A. L., Hamilton, C. W., McEwen, A. S., & Daubar, I. J. (2015). Episodes of fluvial and volcanic activity in Mangala Valles, Mars. *Icarus*, 245, 333–347. <https://doi.org/10.1016/j.icarus.2014.09.040>
- Keszeihelyi, L., McEwen, A. S., & Thordarson, T. (2000). Terrestrial analogs and thermal models for Martian flood lavas. *Journal of Geophysical Research*, 105(E6), 15027–15049. <https://doi.org/10.1029/1999je001191>
- Keszeihelyi, L. P., Denlinger, R. P., O'Connell, D. R. H., & Burr, D. M. (2007). Initial insights from 2.5D hydraulic modeling of floods in Athabasca Valles, Mars. *Geophysical Research Letters*, 34(21), L21206. <https://doi.org/10.1029/2007gl031776>
- Leverington, D. W. (2004). Volcanic ridges, streamlined islands, and the origin of outflow channels on Mars. *Journal of Geophysical Research*, 109(E10), E10011. <https://doi.org/10.1029/2004je002311>
- Leverington, D. W. (2006). Volcanic processes as alternative mechanisms of landform development at a candidate Crater-Lake site near Tyrhenia Patena, Mars. *Journal of Geophysical Research*, 111(E11), E11002. <https://doi.org/10.1029/2004je002382>

- Leverington, D. W. (2011). A volcanic origin for the outflow channels of Mars: Key evidence and major implications. *Geomorphology*, 132(3–4), 51–75. <https://doi.org/10.1016/j.geomorph.2011.05.022>
- Leverington, D. W. (2018). Is Kasei Valles (Mars) the largest volcanic channel in the solar system? *Icarus*, 301, 37–57. <https://doi.org/10.1016/j.icarus.2017.10.007>
- Manga, M. (2004). Martian floods at Cerberus Fossae can be produced by groundwater discharge. *Geophysical Research Letters*, 31(2), L02702. <https://doi.org/10.1029/2003gl018958>
- Manga, M., & Wright, V. (2021). No cryosphere-confined aquifer below insight on Mars. *Geophysical Research Letters*, 48(8), e2021GL093127. <https://doi.org/10.1029/2021gl093127>
- McKenzie, D., & Nimmo, F. (1999). The generation of Martian floods by the melting of ground ice above Dykes. *Nature*, 397(6716), 231–233. <https://doi.org/10.1038/16649>
- Morgan, G. A., Campbell, B. A., Carter, L. M., Plant, J. J., & Phillips, R. J. (2013). 3D reconstruction of the source and scale of buried young flood channels on Mars. *Science*, 340(6132), 607–610. <https://doi.org/10.1126/science.1234787>
- Plescia, J. B. (2003). Cerberus fossae, Elysium, Mars: A source for lava and water. *Icarus*, 164(1), 79–95. [https://doi.org/10.1016/S0019-1035\(03\)00139-8](https://doi.org/10.1016/S0019-1035(03)00139-8)
- Rubin, A. M. (1992). Dike-induced fracturing and graben subsidence in volcanic rift zones. *Journal of Geophysical Research*, 97(B2), 1839–1858. <https://doi.org/10.1029/91j02170>
- Tanaka, K. L., Skinner, J. A., & Hare, T. M. (2005). "Geologic map of the northern plains of Mars," *scientific investigations map*. Preprint. <https://doi.org/10.3133/sim2888>
- Vacher, J., Baratoux, D., Mangold, N., Pinet, P., Karita, K., & Gregoire, M. (2009). The volcanic history of central Elysium Planitia: Implications for Martian magmatism. *Icarus*, 204(2), 418–442. <https://doi.org/10.1016/j.icarus.2009.06.032>
- Vetterlein, J., & Roberts, G. P. (2009). Postdating of flow in Athabasca Valles by faulting of the Cerberus fossae, Elysium Planitia, Mars. *Journal of Geophysical Research*, 114(E7), E07003. <https://doi.org/10.1029/2009je003356>
- Voigt, J. R. C., & Hamilton, C. W. (2018). Investigating the volcanic versus aqueous origin of the surficial deposits in eastern Elysium Planitia, Mars. *Icarus*, 309, 389–410. <https://doi.org/10.1016/j.icarus.2018.03.009>